

**Nanoengineering of the mechanical properties of crystalline calcium-silicate-hydrate
phases via molecular dynamics simulations**

By

Baig Abdullah Al-Muhit

Dissertation

Submitted to the Faculty of the
Graduate School of Vanderbilt University
in partial fulfillment of the requirements
for the degree of

DOCTOR OF PHILOSOPHY

in

Civil Engineering

December 14, 2019

Nashville, Tennessee

Approved:

Florence Sanchez, Ph.D.

Douglas E. Adams, Ph.D.

Prodyot K. Basu, Ph.D.

David S. Kosson, Ph.D.

Norman Tolk, PhD.

Pablo Zavattieri, PhD.

*Dedicated to the Almighty Allah, my aunt, and my wife,
With whom I searched for the silver linings of PhD*

ACKNOWLEDGMENTS

I would like to thank my committee members, Dr. Florence Sanchez, Dr. Douglas Adams, Dr. David Kosson, Dr. Norman Tolk, Dr. Prodyot Basu, and Dr. Pablo Zavattieri for their time and guidance. Dr. Adams and Dr. Kosson serve as the incredible leaders of our department who always showed genuine interest in my research. Dr. Basu taught me how to formulate my theoretical knowledge into mathematical language. Dr. Tolk claimed that his *statistical mechanics* and *quantum mechanics* courses would change my world view, which absolutely did happen. I applied these learnings firsthand in my research and certainly I will use it in the future to come. Finally, I want to thank my PhD adviser and committee chair, Dr. Florence Sanchez, for this amazing opportunity to work on this PhD research project. I graciously want to acknowledge that this research changed the direction of my graduate career. She supported and guided me continuously through the rocky PhD journey. I also want to thank Dr. Suryanarayan at University of Central Florida for his excellent teaching that piqued my interest in the intricacies of materials science. I want to thank my wife, another PhD researcher, whose support through my graduate career was indispensable. My lifelong curiosity and tenacity to creating new knowledge could not have come to fruition without the support structure from my childhood. I want to thank Dr. Lesa Brown for her crucial help and support with my writing.

Finally, I want to thank the National Science Foundation (NSF) under CMMI 1462575 for funding this research. I would like also to thank the U.S Department of Energy funded Consortium for Risk Evaluation with Stakeholder Participation III (CRESP, Cooperative Agreement Number DE-FC01-06EW07053) for providing the computational resources.

Disclaimer: This document was prepared as an account of work sponsored by an Agency of the United States Government. Neither the United States Government nor any agency thereof, nor any of their employees, makes any warranty, express or implied, or assumes any legal liability or responsibility for the accuracy, completeness, or usefulness of any information, apparatus, product, or process disclosed, or represents that its use would not infringe privately owned rights. Reference herein to any specific commercial product, process, or service by trade name, trademark, manufacturer, or otherwise does not necessarily constitute or imply its endorsement, recommendation, or favoring by the United States Government or any agency thereof.

TABLE OF CONTENTS

	Page
DEDICATION	ii
ACKNOWLEDGMENTS	iii
LIST OF TABLES	vii
LIST OF FIGURES	viii
NOMENCLATURE	xxii
Chapter	
1 INTRODUCTION	1
1.1. Overview	1
1.2. Objectives and Approach	2
1.3. Structure of the Dissertation.....	4
2 LITERATURE REVIEW	5
2.1. Overview	5
2.2. Materials modeling with classical molecular dynamics simulation.....	5
2.3. Mechanical properties of single layer graphene sheet.....	8
2.4. Mechanical properties of graphene-reinforced C–S–H nanocomposite.....	9
2.5. Interfacial strength of C–S–H/ graphene nanosheets	12
2.6. Conclusions	14
3 MECHANICAL PROPERTIES OF SINGLE LAYER GRAPHENE SHEET VIA MOLECULAR DYNAMICS SIMULATIONS	16
3.1. Overview	16
3.2. Computational Details.....	18
3.3. Results and Discussion.....	24
3.3.1. Surface topology and internal local stress distribution.....	24
3.3.2. Stress-strain responses	31
3.3.3. Strain energy density	44
3.3.4. Elastic moduli, shear moduli, and linear compressibility.....	47
3.3.5. In-plane Poisson’s ratio	55
3.3.6. Sound wave velocity.....	57
3.4. Conclusions	60
4 MECHANICAL PROPERTIES OF TOBERMORITE/GRAPHENE NANOCOMPOSITES UNDER TENSILE AND SHEAR LOADINGS VIA MOLECULAR DYNAMICS SIMULATIONS	62
4.1. Overview	62
4.2. Computational Details.....	65

4.2.1. Effect of geometric assembly of GS in tobermorite 9 Å (T ₉).....	65
4.2.2. Effect of the surface structure of tobermorite 14 Å (T ₁₄) interfacing with the GS.....	70
4.2.3. Effects of functionalization of FGS on Tobermorite 14 (T ₁₄).....	79
4.3. Results and Discussion.....	85
4.3.1. Effect of geometric assembly of GS in tobermorite 9 Å (T ₉).....	85
4.3.2. Interfacial interactions between GS and Tobermorite 14 Å (T ₁₄) with different interfaces.....	106
4.3.3. Effect of functionalization of GS on Tobermorite 14 Å (T ₁₄).....	136
4.4. Conclusions.....	159
4.4.1. Effect of geometric assembly of GS in tobermorite 9 Å (T ₉).....	159
4.4.2. Effect of the surface structure of tobermorite 14 Å (T ₁₄) interfacing with the GS....	161
4.4.3. Effect of functionalization of GS on tobermorite 14 (T ₁₄).....	162
5 INTERFACIAL MECHANICS OF GRAPHENE BILAYERS WITH NANOCONFINED WATER MONOLAYER.....	164
5.1. Overview.....	164
5.2. Computational Details.....	166
5.2.1. Simulation setup and computational details.....	166
5.2.2. Forcefields.....	168
5.2.3. Equilibration.....	169
5.2.4. Loading methods and simulations.....	170
5.2.5. Data analysis.....	171
5.3. Results and Discussions.....	173
5.3.1. Interfacial strength of GS/FGS bilayer systems.....	173
5.3.2. Interfacial strength of FGS/FGS bilayer systems.....	178
5.3.3. Interfacial strength of GS/FGS bilayer systems with confined water monolayer.....	180
5.3.4. Interfacial strength of FGS/FGS bilayer systems with confined water monolayer...	183
5.3.5. Interaction energy change during normal and shear traction.....	187
5.3.6. Hydrogen bonding characteristics of graphene bilayer interfaces with nanoconfined water monolayer.....	197
5.3.7. Mean squared displacement of the nanoconfined water monolayer in wet interfaces.....	203
5.4. Conclusions.....	209
6 INTERFACIAL MECHANICS OF TOBERMORITE 14 Å/GRAPHENE NANOCOMPOSITE.....	211
6.1. Overview.....	211
6.2. Computational Details.....	213
6.2.1. Simulation models and computational cells.....	213
6.2.2. Force field.....	214
6.2.3. Equilibration.....	215
6.2.4. Traction-separation methods and MD Simulations.....	216
6.2.5. Data collection and analysis.....	217
6.3. Results and Discussion.....	219
6.3.1. Interfacial strength of T ₁₄ /FGS interfaces.....	219

6.3.2. Interaction energy of T ₁₄ /FGS interfaces.....	227
6.3.3. Equilibrium mean squared displacement of the water molecules	228
6.4. Conclusions	232
7 CONCLUSIONS AND FUTURE RESEARCH DIRECTIONS.....	234
REFERENCES	239
Appendix	
A Supplementary materials for Chapter 3	256
B Supplementary materials for Chapter 4.....	277
C Molecular dynamics scripts for Chapter 3	284
D Molecular dynamics scripts for Chapter 4	292
E Molecular dynamics scripts for Chapter 5.....	306
F Molecular dynamics scripts for Chapter 6.....	313

LIST OF TABLES

Table	Page
3.1. Amplitude (maximum height) and wavelength of the initial deformation in functionalized graphene at zero applied strain as a function of –OH coverage for line patterns along the zigzag direction (wavelength along armchair) and line patterns along the armchair direction (wavelength along zigzag).	27
3.2. Poisson’s ratio of GS and FGS for different spatial distribution (random arrangement R, line patterns along zigzag ZZ, and line patterns along armchair AC) and –OH coverage.....	56
3.3. Summary of response behaviors for line pattern arrangements.....	61
4.1. Fracture stress and strain of the T ₉ and T ₉ /GS systems, showing failure of the T ₉ matrix and ultimate fracture of the GS.	89
4.2. Comparison of the tensile and shear strain energy densities of the T ₉ /GS nanolaminates	90
4.3. Bond distances during tensile loading of the T ₉ /GS nanolaminates along the X-direction, shown before loading, at failure of the T ₉ matrix, and at failure of the GS.	92
4.4. Ratio of elastic constants	103
4.5. Strain energy densities of the T ₁₄ systems and T ₁₄ /GS nanocomposites calculated from the tensile (in-plane and out-of-plane) and shear stress-strain responses.	126
4.6. Volume compressibility and bulk moduli for the T ₁₄ systems and T ₁₄ /GS nanocomposites.....	133
4.7. Strain energy densities of T ₁₄ /FGS nanocomposites due to tensile and shear loadings.	155

LIST OF FIGURES

Figure	Page
2.1. Schematic diagram of a generic classical molecular dynamics simulation approach with (a) algorithm and (b) numerical approach to solve Newton's equation of motion.	7
2.2. Models of (a) C–S–H and (b) crystalline analogue of C–S–H, tobermorite 11 Å, comprised of the structural layers are shown (adapted from [115]).	11
2.3. A representative model of the T ₁₄ with defined water, calcium octahedral, and silicate tetrahedral structural layers.	13
3.1. Clustered line pattern arrangements: (a) line patterns along the zigzag (ZZ) direction and (b) line patterns along the armchair (AC) direction. The red and blue balls represent carbon and oxygen atoms, respectively.	23
3.2. Loading modes: (a) uniaxial tension along the zigzag (ZZ) direction, (b) uniaxial tension along the armchair (AC) direction, and (c) shear deformation along the zigzag (ZZ) direction.	24
3.3. Graphene sheet with hydroxyl functionalization after relaxation to equilibrium at zero applied strain (unstrained conditions) exhibiting a change toward a monoclastic surface (cylindrical configuration). Shown for 25% hydroxyl functionalization: (a) random arrangement, (b) –OH line patterns oriented along the zigzag direction, and (c) –OH line patterns oriented along the armchair direction. The red, blue, and yellow balls represent carbon, oxygen, and hydrogen atoms, respectively.	26
3.4. Graphene sheet with 100% hydroxyl functionalization after relaxation to equilibrium at zero applied strain (unstrained conditions) exhibiting an anticlastic surface (saddle-shaped configuration). The red, blue, and yellow balls represent carbon, oxygen, and hydrogen atoms, respectively.	27
3.5. Internal local stress distribution (component of the stress parallel to the load) during tensile loading along the armchair (AC) direction in the graphene sheet with 50% hydroxyl functionalization arranged in a clustered in-line pattern along the zigzag direction (⊥, perpendicular to the tensile loading direction): (a) after	

	relaxation to equilibrium before tensile loading (unstrained conditions); and (b), (c), (d), and (e) as a function of increasing tensile strain, showing stages of slow increasing stress (de-wrinkling and loss of curvature), fast increasing stress (elongation), before fracture (maximum bond elongation), and fracture (release of stress concentration), respectively.	28
3.6.	Internal local stress distribution (component parallel to the load) during tensile loading along the zigzag (ZZ) direction in the graphene sheet with 50% hydroxyl functionalization arranged in an in-line pattern along the armchair direction (\perp , perpendicular to the tensile loading direction): (a) after relaxation to equilibrium before tensile loading (unstrained conditions) leading to initial bending deformation; and (b), (c), (d), and (e) as a function of increasing tensile strain, showing stages of slowly increasing stress (de-wrinkling and loss of curvature), rapidly increasing stress (elongation), before fracture (maximum bond elongation), and at fracture (release of stress concentration), respectively.	29
3.7.	Internal local stress distribution (component of the stress parallel to the load) during tensile loading along the zigzag direction in the graphene sheet with 50% hydroxyl coverage in random arrangement: (a) after relaxation to equilibrium before tensile loading (unstrained conditions), (b) and (c) as a function of increasing tensile strain, and (d) at fracture.	30
3.8.	Internal local stress distribution (component of the stress parallel to the load) during tensile loading along the zigzag (ZZ) direction in the graphene sheet with 50% hydroxyl coverage arranged in an in-line pattern along the ZZ-direction (\parallel , parallel to the tensile loading direction): (a) after relaxation to equilibrium before tensile loading (unstrained conditions), and (b), (c), and (d) as a function of increasing tensile strain, showing stages of rapidly increasing stress (elongation) and fracture.	31
3.9.	Stress-strain response for graphene sheets (GS) under tensile loading along the zigzag direction [(a), (c), and (e)] and tensile loading along the armchair direction [(b), (d), and (f)] as a function of –OH surface coverage (0, 12, 25, 50, 75, and 100%) and spatial distribution (random and in-line pattern arrangements along the zigzag and armchair directions). [R: random; ZZ: line patterns along zigzag; AC: line patterns along armchair].	35
3.10.	Tensile fracture stress and strain as a function of tensile loading direction and –OH surface coverage. (a) fracture stress and strain for tensile loading along the zigzag direction and (b) fracture stress and strain for tensile loading along the	

armchair direction. [R: random; ZZ: line patterns along zigzag; AC: line patterns along armchair].	36
3.11. Shear stress-strain evolution for graphene sheets under shear deformation along the zigzag direction as a function of hydroxyl coverage (0, 12, 25, 50, 75, and 100%) for (a) random distribution, (b) line pattern arrangements along the zigzag direction, and (c) line pattern arrangements along the armchair direction.	38
3.12. Development of wrinkles in the pristine graphene sheet as a function of strain up to fracture during shear deformation along the zigzag direction.	39
3.13. (a) Shear fracture stress and (b) shear fracture strain of graphene systems as a function of –OH surface coverage for different spatial distributions. [R: random; ZZ: line patterns along zigzag; AC: line patterns along armchair].....	40
3.14. Energy changes as a function of strain for tensile loading along the zigzag (ZZ) direction: (a), (b) potential energy (per atom on average); (c), (d) bond-stretching energy; (e), (f) angle-bending energy; and (g), (h) torsional energy (dihedral angles) for line patterns along the zigzag and armchair directions, respectively.	42
3.15. Energy changes as a function of strain for shear loading along the zigzag (ZZ) direction: (a), (b) potential energy (per atom on average); (c), (d) bond-stretching energy; (e), (f) angle-bending energy; and (g), (h) torsional energy (dihedral angles) for line patterns along the zigzag and armchair directions, respectively.	43
3.16. Strain energy density of the FGS systems for (a) tensile strain in zigzag direction, (b) tensile strain in armchair direction, and (c) shear strain in zigzag direction.....	46
3.17. Directional elastic modulus ($N\ m^{-1}$) for (a) random –OH arrangement (R), (b) –OH line patterns along the zigzag direction (ZZ), and (c) –OH line patterns along the armchair direction (AC).	49
3.18. Elastic moduli for applied tensile load in zigzag (E_{11}) and armchair (E_{22}) directions for (a) random –OH arrangement (R), (b) –OH line patterns along the zigzag direction (ZZ), and (c) –OH line patterns along the armchair direction (AC). Elastic moduli shown also for the toe region for the perpendicular cases. (d) Shear moduli (G_{12}) for applied load in zigzag direction.	50

3.19.	Directional shear modulus (N m^{-1}) for (a) random –OH arrangement (R), (b) –OH line patterns along the zigzag direction (ZZ), and (c) –OH line patterns along the armchair direction (AC).....	52
3.20.	Linear compressibility (β , m N^{-1}) as a function of –OH percentages for (a) random arrangement, (b) line patterns along the zigzag direction (ZZ), and (c) line patterns along the armchair direction (AC).	54
3.21.	Internal local stress distribution in the graphene sheet with 75% hydroxyl functionalization in clustered line patterns along the zigzag direction, showing (a) unstrained condition, (b) elongation along the armchair direction at low tensile strain along the zigzag direction, and (c) no elongation nor contraction along the armchair direction at high tensile strain along the zigzag direction.	57
3.22.	Longitudinal sound wave velocities through the GS and FGS for waves traveling along (a) the zigzag direction and (b) the armchair direction of the graphene lattice. [R: random; ZZ: line patterns along zigzag; AC: line patterns along armchair].	59
4.1.	Tobermorite 9 Å (T_9) structure in (a) X- and (b) Y-directions, and (c) structural layers of T_9 in the X-, Y-, and Z-directions.	67
4.2.	Structures of T_9 /GS nanolaminates, (a) T_9 , (b) 3 layers of GS inserted in a hierarchical alternate arrangement in the T_9 matrix, (c) a 3-layer GS stacked in the middle of the T_9 matrix, (e) a planar representation of graphene sheet, GS.....	68
4.3.	(a) and (b) Layered crystal structure of tobermorite 14 Å (T_{14}). (c) Silicate tetrahedra chain along the X-, Y-, and Z-directions [for clarity, structures are shown without water molecules in (b) and (c)].	73
4.4.	(a) Graphene sheet (GS) and (b) monoclinic supercell of tobermorite 14 Å with the exposed water layer surface ($T_{14}^{\text{O}w}$ supercell).	74
4.5.	Models of T_{14} /GS nanocomposites: (a) nanocomposite with the GS interfacing with the bottom surface water at the $(0\ 0\ \bar{1})$ plane of the T_{14} structure ($T_{14}^{\text{O}w}$ /GS nanocomposite), (b) nanocomposite with the GS interfacing with the octahedral calcium layer at the $(0\ 0\ 1)$ plane ($T_{14}^{\text{Ca}o}$ /GS nanocomposite), and (c)	

	nanocomposite with the GS interfacing with the tetrahedral silicate layer at the (0 0 1) plane ($T_{14}^{Si_t}$ /GS nanocomposite).....	75
4.6.	The model of the T_{14} structure nanocomposite showing the three structural layers responsible for building the structural skeleton of T_{14}	80
4.7.	Representative models of the T_{14} /FGS nanocomposite (a) FGS with 25% –OH with random pattern and (b) FGS with 25% –OH with zigzag clustered line pattern of –OH.	81
4.8.	Tensile and shear stress-strain response of the pristine T_9 and T_9 /GS nanolaminate systems, (a) tensile loading along X, (b) tensile loading along Y, (c) shear loading along X.....	88
4.9.	Deformation of the structural layers and fracture mechanisms of T_9 and T_9 /GS systems in the X-direction: (a) T_9 matrix, (b) T_9 /GS ^{3H} nanolaminate, (c) T_9 /GS ^{3S} nanolaminate.	93
4.10.	Detailed deformation process of pristine the T_9 matrix in the X-direction at different strains: (a) equilibrium (strain 0.0), (b) matrix failure (0.125), (c) GS fracture strain (0.25), (d) strain (0.50) at full separation.	94
4.11.	Detailed deformation process of the hierarchical T_9 /GS ^{3H} nanolaminate in the X-direction at different strains: (a) equilibrium (strain 0.0), (b) matrix failure (0.13), (c) GS fracture strain (0.175), (d) final strain (0.50) at full separation.....	95
4.12.	Detailed deformation process of the stacked T_9 /GS ^{3S} nanolaminate in the X-direction at different strains: (a) equilibrium (strain 0.0), (b) matrix failure (0.125), (c) GS fracture strain (0.17), (d) final strain (0.50) at full separation.....	96
4.13.	Deformation of the structural layers and fracture mechanisms of the T_9 and T_9 /GS systems in the Y-direction: (a) T_9 matrix, (b) hierarchical T_9 /GS ^{3H} nanolaminate, (c) stacked T_9 /GS ^{3S} nanolaminate.....	97

4.14.	Detailed deformation process of the pristine T ₉ matrix in the Y-direction at different strains: (a) equilibrium (strain 0.0), (b) matrix failure (0.125), (c) fracture strain (0.25), (d) final strain (0.50) at full separation.	98
4.15.	Detailed deformation process of the pristine T ₉ /GS ^{3H} matrix in the Y-direction at different strains: (a) equilibrium (strain 0.0), (b) matrix failure (0.125), (c) fracture strain (0.25), (d) final strain (0.50) at full separation.	99
4.16.	Detailed deformation process of the pristine T ₉ /GS ^{3S} matrix in the Y-direction at different strains: (a) equilibrium (strain 0.0), (b) matrix failure (0.125), (c) fracture strain (0.25), (d) final strain (0.50) at full separation.	100
4.17.	Comparisons of elastic constants of the T ₉ and T ₉ /GS systems, (a) normal constants, (b) shear constants, and (c) normal coupling constants.	102
4.18.	3D representations of directional anisotropy of elastic modulus for T ₉ and T ₉ /GS systems: (a) T ₉ matrix, (b) hierarchical T ₉ /GS ^{3H} nanolaminate, (c) stacked T ₉ /GS ^{3S} nanolaminate.	104
4.19.	2D representations of directional anisotropy of (a) linear compressibility and (b) elastic modulus of the T ₉ /GS nanolaminates projected on the XY plane, i.e., plane of the GS.	105
4.20.	Stress-strain response under in-plane tensile loading: (a) and (b) stretching along the X-direction of T ₁₄ systems and T ₁₄ /GS nanocomposites, respectively and (c) and (d) stretching along the Y-direction of T ₁₄ systems and T ₁₄ /GS nanocomposites, respectively. [T ₁₄ ^{O_w} : T ₁₄ structure with exposed water layer surface; T ₁₄ ^{Ca_o} : T ₁₄ structure with exposed octahedral calcium surface; T ₁₄ ^{Si_t} : T ₁₄ structure with exposed tetrahedral silicate surface; T ₁₄ ^{O_w} /GS: GS interfacing with the bottom surface water of T ₁₄ ; T ₁₄ ^{Ca_o} /GS: GS interfacing with the octahedral calcium layer of T ₁₄ ; T ₁₄ ^{Si_t} /GS: GS interfacing with the tetrahedral silicate layer of T ₁₄]	110
4.21.	Failure stages of the nanocomposite with the GS interfacing with the bottom surface water of the tobermorite 14 Å (T ₁₄ ^{O_w} /GS nanocomposite) during in-plane tensile loading along the X-direction: (a) after relaxation to equilibrium but before tensile loading (unstrained conditions); (b) at failure of the tobermorite 14 Å (T ₁₄)	

matrix; (c) at fracture of the graphene sheet (GS); and (d) after separation of the structural layers. For clarity, structures in insets are shown without water molecules.	111
4.22. Failure stages of the nanocomposite with the GS interfacing with the bottom surface water of the tobermorite 14 Å ($T_{14}^{O_w}$ /GS nanocomposite) during in-plane tensile loading along the Y-direction: (a) after relaxation to equilibrium but before tensile loading (unstrained conditions); (b) at failure of the tobermorite 14 Å (T_{14}) matrix; (c) at fracture of the graphene sheet (GS); and (d) after separation of the structural layers. For clarity, structures in insets are shown without water molecules.	112
4.23. Evolution of tetrahedral silica–oxygen bond length and carbon–carbon bond length during in-plane tensile loading of the nanocomposite with the GS interfacing with the bottom surface water of the tobermorite 14 Å ($T_{14}^{O_w}$ /GS nanocomposite): (a), (b) Si _r –O bond length and C–C bond length, respectively during stretching along the X-direction and (c), (d) Si _r –O _b bond length and C–C bond length, respectively during stretching along the Y-direction.....	113
4.24. Evolution of the number of broken tetrahedral silicon–oxygen bonds in the pristine T_{14} systems and T_{14} /GS nanocomposites as function of applied strain: (a), (b) during stretching of the pristine T_{14} systems along the X- and Y-directions, respectively and (c), (d) during stretching of the T_{14} /GS nanocomposites along the X- and Y-directions. [$T_{14}^{O_w}$: T_{14} structure with exposed water layer surface; $T_{14}^{Ca_o}$: T_{14} structure with exposed octahedral calcium surface; $T_{14}^{Si_t}$: T_{14} structure with exposed tetrahedral silicate surface; $T_{14}^{O_w}$ /GS: GS interfacing with the bottom surface water of T_{14} ; $T_{14}^{Ca_o}$ /GS: GS interfacing with the octahedral calcium layer of T_{14} ; $T_{14}^{Si_t}$ /GS: GS interfacing with the tetrahedral silicate layer of T_{14}]	114
4.25. Local stress distribution at the graphene sheet (GS) surface before fracture of the GS during tensile loading: (a), (b), and (c) X-direction stretching of the GS reinforced tobermorite 14 Å nanocomposites; and (e), (f), and (g) Y-direction stretching of the GS reinforced tobermorite 14 Å nanocomposites. [$T_{14}^{O_w}$ /GS: GS interfacing with the bottom surface water of T_{14} ; $T_{14}^{Ca_o}$ /GS: GS interfacing with the octahedral calcium layer of T_{14} ; $T_{14}^{Si_t}$ /GS: GS interfacing with the tetrahedral silicate layer of T_{14}]	115

- 4.26. Stress-strain response for out-of-plane (Z-direction) tensile loading of (a) T₁₄ systems and (b) T₁₄/GS nanocomposites. [T₁₄^{O_w} : T₁₄ structure with exposed water layer surface; T₁₄^{Ca_o} : T₁₄ structure with exposed octahedral calcium surface; T₁₄^{Si_t} : T₁₄ structure with exposed tetrahedral silicate surface; T₁₄^{O_w} /GS: GS interfacing with the bottom surface water of T₁₄; T₁₄^{Ca_o} /GS: GS interfacing with the octahedral calcium layer of T₁₄; T₁₄^{Si_t} /GS: GS interfacing with the tetrahedral silicate layer of T₁₄] 119
- 4.27. Separation stage of T₁₄ systems and T₁₄/GS nanocomposites during out-of-plane tensile loading along the Z-direction: (a) T₁₄ structure with exposed water surface (T₁₄^{O_w}); (b) T₁₄ structure with exposed octahedral calcium surface (T₁₄^{Ca_o}); (c) T₁₄ structure with exposed tetrahedral silicate surface (T₁₄^{Si_t}); (d) nanocomposite with the GS interfacing with the bottom surface water of T₁₄ (T₁₄^{O_w} /GS); (e) nanocomposite with the GS interfacing with the octahedral calcium layer of T₁₄ (T₁₄^{Ca_o} /GS); and (f) nanocomposite with the GS interfacing with the tetrahedral silicate layer of T₁₄ (T₁₄^{Si_t} /GS). 120
- 4.28. Evolution of the number of broken Ca_w-O_{bts} bonds as a function of applied strain during out-of-plane (Z-direction) tensile loading of (a) the T₁₄ systems and (b) the T₁₄/GS nanocomposites. [T₁₄^{O_w} : T₁₄ structure with exposed water layer surface; T₁₄^{Ca_o} : T₁₄ structure with exposed octahedral calcium surface; T₁₄^{Si_t} : T₁₄ structure with exposed tetrahedral silicate surface; T₁₄^{O_w} /GS: GS interfacing with the bottom surface water of T₁₄; T₁₄^{Ca_o} /GS: GS interfacing with the octahedral calcium layer of T₁₄; T₁₄^{Si_t} /GS: GS interfacing with the tetrahedral silicate layer of T₁₄] 121
- 4.29. Shear stress-strain evolution of the (a) T₁₄ systems and (b) T₁₄/GS nanocomposites under shear loading along the X-direction. [T₁₄^{O_w} : T₁₄ structure with exposed water layer surface; T₁₄^{Ca_o} : T₁₄ structure with exposed octahedral calcium surface; T₁₄^{Si_t} : T₁₄ structure with exposed tetrahedral silicate surface; T₁₄^{O_w} /GS: GS interfacing with the bottom surface water of T₁₄; T₁₄^{Ca_o} /GS: GS interfacing with the octahedral calcium layer of T₁₄; T₁₄^{Si_t} /GS: GS interfacing with the tetrahedral silicate layer of T₁₄] 123

- 4.30. Energy of interaction between the tobermorite 14 Å (T_{14}) structures and the graphene sheet (GS) as a function of strain during shear loading along the X-direction. [$T_{14}^{O_w}$ /GS: GS interfacing with the bottom surface water of T_{14} ; $T_{14}^{Ca_o}$ /GS: GS interfacing with the octahedral calcium layer of T_{14} ; $T_{14}^{Si_t}$ /GS: GS interfacing with the tetrahedral silicate layer of T_{14}] 124
- 4.31. 2D plots of the directional in-plane elastic modulus: (a) intrinsic elastic modulus of the T_{14} systems, (b) intrinsic elastic modulus of the T_{14} /GS nanocomposites, and (c) effective (elastic loading stage) elastic modulus of the T_{14} /GS nanocomposites. [$T_{14}^{O_w}$: T_{14} structure with exposed water layer surface; $T_{14}^{Ca_o}$: T_{14} structure with exposed octahedral calcium surface; $T_{14}^{Si_t}$: T_{14} structure with exposed tetrahedral silicate surface; $T_{14}^{O_w}$ /GS: GS interfacing with the bottom surface water of T_{14} ; $T_{14}^{Ca_o}$ /GS: GS interfacing with the octahedral calcium layer of T_{14} ; $T_{14}^{Si_t}$ /GS: GS interfacing with the tetrahedral silicate layer of T_{14}] 129
- 4.32. 3D plots of the directional intrinsic elastic modulus of (a), (c), and (e) tobermorite 14 Å (T_{14}) systems with the exposed water layer ($T_{14}^{O_w}$), octahedral calcium ($T_{14}^{Ca_o}$), and tetrahedral silicate surfaces ($T_{14}^{Si_t}$), respectively and (b), (d), and (f) graphene sheet (GS) reinforced tobermorite 14 Å nanocomposites with the GS interfacing with the bottom surface water of T_{14} ($T_{14}^{O_w}$ /GS), octahedral calcium layer ($T_{14}^{Ca_o}$ /GS), and tetrahedral silicate layer ($T_{14}^{Si_t}$ /GS), respectively..... 130
- 4.33. Shear modulus for applied load in the XY plane along the X-direction for the T_{14} systems and T_{14} /GS nanocomposites. [$T_{14}^{O_w}$: T_{14} structure with exposed water layer surface; $T_{14}^{Ca_o}$: T_{14} structure with exposed octahedral calcium surface; $T_{14}^{Si_t}$: T_{14} structure with exposed tetrahedral silicate surface; $T_{14}^{O_w}$ /GS: GS interfacing with the bottom surface water of T_{14} ; $T_{14}^{Ca_o}$ /GS: GS interfacing with the octahedral calcium layer of T_{14} ; $T_{14}^{Si_t}$ /GS: GS interfacing with the tetrahedral silicate layer of T_{14}] 131
- 4.34. 2D plots of the directional linear compressibility: (a) intrinsic linear compressibility of the T_{14} systems, (b) intrinsic linear compressibility of the T_{14} /GS nanocomposites, and (c) effective (elastic loading stage) linear compressibility of the T_{14} /GS nanocomposites. [$T_{14}^{O_w}$: T_{14} structure with exposed

water layer surface; $T_{14}^{Ca_o}$: T_{14} structure with exposed octahedral calcium surface; $T_{14}^{Si_t}$: T_{14} structure with exposed tetrahedral silicate surface; $T_{14}^{O_w}$ /GS: GS interfacing with the bottom surface water of T_{14} ; $T_{14}^{Ca_o}$ /GS: GS interfacing with the octahedral calcium layer of T_{14} ; $T_{14}^{Si_t}$ /GS: GS interfacing with the tetrahedral silicate layer of T_{14}]	135
4.35. Tensile stress-strain responses of the T_{14} /FGS nanocomposites under tensile loadings in the X- and Y-directions shown in (a) and (b) for random arrangements of –OH, and (c) and (d) for ZZ clustered line patterns of –OH.	140
4.36. One dimensional (1D) density profile of interlayer water and structural water as a function of Z-direction for (a) and (b) random arrangement of –OH, and (c) and (d) ZZ clustered line patterns of –OH.	141
4.37. Two-dimensional (2D) density profiles of interlayer and structural water molecules of T_{14} /FGS nanocomposites on the XY plane for (a) and (c) random arrangement of –OH, and (b) and (d) ZZ clustered line patterns of –OH.	142
4.38. One dimensional (1D) density profiles of interlayer calcium cations (Ca_w) of the T_{14} /FGS nanocomposites on the XY plane for (a) random arrangement of –OH, and (b) ZZ clustered line patterns of –OH.	143
4.39. Mean squared displacement of interlayer water molecules with (a) random arrangement of –OH and (b) ZZ clustered line patterns of –OH.	145
4.40. Tensile stress-strain responses for the T_{14} /FGS nanocomposites in the out-of- plane direction (Z-direction) with varying –OH surface coverage (%) for (a) random clustered –OH and (b) ZZ line clustered –OH.	147
4.41. Fracture mechanisms of the T_{14} /FGS nanocomposites attached with random arrangements of –OH with varying surface coverages.	148
4.42. Fracture mechanisms of the T_{14} /FGS nanocomposites attached with ZZ clustered line patterns of –OH with varying surface coverages.	149

4.43.	The number of broken Si–O bonds for T ₁₄ /FGS nanocomposites along the Z-directions with (a) random arrangements of –OH and (b) ZZ clustered line patterns of –OH.....	150
4.44.	Shear Stress- shear strain responses of T ₁₄ /FGS nanocomposites (a) for random FGS and (b) for ZZ-oriented FGS.	151
4.45.	3D representation of the directional anisotropy of elastic modulus for T ₁₄ /FGS nanocomposites with the varying surface coverages and ZZ clustered line pattern of –OH.	157
4.46.	2D representation of the directional anisotropy of elastic modulus for T ₁₄ /FGS nanocomposites with different surface coverages and clustered line patterns.	159
5.1.	Bilayer graphene interface models with and without nanoconfined water monolayer. Dry bilayer interfaces: (a) graphene/functionalized graphene (GS/FGS) and (b) functionalized graphene/functionalized graphene (FGS/FGS). Wet bilayer interfaces: (c) graphene/water/functionalized graphene (GS/Ow/FGS), and (f) functionalized graphene/water/functionalized graphene (FGS/Ow/FGS), where Ow represents the oxygen of the water monolayer. Bilayer systems shown for 2% -OH functionalization with random arrangement.....	168
5.2.	The traction-separation modes of the bilayer systems: (a) the normal separation along the Z-direction and (b) the shear separation along the X- and Y-directions of the bilayer systems.....	171
5.3.	Traction-separation responses of the GS/FGS bilayer systems with varying degrees of –OH (%) coverages undergoing: (a) normal separation in the negative Z-direction (with 2 Å thick atom layers on both ends of the FGS layer pulling downwards), (2) shear separation in the positive X-direction (with a 2 Å thick atom layer on right end of the FGS layer pulling in X-direction), and (3) shear separation in the positive Y-direction (with a 2 Å thick atom layer on right end of the FGS layer pulling in Y-direction). The top sheets were held fixed in space for all bilayer systems.....	177
5.4.	Traction-separation responses for the FGS/FGS bilayer with varying degrees of –OH contents, undergoing (a) normal separation in negative Z-direction (with 2 Å thick atom layers on both ends of the FGS layer pulling downwards), (2) shear separation in the positive X-direction (with a 2 Å thick atom layer on right end of the FGS layer pulling in X), and (3) shear separation in the positive Y-direction	

	(with a 2 Å thick atom layer on right end of the FGS layer pulling in Y). The top FGS were kept fixed in space for all the bilayer systems.	179
5.5.	Traction-separation response of the GS/FGS bilayer systems with varying degrees of –OH coverage (0, 2, 6, 10, and 12%) and monolayer of water (O_w) sandwiched between the GS and FGS (GS/ O_w /FGS): (a) bottom FGS pulled in the positive X-direction and (b) bottom FGS pulled in the positive Y-direction.	182
5.6.	Traction-separation response of the FGS/FGS bilayers with varying degrees of –OH coverage (0, 2, 6, 10, and 12%) and monolayer of water (O_w) sandwiched between two layers of FGS (FGS/ O_w /FGS): (a) bottom FGS pulled in the positive X-direction and (b) bottom FGS pulled in the positive Y-direction.	183
5.7.	Representation of the separation behavior of the GS/FGS bilayer system with water monolayer between the two graphene layers at different displacements for shear in X-direction (shown for 10%–OH content).	185
5.8.	Representation of separation behavior of FGS/FGS interface with mediating water monolayer between two FGS sheets with 10% –OH content at different displacements for shear in X-direction.	186
5.9.	Interaction energy plots (vdW) for the normal traction-separation of (a) GS/FGS bilayer systems and (b) FGS/FGS bilayer systems without water monolayer.	191
5.10.	Interaction energy plots (vdW) for the (a), (b) shear traction-separation behaviors for the GS/FGS interfaces along X and Y, and (c), (d) shear traction separation behaviors in FGS/FGS interfaces along X and Y without the mediating water monolayer.	192
5.11.	Superposition of the shear traction force and the interaction energy plots for the FGS/FGS bilayer systems (a) 2% (b) 6%, (c) 10%, and (d) 12% –OH coverage during shear separation along the X-direction.	193
5.12.	Interaction energy plots for the (a) shear traction-separation for the GS/FGS bilayer systems with water monolayer in the X-direction, (b) shear traction-separation in the X-direction for the FGS/FGS bilayer systems with water monolayer, (d) shear traction-separation in the Y-direction for the FGS/FGS bilayer systems with water monolayer.	196

5.13.	Time evolution of total number of H-bonds with breakdown with different interactions of H-bond for (a) water-water interactions, (b) donor –OH and acceptor water interactions, (c) donor water and acceptor –OH, and (d) donor and acceptor –OH for the GS/O _w /FGS bilayer.	200
5.14.	Time evolution of the total number of H-bonds with breakdown of the different interactions of H-bonds: (a) water-water interactions, (b) donor –OH and acceptor water interactions, (c) donor water and acceptor –OH, and (d) donor and acceptor –OH for the FGS/O _w /FGS bilayer.....	201
5.15.	Time evolution of the total number of H-bonds with (a) donor and acceptor –OH group interactions between the opposite sheet and (b) donor and acceptor –OH group interactions from the same sheet of the FGS/O _w /FGS bilayer.....	202
5.16.	MSD plots of graphene bilayer systems with monolayer of water at equilibrium (zero shear separation) in X-direction for: (a) GS/O _w /FGS systems and (b) FGS/O _w /FGS systems.	205
5.17.	MSD plots of graphene bilayer systems with monolayer of water during shear separation in the X-direction. Total MSD, X-component of MSD, and Y-component of MSD, respectively for: (a), (c), and (e) GS/O _w /FGS systems and (b), (d), and (f) FGS/O _w /FGS systems.	206
6.1.	Tobermorite 14 Å with the (0 0 $\bar{1}$) interface near (a) GS system and (b) FGS system.	214
6.2.	A representative T ₁₄ /FGS nanocomposite with 10 % –OH coverage of FGS was shown for, (a) normal traction-separation and (b) shear traction-separation loading methods.	217
6.3.	Normal traction-separation behavior of the water-rich (0 0 $\bar{1}$) planes of T ₁₄ and FGS with varying –OH coverages (%).	221
6.4.	Atomistic mechanisms at the T ₁₄ /FGS interfaces for the T ₁₄ /FGS nanocomposites with 10% –OH during the normal traction-separation process, (a) at equilibrium, (b) at the hardening regime, (c) at the beginning of the softening regime, and (d) near the end of the softening regime.	222

6.5.	Shear traction-separation behavior of the T ₁₄ /FGS with varying degrees surface coverages of –OH (%) for, (a) along X-directions and (b) along Y-directions.	225
6.6.	Atomistic mechanisms at the T ₁₄ /FGS interfaces for the T ₁₄ /FGS nanocomposites with 10% –OH during the shear traction-separation process, (a) at equilibrium, (b) within the stability regime, (c) near the end of the stability regime, and (d) near the end of the softening regime.....	226
6.7.	Interaction energy between the T ₁₄ /FGS interfaces for, (a) normal traction-separation in the Z-direction and (b) shear traction-separation in the X-direction.....	228
6.8.	Mean squared displacement (MSD) of water molecules in the T ₁₄ /FGS systems: (a) structural water (O _w) and (b) interlayer water (O _{wd}).	230
6.9.	Mean squared displacement (MSD) of interlayer water molecules (O _{wd}) of the T ₁₄ /FGS systems in the X-, Y-, and Z-directions for, (a) 0% –OH (T ₁₄ /GS), (b) 2% –OH, (c) 6% –OH, and (d) 10% –OH.	231
6.10.	Mean squared displacement (MSD) of structural water molecules (O _w) of the T ₁₄ /FGS systems in the X-, Y-, and Z-directions for, (a) 0% –OH i.e., T ₁₄ /GS, (b) 2% –OH, (c) 6% –OH, and (d) 10% –OH.	232

NOMENCLATURE

AC	Armchair
GS/FGS	Bilayer system composed of a GS and an FGS
GS/O _w /FGS	Bilayer system composed of a GS and an FGS with a water monolayer nanoconfined between the two sheets
κ	Bulk modulus
C–S–H	Calcium silicate hydrate
E	Elastic modulus
FGS	Functionalized graphene sheet
GS	Graphene sheet
G _{xy}	In-plane shear modulus
β_L	Linear compressibility
MSD	Mean squared displacement
MD	Molecular dynamics
T ₁₄ /FGS	Nanocomposite constructed from tobermorite 14 Å and functionalized graphene sheet
T ₉ /GS	Nanolaminate constructed from tobermorite 9 Å and graphene sheet
T ₉ ^{3S} /GS	Nanolaminate constructed from tobermorite 9 Å and three graphene sheet organized in stacked (S) formation
T ₉ ^{3H} /GS	Nanolaminate constructed from tobermorite 9 Å and three graphene sheet organized in alternating hierarchical (H) formation
γ	Shear strain
τ	Shear stress
ε	Tensile strain during stretching
σ	Tensile stress during stretching
T ₁₄	Tobermorite 14 Å
T ₁₄ ^{Ca_o}	Tobermorite 14 Å structure cleaved at the calcium octahedra interface
T ₁₄ ^{Si_t}	Tobermorite 14 Å structure cleaved at the silicate tetrahedra interface
T ₁₄ ^{O_w}	Tobermorite 14 Å structure cleaved at the water interface
T ₉	Tobermorite 9 Å
β_V	Volume compressibility
ZZ	Zigzag

CHAPTER 1

INTRODUCTION

1.1. Overview

Cement is the most widely used construction material in the world because of its simple production process, cost effectiveness, and excellent mechanical properties [1]. Despite its ubiquitous usage as a structural material, hydrated cement is weak in tension compared to compression. Calcium-silicate-hydrate (C–S–H), the primary hydration product of cement, is responsible for the strength and also the weakness of hydrated cement. The inherent weakness of C–S–H comes from its layered structure at the nanoscale, which is strong in the in-plane directions, and weak in the out-of-plane direction [2-6]. As cracks originate at the nanoscale and propagate through the different length scales to the macroscale, the inherent tensile capacity of C–S–H diminishes very quickly. This low tensile strength of C–S–H could be overcome by nano-engineering C–S–H using 2D nanomaterials.

One of the best 2D materials known to science is single layer graphene sheet (GS), which possesses remarkable mechanical properties e.g., in-plane tensile strength and stiffness [7-10] as well as electronic, optical, chemical, and magnetic properties [11-15]. Despite its fascinating in-plane mechanical properties (due to the in-plane carbon-carbon covalent bonds), GS has an intrinsic low out-of-plane strength (due to low van-der-Waals force) [16-18] and cannot provide any out-of-plane strength when used in the composites [19]. In contrast, there are numerous evidences that the use of oxygen containing functional groups on the GS basal plane (making it functionalized graphene sheet, FGS) can modulate and enhance the mechanical properties of the polymer composites [19-27]. However, the effect of FGS on the mechanical properties of the nanoscale C–S–H are scarce in the literature. One of the reasons for the scarcity of mechanical properties of the C–S–H/FGS nanocomposites is the difficulty of achieving reliable experimental results. To overcome the difficulty in experimental observations, the molecular dynamics (MD) simulation approach could be a viable alternative. The MD simulations can realistically model and capture the atomic scale intricacies of the physics of the systems and predict the behavior of the system from a bottom-up approach.

As the structural layers of C–S–H are divided into an interlayer (water-rich and calcium cation-rich) region, calcium octahedral layers, and silicate tetrahedral layers, the interaction of C–S–H with the FGS also depends on the interaction between these interfaces with the FGS. Therefore, the modulation of surface chemistry of the C–S–H and FGS is a promising avenue to achieve desired mechanical properties of the C–S–H/FGS nanocomposites. As the arrangement of the nanoconfined water in the C–S–H are very different in the interlayer than in the bulk, the interaction between water and the –OH groups of the FGS has been shown to play an important role in controlling the mechanical properties of the entire nanocomposite [28-33].

In addition to the modulation of the surface chemistry of C–S–H and FGS, the mechanical properties of FGS reinforced C–S–H nanocomposites can be tailored by geometrical manipulations such as nanolaminated formation of GS in the C–S–H matrix [34-38]. However, the mechanical properties and the underlying strengthening mechanisms of C–S–H/GS nanolaminates have not been investigated in the literature.

The goal of the proposed research is to investigate the effects of the coverage (%) of the –OH functionalization on the graphene basal plane, clustered line patterns arrangement of the –OH functionalization, and loading directions on the mechanical properties of crystalline C–S–H (tobermorite 9 Å and 14 Å) nanocomposites. FGS has the potential to modulate the strength, stiffness, toughness, and compressibility of tobermorite-based nanostructures. The –OH groups enhance the interfacial strength between the interfaces. The structural and dynamic properties of the atoms upon loading will be examined because these properties control the failure mechanisms of the nanocomposites upon loading. In addition, the traction-separation behavior (interfacial strength with respect to displacement) between the T₁₄ and FGS interfaces with varying –OH coverages, and clustered line patterns will be investigated. Structural and dynamic properties of the interfacial atoms will also be investigated.

1.2. Objectives and Approach

The goal of the research was to nanoengineer the mutually exclusive mechanical properties (strength, toughness, stiffness, and compressibility) of tobermorite/graphene nanocomposites, and thereby, to understand the underlying mechanisms that contributed to the variations in these properties. The variations in the surface chemistry of tobermorite (three

different surfaces), geometric assembly of tobermorite with the inclusion of GS, and surface chemistry of functionalized graphene ($-OH$ coverage, $-OH$ clustered line pattern) were investigated. The specific objectives of the research are as follows:

Objective 1: Investigate the mechanical properties of single layered functionalized graphene sheets via molecular dynamics simulations

Objective 2: Investigate the mechanical properties of tobermorite/graphene nanocomposites under tensile and shear loading conditions via molecular dynamics simulations

Sub-objective 2.1: *Tailor the mechanical properties of tobermorite 9 Å/graphene nanocomposite by geometrical manipulations*

Sub-objective 2.2: *Determine the effect of the surface structure of tobermorite interfacing with graphene on the mechanical properties of tobermorite 14 Å/graphene nanocomposites*

Sub-objective 2.3: *Tailor the mechanical properties of tobermorite 14 Å/graphene nanocomposite via hydroxyl functionalization of graphene*

Objective 3: Investigate the interfacial interaction properties of tobermorite 14 Å/graphene nanocomposite under normal and shear traction separation via molecular dynamics simulations

Sub-objective 3.1. *Investigate the interfacial interactions of functionalized graphene bilayer systems with and without water monolayer*

Sub-objective 3.2. *Investigate the interfacial strength of tobermorite 14 Å with functionalized graphene*

Molecular dynamics (MD) simulations were used to investigate the mechanical properties of graphene reinforced tobermorite nanocomposites. Hydroxyl ($-OH$) functionalization with varying surface coverages (%) and clustered line patterns (random, zigzag, and armchair) were used to tailor the surface chemistry of the single layer graphene basal plane (FGS) and modulate the mechanical properties of FGS. Three types of tobermorite-graphene interfaces (water-rich, calcium octahedral, and silicate tetrahedral) were studied. The geometry of tobermorite was built by using stacked and hierarchical nanolaminate form of graphene sheet. Also, the water-rich interface of tobermorite was reinforced with varying surface coverages and clustered line patterns (random and zigzag) of $-OH$ groups, and the mechanical properties were investigated.

Finally, the interfacial strength of the water-rich interface of tobermorite and functionalized graphene sheet was investigated and compared with the graphene/graphene interfaces.

1.3. Structure of the Dissertation

This dissertation is organized into seven chapters. Chapter 2 contains the relevant literature pertaining to the research in this dissertation. Chapter 3 discusses the mechanical properties of functionalized graphene sheets. The primary emphasis of this chapter was to determine the effects of clustered line pattern of –OH groups on the stress-strain responses, toughenss, directional anisotropy of elasticity and compressibility, and wave propagation. Chapter 4 discusses the mechanical properties of tobermorite/graphene nanocomposites based on: (1) the geometrical assembly of graphene in the tobermorite matrix, (2) by exposing silicate interface, calcium interface, and water-rich interface of tobermorite to graphene, and (3) by varying the surface coverages (%) of –OH of functionalized graphene and clustered line pattern of –OH in contact with the water-rich interface of tobermorite. Chapter 5 discusses the normal and shear traction-separation properties of functionalized graphene bilayers in dry and wet (nanoconfined water monolayer) conditions. Chapter 6 discusses the normal and shear traction-separation properties of tobermorite/graphene interfaces with varying surface coverages of –OH groups. Chapter 7 summarizes the results of this research and presents recommendations for future work.

CHAPTER 2

LITERATURE REVIEW

2.1. Overview

This chapter provides an overview of the literature relevant to the research provided in this dissertation. An overview of the classical molecular dynamics simulation procedure in materials design is presented. An overview of the mechanical properties of functionalized graphene with varying coverages of surface functionalization is discussed. Also discussed is the effect of geometrical assembly, coverage of –OH groups of functionalized graphene on the mechanical properties of tobermorite 9 Å (T₉) and 14 Å (T₁₄). Also discussed is the effect of different surfaces of T₁₄ near graphene on the mechanical properties. Lastly, the traction-separation behaviors of tobermorite and graphene interfaces are discussed.

2.2. Materials modeling with classical molecular dynamics simulation

Computational materials design. Innovative materials design requires meticulous experimentation to unravel the underlying failure mechanisms. However, these mechanisms originate at the nanoscale and is very difficult to decouple experimentally. Thus, in recent years, computational materials design was integrated as a complement to the experimental materials design process, especially with the development of computer hardwares and softwares. Using computational materials design greatly reduces production cost while accelerates the materials development process. Since most of the fundamental failure mechanisms originates from the nanoscale, ab initio and classical molecular dynamics (MD) methods can be a viable option to design innovative materials because both of these methods explore in the angstrom to nanometer length scales.

Advantage of classical MD approach. For nearly all systems of interest, the most transferrable and fundamental description of matter is one that invokes quantum mechanics. Quantum mechanics provides the highest level of accuracy by solving Schrodinger's equation ($H\varepsilon = E\varepsilon$, where H is Hamiltonian, E is energy, and ε is state of the particle) for all of the

subatomic particles in a system. This method is also known as ab initio MD or density functional theory (DFT) in the computational aspects of materials design. There are several types of ab initio MD methods. One of the methods is the Kohn-Sham equation [39], where one electron Schrodinger's equation is solved. In another, Born-Openheimer approximation (also known as Born-Openheimer molecular dynamics) [40], the trajectories of the electrons and nucleus can be treated separately. So, it is clearly evident that many approximations need to be made in order to use DFT methods, and even these techniques are limited to small numbers of atoms. In contrast, the classical MD simply treats atoms as solid balls interacting with each other with a pre-defined potential (like a linear spring system with a spring constant, i.e., potential).

There are both practical and philosophical reasons for performing simulations on simpler systems that do not entail a full solution of the quantum-mechanical equations (e.g., DFT). Practical reasons stem from the need to treat larger systems and run simulations for longer times than those that ab initio methods can achieve. Philosophically, it is encouraged to use simpler models (e.g., molecular dynamics models) because the driving forces behind the phenomena of interest often naturally manifest at larger length and time scales such that fine-grained details are not needed to understand them. The obvious advantage of MD over DFT is that it gives a route to dynamical properties of the system: transport coefficients, time dependent responses to perturbations, and rheological properties.

MD simulation algorithm. Molecular dynamics simulation consists of the numerical, step-by-step, solution of the classical equations of motion [41], which for a simple atomic system may be written as,

$$F_i = m_i \ddot{r}_i \quad (2.1)$$

$$F_i = -\frac{\partial U}{\partial r_i} \quad (2.2)$$

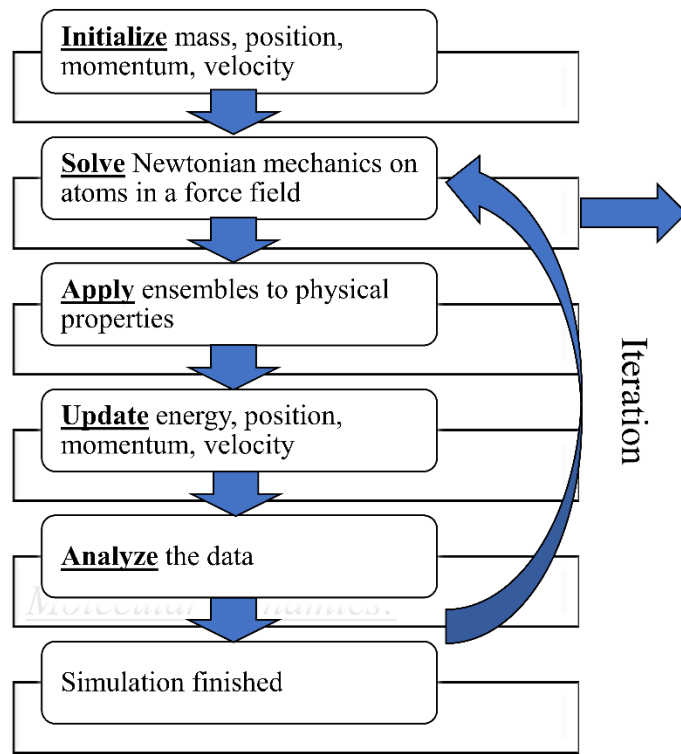
where, m_i = masses of atoms i , U = potential energy acting between the pairs of atoms, \ddot{r}_i = acceleration of atoms, i = Number of atoms. Force, F_i acting on the atoms are calculated from the potential energy $U(r^N)$, where $r^N = (r^1, r^2, \dots, r^N)$ represents the complete set of $3N$ atomic coordinates of the atoms.

The potential energy is calculated using the bonded and non-bonded potential energies of all the atoms in the system as,

$$U = U_{\text{bonded}} + U_{\text{non-bonded}} \quad (2.3)$$

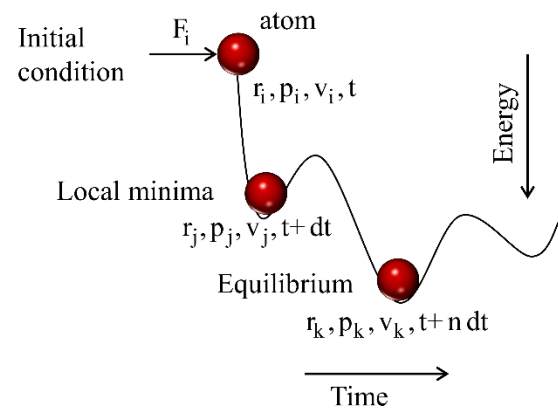
The details of the bonded and non-bonded potential energies in a simulated system are described in the Appendices A and B. A summary of the MD simulation algorithm is described in Figure 2.1.

(a) Molecular dynamics algorithm



(b) Numerical process to solve equation of motion

Numerical method to study many-body systems by solving Newton's equation of motion



Notation:

F_i	= initial force on an atom
r_i	= initial position of the atom
p_i	= initial momentum of the atom
v_i	= initial velocity of the atom
t	= time
n	= number of timesteps
dt	= timestep
r_j, r_k	= positions of the atom after timestep dt and ndt , respectively
p_j, p_k	= momentums of the atom after timestep dt and ndt , respectively
v_j, v_k	= velocities of the atom after timestep dt and ndt , respectively

Figure 2.1. Schematic diagram of a generic classical molecular dynamics simulation approach with (a) algorithm and (b) numerical approach to solve Newton's equation of motion.

MD Softwares. There are numerous commercial molecular dynamics simulation softwares are available such as Materials Studio, GROMACS, CHARMM, AMBER, and LAMMPS. For this study, LAMMPS [42] was chosen as the MD software because of its versatility (LAMMPS is open-source) and ease of compatibility with other geometry building softwares (e.g., MOLTEMPLATE, PACKMOL, etc.) and visualization softwares (e.g., VMD, OVITO, etc.).

2.3. Mechanical properties of single layer graphene sheet

Due to its unique structure and many extraordinary properties (e.g. high tensile strength, low frictional properties, high electrical conductivity), graphene, a two-dimensional (2D) sp^2 hybridized carbon sheet, has attracted significant interest over the last two decades in numerous fields, including engineering, chemistry, physics, biology, material sciences, and medicine [15, 43-47]. Introduction of functional groups onto the graphene surface enables modification of its chemical reactivity and surface topology and, in turn, its electronic, optical, magnetic, and thermal properties [48-52]. Surface chemical modification and functionalization of graphene with various chemical groups containing oxygen, sulfur, nitrogen, phosphorous, and other elements has become central to the realization of a wide range of graphene surface properties and functionalities and for the development of new graphene-based nanocomposites [48, 53-55]. Functionalized graphene has also been shown to provide a route to create 3D graphitic structures with tunable, superior mechanical and electrical properties [56-58]. Recently, novel strategies to locally control and pattern functionalization spatially on the micro and nanoscales have emerged [59-61]. Direct writing techniques capable of patterning surfaces with molecules are expected to enable the realization of new graphene derivatives with locally tunable properties [62]. This could have promising new applications for graphene in electronics, semiconductors, energy storage, biomedical engineering, civil engineering, and aerospace and automotive engineering.

Most studies to date on patterned functionalization have focused on tuning and understanding the local electronic, optical, chemical, and thermal properties of graphene [11, 14, 48, 49, 51, 62-71]. The anisotropic mechanical response of oxide-functionalized graphene has also been reported [72], however, tuning of the mechanical properties of graphene via patterned functionalization remains largely unexplored. The few studies which focus on the mechanical

properties of graphene and functionalized graphene have suggested that the spatial distribution and percent coverage of the functional groups on the graphene have a strong influence on the resulting mechanical properties [7, 8, 73-76] and that the presence of functional groups can change the behavior of the graphene during uniaxial stretching such that the material exhibits negative Poisson's ratios that are characteristic of auxetic materials [77-83]. While these studies have shown great potential for patterned functionalization to modulate the mechanical properties of graphene, the dependence of the mechanical properties on the structure of the graphene surface (i.e., spatial distribution and surface coverage of the functional groups), functionalization induced topology changes, and mechanical loading conditions and strain directions are not yet well understood.

2.4. Mechanical properties of graphene-reinforced C–S–H nanocomposite

Cement-based materials are inherently weak in tension. While nano- and microscale fiber reinforcements have been the method of choice for enhancing the material tensile properties by bridging cracks and improving the material load transfer capacity [84-97], this approach primarily addresses the material tensile property at the macroscale composite level rather than enhancing from the molecular scale of the cement hydrates. Calcium silicate hydrate (C–S–H) is the main binding cement hydrate responsible for the tensile properties of cement-based materials [98-100]. Nanotechnology offers the opportunity for the development of new C–S–H nanocomposites [101, 102]. Nano-engineering of C–S–H through the grafting of graphene-based materials can be a viable option for enhancing the tensile capacity of cement-based materials.

While experimental techniques, including atomic force microscopy and nanoindentation mapping are capable of studying the mechanical properties of cement phases such as C–S–H [103, 104], these techniques provides microscale information from which nanoscale behavior must be deduced and no molecular level detail of the internal, cohesive forces are obtained. Molecular dynamics (MD) modeling provides a useful tool for understanding atomistic scale, reinforcing mechanisms and tuning the mechanical properties of C–S–H. MD has been successfully used to investigate the structural and mechanical properties of C–S–H at the molecular scale, including its tensile and shear strengths [2, 3, 105-107]. While MD studies of the mechanical response of C–S–H with embedded carbon nanotubes, graphene, and graphene

derivatives have been recently reported in the literature [25, 33, 108-111], little is known about the possible influence of the interface composition and structure on the strengthening mechanisms and mechanical properties of the reinforced C–S–H nanocomposites. Yet, understanding the relationship between the surface structure of C–S–H interfacing with graphene and the mechanical properties of the reinforced system is key to being able to realize new C–S–H nanocomposites and enhance the mechanical properties of cement-based materials.

Tobermorite, a naturally occurring mineral with a low calcium-to-silicon (Ca/Si) ratio (< 1.0), has been identified in the literature as a viable analogue of crystalline pristine C–S–H phases (Figure 2.2) due to the structural similarity between the structures [98, 112]. While other C–S–H phase models with variable Ca/Si ratios have been recently proposed as more realistic models [3, 113, 114], the layered structure of T_{14} allowed for the study of three well-defined structures with different, well-defined interfaces that could be interfaced with the graphene (i.e., interlayer water interface, octahedral calcium layer interface, and tetrahedral silicate layer interface). These defectless T_{14} interfaces could provide a blueprint for understanding the in-plane strengthening mechanisms of graphene reinforced tobermorite nanocomposites. The tobermorite family is distinguished based on the interlayer spacings of 9 Å, 11 Å, and 14 Å. In this study, tobermorites 14 Å (T_{14}) and 9 Å (T_9) were studied as the base matrices. The interlayer spacing of T_{14} was 14 Å because of the presence of calcium cations and water molecules. T_9 has a lower interlayer spacing of 9 Å than T_{14} because of the absence of water molecules in the interlayer (resembles dry C–S–H). Nonetheless, both tobermorite structures resembled layered *drierketten* type structures of C–S–H, and allowed for the nanoengineering of the structures with graphene reinforcement.

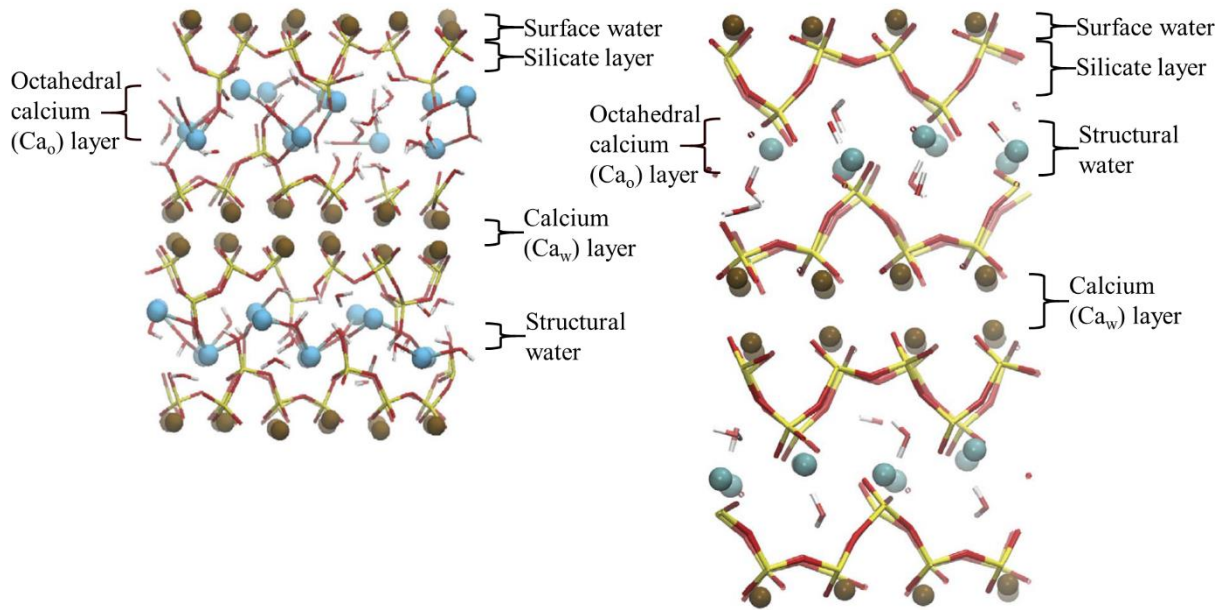
(a) Structure of Calcium Silicate Hydrate (C–S–H)**(b) Structure of Tobermorite 11 Å**

Figure 2.2. Models of (a) C–S–H and (b) crystalline analogue of C–S–H, tobermorite 11 Å, comprised of the structural layers are shown (adapted from [115]).

It has been reported in the literature that the strength and toughness (i.e., ductility) of cement composites could be enhanced by arranging different types of fibers and carbon nanotubes (CNT) in a lamellar formation [108, 116, 117]. Orientating graphene sheet (GS) in a lamellar formation in a copper (Cu) matrix (Cu/GS/...GS/Cu formation) also increased the strength and the plastic strain of the composite, transitioning Cu/GS composite from brittle-to-ductile behavior [34]. As previous findings demonstrated, C–S–H and tobermorite possess a unique layered structure, which could be strengthened further by orienting GS in lamellar formation sandwiched within the matrix. However, this type of geometrical configuration-based studies on the nanoscale mechanical behaviors of the graphene-reinforced tobermorite 9 Å (T₉/GS) nanolaminates has not yet been investigated. The location and geometric arrangement pattern of graphene within the tobermorite systems offer opportunities to modulate the mechanical properties (because of its layered structure).

The interfacial chemical species of the C–S–H or T₁₄ nanostructures has been shown to interact during the external loadings and modulate the mechanical properties of T₁₄ [2, 32, 118].

It has also been observed that graphene oxide (GO) embedded in C–S–H matrix in the interlayer direction increased the failure strength and strains of the GO-reinforced C–S–H (C–S–H/GO) nanocomposite because the hydroxyl groups (–OH) interacted with the interlayer interface of C–S–H [109]. Moreover, it has been shown that the interlayer interface filled with water can create hydrogen bonds with the –OH groups of the functionalized graphene sheet (FGS) and modulate the mechanical properties. It has been shown before that T₁₄ was hydrophilic because the water molecules pointed hydrogen atoms towards the interlayer Ca atoms [119]. In addition to the effect of patterning of –OH groups on the FGS, the –OH groups supposedly attract the mobile water molecules of the T₁₄ away from the core structure which may lead to a difference in the mechanical responses. In addition to the water-rich layer, the structural skeleton of T₁₄ was made of two other layers: calcium octahedral layer, sandwiched between two opposite silicate layers [120]. These layers play significant role in engineering the mechanical properties of T₁₄ and T₁₄-based nanocomposites. Therefore, a thorough understanding of the effect of the interfaces as well as the clustered line patterns and coverage of hydroxyl (–OH) groups associated with the GS on the mechanical properties of the nanocomposites during tensile and shear loading stimulations is necessary to nanoengineer the T₁₄/GS and T₁₄/FGS nanocomposites.

2.5. Interfacial strength of C–S–H/ graphene nanosheets

The crystalline calcium-silicate-hydrate (C–S–H) or its analogue tobermorite 14 Å (T₁₄) is built with a layered structure (Figure 2.3) where the interlayer (parallel to $(0\ 0\ \bar{1})$ plane) is known to be the weakest layer. The structure of this interlayer, i.e., $(0\ 0\ \bar{1})$ plane, is filled with calcium cations and nanoconfined water molecules, which guide the stress transfer within the structure (especially along the out-of-plane tensile and shear loadings). In the literature, the calcium cations in the interlayer have been reported to be almost immobile (very low diffusion constant) [31, 121-123]. Meanwhile, the water molecules transported through the nanoconfined interlayer space by diffusion. However, the diffusion constant of this confined interlayer water was still much slower than that of the bulk water [32, 122]. Therefore, the structural and dynamic nature of calcium and water retained the structural homogeneity near the interfaces, and the overall structural disintegration of T₁₄ were caused by the slight bent in the calcium octahedral

layers and distortion of the silicate tetrahedral layers. However, when stress was accumulated in the interlayer, this weak layer failed at a faster rate than the structural skeletons of the T₁₄.

Structure of Tobermorite 14 Å (T₁₄)

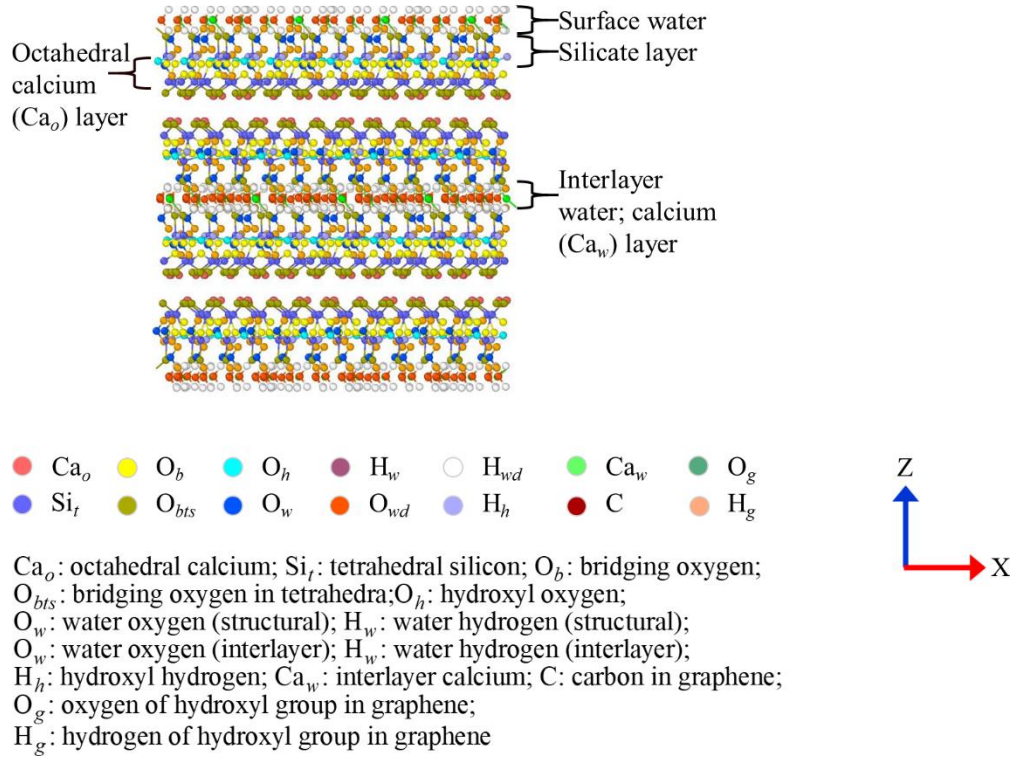


Figure 2.3. A representative model of the T₁₄ with defined water, calcium octahedral, and silicate tetrahedral structural layers.

In the literature, numerous attempts have been undertaken to strengthen the interlayer interface of different composites using graphene-derivatives (e.g., by using graphene, graphene oxide, carbon nanotube etc.) [19, 21, 23, 27, 124-129]. The pull-out test on a wrinkled graphene oxide (GO)/polymer composite had reported that the wrinkled geometry enhanced the interfacial stress transfer between the interfaces [127]. In addition to the variability of material (GO) and geometry (wrinkling), the degree of functionalization of GO (functional group coverage) also influenced the interfacial binding characteristics between the GO and polymer interfaces [130]. Similar to the polymers, it was observed that the interfacial stress transfer between C–S–H and GO was also increased by incorporating GO in the C–S–H matrix [109, 131]. GO was suggested to be a potential strengthening material for the C–S–H interfaces because the oxygen-containing

functional groups increased the dispersion of GO in cement paste [132], and regulate better microstructure by promoting hydration [33]. The hydrophobicity and hydrophilicity of the C–S–H interfaces near interlayer water and calcium ions also controlled these interfacial properties [133]. It was reported that C–S–H was hydrophilic [119, 134] and the nanoconfined water had multi-characteristics [32, 119]. The bond-slip (shear stress-displacement) relationship of C–S–H/GO interface was observed to be enhanced (because of the interaction of oxygen atoms with C–S–H layers) by embedding GO sheet in the C–S–H matrix [135], agreeing with the previous findings. The hydroxyl (–OH) groups of FGS created strong hydrogen bonds in the C–S–H layers, thus, enhancing the overall mechanical properties by increasing the interfacial strength [25]. It was also reported that the development of three dimensional network of hydrogen bonding among the water molecules and the C–S–H matrix in the nanoconfined spaces between the interfaces played a dominant role in controlling the structure and dynamic properties of water [122]. The strengthening effects of GO came from the nanoconfined water between the GO and C–S–H interfaces, even after drying, due to the hydrophilic nature of GO [33]. Since, the interlayer water in tobermorite was nanoconfined, the structural and dynamic behavior was very different than from the bulk. Understanding the structure and dynamics of nanoconfined water was important because it changed the properties of the entire composite in the macroscale [136]. These phenomena could potentially change the mechanical properties of the nanocomposites near the interfaces, thus altering the load transferring capability.

2.6. Conclusions

The literature pertaining to the research in this dissertation was presented. The following research gaps were identified:

- Few studies have been done on the effects of patterned –OH functionalization, surface coverage of –OH, and loading conditions on the mechanical properties of GS and FGS.
- Little research has been performed on the effects of geometrical assembly of GS in the T₉ matrix, exposed silicate, calcium, and water interfaces of T₁₄ near the GS, and the effects of clustered line patterns of –OH on the mechanical properties of T₁₄/FGS nanostructures, which are necessary to nanoengineer the mutually exclusive mechanical properties such as strength, stiffness, toughness, and compressibility.

- Little research has been done on the interfacial traction-separation behaviors of the T_{14}/FGS and the GS/FGS interfaces, which is required to understand the underlying strengthening mechanisms of FGS on the T_{14}/FGS and the GS/FGS interfaces, which also affect the overall mechanical properties of T_{14}/FGS and GS/FGS based nanocomposites.

CHAPTER 3

MECHANICAL PROPERTIES OF SINGLE LAYER GRAPHENE SHEET VIA MOLECULAR DYNAMICS SIMULATIONS

This chapter has been published in the journal Carbon as the following peer-reviewed manuscript: B. Al-Muhit, F. Sanchez, Tunable mechanical properties of graphene by clustered line pattern hydroxyl functionalization via molecular dynamics simulations, Carbon, **146** (2019), p. 680-700 doi.org/10.1016/j.carbon.2019.02.019.

3.1. Overview

Due to its unique structure and many extraordinary properties, graphene, a two-dimensional (2D) sp^2 hybridized carbon sheet, has attracted significant interest over the last decades in numerous fields, including engineering, chemistry, physics, biology, material sciences, and medicine [15, 43-47]. Surface chemical modification and functionalization of graphene with various chemical groups containing oxygen, sulfur, nitrogen, phosphorous, and other elements has become central to the realization of a wide range of graphene surface properties and functionalities and the development of new graphene-based nanocomposites [48, 53-55]. Introduction of functional groups onto the graphene surface enables modification of its chemical reactivity and surface topology and, in turn, its electronic, optical, magnetic, and thermal properties [48-52]. Functionalized graphene has also been shown to provide a route to create 3-dimensional graphitic structures with tunable, superior mechanical and electrical properties [56-58]. Recently, novel strategies to locally control and pattern functionalization spatially on the micro and nanoscales have emerged [59-61]. Direct writing techniques capable of patterning surfaces with molecules are expected to enable the realization of new graphene derivatives with locally tunable properties [62]. This could have promising new applications for graphene in electronics, semiconductors, energy storage, biomedical engineering, civil engineering, and aerospace and automotive engineering.

Most studies to date on patterned functionalization have focused on tuning and understanding the local electronic, optical, chemical, and thermal properties of graphene [63-65].

Tuning of the mechanical properties of graphene via patterned functionalization remains, however, largely unexplored. While chemical functionalization introduces many defects on graphene as a result of the conversion of sp^2 to sp^3 bonding and hence deteriorates its mechanical properties [8, 73], there is evidence that the mechanical properties of functionalized graphene depend greatly on the spatial distribution and coverage of functional groups on the graphene surface [74, 75]. Furthermore, it has been found that hydrogenated graphene and graphene with patterned defects can exhibit expansion instead of contraction during uniaxial stretching, thus exhibiting negative Poisson's ratios that are characteristics of auxetic materials [77-83]. The anisotropic mechanical response of oxide functionalized graphene has also been reported [72]. However, while studies devoted to the mechanical properties of functionalized and corrugated graphene have shown great potential for patterned functionalization to modulate the mechanical properties of graphene, the dependence of the mechanical properties on the structure of the graphene surface (i.e., spatial distribution and surface coverage of the functional groups), functionalization induced topology changes, and mechanical loading conditions and strain directions are not yet well understood.

This chapter focuses on hydroxyl ($-OH$) functionalization and presents a study of the effect of the spatial distribution (random and clustered line patterns along the armchair and zigzag directions of the graphene lattice) and percentage of $-OH$ groups on topological changes and mechanical response of graphene sheets (GS) under tension loading in zigzag and armchair (parallel to C-C bonds) directions and under shear loading in the zigzag direction. Hydroxyl functionalization was chosen because it promotes hydrophilicity of GS and is often the precursor for the covalent attachment of organic groups in many applications [137]. The hydroxyl groups were attached to the carbon atoms on one side of the GS with a coverage spanning the entire range (0-100%) in three arrangements: (i) non-clustered random arrangements, (ii) clustered line pattern arrangements along the zigzag direction, and (iii) clustered line pattern arrangements along the armchair direction. Clustered line pattern arrangements were selected to study the directional effect of functionalization with respect to the loading direction on the mechanical properties. A classical molecular dynamics (MD) method with an empirical interatomic potential force field (consistent valence forcefield, CVFF) was used for the simulations. Stress-strain responses, potential energy changes during loading, strain energy densities, directional elastic and shear moduli, linear compressibility, Poisson's ratios, and sound wave velocities were

determined for the pristine GS and –OH functionalized GS (FGS). It is demonstrated that clustered line pattern functionalization increased the stiffness of the GS along the zigzag direction and stretchability along the armchair direction without significantly stretching the carbon bonds and can enhance the toughness of the GS relative to random functionalization. Also, it is shown that the Poisson's ratio can be tuned from positive to near zero and negative values, leading to auxetic behavior. The auxetic behavior originated from the unique initial functionalization induced bending deformation of the FGS achieved with line pattern arrangements. This work provides new insights into the anisotropic structure-topology-property relations of graphene and possible strategies for the design of new graphene derivatives and other two-dimensional nanomaterials via chemical functionalization.

All simulations were performed with LAMMPS [42] using the CVFF that has been shown to be suitable to describe the interaction between carbon (C), oxygen (O), and hydrogen (H) atoms [138].

3.2. Computational Details

Models and computational cells. A single layer, pristine graphene sheet (GS) made of 252 C atoms arranged in a hexagonal lattice with initial sp^2 C–C bond lengths and \angle C–C–C bond angles of 1.418 Å and 120° , respectively, was constructed using Materials Studio 7.0 (Dassault Systèmes BIOVIA, San Diego, CA). The shorter and longer sides of the GS were terminated by zigzag (X-direction) and armchair (Y-direction) edges, respectively. Hydroxyl (–OH) functionalized graphene sheets (FGS) were then created from the GS by attaching out-of-plane –OH groups to the C atoms on one side of the GS surface using three (3) different functionalization arrangements: random (R), clustered line patterns along the zigzag (ZZ) direction (X-axis) of the graphene lattice, and clustered line patterns along the armchair (AC) direction (Y-axis) of the graphene lattice at five (5) degrees of –OH functionalization, 12%, 25%, 50%, 75%, and 100% (i.e., ratio of number of –OH groups to carbon atoms in graphene). The functionalized C atoms changed from sp^2 to sp^3 hybridization as a result. The initial C–O and O–H bond lengths were 1.39 Å and 0.96 Å, respectively. The initial \angle C–C–O and \angle C–O–H bond-angles were 120° and 109.47° , respectively. For the clustered line pattern arrangements, the –OH groups were attached to the C atoms in an arrangement of parallel adjacent lines that

were oriented either along the zigzag direction or along the armchair direction of the graphene lattice (Figure 3.1). The number of lines was fixed by the percentage of –OH coverage. The clustered line patterns along the zigzag direction were arrays of straight lines of evenly distributed –OH groups along the lines with the spacing between lines alternating between a short and long arrangement. These lines were preferentially located along the zigzag edges of the GS and two lines of atoms from the zigzag edges. The clustered line patterns along the armchair direction were arrays of equally spaced straight lines of –OH groups with alternating short and long spacing between the –OH groups along the lines. These lines were preferentially located along the centerline of the GS (bulk of the GS lattice). These configurations allowed relatively similar, initial, out-of-plane zigzag and armchair deformation amplitudes and wavelengths of the FGS and allowed insights into the directional effect of clustered line patterns on the mechanical properties of the GS. For the random arrangement, the –OH groups were attached to the carbon atoms in a relatively uniform distribution that avoided clustering. Preliminary evaluation of three different configurational non-clustered random distributions showed no significant differences in the tensile stress-strain response (Figure A6.1), indicating that the results were insensitive to the choice of the non-clustered random distribution.

The initial tilt angle and thickness of the GS were selected as zero degree in all directions and 3.35 Å (van der Waals thickness of the C atoms), respectively. To construct the computational cells, a vacuum of 30 Å was placed on both sides of the GS and FGS to create a non-periodic and isolated geometry along the +Z and –Z-directions. The final triclinic computational cell dimensions of the GS and FGS systems were 22×28.5×60 Å³ and 22×29×60 Å³, respectively. The unit cell size of the GS used in this study had a diagonal length of 3.64 nm and was chosen to be large enough to approach the mechanical properties of bulk graphene [139] but small enough to prevent out-of-plane bending deformation of the unstrained GS [140]. 3D periodic boundary conditions were applied to all six (6) directions in all systems. The two 30 Å vacuum slabs placed on both sides of the GS and FGS systems essentially converted the 3D periodicity to a 2D periodicity in the XY plane with the MD simulations performed over an infinite surface of the GS and FGS systems. The FGS systems were represented symbolically as FGS_jⁱ, where $i = \{R, ZZ, AC\}$ corresponded to the arrangement of the –OH groups on the GS surface and $j = \{0, 12, 25, 50, 75, 100\}$ was the percentage of functional groups.

Force field. The CVFF was used to describe the interaction among C, O, and H atoms of the GS and FGS. The CVFF includes terms for the bond-stretching energy, the angle-bending energy, the torsion-angle (dihedral) energy, the out-of-plane energy (improper torsion), the electrostatic energy (Coulombic energy) and the van der Waals energy. Bond energies were calculated by the Morse and harmonic potentials. The Morse potential provides a description for bond breaking and is commonly used in the literature to determine the tensile properties of covalently bonded systems [141, 142]. The applicability of the CVFF for studying the mechanical properties and energetics of graphene and graphene-derived materials has previously been demonstrated in the literature [143, 144]. Angle-bending and torsional energies were incorporated using harmonic potentials. Out-of-plane bending energies were represented using improper torsion terms. During loading, the Morse, angle-bending, and torsion bonds were considered permanently broken when the Morse bond length exceeded 1.7 Å [42]. The equations of the Morse, angle-bending, and torsional (dihedral angles and improper torsions) potentials are provided in the supplementary material, Section A1.1. To keep the FGS charge neutral, partial atomic charges were assigned to the C, O, and H atoms using the built-in QEq charge equilibration method [145] in LAMMPS. The intermolecular interactions were calculated as the sum of an electrostatic term for the Coulombic interaction between partial atomic charges and a 12–6 Lennard–Jones (LJ) term [146] describing the van der Waals (vdW) dispersive interactions. The electrostatic interactions between atoms were calculated as:

$$\Psi^{\text{electrostatic}} = \sum_i \sum_{j>i} \frac{1}{4\pi\epsilon_0} \cdot \frac{q_i q_j}{r_{ij}^2} \quad (3.1)$$

where q_i and q_j are charges on atoms i and j , ϵ_0 is the permittivity of the vacuum (8.85419×10^{-12} F/m), and $r_{ij} = |\mathbf{r}_i - \mathbf{r}_j|$ is the interatomic distance (Å) between the atoms i and j .

The vdW interaction between atoms was calculated as:

$$\Psi^{\text{vdW}} = \sum_i \sum_{j>i} 4\epsilon \left[\left(\frac{\sigma}{r_{ij}} \right)^{12} - \left(\frac{\sigma}{r_{ij}} \right)^6 \right] \quad (3.2)$$

where ϵ is the depth of the potential well (kcal mol^{-1}), σ is the distance (Å) at which the potential is zero, and r_{ij} is the interatomic distance (Å). The Ewald summation method [147] was

used to evaluate the long-range Coulombic interactions in the reciprocal space with a cut-off distance of 10 Å. A neighbor cut-off distance of 3 Å was used.

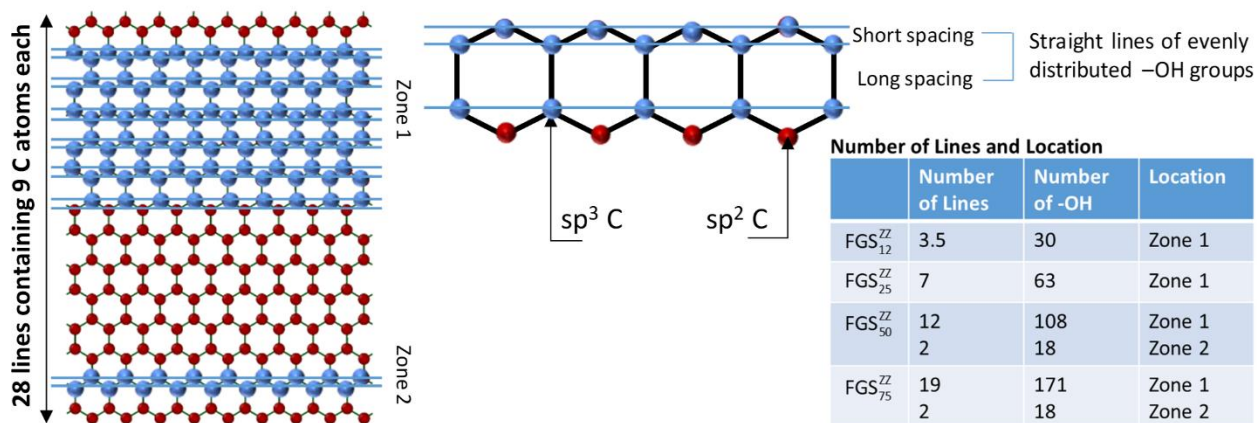
Equilibration. The GS and FGS were energy minimized using the conjugate gradient method. Appropriate force- and energy-cutoff distances were used to reduce the energy and pressure build-up during the geometry optimization. The GS and FGS systems were then equilibrated at a targeted temperature of 300 K and external pressure of 0 atm, using the canonical isothermal-isochoric NVT (fixed number of atoms, volume, and temperature) and isothermal-isobaric NPT (fixed number of atoms, pressure, and temperature) ensembles for 200 ps and 1 ns, respectively. The Nosé-Hoover thermostat and barostat [148, 149] was used to control the temperature and pressure. The equation of motion was integrated over time using the velocity-Verlet algorithm with a time step of 1 fs.

Loading methods and MD simulations. Three different straining modes were studied: (i) uniaxial tension along the zigzag direction (chirality angle, $\theta = 0^\circ$), (ii) uniaxial tension along the armchair direction (chirality angle, $\theta = 30^\circ$), and (iii) shear deformation in XY plane along the zigzag direction. To simulate the loading, atoms at opposite edges of the GS and FGS and within 3 Å of the edges were constrained while subjected to tensile or shear forces as shown in Figure 3.2. The tensile strains along zigzag (ε^{ZZ}) and armchair (ε^{AC}) and the shear strain along zigzag (γ^{ZZ}) were applied with a strain rate of 1×10^{-6} (Å/Å) fs⁻¹, in accordance with typical ranges used in the literature [7, 143, 150].

Data analysis. The atomistic stress was calculated according to the virial stress theorem [151] considering both the potential and kinetic energy terms. The calculated virial stress was time-averaged over 4500 fs for each increment of strain to obtain the engineering stress that was plotted against the corresponding strain to obtain the stress-strain curves. The stress in 3D (GPa) was multiplied by the thickness of the GS or FGS to obtain the stress in 2D (Nm⁻¹). Strain energy densities per unit area for tension (Π) and shear (Γ) were calculated by integrating with the trapezoidal rule to obtain the area under the corresponding stress-strain curves from a strain of 0 to the fracture strain. The strain energy density was used as an indirect measurement of the toughness of the GS and FGS. The total potential energy was calculated as the sum of the bond-stretching energy (sum over C–C, C–O, and O–H bonds), angle-bending energy (sum over \angle C–C–C, \angle C–C–O, and \angle C–O–H angles), and torsional energy (sum over C–C–C–C, C–C–C–O,

O–C–C–O, and C–C–O–H dihedral angles). The internal local atomic stresses of each GS and FGS system were calculated by computing the stress experienced by each atom multiplied by the volume of the atom. The in-plane elastic stiffness constants, C_{ij} ($i, j \in [1-3]$; normal, shear, and coupling constants), were calculated from the slope of stress-strain plots of time averaged stresses obtained at different strains. The systems were deformed at a particular strain for 100,000 fs. Three strains with increments of ± 0.005 were used and the corresponding stresses were obtained every 100 fs and time averaged (1,000 data points) to compute the final stresses. The normal and coupling constants were then calculated from the slope of the stress-strain plots obtained using the NPT ensemble keeping the directions perpendicular to the loading direction free of pressure. The shear component, however, was obtained in the NVT ensemble because of the requirement of the volume preservation during shearing. The compliance components were obtained by inverting the stiffness matrix, $S_{ij} = C_{ij}^{-1}$. From the compliance constants, a full tensorial analysis was performed and key quantities were determined, including the directional elastic moduli (E, uniaxial stiffness), the directional shear moduli (G, resistance to shearing), the linear compressibility (β , deformation as a response to hydrostatic compression), the Poisson's ratios (ν , ratio of transverse strain to axial strain), and sound wave velocities. Details of the calculations can be found in the Appendix A5.0.

(a) Line patterns along ZZ



(b) Line patterns along AC

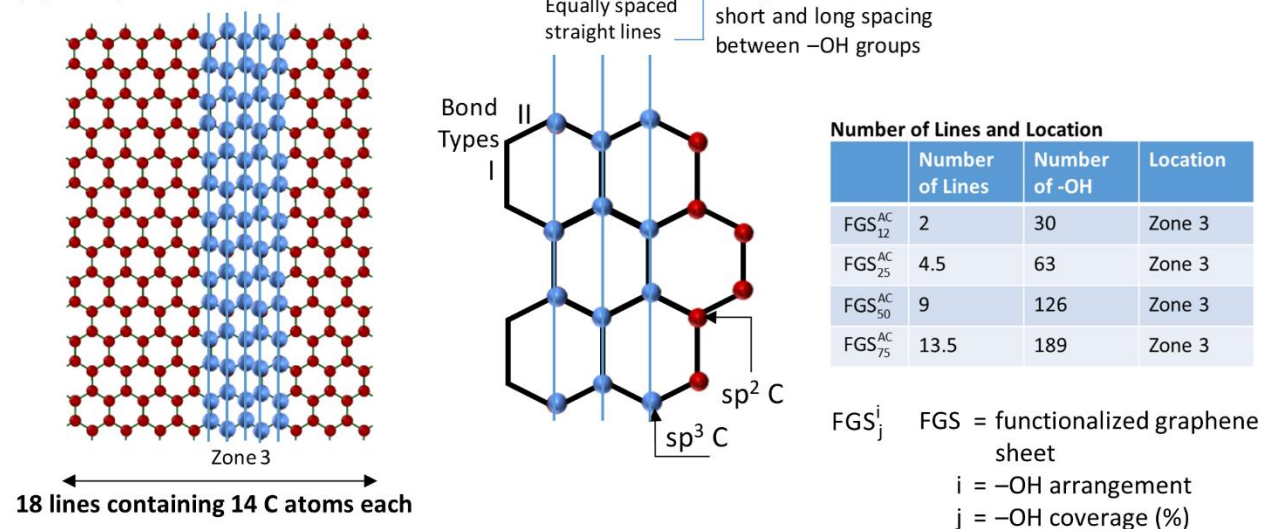


Figure 3.1. Clustered line pattern arrangements: (a) line patterns along the zigzag (ZZ) direction and (b) line patterns along the armchair (AC) direction. The red and blue balls represent carbon and oxygen atoms, respectively.

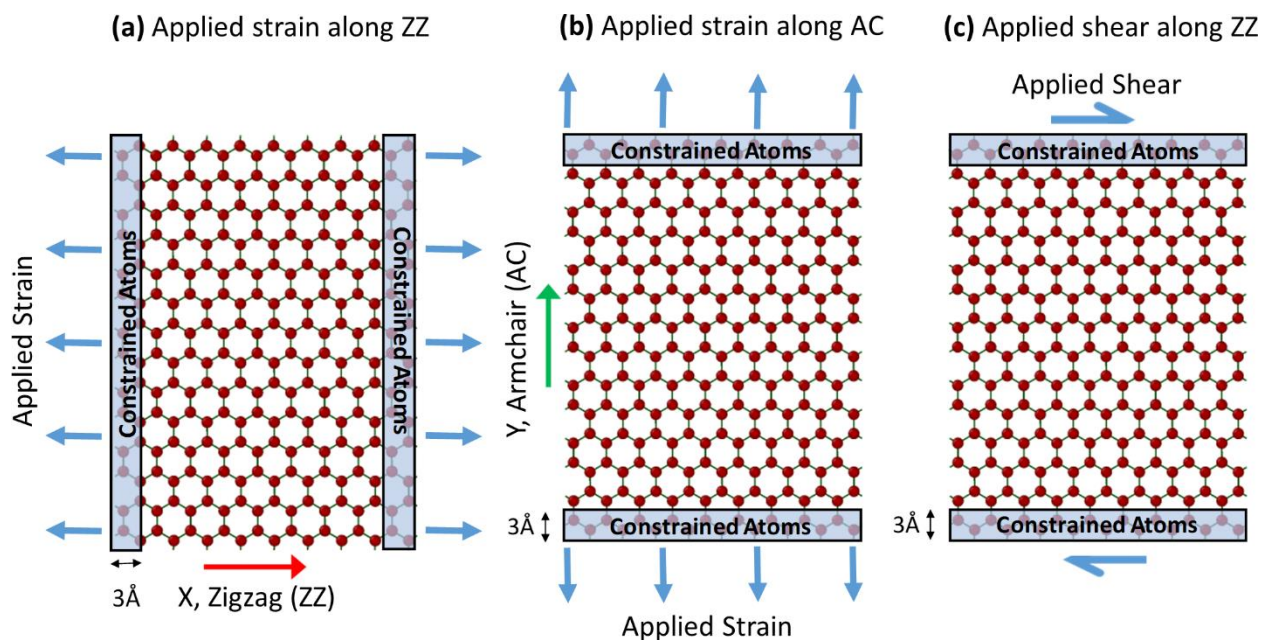


Figure 3.2. Loading modes: (a) uniaxial tension along the zigzag (ZZ) direction, (b) uniaxial tension along the armchair (AC) direction, and (c) shear deformation along the zigzag (ZZ) direction.

3.3. Results and Discussion

3.3.1. Surface topology and internal local stress distribution

Hydroxyl functionalization on one side of the GS caused out-of-plane bending of the GS after relaxation to equilibrium at zero applied strain (unstrained conditions) from its initial flat state. The GS deformation became more prominent with increasing $-OH$ coverage and was larger for the clustered line patterns than the random arrangement of functionalization (Figure 3.3). The FGS deformed into a cylindrical type configuration (monoclastic surface, Figure 3.3) with the axis of bending perpendicular to the direction of the line patterns for 12%, 25%, 50%, and 75% surface coverage, and into a saddle-shaped configuration (anticlastic surface, Figure 3.4) that was symmetrical along the X- and Y-directions for 100% surface coverage. The average amplitude of the deformation (maximum height) and corresponding wavelength increased with increasing $-OH$ coverage (Table 3.1). Consistent with the location of the line patterns, the deformations along the armchair direction were more eccentric than that along the zigzag direction but had overall similar amplitude to wavelength ratios at each $-OH$ percentage. These initial bending deformations were primarily the result of the repulsive interactions between

neighboring –OH groups and the change from sp^2 to sp^3 configuration and arose from the initial minimization of the potential energy and topology of the FGS systems. These interactions were prevalent for the line pattern arrangements because the –OH lines were densely packed. During the minimization process, a few –OH groups reoriented themselves to the opposite side of the FGS. High initial, internal stress concentrations near the –OH sites could be seen from the internal local stress distributions (Figure 3.5a and Figure 3.6a). The C atoms with the attached –OH groups experienced tensile stress, while the other C atoms (no attached –OH groups) experienced compressive stress.

The component of the stress in the direction of the applied load controlled the deformation and the stored strain energy and was strongly influenced by the initial functionalization induced topology change of the FGS. Under tensile loading of the FGS with random –OH arrangement, higher internal local stress concentrations developed at the –OH functionalization sites as strain increased. The randomly functionalized GS elongated until fracture, which occurred perpendicular to the loading direction through a path that followed clustered regions of –OH groups (Figure 3.7). A similar behavior for the clustered line pattern arrangements was observed under tensile loading parallel to the line pattern direction (Figure 3.8). The presence of two distinct zones with and without functionalization on the FGS surface resulted in greater fracture stress than for the random pattern functionalization. In contrast, under tensile loading perpendicular to the line pattern direction, the internal local stress distribution evolved from compressive to tensile stress as the strain increased (Figure 3.5 and Figure 3.6) and the FGS lost the curvature and elongated until the entire FGS structure experienced tensile stress. Subsequently, the bonds ruptured and the FGS fractured in the direction perpendicular to the strain direction, releasing the accumulated stress. The internal stress for loading perpendicular to the line patterns was greater when the line patterns were along the armchair direction than along the zigzag direction. The difference arose from the structural asymmetry of the graphene lattice and the fact that, for line patterns along the armchair direction, stretching occurred along the zigzag direction for which four (4) bonds in one hexagonal graphene unit cell were elongated compared to only two (2) bonds when the line patterns were along the zigzag direction and the stretching occurred along the armchair direction (i.e., only type II bonds were involved during stretching along the zigzag direction while only two (2) type I bonds participated during stretching along the armchair direction). Though the CVFF might not completely capture the

deformation behavior details in the near vicinity of the point of fracture (i.e., high strain region), the effect on the predicted internal local stress distribution at high strain before fracture would be small relative to the overall magnitude of the stress, and the trend of the stress evolution as a function of strain was overall captured. If pre-existing cracks were to exist other potentials might be needed [152]. Table A7 provides a comparison of the mechanical properties of the GS and 100% –OH FGS to that obtained from atomistic studies using different force fields and simulation methods.

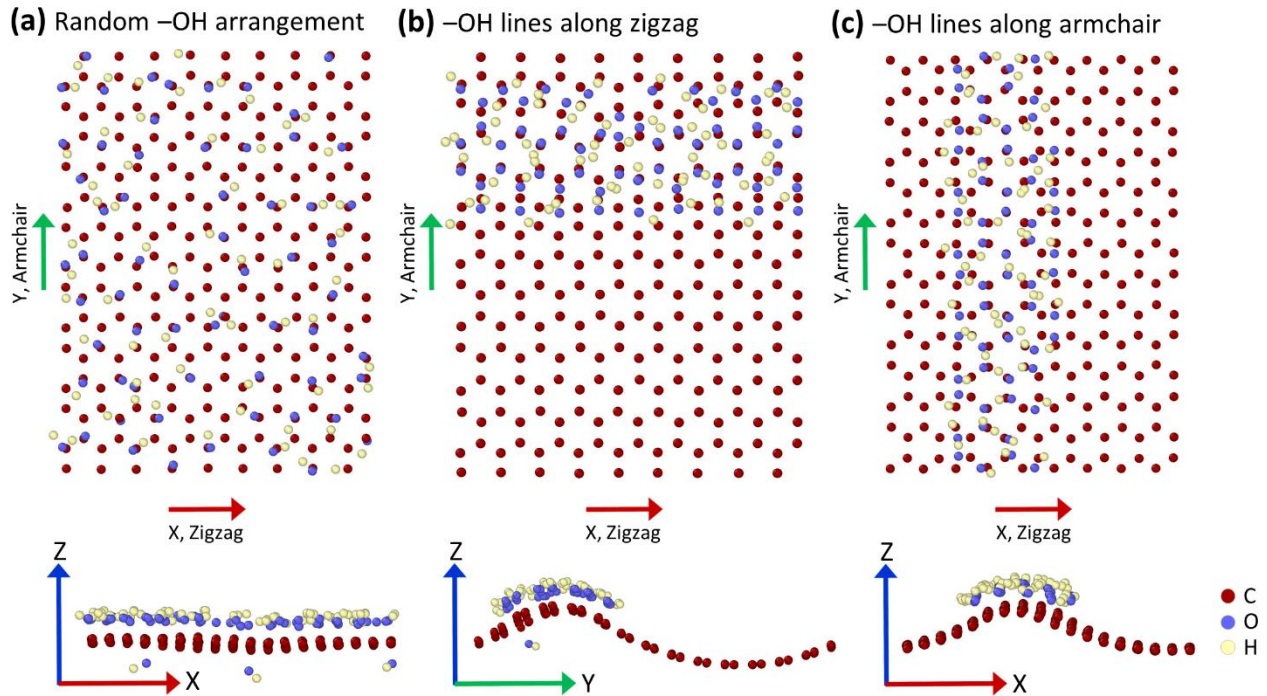


Figure 3.3. Graphene sheet with hydroxyl functionalization after relaxation to equilibrium at zero applied strain (unstrained conditions) exhibiting a change toward a monoclastic surface (cylindrical configuration). Shown for 25% hydroxyl functionalization: (a) random arrangement, (b) –OH line patterns oriented along the zigzag direction, and (c) –OH line patterns oriented along the armchair direction. The red, blue, and yellow balls represent carbon, oxygen, and hydrogen atoms, respectively.

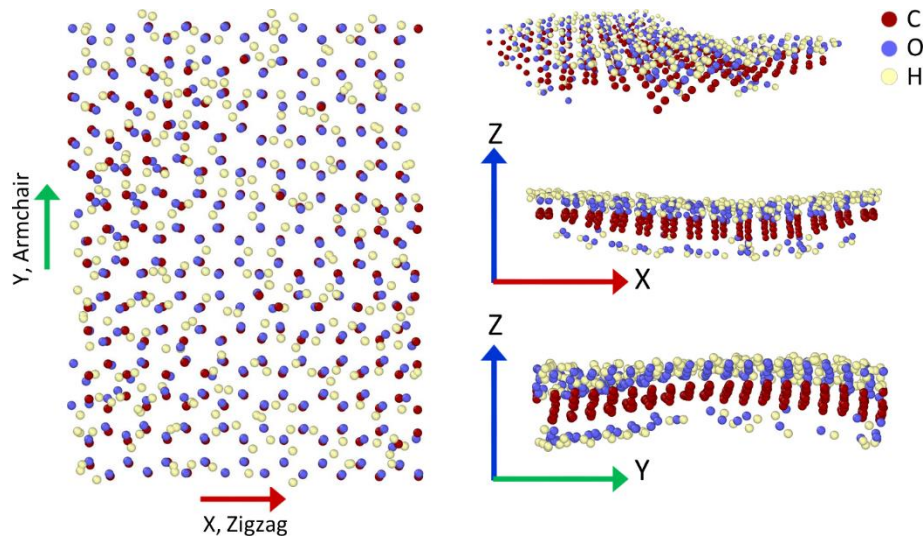


Figure 3.4. Graphene sheet with 100% hydroxyl functionalization after relaxation to equilibrium at zero applied strain (unstrained conditions) exhibiting an anticlastic surface (saddle-shaped configuration). The red, blue, and yellow balls represent carbon, oxygen, and hydrogen atoms, respectively.

Table 3.1. Amplitude (maximum height) and wavelength of the initial deformation in functionalized graphene at zero applied strain as a function of $-OH$ coverage for line patterns along the zigzag direction (wavelength along armchair) and line patterns along the armchair direction (wavelength along zigzag).

Line pattern direction	$-OH$ %	Amplitude h (Å)	Wavelength λ (Å)	Amplitude/wavelength $\alpha = h/\lambda$
Zigzag	0	0	∞	0
	12	0.71	6.57	0.10
	25	2.05	9.88	0.21
	50	2.79	11.79	0.24
	75	3.45	14.52	0.24
Armchair	0	0	∞	0
	12	0.37	5.67	0.07
	25	1.40	7.63	0.18
	50	3.62	12.07	0.30
	75	4.03	16.28	0.25

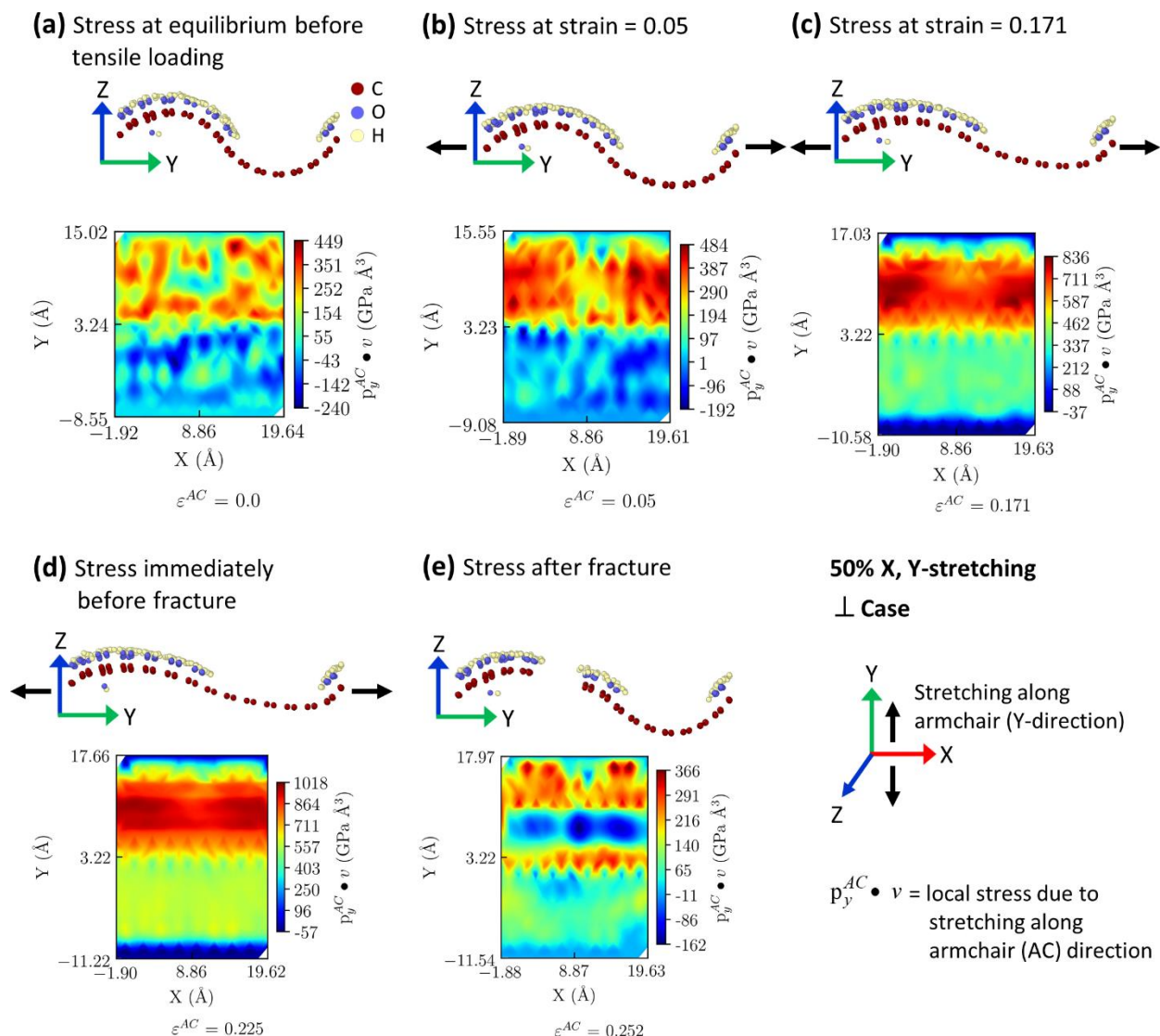


Figure 3.5. Internal local stress distribution (component of the stress parallel to the load) during tensile loading along the armchair (AC) direction in the graphene sheet with 50% hydroxyl functionalization arranged in a clustered in-line pattern along the zigzag direction (\perp , perpendicular to the tensile loading direction): (a) after relaxation to equilibrium before tensile loading (unstrained conditions); and (b), (c), (d), and (e) as a function of increasing tensile strain, showing stages of slow increasing stress (de-wrinkling and loss of curvature), fast increasing stress (elongation), before fracture (maximum bond elongation), and fracture (release of stress concentration), respectively.

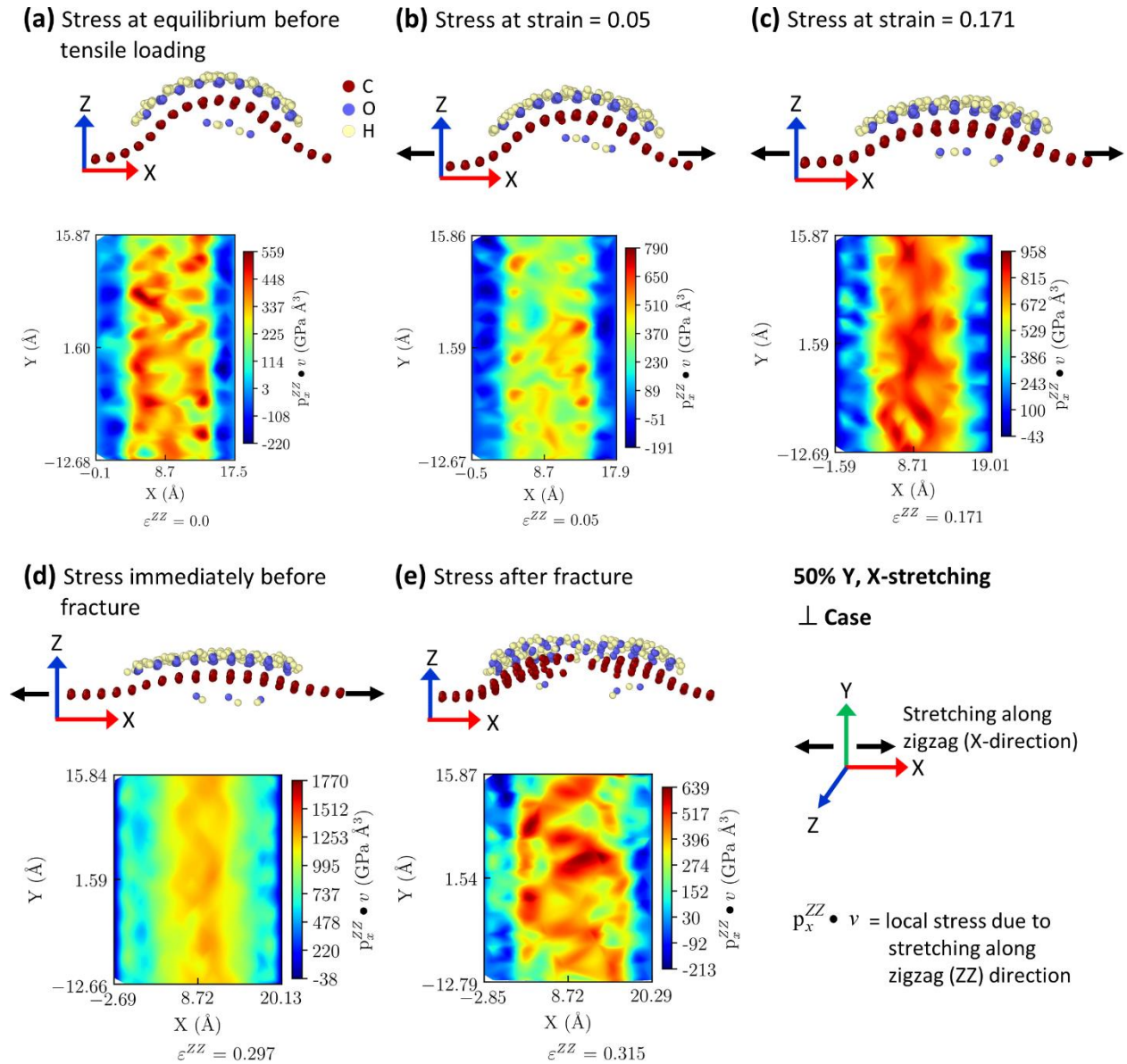


Figure 3.6. Internal local stress distribution (component parallel to the load) during tensile loading along the zigzag (ZZ) direction in the graphene sheet with 50% hydroxyl functionalization arranged in an in-line pattern along the armchair direction (\perp , perpendicular to the tensile loading direction): (a) after relaxation to equilibrium before tensile loading (unstrained conditions) leading to initial bending deformation; and (b), (c), (d), and (e) as a function of increasing tensile strain, showing stages of slowly increasing stress (de-wrinkling and loss of curvature), rapidly increasing stress (elongation), before fracture (maximum bond elongation), and at fracture (release of stress concentration), respectively.

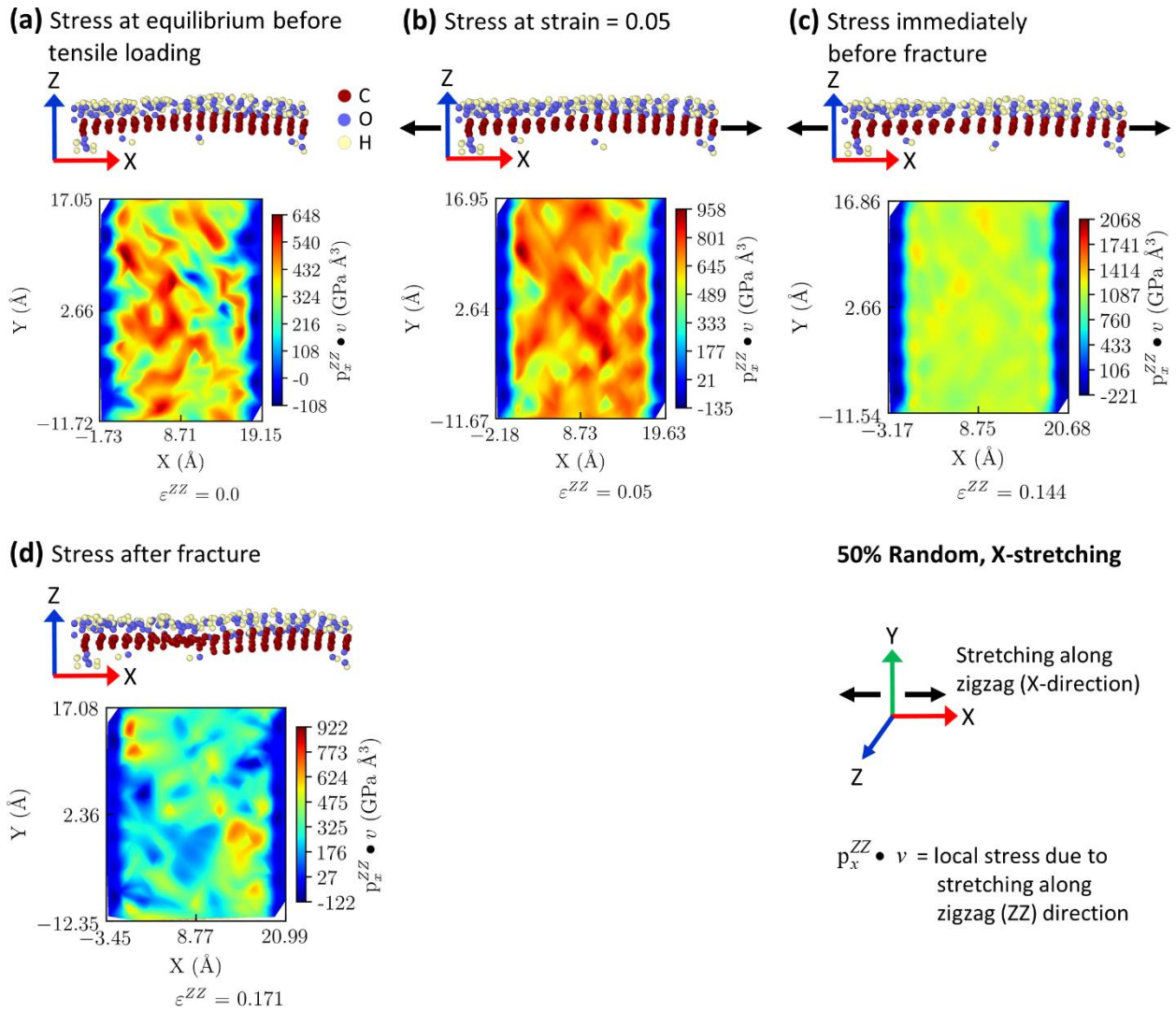


Figure 3.7. Internal local stress distribution (component of the stress parallel to the load) during tensile loading along the zigzag direction in the graphene sheet with 50% hydroxyl coverage in random arrangement: (a) after relaxation to equilibrium before tensile loading (unstrained conditions), (b) and (c) as a function of increasing tensile strain, and (d) at fracture.

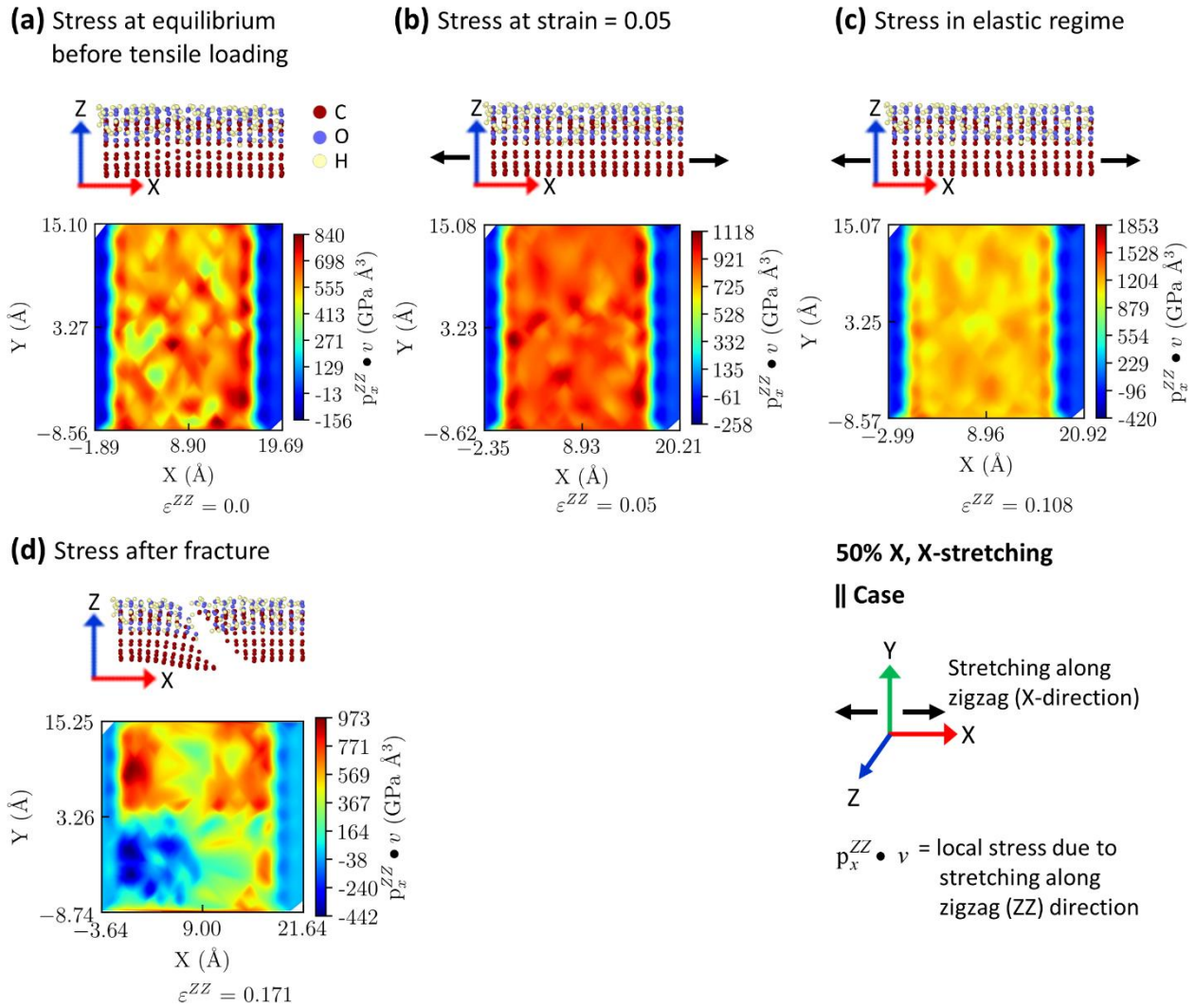


Figure 3.8. Internal local stress distribution (component of the stress parallel to the load) during tensile loading along the zigzag (ZZ) direction in the graphene sheet with 50% hydroxyl coverage arranged in an in-line pattern along the ZZ-direction (||, parallel to the tensile loading direction): (a) after relaxation to equilibrium before tensile loading (unstrained conditions), and (b), (c), and (d) as a function of increasing tensile strain, showing stages of rapidly increasing stress (elongation) and fracture.

3.3.2. Stress-strain responses

3.3.2.1. Uniaxial tensile loading

The tensile stress-strain evolution of –OH functionalized GS (Figure 3.9) not only depended on the percentage of –OH groups but also on their spatial distribution on the surface (i.e., random versus line pattern arrangements) and the applied tensile strain direction (i.e.,

armchair versus zigzag). In all cases, fracture tensile stresses decreased with increasing –OH coverage, and greater fracture tensile stresses were attained for applied tensile strains along the zigzag direction compared to the armchair direction, which was in good agreement with previous studies of functionalized graphene from the literature [7-9]. The zigzag direction of a GS is more stretchable than the armchair direction because of the different bonding arrangements of the hexagonal graphene lattice and differences in bond deformation in the zigzag direction. Whereas, for loading in the armchair direction, the bonds parallel to the tension direction (type I) elongate with increasing strain and break earlier. The results for the pristine GS (without functionalization) also showed good agreement with atomistic studies reported in the literature [153] in the two perpendicular directions (i.e., zigzag and armchair) and showed good agreement with experimental values (see Table A7 for a comparison with atomistic and experimental studies). The fracture stress of the GS was 49.6 Nm^{-1} (148 GPa) along the zigzag direction and 33.4 Nm^{-1} (99.7 GPa) along the armchair direction, which compared well with experimental values that range from 120-140 GPa [154]; the fracture strain was 0.29 along the zigzag direction and 0.19 along the armchair direction, which compared well with the experimental value of 0.25 [154].

The stress-strain evolution of FGS was strongly affected by the initial functionalization induced bending deformation of the FGS and the direction of the applied tensile strain with respect to the direction of the line patterns (parallel versus perpendicular). For –OH line patterns along the zigzag direction, zigzag loading was able to withstand higher stresses than armchair loading (up to 60% at an –OH percentage of 75%) and higher stresses compared to the random functionalization, while armchair loading was able to withstand greater strains than zigzag loading and greater strains compared to the random functionalization (Figure 3.9 and Figure 3.10). For –OH line patterns along the armchair direction, zigzag loading was able to withstand greater strains (up to 50% at –OH percentages of 50% and 75%) than armchair loading and greater strains compared to the random functionalization arrangement at –OH percentages of 25%, 50%, and 75%.

Two different stress-strain behaviors could be observed with line pattern functionalization depending on the direction of the strain. When the tensile strain direction and –OH line patterns were perpendicular to each other (\perp , perpendicular case), the FGS showed an

R-curve behavior for 25%, 50%, and 75% –OH functionalization with an initial minimal stress development for large strains (toe region) as a result of the gradual de-wrinkling and flattening (loss of curvature) of the FGS, followed by a rapidly increasing stress with increasing strain (elastic region) corresponding to the stretching and elongation of the FGS. This R-curve behavior was not observed for 12% –OH functionalization as the initial bending deformation of the FGS was relatively negligible for that percent coverage (Table 3.1). In contrast, when the strain direction and –OH line patterns were parallel (\parallel , parallel case), the stress-strain curve conformed with typical nonlinear stress-strain curve behavior and corresponded to the stretching and elongation (with no flattening) of the FGS in the direction transverse to the curvature. In addition, in the parallel case, greater stresses developed for line patterns along the zigzag direction (Figure 3.9c and Figure 3.9f) while in the perpendicular case, greater stresses developed for line patterns along the armchair direction (Figure 3.9d and Figure 3.9e).

GS functionalized with –OH line pattern arrangements sustained greater fracture strains in the direction perpendicular to the line patterns at –OH percentages greater than 25% but similar or lower fracture stresses than the GS functionalized with random arrangements (Figure 3.10). The greater fracture strains resulted from the gradual de-wrinkling and flattening of the FGS and were correlated with the amplitude of the initial bending deformation seen with increasing –OH coverage. During the gradual de-wrinkling and flattening of the FGS, the initial applied tensile strain did not cause much stress in the FGS structure and the C–C bonds started to elongate at a much higher strain, resulting in a failure bond energy being reached at a higher strain. In contrast, when the applied tensile strains were in the same direction as the –OH line patterns (\parallel , parallel case), FGS sustained greater stresses before failure for the zigzag direction in comparison to the stresses observed for the randomly functionalized GS. This was not the case for the armchair direction which exhibited similar stresses before failure to the randomly functionalized GS. This was consistent with the greater stretchability of graphene in the zigzag direction than the armchair direction.

These results clearly demonstrated the effect of the initial functionalization induced deformation and the dependence between the direction of the –OH line pattern arrangement and the loading direction. When the –OH line patterns were parallel to the applied tensile strain, the mechanism of fracture was the result of bond stretching and breaking of the graphene lattice,

similar to that of graphene without functionalization but at lower stresses and strains. When the OH line patterns were perpendicular to the applied tensile strain, the mechanism of fracture was related to the amplitude and wavelength of the initial bending deformation of the functionalized graphene and was the result of the gradual flattening of the functionalized graphene involving minimal stress followed by the stretching and breaking of the graphene lattice, thus resulting in greater sustained tensile fracture strains than for the random functionalization and in some cases the pristine graphene.

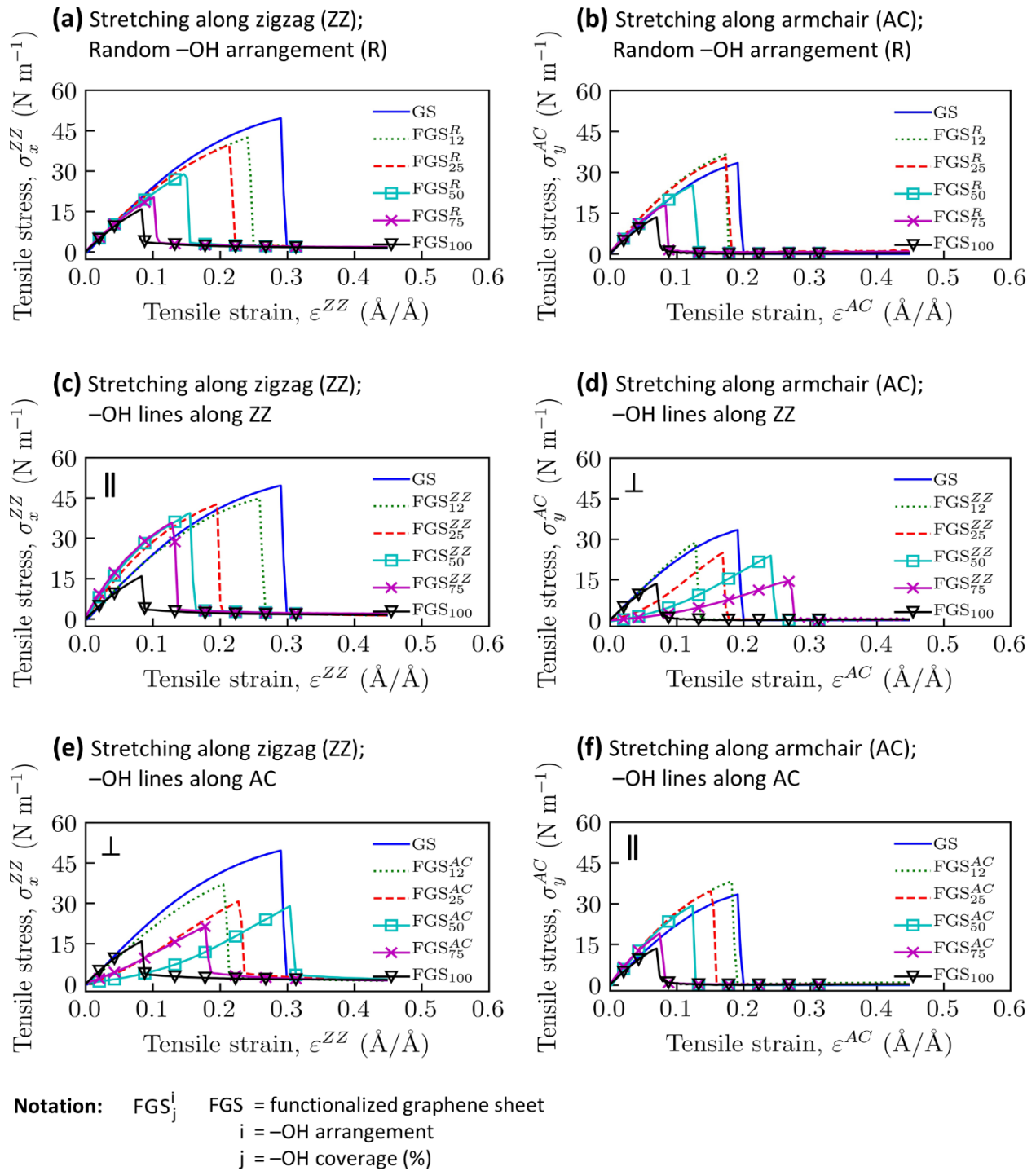
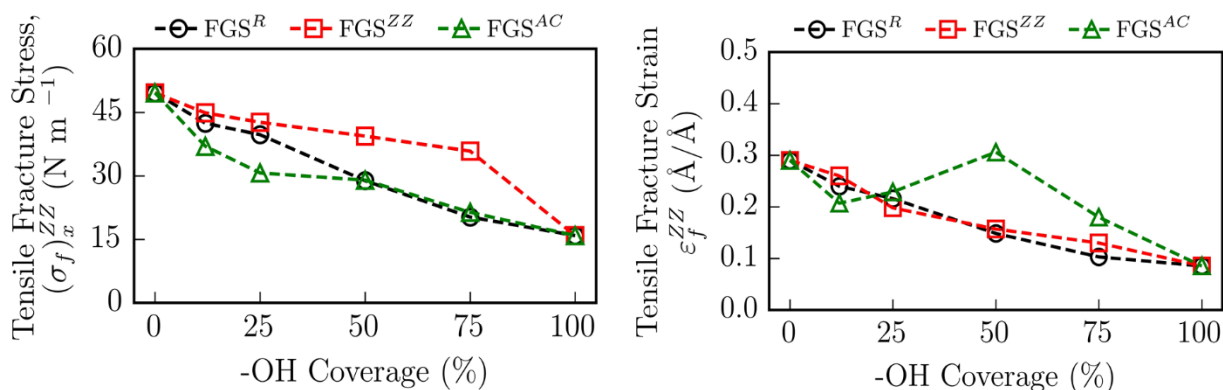
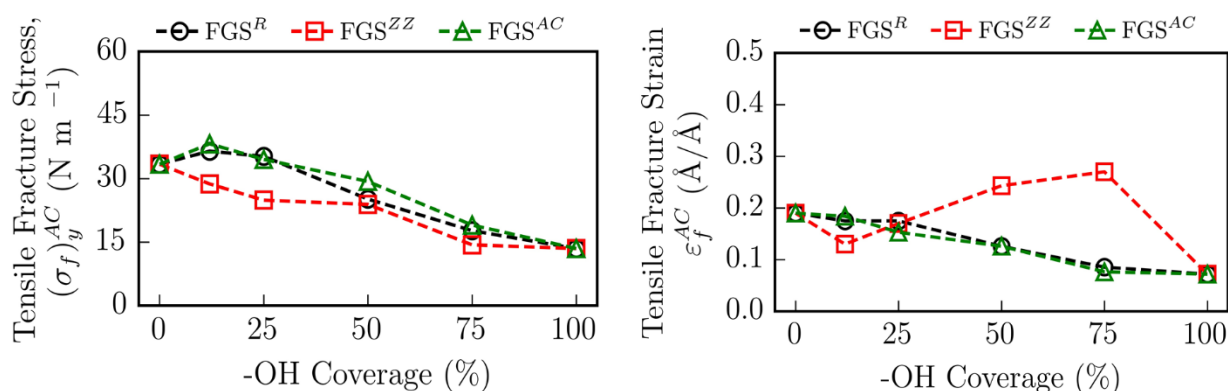


Figure 3.9. Stress-strain response for graphene sheets (GS) under tensile loading along the zigzag direction [(a), (c), and (e)] and tensile loading along the armchair direction [(b), (d), and (f)] as a function of -OH surface coverage (0, 12, 25, 50, 75, and 100%) and spatial distribution (random and in-line pattern arrangements along the zigzag and armchair directions). [R: random; ZZ: line patterns along zigzag; AC: line patterns along armchair].

(a) Stretching along zigzag (ZZ)



(b) Stretching along armchair (AC)



Notation: FGSⁱ FGS = functionalized graphene sheet
i = -OH arrangement

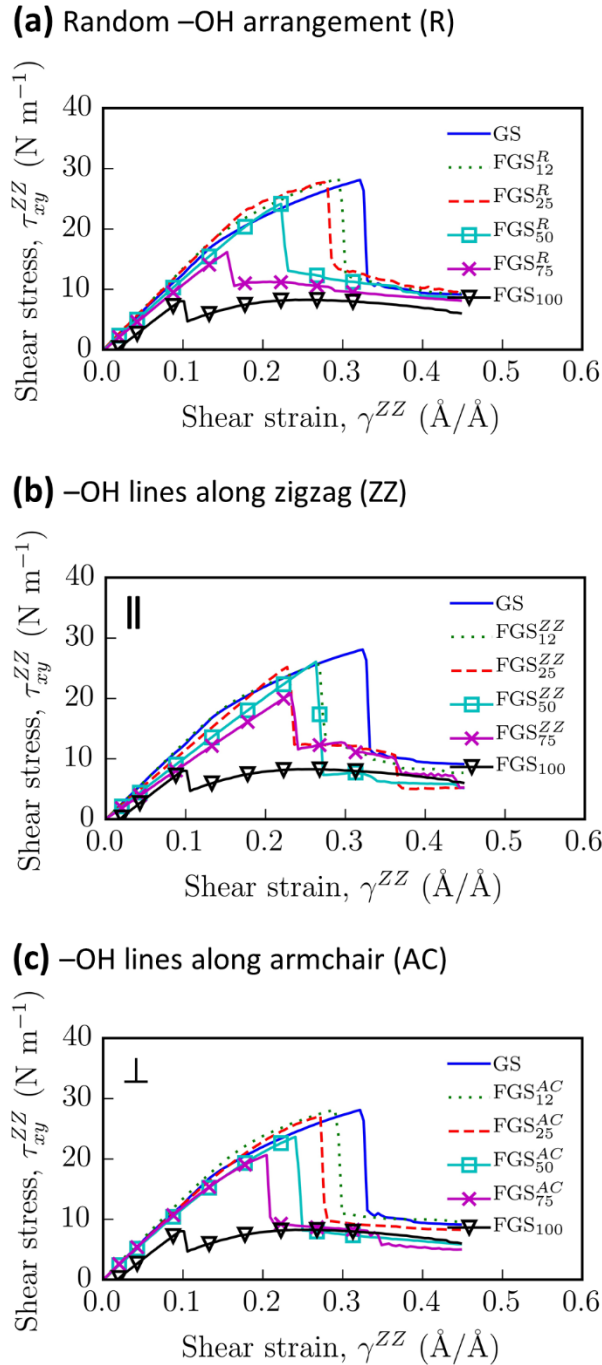
Figure 3.10. Tensile fracture stress and strain as a function of tensile loading direction and -OH surface coverage. (a) fracture stress and strain for tensile loading along the zigzag direction and (b) fracture stress and strain for tensile loading along the armchair direction. [R: random; ZZ: line patterns along zigzag; AC: line patterns along armchair].

3.3.2.2. Shear loading along zigzag direction

Only shear deformations along the zigzag direction were examined. Similar behaviors were expected for shear deformation along the armchair direction but with lower fracture shear stresses and strains as previously reported in the literature for pristine graphene [74] because of the lower stretching capacity of the graphene lattice in that direction. In all cases, a large amount of residual shear stress existed in the GS systems post fracture (Figure 3.11), which was not seen post-tensile fracture. During shear, the angle bending of the \angle C-C-C angles and torsional

deformation of the C–C–C–C dihedral angles were more prominent post failure for the GS lattice. Furthermore, a significant reduction in shear stress and strain was seen for 100% –OH coverage, as a result of the weakening of the graphene lattice due to the change in carbon hybridization from sp^2 to sp^3 with the attachment of the –OH groups. The pristine GS and randomly functionalized GS with 12% and 25% –OH coverage displayed out-of-plane bending (wrinkles) during shear deformation along the zigzag direction to release the strain energy and reach a low energy configuration (Figure 3.12). Out-of-plane bending during shear deformation was not observed at higher –OH percentages with random arrangements as fracturing was then more favorable to release stress than deformation. Out-of-plane bending was also not observed for the FGS with line pattern arrangements because of their initial out-of-plane bending configuration prior to shear loading.

The response to shear deformation of the FGS was influenced by the direction of the –OH line patterns with respect to the shear direction and the percentage of –OH coverage (Figure 3.13). When the –OH line patterns were perpendicular to the shear deformation (line patterns along the armchair direction; Figure 3.11c), the shear fracture stresses and strains steadily decreased with increasing –OH coverage and showed a non-linear response similar to that observed for graphene without functionalization and with random functionalization (Figure 3.11a). The initial stress distribution in the FGS created by the initial bending deformation induced by the functionalization was relatively uniform perpendicular to the shear deformation throughout the surface of the FGS, similar to the GS without functionalization and with random functionalization, thus resulting in a similar shear deformation response. In contrast, when the –OH line patterns were parallel to the shear deformation (line patterns along the zigzag direction; Figure 3.11b), a linear shear stress-strain response was observed for –OH coverage of 25%, 50%, and 75%, with the shear fracture stresses and strains that became independent of the –OH coverage (i.e., no significant change in shear fracture stresses and strains with increasing –OH coverage). The FGS failed during the elastic deformation stage as a result of the presence of two distinct stress distribution zones on the FGS surface corresponding to sp^2 and sp^3 hybridization zones that were parallel to the shear deformation and resulted in a brittle failure.



Notation: FGS_j^i FGS = functionalized graphene sheet
 i = –OH arrangement
 j = –OH coverage (%)

Figure 3.11. Shear stress-strain evolution for graphene sheets under shear deformation along the zigzag direction as a function of hydroxyl coverage (0, 12, 25, 50, 75, and 100%) for (a) random distribution, (b) line pattern arrangements along the zigzag direction, and (c) line pattern arrangements along the armchair direction.

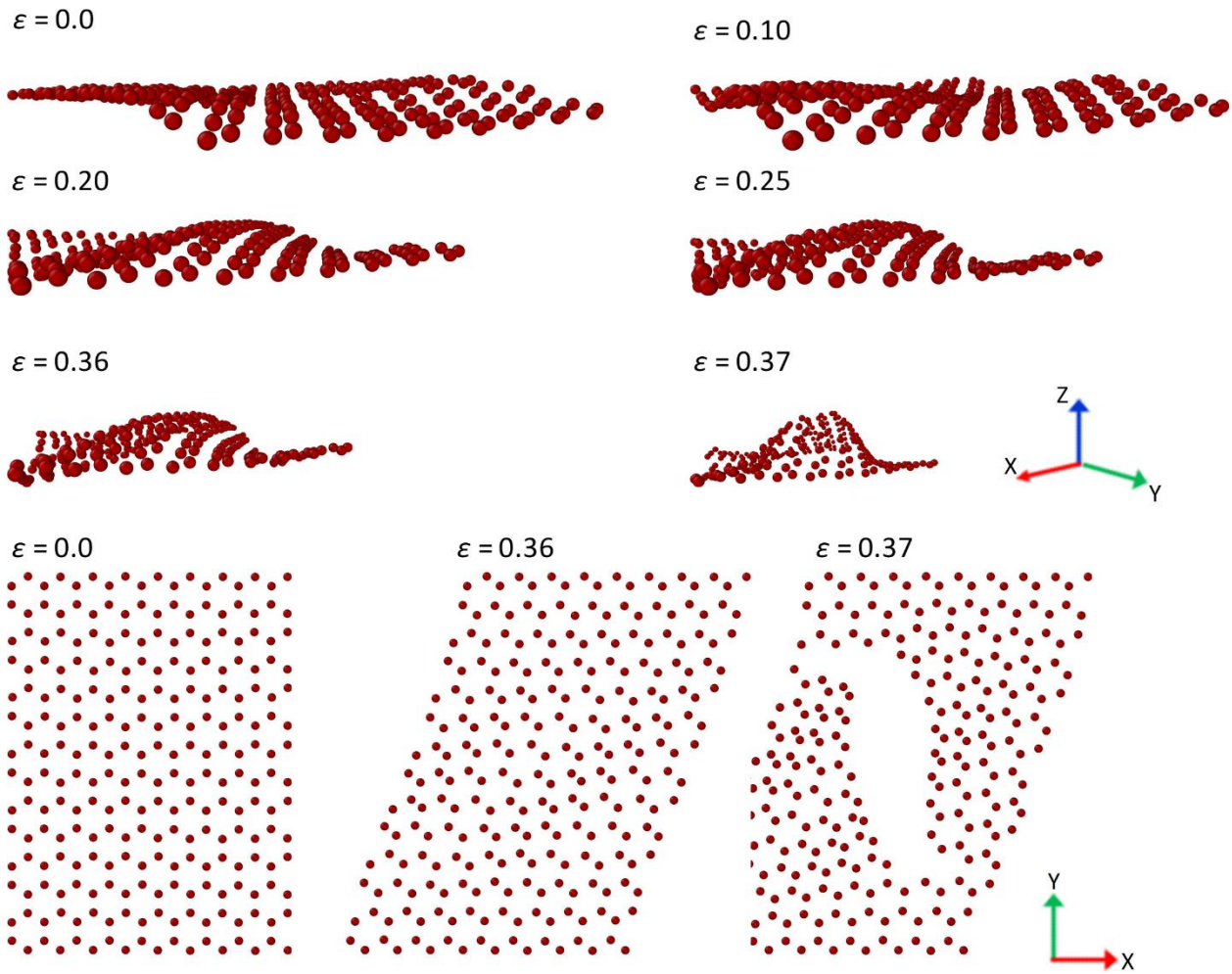
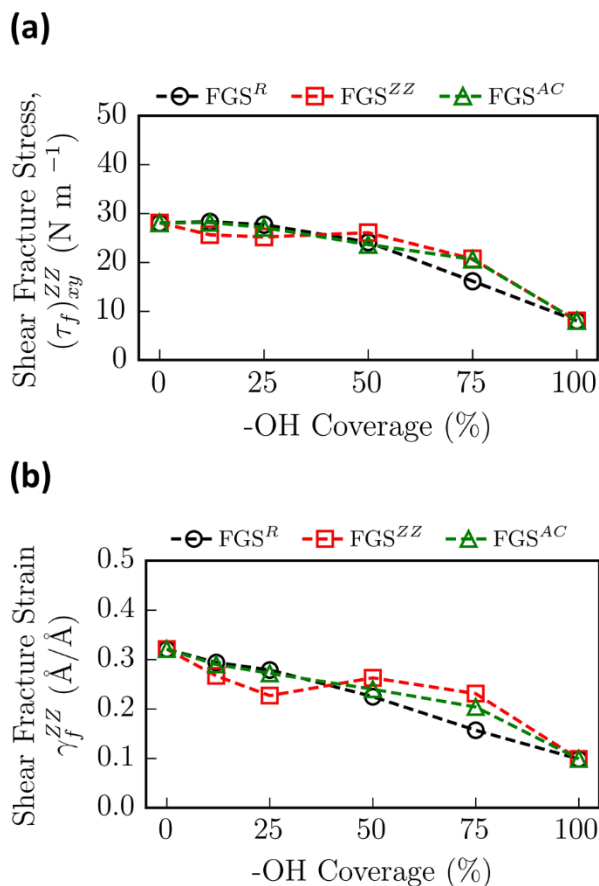


Figure 3.12. Development of wrinkles in the pristine graphene sheet as a function of strain up to fracture during shear deformation along the zigzag direction.



Notation: FGSⁱ FGS = functionalized graphene sheet
i = -OH arrangement

Figure 3.13. (a) Shear fracture stress and (b) shear fracture strain of graphene systems as a function of -OH surface coverage for different spatial distributions. [R: random; ZZ: line patterns along zigzag; AC: line patterns along armchair].

3.3.2.3. Potential energy changes during tensile and shear loadings

The potential energy and relative contributions of the bond-stretching energy, angle-bending, and torsional energy (dihedral angles) provided further insights into the microscopic mechanisms that occurred during tensile and shear loadings of the GS and FGS with clustered -OH line pattern functionalization (Figure 3.14, Figure 3.15, and Appendix A). The variation of potential energy (per atom on average) during tensile loading followed a trend similar to the stress evolution as a function of strain (Figure 3.14a and Appendix A6.1) for tensile loading along the zigzag and armchair directions, respectively) and was predominantly the result of the increase in bond energy (Figure 3.14b and Appendix A6.2). Similar to the fracture tensile stress,

the potential energy at maximum stress decreased with increasing –OH coverage. This was consistent with the decrease in the number of sp^2 and the increase in the number of sp^3 hybridized carbon atoms due to the attachment of –OH groups. Greater energy was required to break the double bond of sp^2 hybridized C atoms. When the tensile loading was perpendicular to the line pattern direction (\perp , perpendicular case), the potential energy (and thus bond energy) of the FGS remained initially close to zero as the strain increased, indicating that no stretching of the C bonds occurred, in agreement with the gradual flattening of the FGS. Subsequently, the potential energy (bond energy) increased rapidly up to fracture as a result of the elongation of the C bonds during stretching. When the tensile loading was parallel to the line pattern direction (\parallel , parallel case), the potential energy (bond energy) increased rapidly as the strain increased as a result of bond elongation until fracture. The flattening of the FGS in the perpendicular case resulted in failure bond energies that were reached at higher strains than for the parallel case. The angle bending energy evolution as a function of tensile strain further indicated that the $\angle C-C-C$ angles were stiffer for the line patterns along the zigzag direction and more compliant for the line patterns along the armchair direction.

In contrast to tensile loading, for shear loading, the angle-bending and torsional energies contributed significantly more to the potential energy than the bond energy (Figure 3.15). The potential energy due to shear along the zigzag direction was greater when the line patterns were oriented along the armchair direction than along the zigzag direction. The –OH line patterns oriented along the zigzag direction created a weak zone where the bonds were easier to twist and distort as a result of sp^3 hybridization, thus leading to brittle fracture. During shear loading, the stress was the result of an interplay between changes in the C–C bond length, bending of the $\angle C-C-C$ angles, and torsional deformations of the C–C–C–C, thus resulting in greater fracture strains than for tensile loading.

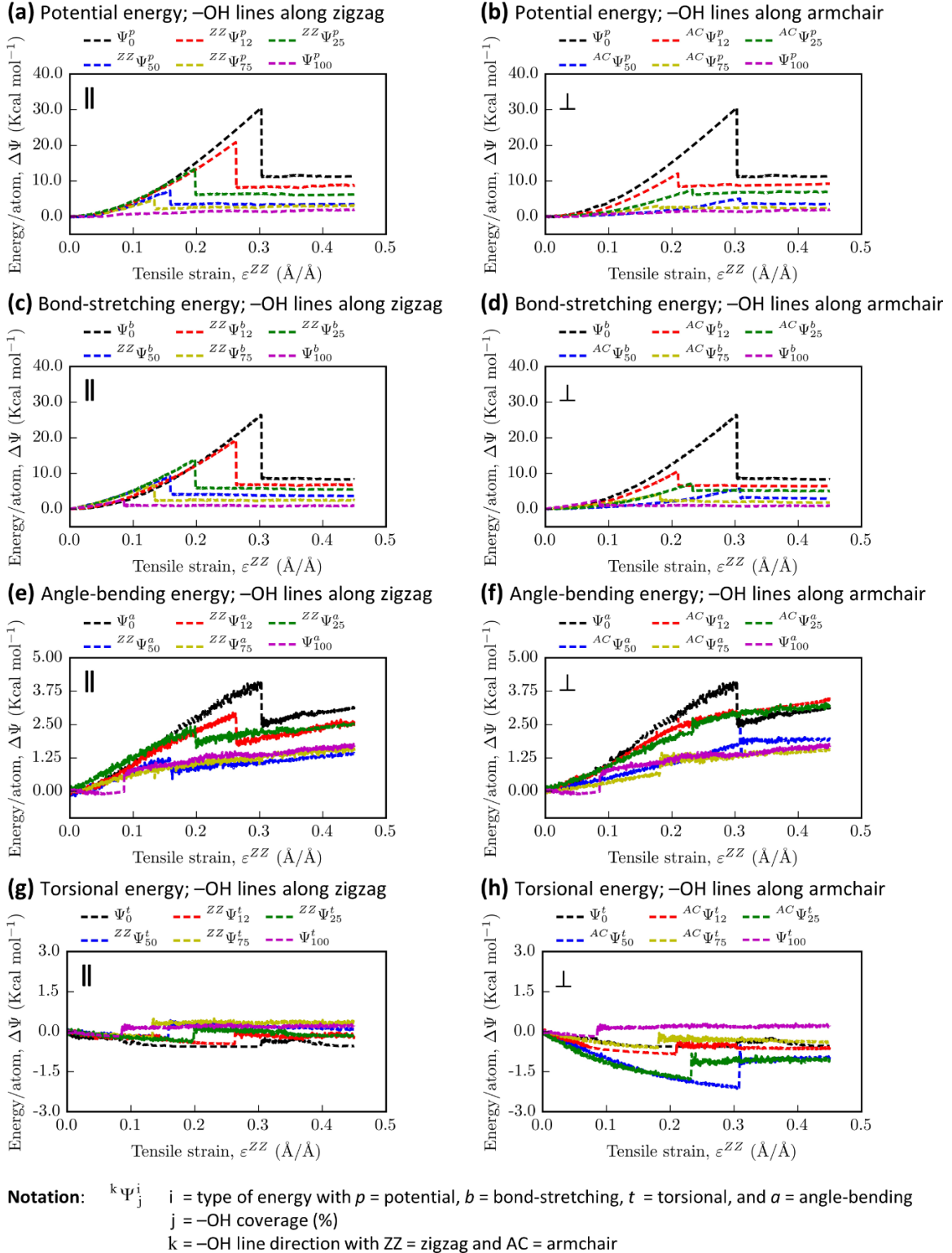


Figure 3.14. Energy changes as a function of strain for tensile loading along the zigzag (ZZ) direction: (a), (b) potential energy (per atom on average); (c), (d) bond-stretching energy; (e), (f) angle-bending energy; and (g), (h) torsional energy (dihedral angles) for line patterns along the zigzag and armchair directions, respectively.

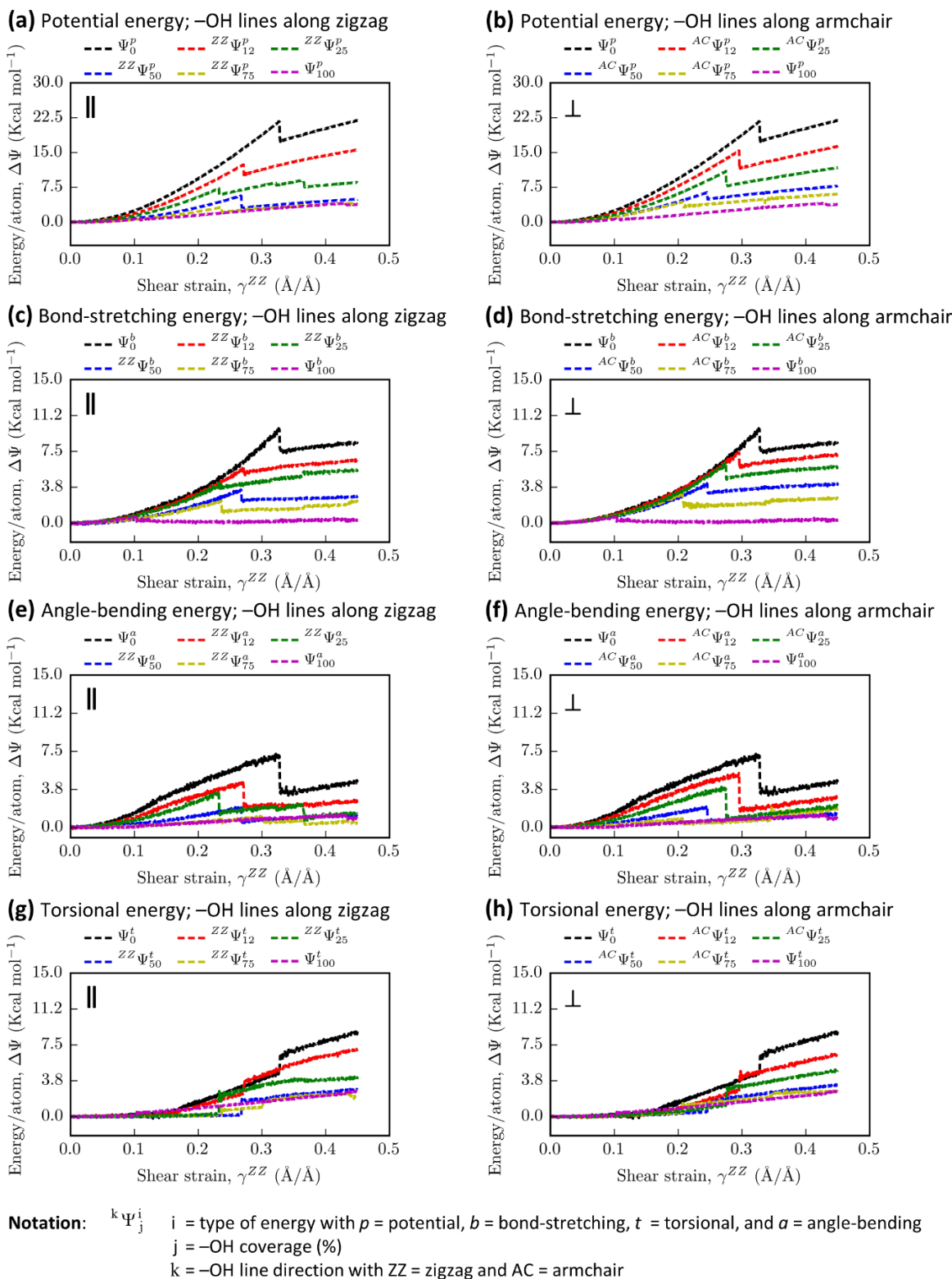


Figure 3.15. Energy changes as a function of strain for shear loading along the zigzag (ZZ) direction: (a), (b) potential energy (per atom on average); (c), (d) bond-stretching energy; (e), (f) angle-bending energy; and (g), (h) torsional energy (dihedral angles) for line patterns along the zigzag and armchair directions, respectively.

3.3.3. Strain energy density

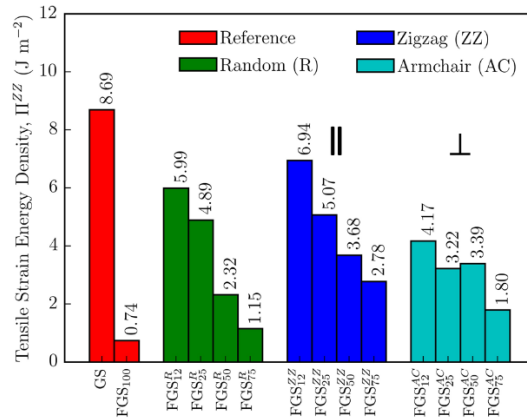
The fracture toughness of graphene is an important property that has been measured experimentally only recently [152] and the brittleness and low fracture toughness of graphene is an area of concern. While the present study was carried out on graphene without cracks, the strain energy density provided important insights into the effect of –OH coverage and spatial arrangement of the –OH groups on the toughness of the FGS. The strain energy density of the GS (Figure 3.16) showed a sharp drop for full –OH coverage (92% and 89% decrease for tensile loading along zigzag and armchair, respectively, and 76% decrease for shear loading), indicating a significant reduction in the material's resistance to fracture (i.e., toughness). The fully –OH functionalized GS showed a greater resistance to fracture under shear deformation (strain energy density *ca.* 2.5 times greater) than under tensile loading contrary to the pristine GS for which the tensile strain energy density was greater than that of the shear deformation. The strain energy densities under tensile loading along the zigzag direction were greater than those under tensile loading along the armchair direction, in agreement with the greater stretching capacity of the graphene lattice in the zigzag direction. However, with increasing –OH percentage, the directional loading dependency of the tensile strain energy diminished (35% difference for pristine GS between zigzag and armchair loading versus only 9% for FGS with full –OH coverage).

The spatial arrangement of the –OH groups on the GS surface (random versus line patterns oriented along zigzag and line patterns oriented along armchair) influenced the strain energy density (and thus toughness) of the FGS. FGS with –OH line pattern arrangement exhibited a lower decrease in tensile and shear strain energy density with increasing –OH percentage than the FGS with random arrangement. A dependence between the direction of the –OH line pattern arrangement and the loading direction on the strain energy stored was seen. This dependence of the toughness was the result of the initial functionalization induced topology changes that provided the FGS with a bending deformation perpendicular to the direction of the line patterns. For tensile loading, the FGS showed a greater toughness when the –OH line patterns and the tensile loading directions were parallel. In that case, the FGS was stretched and elongated with minimal topological change (no flattening of the FGS) and the strain energy density decreased gradually with increasing –OH coverage. The stiffening of the $\angle C-C-C$ angles observed for the –OH line patterns parallel to the loading direction provided a toughening

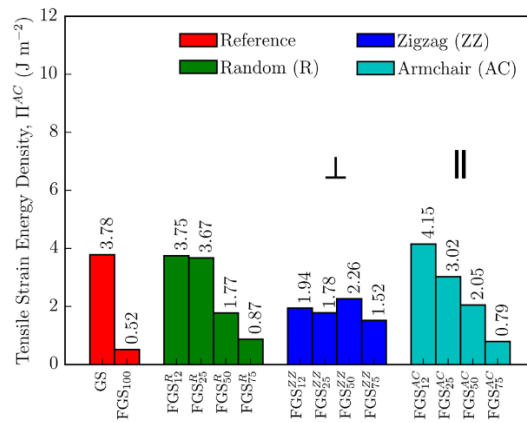
mechanism, resulting in a greater toughness compared to the corresponding –OH random arrangement. When the –OH line patterns and the tensile loading directions were perpendicular, the strain energy density appeared mostly insensitive to the –OH coverage, in particular for the –OH line patterns along the zigzag direction as a result of the unfolding of the FGS. The unfolding of the FGS delayed the occurrence of fracture and provided to some extent a mechanism for energy dissipation and thus greater toughness than the corresponding –OH random arrangement at 50% and 75% –OH coverages. Enhancement of the graphene toughness through wrinkled configurations and controlled distributions of topological defects has been previously reported in the literature [155].

In contrast, for shear loading along the zigzag direction, overall a greater toughness was observed at 12% and 25% –OH coverages when the –OH line patterns were perpendicular to the shear deformation. Indeed, when the –OH line patterns were parallel to the shear deformation (along the zigzag direction in this case), brittle fracture was observed.

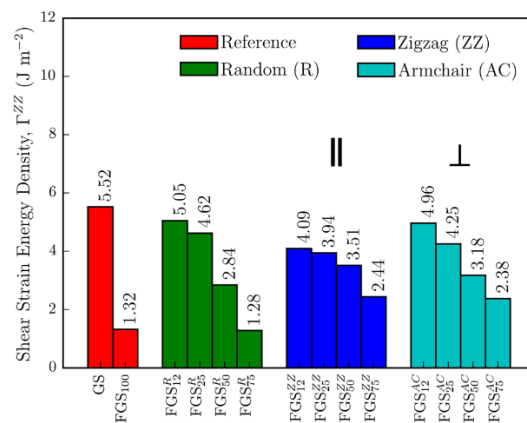
(a) Stretching along zigzag (ZZ)



(b) Stretching along armchair (AC)



(c) Shear along zigzag (ZZ) in XY plane



Notation: FGS_jⁱ FGS = functionalized graphene sheet
 i = -OH arrangement
 j = -OH coverage (%)

Figure 3.16. Strain energy density of the FGS systems for (a) tensile strain in zigzag direction, (b) tensile strain in armchair direction, and (c) shear strain in zigzag direction.

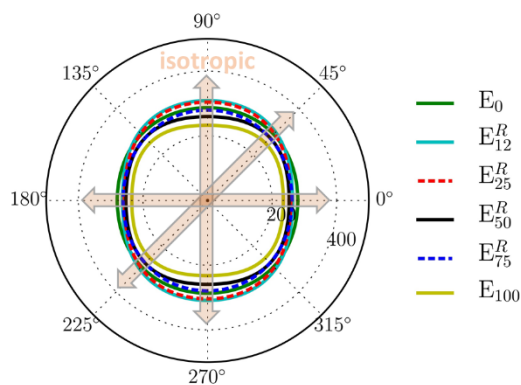
3.3.4. Elastic moduli, shear moduli, and linear compressibility

Line patterned functionalization affected the elastic behavior of the FGS and led to strong elastic anisotropy of the stress flow as seen by the strong deviation from the circular shape of the directional elastic modulus (Figure 3.17). The observed elastic anisotropy was the result of the initial, functionalization induced bending deformation and the associated initial internal local stress distributions. For the random –OH group arrangement, the elastic moduli were overall, relatively insensitive to the increase in –OH coverage and showed similar values (*ca.* 280-310 Nm^{-1}) in all directions, indicating that the FGS with random arrangement was elastically quasi-isotropic. This result agreed with data from atomistic studies reported in the literature in the two perpendicular directions (i.e., zigzag and armchair) for pristine and hydrogenated graphene [7, 73, 153, 156-159]. The elastic modulus of the pristine GS was 838 GPa (280 N m^{-1} ; zigzag direction) and 856 GPa (287 N m^{-1} ; armchair direction), which compared well overall with values from atomistic studies that range from 600-1100 GPa (zigzag and armchair) [7, 156, 160-167] as well as with experimental values reported in the literature from nanoindentation and Raman spectroscopy that range from 900-2400 GPa [154, 168, 169] (see Table A7 for a comparison with atomistic and experimental studies). In addition, the elastic modulus of the FGS with 100% –OH coverage was 700 GPa (234.6 N m^{-1} ; zigzag direction) and 694 GPa (232.4 N m^{-1} ; armchair direction) and agreed well with the simulated result of 720 GPa (zigzag direction) that has been reported in the literature for fully –OH functionalized graphene [73].

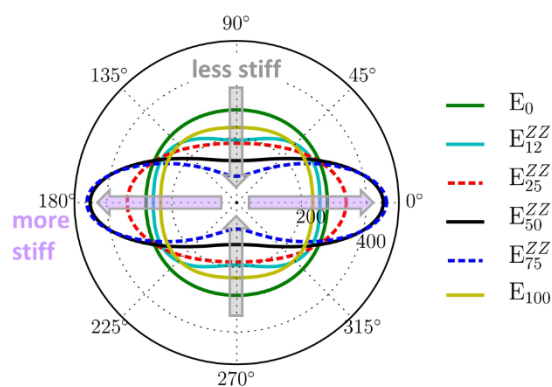
In contrast with the random –OH group arrangement, for the line pattern arrangements, elastic anisotropy was observed with differing effects seen on the elastic moduli, depending on the direction of the line patterns with respect to the loading direction. It was clearly visible that the elastic modulus of the FGS was very anisotropic, with greater-value lobes in the direction parallel to the line patterns compared to the perpendicular direction (Figure 3.17b and Figure 3.17c). When the line patterns and the loading direction were parallel (\parallel , parallel case), the elastic moduli increased with increasing –OH percentage up to 50% –OH coverage and either reached a plateau (line patterns and loading along the zigzag direction; Figure 3.18b) or slightly decreased (line patterns and loading along the armchair direction; Figure 3.18c). When the line patterns and the loading direction were perpendicular (\perp , perpendicular case), the elastic moduli decreased with increasing –OH percentage up to 50% –OH coverage for the line patterns in the

armchair direction (Figure 3.18c) and 75% for the line patterns in the zigzag direction (Figure 3.18b). The perpendicular case resulted in the lowest elastic moduli values (lowest stiffness). These results further indicated that the stiffness of the FGS increased with increasing –OH percentages in the direction parallel to the line patterns while the FGS became more compliant in the direction perpendicular to the line patterns. The stiff direction thus corresponded to the direction of the line patterns of –OH functionalization, while the more compliant direction corresponded to the direction of the curvature and represented the “breathing” mode of deformation (expansion and contraction) for the FGS. During stretching along the direction parallel to the line patterns, the stress could be released through the flattening or curling of the FGS along the direction of the curvature without significantly stretching the carbon bonds. The sp^3 bonds exerted a strengthening influence in the direction parallel to the line patterns and a softening in the perpendicular direction. Greater stiffness and greater compliance in the transverse direction were developed when the line patterns were along the zigzag direction compared to along the armchair direction. The greatest anisotropy as indicated by the ratio between the maximum value of the elastic modulus in the stiffest direction to the minimal elastic modulus was reached at 75% –OH coverage for the line patterns along the zigzag direction while the ratio was the greatest at 50% –OH coverage for the line patterns along the armchair direction (Figure 3.17b and Figure 3.17c).

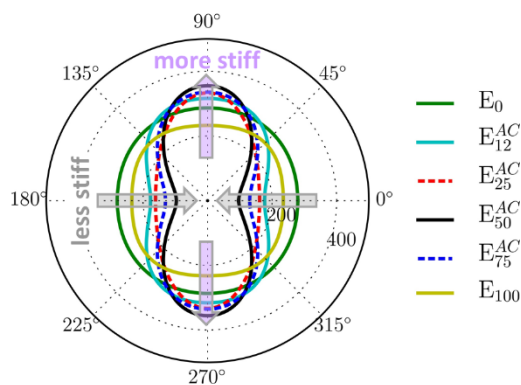
(a) Random –OH arrangement (R)



(b) –OH lines along zigzag (ZZ)



(c) –OH lines along armchair (AC)



Notation: E_j^i E = elastic modulus (N m^{-1})
 i = –OH arrangement
 j = –OH coverage

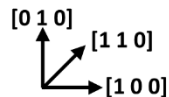
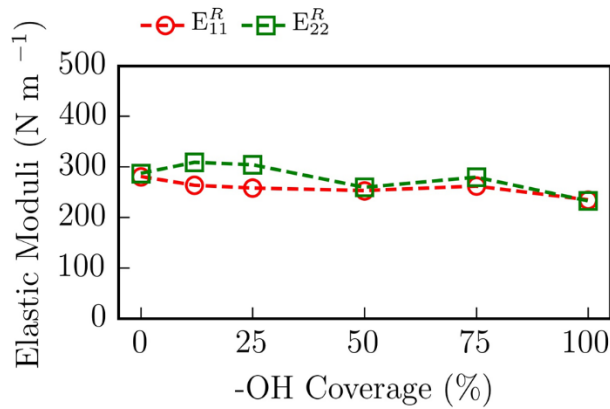
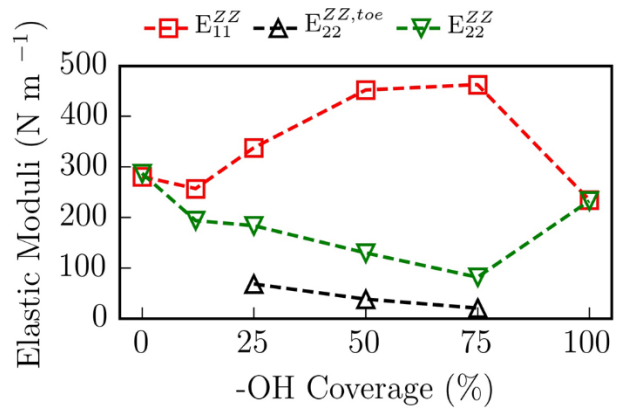


Figure 3.17. Directional elastic modulus (N m^{-1}) for (a) random –OH arrangement (R), (b) –OH line patterns along the zigzag direction (ZZ), and (c) –OH line patterns along the armchair direction (AC).

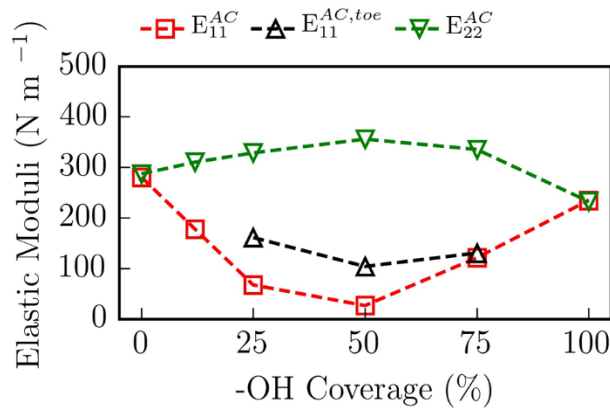
(a) Random -OH arrangement (R)



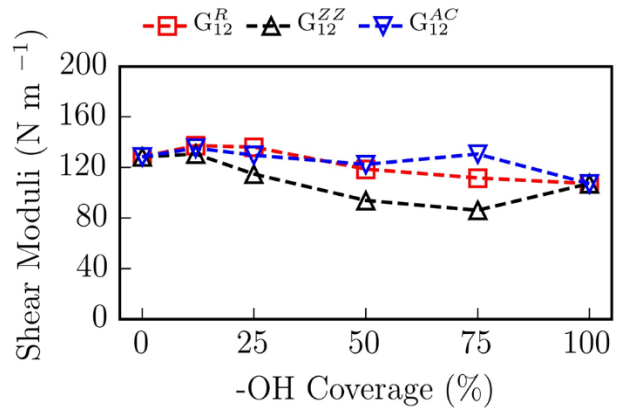
(b) -OH lines along zigzag (ZZ)



(c) -OH lines along armchair (AC)



(d) Shear along zigzag (ZZ)



Notation: E_j^i i = -OH arrangement
 j = stretching directions (11 is along X-direction, 22 is along Y-direction)

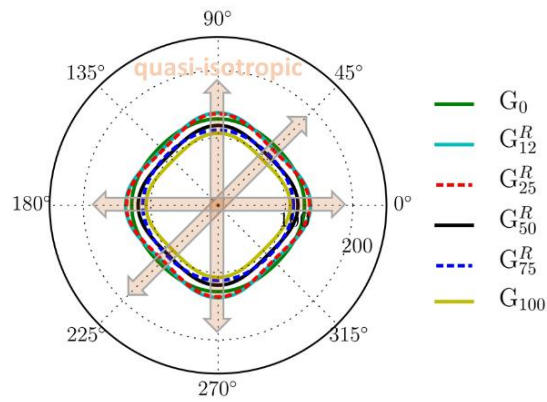
G_n^m m = -OH arrangement
 n = shearing directions (12 is along X-direction of XY-plane)

Figure 3.18. Elastic moduli for applied tensile load in zigzag (E_{11}) and armchair (E_{22}) directions for (a) random -OH arrangement (R), (b) -OH line patterns along the zigzag direction (ZZ), and (c) -OH line patterns along the armchair direction (AC). Elastic moduli shown also for the toe region for the perpendicular cases. (d) Shear moduli (G_{12}) for applied load in zigzag direction.

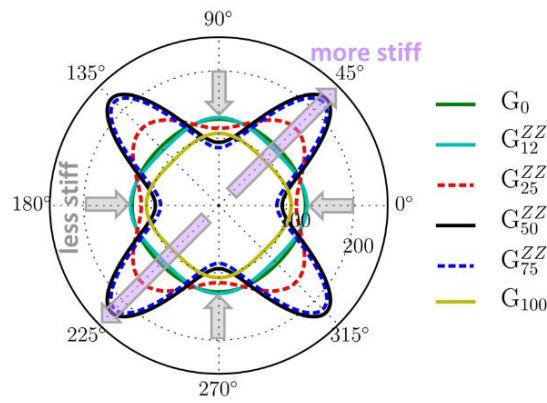
Like for the elastic modulus, the shear modulus showed strong anisotropy for the functionalization with the line pattern arrangements (Figure 3.19). The occurrence of anisotropy for the shear modulus was, however, along different directions than for the elastic modulus. The resistance to shear was the greatest (high value lobes) in the $45-225^\circ$ and $135-315^\circ$ (i.e., $\langle 1\ 1\ 0 \rangle$ family) directions for the line patterns along the zigzag direction while it was the lowest in those

directions for the line patterns along the armchair direction. For the line patterns along the zigzag direction, the shear stiffness in the $\langle 1\ 1\ 0 \rangle$ family of directions increased with increasing $-OH$ percentages. In contrast, for the line patterns along the armchair direction, the shear stiffness decreased in the $\langle 1\ 1\ 0 \rangle$ family of directions with increasing $-OH$ percentages. The resistance to shear loading along the zigzag direction (Figure 3.18d) was greater for the line patterns along the armchair direction (i.e., perpendicular to shear loading) than along the zigzag direction (parallel to shear loading). Additionally, the highest and lowest elastic modulus corresponded to the lowest shear resistance for the line patterns along the zigzag direction, while to the highest shear resistance for the line pattern along the armchair direction. The directional shear modulus furthermore provided information on the bonding directionality. The bond strength increased along the $\langle 1\ 1\ 0 \rangle$ family of directions with increasing $-OH$ percentages for the line patterns along the zigzag directions while it decreased for the line patterns along the armchair directions. All the above discussions indicated that the FGS with line pattern functionalization was elastically highly asymmetric.

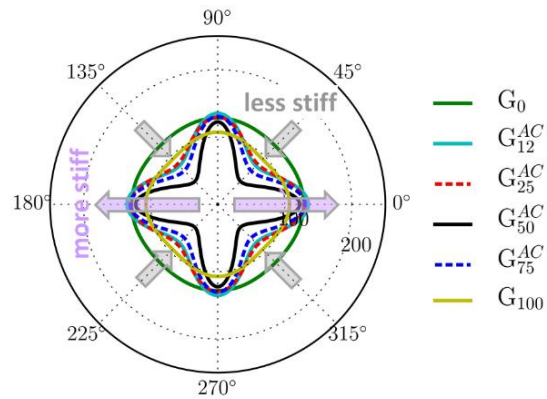
(a) Random -OH arrangement (R)



(b) -OH lines along zigzag (ZZ)



(c) -OH lines along armchair (AC)



Notation: G_j^i G = shear modulus (N m^{-1})
 i = -OH arrangement
 j = -OH coverage

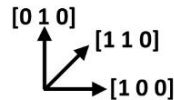
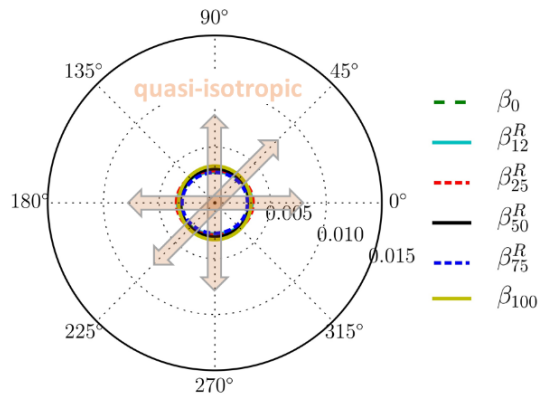


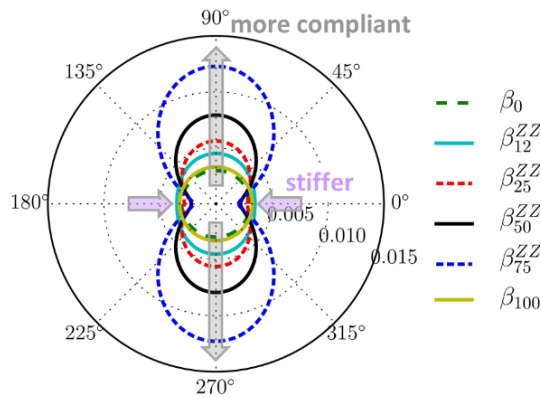
Figure 3.19. Directional shear modulus (N m^{-1}) for (a) random -OH arrangement (R), (b) -OH line patterns along the zigzag direction (ZZ), and (c) -OH line patterns along the armchair direction (AC).

Similar to the elastic moduli, there was no significant spatial dependence and no significant difference in magnitude of the linear compressibility for the pristine GS and all of the FGS with random arrangements of –OH functionalization (Figure 3.20a). In contrast, significant spatial anisotropy was apparent for the clustered line pattern arrangements (Figure 3.20b, c), with much greater compressibility of the FGS seen in the direction perpendicular to the line patterns and slightly reduced compressibility in the direction parallel to the line patterns. This behavior correlated with the direction of the initial functionalization induced bending deformation of the FGS that was also perpendicular to the direction of the line pattern arrangements and thus provided a greater ability for the FGS to deform under loading in that direction. The FGS acted similar to a nanoscale mechanical spring. When the line patterns were oriented along the zigzag direction, the armchair direction of the graphene lattice was the most compressible and the zigzag direction the least compressible as shown from the high-value lobes along the 90° and 270° axis (Figure 3.20b). When the line patterns were oriented along the armchair direction, the zigzag direction of the graphene lattice was then the most compressible and the armchair direction the least compressible as shown from the high-value lobes along the 0° and 180° axis (Figure 3.20c). The compressibility in the direction perpendicular to the line patterns increased by as much 400% relative to the pristine GS for 75% –OH coverage with line patterns along the zigzag direction and by as much as 300% for 50% –OH coverage with line patterns along the armchair direction. Comparing the compressibility values for the direction perpendicular to the line patterns for similar –OH percentages, the compressibility along the zigzag direction (line patterns along armchair) was greater than along the armchair direction (line patterns along zigzag) for 25% and 50% –OH coverages and was consistent with lower stiffness in the zigzag direction than in the armchair direction. This was, however, reversed for 75% –OH coverage, which showed a much greater compressibility in the direction perpendicular to the line patterns when the line patterns were oriented along the zigzag direction than along the armchair direction, in agreement with the stiffness that became lower at that percentage in the armchair direction than in the zigzag direction.

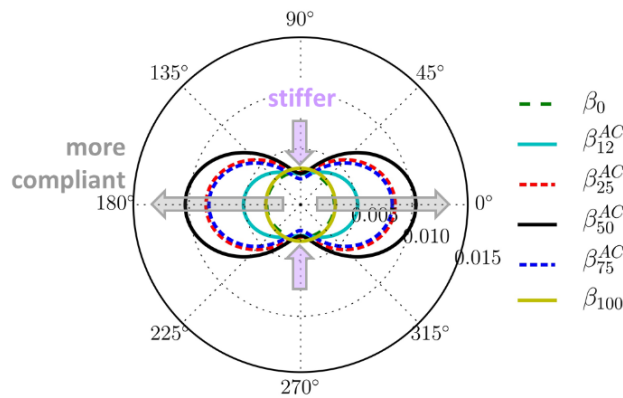
(a) Random –OH arrangement (R)



(b) –OH lines along zigzag (ZZ)



(c) –OH lines along armchair (AC)



Notation: β_j^i β = linear compressibility (m N^{-1})
 i = –OH arrangement
 j = –OH coverage

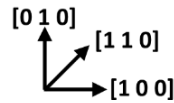


Figure 3.20. Linear compressibility (β , m N^{-1}) as a function of –OH percentages for (a) random arrangement, (b) line patterns along the zigzag direction (ZZ), and (c) line patterns along the armchair direction (AC).

3.3.5. In-plane Poisson's ratio

The in-plane Poisson's ratio of the pristine GS (Table 3.2) was in good agreement with the reported ranges in the literature from ab initio calculations (0.14-0.19, [153, 163, 170-172]; see Table A7) and was insensitive of the loading direction (zigzag vs. armchair), which was in agreement with the isotropic elastic properties of the pristine GS. For the random arrangement of –OH functionalization, the Poisson's ratio decreased for the first increments of functionalization and then increased to the value of the FGS with full (100%) –OH coverage, which exhibited *ca.* 55% increase relative to the pristine GS. The Poisson's ratio of the FGS with random arrangement was overall insensitive to the loading direction and its increase was the result of the weakening of the graphene lattice from the conversion of sp^2 to sp^3 bonding.

In contrast, for clustered line pattern arrangements, a significant reduction in the Poisson's ratios occurred with Poisson's ratios nearing zero or becoming negative, thus revealing auxetic behavior (i.e., lateral expansion under tension). This behavior originated from the unique initial bending deformation induced by the functionalization with line pattern arrangements and resulted from two different mechanisms, depending on the direction of the applied load with respect to the line patterns:

- a) When the line patterns and the loading direction were parallel (i.e., out-of-plane curvature transverse to the direction of the strain), the effect was achieved as a consequence of the initial bending deformation of the GS and the decrease in stiffness in the direction perpendicular to the line patterns. The transverse stress was thought to be released through a combination of (i) change in the bending deformation with the flattening of the FGS as a reaction to strain transverse to the curvature and (ii) the contraction of the graphene lattice in response to strain in the transverse direction similar to that of the pristine GS. Less transverse stress was needed to be released when the line patterns were along the armchair direction (contraction response was predominant) compared to the zigzag direction (flattening response was predominant) because of the lower stiffness of the armchair direction. For the line patterns along the zigzag direction, this resulted in Poisson's ratios nearing zero (no lateral dimensional change) or becoming negative (lateral expansion), while for the line patterns along the armchair direction, this resulted in Poisson's ratios being positive (overall lateral contraction).

b) When the line patterns and the loading direction were perpendicular (i.e., out-of-plane curvature in the direction of the strain), the effect was achieved via the flattening mechanism of the FGS that resulted in no significant change in the transverse dimension (Poisson's ratios nearing zero or slightly negative) because no stretching of the graphene lattice occurred during the de-wrinkling.

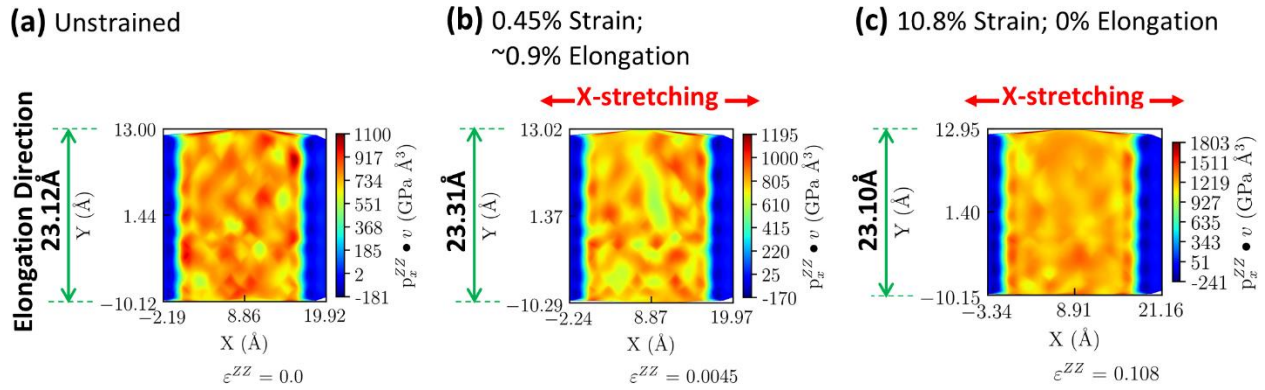
Remarkably, for 25%, 50%, and 75% –OH coverages in clustered line patterns along the zigzag direction, the Poisson's ratios for stretching along the zigzag direction were negative (-0.287 for 75% -OH groups), indicating an auxetic behavior of the FGS for that configuration. The expansion in the armchair direction (Figure 3.21) was then the result of the unfolding of the bending curvature in the direction transverse to the strain as a reaction to stretching (nanoscale mechanical spring effect). The realization of negative Poisson's ratios through the unfolding similar to that occurring when a crumpled sheet of paper is being stretched has been reported in the literature for large graphene sheets with vacancy defects [81], single-layer graphene ribbons [173], oxidized graphene [82], and self-avoiding two-dimensional membranes [174].

Table 3.2. Poisson's ratio of GS and FGS for different spatial distribution (random arrangement R, line patterns along zigzag ZZ, and line patterns along armchair AC) and –OH coverage.

% –OH	Random arrangement, R		Line patterns along ZZ		Line patterns along AC	
	ν_{12}	ν_{21}	ν_{12}	ν_{21}	ν_{12}	ν_{21}
0	0.145	0.148	0.145	0.148	0.145	0.148
12	0.123	0.140	0.070	0.099	0.094	0.146
25	0.112	0.124	-0.086	0.041	0.024	-0.065
50	0.211	0.206	-0.036	0.006	0.006	0.140
75	0.229	0.239	-0.287	0.005	0.084	0.243
100	0.238	0.234	0.238	0.234	0.238	0.234

ν_{12} Poisson's ratio along the zigzag direction.

ν_{21} Poisson's ratio along the armchair direction.



Notation: $p_x^{ZZ} \bullet v$ = local stress due to stretching along zigzag (ZZ) direction

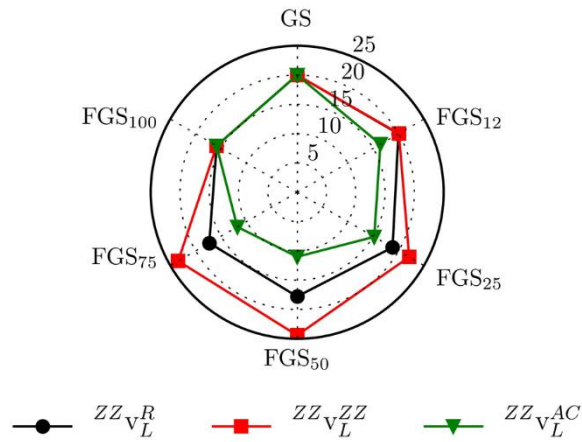
Figure 3.21. Internal local stress distribution in the graphene sheet with 75% hydroxyl functionalization in clustered line patterns along the zigzag direction, showing (a) unstrained condition, (b) elongation along the armchair direction at low tensile strain along the zigzag direction, and (c) no elongation nor contraction along the armchair direction at high tensile strain along the zigzag direction.

3.3.6. Sound wave velocity

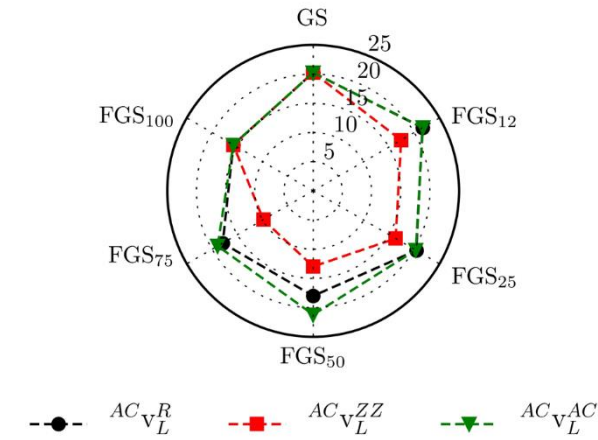
The longitudinal and transverse wave velocities through the pristine GS were independent of the direction of propagation with values of 20 km s^{-1} for the longitudinal and 13.47 km s^{-1} for the transverse velocities that were in good agreement with the experimental and theoretical values reported in the literature for unstrained GS ($15\text{-}22 \text{ km s}^{-1}$ and $10\text{-}14 \text{ km s}^{-1}$ for the longitudinal and transverse velocities, respectively [175-177]). The in-plane longitudinal wave velocity of the GS was affected by the percent coverage and spatial distribution of the -OH groups with the effect more pronounced for the waves traveling in the direction parallel to the zigzag direction compared to those traveling parallel to the armchair direction (Figure 3.22). For the random arrangement, the longitudinal wave velocity decreased with increasing -OH percentages, with a 25% decrease for full (100%) -OH coverage, and was overall insensitive to the direction of the propagation. FGS lost the isotropy with clustered line pattern functionalization. The longitudinal wave velocity of the FGS became dependent upon the direction of propagation relative to the direction of the line patterns. When the wave propagation was parallel to the direction of the line patterns, the waves traveled faster with the line patterns oriented along the zigzag direction (Figure 3.22a) while the velocity remained similar to that of the GS when the line patterns were oriented along the armchair direction (Figure 3.22b). The

faster longitudinal wave propagations along the zigzag direction for line patterns along the zigzag direction were consistent with a stiffening of the GS (larger moduli values) seen with increased –OH percentages for the clustered line patterns along the zigzag direction. The largest velocity reduction was observed when the line patterns were perpendicular to the direction of the wave propagation with slower wave propagation than that of the pristine GS and FGS with random functionalization. The slowest longitudinal wave propagation was seen for waves traveling along the zigzag direction when the line pattern arrangement was in the armchair direction and was the result of the increased stretchability with increasing –OH percentages in that direction. In contrast, the transverse wave velocity was minimally affected by –OH functionalization and reached a value of *ca.* 10 km/s for the FGS with full (100%) –OH coverage (Figure A6.3 shown for waves traveling in the direction parallel to the zigzag direction).

(a) Stretching along zigzag (ZZ)



(b) Stretching along armchair (AC)



Notation: v_L^{ij}

v_L = longitudinal velocity

i = stretching direction

j = -OH arrangement

FGS_k FGS = functionalized graphene sheet

k = -OH coverage (%)

Figure 3.22. Longitudinal sound wave velocities through the GS and FGS for waves traveling along (a) the zigzag direction and (b) the armchair direction of the graphene lattice. [R: random; ZZ: line patterns along zigzag; AC: line patterns along armchair].

3.4. Conclusions

The initial out-of-plane deformation induced by –OH line pattern functionalization affected the mechanical behavior of the GS and caused different stress-strain responses depending on the level and arrangement of –OH functionalization and the direction of the applied load with respect to the line pattern arrangements. The strong elastic anisotropy of the FGS seen for the clustered –OH line pattern arrangements was intrinsic to the initial functionalization induced bending deformation with the direction of the curvature representing the “breathing” mode of deformation (expansion and contraction) of the FGS. Compared with other studies on hydrogenated GS that showed a decrease in the mechanical properties (i.e., decrease in fracture tensile stress, fracture tensile strain, and elastic modulus) with hydrogen functionalization up to 30% coverage [7, 178], the reduction in strength observed with –OH functionalization was accompanied, for the clustered –OH line pattern arrangements, by a stiffening mechanism and an increase in compliance of the FGS. The sp^3 bonds resulting from the attachment of the –OH groups exerted a strengthening influence in the direction parallel to the line patterns and a softening in the perpendicular direction as demonstrated by energy calculations. A summary of the response behaviors seen with clustered line pattern arrangements is provided in Table 3.3.

The FGS with clustered line pattern arrangements acted similar to a nanoscale mechanical spring with an increased stiffness in the direction parallel to the line patterns and increased linear compressibility and fracture tensile strain in the direction perpendicular to the line patterns. Greater stiffness in the parallel direction and greater compliance in the transverse direction were developed when the line patterns were along the zigzag direction compared to along the armchair direction. Furthermore, for the line patterns along the zigzag direction, the shear stiffness in the $\langle 1\ 1\ 0 \rangle$ family of directions increased with increasing –OH percentages while it decreased for the line patterns along the armchair direction. In addition, for the cases studied, the line pattern arrangement along the armchair direction changed the toughness of the FGS from being greater in tensile to being greater in shear. These results indicated that the GS can be uniquely tailored using line pattern functionalization to combine in-plane stiffness, compressibility, and fracture toughness in specific directions.

Additionally, clustered line pattern functionalization was demonstrated to provide a route to convert graphene to a material with auxetic characteristics at ambient conditions. It was found that the Poisson's ratio can be tuned from positive to near zero and negative values through line pattern arrangements. It was shown that the behavior originated from the initial functionalization induced out-of-plane deformation of the GS, allowing the GS to expand or resist transformation in the direction perpendicular to the strain. The orientation dependence of the longitudinal sound wave velocity with line pattern functionalization was also demonstrated with faster longitudinal wave propagations along the zigzag direction when the line patterns were oriented along the zigzag direction and slower when the line patterns were along the armchair direction. This study indicated that clustered line pattern functionalization could be a valuable approach for tuning the mechanical properties of graphene and develop engineered graphene derivatives.

Table 3.3. Summary of response behaviors for line pattern arrangements.

	-OH line patterns along the zigzag (ZZ) direction	-OH line patterns along the armchair (AC) direction
Initial bending direction	Along AC	Along ZZ
Stress-strain response		
Stretching along ZZ	case: typical non-linear behavior	⊥ case: R-curve behavior (gradual flattening) Increased fracture strain along ZZ
Stretching along AC	⊥ case: R-curve behavior (gradual flattening) Increased fracture strain along AC	case: typical non-linear behavior
Elastic modulus (stiffness)	Increased along ZZ (case)	Increased along AC (case)
Linear compressibility	Increased along AC (⊥ case)	Increased along ZZ (⊥ case)
Shear modulus	Increased along the <1 1 0> family	Decreased along the <1 1 0> family
Poisson's ratio		
Along ZZ	Negative (auxetic behavior)	Nearing zero (no lateral expansion)
Along AC	Nearing zero (no lateral expansion)	Positive (lateral contraction)
Longitudinal sound wave velocity		
Along ZZ	Faster (case)	Slower (⊥ case)
Along AC	Slower (⊥ case)	Similar to GS and FGS

CHAPTER 4

MECHANICAL PROPERTIES OF TOBERMORITE/GRAPHENE NANOCOMPOSITES UNDER TENSILE AND SHEAR LOADINGS VIA MOLECULAR DYNAMICS SIMULATIONS

This chapter has three conjoined sections. The first section describes the effects of two types of geometrical assembly (hierarchical and stacked) of graphene sheet (GS) in the tobermorite 9 Å (T_9) matrix on the strength, toughness, and in-plane stiffness of the T_9 /GS nanolaminates. The second section studies the modulation of nanocomposites reinforced with graphene in terms of strength, stiffness, toughness, and directional elasticity near different interfaces of tobermorite 14 Å (T_{14}) (silicate tetrahedra, calcium octahedra, and water interfaces). This second section has resulted in one peer-reviewed manuscript that is published in *Construction and Building Materials* as: B. Al-Muhit, F. Sanchez, *Nano-engineering of the mechanical properties of tobermorite 14Å with graphene via molecular dynamics simulations*. The third section of the chapter investigates the effect of –OH functionalization coverage and patterns on the functionalized graphene sheet (FGS) in terms of the strength, toughness, stiffness, and directional anisotropy of stiffness and compressibility of the T_{14} /FGS nanocomposites. The role of the interlayer and structural water on these mechanical properties of the nanocomposites are also studied.

4.1. Overview

Cement-based materials are inherently weak in tension. While nano- and microscale fiber reinforcements have been the method of choice for enhancing the material tensile properties by bridging cracks and improving the material load transfer capacity [84-97], this approach primarily addresses the material tensile property at the macroscale composite level rather than building on the molecular nature of the cement hydrates. Calcium silicate hydrate (C–S–H) is the main binding cement hydrate responsible for the tensile properties of cement-based materials [98-100]. Nanotechnology offers the opportunity for the development of new C–S–H nanocomposites [101, 102]. Nano-engineering of C–S–H through the grafting of graphene-based materials can be a viable option for enhancing the tensile capacity of cement-based materials.

While experimental techniques, including atomic force microscopy and nanoindentation mapping are capable of studying the mechanical properties of cement phases such as C–S–H [103, 104], these techniques provides microscale information from which nanoscale behavior must be deduced and no molecular level detail of the internal, cohesive forces are obtained. Molecular dynamics (MD) modeling provides a useful tool for understanding atomistic scale, reinforcing mechanisms and tuning the mechanical properties of C–S–H. MD has been successfully used to investigate the structural and mechanical properties of C–S–H at the molecular scale, including its tensile and shear strengths [2, 3, 105-107]. While MD studies of the mechanical response of C–S–H with embedded carbon nanotubes, graphene, and graphene derivatives have been recently reported in the literature [25, 33, 108-111], little is known about the possible influence of the interface composition and structure on the strengthening mechanisms and mechanical properties of the reinforced C–S–H nanocomposites. Yet, understanding the relationship between the surface structure of C–S–H interfacing with graphene and the mechanical properties of the reinforced system is key to being able to realize new C–S–H nanocomposites and enhance the mechanical properties of cement-based materials.

Tobermorite, a naturally occurring mineral with a low calcium-to-silicon (Ca/Si) ratio (< 1), has been identified in the literature as a viable analogue of crystalline pristine C–S–H phases due to the structural similarity between the structures [98, 112]. While other C–S–H phase models with variable Ca/Si ratios have been recently proposed as more realistic models [3, 113, 114], the layered structure of T_{14} allowed for the study of three well-defined structures with different, well-defined interfaces that could be interfaced with the graphene (i.e., interlayer water interface, octahedral calcium layer interface, and tetrahedral silicate layer interface). These defectless T_{14} interfaces could provide a blueprint for understanding the in-plane strengthening mechanisms of graphene reinforced tobermorite nanocomposites. The tobermorite family is distinguished based on the interlayer spacings of 9 Å, 11 Å, and 14 Å. In this study, tobermorites 14 Å (T_{14}) and 9 Å (T_9) were studied as the base matrices. The interlayer spacing of T_{14} was 14 Å because of the presence of calcium cations and water molecules. T_9 has a lower interlayer spacing of 9 Å because of absence of water molecules in the interlayer (resembles dry C–S–H). Nonetheless, both tobermorite structures resembled layered *drierketten* type structures of C–S–H, and allowed for the nanoengineering of the structures with graphene reinforcement.

It has been reported in the literature that the strength and toughness (i.e., ductility) of cement composites could be enhanced by arranging different types of fibers and carbon nanotubes (CNT) in a lamellar formation [108, 116, 117]. Orientating graphene sheet (GS) in a lamellar formation in a copper (Cu) matrix (Cu/GS/...GS/Cu formation) also increased the strength and the plastic strain of the composite, transitioning Cu/GS composite from brittle-to-ductile behavior [34]. As previous findings demonstrated, C–S–H and tobermorite possess a unique layered structure, which could be strengthened further by orienting GS in lamellar formation sandwiched within the matrix. However, this type of geometrical configuration-based studies on the nanoscale mechanical behaviors of the graphene-reinforced tobermorite 9 Å (T₉/GS) nanolaminates has not yet been investigated. The location and geometrical arrangement pattern of graphene within the tobermorite systems offer opportunities to modulate the mechanical properties (because of its layered structure).

The interfacial chemical species of the C–S–H or T₁₄ nanostructures has been shown to interact during the external loadings and modulate the mechanical properties of T₁₄ [2, 32, 118]. It has also been observed that graphene oxide (GO) embedded in C–S–H matrix in the interlayer direction increased the failure strength and strains of the GO-reinforced C–S–H (C–S–H/GO) nanocomposite because the hydroxyl groups (–OH) interacted with the interlayer interface of C–S–H [109]. Moreover, it has been shown that the interlayer interface filled with water can create hydrogen bonds with the –OH groups of the functionalized graphene sheet (FGS) and modulate the mechanical properties. It has been shown before that T₁₄ was hydrophilic because the water molecules pointed hydrogen atoms towards the interlayer Ca atoms [119]. In addition to the effect of patterning of –OH groups on the FGS, the –OH groups supposedly attract the mobile water molecules of the T₁₄ away from the core structure which may lead to a difference in the mechanical responses. In addition to the water-rich layer, the structural skeleton of T₁₄ was made of two other layers: calcium octahedral layer, sandwiched between two opposite silicate layers [120]. These layers play significant role in engineering the mechanical properties of T₁₄ and T₁₄-based nanocomposites. Therefore, a thorough understanding of the effect of the interfaces as well as the clustered line patterns and coverage of hydroxyl (–OH) groups associated with the GS on the mechanical properties of the nanocomposites during tensile and shear loading stimulations is necessary to nanoengineer the T₁₄/GS and T₁₄/FGS nanocomposites.

This chapter was organized as follows: section 4.2.1 described the computational details of the geometrical assemblage of T₉/GS nanolaminates, section 4.2.2 described the computational details of three interface dominated T₁₄/GS nanocomposites, and the computational details of the T₁₄/FGS systems with varying –OH surface coverage was described in the section 4.2.3. The results and discussion sections are explained in the sections, 4.3.1, 4.3.2., and 4.3.3 for the T₉/GS nanolaminates, T₁₄ interface dominated T₁₄/GS nanocomposites, and –OH surface chemistry dominated T₁₄/FGS nanocomposites, respectively. The conclusions were also organized in the same pattern.

4.2. Computational Details

4.2.1. Effect of geometric assembly of GS in tobermorite 9 Å (T₉)

4.2.1.1. Simulation models and computational Cell

A T₉-based C–S–H model and three nanolaminates of T₉ reinforced with stacked and hierarchical assemblies of GS were constructed from the primary skeleton of the T₉ structure.

Tobermorite 9 Å structure. Tobermorite-9Å (T₉) is a defect-free crystalline analogue of C–S–H with the chemical formula, Ca₆Si₆O₁₆(OH)₂ with a Ca/Si of 1.0. The crystal structure of T₉ was triclinic with $C\bar{1}$ space group symmetry (as-per Schoenflies symbol) having the unit cell lattice parameters, a=11.15Å, b=7.303Å, c=9.566Å, α=101.08°, β=92.83°, γ=89.98° according to Bonnacorsi et al. [179]. T₉ consisted of six types of atoms in a layered formation with silicate tetrahedra and calcium octahedra forming the backbone of the system with a layer of Ca atoms in the interlayer regions (Figure 4.1).

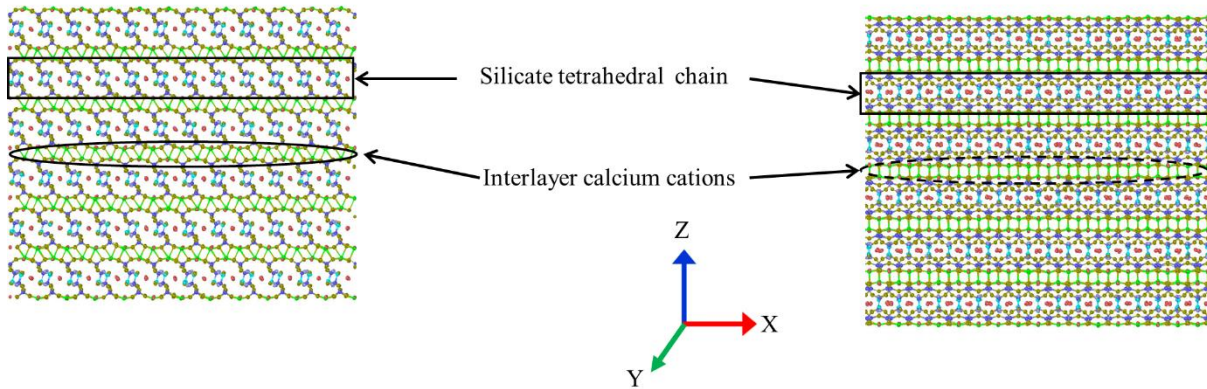
Graphene structure. Three layers of Graphene sheet (GS) were used in a various assemblies as the reinforcing constituent in the T₉ matrix (Figure 4.2). Each GS with a XY planar area of 60×60 Å² was built using Visual Molecular Dynamics (VMD) software [180] with sp² C–C bond lengths of 1.418Å and C–C–C bond-angle of 120°. The armchair (AC) and zigzag (ZZ) directions of the GS were along the X- and Y- Cartesian Coordinate axes, respectively.

T₉/GS nanostructures. Two systems consisting of different arrangements of T₉ and GS were constructed for the MD simulations using VESTA [181] and MOLTEMPLATE [182]

software (Figure 4.2). The structures were designated as (1) T_9 , (2) T_9/GS^{3H} , and (3) T_9/GS^{3S} . The structures consisted of (1) tobermorite-9 Å with a system size of $66 \times 64 \times 56.5$ Å (20736 atoms), named T_9 ; (2) three GS sandwiched in 4 blocks of T_9 in a hierarchical alternate arrangement with a total size of $66 \times 64 \times 54$ Å (18324 atoms), named T_9/GS^{3H} ; and three layers of GS stacked in the middle of two symmetric blocks of T_9 with a total size of $66 \times 64 \times 49.5$ Å (18324 atoms), named T_9/GS^{3S} . The GS were placed 3 Å apart from the interfaces of the T_9 blocks. The visualizations of the T_9/GS nanolaminate composites are shown in Figure 4.2 and were performed using OVITO [183] software.

(a) Tobermorite 9 Å (T_9) along X

(b) Tobermorite 9 Å (T_9) along Y



(c) Structural layers along X, Y, and Z

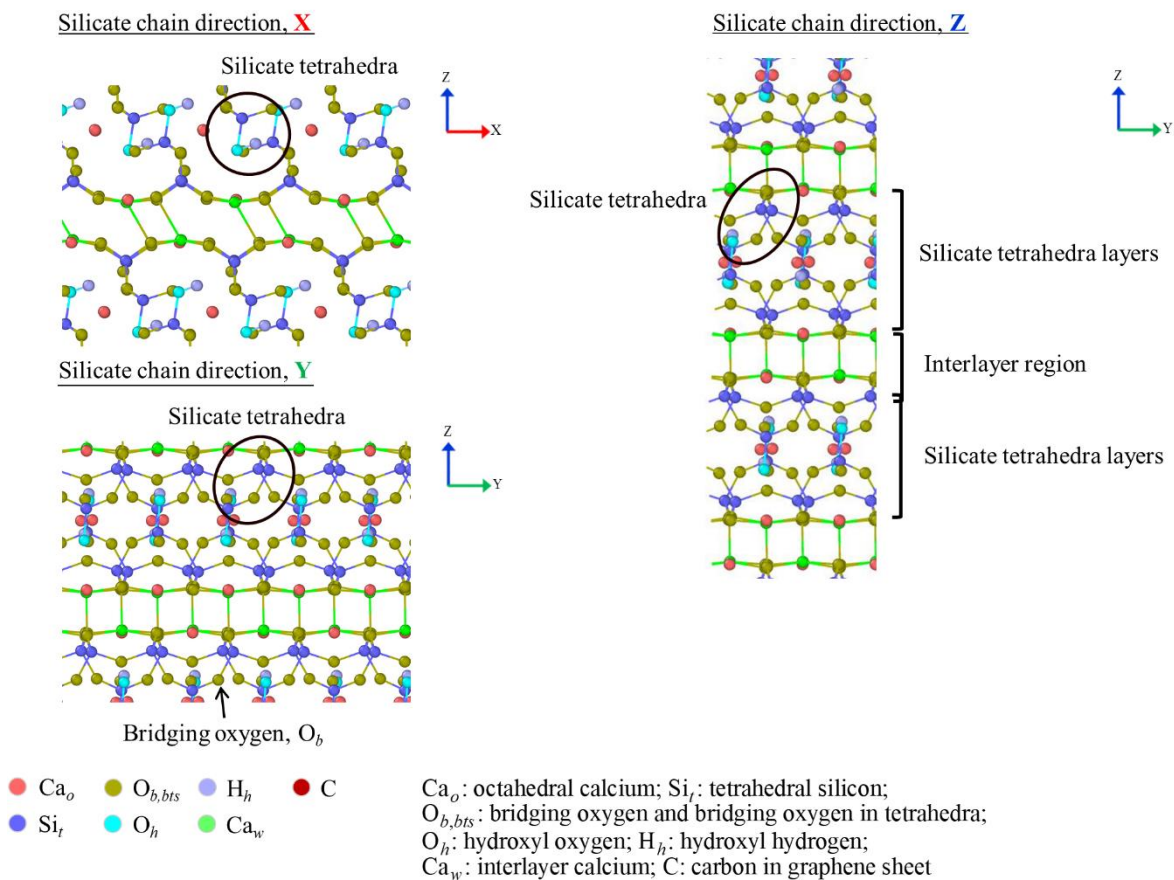


Figure 4.1. Tobermorite 9 Å (T_9) structure in (a) X- and (b) Y-directions, and (c) structural layers of T_9 in the X-, Y-, and Z-directions.

stability of the center-of-mass of the system. The velocities of the atoms were selected using random seed generation in LAMMPS while the linear and angular momentums of the systems were conserved. The Verlet time-integration scheme was used with 1 fs simulation timestep for all the simulations [188].

The equilibrium simulations of the T₉/GS systems were performed for 100 ps in NPT ensembles with Nosé-Hoover thermostat and barostat [148] at 300 K temperature and 0 atm pressure in all directions. The equilibrium thermodynamic parameters such as temperature, pressure, density, total energy and pair interaction energy were observed. The final equilibrated structures were used for further mechanical property simulations such as tension and shear stress-strain curves, and for elastic property calculations.

4.2.1.3. MD simulations and loading directions

Uniaxial tensile loadings on the systems under consideration in the X- and Y-directions were applied on the 8 Å thick boundary atoms. The boundary atoms from both the T₉ and GS systems were selected from the planes parallel (∥) to the loading directions. Shear loadings were applied similarly along the X-direction of the XY plane. A gradual strain increment with strain rate of 1×10^{-5} (Å/Å) fs⁻¹ was applied for both uniaxial tensions and shear tests. This strain rate was extremely high for continuum scale but typically used in the atomistic simulations. A timestep of 1 fs was used for all the simulations.

4.2.1.4. Data collection and analysis

The atomistic stress was calculated according to the virial stress theorem [151] considering both the potential and kinetic energy terms. The calculated virial stress was time-averaged over 500 fs for each increment of strain to obtain the engineering stress that was plotted against the corresponding strain to obtain the stress-strain curves. The strain energy densities per unit area for tension and shear were calculated as the area under the corresponding stress-strain curves.

The in-plane elastic stiffness constants, C_{ij} (normal, shear, and coupling constants) were calculated from the slope of stress-strain plots of time averaged stresses obtained at different strains. The systems were deformed at a particular strain for 5,000 fs. Three strains with increments of ± 0.005 were used and the corresponding stresses were obtained every 100 fs and

time averaged (50 data points) to compute the final stresses. The normal and coupling constants were then calculated from the slope of the stress-strain plots in the NPT ensemble with keeping \perp directions of the loading directions free of pressure. The shear component, however, was obtained in the NVT ensemble because of the requirement of the volume preservation during shearing. The compliance components were obtained by inverting the stiffness matrix, $S_{ij} = C_{ij}^{-1}$. From the compliance constants, a full tensorial analysis was performed and key quantities were determined, including the directional elastic moduli and the directional linear compressibility (β_L , deformation as a response to hydrostatic compression). Details of the calculations can be found in the Appendix B.

4.2.2. Effect of the surface structure of tobermorite 14 Å (T_{14}) interfacing with the GS

4.2.2.1. Simulation models and computational cells

Three T_{14} -based C–S–H models and three nanocomposites of T_{14} reinforced with GS were constructed from the primary skeleton of the T_{14} structure. The T_{14} structure contained octahedral calcium layers sandwiched between tetrahedral chains and surface and interlayer water (Figure 4.3) and provided for three possible tobermorite–graphene interface structures along the basal plane in which the GS was interfaced with the surface water, the octahedral calcium layer, and the tetrahedral silicate layer.

Graphene Sheet (GS). The GS was modeled using the Visual Molecular Dynamics (VMD) software package [189]. The zigzag (ZZ) and armchair (AC) edges of the GS were oriented along the Cartesian coordinate axes X [1 0 0] and Y [0 1 0] directions, respectively (Figure 4.4). The GS was 22 Å × 28 Å in size and consisted of 252 sp^2 hybridized carbon (C) atoms in a hexagonal ring pattern. The C–C bond distances and $\angle C-C-C$ angles were 1.418 Å and 120°, respectively. The thickness of the GS was 3.35 Å.

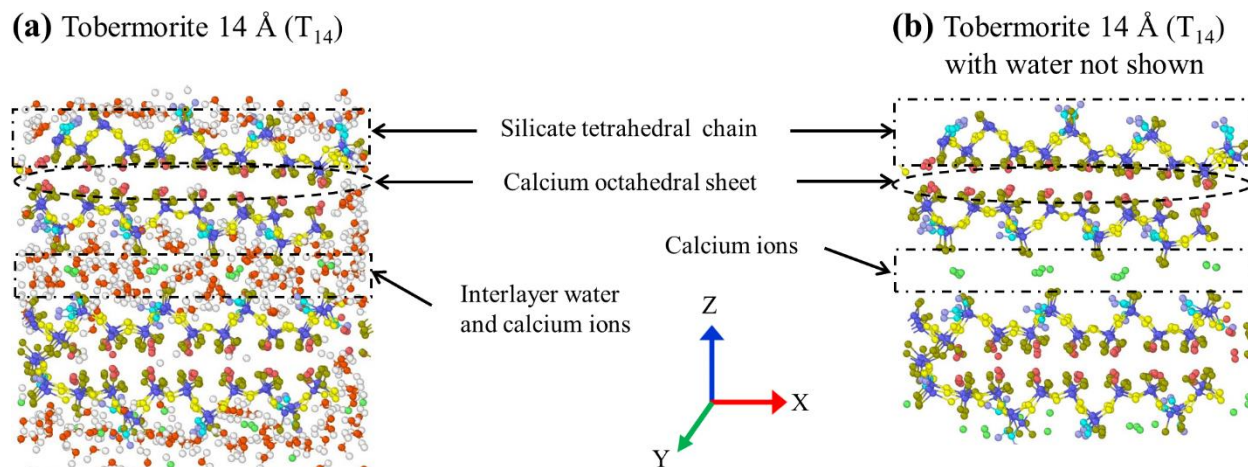
Tobermorite 14 Å-based models for C–S–H. The monoclinic T_{14} structure described by Bonaccorsi et al. [120] was used as the initial model to create T_{14} -based structures with three types of exposed surfaces (i.e, water, octahedral calcium, and tetrahedral silicate chains) to interface with the GS. The unit cell of T_{14} was built using MOLTEMPLATE software [182]. The T_{14} unit cell consisted of 124 atoms per unit cell with space group symmetry of $B11b$ and had a

calcium to silicon (Ca/Si) ratio of 0.833 and lattice parameters $a = 6.735 \text{ \AA}$, $b = 7.425 \text{ \AA}$, $c = 27.987 \text{ \AA}$, $\alpha = \beta = 90^\circ$, and $\gamma = 123.25^\circ$. An occupancy factor of 1.0 was used in this work for the water molecules, resulting in a water to silicon ratio of 1.66. A full site occupancy was chosen to study the effect of the extreme case of water occupancy in the T_{14} structure on the reinforcing effect of graphene. The tensile strength of graphene oxide reinforced C–S–H composites has been shown in the literature to be influenced by the presence of water [33].

The T_{14} structure with the exposed water layer surface ($T_{14}^{O_w}$ structure) was created by replicating the T_{14} unit cell in the X, Y, and Z-directions $4 \times 4 \times 1$ times to form the $T_{14}^{O_w}$ supercell (Figure 4.5). The T_{14} structure with the exposed octahedral calcium surface ($T_{14}^{Ca_o}$ structure) was created by deleting the topmost water layer and silicate chains of the original T_{14} unit cell. To uphold the periodicity of the T_{14} unit cell, the resulting unit cell was mirrored along the negative Z-direction to account for the removal of the layer from the top, resulting in a unit cell with a water to silicon ratio of 1.58. The resulting unit cell was then replicated along the X, Y, and Z-directions $4 \times 4 \times 1$ times to form the $T_{14}^{Ca_o}$ supercell. The T_{14} structure with the exposed tetrahedral silicate surface ($T_{14}^{Si_t}$ structure) was created by stripping off the topmost layer of water molecules from the original T_{14} unit cell, resulting in a water to silicon ratio of 1.5. The resulting unit cell was then replicated $4 \times 4 \times 1$ times to form the $T_{14}^{Si_t}$ supercell. The simulation boxes of all T_{14} -based systems were then changed from monoclinic to $P1$ triclinic symmetry before being interfaced with the GS to allow for the box dimensions to change during the MD simulations. The lattice parameters of the systems became parallel to the triclinic box dimensions after invoking periodicity, resulting in T_{14} -based models with dimensions of $26.94 \text{ \AA} \times 27.50 \text{ \AA}$ along the X and Y-directions and 29.53 \AA , 27.77 \AA , 28.05 \AA along the Z-direction for $T_{14}^{O_w}$, $T_{14}^{Ca_o}$, and $T_{14}^{Si_t}$, respectively.

T_{14} /GS nanocomposite models. To create the different T_{14} /GS nanocomposites, the triclinic T_{14} -based structures were interfaced with the GS. The nanocomposite with the GS interfacing with the surface water ($T_{14}^{O_w}$ /GS nanocomposite; Figure 4.5a) was constructed by placing the GS at a distance of 4 \AA below the $(0 \ 0 \ \bar{1})$ plane of the $T_{14}^{O_w}$ supercell with the ZZ edge of the GS oriented along the X-axis and the AC edge oriented along the Y-axis. Similarly,

the nanocomposite with the GS interfacing with the octahedral calcium layer at the (0 0 1) plane ($T_{14}^{Ca_o}$ /GS nanocomposite; Figure 4.5b) and the nanocomposite with the GS interfacing with the tetrahedral silicate layer at the (0 0 1) plane ($T_{14}^{Si_t}$ /GS nanocomposite; Figure 4.5c) were constructed by placing the GS at a distance of 5 Å above the exposed octahedral calcium surface of the $T_{14}^{Ca_o}$ supercell and the tetrahedral silicate surface of the $T_{14}^{Si_t}$ supercell, respectively, with the ZZ edge of the GS oriented along the X-axis and the AC edge oriented along the Y-axis. The resulting computational cells had dimensions of 26.94 Å×27.50 Å×35 Å and contained a total of 2236 atoms for the $T_{14}^{O_w}$ /GS nanocomposite, 1856 atoms for the $T_{14}^{Ca_o}$ /GS nanocomposite, and 1904 atoms for the $T_{14}^{Si_t}$ /GS nanocomposite.



(c) Silicate tetrahedra chain along X, Y, and Z

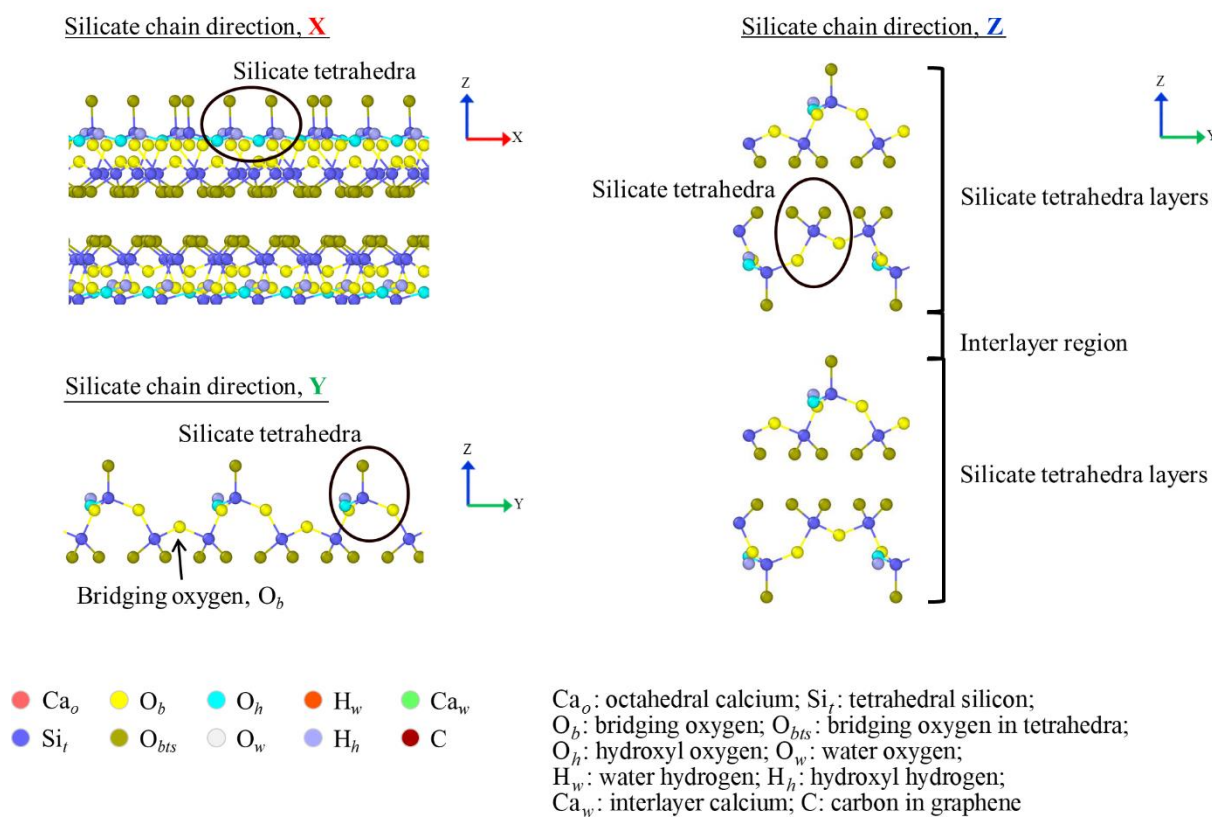


Figure 4.3. (a) and (b) Layered crystal structure of tobermorite 14 Å (T_{14}). (c) Silicate tetrahedra chain along the X-, Y-, and Z-directions [for clarity, structures are shown without water molecules in (b) and (c)].

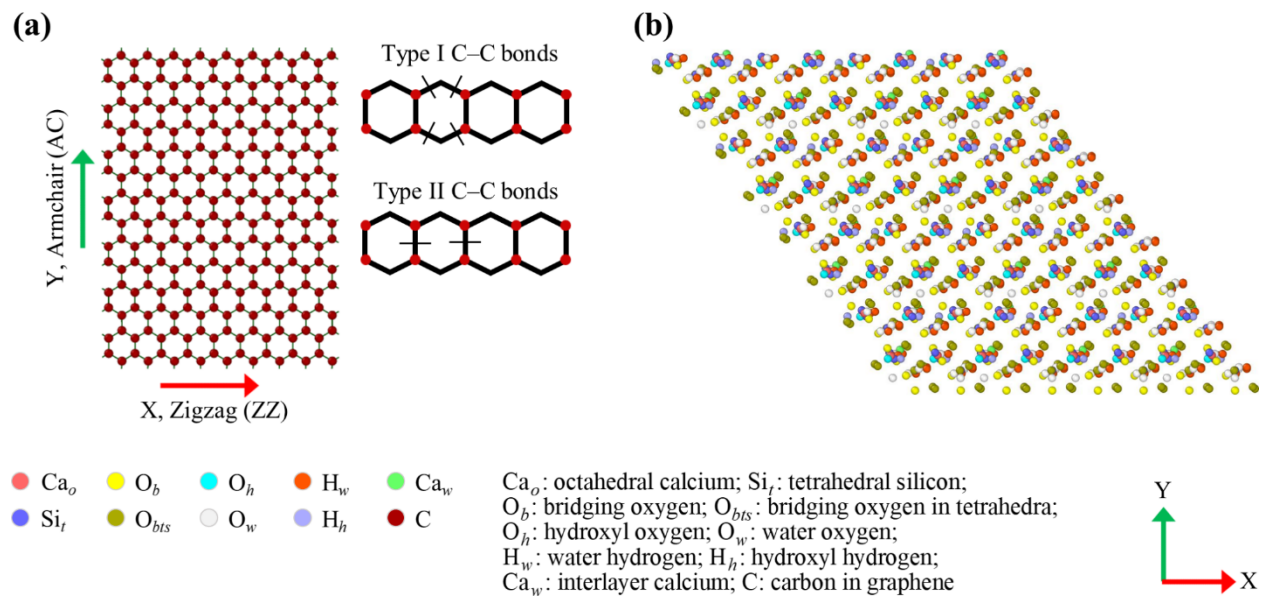


Figure 4.4. (a) Graphene sheet (GS) and (b) monoclinic supercell of tobermorite 14 \AA with the exposed water layer surface ($T_{14}^{O_w}$ supercell).

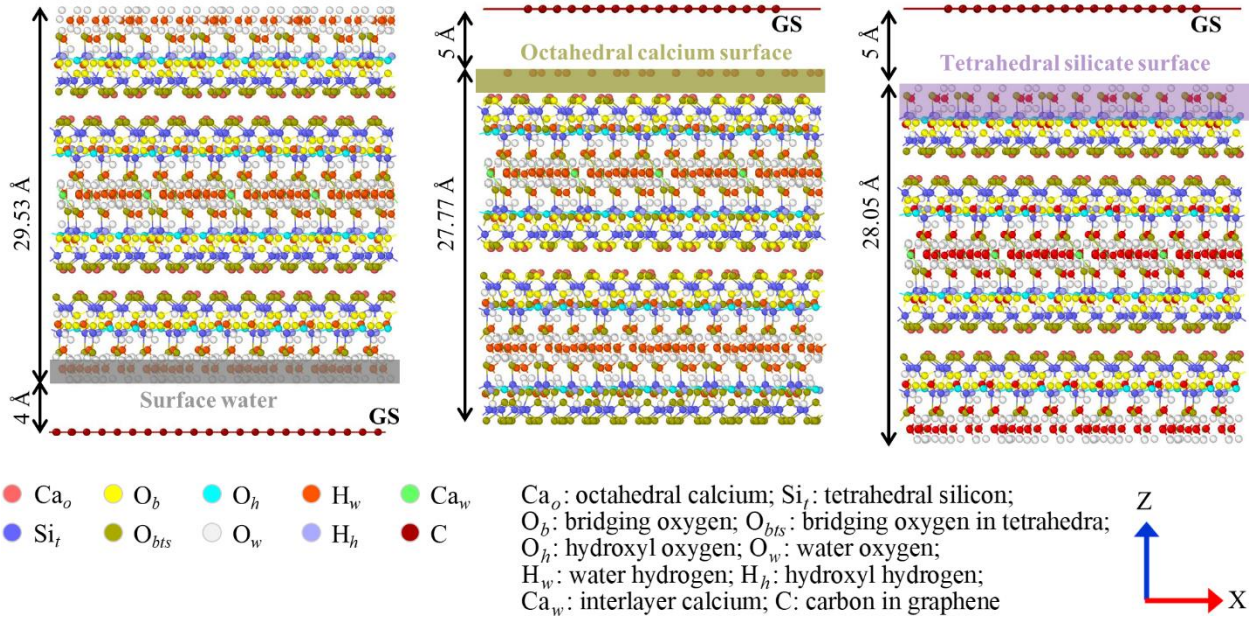
(a) $T_{14}^{O_w}$ /GS nanocomposite(b) $T_{14}^{Ca_o}$ /GS nanocomposite(c) $T_{14}^{Si_t}$ /GS nanocomposite

Figure 4.5. Models of T_{14} /GS nanocomposites: (a) nanocomposite with the GS interfacing with the bottom surface water at the $(0\ 0\ \bar{1})$ plane of the T_{14} structure ($T_{14}^{O_w}$ /GS nanocomposite), (b) nanocomposite with the GS interfacing with the octahedral calcium layer at the $(0\ 0\ 1)$ plane ($T_{14}^{Ca_o}$ /GS nanocomposite), and (c) nanocomposite with the GS interfacing with the tetrahedral silicate layer at the $(0\ 0\ 1)$ plane ($T_{14}^{Si_t}$ /GS nanocomposite).

4.2.2.2. Forcefield

The Consistent Valence Force Field (CVFF) was employed for the simulation of the GS [138]. The CVFF has been previously shown to properly represent the tensile and shear properties of graphene and carbon nanotubes [33, 143, 190] and has been used in the study of the interactions of graphitic structures with tobermorite and aqueous solutions [144, 185]. The C–C bond interaction of the GS was simulated with the Morse potential [141]. The angle bending, torsion, and improper interactions were simulated using the harmonic parameters of the CVFF. The partial atomic charges, non-bonded and bonded interactions among the T_{14} atoms were simulated using the Clay force field (ClayFF), which relied on the flexibility of coulombic interactions between the interacting atoms to represent bonding. The ClayFF was developed to study the structural and dynamic properties of hydrated and mineral systems [184, 186, 191-193] and has been successfully used to study the mechanical and elastic properties of clay-based

minerals and clay-based nanocomposites [193-197]. While using the ClayFF has been reported to generally reproduce well the out-of-plane elastic constants and overpredict the in-plane elastic properties of cement-related phases [193, 194, 198-200], in this study, the response of the GS was dominant in the T₁₄/GS nanocomposite systems and an overprediction of the elastic properties of the T₁₄ systems was thus considered to have a minimal effect on the elastic properties of the overall nanocomposites. In addition, while ClayFF cannot capture chemical reactions, hydrolytic reactions during loading of the T₁₄/GS systems (i.e., formation of silanol, Si–O–H groups and calcium hydroxyl, Ca–O–H groups as Si–O–Si or Si–O–Ca bonds break during loading) were considered to play a minimal role as it has been reported in the literature that water dissociation in graphene oxide reinforced C–S–H with low Ca/Si ratios (less than 1) was minimal for strain less than 0.4 [109] as was the case in this study. The interactions among the carbon atoms of the GS and T₁₄ atoms were modeled using the Lennard-Jones (LJ) potential [201]. The values of the CVFF and ClayFF parameters are provided in the Appendix B.

4.2.2.3. Equilibration

All MD simulations were performed using LAMMPS, an open-source MD simulation software [42]. The pristine T₁₄ systems (i.e., T₁₄^{O_w}, T₁₄^{Ca_o}, and T₁₄^{Si_t}) and the T₁₄/GS nanocomposites (i.e., T₁₄^{O_w}/GS, T₁₄^{Ca_o}/GS, and T₁₄^{Si_t}/GS) were energy minimized at 0 K using the conjugate gradient method to reduce the excess pressure build-up during the geometry setup. The pristine T₁₄ systems and T₁₄/GS nanocomposites were then equilibrated for 1 ns and 500 ps, respectively, at 300 K and 0 atm, using NPT (fixed number of atoms, pressure, and temperature) ensemble conditions. The Nosé-Hoover thermostat and barostat were used for temperature and pressure control of the systems with 100 fs and 1000 fs damping constants, respectively [148, 149]. The neighbor cut-off distance for the interacting atoms was 5 Å, and the neighbor list was updated every timestep. The long-range coulombic interactions were computed in the reciprocal space by the Particle-Particle-Particle-Mesh (PPPM) solver. The short-range coulombic interactions between atoms were calculated as:

$$\Psi^{\text{coul}} = \frac{1}{4\pi\epsilon_0} \cdot \frac{q_i q_j}{r_{ij}^2} \quad (4.1)$$

where q_i and q_j are charges on atoms i and j , ϵ_0 is the permittivity of the vacuum (8.85419×10^{-12} F/m) and $r_{ij} = |r_i - r_j|$ is the interatomic distance. The short-range van-der-Waals (vdW) interaction was computed by the Lennard-Jones (LJ) potential using:

$$\Psi^{\text{LJ}} = 4 \epsilon \left[\left(\frac{\sigma}{r} \right)^{12} - \left(\frac{\sigma}{r} \right)^6 \right] \quad (4.2)$$

where ϵ is the depth of the potential well (kcal mol^{-1}), σ is the distance (\AA) at which the potential was zero, and r is the interatomic distance (\AA). The Lennard-Jones (LJ) and coulombic cut-off distances were 12 \AA and 10 \AA , respectively. The interactions between unlike atoms were calculated using the *Lorentz-Berthelot* mixing rules [202, 203]. The time integration was performed using the velocity-Verlet algorithm. All simulations were performed using a 1 fs timestep. Periodic boundary conditions in the X-, Y-, and Z-directions were used for all systems.

4.2.2.4. Loading methods and MD simulations

Three different loading modes were used: (i) in-plane uniaxial tension along the X- and Y-directions (ZZ edge and AC edge of the graphene sheet, respectively for the nanocomposites), (ii) out-of-plane uniaxial tension along the Z-direction, and (iii) shear loading in the XY plane (perpendicular to the interface with the GS for the nanocomposites) along the X-direction. To simulate the loading and ensure an equal deformation pathway and uniform stress distribution, atoms at opposite edges of the T_{14} systems or T_{14}/GS nanocomposites and within 3 \AA from the edge were constrained while subjected to in-plane tensile (atoms along the direction of stretching) and shear forces (top and bottom atoms) and within 4 \AA (top and bottom atoms) for out-of-plane (Z-direction) tensile loading. A strain rate of $1 \times 10^{-5} \frac{\text{\AA}}{\text{\AA}} \text{ fs}^{-1}$ was used for all loading modes. This strain rate was within the typical ranges used in the literature [4, 204, 205]. While stretching in one direction, the pressure in the other two directions was kept at zero to allow for the Poisson's effect. The time integration of the systems was performed under the NPT condition for tensile loading and NVT (fixed number of atoms, volume, and temperature) conditions for shear loading.

4.2.2.5. Data collection and analysis

The atomistic stress was calculated from the Virial stress theorem [206] considering both the potential and kinetic energy terms. The time-averaged engineering stress was output every 500 fs and plotted against the corresponding strain to obtain the stress-strain (σ - ε) curve of each system. The strain energy densities per unit volume for tensile (Γ) and shear (Π) were calculated by integrating with the trapezoidal rule to obtain the area under the corresponding stress-strain curve from a strain of 0.0 to the fracture strain. The strain energy density was used as an indirect indication of the fracture toughness of the systems.

The intrinsic (equilibrium, zero strain) elastic stiffness constants (C_{ij}) and effective (i.e., during the elastic loading stage) elastic stiffness constants (C_{ij}^{eff}) of the systems were computed in the isothermal-isobaric ensemble (NPT) for the normal constants (C_{ij} and C_{ij}^{eff} , where $i = j = 1, 2, 3$) and the canonical ensemble (NVT) for the shear constants (C_{ij} and C_{ij}^{eff} , where $i = j = 4, 5, 6$). The system under consideration was displaced from its equilibrium position at 0.0 strain (intrinsic elastic constants) or from its position at 0.025 strain (effective elastic constants) to a specified strain, ε_j ($j = X, Y$), and equilibrated for 5000 fs (long enough to reach stress convergence). The collected stress data, σ_i ($i = X, Y$), were then time-averaged to get one σ_i point. The method was repeated for five values of ε_j from -0.01 to +0.01 with 0.005 strain increment (i.e., -0.01, -0.005, 0, 0.005 and 0.01) for the intrinsic constants and three values of ε_j from 0 to 0.05 with 0.025 strain increment (i.e., 0, 0.025, and 0.05) for the effective constants. The C_{ij} and C_{ij}^{eff} were then calculated from the slope of the σ_i - ε_j plot. This method (known as the direct method [190, 207-209]) was used to obtain all independent intrinsic (C_{ij}) and effective (C_{ij}^{eff}) constants of the elastic tensor for all systems. While the triclinic T_{14} systems have twenty one (21) independent C_{ij} and C_{ij}^{eff} , the normal-shear coupling elastic constants (C_{ij} and C_{ij}^{eff} , where $i \neq j$, and $i = 1, 2, 3, j = 4, 5, 6$) were approximately zero compared to the normal and shear elastic stiffness constants. The orthorhombic symmetry with nine (9) elastic constants (including normal, shear, and normal coupling constants) was thus assumed for both the T_{14} systems and T_{14}/GS nanocomposites. The Born mechanical stability criteria were calculated to check for the mechanical stability of all systems [76, 210]. The compliance tensor was calculated by inverting the stiffness matrix, $S \equiv C^{-1}$. The compliance tensor (S) was then used to calculate

the elastic moduli (E), shear moduli (G), bulk moduli (κ), volume compressibility (β_v) and linear compressibility (β_L).

4.2.3. Effects of functionalization of FGS on Tobermorite 14 (T_{14})

Two sets of Tobermorite 14 Å (T_{14})-based C–S–H models reinforced with FGS were constructed. One set consisted of T_{14} /FGS structures with random clustered pattern of –OH groups with varying –OH coverages. Another set consisted of T_{14} /FGS structures with zigzag clustered line pattern of –OH groups. In all cases, the FGS were interfaced with the interlayer ($00\bar{1}$) planes of T_{14} structures.

4.2.3.1. Simulation models and computational cells

Tobermorite 14 Å (T_{14}) structure. The monoclinic T_{14} structure described by Bonaccorsi et al. [120] was used as the model for the structure of crystalline C–S–H in hydrated cement pastes. The T_{14} unit cell consisted of 124 atoms per unit cell with space group symmetry of $B11b$ and had a calcium to silicon (Ca/Si) ratio of 0.833 and lattice parameters $a = 6.735$ Å, $b = 7.425$ Å, $c = 27.987$ Å, $\alpha = \beta = 90^\circ$, and $\gamma = 123.25^\circ$. The T_{14} unit cell was replicated $4 \times 4 \times 1$ times in the X, Y, and Z-directions to represent supercell consisted of T_{14} structures. The symmetry of the simulation box was changed to $P1$ triclinic symmetry to allow for all the box dimensions and the associated T_{14} structures to change during the MD simulations. Since Bonaccorsi's T_{14} model required an occupancy factor of 0.5 for the interlayer calcium ions and interlayer water molecules, 50% of the interlayer calcium atoms and 50% of the interlayer water molecules were deleted from the T_{14} structure before starting the MD simulations. Therefore, the water molecules of the T_{14} structure were of two types: (1) one which had occupancy factor of 1.0 (structural water, O_w) and (2) another with occupancy factor of 0.50 (mobile water or interlayer water, O_{wd}). The final T_{14} structure had X-, Y-, and Z-dimensions of 26.94 Å \times 27.20 Å \times 28.72 Å (Figure 4.6).

Structure of Tobermorite 14 Å (T_{14})

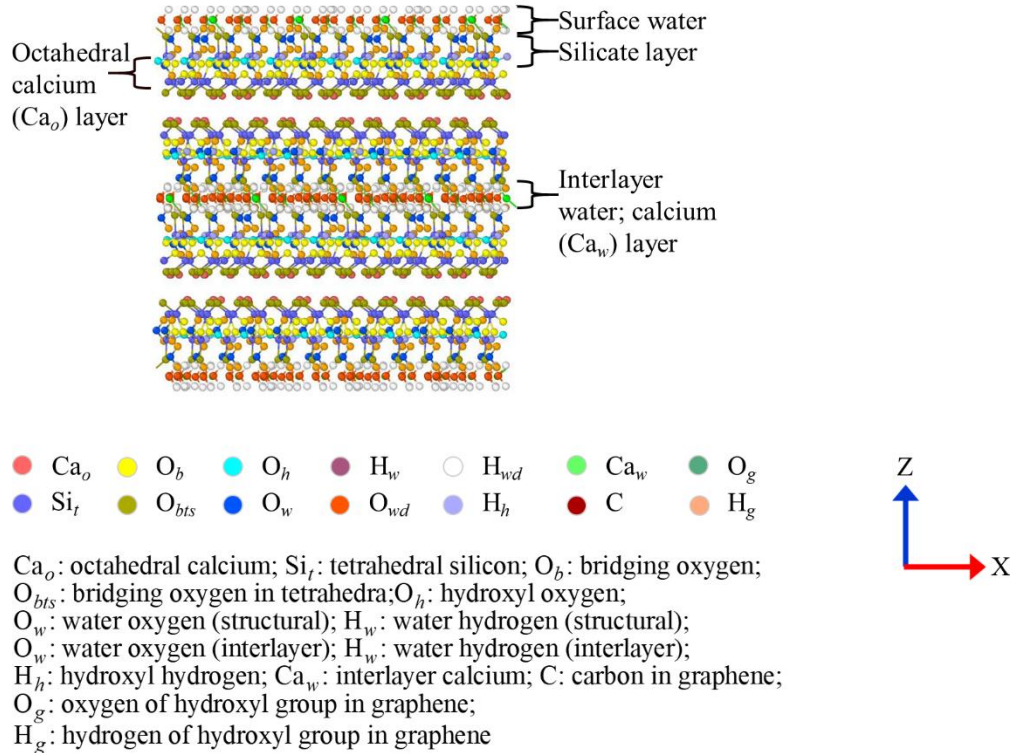


Figure 4.6. The model of the T_{14} structure nanocomposite showing the three structural layers responsible for building the structural skeleton of T_{14} .

FGS structures. The Graphene sheet (GS) and functionalized Graphene sheet (FGS) with four different surface coverages were modeled (25%, 50%, 75%, and 100%) using the Materials Studio software package. The surface coverage was calculated as the ratio of number of $-OH$ groups to the number of carbon atoms in the FGS basal plane. The zigzag (ZZ) and armchair (AC) edges of graphene were oriented along the Cartesian coordinate system X [1 0 0] and Y [0 1 0] directions, respectively. The FGS systems were $22 \text{ \AA} \times 28 \text{ \AA}$ in size and consisted of 252 sp^2 bonded carbon (C) atoms in a hexagonal ring pattern and varying coverages of $-OH$ groups. The $-OH$ groups were oriented on the FGS basal plane in two ways: with a random arrangement (R) and zigzag clustered line pattern (ZZ). The C–C, C–O, and O–H bond lengths were 1.39 \AA and 1.0 \AA , respectively. The $\angle C-C-C$, $\angle C-C-O$, and $\angle C-O-H$ bond-angles were 120° , 109.5° , and 109.5° , respectively. The thickness of the FGS was 3.35 \AA .

T₁₄/GS nanocomposite models. To construct the T₁₄ structures reinforced with FGS with varying surface coverages (T₁₄/FGS nanocomposites), the FGS was placed 4 Å below the (0 0 $\bar{1}$) planes of the T₁₄ systems with the ZZ and AC edges of the FGS oriented along the X- and Y-directions, respectively (Figure 4.7). The –OH groups of the FGS pointed towards the (0 0 $\bar{1}$) plane of the T₁₄. In this paper, the interlayer (0 0 $\bar{1}$) plane of T₁₄ was chosen as opposed to the calcium and silicate layers (Section 4.2.2) because the interaction of water molecules in the (0 0 $\bar{1}$) plane with the –OH groups of FGS was of importance.

(a) Tobermorite 14 Å (T₁₄) and functionalized graphene sheet (FGS) with random clustered 25% –OH (R)

(b) Tobermorite 14 Å (T₁₄) and functionalized graphene sheet (FGS) with 25% –OH in zigzag clustered line pattern (ZZ)

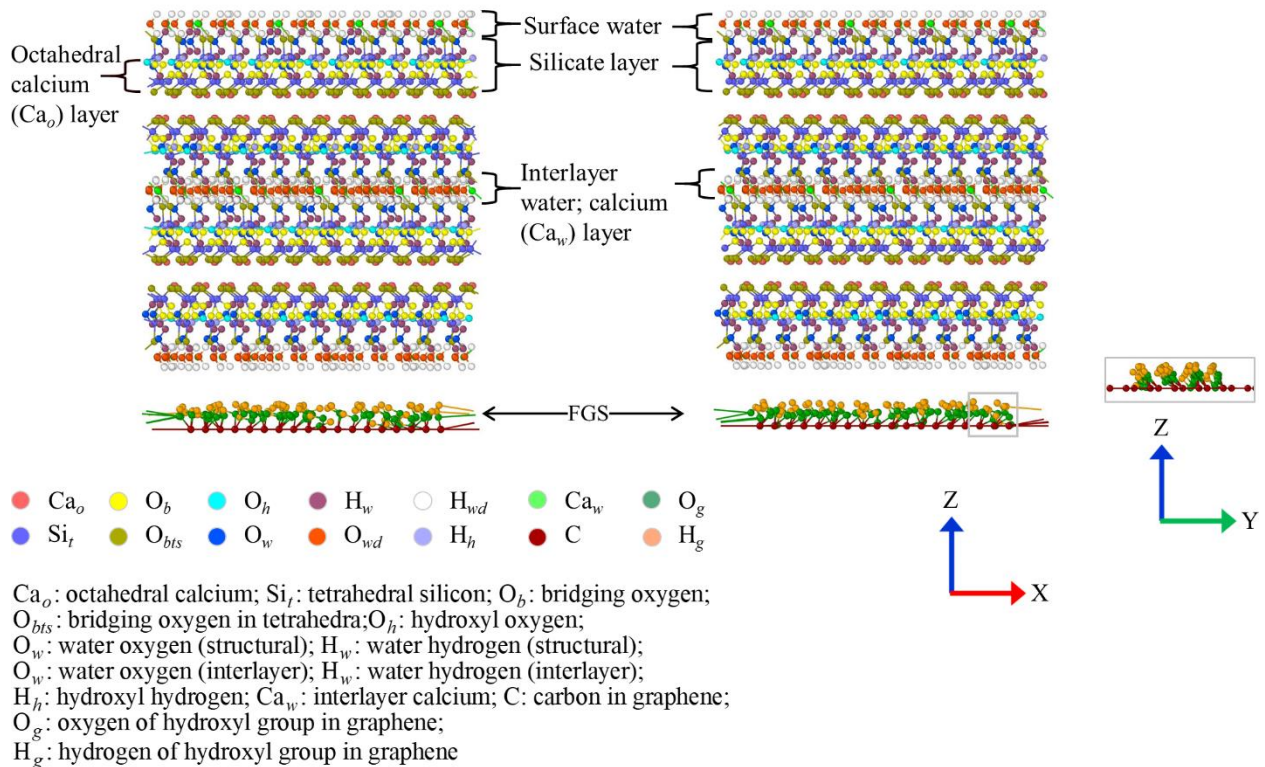


Figure 4.7. Representative models of the T₁₄/FGS nanocomposite (a) FGS with 25% –OH with random pattern and (b) FGS with 25% –OH with zigzag clustered line pattern of –OH.

4.2.3.2. Force field and charge equilibration

Force field. The Consistent Valence Force Field (CVFF) was employed for the simulation of the GS [138]. The CVFF has been previously shown to properly represent the tensile and shear properties of graphene and carbon nanotubes [33, 143, 190] and has been used in the study of the interactions of graphitic structures with tobermorite and aqueous solutions [144, 185]. The C–C bond interaction of the GS was simulated with the Morse potential [141]. The angle bending, torsion, and improper interactions were simulated using the harmonic parameters of the CVFF. The partial atomic charges, non-bonded and bonded interactions among the T₁₄ atoms were simulated using the Clay force field (ClayFF) [184, 186], which relied on the flexibility of coulombic interactions between the interacting atoms to represent bonding. ClayFF was developed to study the structural and dynamic properties of hydrated and mineral systems [184, 186, 191-193] and has been successfully used to study the mechanical and elastic properties of clay-based minerals and clay-based nanocomposites [193-197]. While ClayFF has been reported to generally reproduce well the out-of-plane elastic constants and overpredict the in-plane elastic properties of cement-related phases [193, 194, 198-200], in this study, the response of the GS was dominant in the T₁₄/FGS nanocomposite systems and an over-prediction of the elastic properties of the T₁₄ systems was thus considered to have a minimal effect on the elastic properties of the overall nanocomposites. The interactions among the carbon atoms of the GS and T₁₄ atoms were modeled using the Lennard-Jones (LJ) potential [201]. The values of the CVFF and ClayFF parameters are provided in the Appendix B.

Charge equilibration. The partial atomic charges for the T₁₄ structures were obtained from [184]. For GS, zero charge was assigned to all the carbon atoms (because GS is charge neutral). To keep the FGS charge neutral, partial atomic charges were assigned to the C, O, and H atoms using the built-in QEq charge equilibration method [145] in LAMMPS.

4.2.3.3. Equilibration

All MD simulations were performed using LAMMPS, an open-source MD simulation software [42]. The T₁₄ structure and the T₁₄/FGS nanocomposites were energy minimized at 0 K using the conjugate gradient method to reduce the excess pressure build-up during the geometry setup. The pristine T₁₄ systems and T₁₄/FGS nanocomposites were then equilibrated for 3 ns, respectively, at 300 K and 0 atm, using NPT (fixed number of atoms, pressure, and temperature)

ensemble conditions. The equilibration time of 3 ns was chosen so that the thermodynamic and physical parameters of the system (e.g., temperature, pressure, density, and energy) could reach an equilibrium and it was observed that at least 2 ns was required to reach a stable equilibrium. The Nosé-Hoover thermostat and barostat were used for temperature and pressure control of the systems with 100 fs and 1000 fs damping constants, respectively [148, 149]. The neighbor cut-off distance for the interacting atoms was 5 Å, and the neighbor list was updated every timestep. The long-range coulombic interactions were computed in the reciprocal space by the Particle-Particle-Particle-Mesh (PPPM) solver. The short-range coulombic interactions between atoms were calculated as:

$$\Psi^{\text{coul}} = \frac{1}{4\pi\epsilon_0} \cdot \frac{q_i q_j}{r_{ij}^2} \quad (4.3)$$

where q_i and q_j are charges on atoms i and j , ϵ_0 is the permittivity of the vacuum (8.85419×10^{-12} F/m) and $r_{ij} = |r_i - r_j|$ is the interatomic distance. The short-range van-der-Waals (vdW) interaction was computed by the Lennard-Jones (LJ) potential using:

$$\Psi^{\text{LJ}} = 4\epsilon \left[\left(\frac{\sigma}{r} \right)^{12} - \left(\frac{\sigma}{r} \right)^6 \right] \quad (4.4)$$

where ϵ is the depth of the potential well (kcal mol^{-1}), σ is the distance (Å) at which the potential was zero, and r is the interatomic distance (Å). The Lennard-Jones (LJ) and coulombic cut-off distances were 12 Å and 10 Å, respectively. The interactions between unlike atoms were calculated using the *Lorentz-Berthelot* mixing rules [202, 203]. The time integration was performed using the velocity-Verlet algorithm. All simulations were performed using a 1 fs timestep. Periodic boundary conditions in the X, Y, and Z-directions were used for all systems.

4.2.3.4. Loading methods and MD simulations

Two different loading modes were used: (i) uniaxial tension along the X, Y (ZZ edge and AC edge of the functionalized graphene sheet, respectively for the nanocomposites), and Z-directions and (ii) shear loading in the XY plane (perpendicular to the interface with the FGS for the nanocomposites) along the X-direction. To simulate the loading and ensure an equal deformation pathway, atoms at opposite edges of the pristine T_{14} structures or T_{14}/FGS

nanocomposites and within 3 Å from the edge were constrained while subjected to tensile (atoms along the direction of stretching) and shear loadings (top and bottom atoms). A strain rate of $1 \times 10^{-5} \frac{\text{Å}}{\text{Å}} \text{fs}^{-1}$ was used for both loading modes. This strain rate was within the typical ranges used in the literature [4, 204, 205]. While stretching in one direction, the pressure in the other two directions was kept at zero to allow for the Poisson's effect. The time integration of the systems was performed under the NPT condition for tensile loading and NVT (fixed number of atoms, volume, and temperature) conditions for shear loading.

4.2.3.5. Data collection and analysis

The atomistic stress was calculated from the Virial stress theorem [206] considering both the potential and kinetic energy terms. The time-averaged engineering stress was output every 500 fs and plotted against the corresponding strain to obtain the stress-strain (σ - ε) curve of each system. The strain energy densities per unit volume for tensile (Γ) and shear (Π) were calculated by integrating with the trapezoidal rule to obtain the area under the corresponding stress-strain curve from a strain of 0 to the fracture strain. The strain energy density was used as an indirect indication of the fracture toughness of the system.

The intrinsic (equilibrium, zero strain) elastic stiffness constants (C_{ij}) of the systems were computed in the isothermal-isobaric ensemble (NPT) for the normal constants (C_{ij} where $i = j = 1, 2, 3$) and the canonical ensemble (NVT) for the shear constants (C_{ij} where $i = j = 4, 5, 6$). The system under consideration was displaced from its equilibrium position at 0.0 strain to a specified strain, ε_j ($j = X, Y$) and equilibrated for 5000 fs (long enough to reach stress convergence). The collected stress data, σ_i ($i = X, Y$), were then time-averaged to get one σ_i point. The method was repeated for five values of ε_j from -0.01 to +0.01 with 0.005 strain increment (i.e., -0.01, -0.005, 0, 0.005 and 0.01). The C_{ij} were then calculated from the slope of the σ_i - ε_j plot. This method (known as the direct method [190, 207-209]) was used to obtain all independent intrinsic (C_{ij}) constants of the elastic tensor for all systems. While the triclinic T_{14} systems have twenty-one (21) independent C_{ij} , the normal-shear coupling elastic constants (C_{ij} where $i \neq j$, and $i = 1, 2, 3, j = 4, 5, 6$) were approximately zero compared to the normal and shear elastic stiffness constants. The orthorhombic symmetry with nine (9) elastic constants (including normal, shear, and normal coupling constants) was thus assumed for both the T_{14}

systems and T₁₄/GS nanocomposites. The Born mechanical stability criteria were calculated to check for the mechanical stability of all systems [76, 210]. The compliance tensor was calculated by inverting the stiffness matrix $S \equiv C^{-1}$. The compliance tensor (S) was then used to calculate the elastic moduli (E), shear moduli (G), bulk moduli (κ), and linear compressibility (β_L). These calculations were summarized in the Appendix B.

4.3. Results and Discussion

4.3.1. Effect of geometric assembly of GS in tobermorite 9 Å (T₉)

4.3.1.1. In-plane uniaxial tensile stress-strain responses

The tensile stress-strain (σ - ε) responses of the three T₉/GS nanostructures showed similar type of stress-strain evolutions qualitatively but were varying in the magnitudes of fracture strengths and fracture strains (Figure 4.8). The T₉ systems containing the GS exhibited larger tensile strengths in both the X (Figure 4.8a) and Y-directions (Figure 4.8b) compared to those of pristine T₉ systems, possibly due to the addition of stronger GS in the relatively weaker T₉ matrices. The σ - ε responses could be divided into two distinct regimes that contributed to the overall strengths and strains of the composites. As there was no relative slippage between the T₉ matrix and the GS interfaces (as the boundary atoms of the T₉ and GS were stretched simultaneously), the stress developed simultaneously on both the matrix and the GS.

The σ - ε responses in the X-directions were divided into regime-I and regime-II. The T₉ matrix of pristine T₉ system failed at a strain of 0.125 (regime-I) followed by a sudden stress drop. The stress-strain responses of the composites entered the regime-II after the initial stress drop. This was followed by small but linearly increasing trends of stress development for all the nanolaminate systems, indicating that GS was taking the majority of the loading. For the hierarchical (T₉/GS^{3H}) and stacked nanolaminates (T₉/GS^{3S}), the increasing stress was greater compared to that of the pristine T₉ alone. The AC edge of the GS in the T₉ matrix were oriented along the X-direction which possessed lower fracture stress and fracture strain compared to those of the ZZ edge. Since the T₉ matrix failed in the regime-I, the matrix did not share any more load alongside GS while the loading strain reached regime-II. The C–C bond lengths and the C–C–C bond-angles of the GS increased and deformed as the nanolaminate underwent continuous

increase in the overall strain. The final fractures occurred when the GS reached fracture stress and strain capacity and ruptured suddenly, indicating a brittle type failure at the end of regime-II. It is noteworthy that the final fracture strains of the nanolaminates were not much higher compared to the pristine T₉ system in the X-direction because the fracture strain of GS in the X-direction was very close to the failure strain of T₉ matrix itself. This study revealed that by geometrically varying the arrangement and locations of GS in T₉ matrix, it was possible to enhance both the fracture strengths (strength) and fracture strains of the nanolaminates. It should also be mentioned that despite having an increase in total fracture strain, the final failure pattern of the nanolaminates under tension was still of brittle type because of the brittle failure of GS.

In the Y-direction, the stress-strain responses in regime-I were similar to those of the X-directions. However, the widths of regime-I and regime-II were more distinctive in the Y-direction than in the X-direction. For the stacked and hierarchical nanolaminates, the stress-strain responses followed a similar linearly increasing trend at low strains as in X, thereby, increasing the fracture strengths and fracture strains of the nanolaminates by a substantial amount. The final fracture strains of the nanolaminates indicated the ultimate fracture strains of GS, which was significantly larger due to the orientation of ZZ-direction of GS being in the Y-direction, compared to that of the pristine T₉. The initial slope of the curves in both the X and Y-directions, increased when the GS were included in the systems indicating that the GS partially shared the stress development with the T₉ matrix until failure of the matrix, and hence, the failure stress at regime-I increased slightly with the varying formation of the GS. The stress-strain curves entered regime-II after the matrix failure, at which point the GS shared all the loads, leading to the eventual fracture of the nanolaminates at the maximum fracture strain of the GS. The stacked nanolaminate outperformed the other two systems in strength, stiffness, and strain energy density in the Y-direction.

The increase in strengths and strains of the nanolaminates have positive implications on the elastic moduli, strain energy density, and ductility of the laminate composites which were explored in sections X. The failure strength of the T₉ matrix was far greater compared to the experimental failure strength of cement paste in the macroscale [211]. The T₉ systems in this study were defect free, free of water molecules in the interlayer, and possessed infinite silicate

chain length due to periodic boundary condition, all of which were responsible for high failure strength of the pristine T₉ systems.

4.3.1.2. *In-plane shear stress-strain responses*

The shear stress-shear strain response of the nanolaminates (Figure 4.8c) also showed similar strength development pattern initially as the tensile stress-stress response. The nanolaminates exhibited larger fracture strengths and larger fracture strains compared to those of T₉ because of the high intrinsic larger shear strength of GS. The failure shear strain increased from 0.145 for the pristine T₉ to 0.19 (31% increase) for the stacked nanolaminate and the shear strength increased from 8.06 to 9.88 GPa (22.5% increase). The shear strengths and shear strains also increased similarly for the hierarchical nanolaminate. The shear stress- strain response also could be distinguished by regimes-I and II. The increase in shear strength for the nanolaminates resulted from the large in-plane (XY) shear strength of GS. The post-failure regime (regime II) due to shear followed a less steep slope for the hierarchical and stacked nanolaminate, whereas the slope was steeper, i.e., the failure was comparatively sudden for the pristine T₉ system, indicating a gradual failure mechanism for the stacked and hierarchical nanolaminate. This gradually decreasing shear stress with strain indicated that the shear strength dissipated steadily which led to better ductility of the nanolaminates. Similar to the tensile stress-strain responses, stacked nanolaminate was superior to the other nanolaminates in terms of shear strength. The residual stress in the nanolaminates due to shear were higher compared to those due to tension because of the contribution of larger portion of unrelaxed bond-angle bending energy in the post-failure regime. The slope of the shear stress-strain curve of the stacked nanolaminates were the highest indicating the shear stiffness being the largest of all the systems. The above discussion revealed that geometric arrangement and location of GS within the T₉ matrix also positively affected the shear strength, shear stiffness and shear strain energy density of the nanocomposites. In this section, qualitative observations on the strain energy density and stiffness of the nanolaminate systems were performed. More detailed quantitative analysis on the toughness and the stiffness are presented in sections 4.3.1.3 and 4.3.1.5.

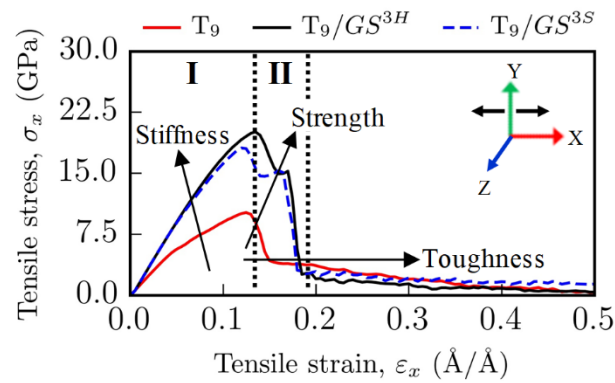
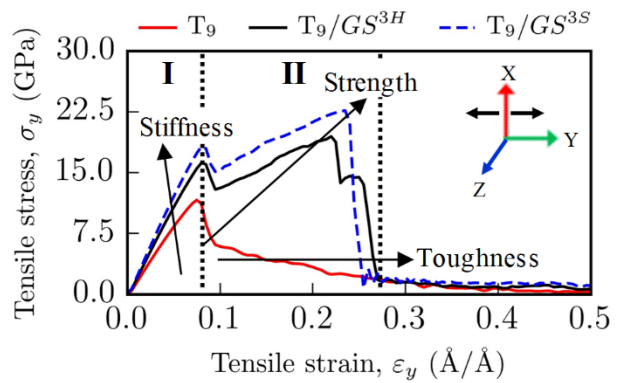
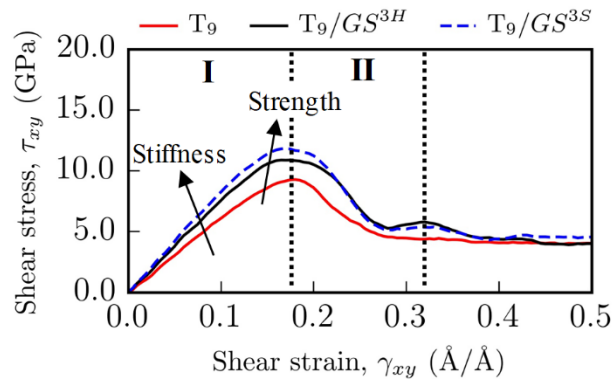
(a) Stretching along X-direction**(b) Stretching along Y-direction****(c) Shear in XY-plane along X-direction**

Figure 4.8. Tensile and shear stress-strain response of the pristine T_9 and T_9/GS nanolaminate systems, (a) tensile loading along X, (b) tensile loading along Y, (c) shear loading along X.

In this study, two key features relating to the stresses and strains were particularly noted, i.e., failure and fracture stresses and failure and fracture strains, respectively, as tabulated in Table 4.1. Failure stress and strain were termed at the stress and strain at which T_9 matrix deformed inelastically, i.e., irreversible deformation occurred in the matrix. At this strain, the bonds and angles of GS were also stretched and deformed, but not fractured yet. The peak stress before the fracture of the nanocomposite was termed as the ultimate fracture stress. The strain at which the nanocomposite experienced peak stress was termed as the ultimate fracture strain.

Table 4.1. Fracture stress and strain of the T₉ and T₉/GS systems, showing failure of the T₉ matrix and ultimate fracture of the GS.

System	Failure strain (Å/Å)			Ultimate fracture strain (Å/ Å)		
	X	Y	XY	X	Y	XY
T ₉	0.125	0.075	0.145	---	---	---
T ₉ /GS ^{3H}	0.135	0.085	0.150	0.170	0.255	0.19
T ₉ /GS ^{3S}	0.120	0.085	0.145	0.165	0.235	0.21
System	Failure stress (GPa)			Ultimate fracture stress (GPa)		
T ₉	10.16	11.60	8.06	---	---	3.85
T ₉ /GS ^{3H}	20.07	16.16	8.84	15.24	19.44/14.29	8.01
T ₉ /GS ^{3S}	18.10	18.17	9.88	15.07	22.64	6.58

4.3.1.3. Strain energy density

Toughness of any material is related to its strain energy density. It is to be acknowledged here that the stress-strain behavior of the nanolaminates resemble that of a snap-through failure and the kinetic energy involved during the fracture is unknown. Therefore, the actual toughness of the nanolaminates cannot be quantified from these strain energy density results and the results from this section are just a prediction about the strain energy density associated with the nanolaminates at the point of fracture.

The inclusion of GS in the T₉ matrix by varying geometrical location increased the strain energy densities of the T₉/GS nanolaminates (Table 4.2). However, the stacking arrangement of GS inside T₉ matrix affected the strain energy densities the most in both the tensile and shear loadings. The strain energy densities for T₉ systems in the Y-direction were lower compared to those in the X-direction because the area under the stress-strain curves for the T₉ systems for loading in the Y-direction was lower. This substantial increase in the nanolaminate strength could be attributed to the ZZ-direction of the GS being in the Y-direction. The ultimate fracture stress and fracture strain of GS in the ZZ-direction were higher than those in the AC direction, leading to an overall higher fracture strengths and fracture strains of the whole nanolaminate (Table 4.1) and eventually, higher strain energy densities in the Y-direction. The stacking nanolaminates led to the higher tensile strain energy density (Table 4.2), although, hierarchical nanolaminate showed higher fracture strain. The failure stress and the ultimate fracture stress

were lower for hierarchical nanolaminate (Table 4.1) to those of the stacking nanolaminate, leading to the lower area under the stress-strain curve, i.e., lower strain energy density in the Y-direction. Interestingly, the hierarchical nanolaminate seemed to be better in taking load than the stacking nanolaminate as the strain energy density in the X-direction for hierarchical nanolaminate was the highest among all systems. In all these systems, strain energy densities significantly increased because the composite systems fractured entirely at the fracture strains of GS which were much higher than those of pristine T₉. Additionally, GS provided very high tensile strength which led to large areas under the stress-strain curves and hence, large strain energy densities. The hierarchical arrangement produced slightly tougher material than the stacked arrangement in the X-direction. Meanwhile, both the stacked and hierarchical arrangements led to tougher nanolaminates than the pristine T₉ system in the X and Y-directions.

Table 4.2. Comparison of the tensile and shear strain energy densities of the T₉/GS nanolaminates.

Systems	Tensile strain energy density, X $\times 10^9$ (J m ⁻³)	Tensile strain energy density, Y $\times 10^9$ (J m ⁻³)	Shear Strain energy density, XY $\times 10^9$ (J m ⁻³)
T ₉	155	79	133
T ₉ /GS ^{3H}	425	565	222
T ₉ /GS ^{3S}	365	620	270

Shear strain energy densities of the nanolaminates also increased due to the presence of GS in the nanocomposite, indicating, it is possible to produce materials that showed high shear strain energy density by geometrically varying the GS location in the T₉ matrix. Similar to the tensile strain energy densities, stacking arrangement also played significant role in increasing the strain energy density by 105% from its pristine counterpart. The reason behind this increase is the large fracture shear strain of the nanolaminate although the fracture shear strength did not increase significantly. Since the shear strain energy density is an approximate measure of a material's shear toughness, evidently, stacked arrangement led to the supposedly toughest nanolaminate composite in the XY plane. By controlling the geometrical layout of GS in the T₉ matrix, tough and damage tolerant nanocomposite could be obtained.

4.3.1.4. Deformation mechanisms of the T₉ and T₉/GS systems due to tensile loadings

Deformation mechanisms in the X-direction. The deformation of the T₉ matrix during the X-direction stretching started at a strain of 0.125 corresponding to the peak failure stress (Figure 4.8a). The deformation then propagated through the T₉ matrix and covered the stress-affected area, termed as the deformation affected zone (DAZ) at a strain of 0.125- 0.13 for both nanolaminates (Figure 4.9). During the deformation process, the octahedral calcium layers, interlayer calcium, and silicate tetrahedra layers were displaced from their original positions, i.e., which broke the symmetry of the T₉ matrix, leading to the eventual failure. The octahedral calcium and silicate tetrahedra also deformed in the vicinity of the direct deformation pathway. However, the deformation at the peripheral region of the DAZ was at minimum or not affected at all. In other words, the deformation was contained in the original deformation zone. The separation of the silicate tetrahedra and calcium octahedral layers created structural cracks (strain of 0.185) in the T₉ system. These cracks continued to agglomerate and propagate through the initially created deformation path, forming nanovoids, eventually leading to a total separation of the T₉ system (Figure 4.9). In contrast, the deformation-to-separation of the T₉/GS nanolaminates followed a two-step process similar to the two regimes seen for the stress-strain responses of the composites. The deformation for the X-direction stretching of the T₉/GS nanolaminates also started at a strain of 0.125 at which point two distinct regions on opposite sides of the GS deformed. Near the vicinity of the DAZ, octahedral calcium layers and the silicate tetrahedral layers were deformed along the out-of-plane Z-direction. As the strain increased (0.13- 0.135), the deformation propagated through the nanolaminates. At a strain of 0.135, the separation of the octahedral calcium layers and silicate tetrahedral layers created nanovoids in the T₉ matrix. At large strains, these nanovoids in the T₉ matrix became more apparent, and most importantly, the GS fractured, at which point the stress of the overall composite dropped significantly in the stress-strain curves (Figure 4.8). This was referred to as the ultimate fracture strain in Table 4.1.

As the strain increased, the atoms near the peripheral region of the DAZ were also displaced. However, the crack propagation followed the original deformation path rather than creating secondary crack fronts. Another interesting observation was that the presence of the GS tended to decrease the width of the DAZ because the GS took a larger portion of the stress compared to the T₉ matrix. The stress could concentrate in a smaller area and propagate by deforming a smaller region.

Interestingly, the averaged $\text{Si}_t\text{-O}_{bts}$ and $\text{Ca}_o\cdots\text{O}_{bts}$ bond lengths and bond distances of the $\text{T}_9 / \text{GS}^{3S}$ nanolaminate shortened as the strain accumulated. However, the bond distances increased for the $\text{T}_9 / \text{GS}^{3H}$ nanolaminates, indicating that the silicate tetrahedra and calcium octahedra layers were less responsible for the failure of the T_9 matrix for the stacked nanolaminate than for the hierarchical nanolaminate (Table 4.3). The $\text{Ca}_w\cdots\text{Ca}_w$ distances increased from 3.91 Å to 4.02 Å (~2.8%) within the regime-I indicating that the interlayer calcium region was responsible for the matrix failure during the X-stretching. Even though the bond distances of the structural layers ($\text{Ca}_o\cdots\text{Ca}_o$ and $\text{Si}_t\cdots\text{Si}_t$) remained unaffected, the displacement of a portion of the structural layers could lead to the disruption of chain arrangement and subsequent failure of the matrix. For the $\text{T}_9 / \text{GS}^{3H}$ nanolaminates, the $\text{Si}_t\text{-O}_{bts}$ and $\text{Ca}_w\text{-O}_{bts}$ bonds were broken due to the tension in X-direction and the disruption of Ca_o layers led to the eventual separation of the pristine T_9 matrix (Figure 4.10). For the nanolaminates, the deformation could not propagate throughout the matrix as it was hindered by the GS. The GS acted as a crack arresting element in the nanolaminates (Figure 4.11 and Figure 4.12). The crack propagation and agglomeration showed that the hierarchical nanolaminate had several isolated growths of cracks in the matrix due to the alternating arrangement of the GS (Figure 4.11d), while the stacked nanolaminate had agglomerated crack growth (Figure 4.12d).

Table 4.3. Bond distances during tensile loading of the T_9/GS nanolaminates along the X-direction, shown before loading, at failure of the T_9 matrix, and at failure of the GS.

System	Strain	$\text{Ca}_o\cdots\text{Ca}_o$	$\text{Ca}_o\cdots\text{O}_{bts}$	$\text{Si}_t\cdots\text{Si}_t$	$\text{Si}_t\text{-O}_{bts}$	$\text{Ca}_w\cdots\text{Ca}_w$	$\text{Ca}_w\text{-O}_{bts}$
	ε						
$\text{T}_9/\text{GS}^{3S}$	0.000	3.248	2.521	2.963	1.532	3.91	2.508
	0.125	3.171	2.509	2.91	1.528	4.02	2.462
	0.17	3.179	2.514	2.93	1.529	3.93	2.521
$\text{T}_9/\text{GS}^{3H}$	0.000	3.156	2.529	2.985	1.525	6.79	2.525
	0.145	3.108	2.523	2.932	1.552	7.069	2.525
	0.175	3.075	2.525	2.97	1.549	7.235	2.499

Note: \cdots denoted bond distances
 $-$ denoted bond lengths

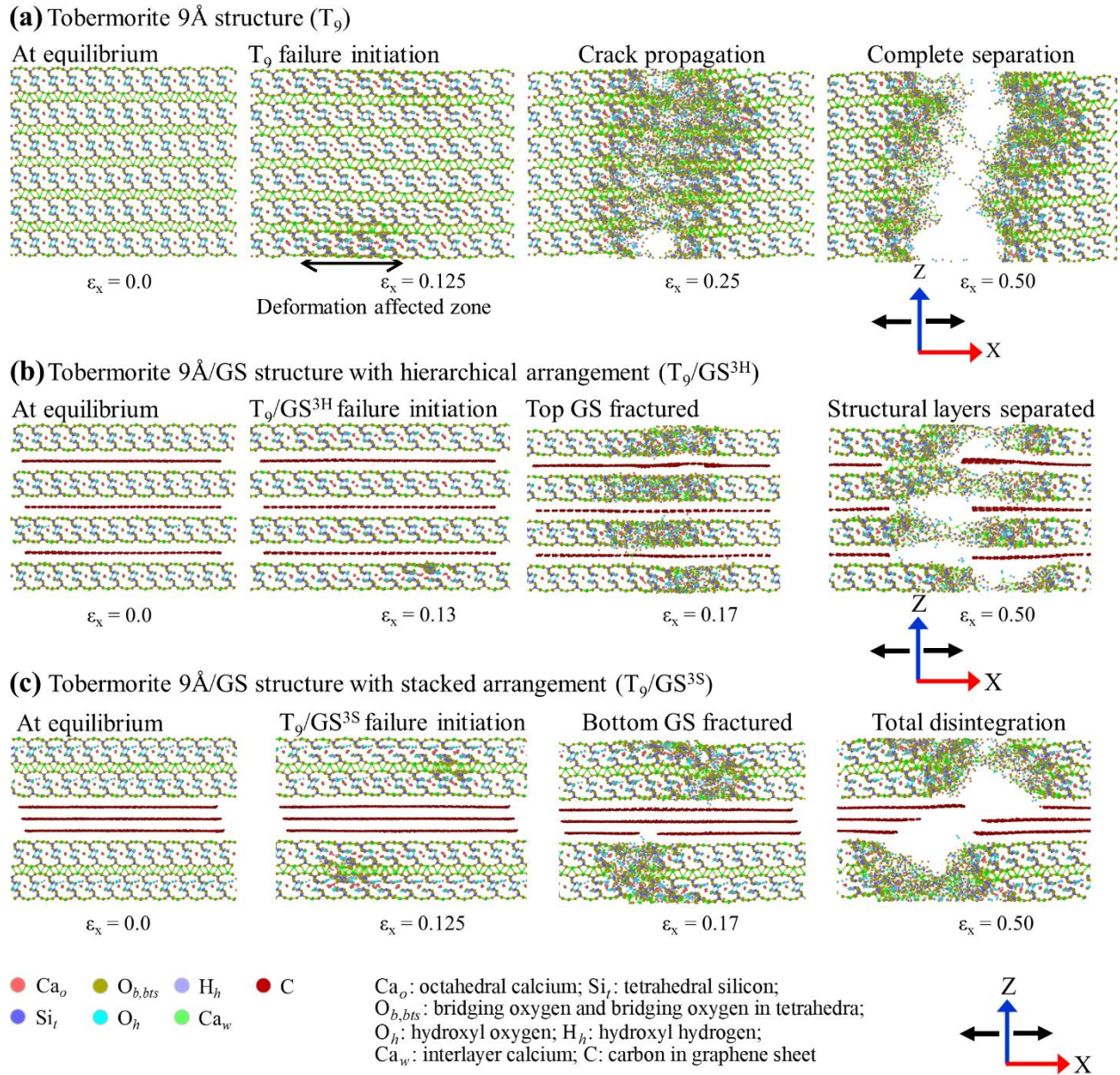
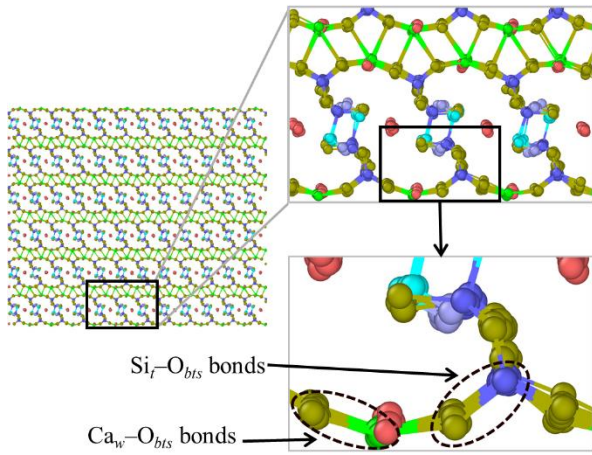
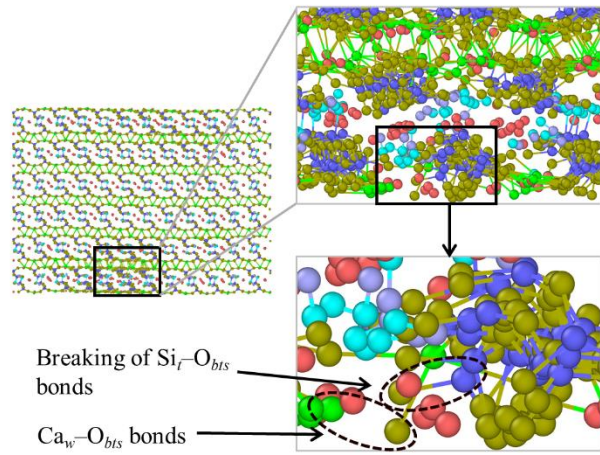


Figure 4.9. Deformation of the structural layers and fracture mechanisms of T_9 and T_9/GS systems in the X-direction: (a) T_9 matrix, (b) T_9/GS^{3H} nanolaminate, (c) T_9/GS^{3S} nanolaminate.

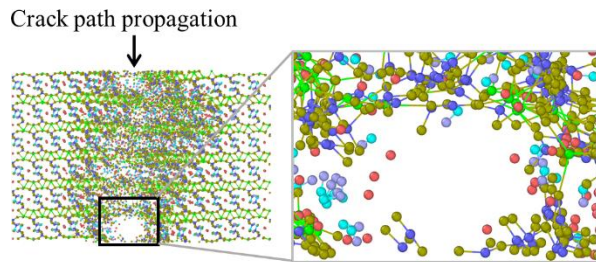
(a) T_9 at equilibrium before loading ($\epsilon_x = 0.0$)



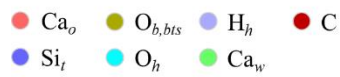
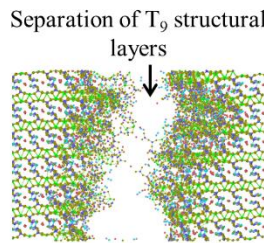
(b) T_9 at failure ($\epsilon_x = 0.125$)



(c) T_9 with further deformation ($\epsilon_x=0.25$)



(d) T_9 at full separation ($\epsilon_x=0.50$)



Ca_o : octahedral calcium; Si_t : tetrahedral silicon;
 $O_{b,bts}$: bridging oxygen and bridging oxygen in tetrahedra;
 O_h : hydroxyl oxygen; H_h : hydroxyl hydrogen;
 Ca_w : interlayer calcium; C: carbon in graphene sheet

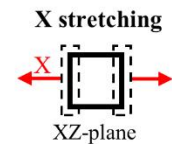
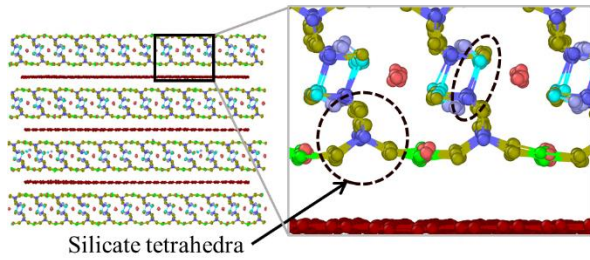
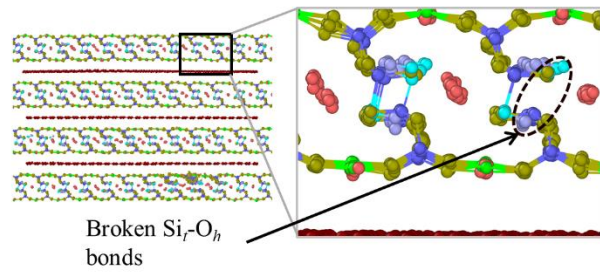


Figure 4.10. Detailed deformation process of pristine the T_9 matrix in the X-direction at different strains: (a) equilibrium (strain 0.0), (b) matrix failure (0.125), (c) GS fracture strain (0.25), (d) strain (0.50) at full separation.

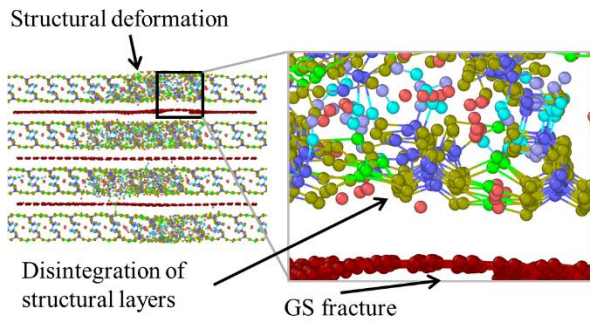
(a) T_9/GS^{3H} at equilibrium before loading ($\epsilon_x = 0.0$)



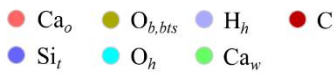
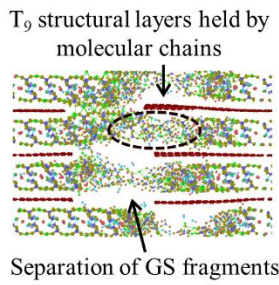
(b) T_9/GS^{3H} at failure ($\epsilon_x = 0.13$)



(c) T_9/GS^{3H} with further deformation ($\epsilon_x=0.175$)



(d) T_9/GS^{3H} at full separation ($\epsilon_x=0.50$)



Ca_o : octahedral calcium; Si_t : tetrahedral silicon;
 $O_{b,bts}$: bridging oxygen and bridging oxygen in tetrahedra;
 O_h : hydroxyl oxygen; H_h : hydroxyl hydrogen;
 Ca_w : interlayer calcium; C: carbon in graphene sheet

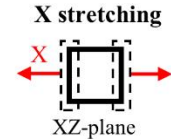


Figure 4.11. Detailed deformation process of the hierarchical T_9/GS^{3H} nanolaminate in the X-direction at different strains: (a) equilibrium (strain 0.0), (b) matrix failure (0.13), (c) GS fracture strain (0.175), (d) final strain (0.50) at full separation.

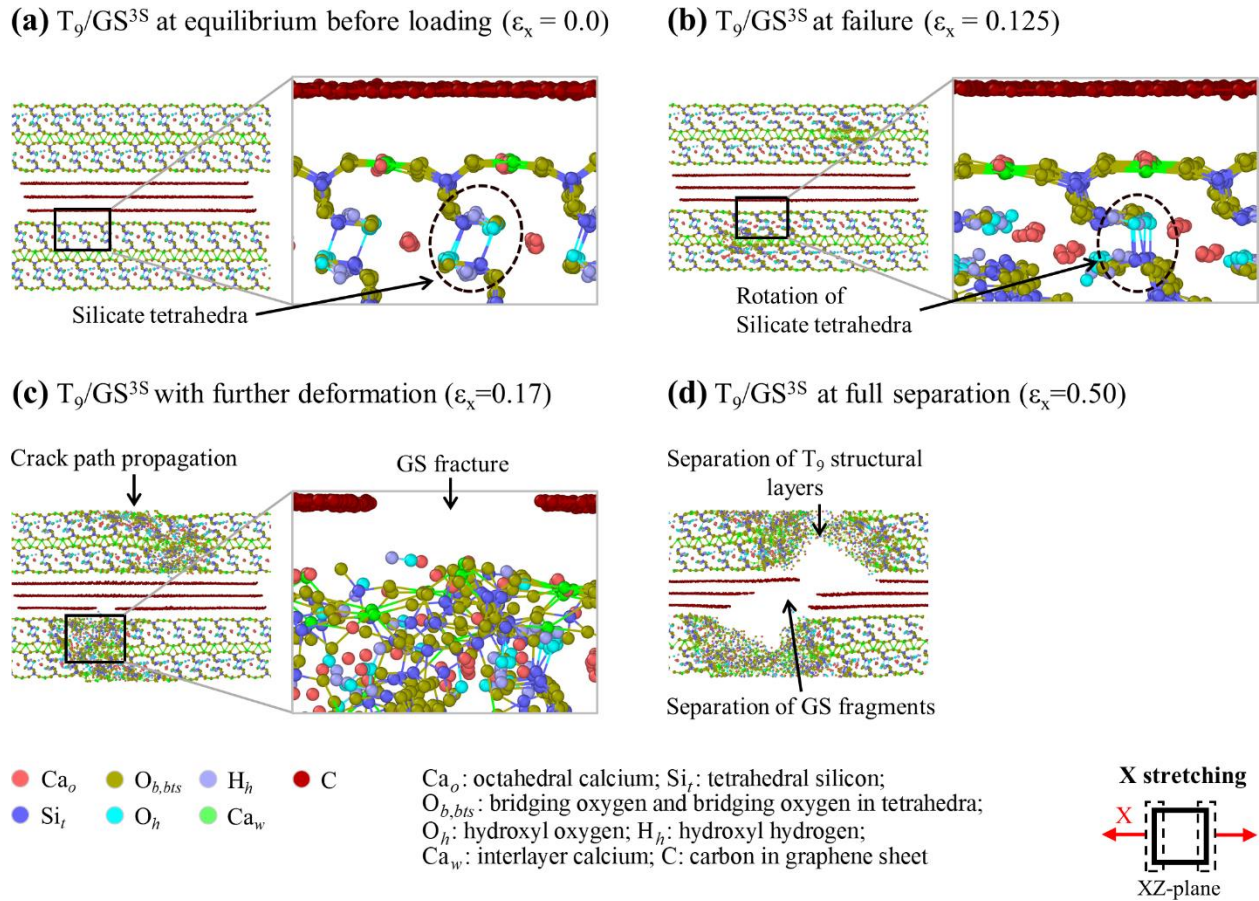
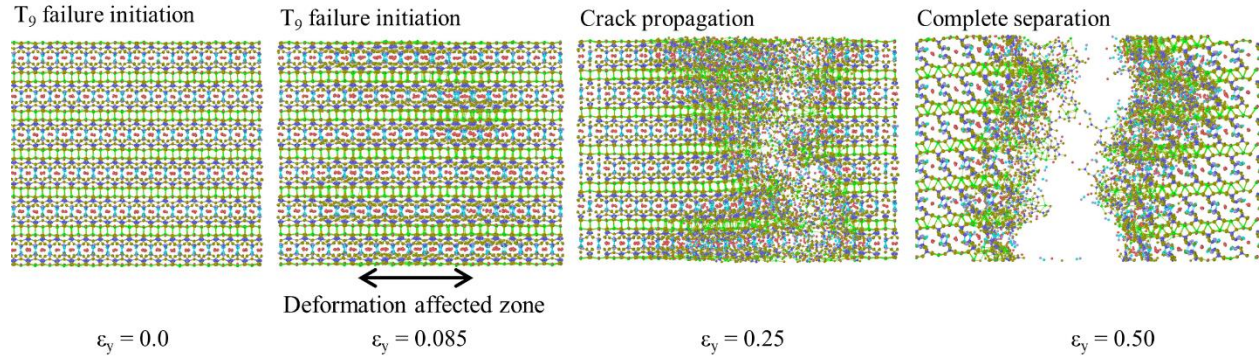


Figure 4.12. Detailed deformation process of the stacked T_9/GS^{3S} nanolaminate in the X-direction at different strains: (a) equilibrium (strain 0.0), (b) matrix failure (0.125), (c) GS fracture strain (0.17), (d) final strain (0.50) at full separation.

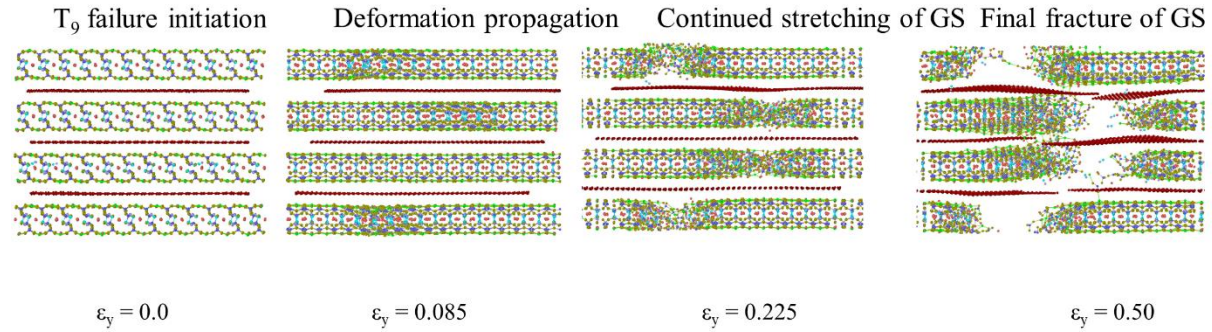
Deformation mechanisms in the Y-direction. The pristine T_9 matrix had a wider DAZ in the Y-direction than in the X-direction (Figure 4.13) The T_9 matrix in the Y-direction had a lower failure strain than in the X-direction because of less rotation of the silicate tetrahedra (Figure 4.14). As a result, the stress could not concentrate in a small region, rather, it was spread out in a larger zone, i.e., a wider DAZ. For the hierarchical nanolaminate, the deformation was symmetrical about the central GS (Figure 4.13 and Figure 4.15). For the stacked nanolaminate, the deformation was also symmetrical with respect to the central GS (Figure 4.16). Like the hierarchical nanolaminate, the stacked nanolaminate experienced deformation originating and propagating through the T_9 matrix during tensile strains ranging from $\epsilon = 0.125$ -0.16. At, $\epsilon = 0.165$, the bottom GS fractured, followed by the fracture of the top GS at $\epsilon = 0.17$, and lastly the middle GS fractured at $\epsilon = 0.175$. Thus, it was possible that similar to the hierarchical

arrangement, the stacked arrangement also shielded the propagation of deformation through the T_9 matrix.

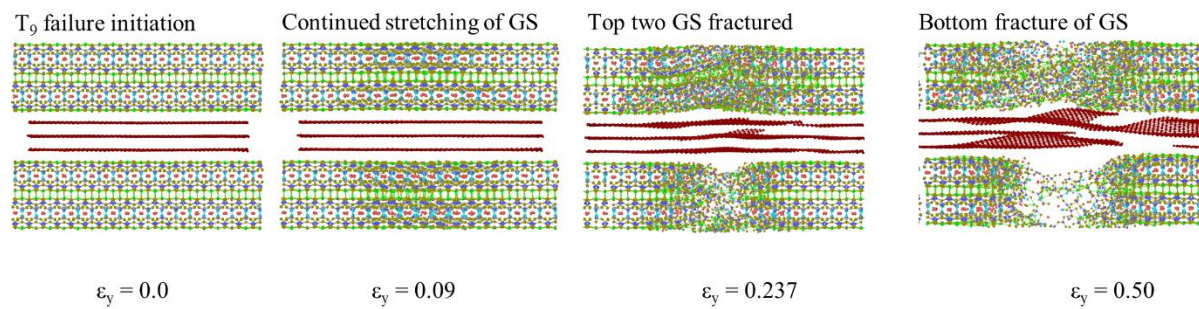
(a) Tobermorite 9Å structure (T_9)



(b) Tobermorite 9Å/GS structure with hierarchical arrangement (T_9/GS^{3H})



(c) Tobermorite 9Å/GS structure with stacked arrangement (T_9/GS^{3S})



- Ca_o ● $O_{b,bts}$ ● H_h ● C
- Si_t ● O_h ● Ca_w

Ca_o : octahedral calcium; Si_t : tetrahedral silicon;
 $O_{b,bts}$: bridging oxygen and bridging oxygen in tetrahedra;
 O_h : hydroxyl oxygen; H_h : hydroxyl hydrogen;
 Ca_w : interlayer calcium; C: carbon in graphene sheet

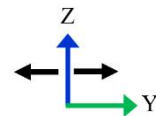
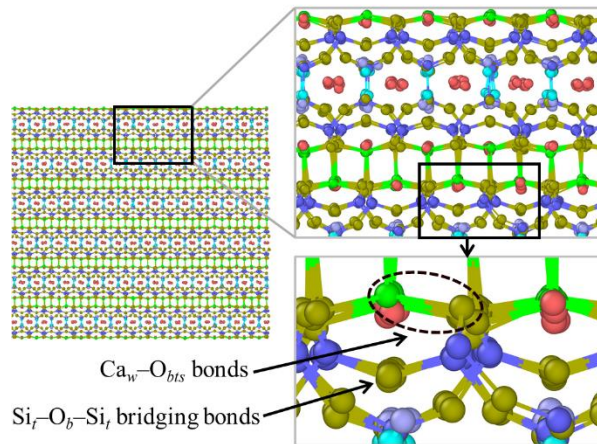
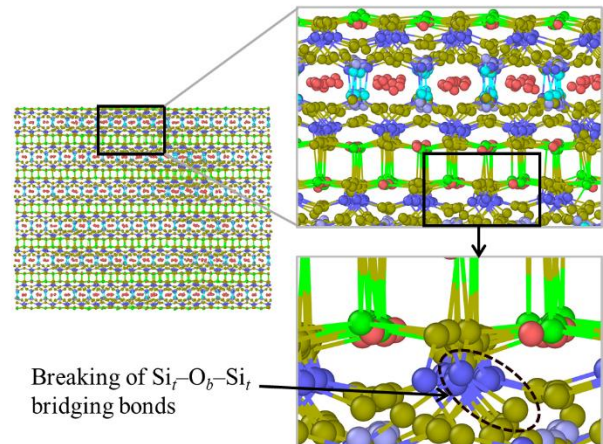


Figure 4.13. Deformation of the structural layers and fracture mechanisms of the T_9 and T_9/GS systems in the Y-direction: (a) T_9 matrix, (b) hierarchical T_9/GS^{3H} nanolaminate, (c) stacked T_9/GS^{3S} nanolaminate.

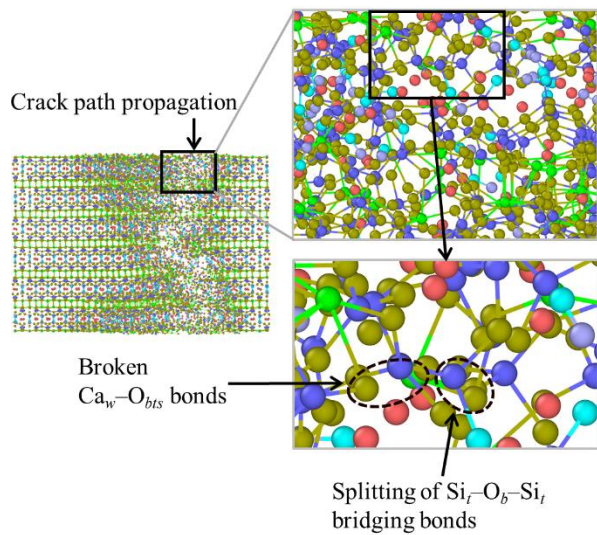
(a) T_9 at equilibrium before loading ($\epsilon_y = 0.0$)



(b) T_9 at failure ($\epsilon_y = 0.08$)



(c) T_9 with further deformation ($\epsilon_y=0.25$)



(d) T_9 at full separation ($\epsilon_y=0.50$)

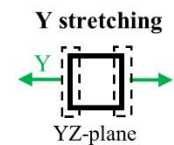
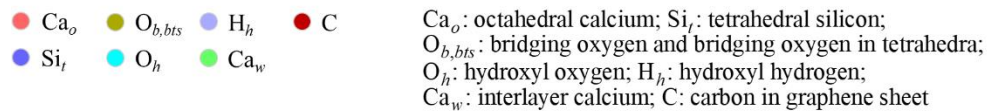
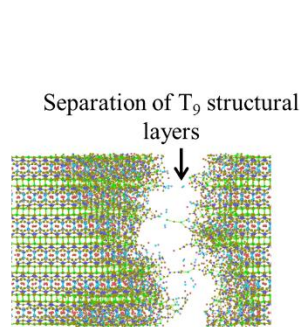
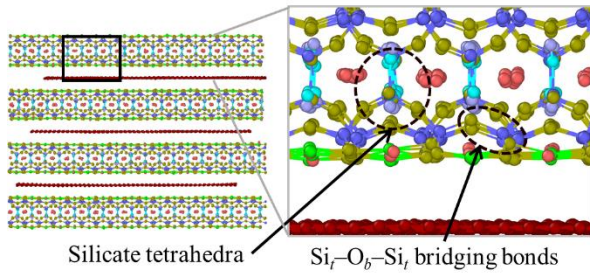
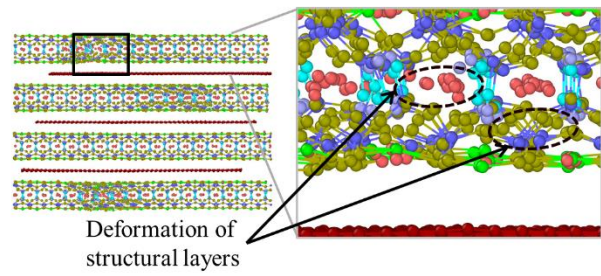


Figure 4.14. Detailed deformation process of the pristine T_9 matrix in the Y-direction at different strains: (a) equilibrium (strain 0.0), (b) matrix failure (0.125), (c) fracture strain (0.25), (d) final strain (0.50) at full separation.

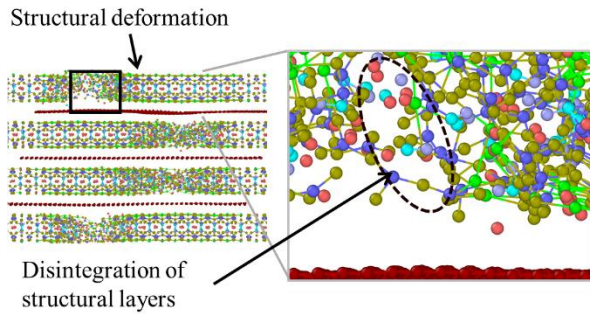
(a) T_9/GS^{3H} at equilibrium before loading ($\epsilon_y = 0.0$)



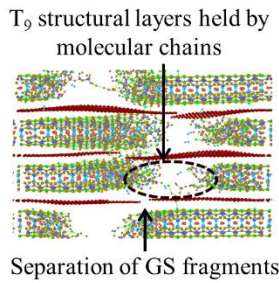
(b) T_9/GS^{3H} at failure ($\epsilon_y = 0.085$)



(c) T_9/GS^{3H} with further deformation ($\epsilon_y=0.225$)



(d) T_9/GS^{3H} at full separation ($\epsilon_y=0.50$)



Ca_o : octahedral calcium; Si_t : tetrahedral silicon;
 $O_{b,bts}$: bridging oxygen and bridging oxygen in tetrahedra;
 O_h : hydroxyl oxygen; H_h : hydroxyl hydrogen;
 Ca_w : interlayer calcium; C: carbon in graphene sheet

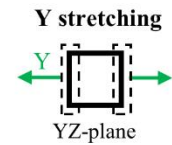
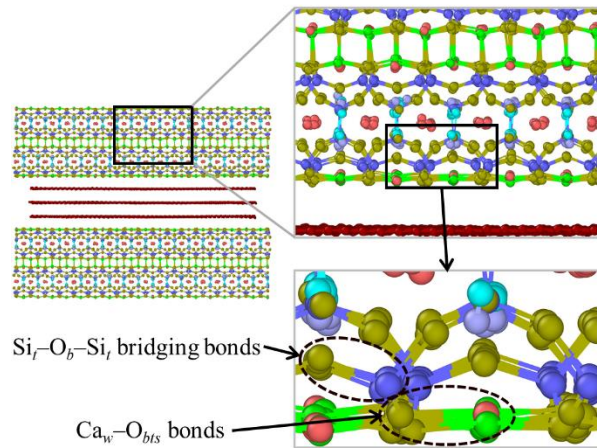
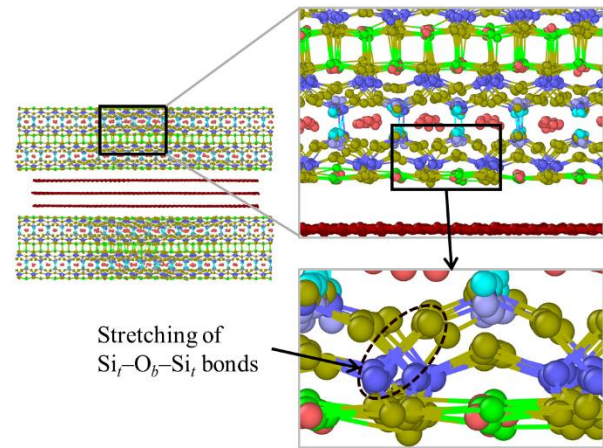


Figure 4.15. Detailed deformation process of the pristine T_9/GS^{3H} matrix in the Y-direction at different strains: (a) equilibrium (strain 0.0), (b) matrix failure (0.125), (c) fracture strain (0.25), (d) final strain (0.50) at full separation.

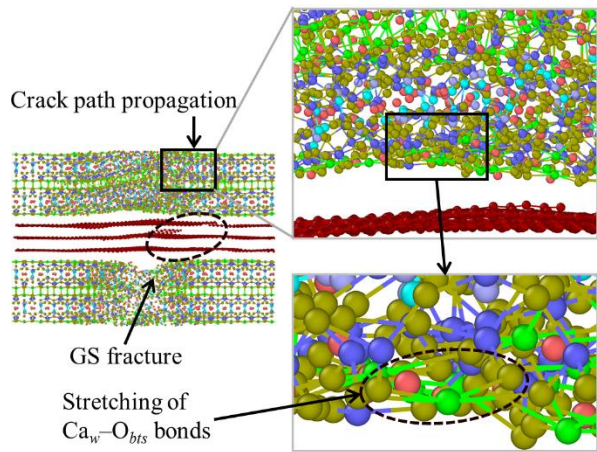
(a) T_9/GS^{3S} at equilibrium before loading ($\epsilon_y = 0.0$)



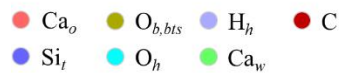
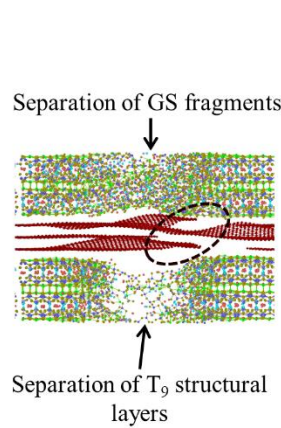
(b) T_9/GS^{3S} at failure ($\epsilon_y = 0.135$)



(c) T_9/GS^{3S} with further deformation ($\epsilon_y=0.25$)



(d) T_9/GS^{3S} at full separation ($\epsilon_y=0.50$)



Ca_o : octahedral calcium; Si_t : tetrahedral silicon;
 $O_{b,bts}$: bridging oxygen and bridging oxygen in tetrahedra;
 O_h : hydroxyl oxygen; H_h : hydroxyl hydrogen;
 Ca_w : interlayer calcium; C: carbon in graphene sheet

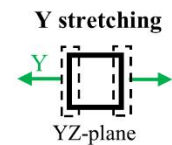


Figure 4.16. Detailed deformation process of the pristine T_9/GS^{3S} matrix in the Y-direction at different strains: (a) equilibrium (strain 0.0), (b) matrix failure (0.125), (c) fracture strain (0.25), (d) final strain (0.50) at full separation.

4.3.1.5. Elastic constants

Greater in-plane normal constants (C_{11} and C_{22}) in Figure 4.17 were seen for the T_9/GS nanolaminates compared to the pristine T_9 matrix due to the large normal constants of the GS. However, the out-of-plane normal constant, C_{33} , of the T_9/GS^{3H} decreased slightly due to the

large number of T₉/GS interfaces, which led to a slower rate of stress development in the nanolaminate. The T₉/GS^{3S} showed similar C₃₃ because interaction between the stacked formation of GS and T₉ led to almost identical rate of initial stress development. The increase in normal constants for the nanolaminates was attributed to the larger intrinsic in-plane stiffness of GS.

The normal-normal coupling constants (C₁₂, C₁₃, and C₂₃) demonstrated stress in the i^{th} (1,1,2) direction for strain in the j^{th} (2,3,3) direction. It was observed that the incorporation of the GS in the T₉ matrix in planar orientation guided an anisotropic stress distribution through the T₉/GS nanolaminates, i.e., the stress flowed mostly in the direction of stretching (GS being anisotropic), leaving the other two directions under-stressed. Therefore, a reduction occurred in the normal-normal coupling constants of the nanolaminates. The stiffness constants, C_{ij}, also revealed that the nanolaminates remained extremely stiff \parallel to the XY plane due to the added stiffness of GS to the already stiff XY plane of the T₉ matrix.

The shear stiffness constants (C₄₄, C₅₅, and C₆₆) represented the resistance of a material against angular distortion. The in-plane shear constant, C₆₆, for the nanolaminates increased compared to that of the T₉ matrix (Figure 4.17). However, not much difference in the C₆₆ constant was observed between the stacked and hierarchical nanolaminates indicating that the in-plane shear resistance was somewhat insensitive to the arrangement of the GS in the T₉ matrix. However, due to the very low shear transfer between the GS and T₉ interfaces, the shear constants C₄₄ and C₅₅ were extremely small. This low out-of-plane stiffness for graphene [18] and graphene-polymer nanocomposite [126] has already been studied in the literature. This issue could be overcome by either embedding GS inside the T₉ matrix instead of building the composite as infinite laminated structure, or by artificially creating covalent bonding between GS layers and T₉ interfaces. From the results obtained, it can also be deduced that the GS could increase the low out-of-plane (Z-direction) stiffness significantly if oriented in a vertically hierarchical or stacked arrangement inside the T₉ matrix. The out-of-plane shear for hierarchical arrangement along YZ due to shear loading along the XY were also higher than all the other systems. The in-plane shear of the nanolaminates was higher compared to that of the T₉ matrix because of the large in-plane shear strength of the GS. Hence, it can be concluded from the elastic constant calculations that the hierarchical configuration of the GS alternatively

sandwiched in the T_9 matrix had advantage in taking shear compared to the stacked configuration.

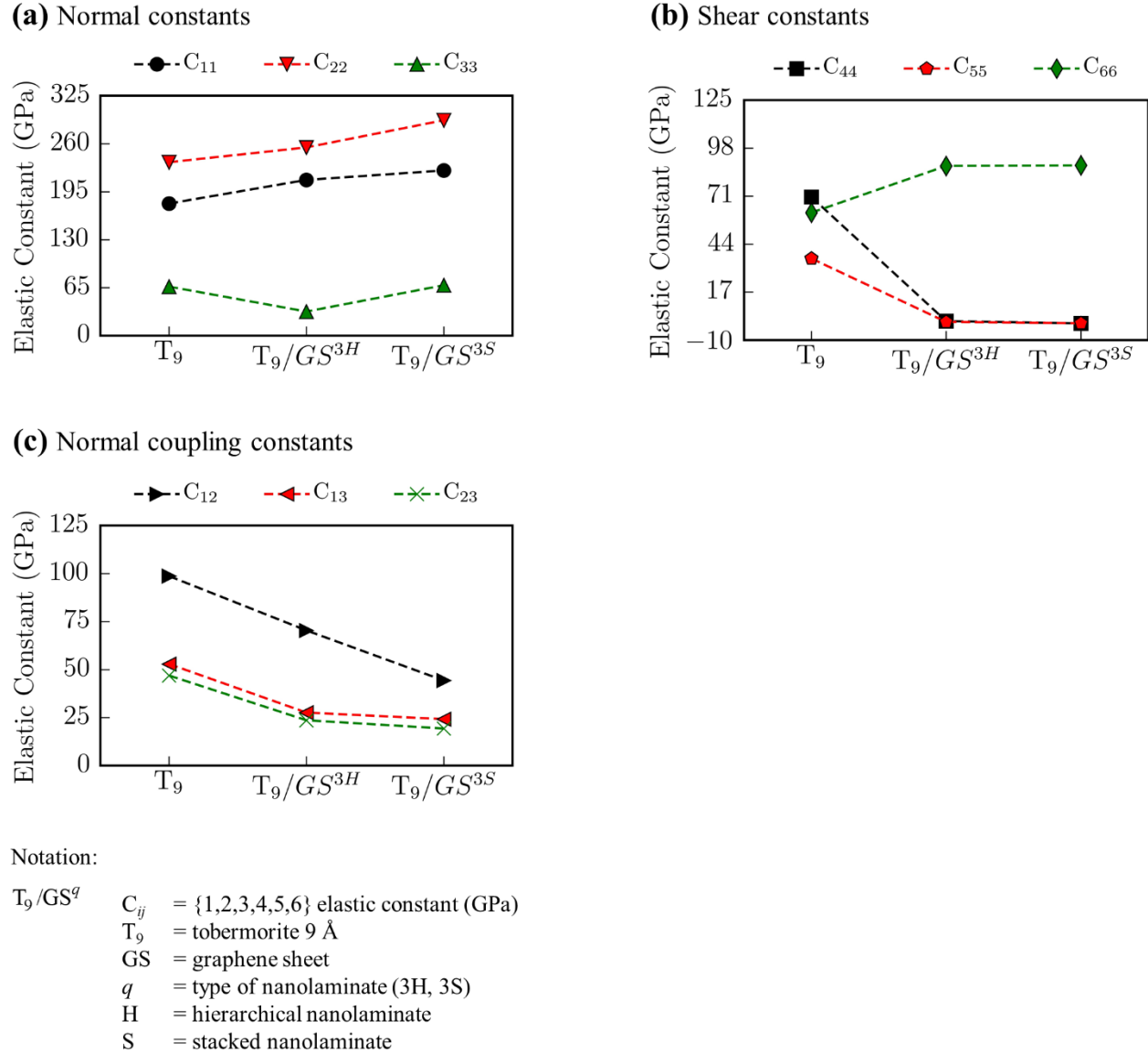


Figure 4.17. Comparisons of elastic constants of the T_9 and T_9/GS systems, (a) normal constants, (b) shear constants, and (c) normal coupling constants.

The density of the T_9 systems decreased from 2.768 g cm^{-3} to 2.47 g cm^{-3} for T_9/GS^{3H} , a 12% decrease. For the stacked nanolaminate, the density was 2.52 g cm^{-3} slightly more than that of the hierarchical nanolaminate. The shear constant-density ratio increased by 64% and 60% for

hierarchical and stacked nanolaminates, respectively, indicating that both arrangements behave positively on geometrical changes in terms of shear resistance. So, it indicated that the same number of total atoms also required less equilibrium volume for the stacked nanolaminate in the T₉ matrix due to the higher GS-GS interfacial interaction than the GS-T₉ interaction. The shear-to-normal constant ratio increased with a decrease in density (Table 4.4) compared to the pristine T₉. For the stacked nanolaminate, the normal constants increased much more compared to the hierarchical nanolaminate but the shear constant remained almost the same as that of the hierarchical GS nanolaminate indicating the insensitivity of shear on geometrical location of the GS in the T₉ matrix. The results demonstrated that higher normal-to-shear coupling can also be obtained through stacked or hierarchical arrangements of GS in T₉ blocks.

Table 4.4. Ratio of elastic constants.

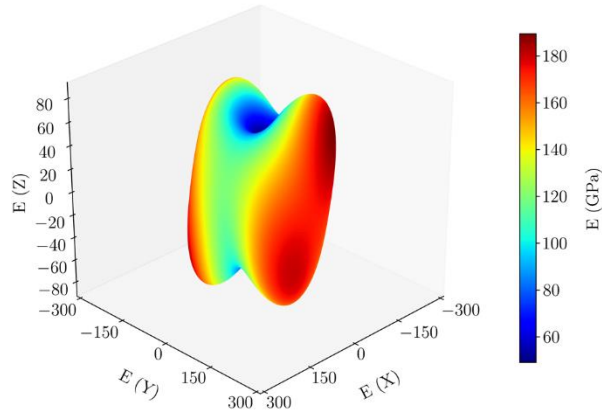
Designation	Density, ρ (g cm ⁻³)	C_{66}/C_{11}	C_{66}/C_{22}	C_{66}/ρ (m ² s ⁻²)
T ₉	2.77	0.34	0.26	21.84×10^6
T ₉ /GS ^{3H}	2.47	0.44	0.36	35.75×10^6
T ₉ /GS ^{3S}	2.52	0.40	0.30	34.92×10^6

4.3.1.6. Directional anisotropy of linear compressibility and elastic modulus

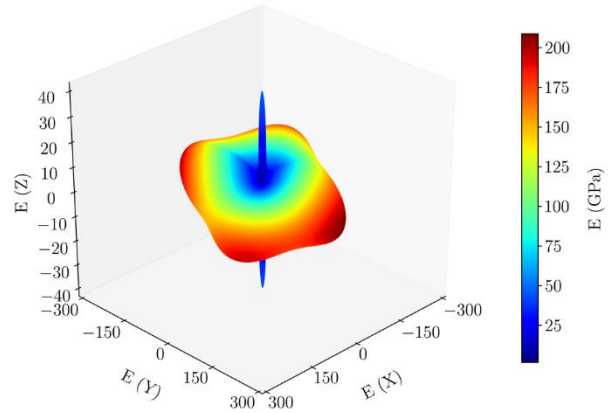
Although, the nanolaminates seemed to possess orthotropic symmetry, the normal-shear coupling constants (C_{14} , C_{15} , C_{16} , C_{24} , C_{25} , C_{26} , C_{34} , C_{35} , and C_{36}) were non-zero, which had immense effects on the directionality of elastic moduli and compressibility. The linear compressibility (β_L) of T₉ showed highly anisotropic behavior with large compressibility in the out-of-plane direction (Z-direction) and very low compressibility in the in-plane (X and Y) directions (large bulk modulus), (Figure 4.19). The in-plane silicate tetrahedral chain and Ca-octahedral framework prevented the T₉ against compression, thus low compressibility was achieved in these planar $[h k 0]$ directions. In the $[0 0 1]$ direction, the interlayer Ca atoms disrupted the silicate and octahedral layered chain connectivity, thus large compressibility was possible in that direction. The incorporation of the GS in the T₉ matrix altered the direction of the linear compressibility anisotropy of the nanolaminates, possibly due to the high in-plane bulk modulus (low compressibility) and relatively insignificant out-of-plane compressibility of the

GS. The location of GS in T_9 played an important role in modulating the linear compressibility of the nanocomposites. For both nanocomposites, the higher linear compressibility occurred closer to the $\langle 1\ 1\ 1 \rangle$ direction, indicating the modulating capability of the GS in terms of compressibility of the T_9 /GS systems.

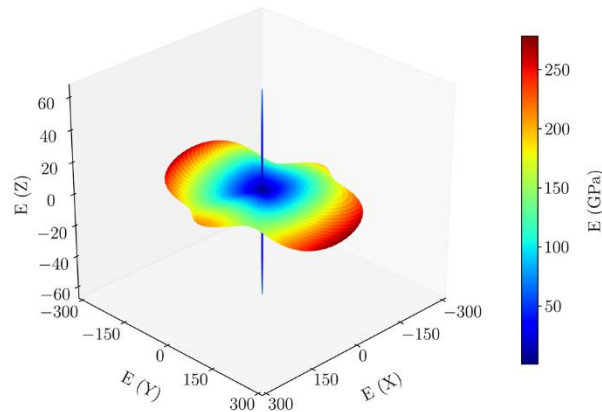
(a) Pristine Tobermorite 9Å (T_9)



(b) Hierarchical nanolaminate (T_9 /GS^{3H})



(c) Stacked arrangement (T_9 /GS^{3S})



Notation:

- E = elastic modulus (GPa)
- T_9 = tobermorite 9 Å
- GS = graphene sheet
- H = hierarchical nanolaminate
- S = stacked nanolaminate

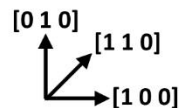
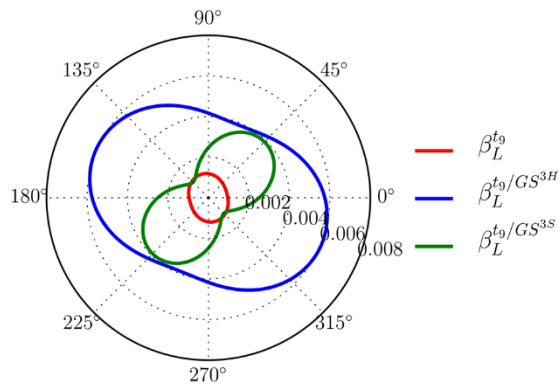
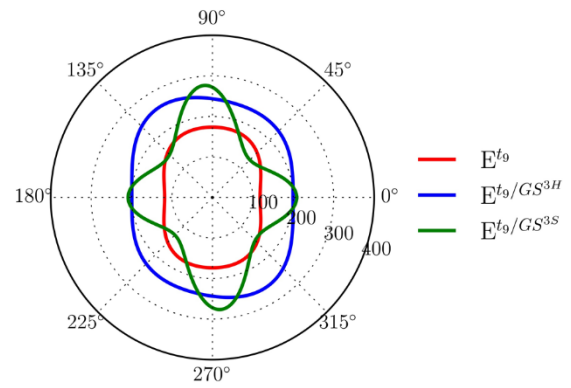
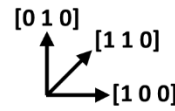


Figure 4.18. 3D representations of directional anisotropy of elastic modulus for T_9 and T_9 /GS systems: (a) T_9 matrix, (b) hierarchical T_9 /GS^{3H} nanolaminate, (c) stacked T_9 /GS^{3S} nanolaminate.

(a) Linear compressibility of T₉/GS nanolaminates**(b)** Elastic modulus of T₉/GS nanolaminates

Notation:

$\beta_L^{T_9/GS^q}$	β_L	= linear compressibility (GPa ⁻¹)
$E_L^{T_9/GS^q}$	E	= elastic modulus (GPa)
	T ₉	= tobermorite 9 Å
	GS	= graphene sheet
	q	= type of nanolaminate (3H, 3S)
	H	= hierarchical nanolaminate
	S	= stacked nanolaminate

Figure 4.19. 2D representations of directional anisotropy of (a) linear compressibility and (b) elastic modulus of the T₉/GS nanolaminates projected on the XY plane, i.e., plane of the GS.

The arrangement of GS in the T₉ matrix, not only produced materials with higher strength, toughness and stiffness, but also with larger compliance along certain crystallographic directions. Evidently, by varying the geometry of the nanolaminate, both T₉/GS^{3H} and T₉/GS^{3S} nanolaminate became relatively more anisotropic than the T₉ matrix. Thus, it is possible to produce mechanically more compliant composite by manipulating the geometry of the nanolaminate. The elastic modulus, E, in the [0 1 0] crystallographic direction was the stiffest for the pristine T₉ (Figure 4.18 and Figure 4.19). However, stacked nanolaminate showed similar behavior, although much higher in magnitude with lowest stiffness along the < 110 > directions, proving the anisotropic properties of stacked nanolaminate. Hierarchical nanolaminate showed slightly lower elasticity in the [0 1 0] directions compared to that of the stacked nanolaminated. However, the hierarchical nanolaminate showed overall higher elasticity in all directions. The minimum stiffness direction of the stacked nanolaminated was in the direction of the maximum compliance because of overall higher flexibility in that direction.

4.3.2. Interfacial interactions between GS and Tobermorite 14 Å (T_{14}) with different interfaces

4.3.2.1. Stress-strain responses

4.3.2.1.1. In-plane uniaxial tensile loading

The GS significantly increased the in-plane (X- and Y-directions) fracture tensile strength and strain of the T_{14} systems (Figure 4.20). For all T_{14} /GS nanocomposites, greater in-plane fracture tensile strength and strain were observed for loading in the X-direction compared to the Y-direction as a result of the orientation of the ZZ and AC edges (along X- and Y-directions, respectively) of the GS in the T_{14} /GS nanocomposites. The GS is more stretchable in the ZZ-direction, whereas it breaks earlier (lower strain and stress) when stressed in the AC direction because of the bonding arrangements of the hexagonal graphene lattice [190]. The GS increased the in-plane failure stress of the T_{14} systems by as much as 180% and 145% in the X- and Y-directions, respectively.

T_{14} systems. The in-plane results for the pristine T_{14} systems (Figure 4.20a and Figure 4.20c) showed overall good agreement with atomistic studies reported in the literature in the X- and Y-directions with a greater in-plane fracture tensile strength in the Y-direction than in the X-direction as a result of the silicate chain of the T_{14} systems running parallel to the Y-direction (greater linear density in that direction). The in-plane fracture tensile strength of the T_{14} systems was 2.8 GPa, 2.2 GPa, and 2.3 GPa for $T_{14}^{O_w}$, $T_{14}^{Ca_o}$, and $T_{14}^{Si_t}$, respectively, in the X-direction and 3.1 GPa, 4.5 GPa, and 4.9 GPa, respectively, in the Y-direction, which compared well with simulation values reported in the literature that ranged from 3-4.5 GPa [2, 212]. The differences observed in the in-plane fracture tensile strength between the T_{14} systems were due to structural differences in their crystal structure assembly with respect to the position of the silicate tetrahedral layer, calcium octahedral layer, and interlayer water within the structure (different representative volume elements, RVE) and were consistent with the water to silicon ratio of the structures (greater ratio, i.e. more water molecules, for $T_{14}^{O_w}$, resulting in a lower tensile strength parallel to the silicate chain). The chemical composition of tobermorite and C-S-H structures has been shown experimentally to affect the atomic packing density of the structure [213]. In addition, the amount of water molecules in the C-S-H structure has been reported, using molecular modeling, to influence its tensile strength with a lower strength seen with increasing

amount of water [214]. After fracture, all T_{14} systems exhibited a plastic regime that was attributed to a local structure rearrangement with internal displacements and rotations of the atoms in the silicate tetrahedral and calcium octahedral layers as a result of the infinite connectivity of the silicate chains, thus allowing the systems to continue to withstand strain. A similar plastic response in the post failure stage of in-plane tensile loading has been reported in the literature for tobermorite and C–S–H with low Ca/Si ratios (i.e., more polymerized and less defective silicate chains) [3, 6].

T_{14}/GS nanocomposites. The in-plane tensile stress-strain response of the T_{14}/GS nanocomposites (Figure 4.20b and Figure 4.20d) was similar to that observed in fiber-matrix composites with lamellar formation [215] and exhibited three main regimes: (i) an elastic regime in which the stress increased quasi-linearly with the strain as T_{14} and the GS shared the stress up to the failure of the T_{14} matrix (regime R_1); (ii) a regime in which the GS controlled the stress-strain evolution of the nanocomposite and was capable of bearing the increasing strain without any bond breaking (GS loading regime, R_{GS}); and (iii) a post failure plastic regime (regime R_2). After failure of the T_{14} matrix and as the stress within the T_{14}/GS nanocomposites increased, internal displacements of the atoms in the silicate tetrahedral and calcium octahedral layers became more prominent, resulting in disordered layers. Meanwhile, the GS provided a crack bridging mechanism, thus allowing the nanocomposites to maintain overall structural integrity until fracture of the GS. Figure 4.21 and Figure 4.22 illustrate the failure stages of the $T_{14}^{O_w}/GS$ nanocomposite during tensile loading along the X- and Y-directions, respectively, showing (i) displacement of atoms in the calcium octahedral and silicate tetrahedral layers, (ii) breaking of bonds between tetrahedral silicon and oxygen atoms ($Si-O$) and between interlayer calcium and bridging oxygen in tetrahedra (Ca_w-O_{bts}), and (iii) the crack path and separation of the structural layers. Similar failure stages were seen for the $T_{14}^{Ca_o}/GS$ and $T_{14}^{Si_t}/GS$ nanocomposites. At the fracture of the GS, the silicate tetrahedral and calcium octahedral layers were critically damaged and had then no capacity to support further loads. At that point, the T_{14}/GS nanocomposites failed abruptly and the stress then went to a plastic plateau. The strengthening effect of the GS, however, still existed even though the GS had ruptured. The T_{14}/GS nanocomposites showed fracture tensile strengths and strains that were as much as 360% and 260% in the X-direction and

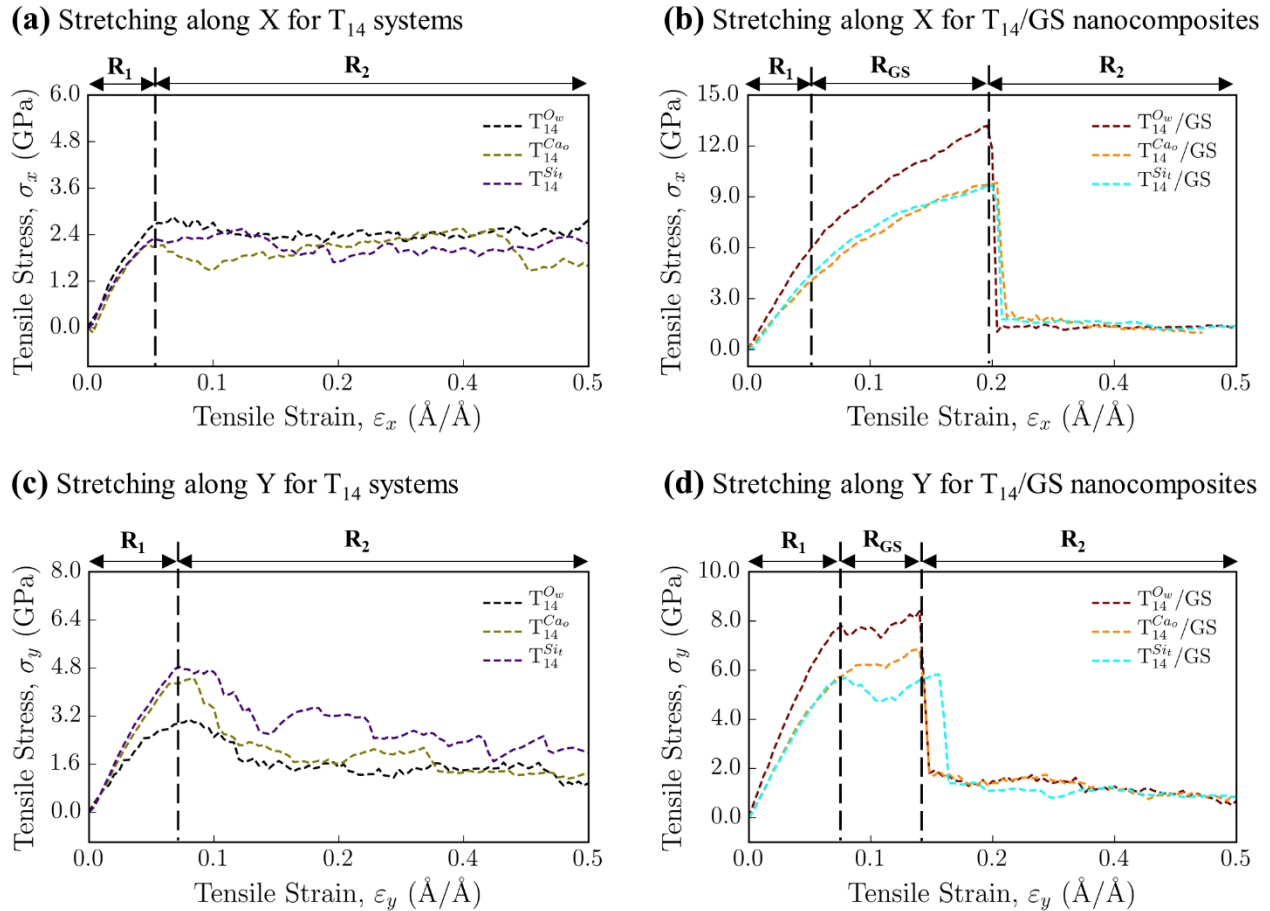
180% and 110% in the Y-direction greater, respectively, than that of the T_{14} systems without the GS reinforcement.

The evolution of the Si_r-O and C-C bond lengths as a function of strain along the X- and Y-directions (Figure 4.23, shown for the $T_{14}^{O_w}$ /GS nanocomposite) further illustrated the strain transfer from the T_{14} structure to the GS with an initial rapid increase in the Si_r-O bond length followed by a gradual decrease that was accompanied by a sharp increase in the C-C bond length for stretching along the X-direction and to a lesser extent along the Y-direction (only type II bonds were involved during stretching along X while two type I bonds participated during stretching along Y). It also further confirmed the role played by the Si_r-O bond stretching in the existence of residual stress in the post failure plastic regime. Analysis of the number of Si_r-O bonds broken (Figure 4.24) revealed a lower number of broken bonds with increasing strain for the nanocomposite with the GS interfacing with the surface water ($T_{14}^{O_w}$ /GS) compared to the nanocomposites with the GS interfacing with the calcium and silicate surfaces ($T_{14}^{Ca_o}$ /GS and $T_{14}^{Si_r}$ /GS). This lower number of broken Si_r-O bonds within the $T_{14}^{O_w}$ /GS nanocomposite became apparent only after failure of the $T_{14}^{O_w}$ matrix when the GS took control of the stress-strain evolution and suggested a different flow of stress within this nanocomposite. A lower number of broken Si_r-O bonds was also observed for the pristine $T_{14}^{O_w}$ structure compared to the $T_{14}^{Ca_o}$ and $T_{14}^{Si_r}$ structures. The water layers within the $T_{14}^{O_w}$ structure were thought to have hindered the propagation of stress across the structure (three water layers within the RVE of the $T_{14}^{O_w}$ system versus two water layers within the RVE of the $T_{14}^{Ca_o}$ and $T_{14}^{Si_r}$ systems). Overall, a lower number of broken bonds was seen for loading in the Y-direction compared to loading in the X-direction because the stress during loading in the Y-direction was transferred through the bridging oxygen, which could twist and rotate upon loading, thus preventing bond breaking.

The GS exhibited more apparent in-plane strengthening effect when interfacing with water than with either of the solid surfaces (i.e., calcium or silicate surfaces). The $T_{14}^{O_w}$ /GS nanocomposite with the GS interfacing with the bottom surface water (water interface) exhibited the highest fracture tensile strengths (13.2 GPa in the X-direction and 8.4 GPa in the Y-

direction). In contrast, the $T_{14}^{Ca_o}$ /GS nanocomposite with the GS interfacing with the octahedral calcium layer (calcium interface) and the $T_{14}^{Si_t}$ /GS nanocomposite with the GS interfacing with the tetrahedral silicate layer (silicate interface) had lower in-plane fracture tensile strengths (9.8 GPa and 9.7 GPa, respectively, in the X-direction and 6.8 GPa and 5.8 GPa, respectively, in the Y-direction). The greater fracture strength seen with the water interface was attributed to the interaction of the water with the GS as confirmed by the local stress distribution at the GS surface. The GS interfacing with water demonstrated the highest local stress distribution compared to that of the GS interfacing with the calcium and silicate surfaces (Figure 4.25). The water molecules at the surface of the T_{14} structure increased the intermolecular forces (i.e., molecular level frictional forces, the forces acting between the molecules of two different surfaces) with the GS most likely because of their preferential orientation in the confined space created by the interface with the GS, which has been reported in the literature to increase the water viscosity [119]. As a result, viscous interfacial water dominated and increased the surface friction, thus leading to a greater strength development of the overall nanocomposite than that seen when the GS interacted with the dry, solid surfaces (i.e., calcium and silicate surfaces) with no mediating water. By analogy, the behavior seen at the water–GS interface was similar to that occurring when water increases the friction between someone’s finger and a sheet of plastic. Molecular level, water mediated friction versus dry friction at solid interfaces has been the focus of numerous studies [216-219] and enhanced friction forces with water have been reported at graphene/copper and graphene/mica interfaces [218, 220].

The effect of the structure of the dry solid surface (calcium vs. silicate) interfacing with the GS was apparent only in the Y-direction (parallel to the silicate chain) with the lowest fracture strength obtained for the nanocomposite with the GS interfacing with the tetrahedral silicate layer. It was hypothesized that the structure of the octahedral calcium layer as an ordered zigzag sheet (corrugated surface) caused greater molecular friction with the GS than that of the tetrahedral silicate layer, which was more prone to twisting and rotating, thus resulting in a lower strength development for the nanocomposite with the silicate interface than that with the calcium interface. Overall greater local stresses at the GS surface were observed for the calcium interface compared to the silicate interface (Figure 4.25).



Notation:

T_{14}^i /GS T_{14} = tobermorite 14Å
 GS = graphene sheet
 $i = \{O_w, Ca_o, Si_t\}$
 O_w = water interface
 Ca_o = calcium interface
 Si_t = silicate interface
 □ boundary atoms

R_1 elastic regime of T_{14} systems or T_{14} /GS nanocomposites
 R_{GS} GS loading regime
 R_2 post-failure plastic regime of T_{14} systems or T_{14} /GS nanocomposites
 (Average locations shown for all regimes)

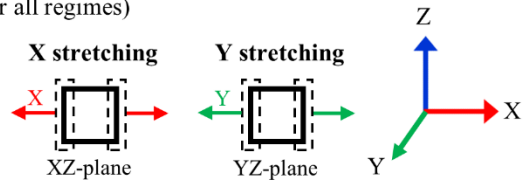
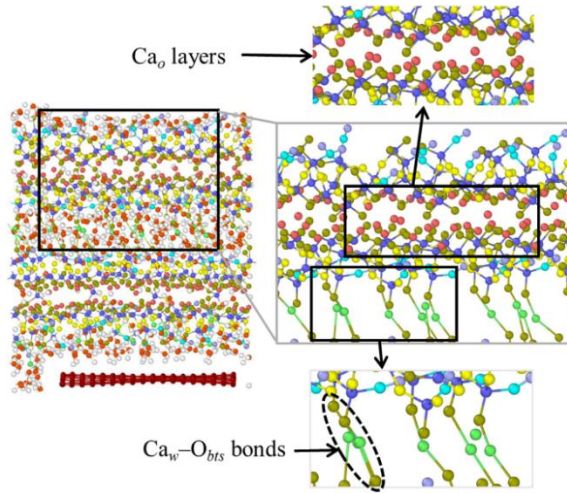
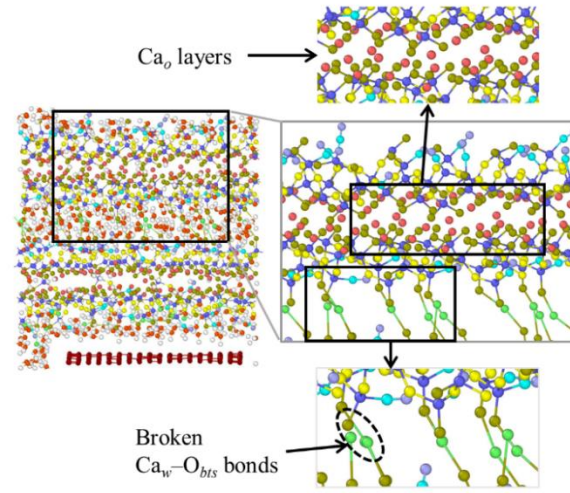


Figure 4.20. Stress-strain response under in-plane tensile loading: (a) and (b) stretching along the X-direction of T_{14} systems and T_{14} /GS nanocomposites, respectively and (c) and (d) stretching along the Y-direction of T_{14} systems and T_{14} /GS nanocomposites, respectively. [$T_{14}^{O_w}$: T_{14} structure with exposed water layer surface; $T_{14}^{Ca_o}$: T_{14} structure with exposed octahedral calcium surface; $T_{14}^{Si_t}$: T_{14} structure with exposed tetrahedral silicate surface; $T_{14}^{O_w}/GS$: GS interfacing with the bottom surface water of T_{14} ; $T_{14}^{Ca_o}/GS$: GS interfacing with the octahedral calcium layer of T_{14} ; $T_{14}^{Si_t}/GS$: GS interfacing with the tetrahedral silicate layer of T_{14}]

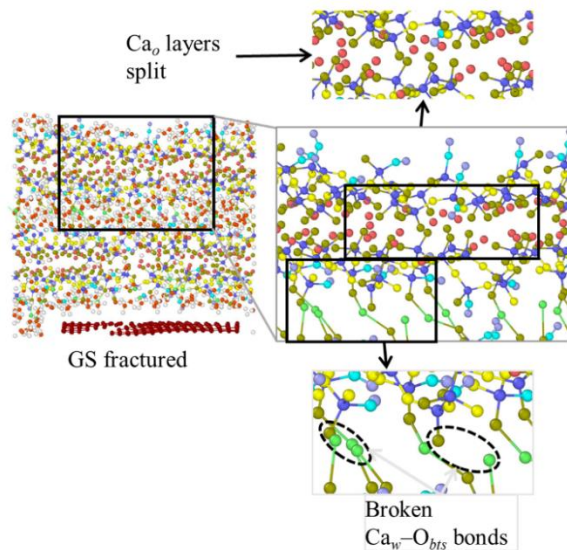
(a) $T_{14}^{O_w}/GS$ at equilibrium before loading
($\epsilon_x = 0.0$)



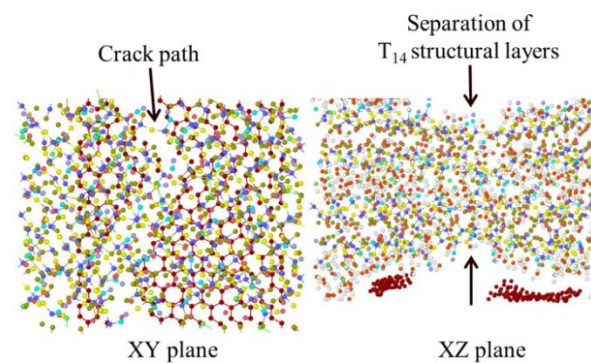
(b) $T_{14}^{O_w}/GS$ at T_{14} failure
($\epsilon_x = 0.085$)



(c) $T_{14}^{O_w}/GS$ at GS fracture
($\epsilon_x = 0.25$)



(d) $T_{14}^{O_w}/GS$ at separation
($\epsilon_x = 0.50$)



● Ca_o ● O_b ● O_h ● H_w ● Ca_w Ca_o : octahedral calcium; Si_t : tetrahedral silicon;
● Si_t ● O_{bts} ● O_w ● H_h ● C O_b : bridging oxygen; O_{bts} : bridging oxygen in tetrahedra;
 O_h : hydroxyl oxygen; O_w : water oxygen;
 H_w : water hydrogen; H_h : hydroxyl hydrogen;
 Ca_w : interlayer calcium; C : carbon in graphene

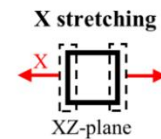


Figure 4.21. Failure stages of the nanocomposite with the GS interfacing with the bottom surface of the tobermorite 14 \AA ($T_{14}^{O_w}/GS$ nanocomposite) during in-plane tensile loading along the X-direction: (a) after relaxation to equilibrium but before tensile loading (unstrained conditions); (b) at failure of the tobermorite 14 \AA (T_{14}) matrix; (c) at fracture of the graphene sheet (GS); and (d) after separation of the structural layers. For clarity, structures in insets are shown without water molecules.

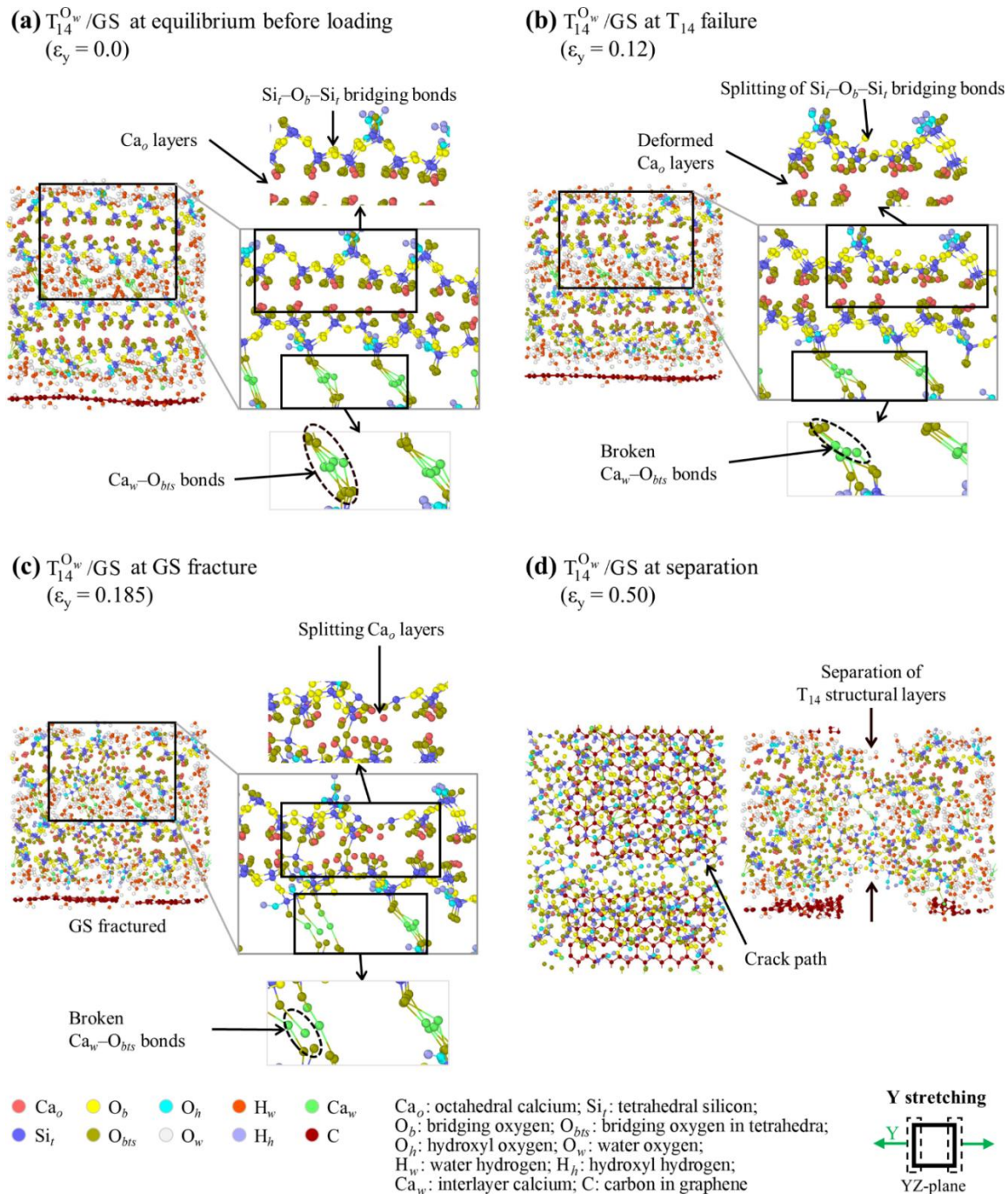


Figure 4.22. Failure stages of the nanocomposite with the GS interfacing with the bottom surface water of the tobermorite 14 Å ($T_{14}^{O_w}/GS$ nanocomposite) during in-plane tensile loading along the Y-direction: (a) after relaxation to equilibrium but before tensile loading (unstrained conditions); (b) at failure of the tobermorite 14 Å (T_{14}) matrix; (c) at fracture of the graphene sheet (GS); and (d) after separation of the structural layers. For clarity, structures in insets are shown without water molecules.

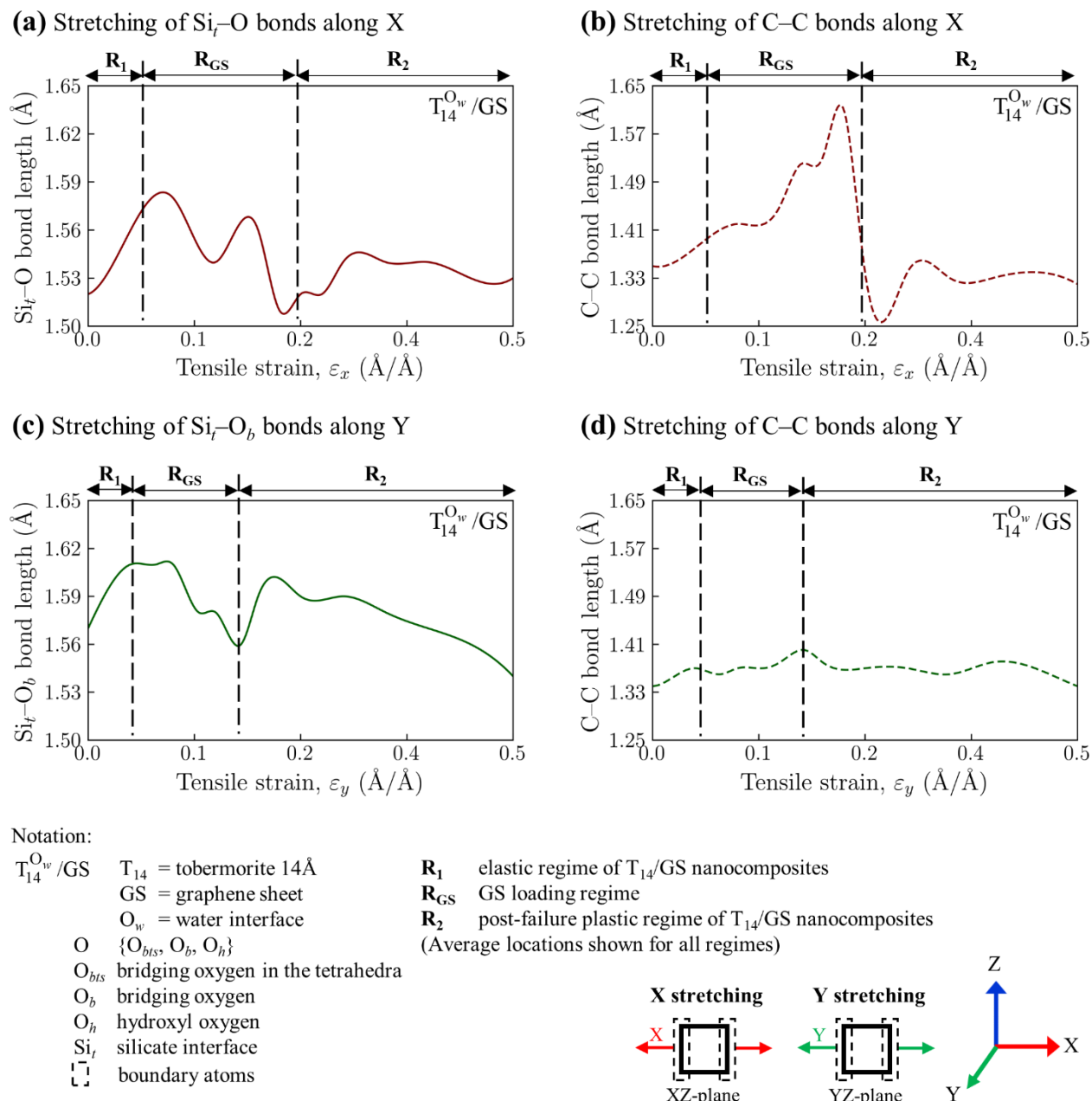
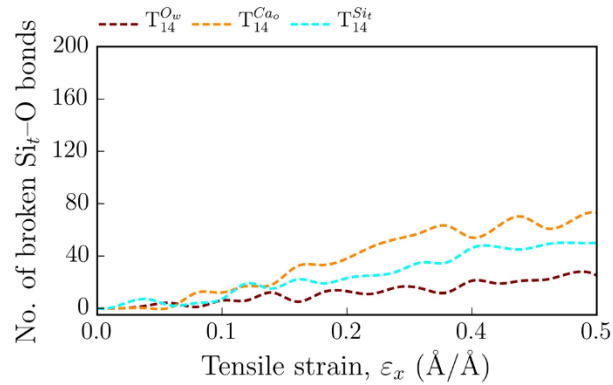
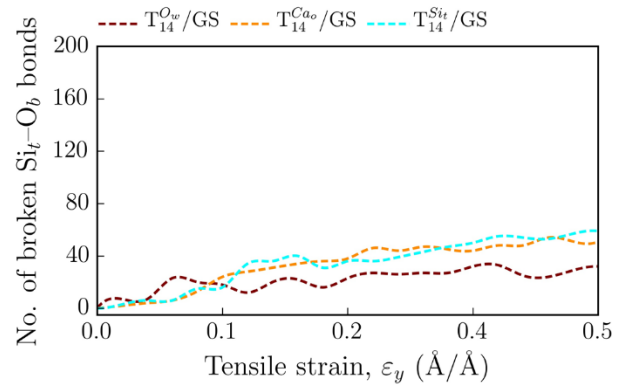
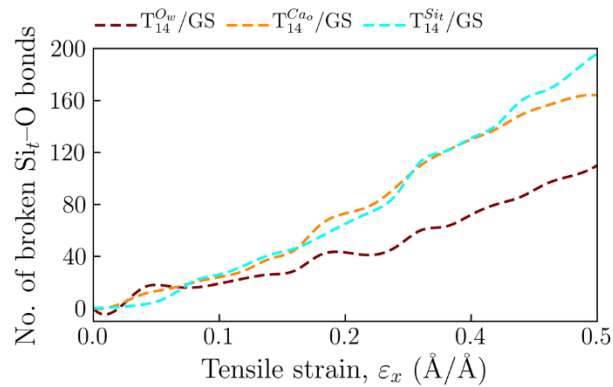
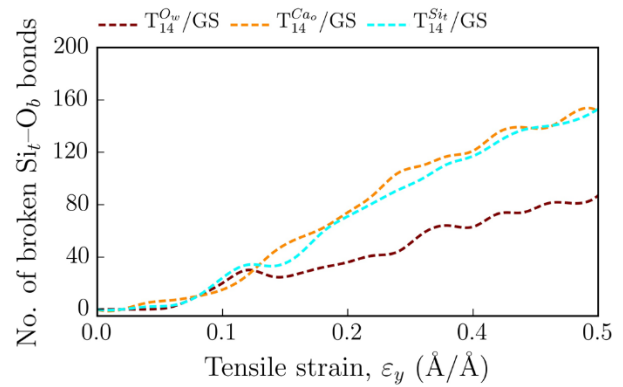


Figure 4.23. Evolution of tetrahedral silica–oxygen bond length and carbon–carbon bond length during in-plane tensile loading of the nanocomposite with the GS interfacing with the bottom surface water of the tobermorite 14 Å ($T_{14}^{O_w}/GS$ nanocomposite): (a), (b) Si_t-O bond length and C-C bond length, respectively during stretching along the X-direction and (c), (d) Si_t-O_b bond length and C-C bond length, respectively during stretching along the Y-direction.

(a) Stretching along X for pristine T_{14} **(b)** Stretching along Y for pristine T_{14} **(c)** Stretching along X for T_{14}/GS nanocomposites**(d)** Stretching along Y for T_{14}/GS nanocomposites

Notation:

T_{14}^i/GS	T_{14} = tobermorite 14Å	O	{ O_{bts} , O_b , O_h }
	GS = graphene sheet	O_{bts}	bridging oxygen in the tetrahedra
	i = { O_w , Ca_o , Si_t }	O_b	bridging oxygen
	O_w = water interface	O_h	hydroxyl oxygen
	Ca_o = calcium interface		
	Si_t = silicate interface		
\square	boundary atoms		

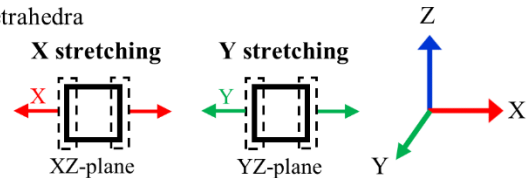
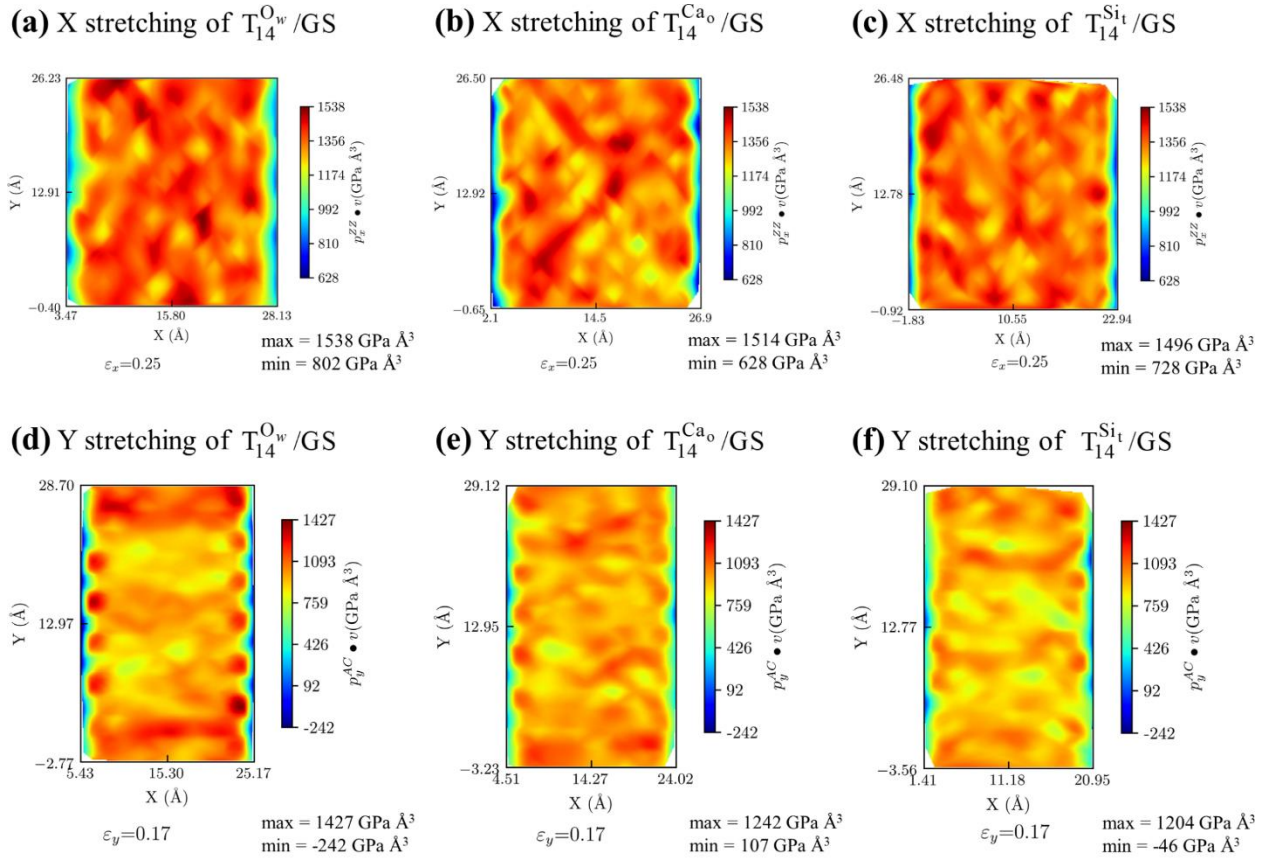


Figure 4.24. Evolution of the number of broken tetrahedral silicon–oxygen bonds in the pristine T_{14} systems and T_{14}/GS nanocomposites as function of applied strain: (a), (b) during stretching of the pristine T_{14} systems along the X- and Y-directions, respectively and (c), (d) during stretching of the T_{14}/GS nanocomposites along the X- and Y-directions. [$T_{14}^{O_w}$: T_{14} structure with exposed water layer surface; $T_{14}^{Ca_o}$: T_{14} structure with exposed octahedral calcium surface; $T_{14}^{Si_t}$: T_{14} structure with exposed tetrahedral silicate surface; $T_{14}^{O_w}/GS$: GS interfacing with the bottom surface water of T_{14} ; $T_{14}^{Ca_o}/GS$: GS interfacing with the octahedral calcium layer of T_{14} ; $T_{14}^{Si_t}/GS$: GS interfacing with the tetrahedral silicate layer of T_{14}]



Notation:

T_{14}^i/GS T_{14} = tobermorite 14Å
 GS = graphene sheet
 $i = \{O_w, Ca_o, Si_t\}$
 O_w = water interface
 Ca_o = calcium interface
 Si_t = silicate interface

$p_x^{ZZ} \cdot v$ local stress distribution on GS along X direction with ZZ orientation ($GPa \text{ \AA}^3$)
 $p_y^{AC} \cdot v$ local stress distribution on GS along Y direction with AC orientation ($GPa \text{ \AA}^3$)
 v atomic volume (Å^3)
 \square boundary atoms

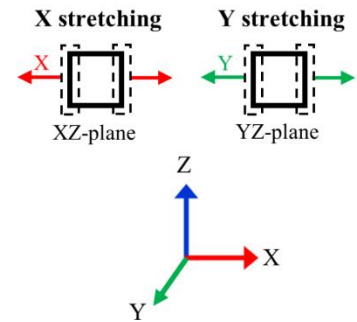


Figure 4.25. Local stress distribution at the graphene sheet (GS) surface before fracture of the GS during tensile loading: (a), (b), and (c) X-direction stretching of the GS reinforced tobermorite 14 Å nanocomposites; and (e), (f), and (g) Y-direction stretching of the GS reinforced tobermorite 14 Å nanocomposites. [$T_{14}^{O_w}/GS$: GS interfacing with the bottom surface water of T_{14} ; $T_{14}^{Ca_o}/GS$: GS interfacing with the octahedral calcium layer of T_{14} ; $T_{14}^{Si_t}/GS$: GS interfacing with the tetrahedral silicate layer of T_{14}]

4.3.2.1.2. Out-of-plane tensile loading

The in-plane GS reinforcement of the T_{14} structures did not show a strengthening of the structures along their weakest direction, i.e. the direction orthogonal to the interlayer water region (Z-direction). On the contrary, the presence of the GS along the basal plane caused a loss (as much as 47% reduction) in the out-of-plane tensile strength capacity of the T_{14} structures (Figure 4.26).

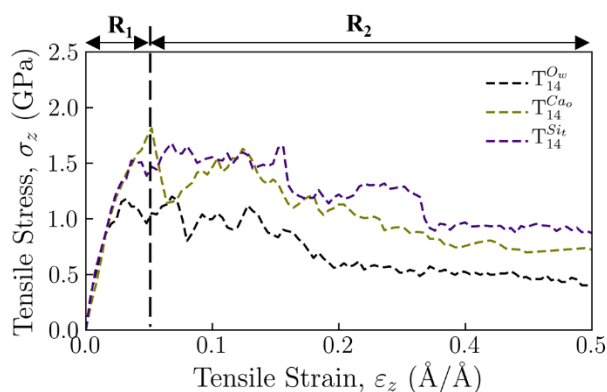
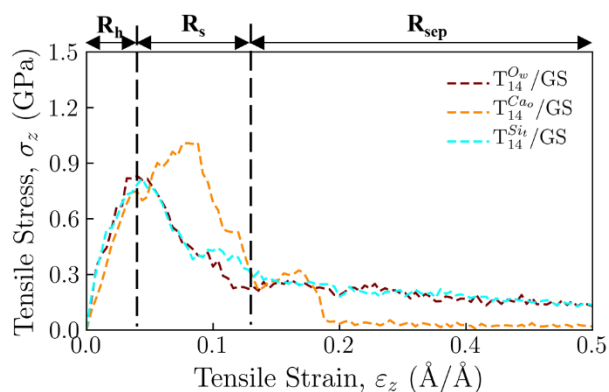
T₁₄ systems. The out-of-plane fracture tensile strength of the T_{14} structures in the Z-direction was controlled by the weak mechanical strength of the interlayer water region and was influenced by the relative position of the different layers through which the stress was transferred (Figure 4.27). The fracture and separation of the structures occurred at the interlayer water region from the breaking of the bonds connecting the calcium-silicate layers (i.e., bonds between bridging oxygen from the silicate chains and the interlayer calcium atoms, $O_{bts}-Ca_w-O_{bts}$ bridging bonds). The T_{14} structure with the exposed octahedral calcium surface ($T_{14}^{Ca_o}$ structure) showed the highest out-of-plane fracture tensile strength (1.7 GPa) in the Z-direction (Figure 4.26a) while that with the exposed water layer surface ($T_{14}^{O_w}$ structure) had the lowest (1.1 GPa). The innermost layer of the $T_{14}^{Ca_o}$ structure was composed of calcium octahedral sandwiched by silicate tetrahedral chains thus providing the $T_{14}^{Ca_o}$ structure with greater stress resistance (greater capability to take up load) in the Z-direction than the two other T_{14} structures ($T_{14}^{O_w}$ and $T_{14}^{Si_t}$) for which the innermost layer was composed of the weak interlayer water region. For all structures, during the separation process, the water molecules clustered within the interlayer water region and formed a water molecule chain connected by a dynamic hydrogen bond network (Figure 4.27). Both ends of this chain were attached to the interlayer calcium atoms or bridging oxygen from the silicate chains, resulting in residual stress characterized by a continued increase in strain capacity with a flattening of the stress retained.

T₁₄/GS nanocomposites. The presence of the GS as in-plane reinforcement had no strengthening effect on the T_{14} structures in the Z-direction (out-of-plane) and, on the contrary, degraded their out-of-plane tensile performance. The failure mode of the T_{14} /GS nanocomposites under tensile loading in the Z-direction differed significantly from that of the in-plane loading. The failure mode of the nanocomposites with the GS interfacing with the surface water and

tetrahedral silicate layer (i.e., $T_{14}^{O_w}/GS$ and $T_{14}^{Si_t}/GS$) was dominated by the failure of the interface between the T_{14} structure and the GS while that of the nanocomposite with the GS interfacing with the octahedral calcium layer (i.e., $T_{14}^{Ca_o}/GS$) was controlled by a failure within the T_{14} structure. For the $T_{14}^{O_w}/GS$ and $T_{14}^{Si_t}/GS$ nanocomposites, the separation of the GS and T_{14} structure as a result of the pulling in the Z-direction occurred at the interface with the GS rather than inside the bulk of the T_{14} structure and no local separation within the T_{14} structure occurred (Figure 4.27d and Figure 4.27f). The clean separation suggested that the surface water–GS interface and tetrahedral silicate layer–GS interface were mechanically weaker than the GS or the T_{14} structures. In contrast, for the $T_{14}^{Ca_o}/GS$ nanocomposite, the separation occurred inside the bulk of the T_{14} structure with fracture of the interlayer water region similar to that of the pristine system with no GS reinforcement (Figure 4.27e). In all cases, the T_{14} structures became elongated as the interatomic bonds were stretched, and some structural water molecules were seen to have migrated towards the interface with the GS. At the peak stress, the T_{14} structures were lengthened in the Z-direction by *ca.* 6% for the $T_{14}^{O_w}/GS$ nanocomposite, *ca.* 9% for the $T_{14}^{Ca_o}/GS$ nanocomposite, and *ca.* 2.4% for the $T_{14}^{Si_t}/GS$ nanocomposite. The greater elongation at peak stress seen for the $T_{14}^{Ca_o}/GS$ nanocomposite indicated a greater resistance of this nanocomposite to tensile loading in the Z-direction. An analysis of the number of broken interlayer calcium–bridging oxygen in tetrahedra (Ca_w-O_{bts}) bonds indicated that the T_{14}/GS nanocomposites with the GS interfacing with the water and silicate surfaces had fewer Ca_w-O_{bts} bonds broken than the pristine T_{14} systems as strain progressed (Figure 4.28), while that with the GS interfacing with the calcium surface demonstrated a similar number of broken Ca_w-O_{bts} bonds compared to its pristine counterpart (without GS reinforcement). The evolution of the number of broken Ca_w-O_{bts} bonds was consistent with the fact that the separation of the $T_{14}^{Ca_o}/GS$ nanocomposite occurred at the interlayer water region versus at the interface between the GS and the T_{14} structure for the $T_{14}^{O_w}/GS$ and $T_{14}^{Si_t}/GS$ nanocomposites.

The out-of-plane stress-strain evolution exhibited three main regimes for all cases (Figure 4.26b): (i) a strain hardening regime (R_h) in which the GS and the T_{14} structure pulled on each other and the nanocomposites started to elongate; (ii) a strain softening regime (R_s) in which the

stress was relaxed with increasing strain as the nanocomposite separated at the fracture region; and (iii) a separation regime (R_{sep}) characterized by the presence of residual stresses. The nanocomposite with the GS interfacing with the octahedral calcium layer ($T_{14}^{\text{Ca}_o}$ /GS) had a higher peak tensile separation stress than the two other T_{14} /GS nanocomposites (1.00 GPa versus 0.81 GPa and 0.78 GPa, for the nanocomposites with the GS interfacing with the water and silicate surfaces, respectively) and also showed a greater fracture strain (0.11 versus 0.055 for both the $T_{14}^{\text{O}_w}$ /GS and $T_{14}^{\text{Si}_t}$ /GS nanocomposites). This indicated that the $T_{14}^{\text{Ca}_o}$ /GS nanocomposite needed more energy to fracture, due to a greater resistance to stress transfer in the Z-direction for the T_{14} structure with the exposed octahedral calcium surface ($T_{14}^{\text{Ca}_o}$ structure) compared to the other T_{14} structures, thus lowering the stress concentration at the interface with the GS and increasing the stress concentration within the interlayer water region. In contrast, the T_{14} /GS nanocomposites with the GS interfacing with the water and silicate surfaces showed similar stress development with increasing separation due to the similar organization within the structure of the different layers through which the stress was transferred. For the $T_{14}^{\text{O}_w}$ /GS and $T_{14}^{\text{Si}_t}$ /GS nanocomposites, after separation of the GS and T_{14} structures, a small residual stress could be seen as a result of the migration of the water molecules out of the T_{14} structures, forming collective hydrogen bond networks (i.e., T_{14} -water-water-[...]-water hydrogen bonds such as in Figure 4.27) that interacted with the GS through repulsive van der Waals forces. For the $T_{14}^{\text{Ca}_o}$ /GS nanocomposite, no more residual stress could be seen beyond a strain of 0.2.

(a) Stretching along Z for T_{14} systems**(b)** Stretching along Z for T_{14} /GS nanocomposites

Notation:

T_{14}^i /GS	T_{14} = tobermorite 14Å GS = graphene sheet $i = \{O_w, Ca_o, Si_t\}$	R_1 elastic regime of T_{14} systems R_2 post-failure plastic regime of T_{14} systems R_h hardening regime of T_{14} /GS systems R_s softening regime of T_{14} /GS systems R_{sep} separation regime of T_{14} /GS systems (Average locations shown for all regimes)
O_w	= water interface	
Ca_o	= calcium interface	
Si_t	= silicate interface	
\square	boundary atoms	

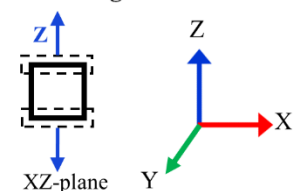
Z stretching

Figure 4.26. Stress-strain response for out-of-plane (Z-direction) tensile loading of (a) T_{14} systems and (b) T_{14} /GS nanocomposites. [$T_{14}^{O_w}$: T_{14} structure with exposed water layer surface; $T_{14}^{Ca_o}$: T_{14} structure with exposed octahedral calcium surface; $T_{14}^{Si_t}$: T_{14} structure with exposed tetrahedral silicate surface; $T_{14}^{O_w}/GS$: GS interfacing with the bottom surface water of T_{14} ; $T_{14}^{Ca_o}/GS$: GS interfacing with the octahedral calcium layer of T_{14} ; $T_{14}^{Si_t}/GS$: GS interfacing with the tetrahedral silicate layer of T_{14}]

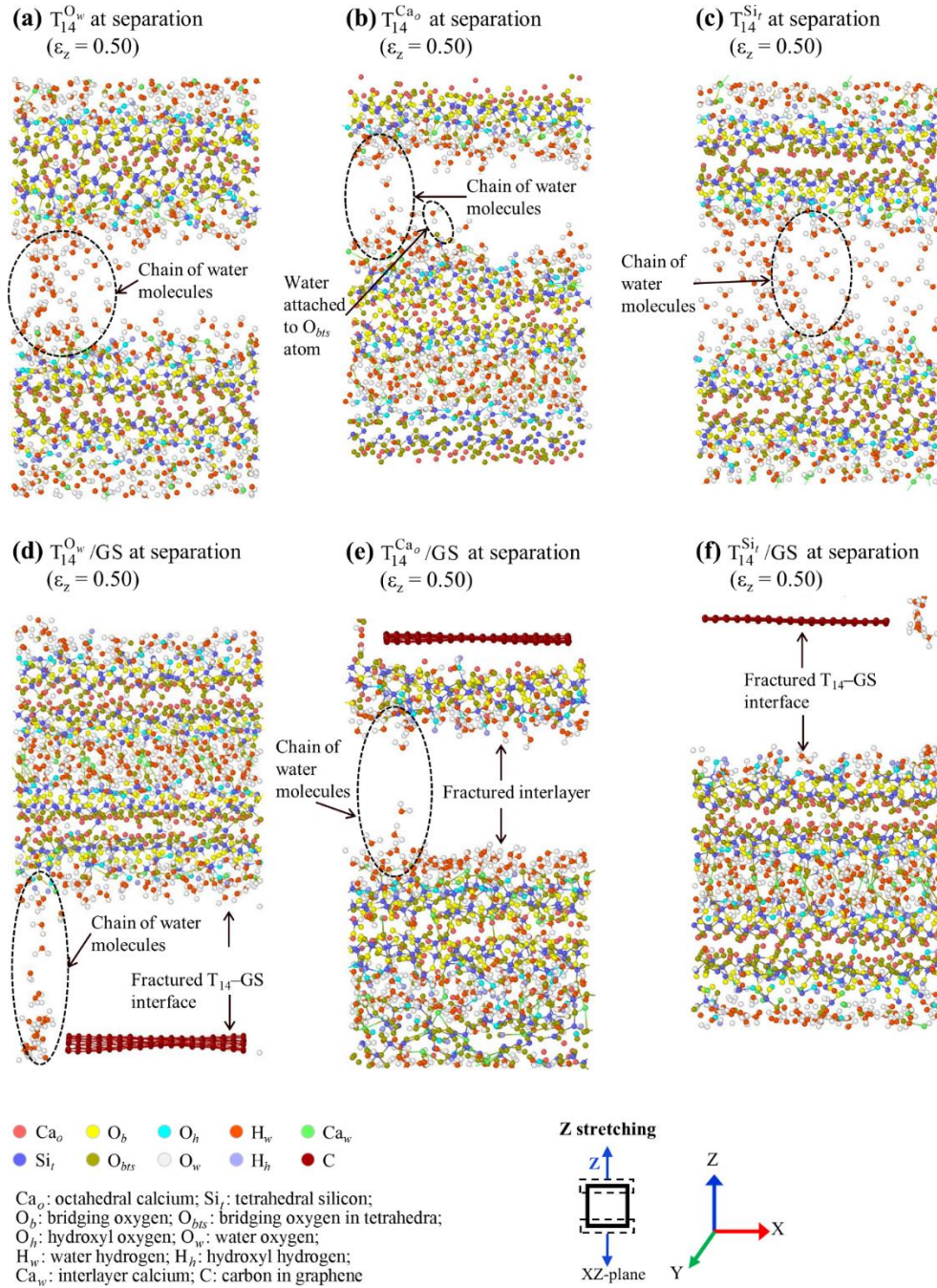
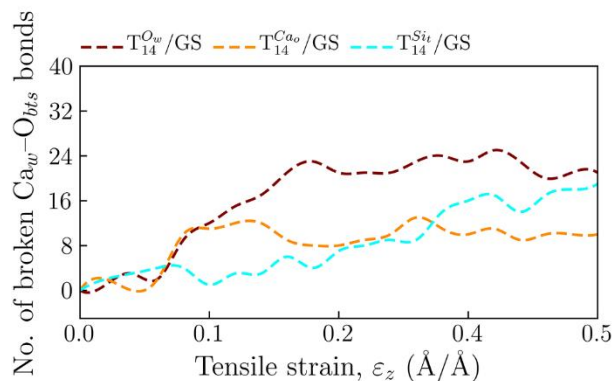
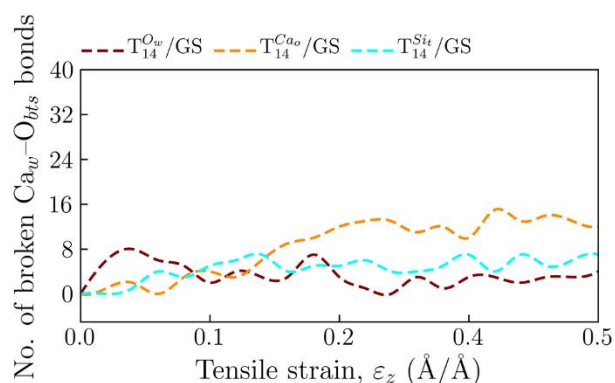


Figure 4.27. Separation stage of T_{14} systems and T_{14}/GS nanocomposites during out-of-plane tensile loading along the Z-direction: (a) T_{14} structure with exposed water surface ($T_{14}^{O_w}$); (b) T_{14} structure with exposed octahedral calcium surface ($T_{14}^{Ca_o}$); (c) T_{14} structure with exposed tetrahedral silicate surface ($T_{14}^{Si_t}$); (d) nanocomposite with the GS interfacing with the bottom surface water of T_{14} ($T_{14}^{O_w}/GS$); (e) nanocomposite with the GS interfacing with the octahedral calcium layer of T_{14} ($T_{14}^{Ca_o}/GS$); and (f) nanocomposite with the GS interfacing with the tetrahedral silicate layer of T_{14} ($T_{14}^{Si_t}/GS$).

(a) Stretching along Z for pristine T_{14} **(b)** Stretching along Z for T_{14} /GS nanocomposites

Notation:

T_{14}^i /GS	T_{14} = tobermorite 14Å
	GS = graphene sheet
	i = { O_w , Ca_o , Si_t }
	O_w = water interface
	Ca_o = calcium interface
	Si_t = silicate interface
Ca_w	interlayer calcium
O_{bts}	bridging oxygen in the tetrahedra
\square	boundary atoms

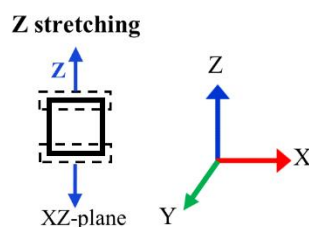


Figure 4.28. Evolution of the number of broken Ca_w-O_{bts} bonds as a function of applied strain during out-of-plane (Z-direction) tensile loading of (a) the T_{14} systems and (b) the T_{14} /GS nanocomposites. [$T_{14}^{O_w}$: T_{14} structure with exposed water layer surface; $T_{14}^{Ca_o}$: T_{14} structure with exposed octahedral calcium surface; $T_{14}^{Si_t}$: T_{14} structure with exposed tetrahedral silicate surface; $T_{14}^{O_w}/GS$: GS interfacing with the bottom surface water of T_{14} ; $T_{14}^{Ca_o}/GS$: GS interfacing with the octahedral calcium layer of T_{14} ; $T_{14}^{Si_t}/GS$: GS interfacing with the tetrahedral silicate layer of T_{14}]

4.3.2.1.3. Shear loading in the XY plane along the X-direction

Only shear loading along the X-direction (i.e., zigzag direction of the GS and the direction perpendicular to that of the running silicate chains) was examined because it was the T_{14} structures' weakest direction and the GS's more stretchable direction.

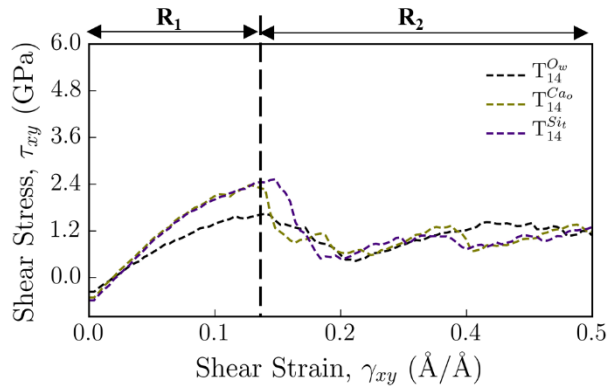
The GS significantly contributed to the fracture shear strength of the T_{14} /GS nanocomposites (Figure 4.29). The T_{14} /GS nanocomposites exhibited fracture shear strengths that were 90% to 225% greater than that of their respective, pristine T_{14} systems without the GS reinforcement. The greatest enhancement of the fracture shear strength was seen for the $T_{14}^{O_w}$

/GS nanocomposite with the GS interfacing with water while the smallest shear strength development was seen for the $T_{14}^{Si_r}$ /GS nanocomposite.

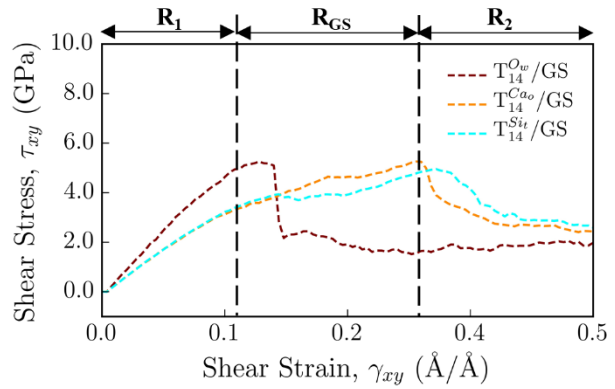
The response of the T_{14} /GS nanocomposites to shear loading in the XY plane was influenced by the molecular friction forces developed at the interface between the T_{14} structures and the GS. While all the T_{14} /GS nanocomposites reached a similar fracture shear strength at fracture (4.9-5.3 GPa), the $T_{14}^{O_w}$ /GS nanocomposite with the GS interfacing with water exhibited a much lower fracture strain than the two other nanocomposites. During shear deformation, the $T_{14}^{O_w}$ /GS nanocomposite displayed a more rapid build-up in shear strength, which resulted in an earlier fracture (i.e., at a lower strain) of the GS than observed for the $T_{14}^{Ca_o}$ /GS and $T_{14}^{Si_r}$ /GS nanocomposites. The GS in the $T_{14}^{O_w}$ /GS nanocomposite failed abruptly before the failure of the T_{14} structure, resulting in a brittle fracture of the nanocomposite, followed by a subsequent plastic behavior. Even after failure, the T_{14} structure was able to withstand some of the load. The plastic behavior was attributed to the internal displacements and rotations of the atoms in the silicate tetrahedral and calcium octahedral layers of the T_{14} structure. The water molecules at the surface of the T_{14} structure were thought to have promoted molecular friction with the GS, building up stresses at the surface of the GS that were greater than the GS intrinsic capability to resist friction, thus causing the GS to fail at a strain lower than its intrinsic fracture shear strain and before the failure of the T_{14} matrix. The water molecules rotated during shear to release stress because of their reduced mobility (confined space of the interface) and the hydrophobic effect of the GS (entropy-driven), thus ripping the GS. In contrast, for the nanocomposites with the dry solid surfaces (calcium and silicate) interfacing with the GS, the shear stress initially increased at a lower rate, and the nanocomposites exhibited a more gradual failure. The shear strain caused distortion of the tetrahedral and octahedral sheets of the T_{14} matrix, in addition to $\angle C-C-C$ angle bending and $C-C-C-C$ dihedral bending of the GS. The shear stress increased initially due to the load being shared by both the T_{14} structure and the GS up to failure of the T_{14} structure at which point the stress increased gradually due to the GS loading regime and plastic behavior of the T_{14} structure until failure of the GS, which occurred at its intrinsic fracture shear strain (i.e., *ca.* 0.321 [190]). The interaction energy as a function of shear loading was 2-3 times greater (more negative) for the water interface compared to the calcium and silicate interfaces

(Figure 4.30), which was consistent with the higher rate of strength development and greater molecular friction forces exerted by the water molecules on the GS compared to that with the dry solid surfaces (calcium and silicate). As discussed in section 4.3.2.1.1, the role of water in enhancing molecular friction between two surfaces has been reported in the literature [217, 218, 220, 221].

(a) Shearing along X for T_{14} systems



(b) Shearing along X for T_{14} /GS nanocomposites



Notation:

T_{14}^i /GS	T_{14} = tobermorite 14 \AA	R_1	elastic regime of T_{14} systems or T_{14} /GS nanocomposites
	GS = graphene sheet	R_{GS}	GS loading regime
	$i = \{O_w, Ca_o, Si_t\}$	R_2	post-failure plastic regime of T_{14} systems or T_{14} /GS nanocomposites
	O_w = water interface		(Average locations shown for all regimes)
	Ca_o = calcium interface		
	Si_t = silicate interface		
\square	boundary atoms		

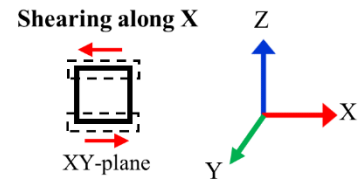
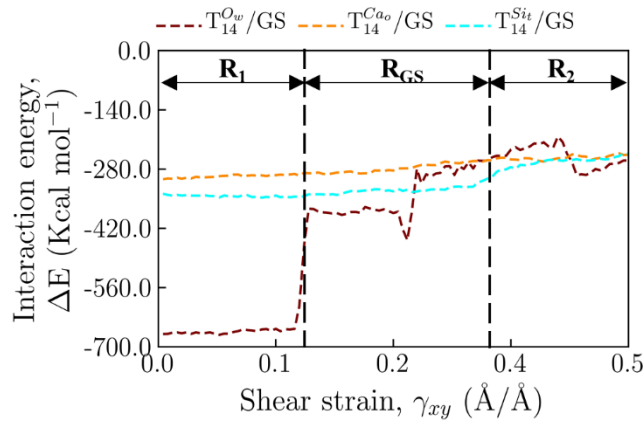


Figure 4.29. Shear stress-strain evolution of the (a) T_{14} systems and (b) T_{14} /GS nanocomposites under shear loading along the X-direction. [$T_{14}^{O_w}$: T_{14} structure with exposed water layer surface; $T_{14}^{Ca_o}$: T_{14} structure with exposed octahedral calcium surface; $T_{14}^{Si_t}$: T_{14} structure with exposed tetrahedral silicate surface; $T_{14}^{O_w}/GS$: GS interfacing with the bottom surface water of T_{14} ; $T_{14}^{Ca_o}/GS$: GS interfacing with the octahedral calcium layer of T_{14} ; $T_{14}^{Si_t}/GS$: GS interfacing with the tetrahedral silicate layer of T_{14}]



Notation:

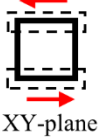
T_{14}^i /GS	T_{14} = tobermorite 14Å GS = graphene sheet i = { O_w , Ca_o , Si_t }	Shearing along X 
O_w	= water interface	
Ca_o	= calcium interface	
Si_t	= silicate interface	
R_1	elastic regime of T_{14} systems or T_{14} /GS nanocomposites	
R_{GS}	GS loading regime	
R_2	post-failure plastic regime of T_{14} systems or T_{14} /GS nanocomposites	
	(Average locations shown for all regimes)	
\square	boundary atoms	

Figure 4.30. Energy of interaction between the tobermorite 14 Å (T_{14}) structures and the graphene sheet (GS) as a function of strain during shear loading along the X-direction. [$T_{14}^{O_w}$ /GS: GS interfacing with the bottom surface water of T_{14} ; $T_{14}^{Ca_o}$ /GS: GS interfacing with the octahedral calcium layer of T_{14} ; $T_{14}^{Si_t}$ /GS: GS interfacing with the tetrahedral silicate layer of T_{14}]

4.3.2.1.4. Strain energy density

The strain energy density indirectly measured the toughness of the T_{14} /GS nanocomposites. The GS significantly enhanced the in-plane tensile and shear toughness of the T_{14} systems, providing the nanocomposites with a greater resistance to fracture. The strain energy densities of the T_{14} /GS nanocomposites were *ca.* 3-18 times greater under in-plane tensile loading and *ca.* 3-5 times greater under shear deformation than their respective T_{14} systems with no GS reinforcement (Table 4.5). Under in-plane tensile loading, the T_{14} /GS nanocomposites showed a greater resistance to fracture in the X-direction (strain energy density *ca.* 2 times

greater than in the Y-direction) contrary to the T₁₄ systems with no GS reinforcement that showed a greater resistance to fracture in the Y-direction (direction of greater linear density of atoms). This result was primarily attributed to the large fracture shear strain of the GS [74, 190, 222] and demonstrated the role of the GS orientation (the most stretchable direction of the GS was along the X-direction) in controlling the tensile toughness of the nanocomposites.

The influence of the water interface versus dry solid interface on the T₁₄/GS nanocomposite toughness was apparent with a greater strain energy density under tension for the T₁₄^{O_w}/GS nanocomposite with the GS interfacing with water and a lower strain energy density under shear compared to the nanocomposites with the dry solid surfaces (calcium and silicate) interfacing with the GS. This behavior correlated with greater molecular friction forces promoted by the water interface and was in agreement with a similar effect of liquid interfaces reported in the literature [218, 220]. The in-plane tensile strain energy density of the T₁₄^{O_w}/GS nanocomposite with the GS interfacing with water was *ca.* 1.3 times greater in the X- and Y-directions than that of the nanocomposites with the GS interfacing with the calcium and silicate surfaces. The shear strain energy density of the T₁₄/GS nanocomposites with the GS interfacing with the calcium and silicate surfaces was approximately twice that of the nanocomposite with the water interface.

In contrast, under out-of-plane (Z-direction) tensile loading, the in-plane GS reinforcement led to a lower resistance to fracture of the nanocomposites with the GS interfacing with the water and silicate surfaces (strain energy densities *ca.* 3 and *ca.* 4 times lower, respectively) and similar resistance to fracture for the nanocomposite with the GS interfacing with the calcium surface as a result of the weak interaction of the GS with the T₁₄ systems.

Table 4.5. Strain energy densities of the T₁₄ systems and T₁₄/GS nanocomposites calculated from the tensile (in-plane and out-of-plane) and shear stress-strain responses.

Systems	Tensile (Γ), X (×10 ⁹ J m ⁻³)	Tensile (Γ), Y (×10 ⁹ J m ⁻³)	Tensile (Γ), Z (×10 ⁹ J m ⁻³)	Shear (Π), XY (×10 ⁹ J m ⁻³)
T ₁₄ ^{O_w}	0.139	0.194	0.079	0.148
T ₁₄ ^{Ca_o}	0.090	0.287	0.072	0.186
T ₁₄ ^{Si_t}	0.096	0.239	0.107	0.239
T ₁₄ ^{O_w} /GS	2.020	1.050	0.026	0.473
T ₁₄ ^{Ca_o} /GS	1.525	0.781	0.074	0.845
T ₁₄ ^{Si_t} /GS	1.520	0.837	0.029	0.877

4.3.2.2. Elastic moduli, shear moduli, bulk moduli, and linear compressibility

4.3.2.2.1. In-plane elastic and shear moduli

The in-plane elastic behavior of the T₁₄ systems was affected by the differences in the stacking and exposure of the calcium, silicate, and water layers within each structure at equilibrium. These differences in structural layer build-up (different representative volume elements, RVE) affected the initial local stress distribution at equilibrium within the structures and resulted in higher stiffness and elastic anisotropy of the T₁₄ structures with the exposed calcium and silicate surfaces (T₁₄^{Ca_o} and T₁₄^{Si_t}, respectively) compared to the T₁₄ structure with the exposed water surface (T₁₄^{O_w}), which exhibited a smaller stiffness and similar intrinsic, in-plane elastic modulus values in all directions (*ca.* 49 GPa), indicating that the T₁₄^{O_w} structure was elastically quasi-isotropic (Figure 4.31a). The most elastic anisotropy was seen for the T₁₄ structure with the exposed calcium surface with the greatest intrinsic stiffness along the 45-225° and 135-315° (i.e., <1 1 0> family) directions and the lowest intrinsic stiffness along the X-direction. The intrinsic elastic modulus values of the T₁₄ systems ranged from 48.9-66.7 GPa in the X-direction and 49.0-74.0 GPa in the Y-direction, which compared well overall with values from atomistic studies that range from 25.0-69.0 GPa [2-4, 204, 205, 223-228] but were, however, higher than experimental values obtained from nanoindentation of low and high density C-S-H, which range from 18.2-41.5 GPa [229-234]. The higher values from the MD

simulations were consistent with the nanoscale size, defect free structure, and infinite silicate chain length of the T₁₄ like C–S–H models compared to real experimental systems.

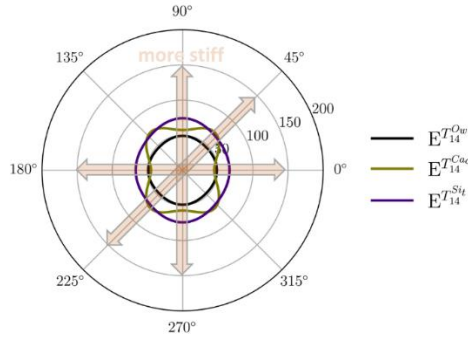
The GS enhanced the intrinsic (equilibrium, zero strain) in-plane elastic modulus of the T₁₄ systems by a factor of *ca.* 2 while decreasing (i.e., flattening) the out-of-plane elastic modulus of the T₁₄ systems as seen from the 3-dimensional, disk-shaped region of the directional elastic modulus values in Figure 4.32. The GS interacted weakly in the [0 0 1] direction with the T₁₄ matrix via van der Waals interaction, which was responsible for the small out-of-plane elastic modulus of the T₁₄/GS nanocomposites. The GS imparted the higher stiffness to the T₁₄/GS nanocomposites while the T₁₄ matrix imparted elastic anisotropy as seen by the deviation from the circular shape of the directional intrinsic elastic modulus (Figure 4.31b). The T₁₄/GS nanocomposite with the GS interfacing with the tetrahedral silicate surface exhibited the most elastic anisotropy with a greater value lobe of the intrinsic elastic modulus (greatest stiffness) along the Y-direction and the lowest intrinsic elastic modulus value (lowest stiffness) along the 45-225° and 135-315° (i.e., <1 1 0> family) directions. The greater stiffness in the Y-direction was the combined result of the AC direction (stiffer direction) of the GS and running silicate chain of the T₁₄ matrix (greater linear density) along the Y-direction.

The influence of the interface between the T₁₄ matrix and the GS on the in-plane elastic modulus of the nanocomposites was revealed upon loading by a change in stiffness behavior that was accompanied by a reduction in the nanocomposite elastic modulus (Figure 4.31b and Figure 4.31c). The non-linear behavior of the elastic modulus as a function of strain resulted in an effective modulus that was lower than the intrinsic modulus (i.e., modulus at equilibrium before loading). During the elastic loading stage, the effect of the GS reinforcement was controlled by the stiffness of the GS and the interactions between the GS and the T₁₄ matrix. Similar effective in-plane elastic modulus values were seen in all directions for each respective nanocomposite, indicating that upon loading, the nanocomposites became elastically quasi-isotropic (Figure 4.31c). Under load, a greater reduction in the elastic modulus (i.e., stiffness) was seen in all directions for the nanocomposites with the calcium and silicate interfaces compared to that of the nanocomposite with the water interface, resulting in a greater effective elastic modulus (i.e., effective stiffness) for the nanocomposite with the water interface and lower but similar effective elastic modulus values for the nanocomposites with the calcium and silicate interfaces with

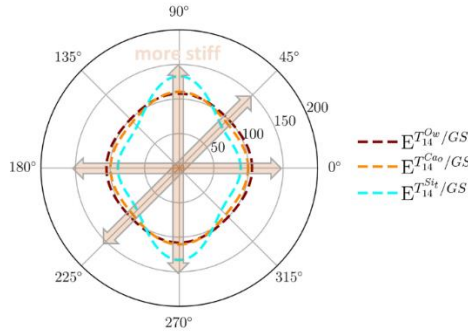
respect to their respective intrinsic values. During loading, the surface friction between the water molecules and the GS were thought to have dominated, thus leading to a greater stiffness of the nanocomposites compared to that seen when the GS interacted with the dry, solid surfaces. The decrease in stiffness for the nanocomposites with the calcium and silicate interfaces relative to their respective intrinsic stiffness (i.e., at equilibrium before loading) was attributed primarily to a reorientation of the atoms within the T_{14} matrix occurring during loading.

Like for the in-plane elastic modulus, the GS increased the shear modulus of the T_{14} systems (Figure 4.33). The influence of the interface between the T_{14} matrix and the GS was apparent for the nanocomposites with the GS interfacing with water. While the T_{14} system with the exposed water surface exhibited a lower shear modulus compared to the T_{14} systems with the exposed calcium and silicate surfaces because of a higher water content within the structure, the GS reinforced nanocomposite with the water interface (i.e., $T_{14}^{O_w}/GS$) showed the highest shear modulus, demonstrating the prominent effect of the water interface and molecular friction forces during shear loading. In contrast, the nanocomposites with the GS interfacing with the calcium and silicate surfaces (i.e., $T_{14}^{Ca_o}/GS$ and $T_{14}^{Si_t}/GS$) had similar shear modulus values.

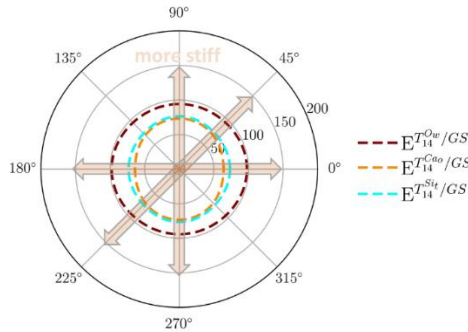
(a) Intrinsic (zero strain) elastic modulus of T_{14}



(b) Intrinsic (zero strain) elastic modulus of T_{14}/GS



(c) Effective (loading) elastic modulus of T_{14}/GS



Notation:

$E^{T_{14}/GS}$ E = elastic modulus (GPa)
 T_{14} = tobermorite 14Å
 GS = graphene sheet
 $i = \{O_w, Ca_o, Si_t\}$
 O_w = water interface
 Ca_o = calcium interface
 Si_t = silicate interface

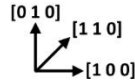
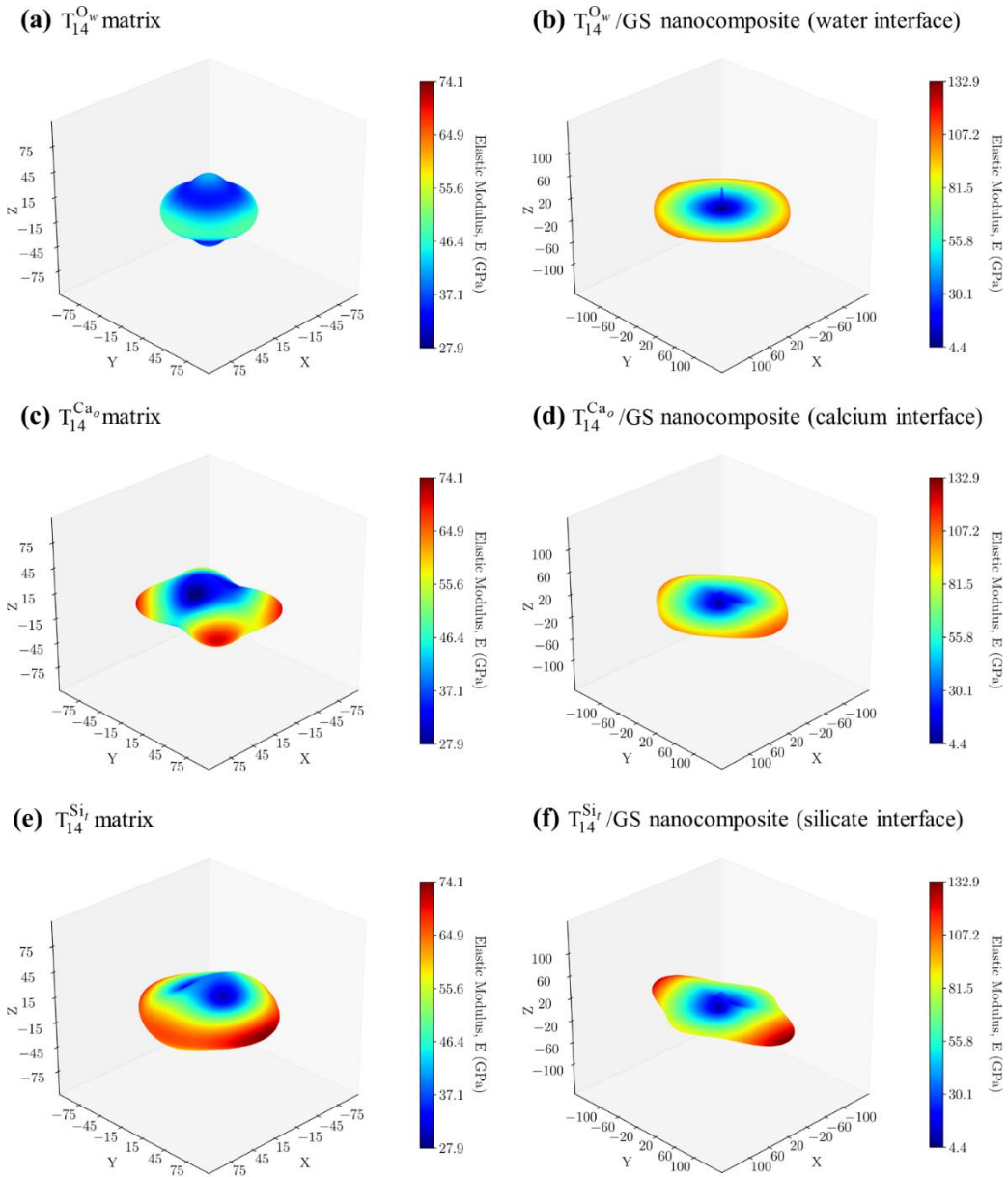


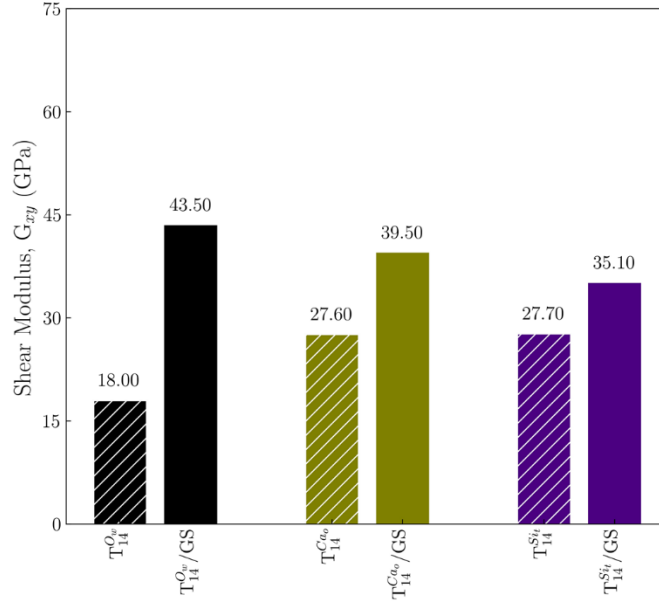
Figure 4.31. 2D plots of the directional in-plane elastic modulus: (a) intrinsic elastic modulus of the T_{14} systems, (b) intrinsic elastic modulus of the T_{14}/GS nanocomposites, and (c) effective (elastic loading stage) elastic modulus of the T_{14}/GS nanocomposites. [$T_{14}^{O_w}$: T_{14} structure with exposed water layer surface; $T_{14}^{Ca_o}$: T_{14} structure with exposed octahedral calcium surface; $T_{14}^{Si_t}$: T_{14} structure with exposed tetrahedral silicate surface; $T_{14}^{O_w}/GS$: GS interfacing with the bottom surface water of T_{14} ; $T_{14}^{Ca_o}/GS$: GS interfacing with the octahedral calcium layer of T_{14} ; $T_{14}^{Si_t}/GS$: GS interfacing with the tetrahedral silicate layer of T_{14}]



Notation:

T_{14}^i /GS T_{14} = tobermorite 14Å
 GS = graphene sheet
 $i = \{O_w, Ca_o, Si_t\}$
 O_w = water interface
 Ca_o = calcium interface
 Si_t = silicate interface

Figure 4.32. 3D plots of the directional intrinsic elastic modulus of (a), (c), and (e) tobermorite 14 Å (T_{14}) systems with the exposed water layer ($T_{14}^{O_w}$), octahedral calcium ($T_{14}^{Ca_o}$), and tetrahedral silicate surfaces ($T_{14}^{Si_t}$), respectively and (b), (d), and (f) graphene sheet (GS) reinforced tobermorite 14 Å nanocomposites with the GS interfacing with the bottom surface water of T_{14} ($T_{14}^{O_w}$ /GS), octahedral calcium layer ($T_{14}^{Ca_o}$ /GS), and tetrahedral silicate layer ($T_{14}^{Si_t}$ /GS), respectively.



Notation:

T_{14}^i/GS T_{14} = tobermorite 14Å
 GS = graphene sheet
 i = { O_w , Ca_o , Si_t }
 O_w = water interface
 Ca_o = calcium interface
 Si_t = silicate interface

Figure 4.33. Shear modulus for applied load in the XY plane along the X-direction for the T_{14} systems and T_{14}/GS nanocomposites. [$T_{14}^{O_w}$: T_{14} structure with exposed water layer surface; $T_{14}^{Ca_o}$: T_{14} structure with exposed octahedral calcium surface; $T_{14}^{Si_t}$: T_{14} structure with exposed tetrahedral silicate surface; $T_{14}^{O_w}/GS$: GS interfacing with the bottom surface water of T_{14} ; $T_{14}^{Ca_o}/GS$: GS interfacing with the octahedral calcium layer of T_{14} ; $T_{14}^{Si_t}/GS$: GS interfacing with the tetrahedral silicate layer of T_{14}]

4.3.2.2.2. Bulk moduli and linear compressibility

A greater bulk modulus (resistance to compression) and thus lower volume compressibility were observed for the T_{14} system with the exposed water surface ($T_{14}^{O_w}$) while a lower bulk modulus and thus greater volume compressibility were observed for the T_{14} system with the exposed calcium octahedral surface ($T_{14}^{Ca_o}$) (Table 4.6). These differences in bulk modulus values were attributed to their differences in crystal structure assembly (i.e., stacking of the octahedral calcium, tetrahedral silicate, and water layers), which was consistent with results

reported in the literature using high-pressure synchrotron X-ray diffraction [235] that indicated that the bulk modulus of tobermorite 14 Å was dominated by the incompressibility (i.e., stiffness) of the structure in the Z-direction. The bulk modulus value of the T₁₄ system with the exposed water surface (34.0 GPa) compared well with values reported in the literature from atomistic modeling and experiments that range from 33.7-47.8 GPa [223-226, 234-236]. The low value of the bulk modulus seen for the T₁₄ system with the exposed octahedral surface (30.1 GPa) was thought to be due to structural defects in the silicate chain caused by the removal of the top silicate layer.

The GS reduced the bulk modulus of the T₁₄ system with the exposed octahedral calcium and tetrahedral silicate surfaces (by *ca.* 15% and 9%, for the T₁₄^{Ca_o}/GS and T₁₄^{Si_t}/GS nanocomposites respectively; Table 4.6). The weak out-of-plane stiffness of the GS was thought to be responsible for the decrease in the bulk modulus. In contrast, for the nanocomposite with the GS interfacing with the water (T₁₄^{O_w}/GS nanocomposite), the GS did not reduce the bulk modulus of the nanocomposite because of the presence of the confined water molecules at the interface with the GS, which provided stiffness in the Z-direction of the nanocomposite (the out-of-plane stiffness was greater for T₁₄^{O_w}/GS nanocomposite with the water interface than the T₁₄^{Ca_o}/GS and T₁₄^{Si_t}/GS nanocomposites with the solid interfaces).

Table 4.6. Volume compressibility and bulk moduli for the T₁₄ systems and T₁₄/GS nanocomposites.

Systems	Volume Compressibility β_v (GPa ⁻¹)	Bulk Modulus κ (GPa)
T ₁₄ ^{O_w}	0.029	34.0
T ₁₄ ^{Ca_o}	0.033	30.1
T ₁₄ ^{Si_t}	0.031	32.4
T ₁₄ ^{O_w} /GS	0.028	35.0
T ₁₄ ^{Ca_o} /GS	0.039	25.6
T ₁₄ ^{Si_t} /GS	0.034	29.6

Notations: T₁₄^{O_w} : T₁₄ structure with exposed water layer surface

T₁₄^{Ca_o} : T₁₄ structure with exposed octahedral calcium surface

T₁₄^{Si_t} : T₁₄ structure with exposed tetrahedral silicate surface

T₁₄^{O_w}/GS: GS interfacing with the bottom surface water of T₁₄

T₁₄^{Ca_o}/GS: GS interfacing with the octahedral calcium layer of T₁₄

T₁₄^{Si_t}/GS: GS interfacing with the tetrahedral silicate layer of T₁₄

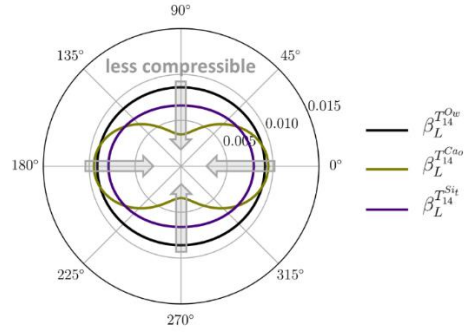
The linear compressibility was affected by the amount of water within the T₁₄ matrix and the structure of the interface between the T₁₄ matrix and the GS (Figure 4.34). A greater compressibility in the Y-direction was observed for the T₁₄ matrix that had the highest water content (i.e., T₁₄^{O_w} with a water to silicon ratio of 1.66). In contrast, the T₁₄ systems with the exposed calcium and silicate surfaces had less water and more solids (i.e., water to silicon ratio of 1.58 and 1.5 for T₁₄^{Ca_o} and T₁₄^{Si_t}, respectively) and were thus less compressible along the direction of the running silicate chains. A strong anisotropy of the linear compressibility was observed for the T₁₄ matrix with the exposed octahedral calcium surface (T₁₄^{Ca_o}) with a greater compressibility along the X-direction and lower compressibility along the Y-direction, as shown from the high value lobes along the X-direction (Figure 4.34a). There was, however, no significant spatial dependence of the linear compressibility in the XY-plane (i.e., quasi-circular shape) for the T₁₄ systems with the exposed water and tetrahedral silicate surfaces (i.e., T₁₄^{O_w} and T₁₄^{Si_t}, respectively). The anisotropy in linear compressibility for the T₁₄^{Ca_o} matrix resulted from its structural differences in the crystal structure assembly compared to the base T₁₄ structure (i.e.,

T₁₄ system with the exposed water surface, T₁₄^{O_w}) that were more prominent than for the T₁₄ system with the exposed tetrahedral silicate surface (T₁₄^{Si_t}).

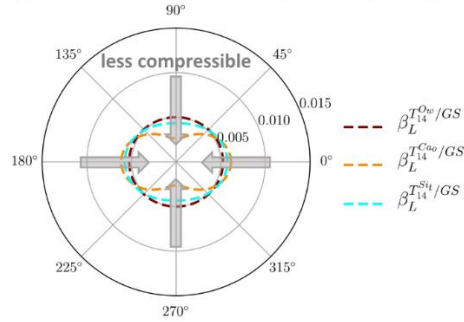
The GS significantly reduced the intrinsic (equilibrium, zero strain) linear compressibility of all T₁₄ systems by *ca.* 45% in all directions of the XY plane by providing stiffness (the GS possesses extraordinary stiffness in both the ZZ and AC directions and a very low compressibility with a value of 0.00084 GPa⁻¹ [190]). The spatial dependence of the intrinsic linear compressibility of the T₁₄/GS nanocomposites, however, remained conserved (i.e., similar shape of the directional compressibility than their respective pristine systems with no GS reinforcement), indicating that the linear compressibility was modulated by the structure of the T₁₄ systems.

Under load (strain of 0.025), the T₁₄/GS nanocomposites exhibited a change in their compressibility behavior (Figure 4.34c) that was accompanied by an increase in compressibility relative to the nanocomposite intrinsic compressibility at zero strain. The linear compressibility of the nanocomposites increased due to the increase in bond lengths during loading of the calcium octahedral and silicate tetrahedral chains in the T₁₄ matrix and carbon bonds in the GS. The nanocomposite with the GS interfacing with the octahedral calcium surface (i.e., T₁₄^{Ca_o}/GS nanocomposite) showed the most significant change in compressibility behavior. While the T₁₄^{Ca_o}/GS nanocomposite exhibited at zero strain its lowest compressibility in the Y-direction, during loading, its compressibility in that direction was significantly increased. The linear compressibility of the T₁₄^{Ca_o}/GS nanocomposite became then relatively independent of the direction (quasi-circular shape of the directional linear compressibility). This change in compressibility behavior during loading demonstrated the influence of the structure of the interface between the T₁₄ matrix and the GS. It was thought that, upon loading, the corrugated surface of the T₁₄ system with the octahedral calcium surface (i.e., zigzag structure of the octahedral calcium layer) became flatter (i.e, stretching of the octahedral calcium chain) thus becoming more compressible.

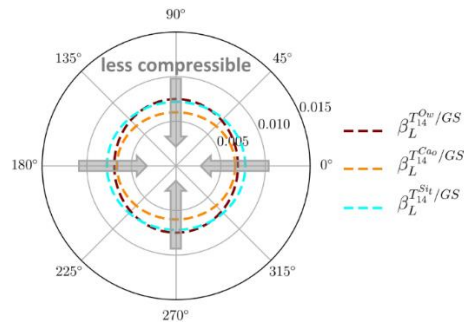
(a) Intrinsic (zero strain) compressibility of T_{14}



(b) Intrinsic (zero strain) compressibility of T_{14}/GS



(c) Effective (loading) compressibility of T_{14}/GS



Notation:

$\beta_L^{T_{14}^i/GS}$ β_L = linear compressibility (GPa⁻¹)
 T_{14} = tobermorite 14Å
 GS = graphene sheet
 i = { O_w , Ca_o , Si_t }
 O_w = water interface
 Ca_o = calcium interface
 Si_t = silicate interface

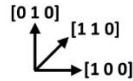


Figure 4.34. 2D plots of the directional linear compressibility: (a) intrinsic linear compressibility of the T_{14} systems, (b) intrinsic linear compressibility of the T_{14}/GS nanocomposites, and (c) effective (elastic loading stage) linear compressibility of the T_{14}/GS nanocomposites. [$T_{14}^{O_w}$: T_{14} structure with exposed water layer surface; $T_{14}^{Ca_o}$: T_{14} structure with exposed octahedral calcium surface; $T_{14}^{Si_t}$: T_{14} structure with exposed tetrahedral silicate surface; $T_{14}^{O_w}/GS$: GS interfacing with the bottom surface water of T_{14} ; $T_{14}^{Ca_o}/GS$: GS interfacing with the octahedral calcium layer of T_{14} ; $T_{14}^{Si_t}/GS$: GS interfacing with the tetrahedral silicate layer of T_{14}]

4.3.3. Effect of functionalization of GS on Tobermorite 14 Å (T_{14})

4.3.3.1. Uniaxial tensile stress-strain responses

4.3.3.1.1. In-plane tensile stress-strain responses

Random arrangement of –OH groups. The tensile stress-strain (σ - ε) responses of the T_{14} /FGS systems (Figure 4.35) were categorized into three regimes, (1) T_{14} /FGS elastic loading regime (linear increase in stress with strain), (2) FGS loading regime (continuous increase in stress with different modulus), and (3) post-failure plastic regime (marked by failure of both T_{14} and FGS). In all these T_{14} /FGS nanocomposites, the –OH groups were randomly arranged on the basal planes of FGS.

The initial elastic regime designated the loading of the T_{14} matrix, with little contribution from the FGS. The beginning of the FGS loading regime marked the transition of the stress-strain behavior from the elastic loading regime (at which the T_{14} matrix failed) to the FGS loading regime, after which the majority of the stress was transferred to the FGS. The FGS systems took the majority of the load in the duration of the FGS loading regime, at the end of which the FGS failed, and the stress-strain curves entered the post-failure regime, where the whole nanocomposite was failed and fractured, and only the residual stress remained.

This type of σ - ε response was commonly encountered in the in-plane (lamellar) structural formation of fiber/matrix nanocomposites [215]. Initially, the T_{14} matrix of the T_{14} /FGS nanocomposite were stretched (alongside FGS) as the whole system was subjected to stretching along the X-direction. The stretching in T_{14} matrix was caused by the elongation of the structural Si_t -O bonds and Ca_w - O_{bts} bonds in the T_{14} structural skeletons, i.e., the silicate tetrahedral (Si_t) and calcium octahedral (Ca_o) layers. This was similar to the σ - ε response of pristine T_{14} where the silicate and calcium layers deformed upon loading, followed by the entrance (of the pristine T_{14}) to the post-failure plastic regime. The pristine T_{14} usually possess noticeable plasticity in the post-failure plastic regime along the X-direction. This behavior was typically encountered in the crystalline C–S–H with low Ca/Si ratio [237]. In the elastic regime, the C–C bonds of the FGS were also stretched (by little amount), in addition to the stretching of T_{14} matrix, which also added to the initial stress development of the T_{14} /FGS nanocomposite. As the stretching increased, the T_{14} /FGS nanocomposite reached the failure strain of T_{14} matrix (0.09) where the failure stress was 7.5 GPa. The noticeable difference between all the nanocomposites in the

elastic regime was the differences in failure stresses. As the –OH coverage increased, the ratio of sp^3 - sp^2 carbon atoms increased, increasing the number of weak single-bonded carbon atoms, resulting in weakened FGS. Therefore, the FGS could not share the load distribution with the T_{14} as effectively as GS, resulting in lower failure stresses for the T_{14} /FGS nanocomposites.

As the T_{14} matrix failed at the end of the elastic regime, the load in the nanocomposite transferred from the T_{14} and FGS to only FGS. The C–C bonds were stretched in this regime which increased both the stress and strain in the nanocomposites until the strain reached fracture strain of the FGS. The T_{14} /GS (FGS without –OH groups) nanocomposite showed the largest fracture stress (13.64 GPa) and fracture strain (0.246) compared to all the T_{14} /FGS systems. These fracture stresses and strains of T_{14} /GS were 380% and 310% more than the pristine T_{14} system (2.84 GPa fracture stress and 0.063 fracture strain). The T_{14} /FGS nanocomposites with 25%, 50%, and 75% –OH coverages showed the fracture strains of 0.236, 0.148, and 0.100, respectively, indicating relative bond-strain losses compared to T_{14} /GS due to the higher –OH coverages (%). In agreement with the above results, the T_{14} /FGS with full coverage (100% –OH) showed the lowest fracture stress and strain (6.64 GPa and 0.076, respectively) because all the C–C bonds of FGS were converted from sp^2 bonded stronger C=C to sp^3 bonded weaker C–C. Although, the fracture stresses and strains of T_{14} /FGS with full coverage were lost, these properties were still larger compared to the pristine T_{14} , (by 130% and 21%, respectively) indicating the advantages of using FGS as the reinforcing material in the T_{14} matrix. It should be noted that the width of the FGS loading regime depended on the fracture strains of the FGS, and thus, a variable parameter. As the fracture strains of the FGS reduced with increasing –OH coverages (%), the width of the FGS loading regimes were increasingly smaller. At large –OH coverages (e.g., 75% and 100% –OH coverage), the FGS loading regimes were not easily discernible from the elastic regimes. For all FGS coverages, the T_{14} matrix failed almost at the same failure strains. The T_{14} /FGS nanocomposites entered the post-failure plastic regimes after the fracture of FGS.

The T_{14} /FGS nanocomposites also showed similar three-regime σ - ε responses in the Y-directions as in the X-directions. The pristine T_{14} usually showed higher fracture stress (5.00 GPa) and fracture strains (0.073) in the Y-direction than in the X-direction because of the orientation of silicate chain along the Y-direction. The silicate chains in Y-direction possessed a

higher linear density, and resisted against the translation, twisting, and rotation upon tensile loading, which resulted in larger stress development in the Y-direction. The failure stresses and strains of the T₁₄ matrices of T₁₄/FGS nanocomposites in the elastic regime resembled that of the pristine T₁₄ in the Y-direction. The transition from the elastic regime to the FGS loading regime could be visible by observing the change in slope in the σ - ε curve. However, the FGS loading regimes showed that the T₁₄/FGS nanocomposites in Y-direction showed much lower stress and strain developments due to the AC orientation of FGS being \parallel to the Y-direction. It is well established in the literature that the tensile fracture stress and strain are smaller in the AC direction of GS than the ZZ-direction [190]. Therefore, the T₁₄/FGS nanocomposites fractured at lower stresses and strains in the Y-directions compared to those of the X-directions. For 25% –OH, the T₁₄ matrix failed at a strain of 0.097 and the corresponding failure stress was 8.00 GPa. The load then transferred onto the FGS, which continued to take the load until the final fracture at the strain of 0.199 (the corresponding fracture stress was 9.42 GPa, 15% after the failure of T₁₄ matrix). Similarly, at full –OH coverage, the fracture stress of the nanocomposite was 5.43 GPa, only a 9% increase after the failure of the T₁₄ matrix (T₁₄ matrix failure stress was 4.94 GPa). For the full coverage, the elastic regime and the FGS loading regime were not easily discernible. At the lower –OH coverages, low stress development was seen from the elastic regime to the FGS loading regime (i.e., almost plateaued region). This was attributed to the lower intrinsic tensile failure stress of the FGS than that of GS, in addition to the lower plasticity of T₁₄ in the Y-direction (than in X-direction).

The incorporation of –OH groups on the FGS basal plane manipulated the fracture stresses, fracture strains, and the fracture patterns of the T₁₄/FGS nanocomposites because the –OH groups attracted the interlayer and structural water molecules from the T₁₄ matrices to the FGS interfaces. The water molecules interacted with the –OH groups of FGS and reduced the fracture stresses of the FGS (Figure 4.36 and Figure 4.37). At low –OH coverages (e.g., 25%), this transition was prominent. It was also evident that the Ca_w cations were also pulled by the –OH groups of FGS (Figure 4.38) from the T₁₄ matrices. The peak positions of the Ca_w atoms in T₁₄/FGS systems shifted to the right because the –OH groups pushed the Ca_w atoms away from the carbon atoms of FGS. However, the peak height increased which indicated the higher fraction of Ca_w atoms near the FGS. These two mechanisms (water molecules and Ca_w cations)

might play a role in reducing the fracture strains of the FGS, thus, those of the whole nanocomposites.

ZZ clustered line patterns of –OH on FGS. The FGS with ZZ clustered line patterns of –OH led to the reduction of the fracture stresses and fracture strains of the T₁₄/FGS nanocomposites (Figure 4.35). The ZZ clustered line patterns created weak zone of sp³ bonded C atoms (C–C) along the X-directions (depending on the % of –OH coverage). As a result, the loading of the T₁₄/FGS with ZZ clustered line pattern in the Y-direction led to lower fracture stress than the T₁₄/FGS with random arrangement of –OH. The increase in the surface coverages of –OH (%) weakened the FGS, which decreased the fracture stresses of the T₁₄/FGS nanocomposites compared to the T₁₄/GS nanocomposite. The peak fracture stresses of the nanocomposites reduced immediately after the fracture of FGS, indicating that the stretched C–C bonds released the bond-stretching energy after the fracture.

Similar to the responses, the T₁₄/FGS nanocomposites with ZZ-oriented –OH also showed three regimes. However, the stress development for the nanocomposites were much lower than those with random clustered –OH. This indicated that even in the elastic regime, the FGS with ZZ –OH orientations could not share the load as much as the T₁₄ with random –OH because FGS was weaker with ZZ patterned –OH. The line patterned –OH groups created to weak zone of sp³ bonded C system while other regions were sp² bonded. The failure stresses and strains of the T₁₄ matrix of the nanocomposites were 5.98 GPa and 0.06 for 25% –OH. As the –OH coverage increased, the fracture strain decreased. The fracture stresses at the end of FGS loading regime were 10.15, 9.13, and 9.21 GPa, while the fracture strains were 0.139, 0.133, and 0.107. During stretching, higher stress could develop along the weak zone and fractured earlier than the randomly clustered FGS. The other nanocomposites also demonstrated reductions in the failure stresses and strains compared to the pristine nanocomposite (T₁₄/GS). From the above discussion, it was evident that random clusters of the –OH groups on the FGS basal plane was better than for the in-plane strength development and for damage resistance (toughness) of the T₁₄/GS nanocomposites than the line patterning. For all the systems, the FGS fractured after the T₁₄ matrix, as a result, the structural stability was still controlled.

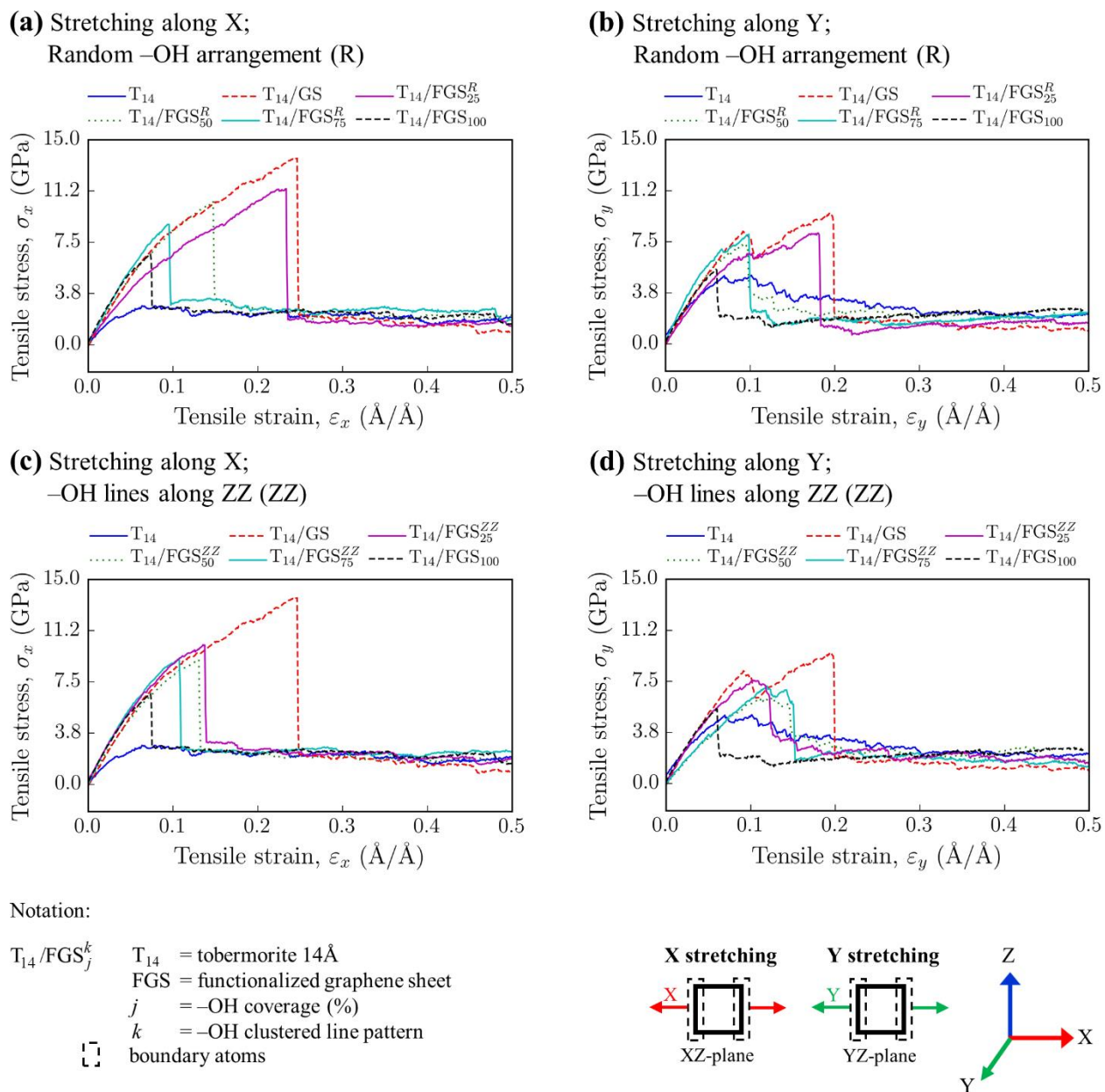
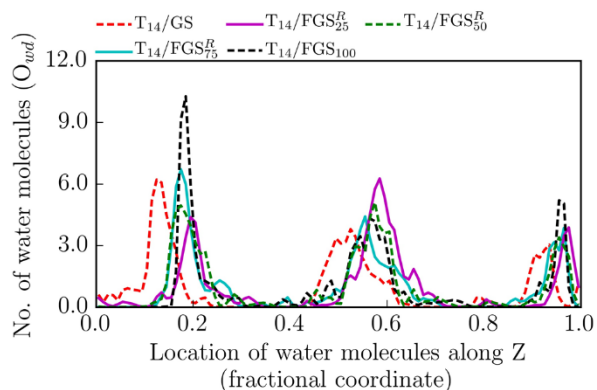
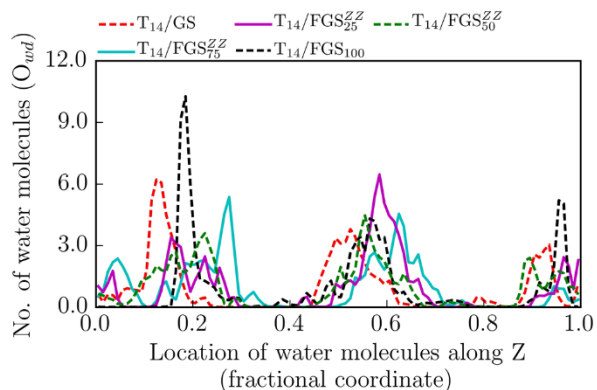


Figure 4.35. Tensile stress-strain responses of the T_{14}/FGS nanocomposites under tensile loadings in the X- and Y-directions shown in (a) and (b) for random arrangements of –OH, and (c) and (d) for ZZ clustered line patterns of –OH.

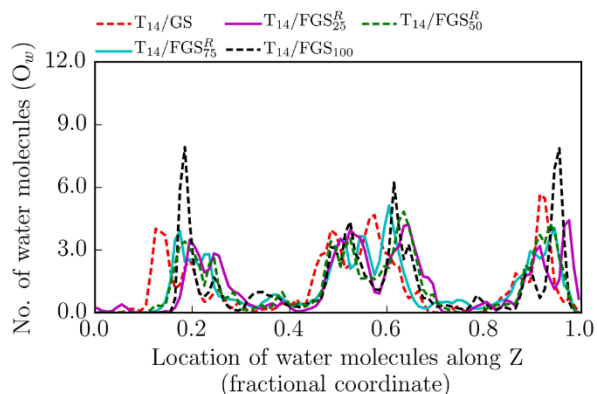
(a) Spatial distribution of interlayer water for T_{14} /FGS with random $-OH$ (R)



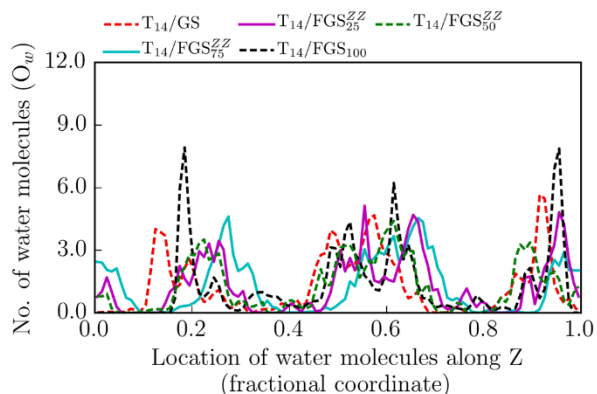
(b) Spatial distribution of interlayer water for T_{14} /FGS with zigzag clustered line pattern of $-OH$ (ZZ)



(c) Spatial distribution of structural water for T_{14} /FGS with random $-OH$ (R)



(d) Spatial distribution of structural water for T_{14} /FGS with zigzag clustered line pattern of $-OH$ (ZZ)

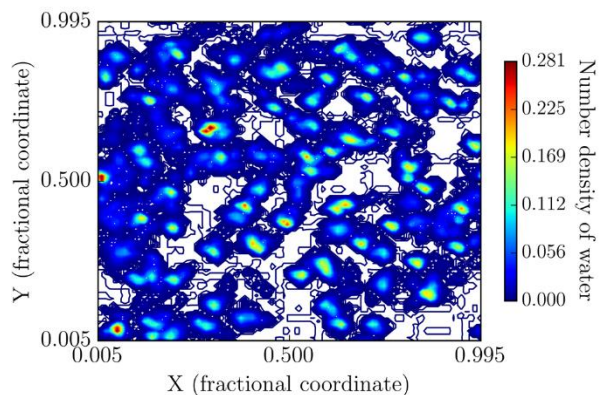


Notation:

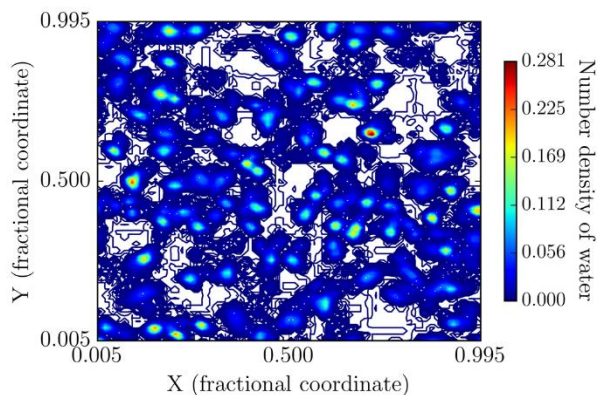
T_{14}/FGS_j^k T_{14} = tobermorite 14\AA
 FGS = functionalized graphene sheet
 j = $-OH$ coverage (%)
 k = $-OH$ clustered line pattern
 O_{wd} oxygen of interlayer water
 O_w oxygen of structural water

Figure 4.36. One dimensional (1D) density profile of interlayer water and structural water as a function of Z-direction for (a) and (b) random arrangement of $-OH$, and (c) and (d) ZZ clustered line patterns of $-OH$.

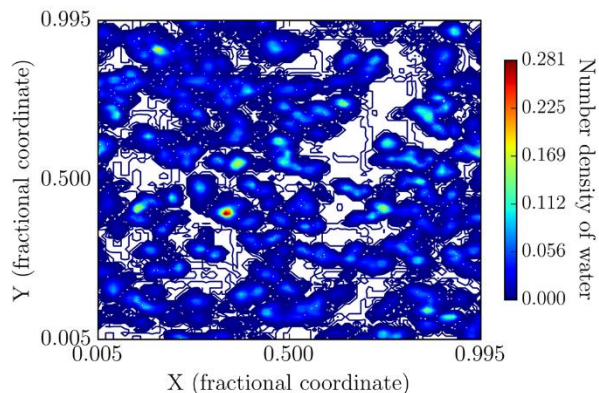
(a) Spatial distribution of interlayer water for T_{14} /FGS with random of 25% $-OH$



(b) Spatial distribution of interlayer water for T_{14} /FGS with zigzag line cluster of 25% $-OH$



(c) Spatial distribution of interlayer water for T_{14} /FGS with random cluster of 75% $-OH$



(d) Spatial distribution of interlayer water for T_{14} /FGS with zigzag line cluster of 75% $-OH$

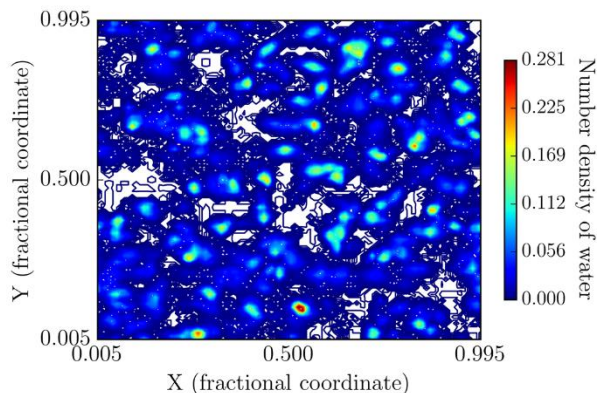
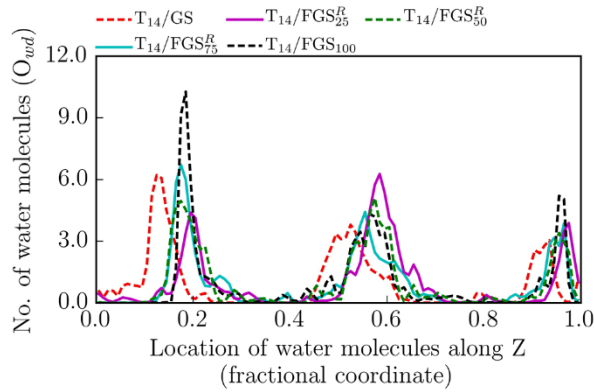
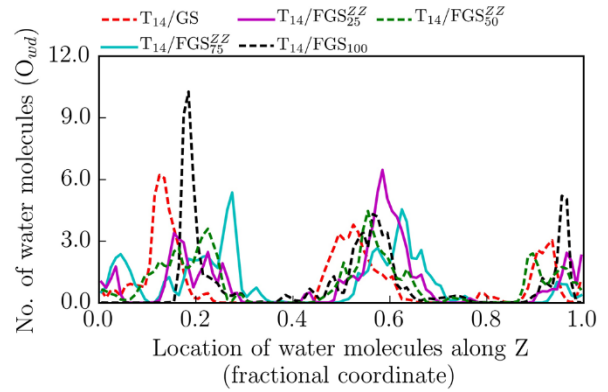


Figure 4.37. Two-dimensional (2D) density profiles of interlayer and structural water molecules of T_{14} /FGS nanocomposites on the XY plane for (a) and (c) random arrangement of $-OH$, and (b) and (d) ZZ clustered line patterns of $-OH$.

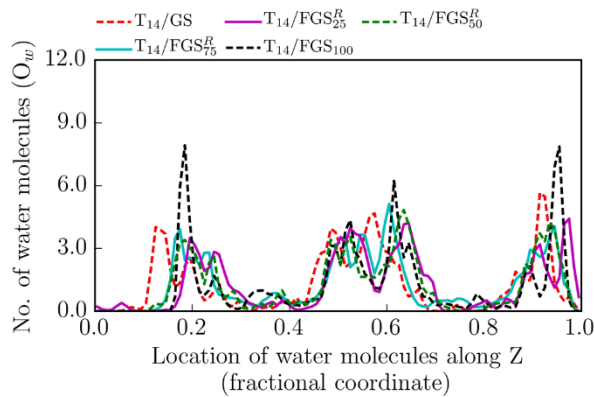
(a) Spatial distribution of interlayer water for T_{14} /FGS with random $-OH$ (R)



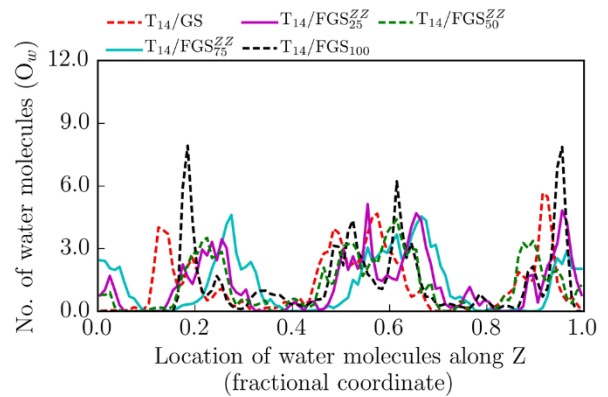
(b) Spatial distribution of interlayer water for T_{14} /FGS with zigzag clustered line pattern of $-OH$ (ZZ)



(c) Spatial distribution of structural water for T_{14} /FGS with random $-OH$ (R)



(d) Spatial distribution of structural water for T_{14} /FGS with zigzag clustered line pattern of $-OH$ (ZZ)



Notation:

T_{14}/FGS_j^k T_{14} = tobermorite 14\AA
 FGS = functionalized graphene sheet
 j = $-OH$ coverage (%)
 k = $-OH$ clustered line pattern
 O_{wd} oxygen of interlayer water
 O_w oxygen of structural water

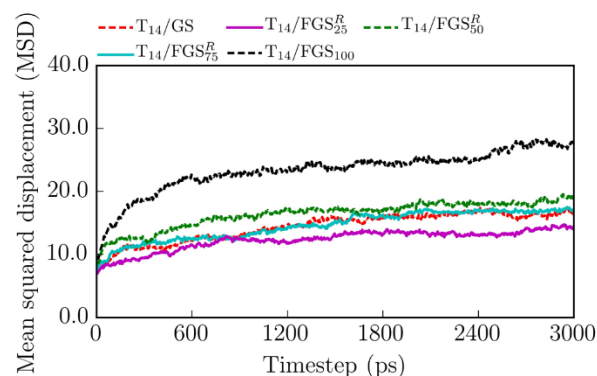
Figure 4.38. One dimensional (1D) density profiles of interlayer calcium cations (Ca_w) of the T_{14} /FGS nanocomposites on the XY plane for (a) random arrangement of $-OH$, and (b) ZZ clustered line patterns of $-OH$.

It was interesting to note that although the strength in Y-direction for T_{14} was higher than the X-direction, the strength of the nanocomposites did not follow the same conclusion. The reason is the strength of GS in the X-direction was higher compared to its Y-direction

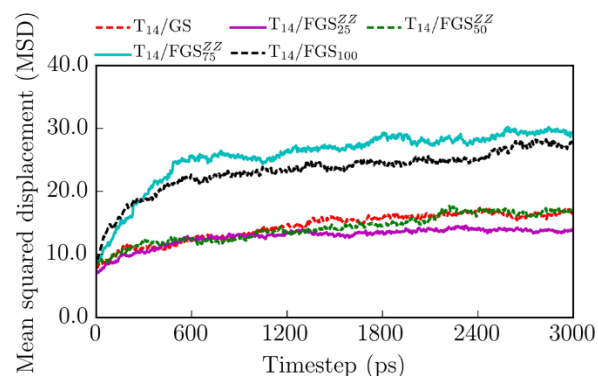
counterpart (due to the ZZ orientation along the X-direction) [190], leading to higher strength for the entire nanocomposite in the X-direction.

Mean squared displacement of water molecules. Mean squared displacement (MSD) of the structural water (O_w) and interlayer water (O_{wd}) were used to explain the effects of –OH groups and –OH arrangements on the molecular environment near the FGS and T_{14} interfaces and the subsequent effects to the mechanical properties of the T_{14} /FGS nanocomposites (Figure 4.39). The MSD of O_w with the FGS surface coverages of 75% and 100% were more than that of the O_w of pristine T_{14} because the –OH groups channeled O_w from their original locations within the T_{14} matrices towards the FGS surface, therefore, increasing the mobility. However, this behavior was not observed for the low surface coverages of –OH such as 25% and 50%, possibly because the surface coverages were not large enough to draw out the O_w . The MSD of O_w for the pristine T_{14} and T_{14} /FGS with 25% and 50% –OH showed that the hydrogen bond (H-bond) network created between the ZZ clustered line patterns of –OH groups and O_w was not strong enough to visibly affect the mobility of O_w . On the other hand, the O_{wd} had high mobility in the T_{14} /FGS with 100% –OH because the –OH/–OH H-bond network severed the H-bond network between the –OH and water, thus, creating more intra-molecular H-bond network among themselves. The 75% also had higher mobility, possibly due to the previous reason. 25 and 50% showed slower mobility because of the temporary cage created by the H-bonds between the water and –OH for the water molecules. It was also evident that as the surface coverage of the –OH increased, the interlayer water density increased near the FGS (Figure 4.37), which might promote the early fracture of the FGS during stretching, thus affecting the mechanical properties.

(a) Mean squared displacement of interlayer water for T_{14} /FGS with random $-OH$ (R)



(b) Mean squared displacement of interlayer water for T_{14} /FGS with zigzag clustered line pattern of $-OH$ (ZZ)



Notation:

T_{14}/FGS_j^k T_{14} = tobermorite 14Å
 FGS = functionalized graphene sheet
 j = $-OH$ coverage (%)
 k = $-OH$ clustered line pattern
 O_w interlayer water

Figure 4.39. Mean squared displacement of interlayer water molecules with (a) random arrangement of $-OH$ and (b) ZZ clustered line patterns of $-OH$.

4.3.3.1.2. Out-of-plane tensile stress-strain responses

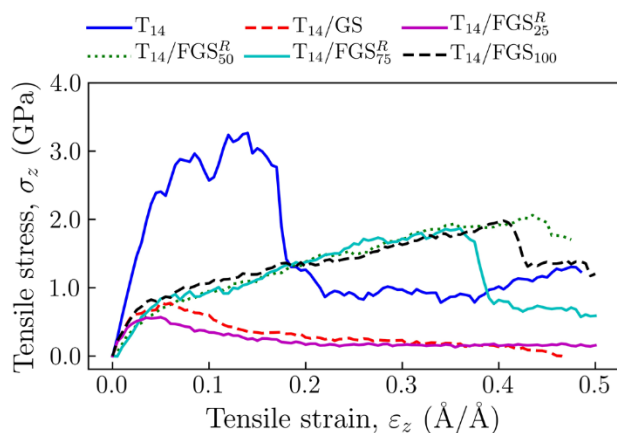
The out-of-plane tensile response (σ - ε) in the Z-directions (Figure 4.40) showed that T_{14} was slightly lower in strength (2.96 GPa) compared to the in-plane strength (2.83 GPa and 4.85 GPa in the X- and Y-directions, respectively). Although, generally, the out-of-plane direction of T_{14} was weaker than the in-plane direction, higher strength in the Z-direction was observed for T_{11} in the literature [5]. It was noteworthy that, the T_{14} structure was also more compliant along Z-direction, possibly due to electrostatic interactions of the Ca_w and O_{bts} atoms, and intermolecular interactions of the water, rather than in-plane covalent type bonding of Si_r-O chains.

Random clusters of $-OH$ groups on FGS. Having GS as an interface to the T_{14} , weakened the strength of T_{14} along Z-direction (0.83 GPa) (Figure 4.40). The reason could be that the interface was weaker than the interlayer. Therefore, when the tension was applied on the GS and T_{14} , the interface separated earlier than the interlayer, resulting in lower stress development

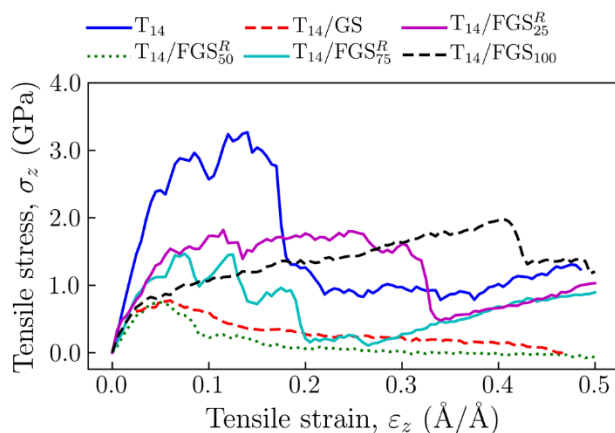
throughout the structure. FGS with 25% –OH groups, lowered the strength even more (0.75 GPa), indicating that –OH groups were not able to create stable structural network with the T₁₄ structures through water molecules (O_w and O_{wd}). However, the toughness of the structures increased substantially for the T₁₄/FGS with –OH coverages over 50%. For 50%, 75%, and 100% FGS, the fracture strains were 0.45, 0.38, and 0.41, respectively, compared to only strain of 0.07 for T₁₄/GS, an increase in the range of 442% to 541%. The –OH groups drew out interlayer and structural water near the T₁₄ and FGS interface and created a structural network which required more strength to break than the interlayer. As a result, the interlayer was broken instead of the interface, preceded by the elongation and breakage of the Si–O bonds in the structural network (Figure 4.41 and Figure 4.43). Thus, strength development occurred alongside gradual strain accumulation before final fracture. A significant strain hardening was observed for the T₁₄/FGS structures above 50% –OH coverage.

Zigzag line clusters of –OH groups on FGS. The 25% FGS had intrinsic curvature which was responsible for rebuilding the interface of T₁₄ (some portion was pushed inward) (Figure 4.42). Therefore, it could build a stronger network, and thus, showed higher fracture strain (0.35), compared to 0.05 from its random counterpart (a 600% increase in strain). FGS with 75% also did not show a significant strengthening. Due to significant amount of curvature, the equilibrated structure of T₁₄ was also extremely deformed from the beginning. Thus, a lower strength was developed during tensile stretching along Z before breaking. 50% FGS showed a separation from the interface instead of the interlayer. The 50% had even more curvature than the 75%. Therefore, the water molecules did not have large enough contact area of FGS to interact and create structural network. Therefore, stress could not propagate throughout the T₁₄ structures during stretching, and the weak T₁₄/FGS interface separated. It was noteworthy that in general, large coverage of –OH groups in a random clustered pattern showed better strength and toughness in the out-of-plane direction.

(a) Random -OH arrangement (R)



(b) -OH lines along ZZ (ZZ)



Notation:

T_{14}/FGS_j^k T_{14} = tobermorite 14Å
FGS = functionalized graphene sheet
 j = -OH coverage (%)
 k = -OH clustered line pattern
□ boundary atoms

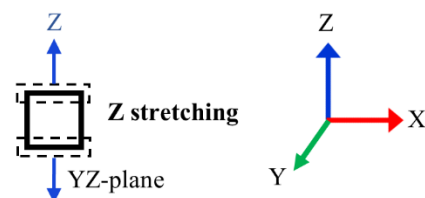
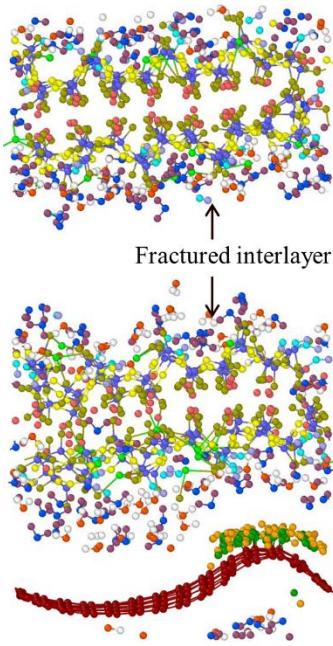
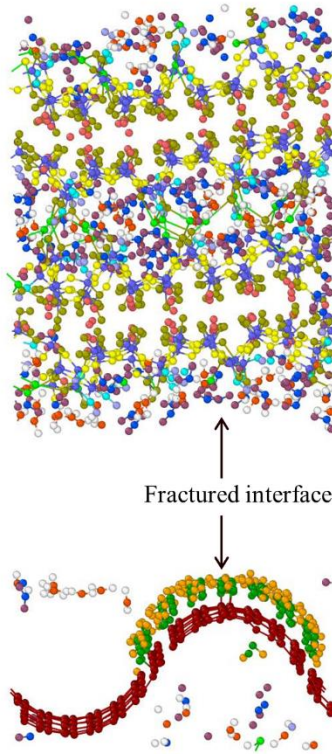


Figure 4.40. Tensile stress-strain responses for the T_{14}/FGS nanocomposites in the out-of-plane direction (Z-direction) with varying -OH surface coverage (%) for (a) random clustered -OH and (b) ZZ line clustered -OH.

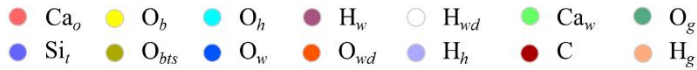
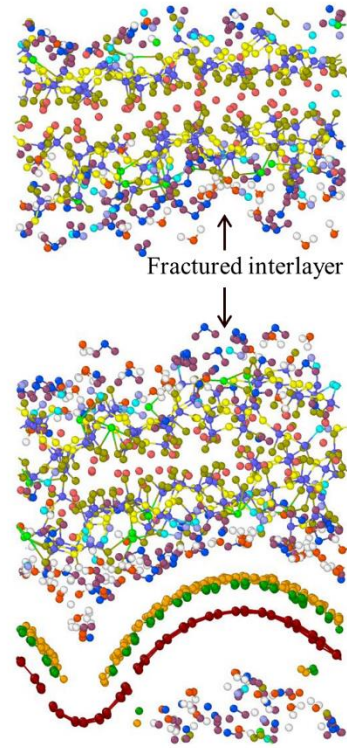
(a) T_{14} /FGS with zigzag 25%
–OH at complete separation
($\epsilon_z = 0.50$)



(b) T_{14} /FGS with zigzag 50%
–OH at complete separation
($\epsilon_z = 0.50$)



(c) T_{14} /FGS with zigzag 75%
–OH at complete separation
($\epsilon_z = 0.50$)



Ca_o : octahedral calcium; Si_t : tetrahedral silicon; O_b : bridging oxygen;
 O_{bts} : bridging oxygen in tetrahedra; O_h : hydroxyl oxygen;
 O_w : water oxygen (structural); H_w : water hydrogen (structural);
 O_w : water oxygen (interlayer); H_w : water hydrogen (interlayer);
 H_h : hydroxyl hydrogen; Ca_w : interlayer calcium; C : carbon in graphene;
 O_g : oxygen of hydroxyl group in graphene;
 H_g : hydrogen of hydroxyl group in graphene

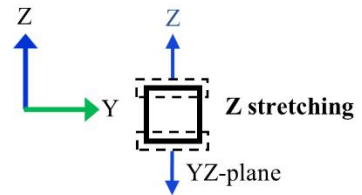


Figure 4.42. Fracture mechanisms of the T_{14} /FGS nanocomposites attached with ZZ clustered line patterns of –OH with varying surface coverages.

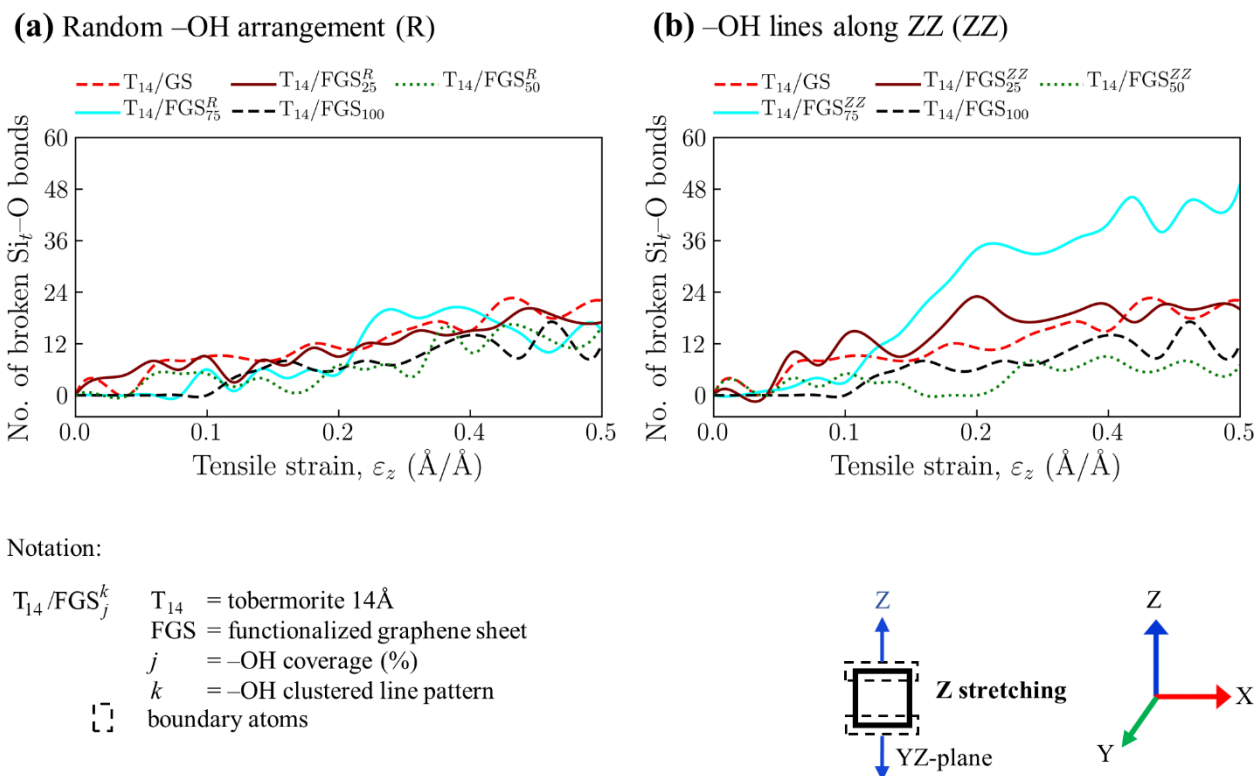


Figure 4.43. The number of broken Si_r-O bonds for T_{14}/FGS nanocomposites along the Z -directions with (a) random arrangements of –OH and (b) ZZ clustered line patterns of –OH.

4.3.3.2. Shear stress-strain responses

Random clusters of –OH groups on FGS. Shear stress-strain (τ - γ) responses of the nanocomposites showed distinct loading regimes similar to the tensile responses, categorized by accounting the responses of T_{14} and FGS at each stage. Due to the mechanism of applied shear strain (γ), the structural layers (tetrahedral silicate and calcium octahedral layers) and the interlayers (water and mobile calcium atoms) of the T_{14} systems were twisted instead of getting stretched. The initial shear stress accumulation and distribution occurred through a large area in the T_{14} system, which resulted in a larger global shear stress (3.92 GPa) compared to X tensile stretching, at a strain of 0.14 at the end of the elastic regime (Figure 4.44).

The random clustered –OH line patterned FGS systems increased the initial failure shear stresses of the nanocomposites in varying amount (3.93, 3.02, 4.62, 4.92, 5.17 GPa for 0%, 25%, 50%, 75%, and 100%, respectively). However, the failure shear strains remained almost the same. In the initial regime, the FGS shared majority of the load as the –OH coverage increased,

with the full coverage taking the largest share of the load. This might be attributed to the interaction of the FGS with the $(00\bar{1})$ interfaces (water-rich interfaces) of the T_{14} during shearing at higher coverages (50%, 75%, and 100%). However, the maximum load transfer could be seen for GS in the FGS loading regime (5.96 GPa from 3.93 GPa). The FGS systems could not increase the stress of the nanocomposite much because their intrinsic strengths were lower. However, even with the full coverage (100% -OH), the shear fracture stress reached ~ 5.85 GPa, at a fracture strain of 0.185. Thus, the fracture shear stresses were very similar for the FGS systems but the fracture shear strain decreased because the intrinsic shear strain reduced with the increase in -OH coverage.

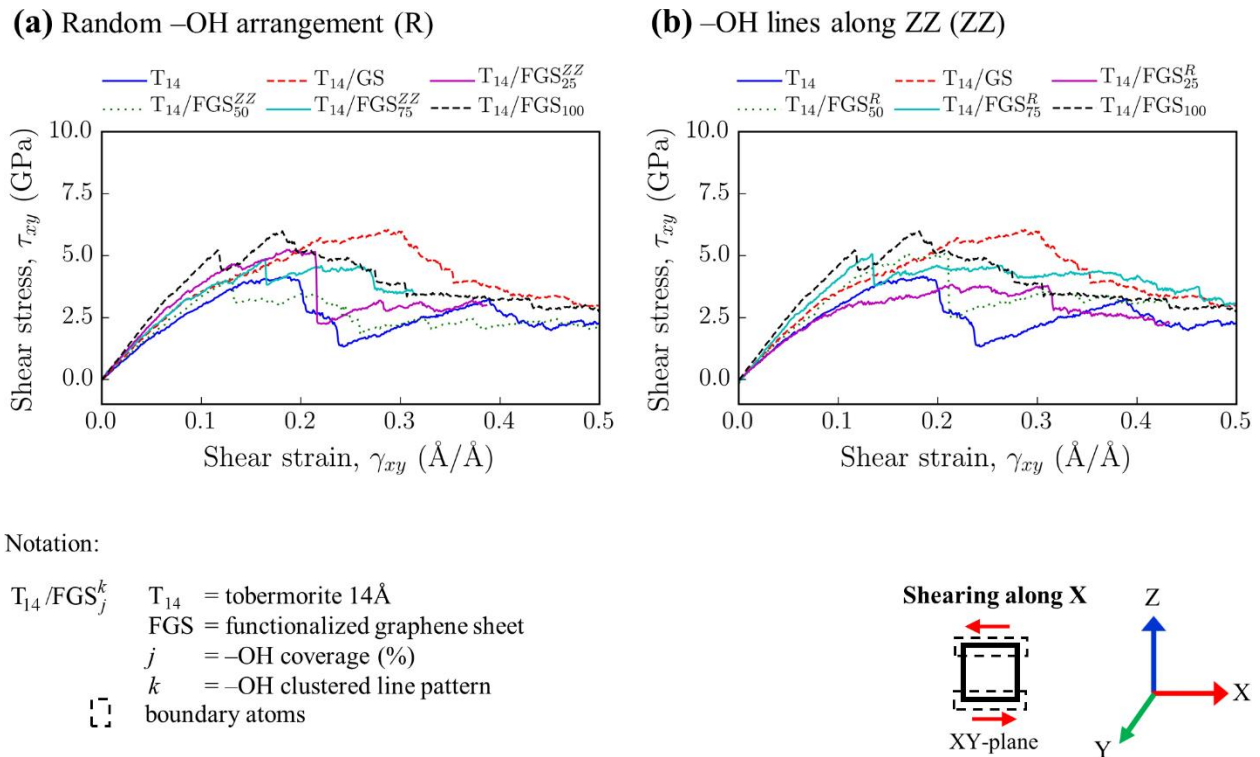


Figure 4.44. Shear Stress- shear strain responses of T_{14}/FGS nanocomposites (a) for random FGS and (b) for ZZ-oriented FGS.

ZZ-clustered line pattern of -OH on FGS. One of the noticeable features of the ZZ-clustered line pattern of -OH groups was the lower shear stress development at fracture at the end of the FGS loading regime than those of T_{14}/FGS nanocomposites with random clustered

line pattern of –OH. This phenomenon could be attributed to the fact that –OH groups were organized in a particular smaller area, which might not be as effective in increasing interfacial friction during shear. Water molecules at the $(0\ 0\ \bar{1})$ interfaces were thought to be responsible for increasing the interfacial interactions between the T₁₄ and FGS interfaces. However, if the –OH groups were ZZ oriented, all the water molecules could not occupy that area, and thus, could not increase the friction effectively. Moreover, having curvature to the FGS did not allow it to have effective interaction with the T₁₄ matrix. Therefore, lower initial shear stresses were observed for the ZZ oriented FGS. In both cases, the nanocomposites retained large residual shear stresses even after the fracture of the FGS in the post-failure plastic regime. Under shear loading, the $\angle\text{C–C–C}$ angles and the structural layers of T₁₄ were subjected to angular distortion. After fracture, the angular distortions could not go back to the equilibrium position as easily as the bond stretching, and hence, large residual shear stress was observed.

4.3.3.3. Strain energy density

Toughness of any material is related to its strain energy density. It is to be acknowledged here that the stress-strain behavior of the nanolaminates resemble that of a snap-through failure and the kinetic energy involved during the fracture is unknown. Therefore, the actual toughness of the nanolaminates cannot be quantified from these strain energy density results and the results from this section are just a prediction about the strain energy density associated with the nanolaminates at the point of fracture. In this study, the tensile (Π) and shear strain energy (Γ_{xy}) densities were used as indirect measurements of the toughness property of T₁₄/FGS nanocomposites. These strain energy densities of the nanocomposites were found to be functions of the surface coverages (%) of –OH, clustered line patterns of –OH on the FGS basal plane, and loading directions.

4.3.3.3.1. In-plane tensile strain energy density for X and Y loading

The T₁₄/GS nanocomposite showed the highest tensile strain energy densities along the X- (Π_x) and Y-directions (Π_y) ($2.10 \times 10^9 \text{ J m}^{-3}$ and $1.26 \times 10^9 \text{ J m}^{-3}$, respectively). According to the literature, FGS lost its intrinsic Π_x and Π_y when the –OH groups were attached to the basal plane (as random arrangement and ZZ clustered line patterns) [9]. As the –OH coverage (%) increased, the Π_x and Π_y of the FGS decreased due to the reduction in intrinsic tensile fracture

stresses and strains of FGS (Table 4.7). Nonetheless, the Π_x and Π_y of T₁₄/FGS nanocomposites were higher than those of the pristine T₁₄ ($0.15 \times 10^9 \text{ J m}^{-3}$ and $0.46 \times 10^9 \text{ J m}^{-3}$, respectively).

The T₁₄/FGS nanocomposites with random arrangement of –OH showed increase in the Π_x and Π_y than those with ZZ clustered line pattern (Table 4.7). In this study, the Π_x of the nanocomposites with low surface coverages of –OH were higher than the Π_y because of the higher fracture stresses and strains of the nanocomposites in the X-directions (due to the ZZ orientations of FGS along X). The effective interactions (i.e., contact areas) between the (0 0 $\bar{1}$) interfaces of the T₁₄ and the FGS were in full effect when the –OH groups were randomly distributed on the FGS basal plane, unlike the ZZ clustered line pattern of –OH, which demonstrated less contact area (because of the bending curvature). Therefore, the lack of Π of the T₁₄/FGS nanocomposites with ZZ clustered line patterns of –OH was thought to be resulted from: (1) the lower intrinsic fracture stresses and strains of the FGS with ZZ clustered line patterns and (2) the smaller but concentrated effective areas of interactions between the water-rich (0 0 $\bar{1}$) interfaces of the T₁₄ and the –OH groups of FGS, which led to even lower fracture strains of the FGS than their intrinsic fracture strains (e.g., FGS with ZZ-clustered line patterns of 25% –OH had a fracture strain of 0.20 when loaded along the X-direction). Therefore, the Π of T₁₄/FGS nanocomposites were found to be interface-controlled. In all cases, damage tolerance (resistance against fracture) of the nanocomposites increased with the incorporation of GS and FGS in the T₁₄ matrices.

4.3.3.3.2. Out-of-plane tensile strain energy density for Z loading

The out-of-plane tensile strain energy density of the T₁₄/GS nanocomposite along the Z-direction (Π_z) was much lower ($0.02 \times 10^9 \text{ J m}^{-3}$) than that of the pristine T₁₄ ($0.32 \times 10^9 \text{ J m}^{-3}$, which was interlayer-dominated) because the GS separated from the (0 0 $\bar{1}$) interface of the T₁₄ easily during the loading along Z-direction, leading to an interface-dominated failure. This result indicated that less amount of energy was required to separate the GS from the T₁₄, which means, the T₁₄/GS nanocomposite was less tough than T₁₄ along the Z direction.

Similar to the T₁₄/GS, an interface-dominated Π_z ($1.60 \times 10^9 \text{ J m}^{-3}$) was observed for the T₁₄/FGS nanocomposites with the FGS having 25% random arrangement of –OH. However, as

the –OH coverage increased, the Π_z of the T₁₄/FGS nanocomposites increased significantly (2850% and 2150% for 50% and 75% –OH coverage) showing a transition in toughness behavior from interface-dominated to interlayer-dominated (due to the interaction of the water-rich interface of the T₁₄ matrix and the –OH groups). Therefore, significant elongation before the ultimate failure was observed, which resulted in a greater strain energy density of the T₁₄/FGS nanocomposites.

The FGS with 25% ZZ clustered line pattern of –OH also led to a higher Π_z of the nanocomposites compared to that of T₁₄. However, the Π_z was lower than those for random arrangements of –OH for 50% and 75% ZZ-clustered line pattern. For the 50% and 75%, the bending curvatures of the FGS were so large that the water molecules of T₁₄ matrices did not have enough contact areas of interactions with the –OH groups of FGS, which led to the interfacial failures as opposed to T₁₄/FGS with random arrangement of –OH (which were interlayer-dominated at higher coverages).

4.3.3.3.3. Shear strain energy density in the XY plane

In this study, the shear strain energy density (Γ_{xy}) of the T₁₄/GS nanocomposite ($1.18 \times 10^9 \text{ J m}^{-3}$) was very similar to the tensile strain energy densities ($2.1 \times 10^9 \text{ J m}^{-3}$ and $1.26 \times 10^9 \text{ J m}^{-3}$ for X- and Y-directions, respectively). Similar to the tensile strain energy densities, the Γ_{xy} of the T₁₄/FGS nanocomposites decreased with the increase in surface coverages of FGS.

The Γ_{xy} of the T₁₄/FGS nanocomposite was found to be generally higher than Γ_y . Also, the ZZ clustered line pattern of –OH created a weak zone on the FGS. Hence, it was easier for the whole FGS to fail under shear along XY plane. Therefore, the Γ_{xy} of the T₁₄/FGS with ZZ clustered line pattern of –OH were lower than the Γ_{xy} of T₁₄/FGS with random arrangement of –OH. Under shear loading, the silicate tetrahedral and $\angle \text{C–C–C}$ angles of T₁₄ and FGS, respectively, were twisting and distorting instead of Si_r–O_{bt}s and C–C bond-stretching. Angular distortion usually led to higher accumulated deformation, i.e., strain before failure, and therefore, higher shear toughness for the T₁₄/FGS nanocomposites could be obtained.

The ZZ clustered line pattern of –OH tend to reduce the Γ_{xy} because the effective interaction area between the $(0\ 0\ \bar{1})$ surface of T₁₄ and the FGS was not large enough to increase the resistance against shear distortion. In addition to that, water molecules of T₁₄ matrix

could create hydrogen bonds with the –OH groups of FGS that improved the interfacial friction even more. A combination of the aforementioned two factors could be responsible for the large Γ_{xy} shown by the T₁₄/GS nanocomposites. The study on the shear strain energy density also demonstrated that the shear toughness of the T₁₄/FGS was interface-dominated.

Table 4.7. Strain energy densities of T₁₄/FGS nanocomposites due to tensile and shear loadings.

–OH clustered line pattern on FGS	–OH coverage (%)	Tensile strain energy density, X, Π_x ($\times 10^9 \text{J m}^{-3}$)	Tensile strain energy density, Y, Π_y ($\times 10^9 \text{J m}^{-3}$)	Tensile strain energy density, Z, Π_z ($\times 10^9 \text{J m}^{-3}$)	Shear strain energy density, XY, Γ ($\times 10^9 \text{J m}^{-3}$)
Control	0	2.10	1.26	0.02	1.18
	100	0.30	0.19	0.42	0.81
Random (R)	25	1.60	0.98	0.02	0.87
	50	0.90	0.44	0.59	0.67
	75	0.50	0.50	0.45	1.52
Zigzag (ZZ)	25	0.87	0.69	0.36	0.75
	50	0.74	0.60	0.02	0.28
	75	0.59	0.65	0.07	0.89

4.3.3.4. Elastic moduli, shear moduli, and linear compressibility

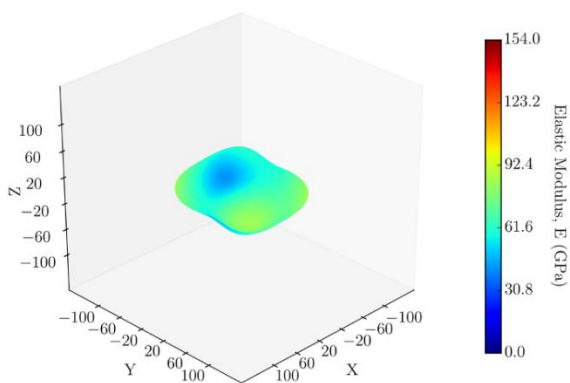
4.3.3.4.1. Elastic moduli and shear moduli

The elastic moduli (E) of the nanocomposites revealed three key variables such as, effect of –OH coverage, –OH line patterning (R or ZZ), and loading directions.

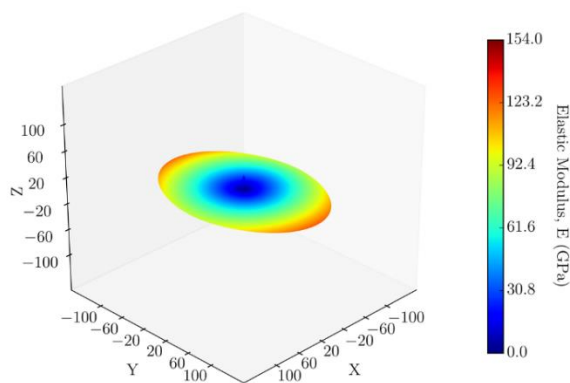
Random arrangement of –OH. The elastic modulus E_x (along [1 0 0] crystallographic directions) was 60.5 GPa for the pristine T₁₄ (Figure 4.46). As the –OH coverage increased, the FGS was stiffened in the XY plane, which increased the overall nanocomposite moduli in the X- and Y-directions (E_x and E_y , respectively). The modulus in Y-direction was usually slightly higher than that in the X-direction for the pristine T₁₄ because the silicate tetrahedra chain with a high linear density ran parallel (\parallel) to the Y-direction, resulting in a faster rate of load resistance response upon straining, i.e., high modulus. Additionally, FGS also possessed higher stiffness along AC direction which was oriented \parallel to Y-direction, resulting in an even higher E_y values for the nanocomposites.

ZZ clustered line pattern of –OH. The intrinsic moduli of the FGS with *ZZ* clustered line pattern of –OH were higher in the X-direction than in the Y-direction, i.e., $E_x > E_y$, especially at large coverages (50% and 75%) [190]. Therefore, the E_x and E_y values were higher for 50% and 75% *ZZ* clustered line pattern of –OH on FGS with T_{14} than those for the T_{14} /FGS with random arrangement of –OH (Figure 4.46). These key variables could be controlled to modulate the elastic modulus of the nanocomposites. However, the in-plane moduli values (E_x and E_y) were the most sensitive to the clustered line pattern of –OH. Most importantly, the in-plane moduli of the T_{14} /FGS nanocomposites could be increased substantially by controlling the surface coverage (%) and line pattern of the –OH.

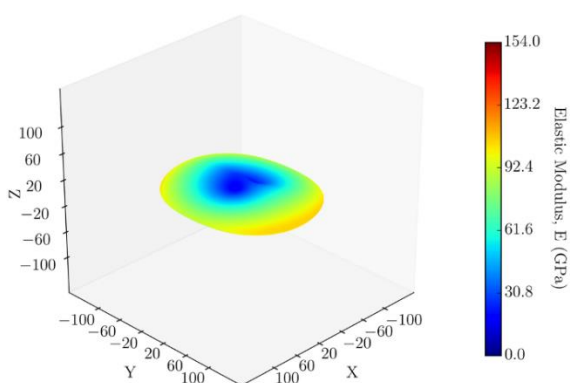
(a) Tobermorite 14 Å (T_{14})



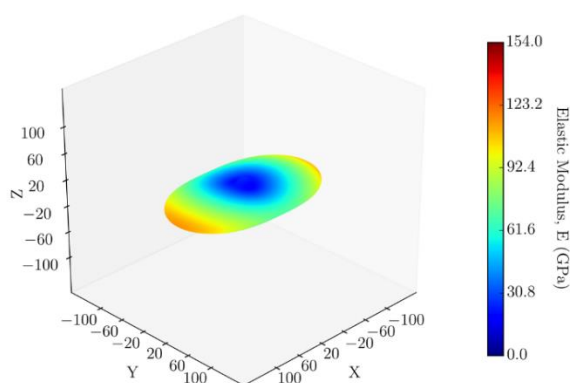
(b) T_{14} /GS nanocomposite



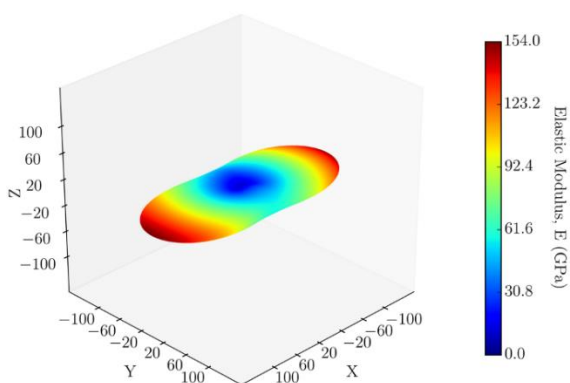
(c) T_{14} /FGS nanocomposite with 25% zigzag (ZZ) -OH



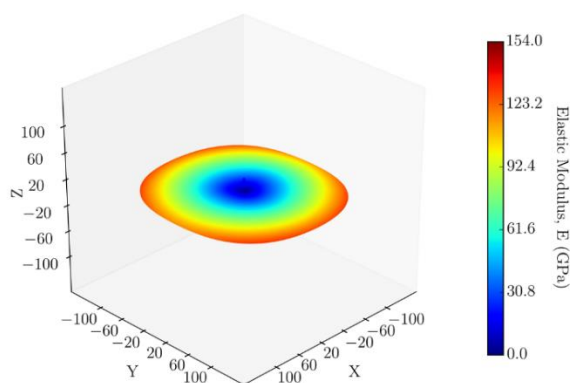
(d) T_{14} /FGS nanocomposite with 50% ZZ -OH



(e) T_{14} /FGS nanocomposite with 75% ZZ -OH



(f) T_{14} /FGS nanocomposite with 100% -OH



Notation:

T_{14}/FGS_j^k T_{14} = tobermorite 14Å
FGS = functionalized graphene sheet
 j = -OH coverage (%)
 k = -OH clustered line pattern

Figure 4.45. 3D representation of the directional anisotropy of elastic modulus for T_{14} /FGS nanocomposites with the varying surface coverages and ZZ clustered line pattern of -OH.

4.3.3.4.2. Directional anisotropy of elastic moduli

Random arrangement of –OH. The pristine T₁₄ systems provided anisotropic directionality of elastic modulus in the X-, Y-, and Z-directions. The elastic modulus for the T₁₄ were similar along the X [1 0 0] and Y [0 1 0] directions, but a slightly higher values along the [1 1 0] - oriented at 45° between the X and Y axes (Figure 4.45 and Figure 4.46) were seen. The T₁₄/FGS nanocomposites with random arrangement of –OH groups showed increased elastic moduli. As the –OH coverage (%) increased, the in-plane elastic moduli (both X and Y) of the T₁₄/FGS nanocomposites also increased. The 3D and 2D shapes suggested that the increase was more along the Y-direction than along the X-direction (Figure 4.45 and Figure 4.46). The FGS with random arrangement of –OH groups also demonstrated higher elastic modulus along the Y-direction [190]. Although, the elastic modulus of the FGS systems were not observed to possess higher modulus with higher coverages, the elastic modulus for the T₁₄/FGS nanocomposites were higher as –OH increased. The reason was attributed to the hydrogen bonds created between the –OH groups of FGS and the water molecules of T₁₄ matrices which provided additional stiffness during loading. The full coverage of –OH reverted to the similar shape of the elastic modulus of pristine T₁₄, although the magnitudes were much higher, i.e., T₁₄/FGS nanocomposites with full coverage was the stiffest.

ZZ clustered line pattern of –OH. In contrast, the ZZ clustered line pattern of –OH created a directional anisotropy in the elastic modulus in the T₁₄/FGS nanocomposites along the X-directions. T₁₄/FGS nanocomposites with 25%, 50%, and 75% ZZ clustered line pattern of –OH experienced substantial increase in the elastic moduli in the X-directions, whereas, the moduli along the Y-directions continued to decrease. The elastic modulus for the 75% –OH decreased in the Y-direction compared to that of 25% so much that it created distinct lobes along the [0 1 0] directions, creating large anisotropy in the elastic modulus envelop of the T₁₄/FGS nanocomposites. This anisotropy in the elastic modulus was created by the FGS with ZZ clustered line pattern of –OH, which possessed very high stiffness in the X-direction. The clustered presence of the –OH groups on the carbon sites of FGS created out-of-plane (Z-direction) curvature along the Y-directions. This bending curvature created a stiffened response upon loading of the T₁₄/FGS nanocomposites along the X-direction, while a flexible response along the Y-direction, resulting in large modulus along the X-directions. This behavior shown by

the T₁₄/FGS nanocomposites was similar to the response shown by FGS only [190]. As the surface coverage of –OH (%) increased, the bending curvature of the FGS also increased, leading to a larger elastic modulus. Therefore, it was evident that the elastic modulus of T₁₄/FGS nanocomposites, similar to the tensile and shear strengths, were dominated by the surface coverage (%) and clustered line pattern of –OH.

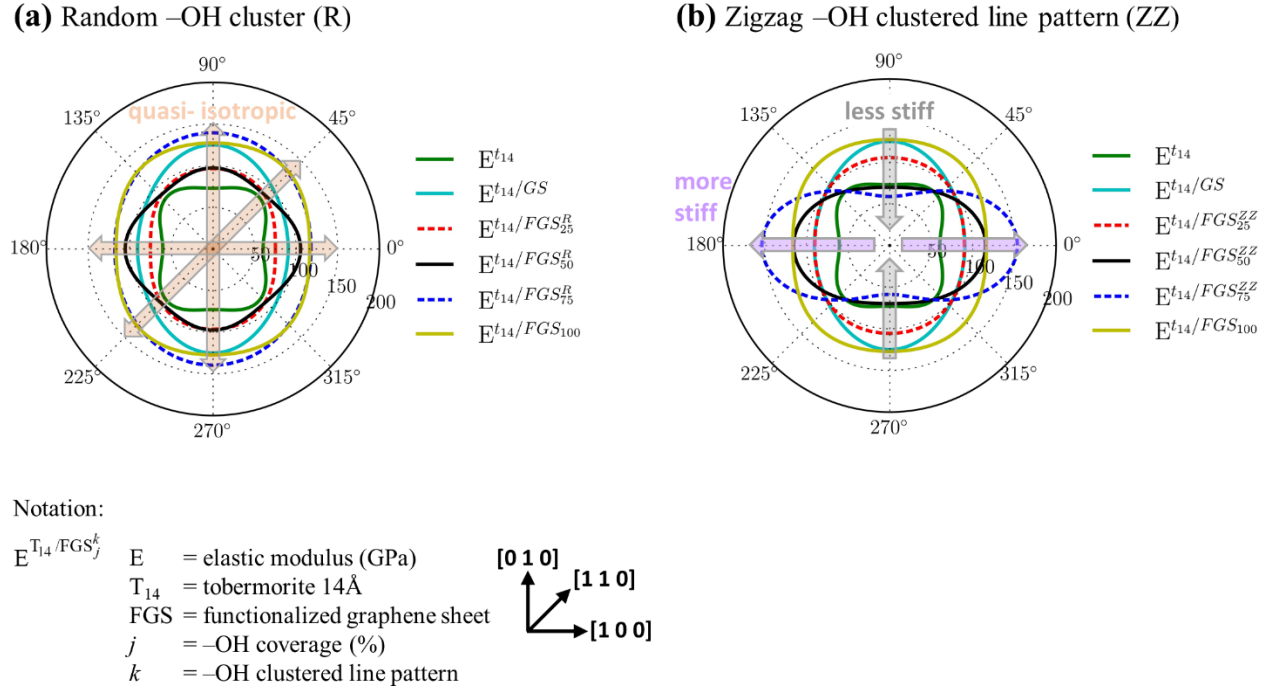


Figure 4.46. 2D representation of the directional anisotropy of elastic modulus for T₁₄/FGS nanocomposites with different surface coverages and clustered line patterns.

4.4. Conclusions

4.4.1. Effect of geometric assembly of GS in tobermorite 9 Å (T₉)

The inclusion of GS in tobermorite 9Å (T₉) matrix in hierarchical and stacked arrangements had positive effects on the strength, stiffness, toughness, and compliance of the nanolaminates. The stacked nanolaminate had a higher ultimate fracture strength compared to the T₉ matrix and the hierarchical nanolaminate due to the bundle effect of the GS. The tensile and shear interaction energies between GS interfaces were higher than those between the GS and T₉ interface, which led to this bundle effect for the stacked nanolaminate. The hierarchical

nanolaminate, due to the uniform separation of the GS layers by T₉ blocks, showed slightly lower ultimate fracture strength and strain compared to those of the stacked nanolaminate. For both nanolaminates, the T₉ matrix failed almost at the same strain, indicating that the inclusion of the GS did not affect the matrix failure mechanism significantly. However, the failure strength increased because the GS shared the load partially in the beginning. The nanolaminates tend to divide the stress-strain curves (not observed in T₉) into regime-I, where the T₉ matrix failed and regime-II, where the GS failed. The shear stress-strain curves of the nanolaminates followed a similar behavior to the tensile stress-strain responses. However, the post-failure regimes for the shear stress-strain responses for the stacked and hierarchical nanolaminates were not as abrupt as the tensile post-failure responses because the relaxation of angular distortions in shear was not as abrupt as the bond-breaking relaxations for tensile failures. Comparing the stress-strain responses in tensile and shear loading, both stacked and hierarchical nanolaminates were relatively much stronger than the pristine T₉ matrix with the stacked nanolaminate being the strongest in the Y-direction while the hierarchical nanolaminate was the strongest in the X-direction. Due to the larger area under the stress-strain curves, the stacked nanolaminate possessed the highest strain energy density in the Y-direction, i.e., it was the toughest, whereas the hierarchical nanolaminate was slightly tougher in the X-direction.

The in-plane normal constants of the stacked nanolaminate were the highest among all systems. The out-of-plane normal constants decreased for the nanolaminates due to weakening effects of the insignificant out-of-plane interaction forces of the GS and disruption of the continuation of the T₉ matrix. The stacked nanolaminate was the stiffest in tension among all systems. Shear constants of the hierarchical and stacked nanolaminates were almost identical and higher than that of the pristine T₉ matrix, indicating that the geometrical variation of the GS within the T₉ matrix did not affect the shear resistance of the nanolaminates. Both the stacked and hierarchical nanolaminates were very stiff in terms of shear. The stacked nanolaminates showed the highest elastic modulus-to-density ratio. However, the hierarchical nanolaminate was the highest among all systems for shear modulus-to-density ratio.

Although the pristine T₉ matrix possessed anisotropic linear compressibility, the inclusion of the GS in the T₉ matrix changed the direction of anisotropy of the nanolaminates due to the strong planar isotropy of GS parallel (∥) to the XY-plane. The projection of the linear

compressibility of the stacked nanolaminate was along the $\langle 1\ 1\ 0 \rangle$ directions. The directional elastic modulus in the XY-plane also showed that the stiffest directions were along the $\langle 0\ 1\ 0 \rangle$ with the $\langle 1\ 1\ 0 \rangle$ directions being the least stiff. It is not surprising that the least stiff directions of the stacked nanolaminate were the most compressible. The hierarchical nanolaminate showed overall quasi-isotropic directional elasticity, although the maximum elastic modulus was smaller than the stacked nanolaminate.

4.4.2. Effect of the surface structure of tobermorite 14 Å (T_{14}) interfacing with the GS

The mechanical properties of tobermorite 14 Å-based structures reinforced with a single graphene sheet interfacing with three well-defined surfaces (i.e., bottom water layer, octahedral calcium layer, and tetrahedral silicate layer) were studied. The graphene sheet contributed to a significant increase in the XY-plane tensile and shear strengths, stiffness, and toughness of the tobermorite 14 Å-based structures. In-plane fracture tensile and shear strengths of the reinforced nanocomposites that were 180% to 360% and 90% to 225% greater, respectively, than those of the tobermorite 14 Å-based structures without the graphene sheet reinforcement as well as intrinsic in-plane elastic moduli that were twice that of the pristine structures could be realized. In contrast, the graphene sheet decreased the out-of-plane tensile strength capacity, stiffness, and bulk modulus of the tobermorite 14 Å-based structures because of the weak interaction of the graphene sheet with the structures. The influence of mediating water at the interface with the graphene sheet versus dry solid surfaces and of the structure of the solid surfaces (i.e., ordered octahedral calcium zigzag sheet versus tetrahedral silicate chain) on the overall nanocomposite behavior was revealed. The graphene sheet exhibited more apparent in-plane strengthening effect when interfacing with water than with either of the solid surfaces (i.e., calcium or silicate surfaces). The confined water molecules interfacing with the graphene sheet promoted surface friction during tensile and shear loading, thus leading to a greater fracture tensile strength, faster rate of shear strength development, and greater toughness under in-plane tensile loading but lower shear toughness compared to the nanocomposites with the dry, solid surfaces (calcium and silicate) interfacing with the graphene sheet. The results further demonstrated the role of the matrix structure in modulating the in-plane stiffness and linear compressibility of the nanocomposites at zero strain and the dominant role of the graphene sheet and interface between the graphene sheet and the matrix upon loading.

4.4.3. Effect of functionalization of GS on tobermorite 14 (T_{14})

The mechanical properties of the T_{14} /FGS nanocomposites with 25%, 50%, 75%, and 100% surface coverage and line arrangements of –OH (random and ZZ clustered line patterns) were investigated in this study. The stress-strain responses of the nanocomposites were divided in three regimes: (1) the elastic regime, where both the T_{14} and FGS shared the load but T_{14} matrix failed, (2) the FGS loading regime, where the total load during tension and shear were taken by the FGS, and (3) the post-failure plastic regime, where, the FGS failed, resulting in the final fracture of the nanocomposite. The incorporation of GS and FGS in the T_{14} matrix increased the peak in-plane tensile fracture stresses (strengths) and strains (elongations) of the nanocomposites compared to those of pristine T_{14} . However, the ZZ clustered line pattern of –OH on FGS increased the molecular friction between the water of T_{14} matrices and the FGS. This molecular friction decreased the intrinsic in-plane tensile fracture strains of the nanocomposites, thus, reducing the peak tensile fracture strains more than those for the nanocomposites with random arrangements of –OH. The out-of-plane tensile behavior of the nanocomposites were found to be interface-dominated at low coverages and interlayer-dominated at large coverages of –OH for the random arrangements. At low coverages, the interfacial interaction between the GS and T_{14} were low, thus, the separation occurred through the interface. However, at large coverages, the interactions between the water and –OH substantially strengthen the interfaces, and therefore, the fracture occurred through the interlayer. The random arrangement of –OH provided more interfacial strengthening because the ZZ clustered line patterns initiated bending curvature to the FGS, which reduced the effective interactions between the water and –OH groups (due to less contact area), thus, fracture occurred through the interfaces (interface-dominated at large coverages).

The T_{14} /GS demonstrated the highest strain energy density among all the nanocomposites. The tensile and shear strain energy density was found to decrease with increase in –OH coverage since that decreased the intrinsic fracture stress and strain of the FGS. However, the out-of-plane strain energy density (and indirectly, toughness) of the nanocomposites increased substantially with increase in –OH coverage and random arrangements of –OH due to significant strengthening of the interfaces.

The elastic modulus of the nanocomposites increased with the incorporation of FGS. The ZZ clustered line patterns of the FGS were seen to increase the elastic modulus of the nanocomposite more than the random arrangements. The increase in -OH coverage increased the modulus of the T14/FGS nanocomposites. The anisotropy in the nanocomposites were more controlled by the ZZ clustered line patterns than the surface coverages of -OH.

CHAPTER 5

INTERFACIAL MECHANICS OF GRAPHENE BILAYERS WITH NANOCONFINED WATER MONOLAYER

This chapter describes the interfacial strength of dry and wet graphene bilayer systems in normal and shear traction-separation modes. The molecular scale mechanisms under shear traction of graphene/functionalized graphene (GS/FGS) and FGS/FGS bilayer systems with nanoconfined water monolayer are elucidated. The competing mechanisms of hydrogen bonding and the effect of the formation of hydrogen bond networks on the mobility of the water molecules and the interfacial shear traction are presented.

5.1. Overview

2D materials have received great attention lately because of their high in-plane stiffness and low interlayer friction. Graphene, such a 2D material, is known to possess impressive in-plane shear strength as opposed to its ultra-low interlayer shear strength, which often leads to remarkably low friction and wear-resistance [238], and eventually induced shear-driven failure. Low interlayer shear might be important for wear-resistant devices or better exfoliation properties, but for structural composite applications, better load transfer for in-plane shear (i.e., high interlayer shear) is, however, necessary. Therefore, in the study presented in this chapter, hydrogen functionalization was explored to enhance the interfacial strength between graphene bilayers while the use of monolayer water as a lubricating agent nanoconfined in graphene bilayer systems was explored to reduce the interfacial strength.

Graphene sheet has a relatively smooth surface, which, in combination with weak van der Waals (vdW) interaction, provides weak graphene-graphene interlayer strength. The graphene-graphene interaction could be enhanced by attaching surface functional groups that increase the surface asperities by mimicking macroscale surface ruggedness, thus, providing enhanced dry adhesion.

The use of water as a lubricating agent in nanoscopic confinements has drawn significant interest in research because of its different behavior from bulk water. The behavior of water in

confined environments (in between two confining plates) has a wide range of applications in chemistry (nanofluidic devices, molecular sieves), tribology [239], biology (protein stability and drug delivery), geology (flow through porous rocks) [240, 241], electrical engineering (nanoresonators) [242], wearable electronics [243], melting/freezing process [244, 245], water desalination [246-248], structural materials [243], humidity sensors [249], and other fields of science. Available studies in the literature have shown that the behavior of water is affected by the type of confining wall (the confining material) and the thickness of the nanoconfinement. In addition, Soler-Crespo et al. [243] studied the mediating effects of multilayer water (which possessed a different mechanism than a monolayer) on the oxide-containing graphitic surfaces, however, did not address the effects of varied amount of –OH groups on the interfacial mechanisms of heterogeneous hydrophobic-hydrophilic graphitic layers containing monolayer water. On another note, the effects of surface roughness provided by varying amount of –OH groups on the transport properties of monolayer water were also not investigated.

Thus, in summary, nanoconfinement of water and flow of water through nanochannels are important characteristics of water, which are not seen in the bulk. Especially, near interfaces, water-layer has been shown to act as 2D or quasi-2D fluid (almost a monolayer), and to show anisotropic behavior. However, little studies have been performed on the dry and wet (with only water monolayer) interfacial adhesion mechanisms regarding hydrophobic and hydrophilic graphitic surfaces upon external stimulations (traction force). This study provided insights into the adhesion properties of graphitic surfaces in the presence of monolayer water (a quasi-2D fluid) in the most nanoconfined region possible (a monolayer). This type of limiting case also provided valuable information about the properties of nanoconfined water under normal and shear traction - the two most widely encountered mechanical loading modes, as opposed to classical continuum hydrodynamic properties.

This chapter is organized as follows: at first, the interfacial strength of dry interfaces containing hydrophobic (graphene sheet, GS) and hydrophilic (–OH functionalized graphene sheet, FGS) graphene surfaces is studied. Then, nanoconfined monolayer water was introduced between the graphene bilayer systems to study the load transfer efficiency of these interfaces in the presence of water monolayer. Then, the interaction energies of the dry (without water) and wet interfaces (with water) were estimated to identify the interfacial adhesion properties with

varying –OH coverages. Finally, the structural (hydrogen bonding analysis) and dynamic properties (mean-squared displacement) of water were investigated to understand the atomistic process of nanoconfined monolayer water sandwiched between the hydrophobic and hydrophilic graphitic bilayer structures. All the studies were performed under normal and shear traction-separation loading modes.

5.2. Computational Details

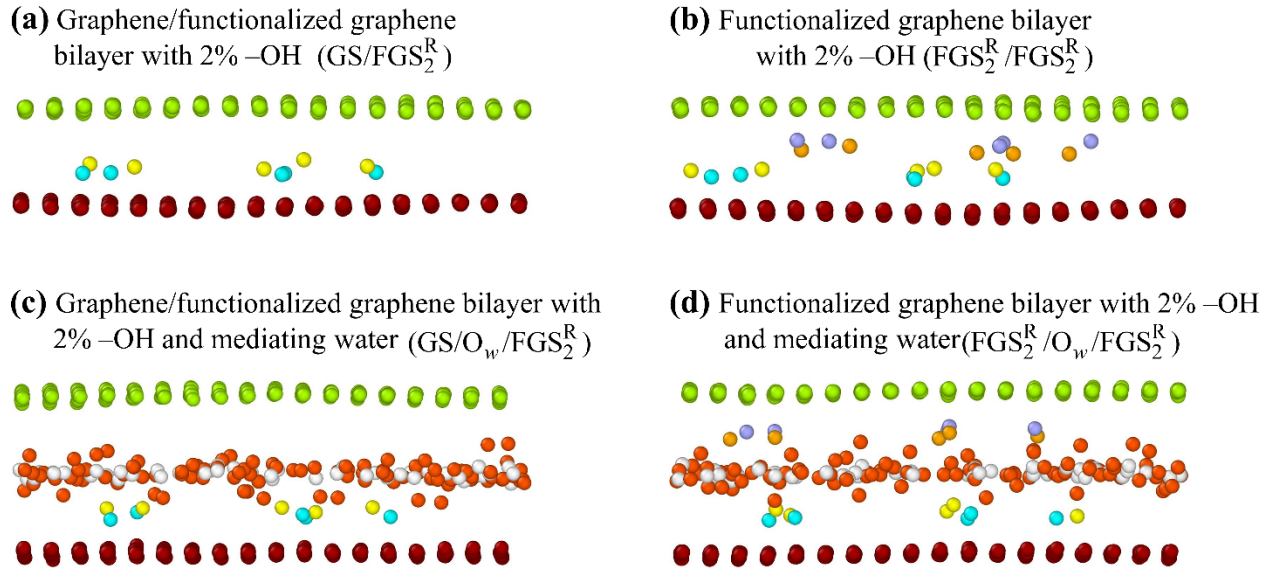
5.2.1. Simulation setup and computational details

In this study, six types of interfaces were investigated, (1) graphene-functionalized graphene (GS/FGS), (2) functionalized graphene-functionalized graphene (FGS/FGS), (3) graphene-water-functionalized graphene (GS/O_w/FGS), and (4) functionalized graphene-water-functionalized graphene (FGS/O_w/FGS). Other two systems, (5) graphene-graphene (GS/GS) and (6) graphene-water-graphene (GS/O_w/GS) interfaces were used as control systems.

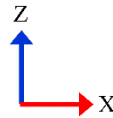
The geometries of single-layered GS and FGS (Figure 5.1a and Figure 5.1b) were modeled using the Materials Studio software package (Materials Studio 7.0, Dassault Systèmes BIOVIA, San Diego, CA). The zigzag (ZZ) and armchair (AC) edges of the GS were oriented along the Cartesian coordinate axes X [1 0 0] and Y [0 1 0] directions, respectively (Figure 5.1a). The GS and FGS had similar planar area and consisted of 252 sp² hybridized carbon (C) atoms in a hexagonal ring pattern. The C–C bond lengths and ∠C–C–C bond-angles were 1.41 Å and 120°, respectively, for the GS and FGS systems. The hydroxyl (–OH) functional groups were attached randomly on one side of the basal plane (XY-plane) of the GS to model the single FGS. For the FGS systems, the C–O and O–H bond-lengths, and C–O–H bond-angles were 1.39 Å and 1.0 Å, and 109.5°, respectively. The C–C–C–C, C–C–C–O, C–C–O–H, O–C–C–O dihedral torsion-angles and C–C–C–C improper torsion-angles for the single layer GS and FGS systems are tabulated in Table A4.3. Five number densities, 2%, 6%, 10%, and 12% of –OH groups relative to the carbon atoms were examined.

The six types of interfaces were created by stacking six types of bilayer systems by organizing six types of bilayer systems. The bilayer systems were created by stacking top and bottom sheets (either GS or FGS) with an approximate distance of C–C van-der-Waals (vdW) radius (~ 4 Å) (Figure 5.1c). These six types of bilayers and interfaces can be categorized into

two types: dry (GS/FGS and FGS/FGS) and wet (GS/O_w/FGS and FGS/O_w/FGS) bilayers and interfaces. The bilayer systems were created using a scripting language *awk* and verified with Visual Molecular Dynamics (VMD) [189], thus creating GS/FGS or FGS/FGS bilayers. The water monolayer was created by replicating one molecule of water with the vdW interaction size of 3.2Å, 7 × 7 times in the XY-plane using LAMMPS, creating a monolayer of water with a total of 49 molecules. Similar to the dry systems, the water monolayer was then inserted in between the two sheets (like a sandwich panel) of graphene-derivatives (such as GS/FGS and FGS/FGS) using *awk* (keeping the interlayer distances of 4 Å), thus creating GS/O_w/FGS or FGS/O_w/FGS bilayers and interfaces. The sizes of the modeled bilayer systems were 19.2 × 26.4 × 7.35 Å³ and 19.2 × 26.4 × 10.55 Å³, for the dry and wet systems, respectively.



Notation: GS = graphene sheet
 FGS = functionalized graphene sheet
 O_w = oxygen of water monolayer
 R = random arrangement of -OH



● C^t ● H_g^t ● O_g^b ● O_w
● O_g^t ● C^b ● H_g^b ● H_w

C^t:Carbon in top GS; O_g^t:Oxygen of -OH in top GS; H_g^t:Hydrogen of -OH in top GS; C^b:Carbon in bottom GS;
 O_g^b:Oxygen of -OH in bottom GS; H_g^b:Hydrogen of -OH in bottom GS; O_w:Oxygen of water; H_w:Hydrogen of water

Figure 5.1. Bilayer graphene interface models with and without nanoconfined water monolayer. Dry bilayer interfaces: (a) graphene/functionalized graphene (GS/FGS) and (b) functionalized graphene/functionalized graphene (FGS/FGS). Wet bilayer interfaces: (c) graphene/water/functionalized graphene (GS/O_w/FGS), and (f) functionalized graphene/water/functionalized graphene (FGS/O_w/FGS), where O_w represents the oxygen of the water monolayer. Bilayer systems shown for 2% -OH functionalization with random arrangement.

5.2.2. Forcefields

The Consistent Valence Forcefield (CVFF) was used for the simulation of bonded and non-bonded interactions of the carbon (C), oxygen (O), and hydrogen atoms (H) of the GS and FGS systems [138]. The CVFF has been previously successfully used for the structural, energy studies, [144, 185] and tensile properties of graphene [190, 212] and other carbon-based materials of graphene family such as carbon nanotubes [143]. Additionally, CVFF has been successfully used to study the traction-separation s of polymer/GS systems [250]. Single Point

Charge (SPC) flexible model of water was used in this study for the nanoconfined water monolayer in between the GS/FGS and FGS/FGS systems. Since a reactive force-field was not used, capturing the splitting of water molecules was not possible. However, because the confined monolayer water was not subjected to a pressure gradient, water-splitting was not considered to be a significant phenomenon.

The interaction between the interfaces was simulated using coulombic and vdW parameters. The long-range coulombic interactions were computed in the reciprocal space by the Particle-Particle-Particle-Mesh (PPPM) solver. The short-range coulombic interactions between atoms were calculated using the formula:

$$\Psi^{\text{coul}} = \frac{1}{4\pi\epsilon_0} \cdot \frac{q_i q_j}{r_{ij}^2} \quad (5.1)$$

where q_i and q_j are charges on atoms i and j , ϵ_0 is the permittivity of the vacuum (8.85419×10^{-12} F/m), and $r_{ij} = |r_i - r_j|$ is the interatomic distance. The short-range vdW interaction was computed by the Lennard-Jones (LJ) potential using:

$$\Psi^{\text{LJ}} = 4 \epsilon \left[\left(\frac{\sigma}{r} \right)^{12} - \left(\frac{\sigma}{r} \right)^6 \right] \quad (5.2)$$

where, ϵ is the depth of the potential well (kcal mol^{-1}), σ is the distance (\AA) at which the potential was zero, and r is the interatomic distance (\AA). Therefore, the total pair interaction energy of the GS/GS bilayer systems were calculated from the following equation:

$$E = \frac{1}{4\pi\epsilon_0} \cdot \frac{q_i q_j}{r_{ij}^2} + 4 \epsilon \left[\left(\frac{\sigma}{r} \right)^{12} - \left(\frac{\sigma}{r} \right)^6 \right] \quad (5.3)$$

The Lennard-Jones (LJ) and coulombic cut-off distances were 12 \AA and 10 \AA , respectively. The interactions between unlike atoms were calculated using the Lorentz-Berthelot mixing rules [202, 203].

5.2.3. Equilibration

For the solid bilayers (GS/FGS and FGS/FGS), three types of traction-separation studies were performed, (1) normal traction in Z-direction, (2) shear traction in X-direction, and (3) shear

traction in Y-direction. For the solid/liquid bilayers (GS/O_w/FGS and FGS/O_w/FGS), only the shear traction-separation studies were performed. During the equilibration, 100 Å thickness of vacuum was kept on both sides of the sheet in the direction of displacement, e.g., 100 Å vacuum was placed on top and bottom sides of the GS-GS bilayer system along Z-direction keeping the X and Y-directions as periodic for the traction-separation study in the Z-direction. All bilayer systems were energy minimized at 0 K using the conjugate gradient method to reduce the excess pressure build-up during geometry setup. The dry bilayer graphene systems were equilibrated for 500 ps and the wet bilayer systems were equilibrated for 1.5 ns with isothermal-isobaric NPT (atoms, pressure, and temperature constant) ensembles. All systems were equilibrated at 300 K and 0 atm. The Nosé-Hoover thermostat and barostat were used for temperature and pressure control of the systems with 100 fs and 1000 fs damping constants, respectively [148, 149]. The neighbor cut-off distance for the interacting atoms was kept at 5 Å, and the neighbor list of the atoms was updated every timestep. The time integration was performed using the velocity-Verlet algorithm. All simulations were performed using a 1 fs timestep.

5.2.4. Loading methods and simulations

Two types of traction-separation simulations i.e., normal and shear, were performed. For the normal separation along Z-direction, the local displacements of the atoms at the two ends of the bottom sheet (either GS or FGS) were kept fixed. The rest of the atoms of the bottom sheet was known as the mobile atoms. The bottom sheet was displaced at a rate of 10^{-5} Å fs⁻¹ in the negative Z-direction while the top sheet (either GS or FGS) was constrained in space (Figure 5.2a). For the shear separation along the X- and Y-directions, the bottom sheet (either GS or FGS) was pulled with the right edge of the sheet fixed (3 Å thick layer of atoms) with a displacement rate of 10^{-5} Å fs⁻¹ in the positive X or Y-directions (Figure 5.2b). For the simulations of the dry systems, the mobile atoms of the bottom sheet were allowed to interact with the constrained top sheet. For the simulations of wet systems, in addition to the mobile atoms of the bottom sheet, the confined water molecules were also kept mobile, i.e., were allowed to interact freely with the top and bottom sheet.

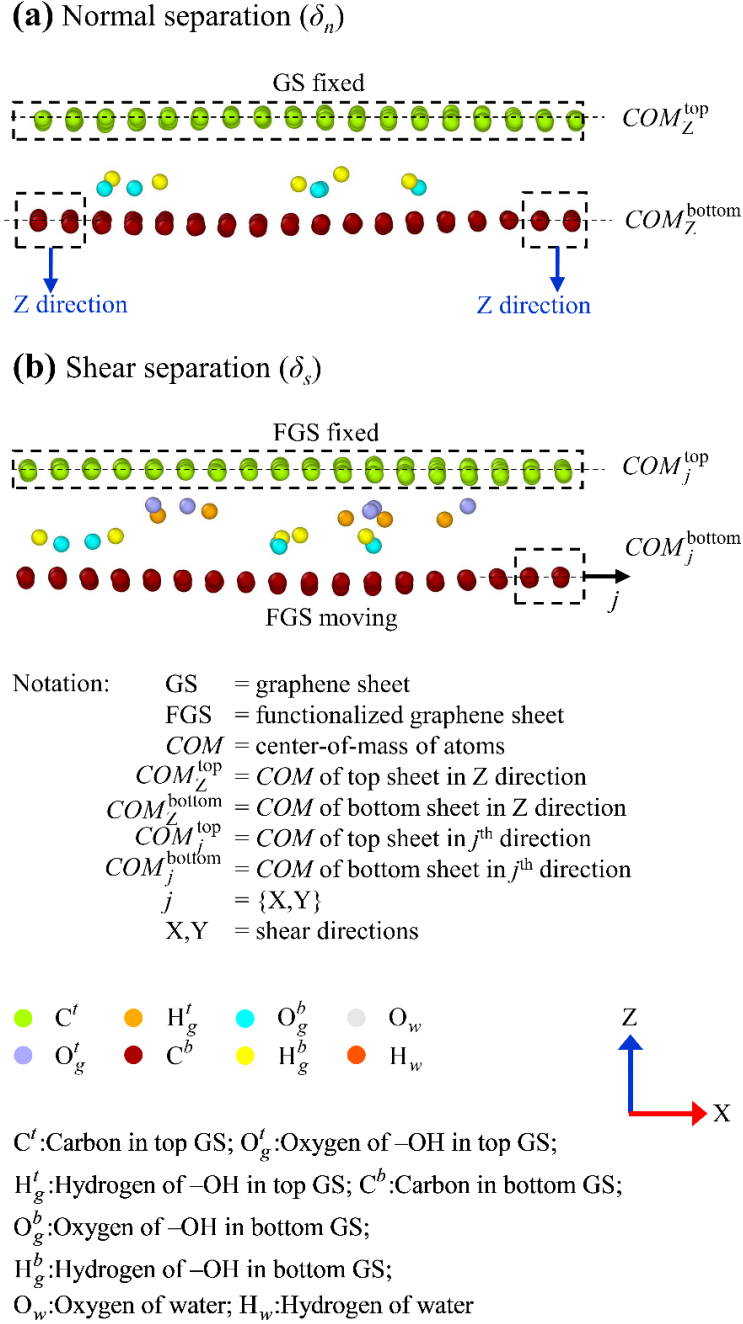


Figure 5.2. The traction-separation modes of the bilayer systems: (a) the normal separation along the Z-direction and (b) the shear separation along the X- and Y-directions of the bilayer systems.

5.2.5. Data analysis

The force developed on the lower sheet was calculated from the pair interaction energy (coulombic and vdW energy) between the top and bottom sheets. The force developed during the

normal separation (δ_n) and shear separation were called normal traction (f_n) and shear traction (f_s), respectively. The displacement and traction data were time-averaged and collected every 10000 fs simulation run. The normal and shear traction-separation simulations were run for 1.2 ns and 4.0 ns, respectively, which resulted in the relative total displacements of 12 Å and 40 Å, respectively (to ensure zero interaction between the sheets). The normal traction-separation and shear traction-separation curves were calculated and plotted. The normal displacement was calculated from difference of the Z- component of the center-of-mass (COM) of the top carbon layer (C atoms of the top sheet) to the Z-component of the COM of the bottom carbon layer (C atoms of the bottom sheet) during the simulation. The X and Y shear displacements were calculated from the X- and Y-component of the COM of the top carbon layers to the X- and Y-components of the COM of the fixed boundary atoms of the bottom carbon layers. The above description of the COM analysis could be expressed as the following:

$$\delta_k = COM_j^{\text{top}} - COM_j^{\text{bottom}} \quad (5.4)$$

where, the traction-separation mode, $k = (n, s)$ with $n =$ normal separation and $s =$ shear separation, and the displacement direction, $j = (Z, X, Y)$, δ_k is the relative displacement of the sheets, $COM =$ center-of-mass of the carbon atoms of the top and bottom sheets.

The interaction energy between the p and q system was calculated from the following formula:

$$\Delta E_{p-q} = E_{p/q} - (E_p + E_q) \quad (5.5)$$

where, $\{p, q\} \in \{GS, FGS\}$. The interaction energy, ΔE , between the p and q systems (ΔE_{p-q}) was obtained by subtracting the potential energy of the p (E_p) and q (E_q) when they were completely separated (theoretically, at infinity distance; for this study, approximately, at 12 Å and 40 Å) from the total potential energy of the p/q at equilibrium ($E_{p/q}$, at zero relative displacement between the p and q). A similar procedure was followed to calculate the interaction energies of all interfaces.

The number of hydrogen bonds (H-bond) between the donor and acceptor atoms of water molecules (O_w) and hydroxyl groups (O_g) of FGS at equilibrium and during shear separation were calculated using the *dreiding* forcefield (available within LAMMPS). Several important

categories of H-bonds were identified and calculated: (1) water/water ($O_w-H_w \cdots O_w$) H-bond where one O_w was the donor and another O_w was the acceptor, (2) water/ $-OH$ ($O_w-H_w \cdots O_g$) H-bond where O_w acted as donor and O_g as acceptor, (3) $-OH$ /water H-bond ($O_g-H_g \cdots O_w$), and (4) $-OH$ / $-OH$ H-bond ($O_g-H_g \cdots O_g$). The summation of (2) and (3) was shown in this paper to obtain the total number of H-bonds between the $-OH$ groups and water. The D-H \cdots A type hydrogen bond ($R_{D \cdots A}$) and angle cutoffs ($\angle D-H \cdots A$) were taken as 3.5 Å and 150°, respectively to quantify both the water/water ($O_w-H_w \cdots O_w$) and water/ $-OH$ ($O_w-H_w \cdots O_g$ and $O_g-H_g \cdots O_w$) hydrogen bonds. Here, D was the donor atom, H was the hydrogen atom to be donated, and A was the acceptor atom, respectively.

The mean squared displacements (MSD) provided information about the mobility of the confined monolayer of water molecules trapped in the bilayer systems with the functional groups on one sheet (GS/FGS) or both sheets (FGS/FGS). The MSD were calculated at the two different stages for all the interfaces; (1) MSD was calculated on the equilibrated structures using the microcanonical NVE (N= number of atoms, V=volume, E=energy) ensemble and (2) MSD of the monolayer water molecules was calculated during the shear separation of the bottom sheet from the top sheet. All visualizations were performed using the VMD [180] and OVITO [183] softwares.

5.3. Results and Discussions

5.3.1. Interfacial strength of GS/FGS bilayer systems

Normal traction-separation of GS/FGS bilayer systems. The normal traction-separation (f_n - δ_n) behavior of the GS/FGS bilayer systems (GS at the top and FGS at the bottom) showed increase in the traction forces (f_n) as the layers were separated (δ_n) gradually in the negative Z-direction (Figure 5.3). The normal traction forces reached their peaks at ~ 1 Å separation, after which the forces started to decrease (indicating the softening part of the curves), and eventually went to zero at ~ 8 Å separation for all the GS/FGS bilayer systems. The highest normal traction force was shown by the pristine GS/GS bilayer (23 nN), followed by reductions in the traction forces as the $-OH$ coverage increased. A cohesive zone model of intergranular fracture of graphene revealed a traction force of ~ 24 nN (agreeing with the present study), with similar traction-separation curve as in this study [251]. After 6% $-OH$ coverage (f_n of 17 nN, a 35%

decrease from the pristine bilayer), the peak traction forces did not decrease any further. It was evident that a high –OH coverage did not have adverse effects on the interfacial normal strengths of the GS/FGS bilayers. The local movement of the boundary atoms were constrained during the normal simulations while the rest of the atoms in the bottom sheets were mobile (allowed to interact freely with the top sheet). Thus, during the hardening portion of the curves, the mobile atoms of the bottom sheet were interacting strongly with the top sheet, and created an inverted-well shaped figure, known as puckering [238] in the literature. The traction force built up during the hardening was due to this puckering behavior. This behavior was observed when the mobile atoms of the bottom sheet during the normal separation were still trying to overcome the interaction force of the bilayer interfaces. According to the literature [252], a similar puckering behavior was observed during the interfacial delamination of a 2D material when a competing vdW energy and elastic energy tried to deform the material.

This type of bilinear hardening-softening traction-separation behavior has been observed for other interfaces associated with graphene [250]. The traction forces for the GS/GS interfaces reached the peak more gradually than the other systems. The reason could be the ease of the $C_g \cdots C_g$ interactions between the two sheets. The direct $C_g \cdots C_g$ interactions were hindered by the –OH groups for the GS/FGS bilayer systems. The traction forces for the GS/GS system went to zero at the separation of $\sim 6.9 \text{ \AA}$, indicating that the –OH groups introduced more interactions (full separation distance, 6.9 \AA vs 8 \AA , respectively) between the GS and FGS but did not necessarily increased the peak traction forces. The GS/FGS bilayer systems with varying degrees of –OH content followed the same bilinear type traction-separation response curves. In this study, GS/GS interface showed the highest peak traction force (23.3 nN). The peak traction force decreased as the % –OH content of the FGS layers increased until 6% –OH coverage (i.e. GS/FGS₆^R), after which the peak traction force did not reduce any further with increasing –OH coverage. Also, having more –OH groups possibly shielded the $C_g \cdots C_g$ interactions of the GS/FGS bilayers, which led to the lower normal traction forces compared to that of the GS/GS bilayer. The softening part of the GS/GS bilayer system was the steepest among all the bilayers, which suggested that the –OH groups also did not allow the GS/FGS bilayers to separate as quickly as the GS/GS bilayer. This study demonstrated that GS/FGS interfaces were weaker in terms of interfacial normal strength than the GS/GS interface. However, the GS/FGS interfaces

remained attached more than the GS/GS interfaces during normal separation due to the interaction of the –OH groups with the GS.

Shear traction-separation of GS/FGS bilayer systems in X and Y-directions. The shear traction-separation ($f_s^X - \delta_s^X$) curves in the X ($f_s^X - \delta_s^X$) and Y-directions ($f_s^Y - \delta_s^Y$) of the GS/FGS bilayers showed three distinct regimes: 1. initial ballistic regime (R_1), 2. stability regime (R_2), and 3. final softening regime (R_3) (Figure 5.3). The shear traction-separation curves in the X-direction showed a sudden increase in the shear traction forces (f_s^X) as the separation between the top and bottom interfaces in the X-direction (δ_s^X) increased. The GS/FGS bilayer systems showed greater slopes initially compared to the GS/GS bilayer system, i.e., possessed greater elastic modulus. Initially, the carbon atoms of the two sheets did not possess an optimum number of interaction sites. As the bottom sheet sled past the top sheet, the atoms had the option to fully interact with each other, thus, increasing the traction forces. The increase in the shear traction forces reached the highest at the separation of $\sim 5 \text{ \AA}$ for all bilayer systems followed by the start of the R_2 regime, which exhibited a plateau region until $\sim 18 \text{ \AA}$. After reaching the separation distance of 18 \AA , the shear traction force dropped and gradually reduced to zero. At that distance, the interfaces were almost $3/4^{\text{th}}$ separated. The number of interacting atoms was then reduced, which resulted in the reduction of the total interfacial shear traction. The fluctuations observed in the traction force was due to a stick-slip behavior [253-255] of the carbon atoms of the GS and FGS. The fluctuations in the shear force increased significantly at the –OH coverage of 2%, possibly due to the friction provided by the interaction between an –OH group and its neighboring carbon atoms. However, as the –OH (%) coverage increased, the number of free carbon neighbors for an –OH group is reduced, thus, provided less fluctuation in shear traction. The coulombic and vdW interactions of the carbon atoms and the –OH groups between the top and bottom sheets controlled the shear traction-separation behavior of the bilayers. The peak shear traction forces in the X-direction (f_s^X) for the GS/FGS bilayer systems were ~ 4 times lower than the normal traction force (f_n), indicating that the shear separation of the GS/FGS bilayer systems required less forces than the normal separation. As the –OH (%) coverage increased, the shear traction also increased due to the larger friction provided by the –OH groups during shear separation. This result has significant implications on the experimental

graphite layer separation process. The shear separation in the X-direction indicated that even after the two sheets were completely separated, the shear traction was not exactly zero, which was believed to be due to the coulombic and vdW interactions between the interacting atoms. The shear traction force reduced to zero completely at $\sim 30.4 \text{ \AA}$, which was 10.2 \AA more than the complete separation distance (19.2 \AA , the length of GS in the X-direction) of the two sheets, indicating that the non-bonded interactions between the sheets required at least 10 \AA separation to completely reduce to zero. The small peak at the beginning of regime R_3 was caused when the two layers being completely separated. The bottom sheet then experienced a sudden dip along the negative Z-direction, possibly due to the loss of interaction that was holding the two sheets together. From the results, the GS/FGS interfaces showed more adhesion energy than the GS/GS interface.

The shear traction-separation curves in the Y-direction (Figure 5.3) generally showed lower shear traction than in the X-directions, due to the armchair orientation of the GS parallel to the Y-direction. While the bottom FGS was sheared, the $-\text{OH}$ groups were seen to interact strongly with the top GS, possibly due the interaction with the carbon atoms. The fluctuations in the traction forces were increased significantly at 2% $-\text{OH}$ coverage. When the $-\text{OH}$ groups sheared past the carbon atoms of the GS, the traction forces increased suddenly due to the vdW interactions and when the separation increased more, the traction forces suddenly fell, making the fluctuations very large. The average shear traction force of the FGS/FGS interfaces was increased, however, compared to that of the GS/GS interface. The amplitude of the fluctuations reduced as the $-\text{OH}$ coverage increased, possibly due to less interaction among the carbon atoms and the $-\text{OH}$ groups. The distance required to separate the interfaces in the Y-direction was larger than the X-direction because the GS was longer (26.7 \AA at equilibrium) in the Y-direction. The increase in shear traction force in the Y-direction was not as apparent as in the X-direction, although the fluctuations in the traction of the GS/FGS bilayer systems surpassed the shear traction forces of the GS/GS bilayer systems. The above discussions indicated that the $-\text{OH}$ groups on FGS systems did not make the traction-separation process of the GS/FGS or FGS/FGS bilayers more difficult compared to that of the GS/GS bilayer, at least in the Y-direction.

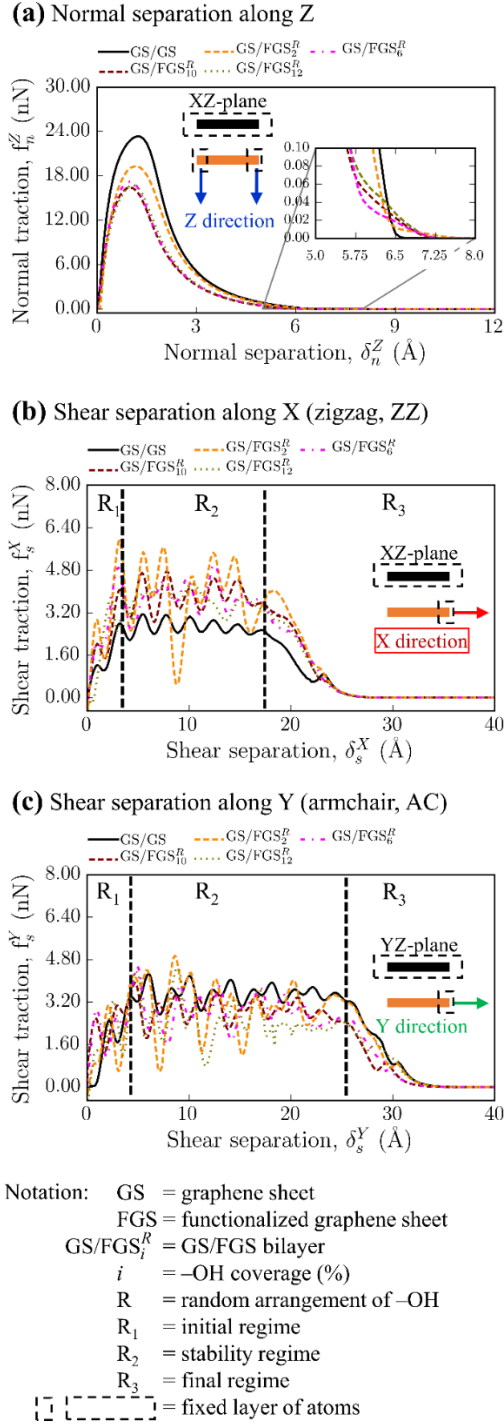


Figure 5.3. Traction-separation responses of the GS/FGS bilayer systems with varying degrees of -OH (%) coverages undergoing: (a) normal separation in the negative Z-direction (with 2 Å thick atom layers on both ends of the FGS layer pulling downwards), (2) shear separation in the positive X-direction (with a 2 Å thick atom layer on right end of the FGS layer pulling in X-direction), and (3) shear separation in the positive Y-direction (with a 2 Å thick atom layer on right end of the FGS layer pulling in Y-direction). The top sheets were held fixed in space for all bilayer systems.

5.3.2. Interfacial strength of FGS/FGS bilayer systems

Normal traction-separation of FGS/FGS bilayer systems. The normal traction-separation responses of the FGS/FGS bilayers were of the bilinear type (similar to those of the GS/FGS bilayers) but differed slightly in peak normal traction force values (Figure 5.4). The –OH groups on both top and bottom layers showed the traction forces for 2% –OH content to be closer to that of the GS/GS bilayer. The interface between top and bottom FGS systems were attached with – the OH groups which sheared past each other during the simulations. The fluctuating peaks for the FGS/FGS bilayer systems were higher than those of GS/FGS bilayers because of the high interaction of the –OH groups from both top and bottom FGS.

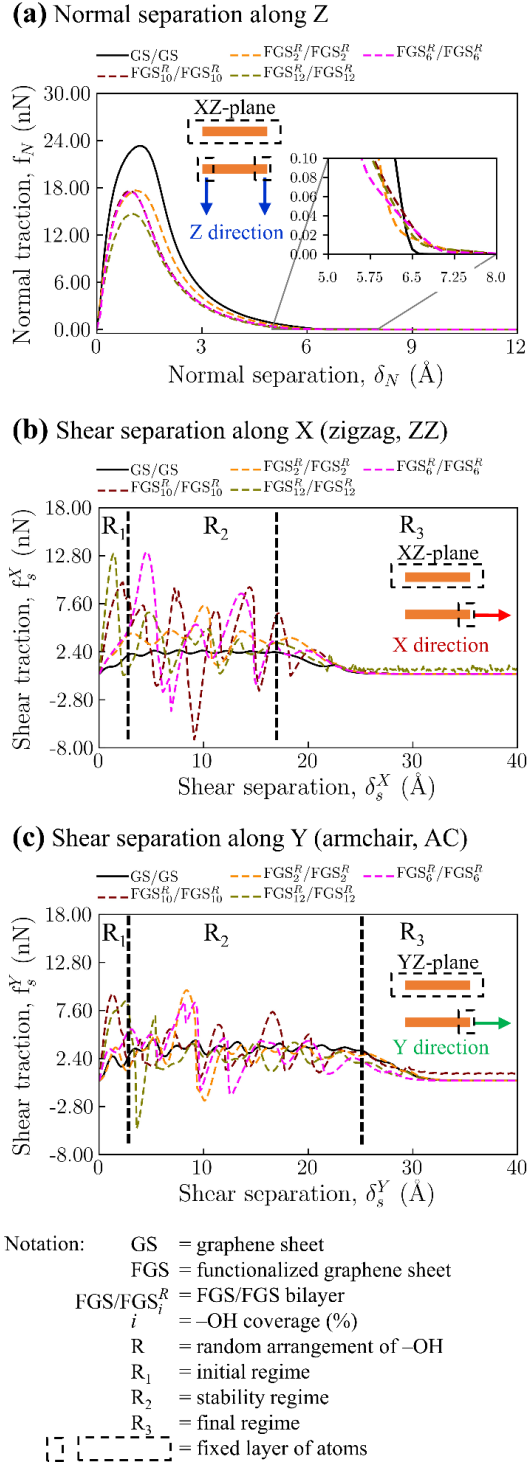


Figure 5.4. Traction-separation responses for the FGS/FGS bilayer with varying degrees of -OH contents, undergoing (a) normal separation in negative Z-direction (with 2 Å thick atom layers on both ends of the FGS layer pulling downwards), (2) shear separation in the positive X-direction (with a 2 Å thick atom layer on right end of the FGS layer pulling in X), and (3) shear separation in the positive Y-direction (with a 2 Å thick atom layer on right end of the FGS layer pulling in Y). The top FGS were kept fixed in space for all the bilayer systems.

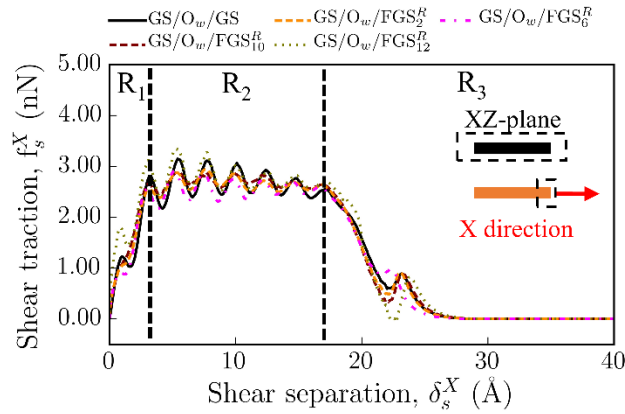
Shear traction-separation of FGS/FGS bilayer systems in X- and Y-directions. Similar to the shear traction-separation behavior of the GS/FGS bilayer systems, the traction-separation responses of the FGS/FGS bilayer systems also depicted (i) an initial regime, R₁, (ii) a stability regime, R₂, and (iii) a final regime, R₃. The shear traction-separation responses ($f_s^X - \delta_s^X$ and $f_s^Y - \delta_s^Y$) of the FGS/FGS bilayer systems started with a large increase in traction force within the first 2.5 Å (Figure 5.4). However, the shear traction peaks and valleys were much larger for the FGS/FGS systems than the GS/FGS systems because of the interactions between the –OH groups from the top and bottom layers as they sled past each other during the separation. Interestingly, while the peak traction forces increased at large –OH coverages (–OH greater than 2%), the average traction force between the interfaces remained approximately same for all the –OH coverages. At low coverage of –OH (e.g., 2%), very few carbon sites of the GS were covered with –OH groups. Therefore, when the bottom FGS sheet sled past the top FGS sheet, the top and bottom –OH groups interacted (shown by the large peak in Figure 5.4b and Figure 5.4c), and the rest of the traction-separation process showed almost identical values of traction forces as the GS/GS bilayers. Meanwhile, at large coverages, most of the areas were filled with protruding –OH groups sticking out from the basal plane, which were responsible for the peaks and valleys in the traction forces.

5.3.3. Interfacial strength of GS/FGS bilayer systems with confined water monolayer

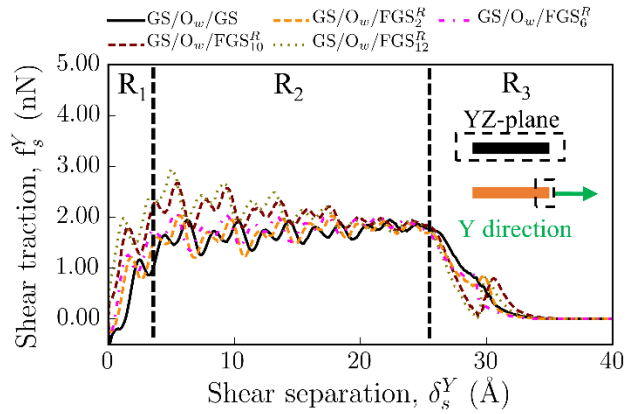
Shear traction-separation of GS/O_w/FGS bilayer systems in X- and Y-direction. The initial regime, R₁, of the shear traction-separation curves ($f_s^X - \delta_s^X$ and $f_s^Y - \delta_s^Y$) for the GS/O_w/FGS bilayer systems started with a large increase in traction force within the first 2.5 Å, similar to the bilayer systems without water (GS/FGS) (Figure 5.5). However, when the traction-separation entered the stability regime (R₂) upon shear separation along the X-direction at about 2.5 Å, the peak traction forces of the bilayer systems were smaller than those of the GS/FGS bilayer systems (dry interfaces), demonstrating the mediating effect of water on the interface between two graphene sheets. The peak traction forces experienced by the bilayer systems held consistency until ~18 Å for the X-direction (the contact length of the GS/FGS) and ~26 Å for the Y-direction, after which the forces started to decrease (final regime R₃). The last small peak in the shear traction seen after the separation of the interfaces originated from the dip that the

bottom FGS experienced after its total loss of interaction with the top GS. For both the X and Y separation of the GS/O_w/FGS bilayer systems, the water molecules (O_w) were seen to reduce the traction forces needed to separate the GS/FGS interfaces. The water molecules possibly shielded the direct interactions between the –OH groups and the carbon atoms of the GS by adhering to the bottom sheet (Figure 5.7), reducing the average traction forces of the GS/FGS bilayer systems by ~ 40% (from 4.5 nN for dry GS/GS to ~3.0 nN for wet GS/O_w/GS). Meanwhile, the shear traction increased as the –OH coverage of the bottom FGS increased, possibly because of the strong –OH/water H-bonded network, also reported in the literature [243]. As the simulation progressed, significant region of the water molecules attached themselves with the moving sheet of the GS/FGS bilayer systems in regime R₂ (Figure 5.7). A similar traction-separation mechanism was evident in both X and Y shear separation.

(a) Shear separation along X (zigzag, ZZ)



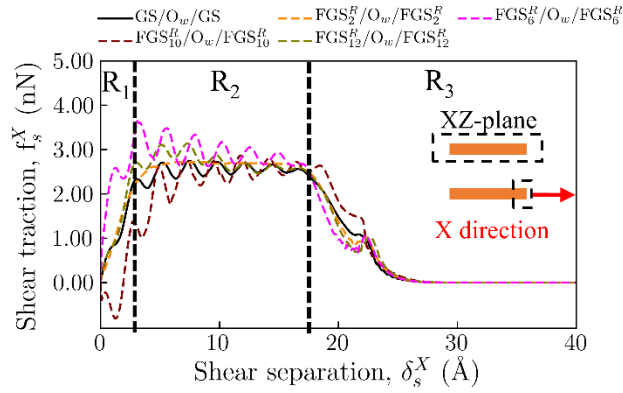
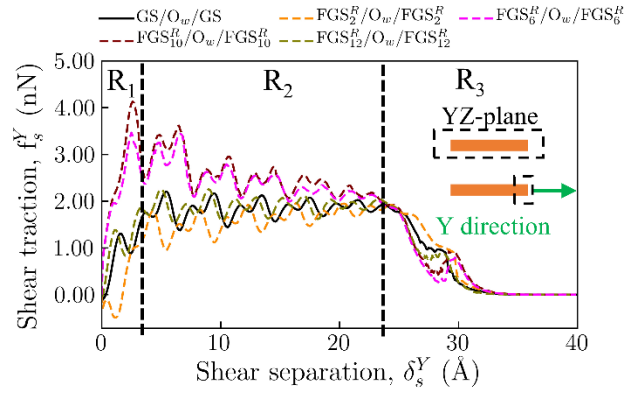
(b) Shear separation along Y (armchair, AC)



Notation: GS = graphene sheet
FGS = functionalized graphene sheet
 O_w = oxygen of water monolayer
 $GS/O_w/FGS_i^R$ = GS/FGS bilayer with confined water monolayer, O_w
 $GS/O_w/GS_i^R$ = GS/GS bilayer with confined water monolayer, O_w
 i = -OH coverage (%)
 R = random arrangement of -OH
[] = fixed atoms

R_1 = initial regime
 R_2 = stability regime
 R_3 = final regime

Figure 5.5. Traction-separation response of the GS/FGS bilayer systems with varying degrees of -OH coverage (0, 2, 6, 10, and 12%) and monolayer of water (O_w) sandwiched between the GS and FGS ($GS/O_w/FGS$): (a) bottom FGS pulled in the positive X-direction and (b) bottom FGS pulled in the positive Y-direction.

(a) Shear separation along X (zigzag, ZZ)**(b) Shear separation along Y (armchair, AC)**

Notation: GS = graphene sheet
 FGS = functionalized graphene sheet
 O_w = oxygen of water monolayer
 $FGS/O_w/FGS_i^R$ = FGS/FGS bilayer with confined water monolayer, O_w
 $GS/O_w/GS_i^R$ = GS/GS bilayer with confined water monolayer, O_w
 i = -OH coverage (%)
 R = random arrangement of -OH groups
 [---] = fixed atoms

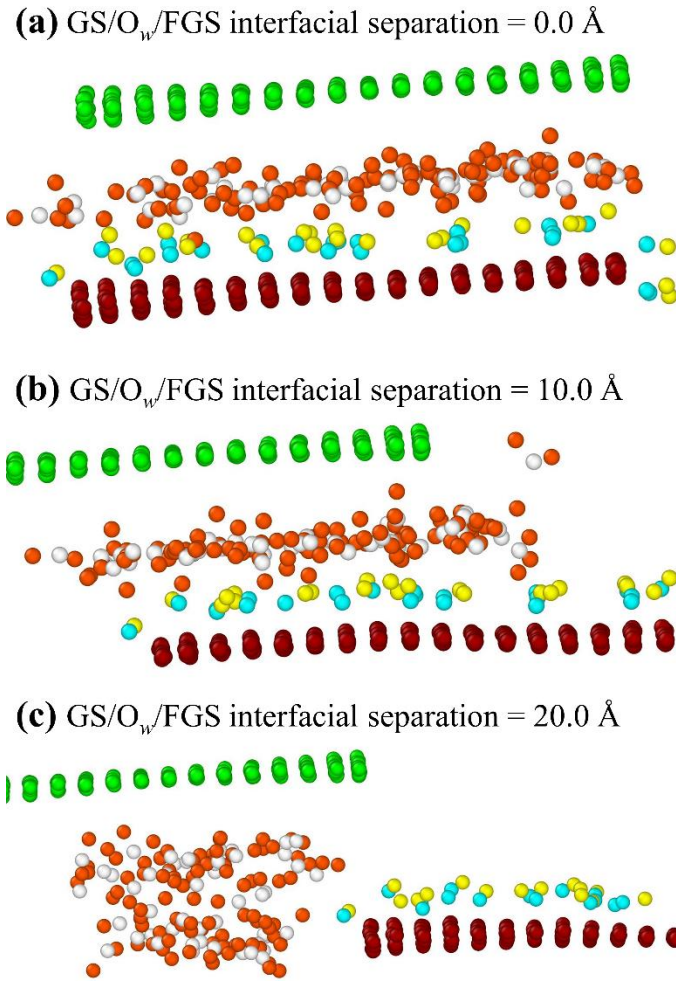
R_1 = initial regime
 R_2 = stability regime
 R_3 = final regime

Figure 5.6. Traction-separation response of the FGS/FGS bilayers with varying degrees of -OH coverage (0, 2, 6, 10, and 12%) and monolayer of water (O_w) sandwiched between two layers of FGS ($FGS/O_w/FGS$): (a) bottom FGS pulled in the positive X-direction and (b) bottom FGS pulled in the positive Y-direction.

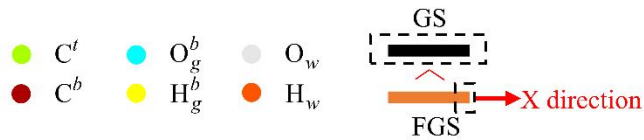
5.3.4. Interfacial strength of FGS/FGS bilayer systems with confined water monolayer

For the $FGS/O_w/FGS$ bilayer systems, the -OH groups were attached to both the top and bottom sheets (Figure 5.6 and Figure 5.8), resulting in stronger interaction than when only present on the bottom sheet, which might be more difficult for the water molecules to reduce effectively. As a result, slightly higher peak traction forces were observed in the stability regime (R_3) for the $FGS/O_w/FGS$ bilayers (for both the X and Y separation) compared to those of the $GS/O_w/FGS$ bilayers. Therefore, similar shear force reduction capability of the mediated water was found for the $FGS/O_w/FGS$ systems, however, to a lesser extent than for the GS/FGS systems. However, the water molecules were seen to be fragmented into several smaller regions from the start of the simulation of the FGS/FGS bilayer systems, suggesting that the water molecules created H-bond networks with both the top and bottom sheets, and thus, inhibited the water/water H-bond networks. This behavior was not observed for the top sheet in the GS/FGS

bilayers. Therefore, when the bottom FGS was sheared relative to the top sheet, the water molecules were attached and moved with the bottom FGS (Figure 5.8). However, as the bottom FGS went past half of the interaction length (the contact length between the top and bottom layers), the water molecules adhered to both the top and bottom FGS. Therefore, far more interactions were seen between the water molecules and the –OH groups for the FGS/FGS bilayers than for the GS/FGS systems. As the simulation progressed, some of the water molecules broke away from the 1st coordination shell of the –OH groups and clustered around the vicinity of the top and bottom FGS, indicating that the strong interaction between the –OH groups and the water remained intact, even after the separation of the sheets. The water molecules possibly created hydrogen bonds (H-bond) between each other and with the –OH groups which resulted in this behavior. However, the breaking of these H-bonds during the relative displacements of the top FGS and bottom FGS still required lower shear traction force (Figure 5.4) than the separation of the FGS/FGS bilayer systems. It seemed that the –OH groups could not have strong interaction when the interfaces were mediated with water, indicating that increase in –OH coverage on the basal plane of the GS could not increase the shear traction force in the presence of water. The interfacial energy and H-bond calculations of these four types of interfaces with varying degrees of –OH contents garnered more insights to these qualitative observations. Interestingly, the water molecules were seen to possess higher friction for the GS/FGS systems. For the FGS/FGS systems, the 12% –OH groups on both surfaces started to create H-bonds with each other, thus breaking the OH-water H-bonds, and improving water mobility, which reduced the shear traction.



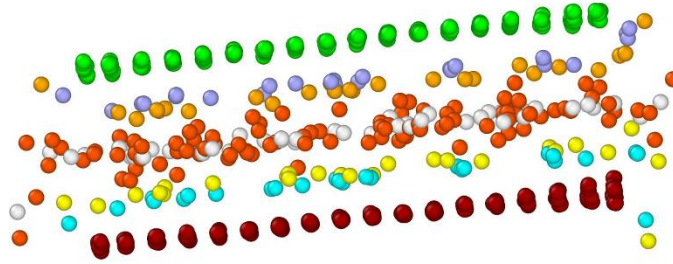
Notation: GS = graphene sheet
 FGS = functionalized graphene sheet
 O_w = oxygen of water monolayer
 [] = fixed atoms



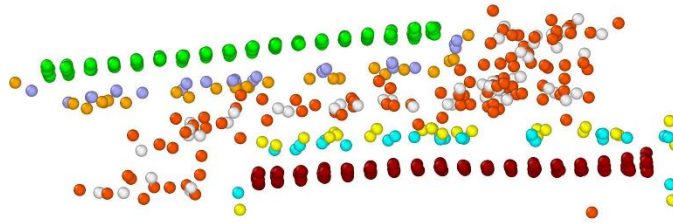
C^t : Carbon in top GS; C^b : Carbon in bottom GS;
 O_g^b : Oxygen of -OH in bottom GS;
 H_g^b : Hydrogen of -OH in bottom GS;
 O_w : Oxygen of water; H_w : Hydrogen of water

Figure 5.7. Representation of the separation behavior of the GS/FGS bilayer system with water monolayer between the two graphene layers at different displacements for shear in X-direction (shown for 10%–OH content).

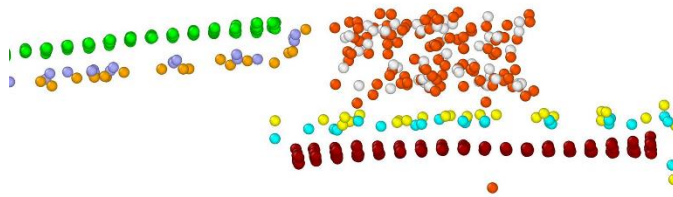
(a) FGS/FGS interfacial separation = 0.0 Å



(b) FGS/FGS interfacial separation = 10.0 Å



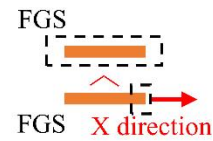
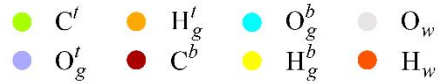
(c) FGS/FGS interfacial separation = 20.0 Å



Notation: FGS = functionalized graphene sheet

O_w = oxygen of water monolayer

$\{ \}$ = fixed atoms



C^t : Carbon in top GS; O_g^t : Oxygen of -OH in top GS;

H_g^t : Hydrogen of -OH in top GS; C^b : Carbon in bottom GS;

O_g^b : Oxygen of -OH in bottom GS;

H_g^b : Hydrogen of -OH in bottom GS;

O_w : Oxygen of water; H_w : Hydrogen of water

Figure 5.8. Representation of separation behavior of FGS/FGS interface with mediating water monolayer between two FGS sheets with 10% -OH content at different displacements for shear in X-direction.

5.3.5. Interaction energy change during normal and shear traction

5.3.5.1. Interaction energy of dry graphene bilayer interfaces

The interfacial energy (ΔE) was divided into three parts: (1) coulombic energy, (2) long-range energy, and (3) vdW energy. The interfacial energy of the dry interfaces showed a similar pattern for both the X and Y separation studies, although the absolute magnitudes were slightly different. The values of the coulombic and long-range interactions of the dry GS/FGS and FGS/FGS interfaces (from the partial charges on the $-OH$ groups) were on the order of $10^{-2} - 10^{-5}$ kcal mol $^{-1}$ during the normal and shear tractions and were, therefore, considered negligible compared to the dominance of the vdW energy and not discussed further.

vdW energy of the GS/FGS bilayer systems. The pristine GS/GS system had the highest normal interaction energy (-767 kcal mol $^{-1}$) among all GS/FGS systems (Figure 5.9). As the $-OH$ coverage increased, the normal interaction energy decreased (from -751 kcal mol $^{-1}$ for 2% $-OH$ to -519 kcal mol $^{-1}$ for 12% $-OH$), indicating that the $-OH$ groups created a shield against the interaction between the top and bottom sheets. The interaction energy behavior of the GS/FGS bilayer systems directly correlated with the traction-separation behavior. The GS/FGS bilayer systems lost their normal interaction energy at a relative distance of $\sim 6 - 8$ Å (i.e., the GS and FGS were totally separated). However, the GS/GS system showed a steeper slope of the total interaction energy as a function of normal separation than the other bilayer systems, i.e., the reduction in interaction energy was more sudden for the pristine GS/GS system, whereas a certain amount of adhesive behavior was observed from the GS/FGS systems. Therefore, the $-OH$ groups might shield the normal interaction energy for the GS/FGS systems but the reduction in the energy envelop was not drastic, rather gradual.

For shear separation in the X-direction, the interaction energy was -679 Kcal mol $^{-1}$ for GS/GS interfaces, whereas, the energy increased to -1247 Kcal mol $^{-1}$ for the GS/FGS interfaces with 2% $-OH$ coverage (Figure 5.10). The $-OH$ groups provided significant friction while sliding against the top GS. The shear traction energy decreased as $-OH$ coverage increased (e.g., -971 Kcal mol $^{-1}$ for 12% $-OH$ coverage). Similar shear mechanism was observed during the shear separation in the Y-direction.

vdW energy of the FGS/FGS bilayer systems. The presence of –OH groups reduced the normal interaction energy (from $-608 \text{ kcal mol}^{-1}$ for 2% –OH to $-480 \text{ kcal mol}^{-1}$ for 12% –OH), in agreement with the observation made for the GS/FGS bilayer systems that –OH groups provided shielding effect against the normal interactions. Having –OH groups on both surfaces (FGS/FGS interfaces) made the shielding effect more prominent, i.e., interaction energy reduced to positive axes (Figure 5.9).

For shear separation in the X-direction, the vdW energy at equilibrium was almost twice ($-1202 \text{ kcal mol}^{-1}$) that of the normal traction energy for 2% –OH at equilibrium, indicating the large friction provided by the interaction of –OH groups from both surfaces (Figure 5.10). The interaction gradually reduced ($-1149 \text{ kcal mol}^{-1}$ for 12% –OH) as the –OH coverage increased. The shear energy plots showed many fluctuations during the separation due to the energy change during the relative orientation and configuration change of the –OH groups, as they sled past each other. As the –OH coverage increased, the shear energy reduced (less negative) in a step-wise manner rather than gradually, which was indicative of the energy peaks and valleys provided by the friction of the –OH groups. Thus, the shear separation showed more adhesive behavior for the FGS/FGS bilayer systems instead of shielding effect provided by the –OH groups during normal traction. As the relative separation reached the length of the FGS, the bottom sheet dipped slightly as it freed itself from the interaction domain provided by the top sheet. However, the non-bonded vdW energy remained active even at 30 \AA distance during shear separation for all interfaces, but was zero after that separation distance. Similar shear mechanism and energy values ($-1248 \text{ kcal mol}^{-1}$ for 2% –OH to $-1017 \text{ kcal mol}^{-1}$ for 12% –OH) were observed in the Y-direction. The shear separation energy at 2% –OH for the GS/FGS and FGS/FGS systems were almost isotropic. As the separation increased, the deviation in shear traction energy from the isotropic behavior was observed because the –OH distribution location and interaction domain played a major role at higher –OH coverages. The interacting –OH groups providing large shear traction force and energy were evident from the superimposed peaks of force and energy (Figure 5.11). However, as the –OH coverage (%) increased, the interactions between the –OH groups, the two sheets, and water molecules became more undulating stick-slip type, and thus, showing the numerous peaks and valleys with smaller amplitudes in the force and energy diagrams, i.e., the number of interactions increased, but due to their large numbers, fluctuations in the shear traction forces were not drastic.

5.3.5.2. Interaction energy of wet graphene bilayer interfaces

The interfacial interaction energy for the wet graphene bilayers during the shear separation studies along the X- and Y-directions was similar in behavior with the dry bilayers. The wet bilayers (GS/O_w/FGS and FGS/O_w/FGS) were only subjected to shear traction-separation. The interaction energies for the wet bilayers were also divided into three parts: (1) coulombic energy, (2) long-range energy, and (3) vdW interaction energy. The vdW energy was the dominant energy for all bilayer systems with the nanoconfined monolayer water.

Coulombic and long-range interaction energies of the GS/O_w/FGS bilayer systems. The coulombic and long-range interaction energies were much lower than the vdW energies, but played an important role in the overall behavior of graphene bilayers with a nanoconfined water monolayer. The GS/O_w/FGS bilayer systems had two types of interaction interfaces to consider: (1) a solid-solid (GS–GS and GS–FGS) interface and (2) a solid-liquid (GS–O_w and FGS–O_w) interface. The GS–GS interface of the GS/O_w/GS bilayer systems did not have coulombic interactions because both sheets were charge neutral, thus, there were no partial charges on the carbon atoms to create electrostatic interactions. Meanwhile, the carbon atoms and the water molecules at the GS–O_w interface of the GS/O_w/GS bilayer systems experienced attractive coulombic interactions at equilibrium ($-20 \text{ kcal mol}^{-1}$). The increase in –OH coverage (%) increased the partial charge available for the electrostatic interactions, and thus, increased the coulombic interactions of the FGS–O_w interfaces. However, above 10% –OH coverage, the FGS–O_w interface experienced the repulsive coulombic energy with the highest value of $\sim 60 \text{ kcal mol}^{-1}$ at $\sim 10 \text{ \AA}$ separation, followed by a gradual transitioning to the attractive coulombic energy within the $10 - 20 \text{ \AA}$ separation range. This phenomenon was attributed to the angular orientational and rotational changes of the –OH groups and water molecules in the $10 - 20 \text{ \AA}$ separation range. The coulombic interaction energy eventually started to fluctuate around zero after 20 \AA separation for all –OH coverages, indicating that the interaction between the water molecules and the –OH groups diminished.

For the GS/O_w/GS bilayer systems, no long-range interactions were present at the GS–GS interfaces. The long-range interactions at the GS–O_w interfaces decreased until 20 \AA separation, and then, fluctuated around zero consistently, similar to the behavior of the coulombic interactions, indicating that the sheets had been separated and the interaction between the water

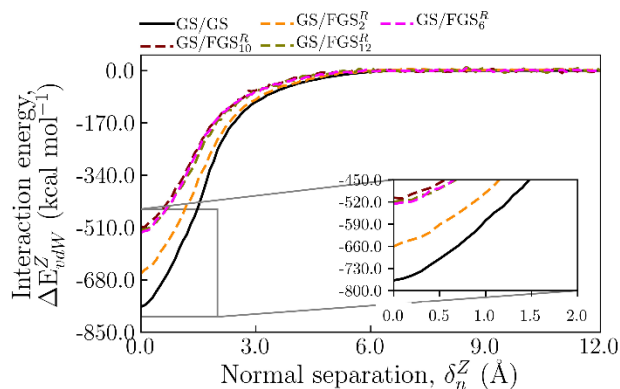
and OH groups were negligible. As the –OH coverage increased, the long-range interaction at the GS–GS interface increased within the interaction area, but reduced to zero as soon as the separation reached the final stage (beyond 20 Å separation). The long-range interactions were much weaker than the Coulombic interactions.

vdW interaction energy of the GS/O_w/FGS bilayer systems. The interaction energy during the shear traction of the bilayer systems revealed the characteristics of the solid-liquid-solid interfaces and supplemented the results from the shear traction-separation plots of the GS/FGS bilayers with water. The vdW interaction energy of the GS–GS interface was much stronger ($-820 \text{ kcal mol}^{-1}$) than the GS–O_w–GS interfacial interaction, e.g., for the top GS–O_w and bottom GS–O_w sheets, the interaction energies were -418 and $-479 \text{ kcal mol}^{-1}$, respectively. The water molecules were responsible for mediating the interaction energy of the GS/O_w/FGS bilayer systems by two mechanisms: (i) by physically pushing the top and bottom sheets further from each other, and thereby, decreasing the interaction energy and (ii) by interacting with the top and bottom sheets, thus, diverting some of the sheet/sheet interaction energy to the sheet/water interaction energy. The interaction energy at the GS–FGS and GS–O_w interfaces at equilibrium (prior to shear separation) increased with –OH coverage. However, the GS–FGS, GS–water, and FGS–water interactions reduced to zero at about the same separation distance for all bilayer systems, indicating that the separation mechanism remained the same. For the FGS with 2% –OH coverage, the vdW interaction energy increased ($-826 \text{ kcal mol}^{-1}$) compared to those of the GS–GS and GS–O_w interfaces (-820 and $-499 \text{ kcal mol}^{-1}$, respectively). Similarly, the shear interaction energy for these interfaces increased as the –OH coverage increased (from $-820 \text{ kcal mol}^{-1}$ for 0% –OH to $-836 \text{ kcal mol}^{-1}$ for 10% –OH coverages). The –OH groups interacted with the water molecules to increase the interaction energy of the GS–O_w interfaces.

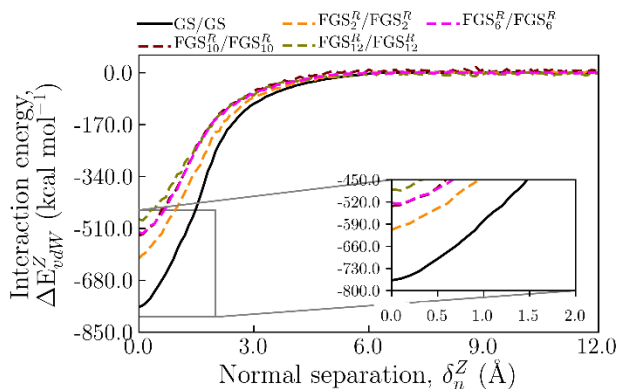
The results provided several significant observations: (i) with the increase in –OH coverage (%), the shear traction energy increased relative to the shear traction energy of the GS/O_w/GS bilayer system, possibly originating from the friction between the –OH groups and the carbon atoms of the GS; (ii) the interaction energy of the FGS–FGS interfaces were slightly higher compared to their GS–FGS counterparts. The –OH groups on both sheets have mechanical interaction when going past each other during the shear separation, rendering larger

interaction energy; and (iii) the water molecules reduced the shear interaction energy for the GS/FGS bilayer systems.

(a) Normal separation of GS/FGS interfaces



(b) Normal separation of FGS/FGS interfaces



Notation: ΔE_{vdW}^Z = vdW interaction energy change in Z direction (kcal mol^{-1})
 GS = graphene sheet
 FGS = functionalized graphene sheet
 GS/FGS_i^R = GS/FGS bilayer
 $\text{FGS}_i^R/\text{FGS}_i^R$ = FGS/FGS bilayer
 i = -OH coverage (%)
 R = random arrangement of -OH
 [] = fixed layer of atoms

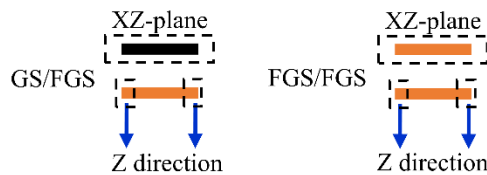
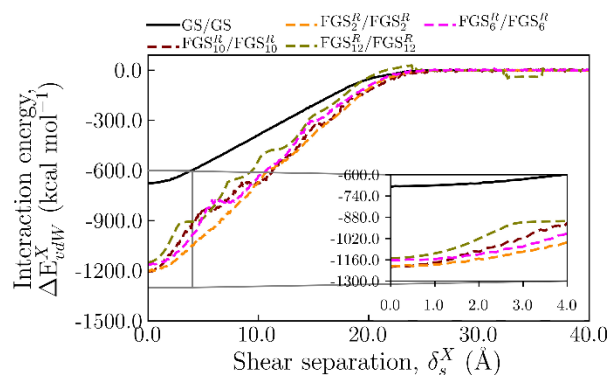
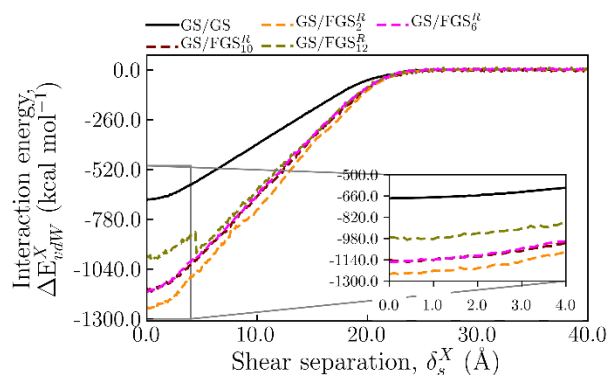
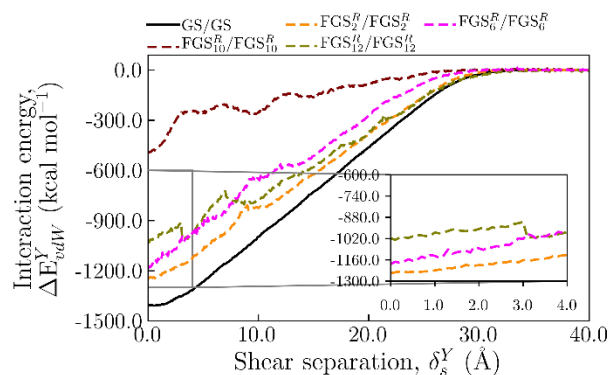
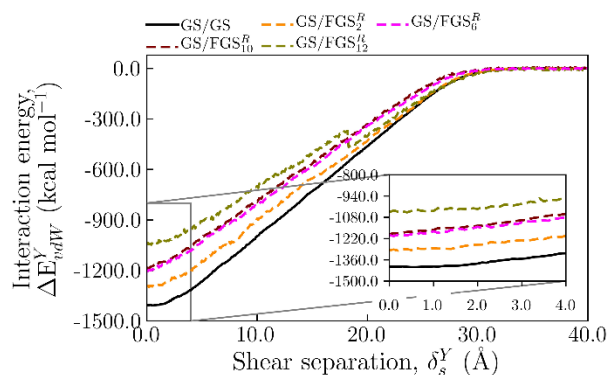


Figure 5.9. Interaction energy plots (vdW) for the normal traction-separation of (a) GS/FGS bilayer systems and (b) FGS/FGS bilayer systems without water monolayer.

(a) Shear separation of GS/FGS interfaces along X **(c)** Shear separation of FGS/FGS interfaces along X



(b) Shear separation of GS/FGS interfaces along Y **(d)** Shear separation of FGS/FGS interfaces along Y



Notation: ΔE_{vdW}^j = vdW interaction energy change in the j^{th} direction (kcal mol⁻¹)
 j = {X, Y}
 GS/FGS_{*i*}^R = GS/FGS bilayer
 FGS_{*i*}^R/FGS_{*i*}^R = FGS/FGS bilayer
i = -OH coverage (%)
 R = random arrangement of -OH
 [] = fixed layer of atoms

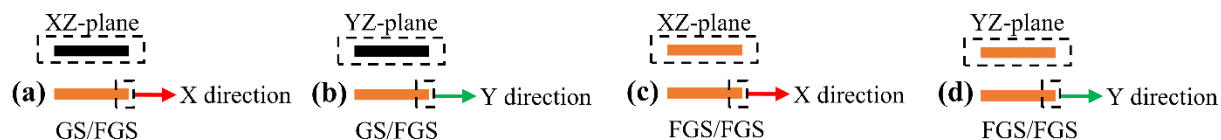
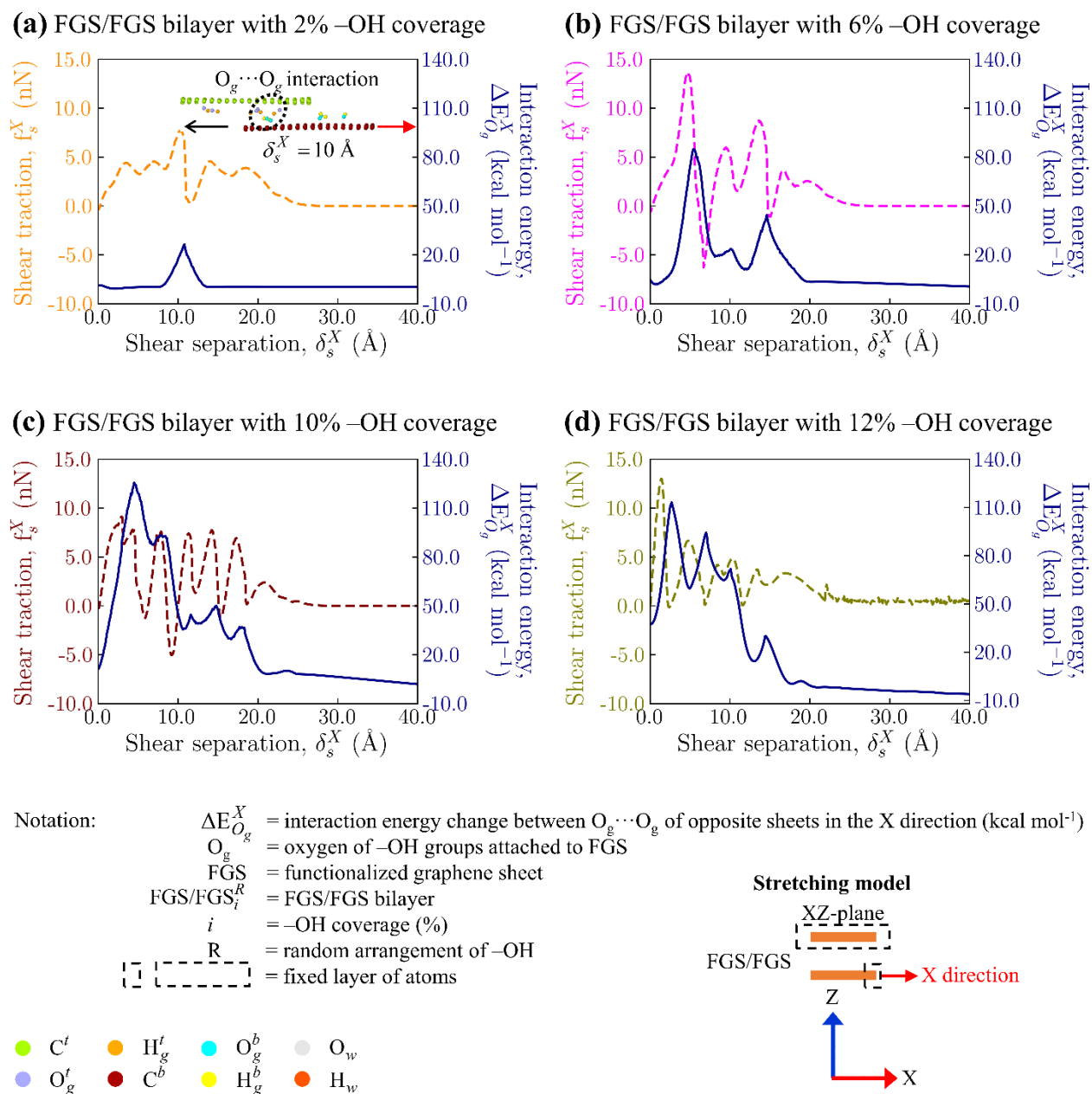


Figure 5.10. Interaction energy plots (vdW) for the (a), (b) shear traction-separation behaviors for the GS/FGS interfaces along X and Y, and (c), (d) shear traction separation behaviors in FGS/FGS interfaces along X and Y without the mediating water monolayer.



C^t : Carbon in top GS; O_g^t : Oxygen of -OH in top GS; H_g^t : Hydrogen of -OH in top GS; C^b : Carbon in bottom GS; O_g^b : Oxygen of -OH in bottom GS; H_g^b : Hydrogen of -OH in bottom GS; O_w : Oxygen of water; H_w : Hydrogen of water

Figure 5.11. Superposition of the shear traction force and the interaction energy plots for the FGS/FGS bilayer systems (a) 2% (b) 6%, (c) 10%, and (d) 12% -OH coverage during shear separation along the X-direction.

Coulombic and long-range interaction energy of the FGS/ O_w /FGS bilayer systems. The peak of the long-range interaction energy for the FGS/FGS interfaces (with water in the middle) were actually lower than that of GS/FGS interfaces for 2% -OH coverage. However, FGS/ O_w

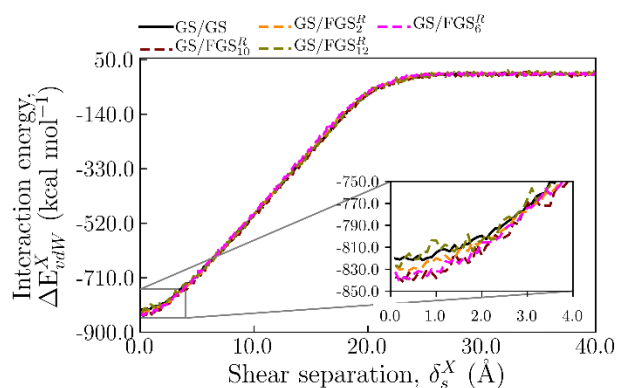
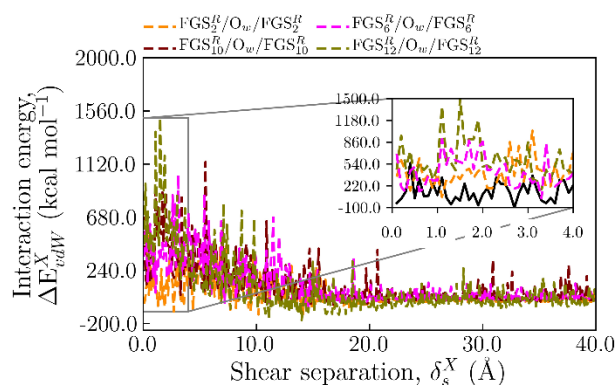
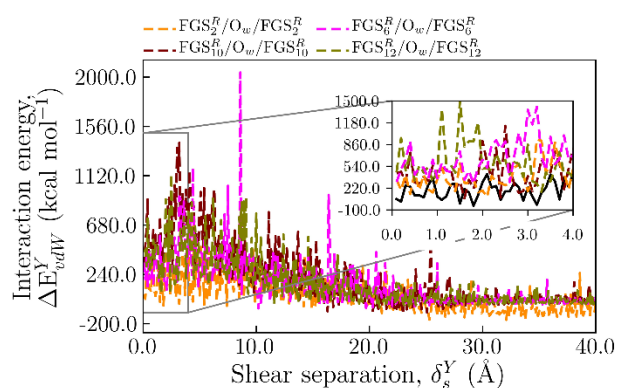
interfaces showed at least 2 times greater interaction than the GS/O_w interfaces at 2% –OH coverage. This was attributed to the presence of –OH groups on both top and bottom sheets pointing towards each other. From the study, it was evident that the long-range interaction between the FGS/FGS interfaces was insensitive to the –OH coverage, however, the FGS–O_w interaction increased as the –OH coverage increased and showed similar switching from repulsive to attractive part at higher –OH coverages (> 10 %), similar to the FGS/O_w/FGS interfaces.

vdW energy of the FGS/O_w/FGS bilayer systems. The mechanism of interfacial interaction energy of the FGS/O_w/FGS bilayer systems during the X and Y separation was the same as those of the GS/O_w/FGS bilayers. The interaction energy of the FGS/FGS bilayers with water monolayer showed a positive energy because of the presence of the –OH groups on both sheets (Figure 5.12). The energy increased as the –OH coverage increased, but reduced to zero for all bilayer systems at about ~15 Å separation, indicating that the separation behavior of the FGS/FGS systems with water monolayer remained the same as that of the GS/FGS bilayers with water monolayer. The interaction energies of the FGS/FGS systems were dominated by the vdW energy at the FGS–FGS interfaces. Meanwhile, the vdW energy between the FGS and water (for all –OH coverage) increased during the shearing and after the separation, the vdW became constant with fluctuating behavior. As the –OH coverage increased, the vdW interaction energy at the FGS–FGS interfaces also increased (with 12% –OH being the highest at equilibrium).

The water molecules separated into different clusters as the separation increased due to the interactions of the water molecules and –OH groups. However, the formation changed again when the sheets were completely separated. This type of grouping and regrouping of water clusters occurred because of the competing interfacial interactions between the water/water and –OH/water molecules. These interactions control and modulate the interfacial mechanical behavior such as adhesion mechanics and exfoliation characteristics of the GS/FGS and FGS/FGS bilayer systems. Having –OH groups on the basal plane of GS made it more hydrophilic, thus, creating H-bond network with the water molecules.

Comparing between the GS/O_w/FGS and FGS/O_w/FGS bilayer systems with water, the latter systems had more interactions between the –OH groups and water molecules. However, the interaction energy between the GS and O_w was higher than the interaction energy GS and GS

when the -OH coverage was large. Hence, it was possible for the FGS/O_w/FGS bilayers with 12% -OH to reduce the shear traction compared to that of GS/O_w/FGS bilayers.

(a) Shear separation along X (zigzag)**(b) Shear separation along X (zigzag)****(c) Shear separation along Y (armchair)**

Notation:

- ΔE_{total}^j = total interaction energy change in the j^{th} direction (kcal mol^{-1})
 $j = \{X, Y\}$
 O_w = oxygen of water monolayer
 $GS/O_w/FGS_i^R$ = GS/FGS bilayer with confined water monolayer, O_w
 $FGS_i^R/O_w/FGS_i^R$ = FGS/FGS bilayer with confined water monolayer, O_w
 i = -OH coverage (%)
 R = random arrangement of -OH groups
 $\boxed{\quad\quad\quad}$ = fixed layer of atoms

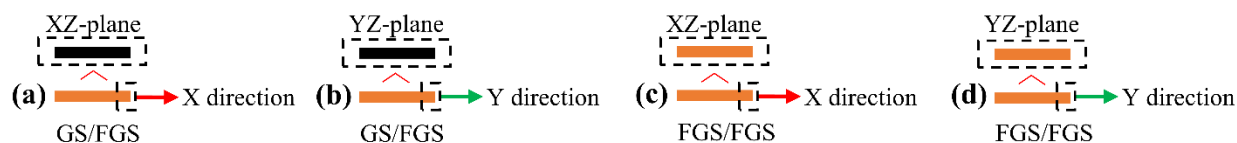


Figure 5.12. Interaction energy plots for the (a) shear traction-separation for the GS/FGS bilayer systems with water monolayer in the X-direction, (b) shear traction-separation in the X-direction for the FGS/FGS bilayer systems with water monolayer, (d) shear traction-separation in the Y-direction for the FGS/FGS bilayer systems with water monolayer.

5.3.6. Hydrogen bonding characteristics of graphene bilayer interfaces with nanoconfined water monolayer

5.3.6.1. Graphene bilayer systems with nanoconfined water monolayer (GS/O_w/FGS)

At the start of the simulation, the geometries of the water molecules ($\angle\text{H-O-H}$ orientation on the XY plane) were planar. The water molecules rearranged and oriented themselves in favor of their respective interactions during the equilibration and sheet-sheet separation process. Four types of H-bonds were identified to play a key role in the mobility of the GS/O_w/FGS systems: (1) H-bond between the water molecules ($\text{O}_w\text{-H}_w\cdots\text{O}_w$), where one oxygen acted as the donor and another oxygen from another molecule acted as the acceptor, (2) H-bond between the water molecules and $-\text{OH}$ groups ($\text{O}_w\text{-H}_w\cdots\text{O}_g$) where the oxygen from the water molecules acted as the donor and the oxygen from the hydroxyl group was the acceptor, (3) H-bond between the water molecules and $-\text{OH}$ groups ($\text{O}_g\text{-H}_g\cdots\text{O}_w$) where the oxygen from the water molecules acted as the acceptor and the oxygen from the hydroxyl group was the donor, and (4) H-bond between the $-\text{OH}$ groups ($\text{O}_g\text{-H}_g\cdots\text{O}_g$) where the oxygen from one hydroxyl group acted as the donor and the oxygen from another neighboring hydroxyl group acted as the acceptor.

The water molecules created H-bonds with each other ($\text{O}_w\text{-H}_w\cdots\text{O}_w$) and with the $-\text{OH}$ groups ($\text{O}_w\text{-H}_w\cdots\text{O}_g$ and $\text{O}_g\text{-H}_g\cdots\text{O}_w$) to form a connected network in all the GS/O_w/FGS bilayer systems. For the GS/O_w/FGS bilayer systems, the confined water molecules created the H-bonds with each other during the equilibration (Figure 5.15). The number of H-bonds-per-water molecule at equilibrium for the GS/O_w/FGS system with 2% $-\text{OH}$ coverage was 2.06, lower than that of bulk water (3.21) because the confined water molecules could not form any H-bonds in the Z-direction. As the separation progressed, the water molecules re-arranged themselves by creating more H-bonds among each other and reached a stable value of ~ 2.46 at the 5 – 15 Å separation range. This value closely matched with the number of H-bonds (~ 2.5) created during the self-assembly of water molecules in a graphene bilayer [242]. However, the structured network of water as seen in the literature [256] was not apparent in this study, possibly because of the presence of only a monolayer of water; although, the local hydrophilicity of water molecules was observed. The number of $\text{O}_w\text{-H}_w\cdots\text{O}_w$ H-bonds followed a decreasing trend with the increase in $-\text{OH}$ coverage (especially the equilibrium value of H-bonds). This initial H-bond

quantification proved the effects of –OH groups on the total H-bond network of the system. During the shear separation in the X-direction, the $O_w-H_w \cdots O_w$ H-bonds remained relatively stable until ~ 12 Å separation, i.e., minimal effects occurred to the internal H-bond stretching within the water network before 12 Å separation. It was observed that, the number of H-bonds between the –OH groups and water molecules started to decrease at ~ 12 Å, which was about half of the length of the GS along the X-direction. Due to the lack of interacting surfaces (half of the GS surface and FGS surface were not in contact), the number of H-bonds decreased. For GS/ O_w /FGS systems with 2%, 6%, and 10% –OH coverages, the number of H-bonds decreased to zero after 20 Å separation because of the lack of physical contact of the two sheets at separation. Understandably, the number of H-bonds for the GS/ O_w /FGS systems with higher –OH coverages (%) was higher than the ones with lower –OH coverage. Within the 10 – 20 Å separation, the number of H-bonds of water molecules gradually increased because the H-bonds that were holding the water molecules with the –OH groups were gradually reduced to zero at 20 Å. The much lower number of –OH/water H-bonds than the water/water H-bonds indicated that the intramolecular interaction (i.e., within water molecules) prevailed. Similar behavior on H-bond creation between the functional groups of graphene oxide sheets and water, and consequently less number of H-bond creation within the water molecules were found for the confined water-bilayer graphene oxide system [249]. Increasing the –OH coverage increased the number of H-bonds to some extent but got saturated at a particular coverage (12%). However, for the 12% –OH, the water molecules were divided into several clusters and formed around the top and bottom sheet, creating a local network of water still possessing some of the residual H-bonds between the –OH groups and water molecules. After that, the number of H-bonds increased, which indicated breaking of the –OH/water H-bonds and creation of more water/water H-bonds. The number of H-bonds between the water and –OH groups of bottom sheet (FGS) was more prominent than the H-bonds within the water molecules. As the –OH coverage increased, the number of H-bonds increased (the number of H-bonds were least for 2% and highest for 12%). The number of H-bonds between the water molecules and –OH groups can be further divided depending on the donor-acceptor behavior, i.e., (1) O_w donor- O_g acceptor and (2) O_g donor – O_w acceptor. In both cases, the H-bonds were totally broken at ~ 20 Å separation, thus, proving the point made earlier, about the number of H-bonds increase within water monolayer after separation (due to the broken H-bonds between water molecules and –OH groups) of the

interfaces. The decreasing trends (between the 10 – 20 Å range) in the H-bond-separation plots indicated that the –OH/water H-bonds were probably stiffer when O_w acted as donor (water donated proton to the –OH group) than the H-bonds when the O_g acted as the donor (–OH group donated proton to water). The –OH groups at 2% coverage were too sparsely distributed on the FGS basal plane to create stable H-bonds, and was not observed to do so in the simulation. However, as the –OH coverage increased, the number of $O_g-H_g \cdots O_g$ H-bonds increased but still remained lower than the number of H-bonds between the water and –OH groups. The –OH groups that are in the same FGS (either top or bottom sheet) were seen to form H-bonds between each other for the coverages of 6% and above. The number of $O_g-H_g \cdots O_g$ H-bonds (intralayer H-bonds between –OH groups) were consistent throughout the simulation. Since, the bottom FGS remained intact during the shear separation, the –OH groups could hold the interactions and the H-bond numbers constant. From the above discussion, it could be summarized that at 12% –OH coverage, the H-bonds between the –OH and water molecules restricted the movement of the water molecules, compared to the GS/ O_w /FGS interface with 12% –OH. However, as the separation increased, the –OH/water H-bonds were broken and the –OH groups started to interact among themselves, which might result in a higher mobility of the water molecules. This phenomenon was responsible for higher shear traction for FGS/ O_w /FGS interfaces compared to the GS/ O_w /FGS interfaces. The combinations of these effects played a role in the interfacial strength and lubricating behavior of the wet interfaces. Therefore, it was evident from this study that the H-bond statistics between the –OH groups and the water molecules played a vital role in modulating the interfacial energetics and frictional properties of the GS/FGS and FGS/FGS bilayers with confined water monolayer, and, the complex interplay of the H-bond breaking and creation indicated that the interfacial strength of the GS/ O_w /FGS was modulated by the water monolayer and –OH (%) coverage.

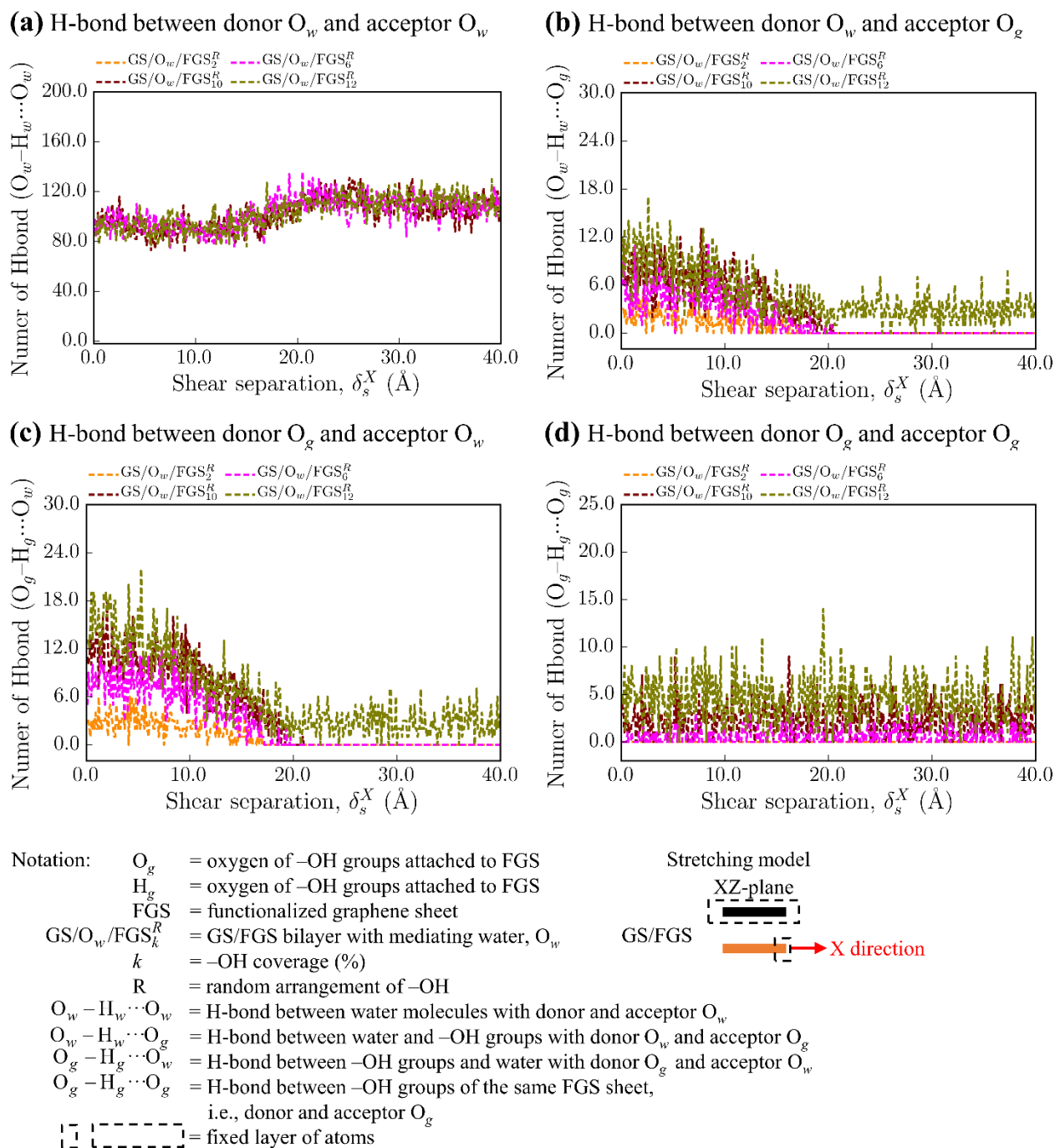
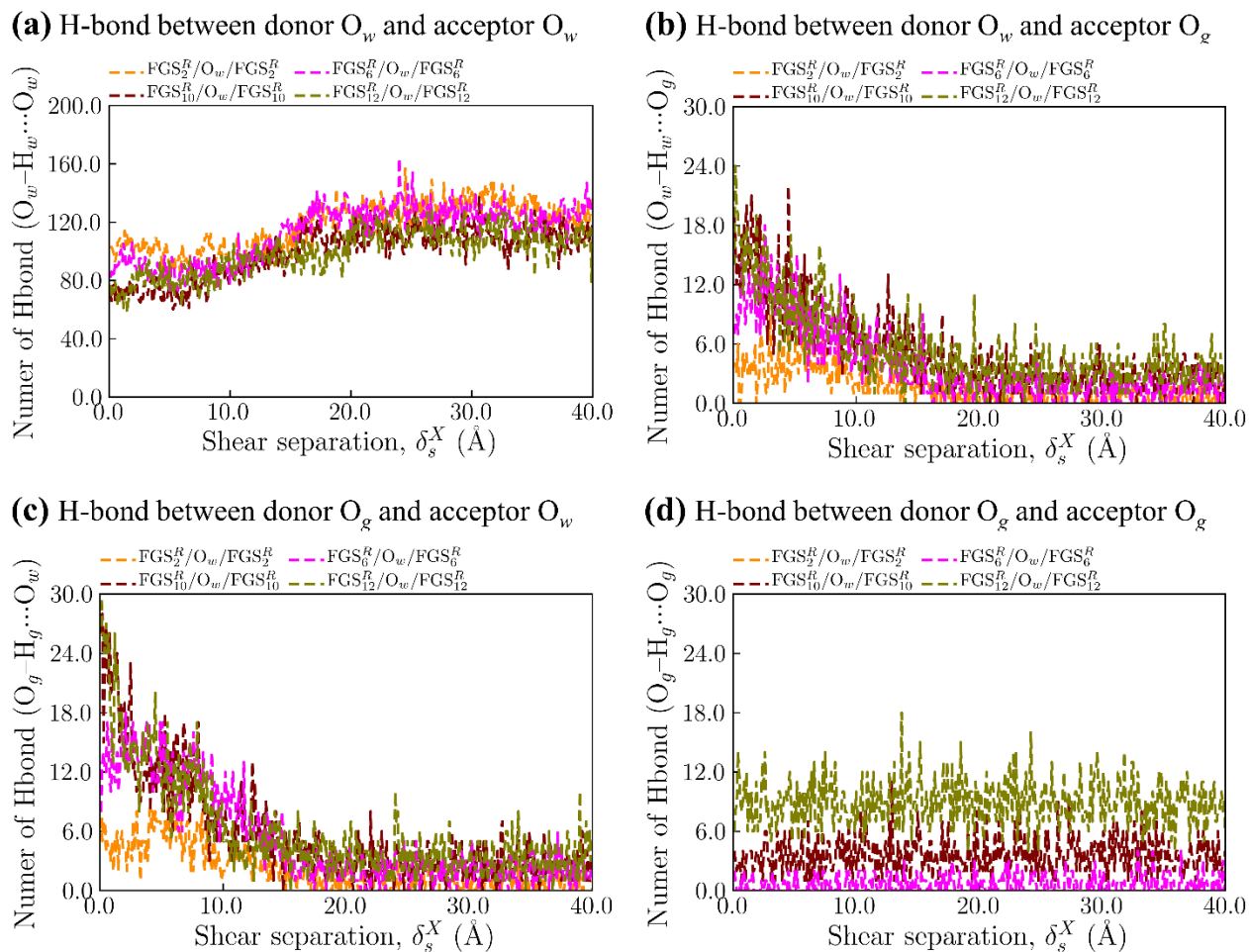


Figure 5.13. Time evolution of total number of H-bonds with breakdown with different interactions of H-bond for (a) water-water interactions, (b) donor -OH and acceptor water interactions, (c) donor water and acceptor -OH, and (d) donor and acceptor -OH for the $GS/O_w/FGS$ bilayer.



Notation: O_g = oxygen of $-OH$ groups attached to FGS
 H_g = oxygen of $-OH$ groups attached to FGS
 FGS = functionalized graphene sheet
 $FGS_k^R/O_w/FGS_k^R$ = FGS/FGS bilayer with mediating water, O_w
 k = $-OH$ coverage (%)
 R = random arrangement of $-OH$
 $O_w-H_w \cdots O_w$ = H-bond between water molecules with donor and acceptor O_w
 $O_w-H_w \cdots O_g$ = H-bond between water and $-OH$ groups with donor O_w and acceptor O_g
 $O_g-H_g \cdots O_w$ = H-bond between $-OH$ groups and water with donor O_g and acceptor O_w
 $O_g-H_g \cdots O_g$ = H-bond between $-OH$ groups of the same FGS sheet,
 i.e., donor and acceptor O_g
 [] [] = fixed layer of atoms

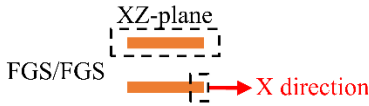
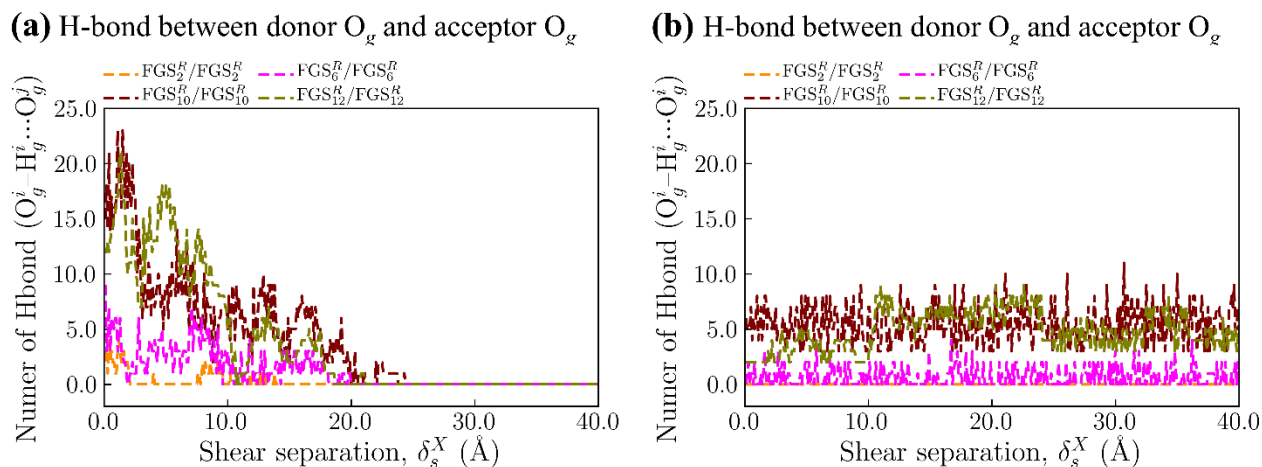
Stretching model


Figure 5.14. Time evolution of the total number of H-bonds with breakdown of the different interactions of H-bonds: (a) water-water interactions, (b) donor $-OH$ and acceptor water interactions, (c) donor water and acceptor $-OH$, and (d) donor and acceptor $-OH$ for the FGS/ O_w /FGS bilayer.



Notation: O_g = oxygen of –OH groups attached to FGS
 H_g = oxygen of –OH groups attached to FGS
 FGS = functionalized graphene sheet
 FGS_k^R/FGS_k^R = FGS/FGS bilayer
 k = –OH coverage (%)
 R = random arrangement of –OH
 $O_g^i - H_g^i \cdots O_g^j$ = H-bond between –OH groups of opposite FGS sheets
 $i O_g^j$ = {top FGS (t), bottom FGS (b)}
 $j O_g^i$ = {bottom FGS (b), top FGS (t)}
 [] = fixed layer of atoms

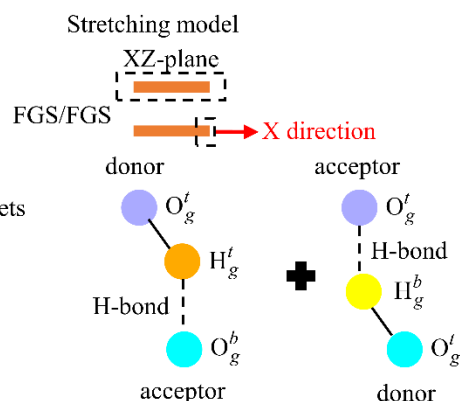


Figure 5.15. Time evolution of the total number of H-bonds with (a) donor and acceptor –OH group interactions between the opposite sheet and (b) donor and acceptor –OH group interactions from the same sheet of the FGS/ O_w /FGS bilayer.

5.3.6.2. FGS/ O_w /FGS interfaces with nanoconfined water monolayer

In general, H-bonding behavior of the water monolayer for the FGS/ O_w /FGS interfaces (Figure 5.14) for shear separation along X-direction showed similar pattern as the GS/ O_w /FGS interfaces (Figure 5.13) during the shear separation in the X-direction. The equilibrium number of H-bonds created within the water molecules were slightly smaller than that of GS/ O_w /FGS interfaces, although the total number of H-bonds was higher for the FGS/ O_w /FGS interfaces compared to that of the GS/ O_w /FGS interfaces. This was attributed to the larger number of –OH/water H-bond creation (because of –OH on both sheets) than the GS/ O_w /FGS interfaces. The number of H-bonds within the water molecules increased from 10 Å to 20 Å range, similar to the GS/ O_w /FGS interfaces, indicating that the H-bond creation and breaking were also geometry

dependent (i.e., related to the interfacial contact area). After the 20 Å separation of the interfaces, the number of H-bonds within the water monolayer held constant values for all the FGS/O_w/FGS interfaces with varying –OH coverages. The –OH groups on the top and bottom FGS formed H-bonds with the water molecules during the equilibration process. However, during the shear separation in X-direction, the H-bonds created by the two interfaces with the water molecules appeared to be broken faster than the H-bonds created by one interface only (i.e., GS/O_w/FGS interface). The H-bonds between the –OH groups and water molecules could be subdivided into two groups: (1) the H-bonds created between the –OH groups of the top FGS and water and (2) the H-bonds created between the –OH groups of the bottom FGS and water. Since the top sheet was immobile, the H-bonds created from the top –OH groups were broken rapidly during the shear separation of the interfaces (since water molecules were more prone to moving with the bottom sheet), thus, decreasing the number of H-bonds at a rapid rate. On the contrary, the mobile water molecules could re-arrange themselves and held the H-bonds when these H-bonds were stretched during the shear separation. The intralayer –OH/–OH groups for FGS/O_w/FGS system have larger number of interactions than the GS/O_w/FGS interfaces. However, the number of H-bonds for the –OH/–OH groups (Figure 5.15) remained consistent throughout the simulation (for 6%, 10%, and 12% –OH), similar to the GS/O_w/FGS interfaces. Having larger number of O_g–H_g···O_g H-bonds also presumably affected the diffusion and mobility of the water molecules in a different way than the GS/O_w/FGS interface.

5.3.7. Mean squared displacement of the nanoconfined water monolayer in wet interfaces

5.3.7.1. Mean squared displacement at equilibrium

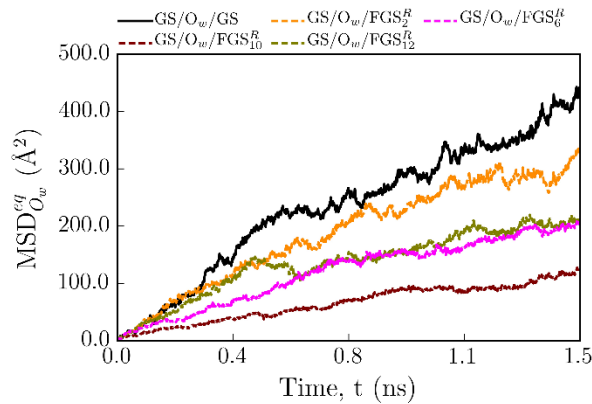
GS/FGS systems with water monolayer. The mean squared displacement (MSD) studies of the monolayer water nanoconfined between two layers of graphene (GS/FGS and FGS/FGS) at equilibrium (zero shear separation) revealed that the mobility of the nano-confined water depended on the surface chemistry of the FGS basal plane, i.e., –OH coverage (%) and location of the –OH groups (on one sheet or both sheets) (Figure 5.16). The equilibrium self-diffusivity of nano-confined water monolayer within the GS/O_w/GS system without any functionalization was $7.7 \times 10^{-10} \text{ m}^2 \text{ s}^{-1}$, lower than bulk water reported in the literature [249] and nano-confined water in large confinements [257]. It has also been reported in the literature that the diffusion

coefficient of nanoconfined water is one order of magnitude lower than that in the bulk water due to the strong H-bonded interactions [258]. The diffusion coefficient of nanoconfined water has been shown to be reduced not only within the graphene bilayers but other types of nanoconfinements (e.g., aluminosilicate) [259]. The in-plane self-diffusion coefficient (D_{xy}) of the monolayer water was closer to that of the bulk water. However, due to the almost non-existent out-of-plane mobility (Z-component of the diffusion coefficient, D_z , along the Z-direction; the direction of confinement) of the water molecules, the total diffusivity (D_r) was lower than that of the bulk water. The presence of –OH groups on the basal plane of FGS tend to reduce the self-diffusivity of the water molecules even more, attesting to the similar findings for bilayer graphene [260, 261] and graphene-oxide sheets with nano-confined water [249]. The MSD values at equilibrium ($MSD_{O_w}^{eq}$) indicated that the presence of –OH groups reduced the mobility of the water monolayer as the –OH coverage (%) increased. The presence of –OH groups on both graphene surfaces adjacent to the water monolayer (FGS/ O_w /FGS) restricted the mobility of water more than that of with the –OH attached to one graphene surface (GS/ O_w /FGS bilayer). The creation of more H-bonds between –OH groups and water molecules led to the restrictive mobility of the water molecules for FGS/FGS bilayer systems. Understandably, the water molecules in GS/FGS with 2% –OH coverage showed a reducing MSD trend compared to the GS/ O_w /GS bilayer. Similarly, as the –OH coverage (%) increased, the MSD values for the GS/ O_w /FGS systems followed a decreasing trend. However, the water molecules in the FGS/ O_w /FGS bilayers with 12% –OH showed almost similar MSD trend before 0.5 ns as the water with the bilayers having 2% –OH. Within 0.40-0.65 ns timestep, the water molecules broke the temporary cage (known as “caging effect”) created by the network of –OH/water H-bonds (shown by decreasing MSD values followed by a sudden surge in MSD values), and then followed an increasing trend similar to that of –OH with 6% coverage. The water molecules in the bilayers with 12% –OH groups were freed from the cage due to the formation of large number of H-bonds between the –OH groups while breaking the –OH/water H-bond. Thus, the water molecules could form H-bonds among each other which increased the probability of clustered mobility, and enhance the water molecules’ overall mobility. The MSD values of the water molecules in all bilayer systems showed fluctuations compared to the usual bulk water MSD values because the –OH/water interactions led to the continuous creation and breaking of

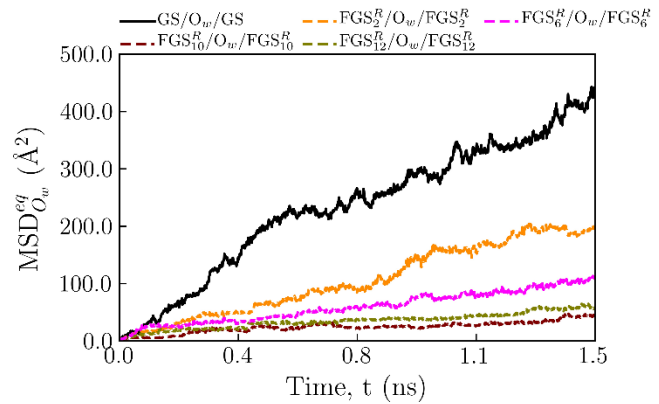
the –OH/water H-bond interactions and thus, led to continuous fluctuation in the H-bond creation and breaking within the water molecules.

FGS/FGS system with water monolayer. The FGS/FGS bilayer systems showed lower MSD values than the GS/FGS systems due to added H-bonding provided by the top FGS with –OH groups that were missing in the GS/FGS system. Similar to the GS/FGS systems, for FGS/FGS systems, the MSD values reduced with increase in –OH coverages. However, 12% –OH groups showed more MSD than 10% which indicated, intra-layer H-bonding among the –OH groups, hindering the –OH/water H-bonding. Thus, the water molecules had greater mobility for 12%, and it was reflected on the shear traction-shear separation plots, indicating less fluctuation in the shear traction forces. This result was also evident from the –OH/–OH interaction, that for 12%, the interaction energy had lesser amplitude of peaks, and more frequency of peaks.

(a) Mean square displacement of water for GS/O_w/FGS bilayers



(b) Mean square displacement of water for FGS/O_w/FGS bilayers



Notation: $MSD_{O_w}^{eq}$ = mean square displacement of O_w at equilibrium (*eq*)
 GS^w = graphene sheet
 FGS = functionalized graphene sheet
 FGS_k^R/O_w/FGS_k^R = FGS/FGS bilayer with water monolayer
 O_w = oxygen of water monolayer
 k = –OH coverage (%)
 R = random arrangement of –OH
 [] = fixed layer of atoms

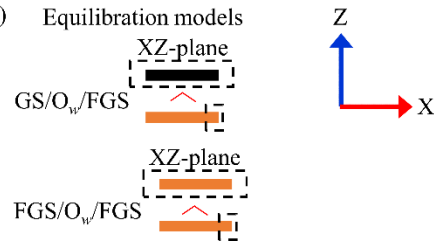


Figure 5.16. MSD plots of graphene bilayer systems with monolayer of water at equilibrium (zero shear separation) in X-direction for: (a) GS/O_w/FGS systems and (b) FGS/O_w/FGS systems.

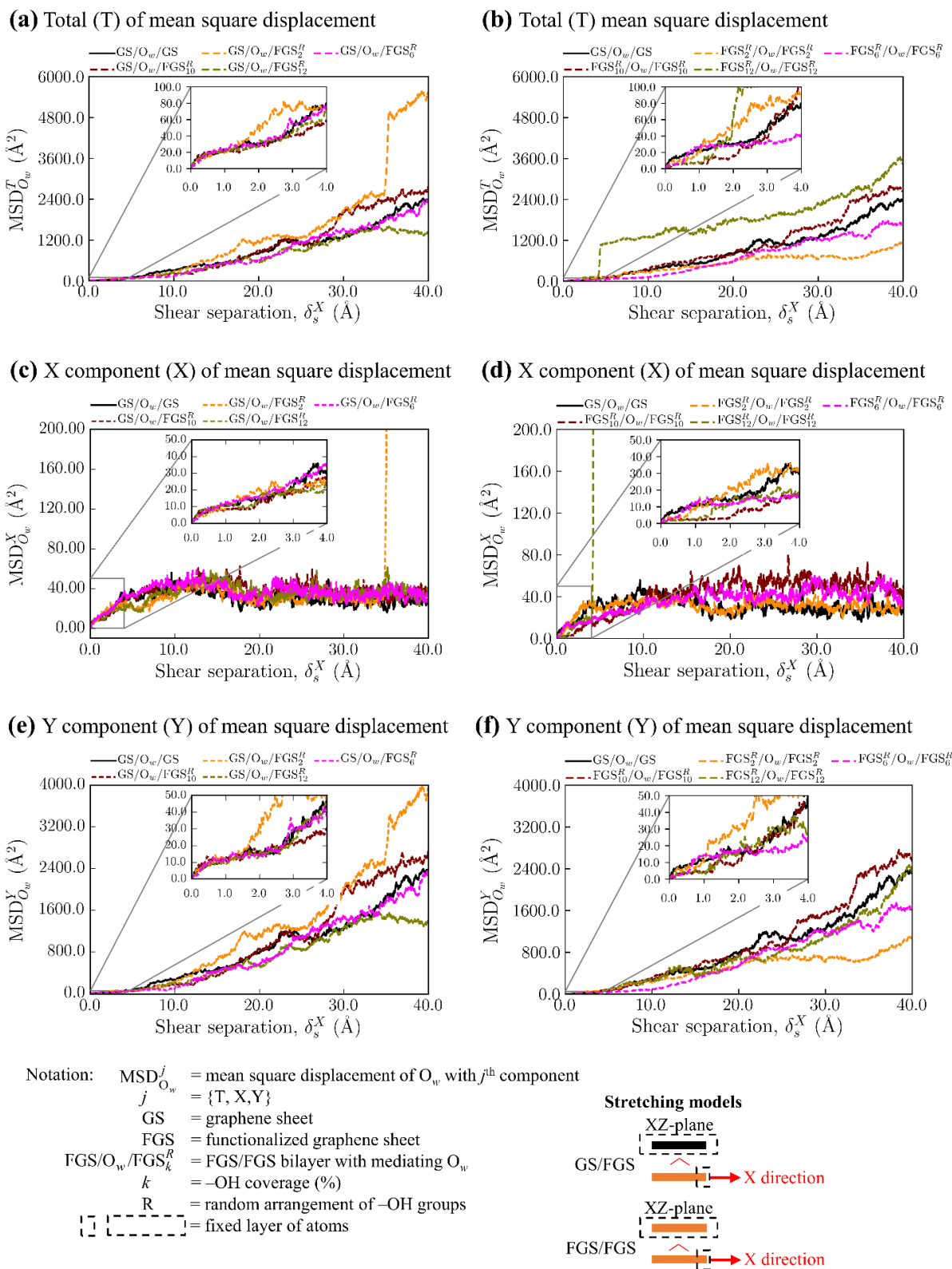


Figure 5.17. MSD plots of graphene bilayer systems with monolayer of water during shear separation in the X-direction. Total MSD, X-component of MSD, and Y-component of MSD, respectively for: (a), (c), and (e) GS/ O_w /FGS systems and (b), (d), and (f) FGS/ O_w /FGS systems.

The FGS/O_w/FGS systems restricted the mobility of water molecules more than the GS/O_w/FGS bilayer systems. Having lower % of –OH coverage reduced the mobility of water in both the GS/O_w/FGS and FGS/O_w/FGS bilayer cases. However, when the –OH coverage was more than 6%, the mobility increased for the FGS/O_w/FGS bilayers than the 10% and 12%. It appeared that the –OH groups interacted with themselves and created H-bonds instead of creating H-bonds with the water, which led to the removal of “caging effect” of the water molecules. After 10 Å separation, the MSD value of 2% FGS/O_w/FGS indicated that the water molecules were restricted to move and they traveled with the movable bottom FGS.

5.3.7.2. Mean squared displacement during shear traction-separation

GS/FGS bilayer systems with water monolayer. During the separation of GS/FGS bilayer with water monolayer (GS/O_w/FGS) in the X-direction, the mobility of water molecules was significantly greater in the Y-direction than in the X-direction (Figure 5.17), possibly because the water molecules could escape in the Y-direction when the H-bonds were broken. The magnitudes of the MSD in the X-direction increased until the separation of ~10 Å, followed by a plateau. Meanwhile, the MSD values kept increasing in the Y-direction during shear separation along the X-direction. Interestingly, the mobility of the water molecules showed a different behavior during separation compared to at the equilibrium conditions. During the shear separation, water molecules confined between the GS/FGS with 2% –OH coverage showed the highest mobility than any other system, even more mobility than the water monolayer nanoconfined between the GS/GS bilayer (Figure 5.17). Because, as the bottom FGS was sheared, the –OH/water (both O_w–H_w···O_g and O_g–H_g···O_w) H-bonds were broken while the recently freed water molecules created more O_w–H_w···O_w H-bonds and formed a clustered network. Therefore, the water monolayer possibly traveled as clusters rather than individual molecules, which increased the overall MSD values. As the simulation progressed, the 2% –OH for the FGS/O_w/FGS system showed the least MSD values. The number of H-bonds decreased until a separation of 10 Å, possibly due to the broken –OH/water H-bonds, followed by an increase and then plateaued formation, after a separation of about 20 Å. After 20 Å separation, the top and bottom layers were almost separated with the water molecules settling with the FGS systems. Thus, the H-bonds between the water molecules remained usually constant. For the FGS systems with 6%, 10%, and 12% –OH coverage, the MSD values increased monotonously up to a separation of 10 Å, followed by a

lower increasing slope due to the breaking of H-bonds between the –OH/water molecules. Fluctuations in the MSD values observed after 20-25 Å indicated the complete separation of the GS and FGS, and the water molecules had to vigorously break bonds and create new bonds to form stable structures. The GS/O_w/FGS system with 10% –OH coverage showed similar mobility behavior initially as the GS/O_w/FGS system, because the –OH groups possibly had more interactions with themselves than with the water molecules. After the separation of the top and bottom sheets (~25 Å), where the water molecules were showed higher mobility due to the sudden change in the confining space. The water in the bilayer with 12% –OH showed slightly higher mobility initially, but after 10 Å, the mobility of the water molecules stayed below that of the pristine GS/O_w/GS bilayer system. This was understandable because there were some interactions of the –OH/water in the system even after the inter-sheet separation. After the separation of the GS and FGS with 2% –OH, the water molecules had much more restrictive movement than the water in the FGS with 12% –OH. The water molecules in the FGS with 12% –OH had more interactions with the –OH/–OH than the water/–OH, and, thus, water moved as clusters showing more mobility.

FGS/FGS bilayer systems with water monolayer. The FGS/O_w/FGS systems with 2% –OH showed (within the initial 4 Å separation) slightly higher total MSD of the water molecules than the pristine systems (GS/O_w/GS) (95 Å² for FGS/O_w/FGS vs. 80 Å² GS/O_w/GS) due to the interactions between the –OH groups of FGS and the water molecules (Figure 5.17a). During the separation, the –OH/water H-bonds were broken, resulting in the creation of more H-bonds between the water clusters, which might be responsible for higher mobility. The FGS/O_w/FGS systems with 6, 10, and 12% –OH groups showed restrictive mobility of water initially than the the water in the pristine GS/O_w/GS bilayer systems due to the interactions between the –OH groups and the water molecules. The MSD values of the water molecules within the 20 Å separation of the sheets were of the most interest, because the movement of water while they were still trapped in the nanoconfinement revealed some interesting features, e.g., H-bonds breaking and creation and the creation of clusters of water network. The total MSD of the water molecules were dominated by the Y-component of the MSD, while the X-component was very small. The X-components of the MSD increased initially, but reached somewhat a constant value, indicating that water molecules reached a stable mobility along X-direction (after 4 Å) while the separation continued along the X-direction. When the sheets were separated along the

X-direction, the water molecules could break the H-bonds with the –OH groups, which freed them from the –OH/water coordination shell and escape along the Y-direction, resulting in the greater mobility along the Y-direction. The mobility of the water had direct consequences to the shear traction force and shear interaction energy of the GS/O_w/FGS and FGS/O_w/FGS wet systems, as discussed previously. Increase in the –OH coverage (%) on a sheet in a bilayer FGS systems did not have disadvantage over the pristine GS/O_w/GS systems in terms of MSD values, i.e., did not restrict the mobility of water significantly for the GS/O_w/FGS and FGS/O_w/FGS interfaces.

5.4. Conclusions

The traction-separation behavior of six types of GS/FGS interfaces combined with different coverages of –OH groups and with and without monolayer of water were studied. For the dry interfaces (GS/FGS and FGS/FGS), the increase in –OH coverage (%) decreased the normal traction forces of the bilayers due to the shielding effect of the –OH groups. However, the presence of –OH groups increased the average shear traction forces between the top and bottom sheets, demonstrated uniquely by the stick-slip traction force behavior. The amplitudes of the traction forces remained high for low coverage (2% –OH). The frequency of peaks and valleys of these traction forces (shown in the traction-separation plots) increased with increasing –OH coverage, but the amplitudes decreased because the frequent spatial distributions of the –OH groups led to softer interactions between the –OH groups of the opposite sheets (FGS/FGS systems). The shear traction forces (and fluctuation amplitude) were higher when both the top and bottom sheets were functionalized, while, the response to the normal traction forces remained similar to those of the GS/FGS systems. The above results indicated that the presence of –OH groups on the FGS basal plane decreased the interfacial normal adhesion, significantly increased the interfacial shear adhesion.

The presence of nanoconfined water monolayer significantly reduced the peak shear traction of the functionalized graphene bilayers (for both GS/O_w/FGS and FGS/O_w/FGS), therefore, increasing the lubrication behavior. However, water molecules can increase the lubrication ability during the shear traction-separation more if the –OH groups were present on one sheet instead of both sheets, e.g., the GS/O_w/FGS have more lubrication than the

FGS/O_w/FGS. An increase in –OH coverage (%) did not increase the lubrication ability significantly even when the water molecules were present, as represented by both the wet interfaces. As the –OH coverage (%) increased, the intramolecular H-bonds within the water network decreased, and consequently, the H-bonds between the –OH groups of FGS and the water molecules increased, thus reducing the mobility of water clusters trapped inside the graphene bilayers. However, for high –OH coverage (e.g., 12% –OH), the –OH groups created H-bonds between each other, meanwhile broke the –OH/water H-bonds, thus increased the mobility of water molecules (as shown by the mean squared displacement results). Therefore, the presence of water monolayer between the graphene bilayer systems lubricated the systems by shielding the –OH/–OH interactions but created H-bonds with the –OH groups, resulting in lower shear traction forces compared to the dry interfaces. Depending on the –OH coverage, the water mobility can increase, thus, increasing the lubrication ability of the wet interfaces even more.

CHAPTER 6

INTERFACIAL MECHANICS OF TOBERMORITE 14 Å/GRAPHENE NANOCOMPOSITE

This chapter described the interfacial traction-separation behavior of the T₁₄/FGS nanocomposite at the water-rich (0 0 $\bar{1}$) interface of T₁₄ and the FGS with varying surface coverages of random arrangement of –OH groups. The interfacial strengths and interaction energies of the T₁₄/FGS during normal and shear traction were investigated. The molecular environment at the interfaces e.g., mobility of the interlayer and structural water during shear traction was also studied using the mean squared displacement method, and its (molecular environment) effects on the interfacial strength of T₁₄/FGS was also addressed.

6.1. Overview

The crystalline calcium-silicate-hydrate (C–S–H) or its analogue tobermorite 14 Å (T₁₄) is built with a layered structure where the interlayer (parallel, \parallel , to the water-rich (0 0 $\bar{1}$) plane) is known to be the weakest layer. The structure of this interlayer, i.e., (0 0 $\bar{1}$) plane, is filled with calcium cations and water molecules (known as interlayer water), which guides the stress transfer within the structure (especially along the out-of-plane tensile and shear loadings). In the literature, the calcium cations in the interlayer were reported to be almost immobile (very low diffusion constant) [31, 121-123]. Meanwhile, the water molecules transported through the nanoconfined interlayer space by molecular diffusion mechanism. However, the diffusion constant of this confined interlayer water was still much slower than that of the bulk water [32, 122]. Therefore, the structural and dynamic nature of calcium cations and interlayer water retained the structural homogeneity near the interfaces, and the overall structural disintegration of T₁₄ were caused by the slight bent in the calcium octahedral layers and distortion of the silicate tetrahedral layers. However, when stress was accumulated in the interlayer, this weak layer failed at a faster rate than the structural skeletons of the T₁₄.

In the literature, numerous attempts were undertaken to strengthen the interfaces of different composites using graphene-derivatives (e.g., by using graphene, graphene oxide, carbon

nanotube etc.) [19, 21, 23, 27, 124-129]. The pull-out test on a wrinkled graphene oxide (GO)/polymer composite had reported that the wrinkled geometry enhanced the interfacial stress transfer between the interfaces [127]. In addition to the variability of material (GO) and geometry (wrinkling), the degree of functionalization of GO (functional group coverage) also influenced the interfacial binding characteristics between the GO and polymer interfaces [130]. Similar to the polymers, it was observed that the interfacial stress transfer between C–S–H and GO was also increased by incorporating GO in the C–S–H matrix [109, 131]. GO was suggested to be a potential strengthening material for the C–S–H interfaces because the oxygen-containing functional groups increased the dispersion of GO in cement paste [132], and regulate better microstructure by promoting hydration [33]. The hydrophobicity and hydrophilicity of the C–S–H interfaces near interlayer water and calcium ions also controlled these interfacial properties [133]. It was reported that C–S–H was hydrophilic [119, 134] and the nanoconfined water had multi-characteristics [32, 119]. The bond-slip (shear stress-displacement) relationship of C–S–H/GO interface was observed to be enhanced (because of the interaction of oxygen atoms with C–S–H layers) by embedding GO sheet in the C–S–H matrix [135], agreeing with the previous findings. The hydroxyl (–OH) groups of FGS created strong hydrogen bonds in the C–S–H layers, thus, enhancing the overall mechanical properties by increasing the interfacial strength [25]. It was also reported that the development of three dimensional network of hydrogen bonding among the water molecules and the C–S–H matrix in the nanoconfined spaces between the interfaces played a dominant role in controlling the structure and dynamic properties of water [122]. The strengthening effects of GO came from the nanoconfined water between the GO and C–S–H interfaces, even after drying, due to the hydrophilic nature of GO [33]. Since, the interlayer water in tobermorite was nanoconfined, the structural and dynamic behavior was very different than from the bulk. Understanding the structure and dynamics of nanoconfined water was important because it changed the properties of the entire composite in the macroscale [136]. These phenomena could potentially change the mechanical properties of the T₁₄/FGS nanocomposites near the interfaces, thus modifying the load transfer capability between T₁₄ matrix and FGS.

Therefore, this study focused on the interfacial normal and shear traction-separation behaviors of the T₁₄/FGS nanocomposites to understand the underlying mechanisms of separation characteristics of the T₁₄/FGS interfaces.

6.2. Computational Details

6.2.1. Simulation models and computational cells

Tobermorite 14 Å (T_{14}) structure. The monoclinic T_{14} structure described by Bonaccorsi et al. [120] was used as the model for the structure of crystalline C–S–H in hydrated cement pastes. The T_{14} unit cell consisted of 124 atoms per unit cell with space group symmetry of $B11b$ and had a calcium to silicon (Ca/Si) ratio of 0.833 and lattice parameters: $a = 6.735 \text{ \AA}$, $b = 7.425 \text{ \AA}$, $c = 27.987 \text{ \AA}$, $\alpha = \beta = 90^\circ$, and $\gamma = 123.25^\circ$. The calcium to silicon (Ca/Si) ratio of T_{14} was 0.833. The T_{14} unit cell was replicated $4 \times 4 \times 1$ times in the X-, Y-, and Z-directions to represent supercell consisted of T_{14} structures. The symmetry of the simulation box was changed to $P1$ triclinic symmetry to allow for all the box dimensions and the associated T_{14} structures to change during the MD simulations. Since Bonaccorsi's T_{14} model required the occupancy factor of 0.5 for the interlayer calcium ions and interlayer water molecules, 50% of the interlayer calcium atoms and 50% of the interlayer water molecules were deleted from the T_{14} structure before starting the MD simulations. Therefore, the water molecules of the T_{14} structure were of two types: (1) one which had occupancy factor of 1.0 (structural water, O_w) and (2) another with occupancy factor of 0.50 (mobile water or interlayer water, O_{wd}). The final T_{14} structure had X-, Y-, and Z-dimensions of $26.94 \text{ \AA} \times 27.20 \text{ \AA} \times 28.72 \text{ \AA}$.

FGS structures. The Graphene sheet (GS) and functionalized Graphene sheet (FGS) with five different surface coverages were modeled (2 %, 6 %, 10 %, and 12 %) using the Materials Studio software package. The surface coverage was calculated as the ratio of number of –OH groups to the number of carbon atoms in the FGS basal plane. The zigzag (ZZ) and armchair (AC) edges of graphene were oriented along the Cartesian coordinate system, X [1 0 0] and Y [0 1 0] directions, respectively. The FGS systems were $22 \text{ \AA} \times 28 \text{ \AA}$ in size and consisted of 252 sp^2 bonded carbon (C) atoms in a hexagonal ring pattern and varying coverages of –OH groups. The –OH groups were oriented on the FGS basal plane in two ways: with a random arrangement (R) and zigzag clustered line pattern (ZZ). The C–C, C–O, and O–H bond lengths were 1.39 Å and 1.0 Å, respectively. The $\angle C-C-C$, $\angle C-C-O$, and $\angle C-O-H$ bond-angles were 120° , 109.5° , and 109.5° , respectively. The thickness of the FGS was taken as 3.35 Å.

T_{14} /GS interface models. To construct the T_{14} structures reinforced with FGS with varying surface coverages (T_{14} /FGS nanocomposites), the FGS was placed 4 Å below the

(0 0 $\bar{1}$) planes of the T_{14} systems with the ZZ and AC edges of the FGS oriented along the X- and Y-directions, respectively (Figure 6.1). The –OH groups of the FGS pointed towards the (0 0 $\bar{1}$) plane of the T_{14} . The (0 0 $\bar{1}$) plane was chosen because the interaction of the water molecules with the –OH groups of FGS and the subsequent effects on the interfacial mechanical properties was of importance.

(a) Tobermorite 14 Å (T_{14}) with graphene sheet (GS) **(b)** Tobermorite 14 Å (T_{14}) and functionalized graphene sheet (FGS) with 10% –OH in random arrangement

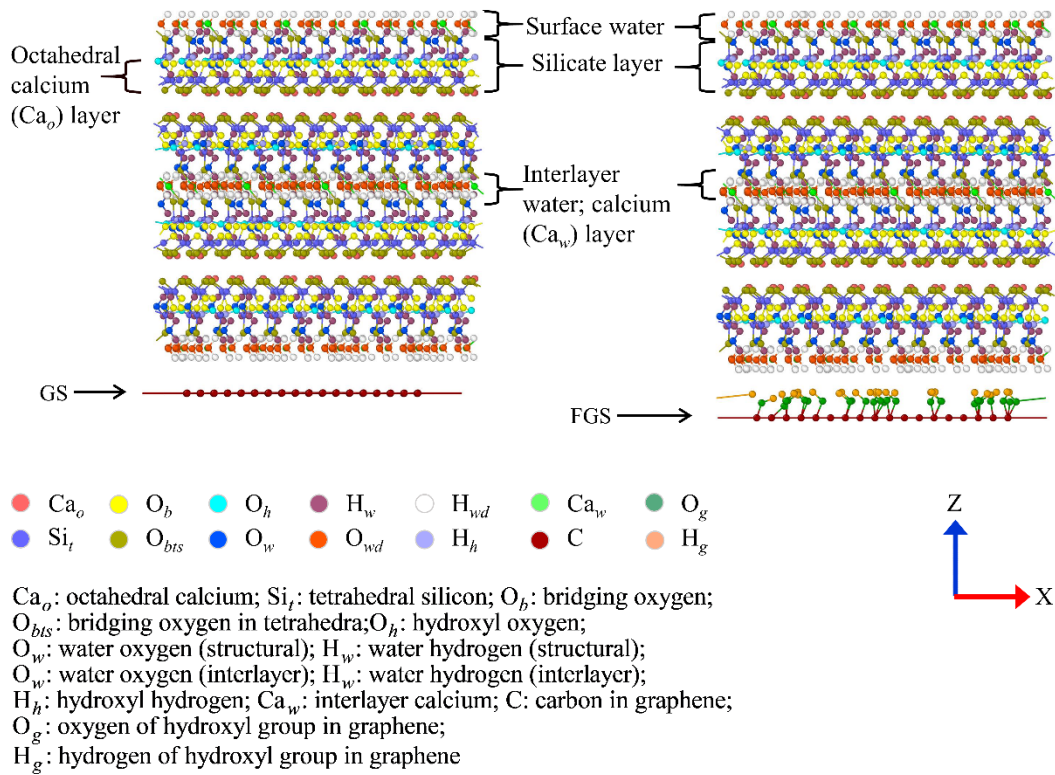


Figure 6.1. Tobermorite 14 Å with the (0 0 $\bar{1}$) interface near (a) GS system and (b) FGS system.

6.2.2. Force field

Force field. The Consistent Valence Force Field (CVFF) was employed for the simulation of the GS [138]. The CVFF has been previously shown to properly represent the tensile and shear properties of graphene and carbon nanotubes [33, 143, 190] and has been used in the study of the interactions of graphitic structures with tobermorite and aqueous solutions

[144, 185]. The C–C bond interaction of the GS was simulated using the Morse potential [141]. The angle bending, torsion, and improper interactions were simulated using the harmonic parameters of the CVFF. The angle bending, torsion, and improper interactions were simulated using the harmonic parameters of the CVFF. The partial atomic charges, non-bonded and bonded interactions among the T₁₄ atoms were simulated using the Clay force field (ClayFF) [184, 186], which relied on the flexibility of coulombic interactions between the interacting atoms to represent bonding. The ClayFF was developed to study the structural and dynamic properties of hydrated and mineral systems [184, 186, 191-193] and has been successfully used to study the mechanical and elastic properties of clay-based minerals and clay-based nanocomposites [193-197]. The interactions among the carbon atoms of the GS and T₁₄ atoms were modeled using the Lennard-Jones (LJ) potential [201]. The values of the CVFF and ClayFF parameters are provided in the Appendix B.

Charge equilibration. The partial atomic charges for the T₁₄ structures were obtained from [184]. For GS, zero charge was assigned to all the carbon atoms (because GS is charge neutral). To keep the FGS charge neutral, partial atomic charges were assigned to the C, O, and H atoms using the built-in QEq charge equilibration method [145] in LAMMPS.

6.2.3. Equilibration

All MD simulations were performed using LAMMPS, an open-source MD simulation software [42]. Three types of traction-separation studies were performed for the T₁₄/FGS systems, (1) normal traction in Z-direction, (2) shear traction in X-direction, and (3) shear traction in Y-direction. During the equilibration, 100 Å thick of vacuums were added to both sides of the nanocomposite in the direction of displacement (making the system non-periodic in that direction), e.g., 100 Å vacuum was placed on top and bottom surfaces of the T₁₄/FGS systems along the Z-direction keeping the X- and Y-directions as periodic for the traction-separation study in the Z-direction. The T₁₄/FGS nanocomposites were energy minimized at 0 K using the conjugate gradient method to reduce the excess pressure build-up during the geometry setup. The T₁₄/FGS nanocomposites were then equilibrated for 500 ps, respectively, at 300 K and 0 atm, using NPT (fixed number of atoms, pressure, and temperature) ensemble conditions. For the system with traction-separation simulation in the *i*-direction, the pressure equilibration was

done on the j - and k -directions. The Nosé-Hoover thermostat and barostat were used for temperature and pressure control of the systems with 100 fs and 1000 fs damping constants, respectively [148, 149]. The neighbor cut-off distance for the interacting atoms was 5 Å, and the neighbor list was updated every timestep. The long-range coulombic interactions were computed in the reciprocal space by the Particle-Particle-Particle-Mesh (PPPM) solver. The short-range coulombic interactions between the interacting atoms were calculated as:

$$\Psi^{\text{coul}} = \frac{1}{4\pi\epsilon_0} \cdot \frac{q_i q_j}{r_{ij}^2} \quad (6.1)$$

where q_i and q_j are charges on atoms i and j , ϵ_0 is the permittivity of the vacuum (8.85419×10^{-12} F/m) and $r_{ij} = |r_i - r_j|$ is the interatomic distance. The short-range van-der-Waals (vdW) interaction was computed by the Lennard-Jones (LJ) potential using:

$$\Psi^{\text{LJ}} = 4\epsilon \left[\left(\frac{\sigma}{r} \right)^{12} - \left(\frac{\sigma}{r} \right)^6 \right] \quad (6.2)$$

where ϵ is the depth of the potential well (kcal mol^{-1}), σ is the distance (Å) at which the potential was zero, and r is the interatomic distance (Å). The Lennard-Jones (LJ) and coulombic cut-off distances were 12 Å and 10 Å, respectively. The interactions between unlike atoms were calculated using the *Lorentz-Berthelot* mixing rules [202, 203]. The time integration was performed using the velocity-Verlet algorithm. All simulations were performed using a 1 fs timestep. Periodic boundary conditions were used in the directions other than the loading directions for all systems.

6.2.4. Traction-separation methods and MD Simulations

In this study, two types of traction-separation simulations i.e., normal and shear, were performed. For the normal traction-separation studies, the local displacements of the atoms at the two opposite boundary layers of atoms of either the GS or FGS were kept fixed. The top layer of T₁₄ with a thickness of 4 Å was also held fixed in space. The rest of the atoms was known as the mobile atoms. The boundary atoms were displaced at a rate of 10^{-5} Å fs⁻¹ in the negative Z-

direction while top layer was constrained in space (Figure 6.2) for the normal traction-separation studies. For the shear separation studies, the GS or FGS was pulled with the right edge of the sheet fixed (3 Å thick layer of atoms) with a displacement rate of 10^{-5} Å fs⁻¹ in the positive X- or Y- directions (Figure 6.2).

(a) Tobermorite 14 Å (T₁₄) and functionalized graphene sheet (FGS) with 10% –OH in random arrangement

(b) Tobermorite 14 Å (T₁₄) and functionalized graphene sheet (FGS) with 10% –OH in random arrangement

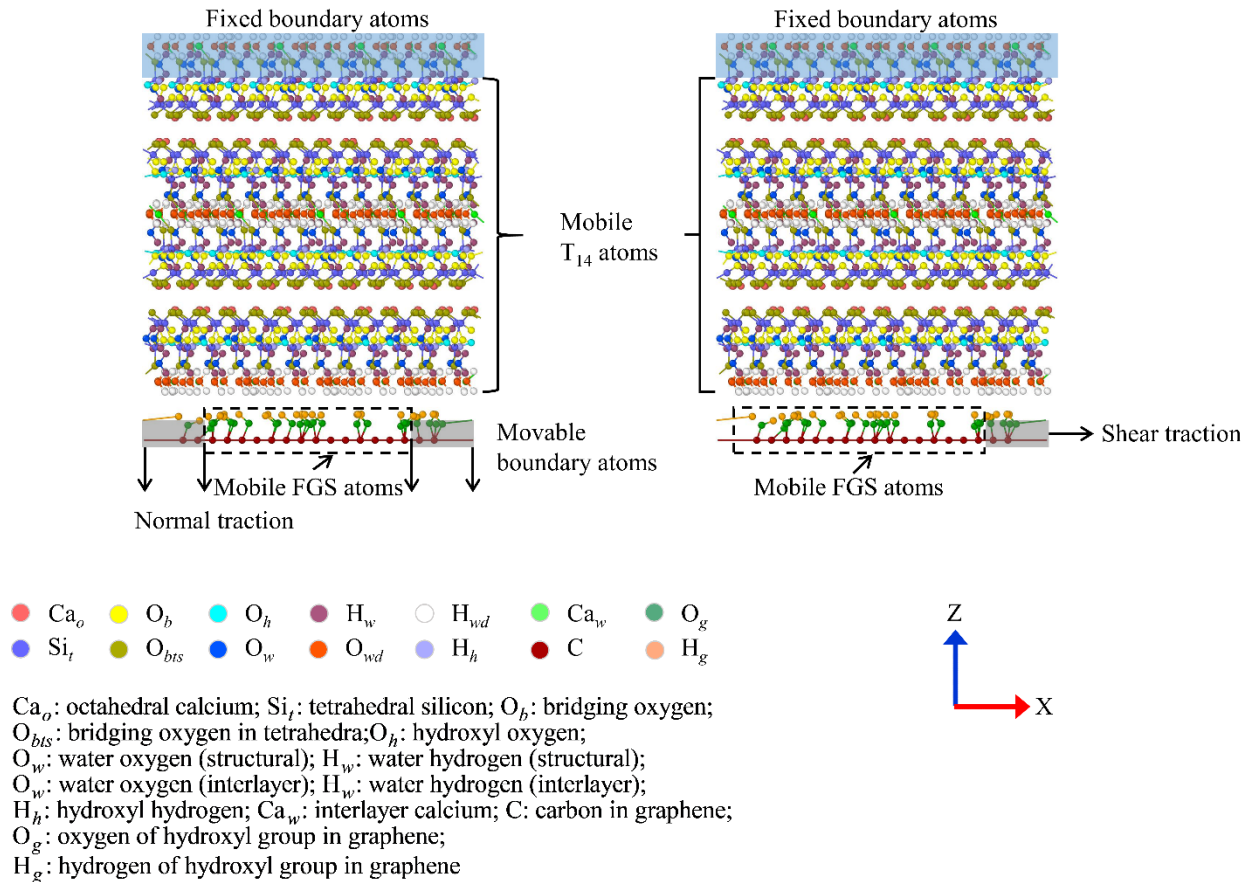


Figure 6.2. A representative T₁₄/FGS nanocomposite with 10 % –OH coverage of FGS was shown for, (a) normal traction-separation and (b) shear traction-separation loading methods.

6.2.5. Data collection and analysis

The force developed on the FGS was calculated from the pair interaction energy (included coulombic and vdW energy) between the FGS and T₁₄. The force developed during the normal separation (δ_n) and shear separation were called normal traction (f_n) and shear traction

(f_s), respectively. The displacement and traction data were time-averaged and collected every 10000 fs simulation run. The normal and shear traction-separation simulations were run for 1.2 ns and 4.0 ns, respectively, which resulted in the relative total displacements of 12 Å and 40 Å, respectively (to ensure zero interaction between the FGS and T_{14}). The normal traction-separation and shear traction-separation curves were calculated and plotted. The normal displacement was calculated from difference of the Z- component of the center-of-mass (COM) of the top layer of the T_{14} to the Z-component of the COM of the FGS (C atoms of the bottom sheet) during the simulation. The X and Y shear displacements were calculated from the X- and Y-components of the COM of the top layers and the COM of the fixed boundary atoms of FGS. The above description of the COM analysis could be expressed as the following,

$$\delta_k = COM_j^{\text{top}} - COM_j^{\text{bottom}} \quad (6.3)$$

where, the direction of traction, $k = (n, s)$ with $n = \text{normal}$ and $s = \text{shear}$, and $j = (Z, X, Y)$, δ_k designated relative displacement of the FGS and T_{14} matrix at every timestep, COM = center-of-mass of the carbon layers of the FGS and top boundary layer of T_{14} .

The interaction energy between the FGS and T_{14} matrix of a T_{14} /FGS nanocomposite was calculated from the following formula:

$$\Delta E_{T_{14}-GS} = E_{T_{14}/FGS} - (E_{T_{14}} + E_{FGS}) \quad (6.4)$$

where, the interaction energy between the T_{14} and FGS system ($\Delta E_{T_{14}-GS}$) was obtained by subtracting the potential energy of the GS (E_{FGS}) and T_{14} ($E_{T_{14}}$) when they were completely separated (theoretically, at infinity distance; for this study, approximately, at 12 Å and 40 Å) from the total potential energy of the T_{14} /FGS at equilibrium ($E_{T_{14}/FGS}$, at zero relative displacement between the T_{14} and FGS). Similar procedure was followed to calculate the interaction energies of all interfaces.

The total mean squared displacement (MSD) of the interlayer and structural water molecules in X-, Y-, and Z-directions were obtained from the equilibrated structures using the microcanonical NVE (N= number of atoms, V=volume, E=energy) ensemble by performing the

simulations for 1 ns. All visualizations were performed using the VMD [180] and OVITO [183] software.

6.3. Results and Discussion

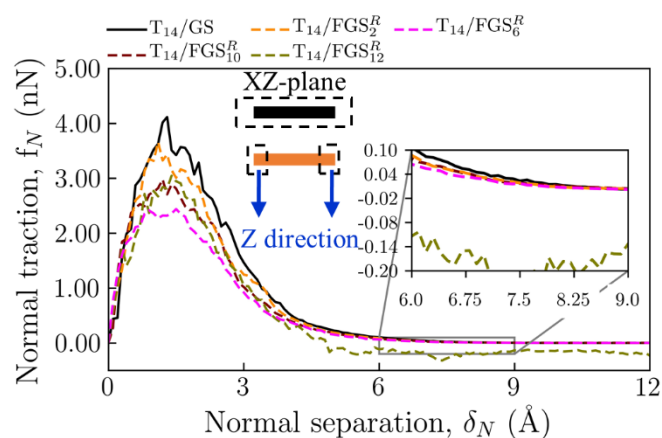
6.3.1. Interfacial strength of T_{14} /FGS interfaces

6.3.1.1. Normal traction-separation behavior

The normal traction-separation response (f_n - δ_n) between the interlayer $(0\ 0\ \bar{1})$ plane of T_{14} and the GS showed a bilinear-type behavior which consisted of two regimes: (1) a hardening regime and (2) a softening regime, similar to that of the GS/GS and FGS/FGS interfaces studied in Chapter 5. The normal traction force (f_n) increased rapidly as the initial separation (δ_n) was provided between the T_{14} and GS interfaces by pulling the GS away from the $(0\ 0\ \bar{1})$ plane of T_{14} . The peak f_n for the T_{14} /GS was much lower than that of GS/GS (4.16 nN vs 23.2 nN, respectively) interface, indicating that it was far easier to separate the T_{14} and GS interfaces via normal force (Figure 6.3) than the GS/GS interface. However, with the incorporation of $-\text{OH}$ groups on the FGS basal plane, the peak f_n between the T_{14} and FGS interfaces decreased slightly when compared with the T_{14} /GS interface. The peak f_n of between T_{14} and FGS interfaces with 2% $-\text{OH}$ was 3.66 nN, a decrease of 12% from that of T_{14} /GS. For 6, 10, and 12% $-\text{OH}$, the peak f_n were 2.43, 2.97, and 3.8 nN, respectively, indicating that the peak f_n between the T_{14} and FGS increased as the $-\text{OH}$ coverage increased (after the initial decrease from the T_{14} /GS interface). The $-\text{OH}$ groups generally increased the distance between the FGS basal plane and the $(0\ 0\ \bar{1})$ plane of the T_{14} , which decreased the interactions between the carbon atoms of FGS and the interfacial atoms (primarily, water molecules and Ca_w cations) of T_{14} in the vicinity of the FGS, therefore, reducing the interfacial strength. However, the reduction in strength for the T_{14} /FGS interfaces was not substantial (e.g., a reduction of 18% for 12% $-\text{OH}$ from GS), very similar to the f_n - δ_n responses captured by the GS/FGS and FGS/FGS interfaces (Chapter 5). The δ_n to reach peak f_n decreased as the $-\text{OH}$ coverage increased, indicating that the $-\text{OH}$ increased the initial stiffness of the T_{14} /FGS interfaces more than the T_{14} /GS interface. The softening regime (after the interfacial strength reached peak strength) demonstrated that the f_n between the T_{14} and GS interface decreased slightly quicker than the f_n between the T_{14} and FGS interfaces, which indicated higher plasticity for the T_{14} /FGS.

The –OH groups were seen to create hydrogen bonds (H-bond) with the interlayer (O_{wd}) and structural water molecules (O_w) of the T_{14} during the f_n - δ_n (Figure 6.4). The internal H-bonds between the water molecules (combining both O_w and O_{wd}) were broken in the process and new H-bonds between the water and –OH groups were created. These mechanisms altered the structural response of T_{14} against normal traction. When the FGS was pulled away from the T_{14} , the interaction between the –OH groups of FGS and T_{14} elongated the T_{14} matrix slightly against the normal force. As the distance between the T_{14} and GS increased, the T_{14} matrix was no longer elongated (i.e., the peak f_n - δ_n was reached), and the FGS was separated from the T_{14} with a minimal increase in force. The range of H-bond distances between water molecules were 1.9 Å to 2.7 Å and the H-bond distances between water and –OH groups of FGS were of a slightly larger range (1.6 Å to 3.2 Å). As the FGS were pulled away from the T_{14} matrix, the intermolecular distances between the O_{wd} and O_g increased and, thus, the $O_{wd} \cdots O_g$ H-bonds (included both the O_{wd} and O_g as donors and acceptors) were broken. It is to be noted that the intermolecular distances between the O_w and O_g also increased, however, the number of O_w at the interlayer was very low because the mobility of O_w was mostly restricted within the T_{14} matrix, not at the interlayer. These free water molecules could create new H-bonds with other water molecules within the T_{14} matrix. This mechanism was mostly observed in the low –OH coverages where there were not enough –OH groups to create stable chains of –OH/water network through H-bonds.

Normal separation along Z



Notation:

T_{14}/FGS_j^R T_{14} = tobermorite 14Å
 FGS = functionalized graphene sheet
 j = -OH coverage (%)
 R = random clustered line pattern of -OH
 [] [] [] [] [] = fixed layers of boundary atoms

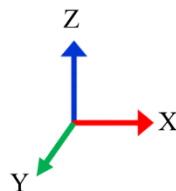
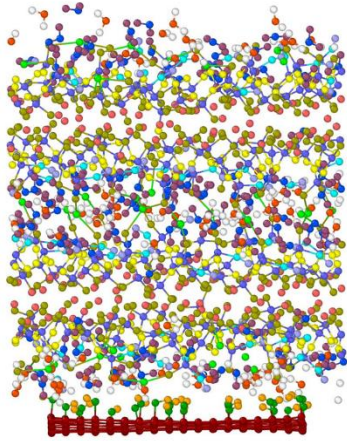
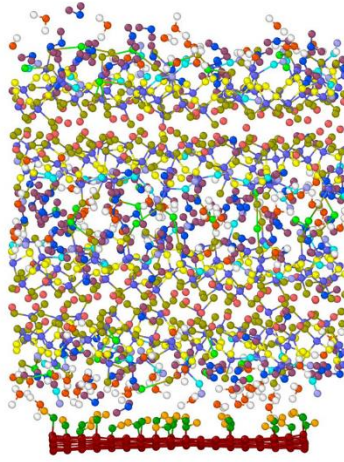


Figure 6.3. Normal traction-separation behavior of the water-rich $(00\bar{1})$ planes of T_{14} and FGS with varying -OH coverages (%).

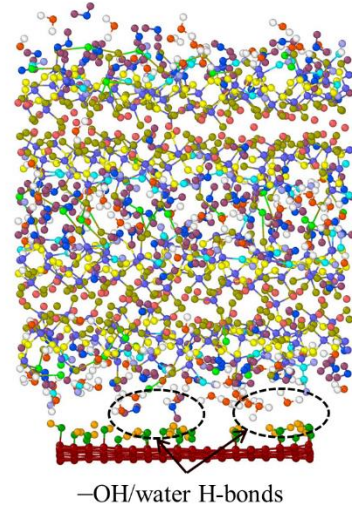
(a) T_{14} /FGS with 10% -OH at equilibrium ($\delta_n = 0$)



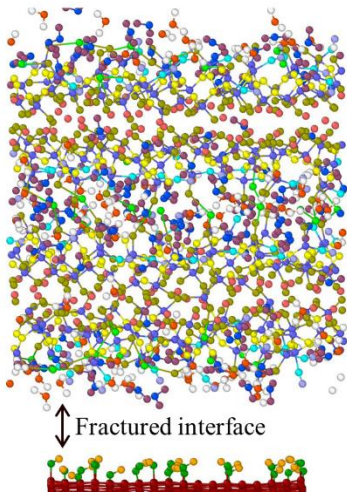
(b) T_{14} /FGS with 10% -OH at hardening regime ($\delta_n = 1 \text{ \AA}$)



(c) T_{14} /FGS with 10% -OH at beginning of softening regime ($\delta_n = 2 \text{ \AA}$)



(d) T_{14} /FGS with 10% -OH near the end of softening regime ($\delta_n = 5 \text{ \AA}$)



Ca_o : octahedral calcium; Si_t : tetrahedral silicon; O_b : bridging oxygen;
 O_{bts} : bridging oxygen in tetrahedra; O_h : hydroxyl oxygen;
 O_w : water oxygen (structural); H_w : water hydrogen (structural);
 O_w : water oxygen (interlayer); H_w : water hydrogen (interlayer);
 H_h : hydroxyl hydrogen; Ca_w : interlayer calcium; C : carbon in graphene;
 O_g : oxygen of hydroxyl group in graphene;
 H_g : hydrogen of hydroxyl group in graphene

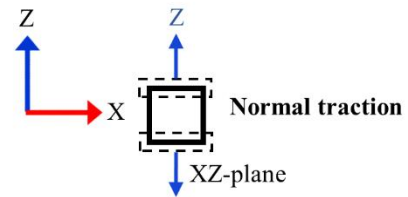


Figure 6.4. Atomistic mechanisms at the T_{14} /FGS interfaces for the T_{14} /FGS nanocomposites with 10% -OH during the normal traction-separation process, (a) at equilibrium, (b) at the hardening regime, (c) at the beginning of the softening regime, and (d) near the end of the softening regime.

6.3.1.2. Shear traction-separation behavior

The shear traction-separation responses (f_s - δ_s) of the T₁₄/FGS interfaces in the X- and Y-directions described the interfacial shear strengths of the T₁₄ and FGS interfaces while the FGS were sheared away against the (0 0 $\bar{1}$) planes of T₁₄ matrices (Figure 6.5). The f_s - δ_s responses of the T₁₄/FGS nanocomposites in both X- and Y-directions showed three distinct regimes: (i) an initial hardening regime, R₁, (ii) a stability regime, R₂, and (iii) a softening regime, R₃.

Shear traction-separation along X-direction. As the FGS was sheared away in the X-direction from the (0 0 $\bar{1}$) plane of T₁₄, there was a substantial resistance against the shearing initially, induced by an increase in the shear traction force (Figure 6.5a). In the R₁ regime, the carbon atoms of GS could interact with all the atoms in the vicinity of GS, thus, increasing the f_s^X . As the GS reached a critical separation, δ_s^X (at ~ 4.5 Å), the f_s^X reached a stable value (~ 0.6 nN), after which the f_s^X continued to fluctuate with a stick-slip type motion as the δ_s^X between the T₁₄ and FGS continued to increase. The T₁₄/GS systems showed stick-slip type of behavior similar to the GS/GS bilayer systems (Chapter 5), possibly because of the interaction of carbon with other atomic species. The crystalline pattern of carbon atoms in the GS and FGS interacted with the other atoms of the T₁₄ via vdW interaction. As the carbon atoms approached and reached near the other atoms, the vdW interaction force increased, and as the carbon atoms moved away from the T₁₄ atoms, the vdW interaction force decreased. This mechanism created a wavy-like pattern in the traction-separation diagram, and was known as stick (approaching)-slip (moving away) behavior. With the increase in -OH coverage, the average f_s^X increased to stable values of ~ 0.8 nN and 0.75 nN for 10% and 12% -OH, respectively. However, the peak f_s^X increased significantly with increase in -OH coverage (e.g., 1.3 nN for 12% FGS vs 0.7 nN for GS). The -OH groups increased the distance between the carbon atoms and the (0 0 $\bar{1}$) plane of T₁₄, which might be responsible for the slight reduction in shear traction away from the peaks. The fluctuation in f_s^X varied significantly as the -OH coverage increased. The -OH groups produced a corrugated type surface on the FGS, which might act as nanoscale rough surface and produced large fluctuation in the f_s^X . As the FGS was sheared further away from the T₁₄, the interaction between the T₁₄ and FGS decreased, which resulted in the end of R₂ regime (at ~ 20

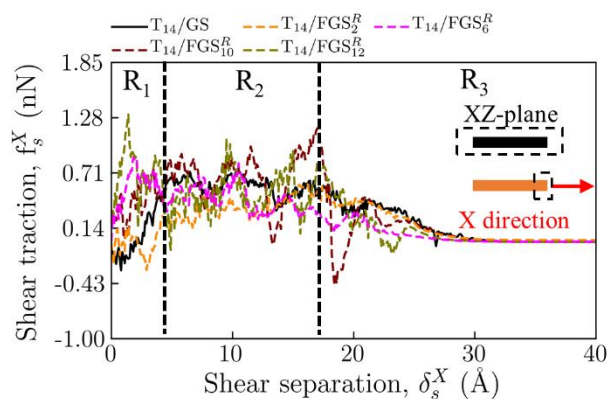
Å, the length of FGS in X-direction) and start of the R₃ regime. In the beginning of the R₃ regime, the FGS was almost separated from the $0\ 0\ \bar{1}$ plane of T₁₄. However, even if the T₁₄ was not physically attached to the FGS, some f_s^X remained, which went to zero at a δ_s^X of ~30 Å.

As the FGS was sheared against the T₁₄, the interface near the vicinity of the FGS became heterogeneous due to the shear force acting on the atoms (Figure 6.6). Further away from the interface, the atoms retained their homogeneity. It could be observed from the Figure 6.6 that, the bottom half of the T₁₄ was continued to be pulled as the FGS sheared away. However, the interfacial strength of the T₁₄/FGS interfaces were lower than that of the interlayer, and, eventually, the fracture occurred through the interface, not through the interlayer. This attribute was also observed in the C–S–H/GO nanocomposite, where the failure also occurred through the interface due to the inherent weakness of the interfacial atomic construction [131]. As the FGS reached near the end of the stability regime, most of the FGS was out of the interaction radius of the T₁₄/FGS, thus, could not contribute to the shear force development. Therefore, the softening regime started, which led to the eventual reduction in strength. The small peak on the $f_s^X - \delta_s^X$ near the beginning of the softening regime was due to the decrease in interaction between the FGS and T₁₄, which led to the release of stress, mirrored by a physical separation of the FGS from T₁₄ (Figure 6.6).

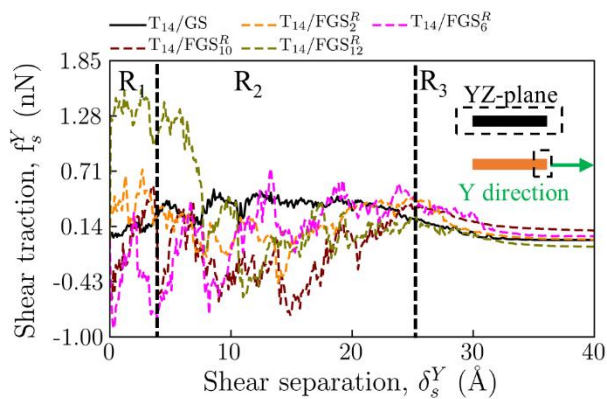
Shear traction-separation along Y-direction. Similar to the traction-separation responses along the X-direction, the T₁₄/FGS interfaces also showed resistance against the shearing initially while the FGS was sheared away in the Y-direction from the $(0\ 0\ \bar{1})$ plane of T₁₄ (Figure 6.5b). However, the increase in shear force f_s^Y for the T₁₄/GS in the Y-direction in the R₁ and R₂ regimes was lower than that in the X-direction. This was attributed to the different type of bonding arrangement of the AC edge (as opposed to the ZZ edge) of GS in the Y-direction. Large fluctuations in the f_s^Y were observed from the $f_s^Y - \delta_s^Y$ responses when the FGS was sheared away from the T₁₄ matrix. For the T₁₄/FGS with 6%, 10%, and 12% –OH, the stick-slip type of f_s^Y responses were seen (just like X-direction) due to the interaction of the –OH and the atomic species of the T₁₄ matrix (attributed to the nanoscale friction and H-bonding mechanisms) while the FGS were sheared along the Y-direction. When the separation δ_s^Y reached critical value

of 26 Å (~ the length of FGS in Y-direction), the f_s^Y reduced due to a loss of interaction between the T₁₄ and FGS. However, at large surface coverages of –OH, some residual stress remained even after the full separation between the FGS and T₁₄.

(a) Shear separation along X (zigzag, ZZ)



(b) Shear separation along Y (armchair, AC)



Notation:

- T_{14}/FGS_j^R T_{14} = tobermorite 14Å
- FGS = functionalized graphene sheet
- j = –OH coverage (%)
- R = random clustered line pattern of –OH
- R₁ = initial regime
- R₂ = stability regime
- R₃ = final regime
- = fixed layer of boundary atoms

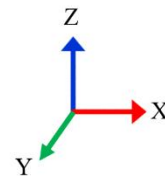
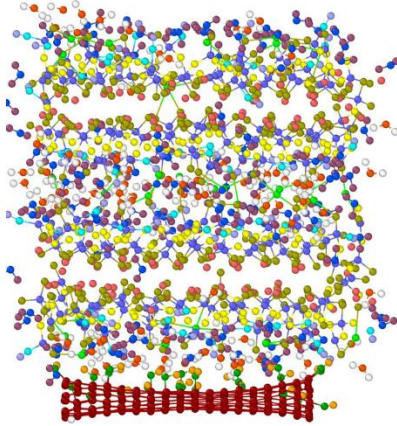


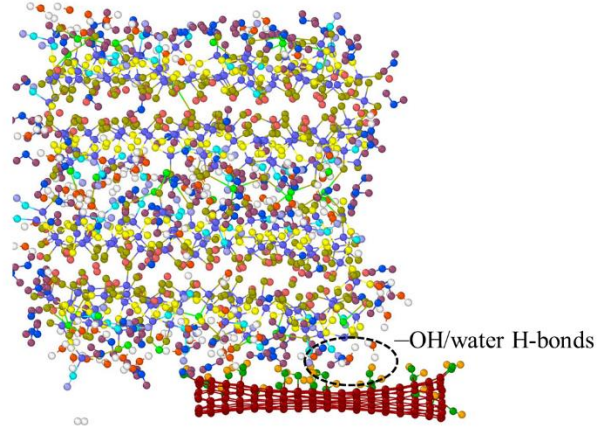
Figure 6.5. Shear traction-separation behavior of the T₁₄/FGS with varying degrees surface coverages of –OH (%) for, (a) along X-directions and (b) along Y-directions.

From the studies of the shear traction-separation responses along the X- and Y-directions, it was evident that the local molecular environments played an important role in modifying the inter- and intra-molecular bonding mechanisms among the different atomic species, consequently controlling the interfacial shear traction forces.

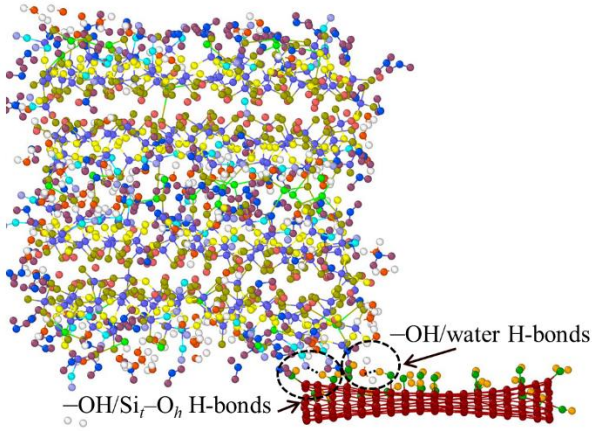
(a) T_{14} /FGS with 10% -OH at equilibrium ($\delta_s = 0$)



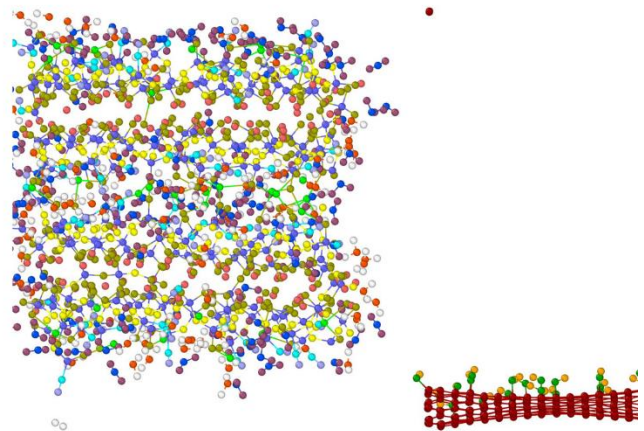
(b) T_{14} /FGS with 10% -OH within stability regime ($\delta_s = 10 \text{ \AA}$)



(c) T_{14} /FGS with 10% -OH near the end of stability regime ($\delta_s = 19 \text{ \AA}$)



(d) T_{14} /FGS with 10% -OH near the end of softening regime ($\delta_s = 30 \text{ \AA}$)



● Ca_o ● O_b ● O_h ● H_w ○ H_{wd} ● Ca_w ● O_g
● Si_t ● O_{bts} ● O_w ● O_{wd} ● H_h ● C ● H_g

Ca_o : octahedral calcium; Si_t : tetrahedral silicon; O_b : bridging oxygen;
 O_{bts} : bridging oxygen in tetrahedra; O_h : hydroxyl oxygen;
 O_w : water oxygen (structural); H_w : water hydrogen (structural);
 O_w : water oxygen (interlayer); H_w : water hydrogen (interlayer);
 H_h : hydroxyl hydrogen; Ca_w : interlayer calcium; C : carbon in graphene;
 O_g : oxygen of hydroxyl group in graphene;
 H_g : hydrogen of hydroxyl group in graphene

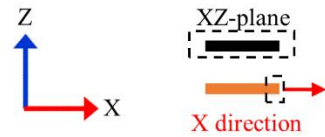


Figure 6.6. Atomistic mechanisms at the T_{14} /FGS interfaces for the T_{14} /FGS nanocomposites with 10% -OH during the shear traction-separation process, (a) at equilibrium, (b) within the stability regime, (c) near the end of the stability regime, and (d) near the end of the softening regime.

6.3.2. Interaction energy of T₁₄/FGS interfaces

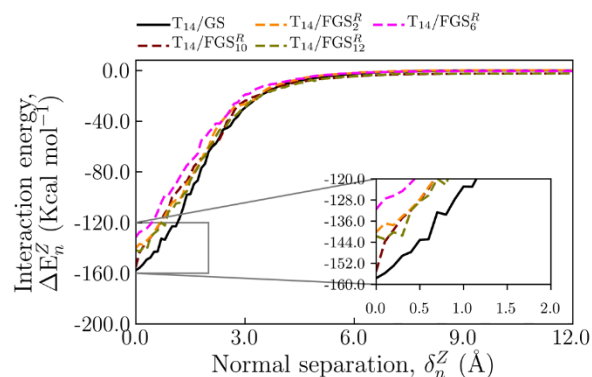
6.3.2.1. Normal traction-separation

The interaction energy for the normal traction-separation (ΔE_n) between the FGS and T₁₄ of the T₁₄/FGS nanocomposites indicated that the energy decreased with the incorporation of –OH groups on the FGS basal plane compared to that of T₁₄/GS (Figure 6.7a). The highest interaction energy was shown by T₁₄/GS (-157 Kcal mol⁻¹), whereas the lowest was from the T₁₄/FGS with 6% –OH (-131 Kcal mol⁻¹). However, the ΔE_n increased for the 10% and 12% –OH (-155 and -141 Kcal mol⁻¹, respectively), indicated that the H-bonding existed at large –OH coverages. It was observed that the overall ΔE_n between the T₁₄ and FGS which included both vdW and coulombic energy, decreased. The reduction in ΔE_n was in agreement with the reduction in f_n also. The ΔE_n between the T₁₄ and FGS also rapidly decreased as the δ_n between the interfaces increased. The curvature of the ΔE_n - δ_n plots (Figure 6.7a) changed at ~ 3 Å separation, after which the rate of ΔE_n decreased. The bend in the ΔE_n mirrored the rapid decrease in the f_n between the T₁₄/FGS interfaces.

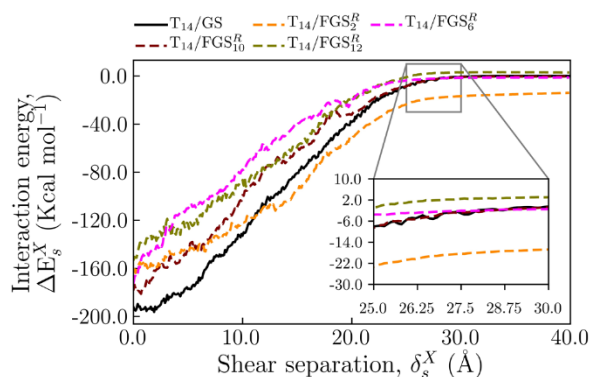
6.3.2.2. Shear traction-separation along X-direction

The shear interaction energy along the X-direction (ΔE_S^X) between the T₁₄ and FGS interfaces was found to be higher compared to the normal interfacial energy (Figure 6.7b). The ΔE_S^X between the T₁₄ and GS was -191 Kcal mol⁻¹, slightly higher than those between the T₁₄ and FGS with 2%, 6%, and 10% –OH coverages (-161, -173, and -178 Kcal mol⁻¹, respectively). Therefore, in all cases, the ΔE_S^X decreased compared to that of T₁₄/GS interfaces. The –OH groups might have higher interaction between the different atomic species of T₁₄ but the increase in distance between the T₁₄ and FGS (caused by the height of –OH groups from the FGS basal plane) resulted in a lower interaction between the carbon atoms of FGS and the T₁₄.

(a) Interaction energy between T₁₄ and FGS during normal separation along Z-direction



(b) Interaction energy between T₁₄ and FGS during shear separation along X-direction



Notation:

T₁₄/FGS_j^R T₁₄ = tobermorite 14Å
 FGS = functionalized graphene sheet
 R = random clustered line pattern of -OH
 j = -OH coverage (%)

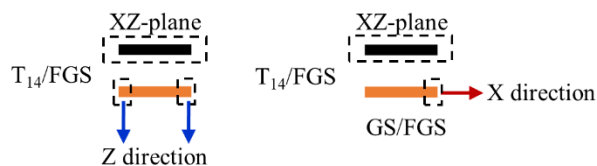


Figure 6.7. Interaction energy between the T₁₄/FGS interfaces for, (a) normal traction-separation in the Z-direction and (b) shear traction-separation in the X-direction.

6.3.3. Equilibrium mean squared displacement of the water molecules

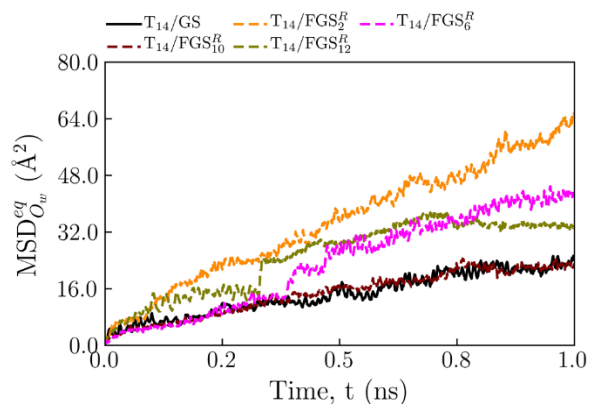
The total mean squared displacement (MSD) of the structural water molecules (O_w) of T₁₄/FGS nanocomposites with 10% -OH had similar response as the O_w in T₁₄/GS (Figure 6.8). The T₁₄/FGS with 2% -OH showed the highest MSD at equilibrium, followed by that of the T₁₄/FGS with 6% -OH. The presence of -OH disrupted the internal H-bond network and surface chemistry near the $(00\bar{1})$ interface of T₁₄. As the -OH coverage increased, the MSD values decreased, indicating the restriction on the mobility of water molecules, possibly because of the increase in the number of $O_g \cdots O_w$ H-bonds.

The mobility of interlayer water, O_{wd} for T₁₄/GS was almost twice that of structural water of the T₁₄/GS. The structural water molecules were restricted because of the H-bonds created between the O_w and O_{bts} , O_b , O_{wd} , and O_h atoms of T₁₄. Therefore, structural water had higher probability of possessing lower mobility than the mobility of interlayer water. Interlayer water molecules played more direct role in modulating the interfacial mechanical properties at the interfaces of T₁₄ and FGS. The presence of -OH groups (2%, 6%, and 10%) showed more

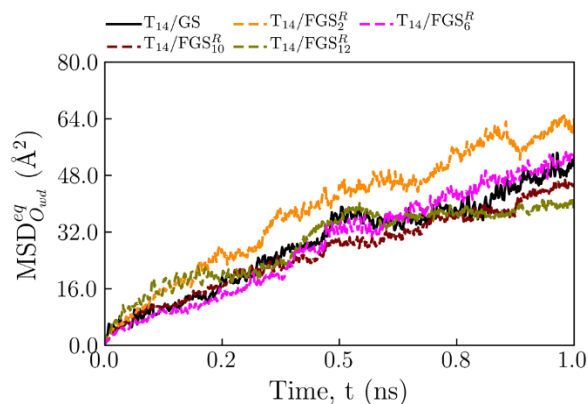
mobility of interlayer and structural water along the Y-direction compared to the X- and Z-directions (Figure 6.9 and Figure 6.10). Interestingly, for 2% –OH, the mobility of interlayer water along the Z-direction was lower than that of the structural water (Figure 6.9 and Figure 6.10), indicating that the interlayer water molecules were more susceptible to the caging effect (trapping of water molecules by H-bonds between water and –OH groups in a cage-like situation) induced by the –OH groups. For the T₁₄/FGS with 10% –OH, the H-bond networks restricted the mobility of water molecules such that the slope of MSD became nearly zero within 0.5 ns – 1.0 ns. For this system, the restriction in the X-direction was significant enough to be similar to that of the GS.

It was evident that both the structural and interlayer water in the presence of –OH groups (T₁₄/FGS) had higher mobility compared to those with no –OH present (T₁₄/GS). The –OH groups increased the distance between the GS and the water molecules by adding height to the GS. Therefore, the interaction between the carbon atoms and water molecules were hindered. Meanwhile, the sporadically created H-bonds between the O_g and O_w disrupted the H-bond network of water in the T₁₄ matrix, thus freeing the water molecules, and increasing the mobility. These two mechanisms played the prominent role in increasing the mobility of water. However, as the –OH coverage increased, the number of H-bond between the O_g and O_w increased and formed a stable O_g···O_w H-bond network, which in turn, decreased the mobility of O_w due to the caging effect, therefore, increasing molecular friction, and interfacial shear traction. The modulation of interfacial strength by creation of H-bond network between the GO and interlayer water of C–S–H were observed elsewhere [109, 243]. Therefore, the MSD of the water molecules was attributed to maintain direct role in modulating the interfacial strength of the T₁₄/FGS interfaces because of this complex interplay of H-bond networks.

(a) Equilibrium mean squared displacement (MSD) of structural water



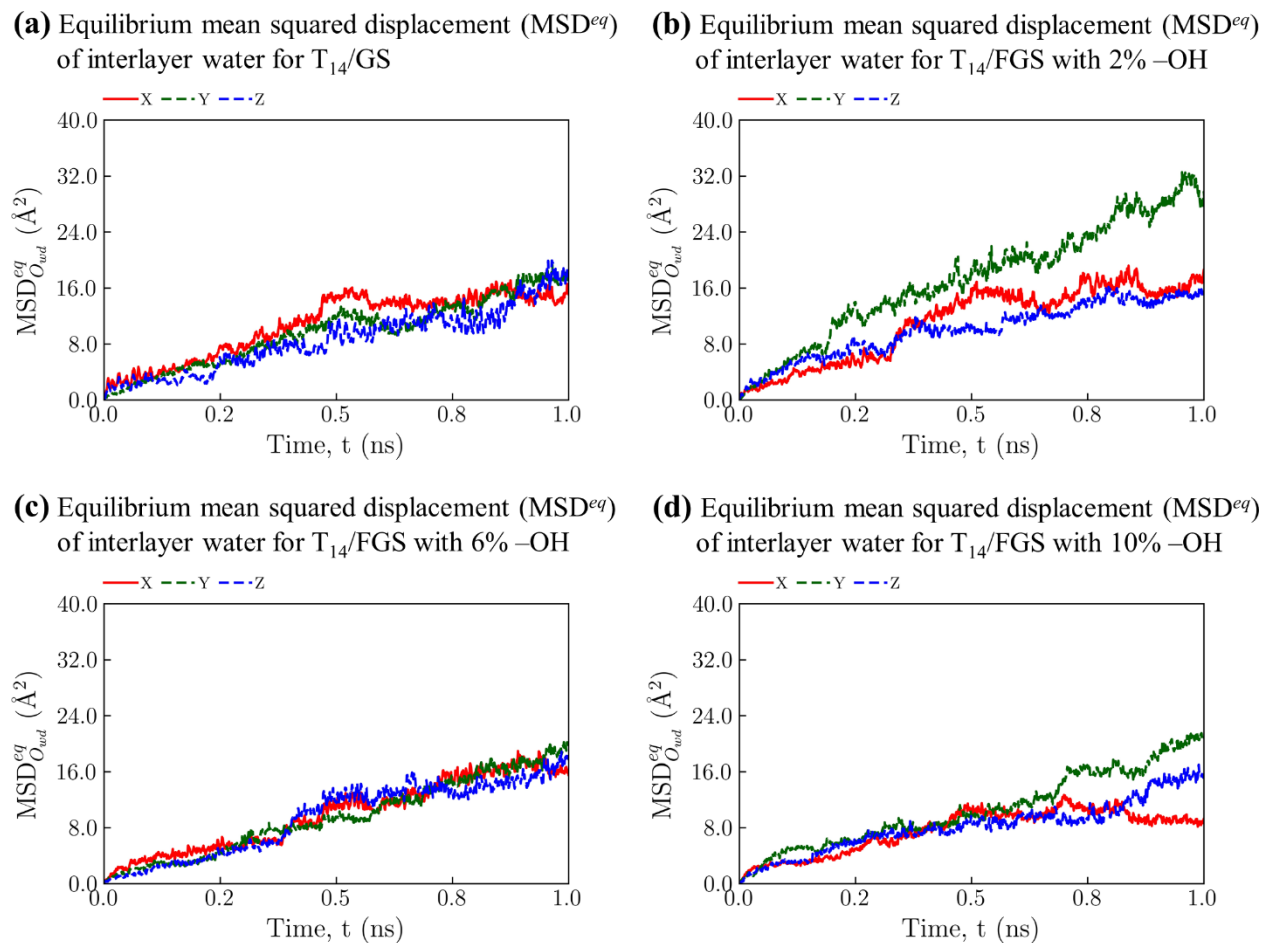
(b) Equilibrium mean squared displacement (MSD) of interlayer water



Notation:

T_{14}/FGS_j^R T_{14} = tobermorite 14Å
 FGS = functionalized graphene sheet
 R = random clustered line pattern of -OH
 j = -OH coverage (%)
 O_w structural water
 O_{wd} interlayer water

Figure 6.8. Mean squared displacement (MSD) of water molecules in the T_{14}/FGS systems: (a) structural water (O_w) and (b) interlayer water (O_{wd}).



Notation:

T_{14}/FGS_j^R T_{14} = tobermorite 14\AA
 FGS = functionalized graphene sheet
 R = random clustered line pattern of $-OH$
 j = $-OH$ coverage (%)
 O_{wd} interlayer water

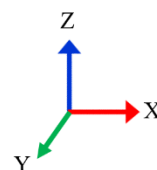
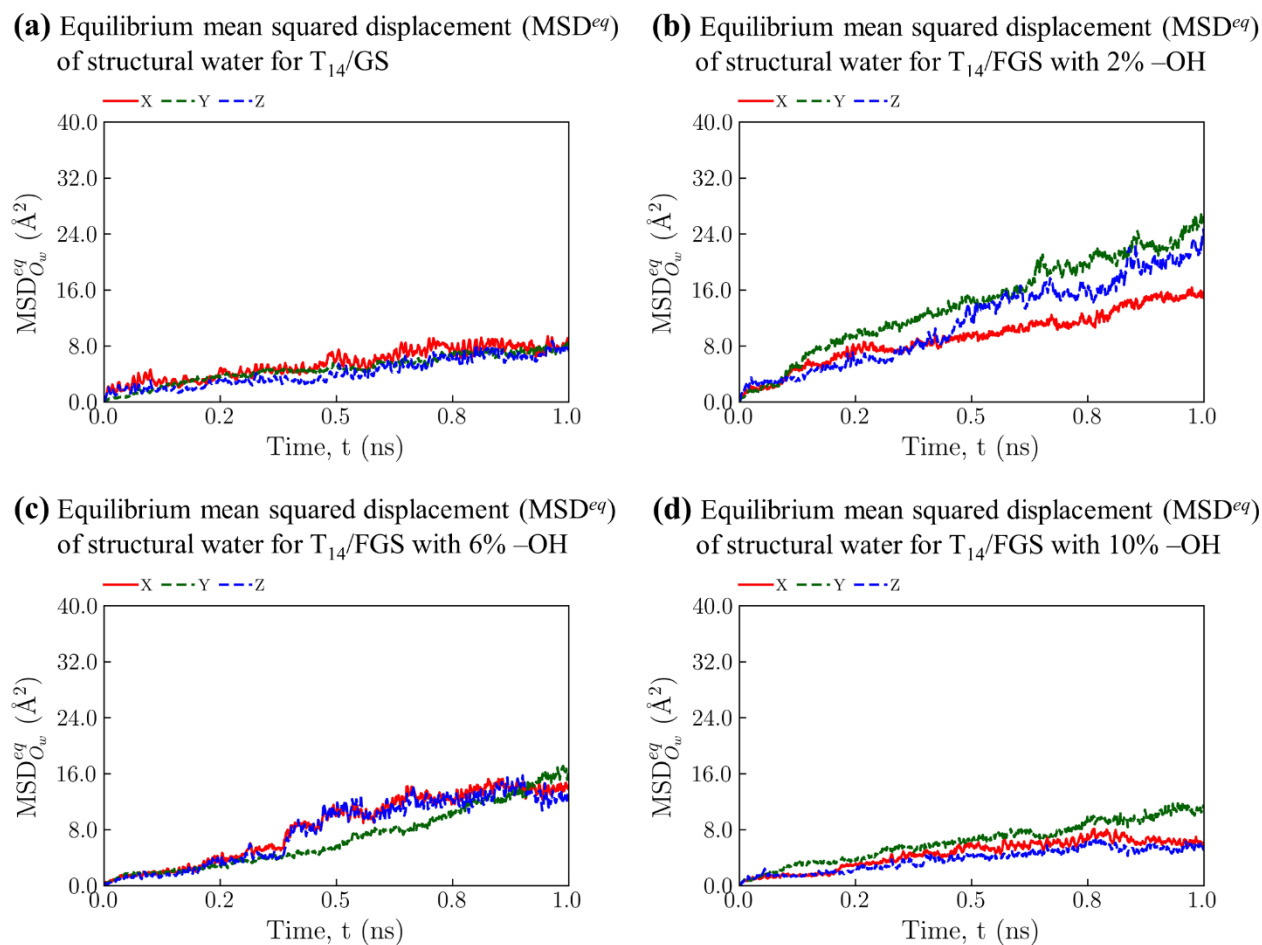


Figure 6.9. Mean squared displacement (MSD) of interlayer water molecules (O_{wd}) of the T_{14}/FGS systems in the X-, Y-, and Z-directions for, (a) 0% $-OH$ (T_{14}/GS), (b) 2% $-OH$, (c) 6% $-OH$, and (d) 10% $-OH$.



Notation:

T_{14}/FGS_j^R T_{14} = tobermorite 14Å
 FGS = functionalized graphene sheet
 R = random clustered line pattern of -OH
 j = -OH coverage (%)
 O_w structural water

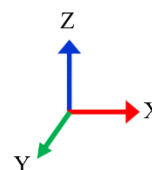


Figure 6.10. Mean squared displacement (MSD) of structural water molecules (O_w) of the T_{14}/FGS systems in the X-, Y-, and Z-directions for, (a) 0% -OH i.e., T_{14}/GS , (b) 2% -OH, (c) 6% -OH, and (d) 10% -OH.

6.4. Conclusions

Interfacial strengths of the T_{14} and FGS interfaces (FGS with 2%, 6%, 10%, and 12% -OH coverages) were evaluated via classical MD simulations. The normal interfacial strength of the T_{14}/GS nanocomposite was the highest among all the other systems. The -OH groups increased the distance between the T_{14} and FGS interfaces, thus, reducing direct interaction

between the FGS and nearby atoms of T₁₄ which resulted in a lower normal interfacial strength (indicated as the peak strength). Therefore, the normal interfacial strengths were seen to decrease as –OH coverage increase. However, the –OH groups were seen to increase the interaction in the softening portion of the traction-separation curves, thus increasing plasticity of the interfaces slightly during the normal separation.

For shear separation, the T₁₄/GS nanocomposites showed highest peak strength initially. However, the –OH groups increased the average shear interfacial strength when large –OH coverages were used. The shear strength of the T₁₄/GS s nanocomposites showed the well-known stick-slip behavior of interacting carbon atoms. Because of the –OH groups, the stick-slip traction response between the T₁₄/FGS interfaces was more erratic than that of the GS/FGS interfaces. However, the stick-slip behavior was the consequence of a significant physical interaction between the –OH groups and other chemical species near the interfaces (e.g., water molecules). As the –OH coverage increased, the fluctuation in the shear traction with separation reduced, and the overall shear strength during the separation increased.

The interfacial strengths of the T₁₄/FGS nanocomposites were modulated due to the alteration of the surface chemistries near the T₁₄ and FGS interfaces. The –OH groups disrupted and altered the H-bond network system near the interfaces. At low –OH coverages, the –OH groups broke the H-bond between the water molecules, thus freeing the water, and increasing the mobility. At large –OH coverages, –OH groups formed a stable network of H-bonds with the other water molecules, thus decreasing the mobility of water molecules by effectively trapping the water molecules in a cage-like situation (i.e., caging effect). This mechanism increased the molecular friction near the interfaces, which resulted in higher shear interfacial strength near the T₁₄ and FGS interfaces.

CHAPTER 7

CONCLUSIONS AND FUTURE RESEARCH DIRECTIONS

A summary of the main conclusions from the chapters of this dissertation is provided in the following. The research provides insights into the molecular mechanisms at the interface of tobermorite and GS systems via molecular dynamics simulations and reveals the effects of surface coverage, clustered line pattern arrangement of hydroxyl functionalization, and loading directions on the mechanical properties of graphene-reinforced tobermorite nanocomposites.

Chapter 3. The out-of-plane deformation induced by –OH line pattern functionalization affected the mechanical behavior of the GS and modulated the stress-strain responses depending on the level and arrangement of –OH functionalization and the direction of the applied load with respect to the line pattern arrangements. The strong elastic and shear anisotropy of the FGS seen for the clustered –OH line pattern arrangements were intrinsic to the initial functionalization induced bending deformation with the direction of the curvature representing the “breathing” mode of deformation (expansion and contraction) of the FGS. The FGS with clustered line pattern arrangements acted similar to a nanoscale mechanical spring with an increased stiffness in the direction parallel to the line patterns and increased linear compressibility and fracture tensile strain in the direction perpendicular to the line patterns. Additionally, clustered line pattern functionalization was demonstrated to provide a route to convert graphene to a material with auxetic characteristics at ambient conditions. It was found that the Poisson’s ratio can be tuned from positive to near zero and negative values through line pattern arrangements. The orientation dependence of the longitudinal sound wave velocity with line pattern functionalization was also demonstrated with faster longitudinal wave propagations along the zigzag direction when the line patterns were oriented along the zigzag direction and slower when the line patterns were along the armchair direction. This study indicated that clustered line pattern functionalization could be a valuable approach for tuning the mechanical properties of graphene and develop engineered graphene derivatives.

Chapter 4. The geometrical assembly of the GS in the tobermorite 9 Å (T₉) matrix and the orientation of the edge of the GS modulated the in-plane (XY) tensile and shear strength, in-

plane stiffness, and strain energy density of the T₉/GS nanolaminates. The in-plane strength of the stacked nanolaminate was higher than that of the hierarchical nanolaminate due to the bundle effect provided by the stacked assembly of GSs, i.e. effect of the lower number of T₉/GS interfaces (two for T₉/GS^{3S} vs. six for T₉/GS^{3H}) and higher number of GS/GS interfaces (two for T₉/GS^{3S} vs. none for T₉/GS^{3H}), where the GS/GS interface was found to be stronger than the T₉/GS interface. In contrast, the in-plane shear strength and out-of-plane stiffness were found to be generally insensitive to the geometrical assembly of GSs in the T₉ matrix. Despite the relative differences in mechanical properties between the T₉/GS^{3H} and the T₉/GS^{3S}, the properties of both nanolaminates improved substantially compared to the pristine T₉, suggesting that both arrangements were viable options to improve the in-plane mechanical properties.

The orientation of the edge of the GS and the surface chemistry and structure of tobermorite 14 Å (T₁₄) interfaced with the GS controlled the in-plane (XY) tensile and shear strengths, stiffness, strain energy density, and directional anisotropy of elasticity of the T₁₄/GS nanocomposites. In-plane fracture tensile and shear strengths of the reinforced nanocomposites that were 180% to 360% and 90% to 225% greater, respectively, than those of the tobermorite 14 Å-based structures without the graphene sheet reinforcement as well as intrinsic in-plane elastic moduli that were twice that of the pristine structures could be realized. The GS exhibited more apparent in-plane strengthening effect when interfacing with water than with either of the solid surfaces (i.e., calcium or silicate surfaces). The confined water molecules interfacing with the GS promoted surface friction during tensile and shear loading, thus leading to a greater fracture tensile strength and faster rate of shear strength development. In contrast, the GS decreased the out-of-plane tensile strength, stiffness, and bulk modulus of the T₁₄-based structures because of the weak interaction of the GS with the structures.

Hydroxyl functionalization of the GS with –OH groups in either a random arrangement or a clustered line pattern arrangement along the ZZ direction of the graphene lattice (i.e., ZZ clustered line pattern) reduced the in-plane (XY) tensile and shear strengths of the T₁₄/FGS nanocomposites relative to the T₁₄/GS nanocomposites (without functionalization of the GS) but increased the in-plane tensile and shear strengths relative to the pristine T₁₄ matrix. The FGSs with a random arrangement of –OH groups with high coverages (50%, 75% and 100%) substantially increased the out-of-plane tensile strength (Z-direction) and ductility of the T₁₄

matrix by transitioning the fracture mechanisms from interface-dominated to interlayer-dominated. Similarly, at low –OH coverages (e.g., 25%), the FGSs with a ZZ clustered line pattern arrangement of –OH groups increased the out-of-plane tensile strength due to the low bending curvature of the GS, which provided enough contact area between the –OH groups and the interfacial atoms of the T₁₄ matrix. In contrast, at high –OH coverages of the FGSs with a ZZ clustered line pattern arrangement, the fracture mechanism became interface-dominated because of the lower T₁₄/FGS contact area (i.e. caused by higher bending curvature of the GS). The ZZ clustered line pattern arrangement of –OH groups also modulated the directional elasticity of the T₁₄/FGS nanocomposites parallel (l) to the direction of the line patterns. While the random arrangements of the –OH groups are better where isotropic in-plane and out-of-plane strength is required (e.g., nanocomposites), the ZZ clustered line pattern is better suited where directionality of the mechanical property is the priority (e.g., sensors).

Chapter 5. The presence of –OH functionalization on one or both sheets of graphene bilayer systems decreased the interfacial normal adhesion due to the shielding effect of the –OH groups while significantly increased the average interfacial shear adhesion, thus reducing the lubrication ability of graphene bilayers. The presence of water monolayer in between the graphene sheets of the bilayer systems reduced the interfacial shear adhesion. The water molecules shielded the interactions between the –OH groups and the carbon atoms of the GS (GS/FGS interfaces) and between the –OH groups from opposite GSs (FGS/FGS systems), thus decreasing the molecular friction and thereby increasing the lubrication ability during shear traction as a result of the complex interactions between the water molecules and the –OH groups. While the dry bilayers would perform better in a nanocomposite matrix than the wet bilayers due to their higher interfacial shear strength, the results suggested that the presence of water monolayer confined into the bilayers can modulate the molecular friction, which could prove to be important for exfoliating graphene membranes and nanotribology applications.

Chapter 6. The presence of –OH functionalization on the GS reduced the normal strength (adhesion) of the T₁₄/GS interface by shielding the FGS from the T₁₄ matrix (i.e., increased distance between the carbon atoms of the FGS and atoms of the T₁₄ matrix compared to the GS without –OH functionalization) while increased the plasticity of the interface as seen from the softening portion of the traction-separation curves. In contrast, functionalization with random

arrangement of the –OH groups (10% surface coverage and higher) increased the shear traction strength of the T₁₄/GS interface compared to without functionalization, as a result of molecular friction through –OH/water hydrogen bonding mechanisms. Results from this chapter provide insights into the fundamental molecular mechanisms of interfacial strengthening via hydroxyl functionalization, which are important for the development of composite materials with superior mechanical properties, high adhesive coatings, and better exfoliation methods.

Future work: This work had led to the following future research questions and directions:

- 2D materials research.
 - Can other functional groups (e.g., –COOH, CH₃, –C=O, etc.) in clustered line patterns modulate the mechanical properties of graphene?
 - Can these functional groups also modulate the mechanical properties of other 2D materials (MoS₂, hBN, borofin, etc.)?
- Geometry-driven tobermorite/2D material nanolaminates.
 - What implications would occur if graphene was incorporated in the tobermorite matrix at different angles?
 - Will hydroxyl functionalization in random and clustered line patterns on both sides of the graphene sheet affect the mechanical properties of the nanolaminates?
 - Will other 2D materials modulate the mechanical properties of the tobermorite-based nanolaminates?
- Modulation of surface chemistry and structure of tobermorite and 2D materials.
 - Will the hydroxyl or other types of functionalization at the surface of the 2D materials alter the chemical environment near the calcium and silicate interfaces of tobermorite and modulate the mechanical properties of the nanocomposite?
 - How different will the molecular mechanisms be if a realistic model of C–S–H is used as the base matrix with 2D materials as reinforcement?
 - How the mechanical properties will be affected if 2D materials with patterned functionalization are used near the tobermorite or C–S–H interfaces?
- Interfacial strength between tobermorite and 2D materials.

- Will hydroxyl or other types of functionalization enhance or decrease the interfacial strength between tobermorite with silicate and calcium surfaces and graphene sheet?
- If functionalized graphene sheets were embedded in the tobermorite matrix with both side of the sheets attached with functionalization, how much alteration will occur in the chemical environment of tobermorite/graphene interfaces and in modulation of the mechanical properties of the nanocomposites?

REFERENCES

- [1] He, Z., Shen, A., Guo, Y., Lyu, Z., Li, D., Qin, X., Zhao, M., and Wang, Z., 2019. Cement-based materials modified with superabsorbent polymers: A review. *Construction and Building Materials*, **225** pp. 569-590.
- [2] Hou, D., Zhang, J., Li, Z., and Zhu, Y., 2015. Uniaxial tension study of calcium silicate hydrate (C–S–H): structure, dynamics and mechanical properties. *Materials and Structures*, **48(11)**, pp. 3811-3824.
- [3] Hou, D., Zhao, T., Jin, Z., Ma, H., and Li, Z., 2015. Molecular Simulation of Calcium Silicate Composites: Structure, Dynamics, and Mechanical Properties. *Journal of the American Ceramic Society*, **98(3)**, pp. 758-769.
- [4] Hou, D., Zhu, Y., Lu, Y., and Li, Z., 2014. Mechanical properties of calcium silicate hydrate (C–S–H) at nano-scale: A molecular dynamics study. *Materials Chemistry and Physics*, **146(3)**, pp. 503-511.
- [5] Jiang, J., Yan, Y., Hou, D., and Yu, J., 2018. Understanding the deformation mechanism and mechanical characteristics of cementitious mineral analogues from first principles and reactive force field molecular dynamics. *Physical Chemistry Chemical Physics*, **20(20)**, pp. 13920-13933.
- [6] Tao, L. and Shahsavari, R., 2017. Diffusive, Displacive Deformations and Local Phase Transformation Govern the Mechanics of Layered Crystals: The Case Study of Tobermorite. *Scientific Reports*, **7(1)**, pp. 5907.
- [7] Pei, Q. X., Zhang, Y. W., and Shenoy, V. B., 2010. A molecular dynamics study of the mechanical properties of hydrogen functionalized graphene. *Carbon*, **48(3)**, pp. 898-904.
- [8] Pei, Q. X., Zhang, Y. W., and Shenoy, V. B., 2010. Mechanical properties of methyl functionalized graphene: a molecular dynamics study. *Nanotechnology*, **21(11)**, pp. 115709.
- [9] Li, Y., Datta, D., Li, Z., and Shenoy, V. B., 2014. Mechanical properties of hydrogen functionalized graphene allotropes. *Computational Materials Science*, **83** pp. 212-216.
- [10] Qing-Xiang, P., Yong-Wei, Z., and Vivek, B. S., 2010. Mechanical properties of methyl functionalized graphene: a molecular dynamics study. *Nanotechnology*, **21(11)**, pp. 115709.
- [11] Yuan, J., Ma, L.-P., Pei, S., Du, J., Su, Y., Ren, W., and Cheng, H.-M., 2013. Tuning the Electrical and Optical Properties of Graphene by Ozone Treatment for Patterning Monolithic Transparent Electrodes. *ACS Nano*, **7(5)**, pp. 4233-4241.
- [12] Ng, S.-W., Noor, N., and Zheng, Z., 2018. Graphene-based two-dimensional Janus materials. *NPG Asia Materials*, **10(4)**, pp. 217-237.
- [13] Galashev, A. E. and Rakhmanova, O. R., 2014. Mechanical and thermal stability of graphene and graphene-based materials. *Physics-Uspekhi*, **57(10)**, pp. 970.
- [14] Lee, B., Chen, Y., Duerr, F., Mastrogiovanni, D., Garfunkel, E., Andrei, E. Y., and Podzorov, V., 2010. Modification of Electronic Properties of Graphene with Self-Assembled Monolayers. *Nano Letters*, **10(7)**, pp. 2427-2432.
- [15] Bharech, S. and Kumar, R., 2015. A Review on the Properties and Applications of Graphene. *Journal of Material Science and Mechanical Engineering (JMSME)*, **2** pp. 70-73.

- [16] Geim, A. K. and Grigorieva, I. V., 2013. Van der Waals heterostructures. *Nature*, **499** pp. 419.
- [17] Li, C., Zhou, P., and Zhang, D. W., 2017. Devices and applications of van der Waals heterostructures. *Journal of Semiconductors*, **38**(3), pp. 031005.
- [18] Hajgató, B., Güryel, S., Dauphin, Y., Blairon, J.-M., Miltner, H. E., Van Lier, G., De Proft, F., and Geerlings, P., 2013. Out-of-plane shear and out-of plane Young's modulus of double-layer graphene. *Chemical Physics Letters*, **564** pp. 37-40.
- [19] Ramanathan, T., Abdala, A. A., Stankovich, S., Dikin, D. A., Herrera-Alonso, M., Piner, R. D., Adamson, D. H., Schniepp, H. C., Chen, X., Ruoff, R. S., Nguyen, S. T., Aksay, I. A., Prud'Homme, R. K., and Brinson, L. C., 2008. Functionalized graphene sheets for polymer nanocomposites. *Nature Nanotechnology*, **3** pp. 327.
- [20] Jin, Y., Duan, F., and Mu, X., 2016. Functionalization enhancement on interfacial shear strength between graphene and polyethylene. *Applied Surface Science*, **387** pp. 1100-1109.
- [21] Li, Y., Wang, S., and Wang, Q., 2017. Enhancement of tribological properties of polymer composites reinforced by functionalized graphene. *Composites Part B: Engineering*, **120** pp. 83-91.
- [22] Skountzos, E. N., Anastassiou, A., Mavrantzas, V. G., and Theodorou, D. N., 2014. Determination of the Mechanical Properties of a Poly(methyl methacrylate) Nanocomposite with Functionalized Graphene Sheets through Detailed Atomistic Simulations. *Macromolecules*, **47**(22), pp. 8072-8088.
- [23] Wang, X., Tan, D., Chu, Z., Chen, L., Chen, X., Zhao, J., and Chen, G., 2016. Mechanical properties of polymer composites reinforced by functionalized graphene prepared via direct exfoliation of graphite flakes in styrene. *RSC Advances*, **6**(113), pp. 112486-112492.
- [24] Pan, L., Ban, J., Lu, S., Chen, G., Yang, J., Luo, Q., Wu, L., and Yu, J., 2015. Improving thermal and mechanical properties of epoxy composites by using functionalized graphene. *RSC Advances*, **5**(74), pp. 60596-60607.
- [25] Hou, D., Yang, T., Tang, J., and Li, S., 2018. Reactive force-field molecular dynamics study on graphene oxide reinforced cement composite: functional group de-protonation, interfacial bonding and strengthening mechanism. *Physical Chemistry Chemical Physics*, **20**(13), pp. 8773-8789.
- [26] Melro, L. S., Pyrz, R., and Jensen, L. R., 2016. A molecular dynamics study on the interaction between epoxy and functionalized graphene sheets. *IOP Conference Series: Materials Science and Engineering*, **139**(1), pp. 012036.
- [27] Zhang, J. and Jiang, D., 2014. Molecular dynamics simulation of mechanical performance of graphene/graphene oxide paper based polymer composites. *Carbon*, **67** pp. 784-791.
- [28] Bonnaud, P. A., Manzano, H., Miura, R., Suzuki, A., Miyamoto, N., Hatakeyama, N., and Miyamoto, A., 2016. Temperature Dependence of Nanoconfined Water Properties: Application to Cementitious Materials. *The Journal of Physical Chemistry C*, **120**(21), pp. 11465-11480.
- [29] Foroutan, M., Fatemi, S. M., and Esmailian, F., 2017. A review of the structure and dynamics of nanoconfined water and ionic liquids via molecular dynamics simulation. *The European Physical Journal E*, **40**(2), pp. 19.

- [30] Hou, D. and Li, Z., 2014. Molecular Dynamics Study of Water and Ions Transported during the Nanopore Calcium Silicate Phase: Case Study of Jennite. *Journal of Materials in Civil Engineering*, **26**(5), pp. 930-940.
- [31] Hou, D., Li, Z., Zhao, T., and Zhang, P., 2015. Water transport in the nano-pore of the calcium silicate phase: reactivity, structure and dynamics. *Physical Chemistry Chemical Physics*, **17**(2), pp. 1411-1423.
- [32] Hou, D., Zhao, T., Ma, H., and Li, Z., 2015. Reactive Molecular Simulation on Water Confined in the Nanopores of the Calcium Silicate Hydrate Gel: Structure, Reactivity, and Mechanical Properties. *The Journal of Physical Chemistry C*, **119**(3), pp. 1346-1358.
- [33] zhang, Y., Yang, T., Jia, Y., Hou, D., Li, H., Jiang, J., and Zhang, J., 2018. Molecular dynamics study on the weakening effect of moisture content on graphene oxide reinforced cement composite. *Chemical Physics Letters*, **708** pp. 177-182.
- [34] Weng, S., Ning, H., Fu, T., Hu, N., Zhao, Y., Huang, C., and Peng, X., 2018. Molecular dynamics study of strengthening mechanism of nanolaminated graphene/Cu composites under compression. *Scientific Reports*, **8**(1), pp. 3089.
- [35] Liu, X., Cai, J., and Luo, S.-N., 2018. Interfacial anti-fatigue effect in graphene–copper nanolayered composites under cyclic shear loading. *Physical Chemistry Chemical Physics*, **20**(11), pp. 7875-7884.
- [36] Rahman, R., Foster, J. T., and Haque, A., 2013. Molecular Dynamics Simulation and Characterization of Graphene–Cellulose Nanocomposites. *The Journal of Physical Chemistry A*, **117**(25), pp. 5344-5353.
- [37] Weng, S., Ning, H., Fu, T., Hu, N., Wang, S., Huang, K., Peng, X., Qi, H. J., and Yan, C., 2019. Anisotropic and asymmetric deformation mechanisms of nanolaminated graphene/Cu composites. *Nano Materials Science*, **1**(2), pp. 121-130.
- [38] Li, Z., Guo, Q., Li, Z., Fan, G., Xiong, D.-B., Su, Y., Zhang, J., and Zhang, D., 2015. Enhanced Mechanical Properties of Graphene (Reduced Graphene Oxide)/Aluminum Composites with a Bioinspired Nanolaminated Structure. *Nano Letters*, **15**(12), pp. 8077-8083.
- [39] Kohn, W. and Sham, L. J., 1965. Self-Consistent Equations Including Exchange and Correlation Effects. *Physical Review*, **140**(4A), pp. A1133-A1138.
- [40] Born, M. and Oppenheimer, R., 1927. Zur Quantentheorie der Molekeln. *Annalen der Physik*, **389**(20), pp. 457-484.
- [41] Allen, M. P. and Tildesley, D. J., Computer Simulation of Liquids. 2017, USA: Oxford University Press.
- [42] Plimpton, S., 1995. Fast Parallel Algorithms for Short-Range Molecular Dynamics. *Journal of Computational Physics*, **117**(1), pp. 1-19.
- [43] Nguyen, B. H. and Nguyen, V. H., 2016. Promising applications of graphene and graphene-based nanostructures. *Advances in Natural Sciences: Nanoscience and Nanotechnology*, **7** pp.
- [44] Randviir, E. P., Brownson, D. A. C., and Banks, C. E., 2014. A decade of graphene research: production, applications and outlook. *Materials Today*, **17**(9), pp. 426-432.
- [45] Allen, M. J., Tung, V. C., and Kaner, R. B., 2010. Honeycomb Carbon: A Review of Graphene. *Chemical Reviews*, **110**(1), pp. 132-145.
- [46] Choi, W., Lahiri, I., Seelaboyina, R., and Kang, Y. S., 2010. Synthesis of Graphene and Its Applications: A Review. *Critical Reviews in Solid State and Materials Sciences*, **35**(1), pp. 52-71.

- [47] Akinwande, D., Brennan, C. J., Bunch, J. S., Egberts, P., Felts, J. R., Gao, H., Huang, R., Kim, J.-S., Li, T., Li, Y., Liechti, K. M., Lu, N., Park, H. S., Reed, E. J., Wang, P., Yakobson, B. I., Zhang, T., Zhang, Y.-W., Zhou, Y., and Zhu, Y., 2017. A review on mechanics and mechanical properties of 2D materials—Graphene and beyond. *Extreme Mechanics Letters*, **13** pp. 42-77.
- [48] Tang, Q., Zhou, Z., and Chen, Z., 2013. Graphene-related nanomaterials: Tuning properties by functionalization. *Nanoscale*, **5**(11), pp.
- [49] Kim, J. Y., Lee, J.-H., and Grossman, J. C., 2012. Thermal Transport in Functionalized Graphene. *ACS Nano*, **6**(10), pp. 9050-9057.
- [50] Guilhon, I., Bechstedt, F., Botti, S., Marques, M., and Teles, L. K., 2017. Thermodynamic, electronic, and optical properties of graphene oxide: A statistical ab initio approach. *Physical Review B*, **95**(24), pp. 245427.
- [51] Johari, P. and Shenoy, V. B., 2011. Modulating Optical Properties of Graphene Oxide: Role of Prominent Functional Groups. *ACS Nano*, **5**(9), pp. 7640-7647.
- [52] Le Ferrand, H., Bolisetty, S., Demirörs, A. F., Libanori, R., Studart, A. R., and Mezzenga, R., 2016. Magnetic assembly of transparent and conducting graphene-based functional composites. *Nature Communications*, **7** pp. 12078.
- [53] Sturala, J., Luxa, J., Pumera, M., and Sofer, Z., 2018. Chemistry of Graphene Derivatives: Synthesis, Applications, and Perspectives. *Chemistry – A European Journal*, **24**(23), pp. 5992-6006.
- [54] Georgakilas, V., Otyepka, M., Bourlinos, A. B., Chandra, V., Kim, N., Kemp, K. C., Hobza, P., Zboril, R., and Kim, K. S., 2012. Functionalization of Graphene: Covalent and Non-Covalent Approaches, Derivatives and Applications. *Chemical Reviews*, **112**(11), pp. 6156-6214.
- [55] Barhoumi, M., Rocca, D., Said, M., and Lebègue, S., 2017. A first principle study of graphene functionalized with hydroxyl, nitrile, or methyl groups. *The Journal of Chemical Physics*, **146**(4), pp. 044705.
- [56] Kabbani, M. A., Kochat, V., Bhowmick, S., Soto, M., Som, A., Krishnadas, K. R., Woellner, C. F., Jaques, Y. M., Barrera, E. V., Asif, S., Vajtai, R., Pradeep, T., Galvão, D. S., Kabbani, A. T., Tiwary, C. S., and Ajayan, P. M., 2018. Consolidation of functionalized graphene at ambient temperature via mechano-chemistry. *Carbon*, **134** pp. 491-499.
- [57] Vinod, S., Tiwary, C. S., Machado, L. D., Ozden, S., Cho, J., Shaw, P., Vajtai, R., Galvão, D. S., and Ajayan, P. M., 2016. Strain Rate Dependent Shear Plasticity in Graphite Oxide. *Nano Letters*, **16**(2), pp. 1127-1131.
- [58] Romero Aburto, R., Alemany, L. B., Weldeghiorghis, T. K., Ozden, S., Peng, Z., Lherbier, A., Botello Méndez, A. R., Tiwary, C. S., Taha-Tijerina, J., Yan, Z., Tabata, M., Charlier, J.-C., Tour, J. M., and Ajayan, P. M., 2015. Chemical Makeup and Hydrophilic Behavior of Graphene Oxide Nanoribbons after Low-Temperature Fluorination. *ACS Nano*, **9**(7), pp. 7009-7018.
- [59] De Sanctis, A., Russo, S., Craciun, M. F., Alexeev, A., Barnes, M. D., Nagareddy, V. K., and Wright, C. D., 2018. New routes to the functionalization patterning and manufacture of graphene-based materials for biomedical applications. *Interface Focus*, **8**(3), pp.
- [60] Thiha, A., Ibrahim, F., Abd Hamid, S. B., and Madou, M., 2016. A New Approach for Selective Surface Functionalization of Carbon Electrodes in Biosensing by Plasma Direct-Writing. *ECS Transactions*, **72**(1), pp. 51-57.

- [61] Ye, D., Wu, S.-Q., Yu, Y., Liu, L., Lu, X.-P., and Wu, Y., 2014. Patterned graphene functionalization via mask-free scanning of micro-plasma jet under ambient condition. *Applied Physics Letters*, **104**(10), pp. 103105.
- [62] Mali, K. S., Greenwood, J., Adisoejoso, J., Phillipson, R., and De Feyter, S., 2015. Nanostructuring graphene for controlled and reproducible functionalization. *Nanoscale*, **7**(5), pp. 1566-1585.
- [63] Marsden, A. J., Brommer, P., Mudd, J. J., Dyson, M. A., Cook, R., Asensio, M., Avila, J., Levy, A., Sloan, J., Quigley, D., Bell, G. R., and Wilson, N. R., 2015. Effect of oxygen and nitrogen functionalization on the physical and electronic structure of graphene. *Nano Research*, **8**(8), pp. 2620-2635.
- [64] Zhang, H., Fonseca, A. F., and Cho, K., 2014. Tailoring Thermal Transport Property of Graphene through Oxygen Functionalization. *The Journal of Physical Chemistry C*, **118**(3), pp. 1436-1442.
- [65] Zhang, X.-L., Zhao, X., Liu, Z.-B., Liu, Y.-S., Chen, Y.-S., and Tian, J.-G., 2009. Enhanced nonlinear optical properties of graphene-oligothiophene hybrid material. *Optics Express*, **17**(26), pp. 23959-23964.
- [66] Pykal, M., Jurečka, P., Karlický, F., and Otyepka, M., 2016. Modelling of graphene functionalization. *Physical Chemistry Chemical Physics*, **18**(9), pp. 6351-6372.
- [67] Gao, G., Liu, D., Tang, S., Huang, C., He, M., Guo, Y., Sun, X., and Gao, B., 2016. Heat-Initiated Chemical Functionalization of Graphene. *Scientific Reports*, **6** pp. 20034.
- [68] Pei, Q.-X., Sha, Z.-D., and Zhang, Y.-W., 2011. A theoretical analysis of the thermal conductivity of hydrogenated graphene. *Carbon*, **49**(14), pp. 4752-4759.
- [69] Suggs, K., Reuven, D., and Wang, X.-Q., 2011. Electronic Properties of Cycloaddition-Functionalized Graphene. *The Journal of Physical Chemistry C*, **115**(8), pp. 3313-3317.
- [70] Withers, F., Russo, S., Dubois, M., and Craciun, M. F., 2011. Tuning the electronic transport properties of graphene through functionalisation with fluorine. *Nanoscale Research Letters*, **6**(1), pp. 526.
- [71] Garg, R., Dutta, K. N., and Choudhury, R. N., 2014. Work Function Engineering of Graphene. *Nanomaterials*, **4**(2), pp.
- [72] Khoei, A. R. and Khorrami, M. S., 2016. Mechanical properties of graphene oxide: A molecular dynamics study. *Fullerenes, Nanotubes and Carbon Nanostructures*, **24**(9), pp. 594-603.
- [73] Shah, P. H. and Batra, R. C., 2014. Elastic moduli of covalently functionalized single layer graphene sheets. *Computational Materials Science*, **95** pp. 637-650.
- [74] Hadizadeh Kheirkhah, A., Saeivar Iranizad, E., Raeisi, M., and Rajabpour, A., 2014. Mechanical properties of hydrogen functionalized graphene under shear deformation: A molecular dynamics study. *Solid State Communications*, **177** pp. 98-102.
- [75] Zhan, H., Zhang, G., Bell, J. M., and Gu, Y., 2015. Graphene with Patterned Fluorination: Morphology Modulation and Implications. *The Journal of Physical Chemistry C*, **119**(49), pp. 27562-27568.
- [76] Mouhat, F. and Coudert, F.-X., 2014. Necessary and sufficient elastic stability conditions in various crystal systems. *Physical Review B*, **90**(22), pp. 224104.
- [77] Grima, J. N., Grech, M. C., Grima-Cornish, J. N., Gatt, R., and Attard, D., 2018. Giant Auxetic Behaviour in Engineered Graphene. *Annalen der Physik*, **530**(6), pp. 1700330.
- [78] Jiang, J.-W., Kim, S. Y., and Park, H. S., 2016. Auxetic nanomaterials: Recent progress and future development. *Applied Physics Reviews*, **3**(4), pp. 041101.

- [79] Jiang, J.-W., Chang, T., and Guo, X., 2016. Tunable negative Poisson's ratio in hydrogenated graphene. *Nanoscale*, **8**(35), pp. 15948-15953.
- [80] Ho, V. H., Ho, D. T., Kwon, S.-Y., and Kim, S. Y., 2016. Negative Poisson's ratio in periodic porous graphene structures. *physica status solidi (b)*, **253**(7), pp. 1303-1309.
- [81] Grima, J. N., Winczewski, S., Mizzi, L., Grech, M. C., Cauchi, R., Gatt, R., Attard, D., Wojciechowski, K. W., and Rybicki, J., 2015. Tailoring Graphene to Achieve Negative Poisson's Ratio Properties. *Advanced Materials*, **27**(8), pp. 1455-1459.
- [82] Wan, J., Jiang, J.-W., and Park, H. S., 2017. Negative Poisson's ratio in graphene oxide. *Nanoscale*, **9**(11), pp. 4007-4012.
- [83] Jiang, J.-W. and Park, H. S., 2014. Negative poisson's ratio in single-layer black phosphorus. *Nature Communications*, **5** pp. 4727.
- [84] Faghieh, F., Das, D., and Ayoub, A., 2017. Seismic Behavior of Fiber Reinforced Steel-concrete Composite Systems. *Procedia Engineering*, **171** pp. 899-908.
- [85] Sharma, S. K., Kumar, A. A., N., G. D. R. R., and Kumar, P., 2013. Micro Fiber Reinforced Cement Paste and Mortar Overlays-A Review. *International Journal of Pavement Research and Technology*, **6**(6), pp. 765-772.
- [86] Muzenski, S., Flores-Vivian, I., and Sobolev, K., 2019. Ultra-high strength cement-based composites designed with aluminum oxide nano-fibers. *Construction and Building Materials*, **220** pp. 177-186.
- [87] Barbhuiya, S. and Chow, P., 2017. Nanoscaled Mechanical Properties of Cement Composites Reinforced with Carbon Nanofibers. *Materials (Basel, Switzerland)*, **10**(6), pp. 662.
- [88] Metaxa, Z. S., Konsta-Gdoutos, M. S., and Shah, S. P., 2010. Carbon Nanofiber-Reinforced Cement-Based Materials. *Transportation Research Record*, **2142**(1), pp. 114-118.
- [89] Sbia, L. A., Peyvandi, A., Soroushian, P., and Balachandra, A. M., 2014. Optimization of ultra-high-performance concrete with nano- and micro-scale reinforcement. *Cogent Engineering*, **1**(1), pp. 990673.
- [90] Jiao, L., Su, M., Chen, L., Wang, Y., Zhu, H., and Dai, H., 2016. Natural Cellulose Nanofibers As Sustainable Enhancers in Construction Cement. *PLOS ONE*, **11**(12), pp. e0168422.
- [91] Al-Rub, R. K. A., Tyson, B. M., Yazdanbakhsh, A., and Grasley, Z., 2012. Mechanical Properties of Nanocomposite Cement Incorporating Surface-Treated and Untreated Carbon Nanotubes and Carbon Nanofibers. *Journal of Nanomechanics and Micromechanics*, **2**(1), pp. 1-6.
- [92] Nelson, P. K., Li, V. C., and Kamada, T., 2002. Fracture Toughness of Microfiber Reinforced Cement Composites. *Journal of Materials in Civil Engineering*, **14**(5), pp. 384-391.
- [93] Bantia, N. and Sheng, J., 1996. Fracture toughness of micro-fiber reinforced cement composites. *Cement and Concrete Composites*, **18**(4), pp. 251-269.
- [94] Cao, M., Zhang, C., and Wei, J., 2013. Microscopic reinforcement for cement based composite materials. *Construction and Building Materials*, **40** pp. 14-25.
- [95] Yi, C. and Ostertag, C. P., 2001. Strengthening and toughening mechanisms in microfiber reinforced cementitious composites. *Journal of Materials Science*, **36**(6), pp. 1513-1522.
- [96] Shah, S. P. and Ouyang, C., 1991. Mechanical Behavior of Fiber-Reinforced Cement-Based Composites. *Journal of the American Ceramic Society*, **74**(11), pp. 2727-2953.

- [97] Pereira, E. B., Fischer, G., and Barros, J. A. O., *Hybrid Fiber Reinforcement and Crack Formation in Cementitious Composite Materials*, in *High Performance Fiber Reinforced Cement Composites 6: HPFRCC 6*, G.J. Parra-Montesinos, H.W. Reinhardt, and A.E. Naaman, Editors. 2012, Springer Netherlands: Dordrecht. p. 535-542.
- [98] Taylor, H. F. W., *Cement Chemistry*. 1990, London: ACADEMIC PRESS.
- [99] Richardson, I. G., 1999. The nature of C-S-H in hardened cements. *Cement and Concrete Research*, **29**(8), pp. 1131-1147.
- [100] Tajuelo Rodriguez, E., Garbev, K., Merz, D., Black, L., and Richardson, I. G., 2017. Thermal stability of C-S-H phases and applicability of Richardson and Groves' and Richardson C-(A)-S-H(I) models to synthetic C-S-H. *Cement and Concrete Research*, **93** pp. 45-56.
- [101] Raki, L., Beaudoin, J., Alizadeh, R., Makar, J., and Sato, T., 2010. Cement and Concrete Nanoscience and Nanotechnology. *Materials*, **3**(2), pp. 918-942.
- [102] Sanchez, F. and Sobolev, K., 2010. Nanotechnology in concrete – A review. *Construction and Building Materials*, **24**(11), pp. 2060-2071.
- [103] Ulm, F.-J., Vandamme, M., Bobko, C., Alberto Ortega, J., Tai, K., and Ortiz, C., 2007. Statistical Indentation Techniques for Hydrated Nanocomposites: Concrete, Bone, and Shale. *Journal of the American Ceramic Society*, **90**(9), pp. 2677-2692.
- [104] Reda Taha, M., Soliman, E., Sheyka, M., Reinhardt, A., and Al-Haik, M., Fracture toughness of hydrated cement paste using nanoindentation. 2010. 105-111.
- [105] Faucon, P., Delaye, J. M., and Virlet, J., 1996. Molecular Dynamics Simulation of the Structure of Calcium Silicate Hydrates: I. $\text{Ca}_{4+x}\text{Si}_6\text{O}_{14}+2x(\text{OH})_4-2x(\text{H}_2\text{O})_2$ ($0 \leq x \leq 1$). *Journal of Solid State Chemistry*, **127**(1), pp. 92-97.
- [106] Manzano, H., Masoero, E., Lopez-Arbeloa, I., and Jennings, H. M., 2013. Shear deformations in calcium silicate hydrates. *Soft Matter*, **9**(30), pp. 7333-7341.
- [107] Palkovic, S. D., Yip, S., and Büyüköztürk, O., 2017. Constitutive response of calcium-silicate-hydrate layers under combined loading. *Journal of the American Ceramic Society*, **100**(2), pp. 713-723.
- [108] Eftekhari, M. and Mohammadi, S., 2016. Molecular dynamics simulation of the nonlinear behavior of the CNT-reinforced calcium silicate hydrate (C-S-H) composite. *Composites Part A: Applied Science and Manufacturing*, **82**(Supplement C), pp. 78-87.
- [109] Hou, D., Lu, Z., Li, X., Ma, H., and Li, Z., 2017. Reactive molecular dynamics and experimental study of graphene-cement composites: Structure, dynamics and reinforcement mechanisms. *Carbon*, **115** pp. 188-208.
- [110] Kai, M. F., Zhang, L. W., and Liew, K. M., 2019. Graphene and graphene oxide in calcium silicate hydrates: Chemical reactions, mechanical behavior and interfacial sliding. *Carbon*, **146** pp. 181-193.
- [111] Lu, Z., Hou, D., Meng, L., Sun, G., Lu, C., and Li, Z., 2015. Mechanism of cement paste reinforced by graphene oxide/carbon nanotubes composites with enhanced mechanical properties. *RSC Advances*, **5**(122), pp. 100598-100605.
- [112] Richardson, I. G., 2004. Tobermorite/jennite- and tobermorite/calcium hydroxide-based models for the structure of C-S-H: applicability to hardened pastes of tricalcium silicate, β -dicalcium silicate, Portland cement, and blends of Portland cement with blast-furnace slag, metakaolin, or silica fume. *Cement and Concrete Research*, **34**(9), pp. 1733-1777.

- [113] Kunhi Mohamed, A., Parker, S. C., Bowen, P., and Galmarini, S., 2018. An atomistic building block description of C-S-H - Towards a realistic C-S-H model. *Cement and Concrete Research*, **107** pp. 221-235.
- [114] Pellenq, R. J.-M., Kushima, A., Shahsavari, R., Van Vliet, K. J., Buehler, M. J., Yip, S., and Ulm, F.-J., 2009. A realistic molecular model of cement hydrates. *Proceedings of the National Academy of Sciences*, **106**(38), pp. 16102-16107.
- [115] Abdolhosseini Qomi, M. J., Krakowiak, K. J., Bauchy, M., Stewart, K. L., Shahsavari, R., Jagannathan, D., Brommer, D. B., Baronnet, A., Buehler, M. J., Yip, S., Ulm, F. J., Van Vliet, K. J., and Pellenq, R. J. M., 2014. Combinatorial molecular optimization of cement hydrates. *Nature Communications*, **5** pp. 4960.
- [116] Hakamy, A., Shaikh, F. U. A., and Low, I. M., *12 - High-performance natural fiber-reinforced cement composites*, in *Advances in Ceramic Matrix Composites (Second Edition)*, I.M. Low, Editor. 2018, Woodhead Publishing. p. 277-305.
- [117] Askarinejad, S. and Rahbar, N., 2017. Effects of Cement–Polymer Interface Properties on Mechanical Response of Fiber-Reinforced Cement Composites. *Journal of Nanomechanics and Micromechanics*, **7**(2), pp. 04017002.
- [118] Hou, D., Lu, Z., Zhao, T., and Ding, Q., 2016. Reactive molecular simulation on the ordered crystal and disordered glass of the calcium silicate hydrate gel. *Ceramics International*, **42**(3), pp. 4333-4346.
- [119] Youssef, M., Pellenq, R. J. M., and Yildiz, B., 2011. Glassy Nature of Water in an Ultraconfining Disordered Material: The Case of Calcium–Silicate–Hydrate. *Journal of the American Chemical Society*, **133**(8), pp. 2499-2510.
- [120] Bonaccorsi, E., Merlino, S., and Kampf, A. R., 2005. The Crystal Structure of Tobermorite 14 Å (Plombierite), a C–S–H Phase. *Journal of the American Ceramic Society*, **88**(3), pp. 505-512.
- [121] Yoon, S. and Monteiro, P. J. M., 2013. Molecular Dynamics Study of Water Molecules in Interlayer of 14 Åring; Tobermorite. *Journal of Advanced Concrete Technology*, **11**(6), pp. 180-188.
- [122] Kalinichev, A. G., Wang, J., and Kirkpatrick, R. J., 2007. Molecular dynamics modeling of the structure, dynamics and energetics of mineral–water interfaces: Application to cement materials. *Cement and Concrete Research*, **37**(3), pp. 337-347.
- [123] Hou, D. and Li, Z., 2014. Molecular dynamics study of water and ions transport in nanopore of layered structure: A case study of tobermorite. *Microporous and Mesoporous Materials*, **195**(Supplement C), pp. 9-20.
- [124] Amnaya, P. A., Dimitris, C. L., and Daniel, C. H., 2009. Modeling of graphene–polymer interfacial mechanical behavior using molecular dynamics. *Modelling and Simulation in Materials Science and Engineering*, **17**(1), pp. 015002.
- [125] Li, Y., Wang, S., and Wang, Q., 2017. A molecular dynamics simulation study on enhancement of mechanical and tribological properties of polymer composites by introduction of graphene. *Carbon*, **111** pp. 538-545.
- [126] Lin, F., Xiang, Y., and Shen, H.-S., 2017. Temperature dependent mechanical properties of graphene reinforced polymer nanocomposites – A molecular dynamics simulation. *Composites Part B: Engineering*, **111** pp. 261-269.
- [127] Liu, F., Hu, N., Ning, H., Liu, Y., Li, Y., and Wu, L., 2015. Molecular dynamics simulation on interfacial mechanical properties of polymer nanocomposites with wrinkled graphene. *Computational Materials Science*, **108** pp. 160-167.

- [128] Wang, Y., Yang, C., Cheng, Y., and Zhang, Y., 2015. A molecular dynamics study on thermal and mechanical properties of graphene-paraffin nanocomposites. *RSC Advances*, **5**(101), pp. 82638-82644.
- [129] Zhang, Y., Zhuang, X., Muthu, J., Mabrouki, T., Fontaine, M., Gong, Y., and Rabczuk, T., 2014. Load transfer of graphene/carbon nanotube/polyethylene hybrid nanocomposite by molecular dynamics simulation. *Composites Part B: Engineering*, **63** pp. 27-33.
- [130] Ding, N., Chen, X., Wu, C.-M. L., and Lu, X., 2012. Computational Investigation on the Effect of Graphene Oxide Sheets as Nanofillers in Poly(vinyl alcohol)/Graphene Oxide Composites. *The Journal of Physical Chemistry C*, **116**(42), pp. 22532-22538.
- [131] Alkhateb, H., Al-Ostaz, A., Cheng, A. H.-D., and Li, X., 2013. Materials Genome for Graphene-Cement Nanocomposites. *Journal of Nanomechanics and Micromechanics*, **3**(3), pp. 67-77.
- [132] Si, Y. and Samulski, E. T., 2008. Synthesis of Water Soluble Graphene. *Nano Letters*, **8**(6), pp. 1679-1682.
- [133] Levitz, P., Bonnaud, P. A., Cazade, P. A., Pellenq, R. J. M., and Coasne, B., 2013. Molecular intermittent dynamics of interfacial water: probing adsorption and bulk confinement. *Soft Matter*, **9**(36), pp. 8654-8663.
- [134] Bonnaud, P. A., Ji, Q., Coasne, B., Pellenq, R. J. M., and Van Vliet, K. J., 2012. Thermodynamics of Water Confined in Porous Calcium-Silicate-Hydrates. *Langmuir*, **28**(31), pp. 11422-11432.
- [135] Fan, D., Lue, L., and Yang, S., 2017. Molecular dynamics study of interfacial stress transfer in graphene-oxide cementitious composites. *Computational Materials Science*, **139**(Supplement C), pp. 56-64.
- [136] Monasterio, M., Gaitero, J. J., Manzano, H., Dolado, J. S., and Cerveny, S., 2015. Effect of Chemical Environment on the Dynamics of Water Confined in Calcium Silicate Minerals: Natural and Synthetic Tobermorite. *Langmuir*, **31**(17), pp. 4964-4972.
- [137] Neto, A. J. P., Chaban, V. V., and Fileti, E. E., 2017. Hydration peculiarities of graphene oxides with multiple oxidation degrees. *Physical Chemistry Chemical Physics*, **19**(48), pp. 32333-32340.
- [138] Dauber-Osguthorpe, P., Roberts, V. A., Osguthorpe, D. J., Wolff, J., Genest, M., and Hagler, A. T., 1988. Structure and energetics of ligand binding to proteins: Escherichia coli dihydrofolate reductase-trimethoprim, a drug-receptor system. *Proteins: Structure, Function, and Bioinformatics*, **4**(1), pp. 31-47.
- [139] Agius Anastasi, A., Ritos, K., Cassar, G., and Borg, M. K., 2016. Mechanical properties of pristine and nanoporous graphene. *Molecular Simulation*, **42**(18), pp. 1502-1511.
- [140] Zhiqiang, S., Huilin, Y., Chi, Z., Martin, K., and Ying, L., 2018. Size of graphene sheets determines the structural and mechanical properties of 3D graphene foams. *Nanotechnology*, **29**(10), pp. 104001.
- [141] Morse, P. M., 1929. Diatomic Molecules According to the Wave Mechanics. II. Vibrational Levels. *Physical Review*, **34**(1), pp. 57-64.
- [142] Kalosakas, G., Lathiotakis, N. N., Galiotis, C., and Papagelis, K., 2013. In-plane force fields and elastic properties of graphene. *Journal of Applied Physics*, **113**(13), pp. 134307.
- [143] Zang, J.-L., Yuan, Q., Wang, F.-C., and Zhao, Y.-P., 2009. A comparative study of Young's modulus of single-walled carbon nanotube by CPMD, MD and first principle simulations. *Computational Materials Science*, **46**(3), pp. 621-625.

- [144] Sanchez, F. and Zhang, L., 2008. Molecular dynamics modeling of the interface between surface functionalized graphitic structures and calcium–silicate–hydrate: Interaction energies, structure, and dynamics. *Journal of Colloid and Interface Science*, **323**(2), pp. 349-358.
- [145] Rappe, A. K. and Goddard, W. A., 1991. Charge equilibration for molecular dynamics simulations. *The Journal of Physical Chemistry*, **95**(8), pp. 3358-3363.
- [146] Jones, J. E. and Chapman, S., 1924. On the determination of molecular fields. —II. From the equation of state of a gas. *Proceedings of the Royal Society of London. Series A, Containing Papers of a Mathematical and Physical Character*, **106**(738), pp. 463-477.
- [147] Darden, T., York, D., and Pedersen, L., 1993. Particle mesh Ewald: An N·log(N) method for Ewald sums in large systems. *The Journal of Chemical Physics*, **98**(12), pp. 10089-10092.
- [148] Nosé, S., 1984. A molecular dynamics method for simulations in the canonical ensemble. *Molecular Physics*, **52**(2), pp. 255-268.
- [149] Hoover, W. G., 1985. Canonical dynamics: Equilibrium phase-space distributions. *Physical Review A*, **31**(3), pp. 1695-1697.
- [150] Zaminpayma, E. and Nayebi, P., 2015. Mechanical and electrical properties of functionalized graphene nanoribbon: A study of reactive molecular dynamic simulation and density functional tight-binding theory. *Physica B: Condensed Matter*, **459** pp. 29-35.
- [151] Zimmerman, J. A., WebbIII, E. B., Hoyt, J. J., Jones, R. E., Klein, P. A., and Bammann, D. J., 2004. Calculation of stress in atomistic simulation. *Modelling and Simulation in Materials Science and Engineering*, **12**(4), pp. S319.
- [152] Zhang, P., Ma, L., Fan, F., Zeng, Z., Peng, C., Loya, P. E., Liu, Z., Gong, Y., Zhang, J., Zhang, X., Ajayan, P. M., Zhu, T., and Lou, J., 2014. Fracture toughness of graphene. *Nature Communications*, **5** pp. 3782.
- [153] Cao, G., 2014. Atomistic Studies of Mechanical Properties of Graphene. *Polymers*, **6**(9), pp. 2404.
- [154] Lee, C., Wei, X., Kysar, J. W., and Hone, J., 2008. Measurement of the Elastic Properties and Intrinsic Strength of Monolayer Graphene. *Science*, **321**(5887), pp. 385.
- [155] Zhang, T., Li, X., and Gao, H., 2014. Designing graphene structures with controlled distributions of topological defects: A case study of toughness enhancement in graphene ruga. *Extreme Mechanics Letters*, **1** pp. 3-8.
- [156] Tsai, J.-L. and Tu, J.-F., 2010. Characterizing mechanical properties of graphite using molecular dynamics simulation. *Materials & Design*, **31**(1), pp. 194-199.
- [157] Sadeghzadeh, S. and Rezapour, N., 2016. The mechanical design of graphene nanodiodes and nanotransistors: geometry, temperature and strain effects. *RSC Advances*, **6**(89), pp. 86324-86333.
- [158] Zhao, H., Min, K., and Aluru, N. R., 2009. Size and Chirality Dependent Elastic Properties of Graphene Nanoribbons under Uniaxial Tension. *Nano Letters*, **9**(8), pp. 3012-3015.
- [159] Zheng, Q., Geng, Y., Wang, S., Li, Z., and Kim, J.-K., 2010. Effects of functional groups on the mechanical and wrinkling properties of graphene sheets. *Carbon*, **48**(15), pp. 4315-4322.
- [160] Zhang, Y. Y. and Gu, Y. T., 2013. Mechanical properties of graphene: Effects of layer number, temperature and isotope. *Computational Materials Science*, **71** pp. 197-200.

- [161] Ito, A. and Okamoto, S., 2011. Mechanical Properties of Vacancy-containing Graphene and Graphite Estimated by Molecular Dynamics Simulations. *MRS Proceedings*, **1362** pp. mrss11-1362-qq09-24.
- [162] Ansari, R., Ajori, S., and Motevalli, B., 2012. Mechanical properties of defective single-layered graphene sheets via molecular dynamics simulation. *Superlattices and Microstructures*, **51**(2), pp. 274-289.
- [163] Liu, F., Ming, P., and Li, J., 2007. Ab initio calculation of ideal strength and phonon instability of graphene under tension. *Physical Review B*, **76**(6), pp. 064120.
- [164] Andrew, R. C., Mapasha, R. E., Ukpong, A. M., and Chetty, N., 2012. Mechanical properties of graphene and boronitrene. *Physical Review B*, **85**(12), pp. 125428.
- [165] Gao, Y. and Hao, P., 2009. Mechanical properties of monolayer graphene under tensile and compressive loading. *Physica E: Low-dimensional Systems and Nanostructures*, **41**(8), pp. 1561-1566.
- [166] Sakhaee-Pour, A., 2009. Elastic properties of single-layered graphene sheet. *Solid State Communications*, **149**(1), pp. 91-95.
- [167] Jensen, B. D., Wise, K. E., and Odegard, G. M., 2015. Simulation of the Elastic and Ultimate Tensile Properties of Diamond, Graphene, Carbon Nanotubes, and Amorphous Carbon Using a Revised ReaxFF Parametrization. *The Journal of Physical Chemistry A*, **119**(37), pp. 9710-9721.
- [168] Lee, J.-U., Yoon, D., and Cheong, H., 2012. Estimation of Young's Modulus of Graphene by Raman Spectroscopy. *Nano Letters*, **12**(9), pp. 4444-4448.
- [169] Suk, J. W., Piner, R. D., An, J., and Ruoff, R. S., 2010. Mechanical Properties of Monolayer Graphene Oxide. *ACS Nano*, **4**(11), pp. 6557-6564.
- [170] Kudin, K. N., Scuseria, G. E., and Yakobson, B. I., 2001. C₂F, BN and C nanoshell elasticity from ab initio computations. *Physical Review B*, **64**(23), pp. 235406.
- [171] Sánchez-Portal, D., Artacho, E., Soler, J. M., Rubio, A., and Ordejón, P., 1999. Ab initio structural, elastic, and vibrational properties of carbon nanotubes. *Physical Review B*, **59**(19), pp. 12678-12688.
- [172] Wei, X., Fragneaud, B., Marianetti, C. A., and Kysar, J. W., 2009. Nonlinear elastic behavior of graphene: Ab initio calculations to continuum description. *Physical Review B*, **80**(20), pp. 205407.
- [173] Jiang, J.-W. and Park, H. S., 2016. Negative Poisson's Ratio in Single-Layer Graphene Ribbons. *Nano Letters*, **16**(4), pp. 2657-2662.
- [174] Ulissi, Z. W., Govind Rajan, A., and Strano, M. S., 2016. Persistently Auxetic Materials: Engineering the Poisson Ratio of 2D Self-Avoiding Membranes under Conditions of Non-Zero Anisotropic Strain. *ACS Nano*, **10**(8), pp. 7542-7549.
- [175] Baimova, Y. A., Dmitriev, S. V., Savin, A. V., and Kivshar, Y. S., 2012. Velocities of sound and the densities of phonon states in a uniformly strained flat graphene sheet. *Physics of the Solid State*, **54**(4), pp. 866-874.
- [176] Dmitriev, S. V., Baimova, J. A., Savin, A. V., and Kivshar, Y. S., 2012. Ultimate strength, ripples, sound velocities, and density of phonon states of strained graphene. *Computational Materials Science*, **53**(1), pp. 194-203.
- [177] Bosak, A., Krisch, M., Mohr, M., Maultzsch, J., and Thomsen, C., 2007. Elasticity of single-crystalline graphite: Inelastic x-ray scattering study. *Physical Review B*, **75**(15), pp. 153408.

- [178] Zhang, Y.-Y., Pei, Q.-X., Wang, C.-M., Cheng, Y., and Zhang, Y.-W., 2013. A molecular dynamics investigation on mechanical properties of hydrogenated graphynes. *Journal of Applied Physics*, **114**(7), pp. 073504.
- [179] Merlino, S., Bonaccorsi, E., and Armbruster, T., 1999. Tobermorites; their real structure and order-disorder (OD) character. *American Mineralogist*, **84**(10), pp. 1613-1621.
- [180] Humphrey, W., Dalke, A., and Schulten, K., 1996. VMD: visual molecular dynamics. *J Mol Graph*, **14**(1), pp. 33-8, 27-8.
- [181] Momma, K. and Izumi, F., VESTA 3 for Three-Dimensional Visualization of Crystal, Volumetric and Morphology Data. Vol. 44. 2011.
- [182] Jewett, A. I., Zhuang, Z., and Shea, J.-E., 2013. Moltemplate a Coarse-Grained Model Assembly Tool. *Biophysical Journal*, **104**(2), pp. 169a.
- [183] Alexander, S., 2010. Visualization and analysis of atomistic simulation data with OVITO—the Open Visualization Tool. *Modelling and Simulation in Materials Science and Engineering*, **18**(1), pp. 015012.
- [184] Cygan, R. T., Liang, J.-J., and Kalinichev, A. G., 2004. Molecular Models of Hydroxide, Oxyhydroxide, and Clay Phases and the Development of a General Force Field. *The Journal of Physical Chemistry B*, **108**(4), pp. 1255-1266.
- [185] Sanchez, F. and Zhang, L., 2010. Interaction energies, structure, and dynamics at functionalized graphitic structure–liquid phase interfaces in an aqueous calcium sulfate solution by molecular dynamics simulation. *Carbon*, **48**(4), pp. 1210-1223.
- [186] Skelton, A. A., Fenter, P., Kubicki, J. D., Wesolowski, D. J., and Cummings, P. T., 2011. Simulations of the Quartz(10 $\bar{1}$)/Water Interface: A Comparison of Classical Force Fields, Ab Initio Molecular Dynamics, and X-ray Reflectivity Experiments. *The Journal of Physical Chemistry C*, **115**(5), pp. 2076-2088.
- [187] Sheppard, D., Terrell, R., and Henkelman, G., 2008. Optimization methods for finding minimum energy paths. *The Journal of Chemical Physics*, **128**(13), pp. 134106.
- [188] Tuckerman, M., Berne, B. J., and Martyna, G. J., 1992. Reversible multiple time scale molecular dynamics. *The Journal of Chemical Physics*, **97**(3), pp. 1990-2001.
- [189] Humphrey, W., Dalke, A., and Schulten, K., 1996. VMD - Visual Molecular Dynamics. *Journal of Molecular Graphics*, **14** pp. 33-38.
- [190] Al-Muhit, B. and Sanchez, F., 2019. Tunable mechanical properties of graphene by clustered line pattern hydroxyl functionalization via molecular dynamics simulations. *Carbon*, **146** pp. 680-700.
- [191] Larentzos, J. P., Greathouse, J. A., and Cygan, R. T., 2007. An ab Initio and Classical Molecular Dynamics Investigation of the Structural and Vibrational Properties of Talc and Pyrophyllite. *The Journal of Physical Chemistry C*, **111**(34), pp. 12752-12759.
- [192] Fazelabdolabadi, B. and Alizadeh-Mojarad, A., 2017. A molecular dynamics investigation into the adsorption behavior inside {001} kaolinite and {1014} calcite nano-scale channels: the case with confined hydrocarbon liquid, acid gases, and water. *Applied Nanoscience*, **7**(5), pp. 155-165.
- [193] Teich-McGoldrick, S. L., Greathouse, J. A., and Cygan, R. T., 2012. Molecular Dynamics Simulations of Structural and Mechanical Properties of Muscovite: Pressure and Temperature Effects. *The Journal of Physical Chemistry C*, **116**(28), pp. 15099-15107.

- [194] Hantal, G., Brochard, L., Laubie, H., Ebrahimi, D., Pellenq, R. J. M., Ulm, F.-J., and Coasne, B., 2014. Atomic-scale modelling of elastic and failure properties of clays. *Molecular Physics*, **112**(9-10), pp. 1294-1305.
- [195] Zhang, J., Pervukhina, M., and Clennell, M. B., 2018. NANOSCALE ELASTIC PROPERTIES OF DRY AND WET SMECTITE. *Clays and Clay Minerals*, **66**(3), pp. 209-219.
- [196] Suter, J. L., Coveney, P. V., Greenwell, H. C., and Thyveetil, M.-A., 2007. Large-Scale Molecular Dynamics Study of Montmorillonite Clay: Emergence of Undulatory Fluctuations and Determination of Material Properties. *The Journal of Physical Chemistry C*, **111**(23), pp. 8248-8259.
- [197] Vo, V. S., Nguyen, V.-H., Mahouche-Chergui, S., Carbonnier, B., Di Tommaso, D., and Naili, S., 2017. From atomistic structure to thermodynamics and mechanical properties of epoxy/clay nanocomposites: Investigation by molecular dynamics simulations. *Computational Materials Science*, **139** pp. 191-201.
- [198] Mazo, M., Manevitch, L., Balabaev, N., Berlin, A., B. Gusarova, E., and Rutledge, G., Temperature dependence of elastic properties of a pyrophyllite plate by molecular dynamics simulation. Proceedings of Second International Conference on Mathematical Modeling and Computer Simulation of Metal Technologies, MMT-2006. Israel, 2006, vol. 2, part 4, p. 97-106. 2006.
- [199] Mishra, R. K., Mohamed, A. K., Geissbühler, D., Manzano, H., Jamil, T., Shahsavari, R., Kalinichev, A. G., Galmarini, S., Tao, L., Heinz, H., Pellenq, R., van Duin, A. C. T., Parker, S. C., Flatt, R. J., and Bowen, P., 2017. cemff: A force field database for cementitious materials including validations, applications and opportunities. *Cement and Concrete Research*, **102** pp. 68-89.
- [200] Mazo, M. A., Manevitch, L. I., Gusarova, E. B., Shamaev, M. Y., Berlin, A. A., Balabaev, N. K., and Rutledge, G. C., 2008. Molecular Dynamics Simulation of Thermomechanical Properties of Montmorillonite Crystal. 1. Isolated Clay Nanoplate. *The Journal of Physical Chemistry B*, **112**(10), pp. 2964-2969.
- [201] Jones, J. E. and Chapman, S., 1924. On the determination of molecular fields. - II. From the equation of state of a gas. *Proceedings of the Royal Society of London. Series A, Containing Papers of a Mathematical and Physical Character*, **106**(738), pp. 463-477.
- [202] Lorentz, H. A., 1881. Ueber die Anwendung des Satzes vom Virial in der kinetischen Theorie der Gase. *Annalen der Physik*, **248**(1), pp. 127-136.
- [203] Berthelot, D., 1898. Sur le mélange des gaz. *Comptes Rendus Hebdomadaires des Séances de l'Académie des Sciences*, **126** pp. 1703-1855.
- [204] Hou, D., Zhao, T., Wang, P., Li, Z., and Zhang, J., 2014. Molecular dynamics study on the mode I fracture of calcium silicate hydrate under tensile loading. *Engineering Fracture Mechanics*, **131**(Supplement C), pp. 557-569.
- [205] Fu, J., Bernard, F., and Kamali-Bernard, S., 2018. Assessment of the elastic properties of amorphous calcium silicates hydrates (I) and (II) structures by molecular dynamics simulation. *Molecular Simulation*, **44**(4), pp. 285-299.
- [206] Subramaniyan, A. K. and Sun, C. T., 2008. Continuum interpretation of virial stress in molecular simulations. *International Journal of Solids and Structures*, **45**(14), pp. 4340-4346.

- [207] Sun, L., Gao, Y., Li, Y., Yoshida, K., Yano, T., and Yi, D., 2016. Structural, bonding, anisotropic mechanical and thermal properties of Al₄SiC₄ and Al₄Si₂C₅ by first-principles investigations. *Journal of Asian Ceramic Societies*, **4**(3), pp. 289-298.
- [208] Zhou, X. W., Heo, T. W., Wood, B. C., Stavila, V., Kang, S., and Allendorf, M. D., 2017. Finite-temperature behavior of PdH_x elastic constants computed by direct molecular dynamics. pp.
- [209] Stetsenko, M. S., 2015. Determining the elastic constants of hydrocarbons of heavy oil products using molecular dynamics simulation approach. *Journal of Petroleum Science and Engineering*, **126** pp. 124-130.
- [210] Born, M. and Huang, K., *Dynamical Theory of Crystal Lattices*. 1962, London: Oxford University Press.
- [211] Selvam, R. P., Subramani, V. J., Murray, S., and Hall, K. D., *Potential Application of Nanotechnology on Cement Based Materials*, TRID, Editor. 2009. p. 158.
- [212] Zhou, Y., Hou, D., Geng, G., Feng, P., Yu, J., and Jiang, J., 2018. Insights into the interfacial strengthening mechanisms of calcium-silicate-hydrate/polymer nanocomposites. *Physical Chemistry Chemical Physics*, **20**(12), pp. 8247-8266.
- [213] Thomas, J. J., Jennings, H. M., and Allen, A. J., 2010. Relationships between Composition and Density of Tobermorite, Jennite, and Nanoscale CaO–SiO₂–H₂O. *The Journal of Physical Chemistry C*, **114**(17), pp. 7594-7601.
- [214] Hou, D., Ma, H., Zhu, Y., and Li, Z., 2014. Calcium silicate hydrate from dry to saturated state: Structure, dynamics and mechanical properties. *Acta Materialia*, **67** pp. 81-94.
- [215] Hull, D. and Clyne, T. W., *An Introduction to Composite Materials*. 1996, Cambridge, UK: Cambridge University Press.
- [216] Schlaich, A., Kappler, J., and Netz, R. R., 2017. Hydration Friction in Nanoconfinement: From Bulk via Interfacial to Dry Friction. *Nano Letters*, **17**(10), pp. 5969-5976.
- [217] Dhopatkar, N., Defante, A. P., and Dhinojwala, A., 2016. Ice-like water supports hydration forces and eases sliding friction. *Science Advances*, **2**(8), pp. e1600763.
- [218] Lee, H., Ko, J.-H., Choi, J. S., Hwang, J. H., Kim, Y.-H., Salmeron, M., and Park, J. Y., 2017. Enhancement of Friction by Water Intercalated between Graphene and Mica. *The Journal of Physical Chemistry Letters*, **8**(15), pp. 3482-3487.
- [219] Lee, M., Kim, B., Kim, J., and Jhe, W., 2015. Noncontact friction via capillary shear interaction at nanoscale. *Nature Communications*, **6** pp. 7359.
- [220] Cai, H., Guo, Y., and Guo, W., 2018. Friction induced structural transformations of water monolayers at graphene/Cu interfaces. *Physical Chemistry Chemical Physics*, **20**(6), pp. 4137-4143.
- [221] Goharshadi, E. K., Akhlagi, G., and Mahdizadeh, S. J., 2015. Investigation of graphene oxide nanosheets dispersion in water based on solubility parameters: a molecular dynamics simulation study. *RSC Advances*, **5**(129), pp. 106421-106430.
- [222] Min, K. and Aluru, N. R., 2011. Mechanical properties of graphene under shear deformation. *Applied Physics Letters*, **98**(1), pp. 013113.
- [223] Shahsavari, R., Buehler, M. J., Pellenq, R. J. M., and Ulm, F.-J., 2009. First-Principles Study of Elastic Constants and Interlayer Interactions of Complex Hydrated Oxides: Case Study of Tobermorite and Jennite. *Journal of the American Ceramic Society*, **92**(10), pp. 2323-2330.
- [224] Manzano, H., Dolado, J. S., and Ayuela, A., 2009. Elastic properties of the main species present in Portland cement pastes. *Acta Materialia*, **57**(5), pp. 1666-1674.

- [225] Manzano, H., Dolado, J. S., Guerrero, A., and Ayuela, A., 2007. Mechanical properties of crystalline calcium-silicate-hydrates: comparison with cementitious C-S-H gels. *physica status solidi (a)*, **204**(6), pp. 1775-1780.
- [226] Pellenq, R. J.-M., Lequeux, N., and Van Damme, H., 2007. Engineering the bonding scheme in C-S-H : The iono-covalent framework. *Cement and Concrete Research*, **38** pp. 159-174.
- [227] Shirley, M. and Bibian, H., 2016. Changes in the elastic moduli of C-S-H due to presence of interlaminar cations. *Modelling and Simulation in Materials Science and Engineering*, **24**(3), pp. 035018.
- [228] Hajilar, S. and Shafei, B. *Molecular Dynamics Simulation of Elastic Properties of Ordered CSH Gel: Case Study of Tobermorite and Jennite*. in *Proceedings of the 5th International Symposium on Nanotechnology in Construction (NICOM-5)*. 2015. Chicago, Illinois.
- [229] Constantinides, G., Ulm, F. J., and Van Vliet, K., 2003. On the use of nanoindentation for cementitious materials. *Materials and Structures*, **36**(3), pp. 191-196.
- [230] Constantinides, G. and Ulm, F.-J., 2004. The effect of two types of C-S-H on the elasticity of cement-based materials: Results from nanoindentation and micromechanical modeling. *Cement and Concrete Research*, **34**(1), pp. 67-80.
- [231] Pelisser, F., Gleize, P. J. P., and Mikowski, A., 2012. Effect of the Ca/Si Molar Ratio on the Micro/nanomechanical Properties of Synthetic C-S-H Measured by Nanoindentation. *The Journal of Physical Chemistry C*, **116**(32), pp. 17219-17227.
- [232] Jennings, H. M., Thomas, J. J., Gevrenov, J. S., Constantinides, G., and Ulm, F.-J., 2007. A multi-technique investigation of the nanoporosity of cement paste. *Cement and Concrete Research*, **37**(3), pp. 329-336.
- [233] Hughes, J. J. and Trtik, P., 2004. Micro-mechanical properties of cement paste measured by depth-sensing nanoindentation: a preliminary correlation of physical properties with phase type. *Materials Characterization*, **53**(2), pp. 223-231.
- [234] Vandamme, M., Ulm, F.-J., and Fonollosa, P., 2010. Nanogranular packing of C-S-H at substoichiometric conditions. *Cement and Concrete Research*, **40**(1), pp. 14-26.
- [235] Oh, J. E., Clark, S. M., Wenk, H.-R., and Monteiro, P. J. M., 2012. Experimental determination of bulk modulus of 14Å tobermorite using high pressure synchrotron X-ray diffraction. *Cement and Concrete Research*, **42**(2), pp. 397-403.
- [236] Al-Ostaz, A., Wu, W., Cheng, A. H. D., and Song, C. R., 2010. A molecular dynamics and microporomechanics study on the mechanical properties of major constituents of hydrated cement. *Composites Part B: Engineering*, **41**(7), pp. 543-549.
- [237] Al-Muhit, B. and Sanchez, F., 2020. Nano-engineering of the mechanical properties of tobermorite 14 Å with graphene via molecular dynamics simulations. *Construction and Building Materials*, **233** pp. 117237.
- [238] Liu, L., Zhou, M., Jin, L., Li, L., Mo, Y., Su, G., Li, X., Zhu, H., and Tian, Y., 2019. Recent advances in friction and lubrication of graphene and other 2D materials: Mechanisms and applications. *Friction*, pp.
- [239] Yang, Z., Bhowmick, S., Sen, F. G., Banerji, A., and Alpas, A. T., 2018. Roles of sliding-induced defects and dissociated water molecules on low friction of graphene. *Scientific reports*, **8**(1), pp. 121-121.

- [240] De Luca, S., Todd, B. D., Hansen, J. S., and Daivis, P. J., 2014. Molecular Dynamics Study of Nanoconfined Water Flow Driven by Rotating Electric Fields under Realistic Experimental Conditions. *Langmuir*, **30**(11), pp. 3095-3109.
- [241] Yi-Ran SUN, F. Y., Jie MA, 2017. Research Progress of Nanoconfined Water. *Acta Physico-Chimica Sinica*, **33**(11), pp. 2173-2183.
- [242] Wang, C., Zhang, C., Jiang, J.-W., Wei, N., Park, H. S., and Rabczuk, T., 2016. Self-assembly of water molecules using graphene nanoresonators. *RSC Advances*, **6**(112), pp. 110466-110470.
- [243] Soler-Crespo, R. A., Gao, W., Mao, L., Nguyen, H. T., Roenbeck, M. R., Paci, J. T., Huang, J., Nguyen, S. T., and Espinosa, H. D., 2018. The Role of Water in Mediating Interfacial Adhesion and Shear Strength in Graphene Oxide. *ACS Nano*, **12**(6), pp. 6089-6099.
- [244] Zokaie, M. and Foroutan, M., 2015. Confinement effects of graphene oxide nanosheets on liquid–solid phase transition of water. *RSC Advances*, **5**(118), pp. 97446-97457.
- [245] Foroutan, M., Fatemi, S. M., and Shokouh, F., 2016. Graphene confinement effects on melting/freezing point and structure and dynamics behavior of water. *Journal of Molecular Graphics and Modelling*, **66** pp. 85-90.
- [246] Cohen-Tanugi, D. and Grossman, J. C., 2012. Water Desalination across Nanoporous Graphene. *Nano Letters*, **12**(7), pp. 3602-3608.
- [247] Dreyer, D. R., Park, S., Bielawski, C. W., and Ruoff, R. S., 2010. The chemistry of graphene oxide. *Chemical Society Reviews*, **39**(1), pp. 228-240.
- [248] Soleimani, E. and Foroutan, M., 2018. Multilayer graphene with a rippled structure for water desalination. *Journal of Molecular Liquids*, **265** pp. 208-215.
- [249] Zokaie, M. and Foroutan, M., 2015. Comparative study on confinement effects of graphene and graphene oxide on structure and dynamics of water. *RSC Advances*, **5**(49), pp. 39330-39341.
- [250] Lee, S., Park, J., Yang, J., and Lu, W., 2014. Molecular Dynamics Simulations of the Traction-Separation Response at the Interface between PVDF Binder and Graphite in the Electrode of Li-Ion Batteries. *Journal of The Electrochemical Society*, **161**(9), pp. A1218-A1223.
- [251] Guin, L., Raphanel, J. L., and Kysar, J. W., 2016. Atomistically derived cohesive zone model of intergranular fracture in polycrystalline graphene. *Journal of Applied Physics*, **119**(24), pp. 245107.
- [252] Kumar, H., Dong, L., and Shenoy, V. B., 2016. Limits of Coherency and Strain Transfer in Flexible 2D van der Waals Heterostructures: Formation of Strain Solitons and Interlayer Debonding. *Scientific reports*, **6** pp. 21516-21516.
- [253] Awad, I. and Ladani, L., 2014. Interfacial Strength Between Single Wall Carbon Nanotubes and Copper Material: Molecular Dynamics Simulation. *Journal of Nanotechnology in Engineering and Medicine*, **4**(4), pp. 041001-041001-6.
- [254] Awad, I. and Ladani, L., 2014. Cohesive Zone Model for the Interface of Multiwalled Carbon Nanotubes and Copper: Molecular Dynamics Simulation. *Journal of Nanotechnology in Engineering and Medicine*, **5**(3), pp. 031007-031007-7.
- [255] Awad, I. and Ladani, L., 2016. Multiscale Modeling of Novel Carbon Nanotube/Copper-Composite Material Used in Microelectronics. *Journal of Multiscale Modelling*, **07**(02), pp. 1650001.

- [256] Zaragoza, A., Gonzalez, M. A., Joly, L., López-Montero, I., Canales, M. A., Benavides, A. L., and Valeriani, C., 2019. Molecular dynamics study of nanoconfined TIP4P/2005 water: how confinement and temperature affect diffusion and viscosity. *Physical Chemistry Chemical Physics*, **21**(25), pp. 13653-13667.
- [257] Jaeger, F., Matar, O., and Müller, E., Transport Properties of Water Confined in a Graphene Nanochannel. 2019.
- [258] Devanathan, R., Chase-Woods, D., Shin, Y., and Gotthold, D. W., 2016. Molecular Dynamics Simulations Reveal that Water Diffusion between Graphene Oxide Layers is Slow. *Scientific Reports*, **6** pp. 29484.
- [259] Ohkubo, T., Gin, S., Collin, M., and Iwadate, Y., 2018. Molecular Dynamics Simulation of Water Confinement in Disordered Aluminosilicate Subnanopores. *Scientific Reports*, **8**(1), pp. 3761.
- [260] Mozaffari, F., 2016. A molecular dynamics simulation study of the effect of water–graphene interaction on the properties of confined water. *Molecular Simulation*, **42**(17), pp. 1475-1484.
- [261] Ho, T. A. and Striolo, A., 2014. Molecular dynamics simulation of the graphene–water interface: comparing water models. *Molecular Simulation*, **40**(14), pp. 1190-1200.

APPENDIX A Supplementary materials for Chapter 3

This appendix includes the supplementary material for the paper that was published from the results of Chapter 3: B. Al-Muhit, F. Sanchez, *Tunable mechanical properties of graphene by clustered line pattern hydroxyl functionalization via molecular dynamics simulations*, Carbon, 146 (2019), 680-700, doi.org/10.1016/j.carbon.2019.02.019

A1.0 Force field

The consistent valence force field (CVFF) includes both bonded and non-bonded (pair) energy terms, including the bond-stretching energy ($\Psi^{\text{bond-stretching}}$), the angle-bending energy ($\Psi^{\text{angle-bending}}$), the torsion-angle (dihedral) energy (Ψ^{torsion}), the out-of-plane energy (improper torsion) (Ψ^{improper}), the electrostatic energy ($\Psi^{\text{electrostatic}}$), and the van der Waals energy (Ψ^{vdW}). The total potential energy (Ψ^{total}) in the CVFF was calculated using the following expression:

$$\Psi^{\text{total}} = \Psi^{\text{bonded}} + \Psi^{\text{non-bonded}} \quad (1)$$

The bonded energy (Ψ^{bonded}) was defined as follows:

$$\Psi^{\text{bonded}} = \Psi^{\text{bond-stretching}} + \Psi^{\text{angle-bending}} + \Psi^{\text{torsion}} + \Psi^{\text{improper}} \quad (2)$$

And, the non-bonded energy ($\Psi^{\text{non-bonded}}$) was written as:

$$\Psi^{\text{non-bonded}} = \Psi^{\text{electrostatic}} + \Psi^{\text{vdW}} \quad (3)$$

A1.1 Bonded energy

A1.1.1 Bond-stretching energy

The bond-stretching energy was defined as the energy required to stretch a bond between two atoms from their equilibrium positions. The total bond-stretching energy (Ψ^b) was the sum of the energy from two bond-stretching potentials, i.e., the Morse ($\Psi^{b(\text{Morse})}$) and harmonic ($\Psi^{b(\text{harmonic})}$) potentials, written as follows:

$$\Psi^b = \Psi^{b(\text{Morse})} + \Psi^{b(\text{harmonic})} \quad (4)$$

Morse potential. The Morse bond potential [1] was used to simulate the bond-stretching and bond-breaking of the carbon atoms associated with the graphene sheet (GS) and functionalized graphene sheet (FGS) systems, and was defined as:

$$\Psi^{b(\text{Morse})} = \sum_{N_b^{\text{Morse}}} D_b \left[1 - e^{-\alpha(\mathbf{r}-\mathbf{r}_0)} \right]^2 \quad (5)$$

$$\text{with } \alpha = \sqrt{\frac{K_b}{2D_b}} \quad (6)$$

where $\Psi^{b(\text{Morse})}$ is the bond-stretching energy ($\text{kcal mol}^{-1} \text{ \AA}^{-2}$) described by the Morse potential; D_b is the bond dissociation energy; \mathbf{r} and \mathbf{r}_0 are the current and equilibrium bond lengths in angstrom ($1 \text{ \AA} = 10^{-10} \text{ m}$); α is the Morse anharmonicity parameter; N_b^{Morse} is the number of Morse bonds; and K_b is the force constant at the minimum of the potential well.

Harmonic potential. The harmonic potential was used to simulate the bond-stretching between the out-of-plane atoms (carbon-oxygen, C–O and oxygen-hydrogen, O–H) in the FGS systems as follows:

$$\Psi^{b(\text{harmonic})} = \sum_{N_b^{\text{harmonic}}} \frac{K_0}{2} (\mathbf{r}-\mathbf{r}_0)^2 \quad (7)$$

where $\Psi^{b(\text{harmonic})}$ is the harmonic bond-stretching energy ($\text{kcal mol}^{-1} \text{ \AA}^{-2}$); K_0 is the force constant at the minimum of the potential well; \mathbf{r} and \mathbf{r}_0 are the current and equilibrium bond lengths in angstrom ($1 \text{ \AA} = 10^{-10} \text{ m}$), respectively; and N_b^{harmonic} is the number of Morse bonds. The total bond energies of the FGS were calculated for carbon-carbon (C–C), carbon-oxygen (C–O), and oxygen-hydrogen (O–H) bond types.

A1.1.2 Angle-bending potential

The angle-bending energy ($\Psi^{\text{angle-bending}}$) was defined as the energy required for the GS and FGS to resist against angular deformation from their equilibrium position. The angle-bending potential expresses the bending energy change of angles as:

$$\Psi^{\text{angle-bending}} = \sum_{N_a} \frac{K_0}{2} (\theta - \theta_0)^2 \quad (8)$$

where K_0 is the angle-bending energy ($\text{kcal mol}^{-1} \text{ rad}^{-2}$); θ and θ_0 are current and equilibrium bond-angles in degrees, respectively; and N_a is the number of angles. The angle-bending energies for the FGS systems were calculated for the angle types $\angle \text{C-C-C}$, $\angle \text{C-C-O}$, and $\angle \text{C-O-H}$.

A1.1.3 Torsion potential

The torsional (dihedral) energy (Ψ^{torsion}) was expressed as the angle twisting energy between a quadruple of atoms of the FGS, which was defined by the following expression:

$$\Psi^{\text{torsion}} = \sum_{N_t} V [1 + \cos(n\varphi - \varphi_0)] \quad (9)$$

where V is the half-height of the energy barrier (kcal mol^{-1}); n is the periodicity (multiplicity) of torsion (n always equal to 2); φ and φ_0 are the current and equilibrium torsion angles with φ_0 equal to either 0° or 180° ; and N_t is the number of torsion angles. The torsion angles were calculated between the quadruples of atoms. The torsional twisting energies were calculated for C-C-C-C , C-C-C-O , O-C-C-O , and C-C-O-H types of torsional angles.

A1.1.4 Out-of-plane bending potential

The improper (out-of-plane) deformation energy (Ψ^{improper}) of the FGS was evaluated between a quadruple of atoms using the following expression:

$$\Psi^{\text{improper}} = \sum_{\text{improper}} V [1 + \cos(n\chi - \chi_0)]^2 \quad (10)$$

where V is the half of the energy barrier height of improper angle (kcal mol^{-1}); n is the periodicity (multiplicity) of improper torsion (n always equal to 2); χ and χ_0 are the current and equilibrium improper torsion angles, respectively, with χ_0 always equal to 180° ; and N_i is the number of improper torsion angle. The CVFF converted the degrees ($^\circ$) into radians

automatically. The improper (out-of-plane) bending energies for the FGS systems were computed for the quadruple improper bending types C–C–C–C.

A1.2 Non-bonded energy (pair energy)

A1.2.1 Electrostatic energy

The electrostatic (Coulombic) energy ($\Psi^{\text{electrostatic}}$) between any pair of atoms were calculated and summed over all of the atoms of the system using the following expression:

$$\Psi^{\text{electrostatic}} = \sum_i \sum_{j>i} \frac{1}{4\pi \epsilon_0} \cdot \frac{q_i q_j}{r_{ij}^2} \quad (11)$$

$$\text{with } r_{ij} = |\mathbf{r}_i - \mathbf{r}_j| \quad (12)$$

where q_i and q_j are the partial charges on the atoms i and j ; ϵ_0 is the permittivity in the vacuum (8.85419×10^{-12} F/m); and r_{ij} is the interatomic distance (Å) between the atoms i and j .

The short-range electrostatic attraction energy was calculated in the real space whereas the long-range portion of the electrostatic energy was calculated in the reciprocal space with a cut-off distance of 10 Å using the Ewald summation approach [2] to increase computational efficiency.

A1.2.2 van der Waals (vdW) energy

The vdW energy observed between atoms was calculated using the 12-6 Lennard-Jones (LJ) potential [3]:

$$\Psi^{\text{vdW}} = \sum_i \sum_{j>i} 4\epsilon \left[\left(\frac{\sigma}{r_{ij}} \right)^{12} - \left(\frac{\sigma}{r_{ij}} \right)^6 \right] \quad (13)$$

where ϵ is the depth of the potential well (kcal mol^{-1}); σ is the distance in angstrom (Å) at which the potential is zero; and r_{ij} is the interatomic distance (Å) between the atoms i and j .

The short-range repulsion and long-range attraction energies were calculated using the 12-6 LJ potential. The long-range attraction energies were calculated in the reciprocal space with a vdW

cut-off distance of 10 Å using the Ewald summation approach [2] to increase computational efficiency.

A2.0 Interaction calculation between unlike atoms

The Lorentz-Berthelot mixing rules [4, 5] were applied for the calculation of the energy and interatomic distances between unlike atoms. In the CVFF, this rule is known as the arithmetic rule:

$$\sigma_{ij} = \left(\frac{\sigma_{ii} + \sigma_{jj}}{2} \right) \quad (14)$$

$$\epsilon_{ij} = \sqrt{\epsilon_{ii}\epsilon_{jj}} \quad (15)$$

where σ_{ij} is the distance between unlike atoms i and j , which is calculated from the mean distance of the like-atoms i, i and j, j . Similarly, ϵ_{ij} is the energy between unlike atoms i and j , which is termed as the square root of the multiplication of the energy of the like-atoms i, i and j, j .

A3.0 Charge equilibration

To keep the entire FGS system charge neutral, QEq/point method (matrix inversion method [6, 7]) in LAMMPS was adopted for one-time partial charge assignment on the C, O, and H atoms of the FGS system. The required electronegativity (χ) and self-coulomb potential (η) parameters were obtained from the ffield.reax.CHO file in LAMMPS, and appropriate conversion from the metal to real unit was performed before using the parameters in the current study. The assigned partial atomic charges were used to calculate the short-range attractive energy (electrostatic energy, $\Psi^{\text{electrostatic}}$) of the FGS system.

A4.0 Forcefield parameters for energy calculation

The CVFF parameters necessary to calculate the bonded and non-bonded (pair) interactions of the GS and FGS systems are tabulated in Tables A4.1 and A4.2.

Table A4.1. Forcefield parameters for the bonded energies of the GS and FGS systems using CVFF.

Parameters	Interactions	D_b	α	r_{ij}	K	θ_0	V	n	φ_0	χ_0
Bond-stretching	C–C	120.00	2.0	1.34	---	---	---	---	---	---
	C–O	384.00	---	1.37	---	---	---	---	---	---
	O–H	540.63	---	0.96	---	---	---	---	---	---
Angle-bending	C–C–C	---	---	---	90	120	---	---	---	---
	C–C–O	---	---	---	60	120	---	---	---	---
	C–O–H	---	---	---	50	109	---	---	---	---
Dihedral/torsional	C–C–C–C	---	---	---	---	---	120	2	-1	---
	C–C–C–O	---	---	---	---	---	1.80	2	-1	---
	O–C–C–O	---	---	---	---	---	3.00	2	-1	---
	C–C–O–H	---	---	---	---	---	1.50	2	1	---
Improper	C–C–C–C	---	---	---	---	---	0.37	2	---	-1

Notation: D_b = disassociation energy; α = Morse anharmonicity parameter; r_{ij} = distance between interacting atoms; K_0 = angle-bending energy; θ_0 = current angle; V = half of the energy barrier height; n = periodicity; φ_0 = current torsion angle; χ_0 = current improper (out-of-plane bending) angle.

Table A4.2. Parameters for the Lennard-Jones (LJ) potential for the calculation of vdW non-bonded energies of the GS and FGS systems.

Parameters	Interacting types of atoms	Energy, ϵ (kcal mol ⁻¹)	Distance, σ (Å)
Lennard-Jones (LJ)	C–C	0.14799	3.617
	O–O	0.227	3.21
	H–H	0.0	0.0

A5.0 Data Analysis: Stress tensor, in-plane elastic constants, directional elastic and shear modulus, linear compressibility, Poisson's ratio, and sound wave velocities

A5.1 Stress tensor

Engineering Stress. The atomistic stress was calculated according to the Virial stress theorem considering both potential and kinetic energy terms as follows:

$$\boldsymbol{\sigma} = \frac{1}{\Omega} \sum_i \left(-m_i \dot{\mathbf{u}}_i \otimes \dot{\mathbf{u}}_i + \frac{1}{2} \sum_{j \neq i} \mathbf{r}_{ij} \otimes \mathbf{f}_{ij} \right) \quad (16)$$

$$\text{with } \mathbf{r}_{ij} = |\mathbf{r}_i - \mathbf{r}_j| \quad (17)$$

where $\boldsymbol{\sigma}$ is the calculated stress; i and j are atom indices, m_i is the mass of atom i , $\dot{\mathbf{u}}_i$ is the time-derivative of the displacement vector \mathbf{u}_i (essentially, the velocity vector); \mathbf{r}_{ij} is the interatomic distance (position vector) between atoms i and j ; \mathbf{f}_{ij} is the force vector on atom i due to atom j ; Ω is the volume of the system; and \otimes is the dyadic product between two vectors.

As GS and FGS were 2D systems, the calculated 3D stress from equation (16), $\boldsymbol{\sigma}^{3D}$, was then transformed from the simulation box to a 2D stress ($\boldsymbol{\sigma}^{2D}$) on the GS or FGS plane:

$$\boldsymbol{\sigma}^{2D} = \boldsymbol{\sigma}^{3D} \cdot \mathbf{s} \cdot h_{GS} \quad (18)$$

$$\text{with } \mathbf{s} = h_{\text{box}} / h_{GS} \quad (19)$$

where h_{box} is the height of the simulation box and h_{GS} is the thickness of the GS (3.35 Å). The stress was time-averaged over 4500 fs for each increment of strain to obtain the engineering stress.

Local atomic stress. The local atomic stress was evaluated by computing the stress of each atom as stress \times volume ($p \cdot v$) (GPa Å³), where p is the local stress experienced by an atom and v is the volume of the atom.

A5.2 In-plane elastic stiffness constants, moduli, and Poisson's ratio

The general elastic stiffness tensor for the GS and FGS systems was written as a 3×3 matrix in the Voigt notation as follows:

$$\mathbb{C} = \begin{bmatrix} C_{11} & C_{12} & 0 \\ C_{21} & C_{22} & 0 \\ 0 & 0 & C_{66} \end{bmatrix} \quad (20)$$

The normal (C_{11} , C_{22}) and coupling stiffness constants (C_{12} and C_{21}) of the \mathbb{C} -tensor were calculated from the slope of the stress-strain ($\sigma - \varepsilon$) plots in the NPT ensemble. The shear component (C_{66}) was obtained in the NVT ensemble because of the requirement of the volume preservation during shearing.

From the stiffness constants (C_{ij}), the compliance constants (S_{ij}) were obtained by matrix inversion of the stiffness tensor \mathbb{C} . The elastic moduli in the X- and Y-directions (E_{11} and E_{22} , respectively) were then calculated from the expression:

$$E_{ii} = \frac{1}{S_{ii}} \quad (21)$$

where S_{ii} are the diagonal components of the S-matrix with $i \in [1,2]$.

The Poisson's ratio (ν_{ij}) in any general direction was calculated using the compliance constants (S_{ii} and S_{ij}) from the expression:

$$\nu_{ij} = \frac{S_{iijj}}{S_{iiii}} = \frac{S_{ij}}{S_{ii}} \quad (22)$$

where S_{iijj} and S_{iiii} are the elements of the fourth order compliance matrix with $i, j \in [1,2]$.

A5.2.1 Directional linear compressibility

The directional dependence of the linear compressibility (β_L) was determined according to the following expression:

$$\beta_L = S_{ijkk} l_i l_j \quad (23)$$

where S_{ijkk} are the elements of the fourth order compliance matrix; $i, j, k \in [1,2]$; and l_i and l_j are the direction cosines. Due to the symmetry of the GS and FGS, the equation for the linear compressibility could be reduced to the following expression:

$$\beta_L = (S_{11} + S_{12}) l_1^2 + (S_{22} + S_{21}) l_2^2 \quad (24)$$

A5.2.2 Directional elastic and shear modulus

The directional elastic modulus in any $\langle h k l \rangle$ direction on the (0 0 1) plane (or X-Y plane) was calculated by expanding the expression of the compliance tensor in the new coordinate system, (S') as follows:

$$S'_{ijkl} = Q_{im} Q_{jn} Q_{ko} Q_{lp} S_{mnop} \quad (25)$$

Expanding and writing equation (25) in Voigt notation yields:

$$\frac{1}{E} = S'_{11} = S_{11} l_1^4 + S_{22} l_2^4 + (S_{12} + S_{21} + S_{66}) l_1^2 l_2^2 \quad (26)$$

where Q_{im} , Q_{jn} , Q_{ko} , and Q_{lp} are the components of the rotation matrix Q that represents the direction cosines between the new compliance tensor axes (S') and the old compliance tensor axes (S); and the indices $i, j, k, l, m, n, o, p \in [1,2]$; and l_1 and l_2 are the direction cosines.

The directional shear modulus on the (0 0 1) plane was calculated following the equation provided by Knowles and Howie [8]:

$$4S'_{ijkl} = 4S_{12} \delta_{ij} \delta_{kl} + 4S_{44} (\delta_{ij} \delta_{kl} + \delta_{il} \delta_{jk}) + (4S_{11} - 4S_{12} - 2S_{66}) Q_{im} Q_{jn} Q_{km} Q_{ln} \quad (27)$$

where Q_{im} , Q_{jm} , Q_{km} , and Q_{lm} are the components of the rotation matrix Q ; and δ_{ij} and δ_{kl} are the Kronecker delta functions with $i, j, k, l \in [1,3]$ that are represented by 3×3 identity matrices.

The directional shear modulus in any direction $\langle h k l \rangle$ (0 0 1) for the GS and FGS systems was then calculated as:

$$\frac{1}{G} = 4S'_{1212} = S_{66} + (4S_{11} - 4S_{12} - 2S_{66})(l_1^2 l_2^2 + m_1^2 m_2^2) \quad (28)$$

where l_1 , l_2 , m_1 , and m_2 are the direction cosines.

A5.3 Sound wave velocities

The longitudinal (V_L) and transversal (V_T) wave velocities were computed for waves traveling along the zigzag direction as follows:

$${}^{ZZ}V_L = \sqrt{\frac{C_{11}^{2D}}{\rho_{GS \text{ or FGS}}}} \quad (\text{longitudinal}) \quad (29)$$

$${}^{ZZ}V_T = \sqrt{\frac{C_{66}^{2D}}{\rho_{GS \text{ or FGS}}}} \quad (\text{transverse}) \quad (30)$$

where C_{11} and C_{66} are the normal and shear stiffness constants, respectively; and $\rho_{GS \text{ or FGS}}^{2D}$ is the mass per unit area (g cm^{-2}) of the GS or FGS. For waves traveling along the armchair direction, the longitudinal (V_L) wave velocities were computed as follows:

$${}^{AC}V_L = \sqrt{\frac{C_{22}^{2D}}{\rho_{GS \text{ or FGS}}}} \quad (\text{longitudinal}) \quad (31)$$

where C_{22} is the normal stiffness constant and $\rho_{GS \text{ or FGS}}^{2D}$ is the mass per unit area (g cm^{-2}) of the GS or FGS.

A6.0 Supplementary Figures

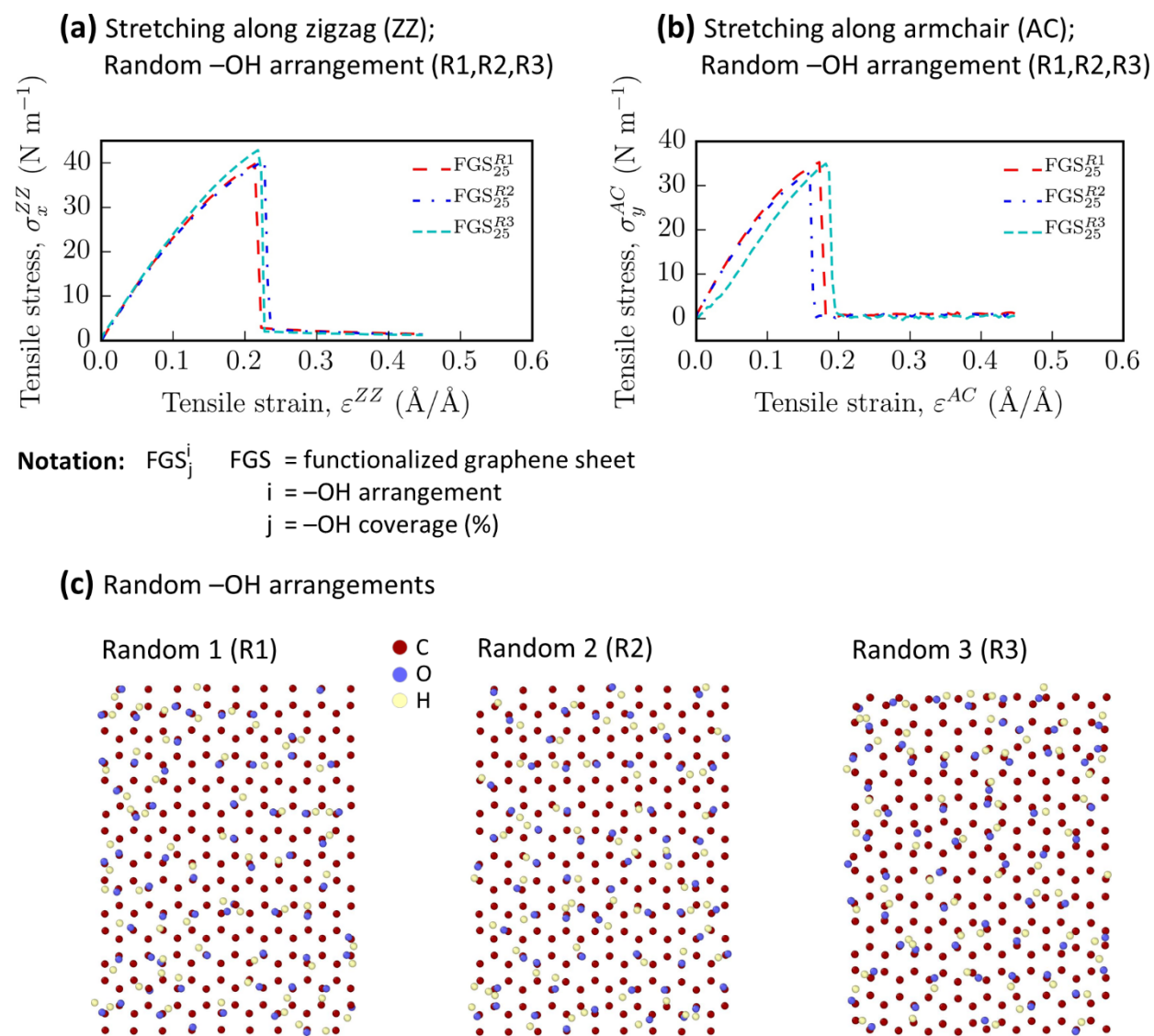


Figure A6.1. Stress-strain response for three different non-clustered random distributions of –OH functionalization for uniaxial tensile loading along (a) the zigzag direction and (b) the armchair direction. (c) Graphene sheet with 25% hydroxyl functionalization shown for three (3) different non-clustered random distributions. [R1: Random 1; R2: Random 2; and R3: Random 3]. The red, blue, and yellow balls represent carbon, oxygen, and hydrogen atoms, respectively.

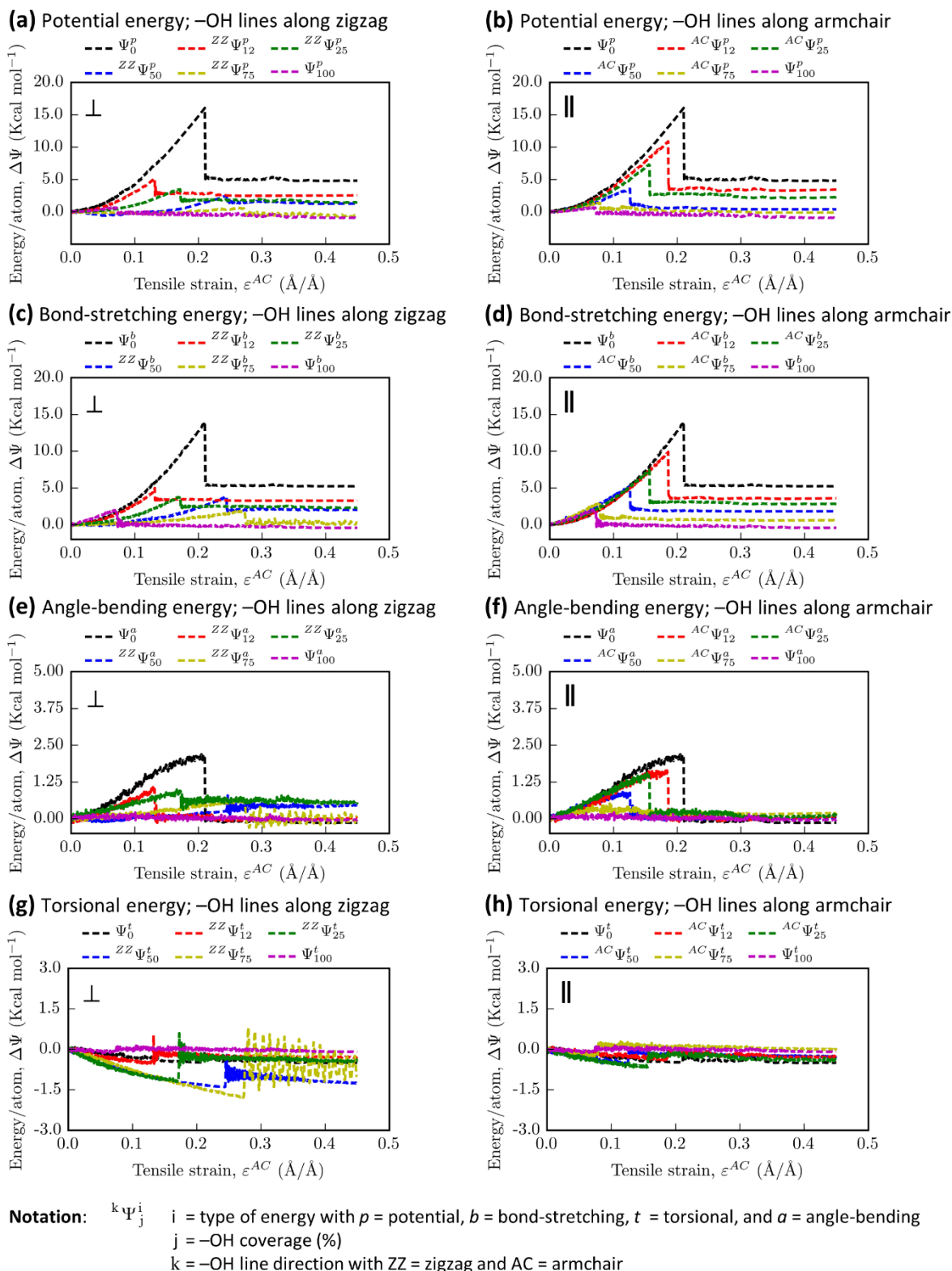


Figure A6.2. Energy changes as a function of strain for tensile loading along the armchair (AC) direction: (a), (b) potential energy (per atom on average); (c), (d) bond-stretching energy; (e), (f) angle-bending energy; and (g), (h) torsional energy (dihedral angles) for line patterns along the zigzag and armchair directions, respectively.

Stretching along zigzag (ZZ)

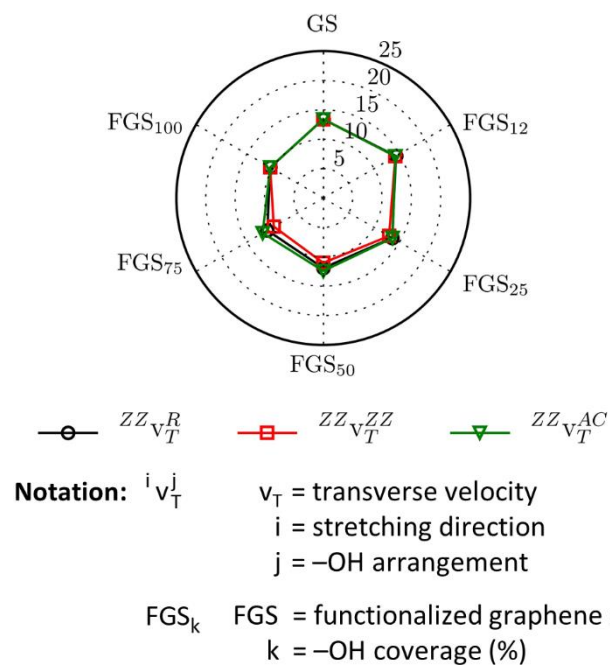


Figure A6.3. Transversal sound wave velocities through the GS and FGS for waves traveling along the zigzag direction. [R: random; ZZ: -OH line patterns along zigzag; AC: -OH line patterns along armchair].

A7.0 Supplementary Table

Table A1.3. Mechanical properties of graphene and functionalized graphene in the two perpendicular directions (i.e., zigzag and armchair) from atomistic and experimental studies reported in the literature. Results from this study shown for comparison.

Method	Potential	System	Loading direction	Fracture stress (GPa)	Fracture strain	Modulus (GPa)		Poisson's ratio	Papers
						Elastic	Shear		
ATOMISTIC STUDIES									
Pristine Graphene Sheet (GS)									
MD	CVFF	GS	ZZ	148 (49.6 Nm ⁻¹)*	0.29	838 (280 Nm ⁻¹)*	383 (127 Nm ⁻¹)*	0.145	This study
			AC	99.7 (33.4 Nm ⁻¹)*	0.19	856 (287 Nm ⁻¹)*	---	0.148	
MD	AIREBO	GS	ZZ	120	0.27	---	---	---	Degefe et al. [9]
			AC	100	0.19	---	---	---	
MD	AIREBO	GS	ZZ	137	0.268	832	---	---	Pei et al. [10]
			AC	105	0.172	893	---	---	
MD	AIREBO	GS	ZZ	141.5	0.2	1060	---	---	Zhang et al. [11]
			AC	115.9	0.138	1090	---	---	
MD	AIREBO	GS	ZZ	107	0.2	1010±30	---	0.21	Zhao et al. [12] [158][160][160][161][158][158]
			AC	90	0.13	1010±30	---	0.21	
MD	AIREBO	GS	ZZ	180	0.32	1090	---	---	Ni et al. [13]
			AC	210	0.44	---	---	---	
MD	Modified AIREBO	GS	ZZ	---	---	1025	---	---	Shen et al. [14]
MD	REBO	GS	ZZ	91	0.17	794	---	---	Ito et al. [15]
			AC	76	0.17	879	---	---	
MM	REBO	GS	AC	---	---	725	---	0.398	Lu et al. [16]
MD	ReaxFF	GS	ZZ	180	0.17	1074	---	---	Nayebi et al. [17]

Method	Potential	System	Loading direction	Fracture stress (GPa)	Fracture strain	Modulus (GPa)		Poisson's ratio	Papers
						Elastic	Shear		
MD	ReaxFF	GS	ZZ	138	0.28	751	186	0.502	Jensen et al. [18]
			AC	125	0.24	751	186	0.502	
MD	Tersoff-Brenner	GS	ZZ	127	0.233	800	---	---	Ansari et al. [19]
			AC	123	0.218	800	---	---	
MM	Tersoff-Brenner	GS	ZZ	---	---	669	---	0.416	Reddy et al. [20]
			AC	---	---			0.416	
MD	Brenner	GS	ZZ	---	---	---	---	-0.05 to 0.30 [†]	Jiang et al. [21]
MD	AMBER	GS	ZZ	---	---	912	358	0.26	Tsai et al. [22]
MD	Lennard-Jones	GS	ZZ	---	---	---	---	-0.9 to >0.5 ^{††}	Ulissi et al. [23]
MM	Morse	GS	ZZ	---	---	958	---	---	Meo et al. [24]
			AC	---	---	931	---	---	
DFPT	Trouller-Martin	GS	ZZ	121	0.266	1050	---	0.186	Liu et al. [25]
			AC	110	0.194	1050	---	0.186	
DFT	PBE	GS	ZZ	---	---	1021	435	0.173	Andrew et al. [26]
			AC	---	---	1021	435	0.173	
DFT	PBE	GS	ZZ	95.5	0.24	---	---	---	Wei et al. [27]
DFT	Pseudo-potential	GS	AC	---	---	---	---	0.14	Sanchez-Portal et al. [28]
EOS	PBE	GS	ZZ	---	---	1088	443	0.185	Tsai et al. [22]
			AC	---	---	1088	443	0.185	
QMD	Semi-empirical QM	GS	ZZ	~168	0.38	600	---	---	Gao et al. [29]
			AC	~119	0.14	1100	---	---	
MSM	NA	GS	ZZ	---	---	1040	213	1.441	Sakhaee-Pour [30]
			AC	---	---	1042	228	1.285	
CE	NA	GS	ZZ	---	---	1029	447	0.149	Kudin et al. [31]
			AC	---	---	1029	447	0.149	

Method	Potential	System	Loading direction	Fracture stress (GPa)	Fracture strain	Modulus (GPa)		Poisson's ratio	Papers
						Elastic	Shear		
Functionalized Graphene Sheet (FGS)									
MD	CVFF	-OH FGS (100%)	ZZ	47.8 (15.9 Nm ⁻¹)*	0.08	700 (234.6 Nm ⁻¹)*	320 (107 Nm ⁻¹)*	0.238	This study
			AC	40.3 (13.5 Nm ⁻¹)*	0.07	694 (232.4 Nm ⁻¹)*	---	0.234	
MD	MM3	-OH FGS (100%)	ZZ	---	---	720	150	---	Shah et al. [32]
MD	COMPASS	-OH FGS (7.5%)	ZZ	---	---	---	166	---	Zheng et al. [33]
MD	AIREBO	-H FGS (100%)	AC	35.4	0.095	---	---	---	Zhang et al. [34]
MD	AIREBO	-H FGS (100%)	AC	~34	0.06	---	---	---	Pei et al. [35]
MD	AIREBO	-CH ₃ FGS (1 line , 2%)	AC	132	0.239	801	---	---	Pei et al. [10]
MD	AIREBO	-CH ₃ FGS (1 line ⊥, 1.25%)	AC	87.2	0.128	766	---	---	Pei et al. [10]

Method	Potential	System	Loading direction	Fracture stress (GPa)	Fracture strain	Modulus (GPa)		Poisson's ratio	Papers
						Elastic	Shear		
EXPERIMENTAL STUDIES									
Pristine Graphene Sheet (GS)									
AFM - Nanoindentation	NA	GS	NA	130 ± 10	0.25	1014 ± 90	---	---	Lee et al. [36]
Raman spectroscopy	NA	GS	NA	---	---	2400	---	---	Lee et al. [37]
Mechanical double-paddle oscillator	NA	GS	NA	---	---	---	280 ± 36	---	Liu et al. [38]
Graphene Oxide (GO)									
AFM in contact mode	NA	GO	NA	---	---	156.5 ± 24	---	---	Suk et al. [39]
Multiwall Carbon Nanotubes (MWCNT)									
TEM w/ tensile testing stage	NA	MWCNT	NA	150	---	900	---	---	Demczyk et al. [40]

* The stress (modulus) in 2D (N m^{-1}) was obtained by multiplying the stress (modulus) in 3D (GPa) by the thickness of the GS or FGS as follows:

$$X^{3\text{D}} (\text{GPa}) = 10 \times (X^{2\text{D}} (\text{N m}^{-1})) \times (\text{Thickness} (\text{\AA}))^{-1}, \text{ where, } X = \text{stress or modulus and Thickness} = 3.35 \text{ \AA}.$$

† Poisson's ratio with respect to applied strain, where strain varies from 0 to 0.15.

†† Poisson's ratio with respect to longitudinal extension, where the extension varies from -5 to 30 (%).

--- Not reported

NA Not applicable

Directions

AC Armchair

ZZ Zigzag

Methods

CE Continuum elasticity

EOS Energy of state

MD Molecular dynamics modeling

MM Molecular mechanics

MSM Molecular structural mechanics

QM Quantum mechanics
QMD Quantum molecular dynamics

Potentials

AIREBO Adaptive Intermolecular Reactive Empirical Bond Order
AMBER Assisted Model Building and Energy Refinement
COMPASS Condensed-phase Optimized Molecular Potentials for Atomistic Simulation Studies
MM3 Molecular mechanics force field
ReaxFF Reactive force field
REBO Reactive Empirical Bond Order
PBE Perdew-Burke-Ernzerhof exchange-correlation functional

Experimental methods

AFM Atomic force microscopy
TEM Transmission electron microscopy

Appendix A References

- [1] P.M. Morse, Diatomic Molecules According to the Wave Mechanics. II. Vibrational Levels, *Physical Review* 34(1) (1929) 57-64.
- [2] T. Darden, D. York, L. Pedersen, Particle mesh Ewald: An $N \cdot \log(N)$ method for Ewald sums in large systems, *The Journal of Chemical Physics* 98(12) (1993) 10089-10092.
- [3] J.E. Jones, S. Chapman, On the determination of molecular fields. —II. From the equation of state of a gas, *Proceedings of the Royal Society of London. Series A, Containing Papers of a Mathematical and Physical Character* 106(738) (1924) 463-477.
- [4] H.A. Lorentz, Ueber die Anwendung des Satzes vom Virial in der kinetischen Theorie der Gase, *Annalen der Physik* 248(1) (1881) 127-136.
- [5] D. Berthelot, Sur Le Melange Des Gaz, *Comptes Rendus Hebdomadaires des Seances de l'Academie des Sciences* 126 (1898) 1703-1855.
- [6] A.K. Rappe, W.A. Goddard, Charge equilibration for molecular dynamics simulations, *The Journal of Physical Chemistry* 95(8) (1991) 3358-3363.
- [7] A. Nakano, Parallel multilevel preconditioned conjugate-gradient approach to variable-charge molecular dynamics, *Computer Physics Communications* 104(1) (1997) 59-69.
- [8] K.M. Knowles, P.R. Howie, The Directional Dependence of Elastic Stiffness and Compliance Shear Coefficients and Shear Moduli in Cubic Materials, *Journal of Elasticity* 120(1) (2015) 87-108.
- [9] M. Degefe, A. Parashar, Effect of non-bonded interactions on failure morphology of a defective graphene sheet, *Materials Research Express* 3(4) (2016) 045009.
- [10] Q.X. Pei, Y.W. Zhang, V.B. Shenoy, Mechanical properties of methyl functionalized graphene: a molecular dynamics study, *Nanotechnology* 21(11) (2010) 115709.
- [11] Y.Y. Zhang, Y.T. Gu, Mechanical properties of graphene: Effects of layer number, temperature and isotope, *Computational Materials Science* 71 (2013) 197-200.
- [12] H. Zhao, K. Min, N.R. Aluru, Size and Chirality Dependent Elastic Properties of Graphene Nanoribbons under Uniaxial Tension, *Nano Letters* 9(8) (2009) 3012-3015.
- [13] Z. Ni, H. Bu, M. Zou, H. Yi, K. Bi, Y. Chen, Anisotropic mechanical properties of graphene sheets from molecular dynamics, *Physica B: Condensed Matter* 405(5) (2010) 1301-1306.
- [14] Y. Shen, H. Wu, Interlayer shear effect on multilayer graphene subjected to bending, *Applied Physics Letters* 100(10) (2012) 101909.
- [15] A. Ito, S. Okamoto, Mechanical Properties of Vacancy-containing Graphene and Graphite Estimated by Molecular Dynamics Simulations, *MRS Proceedings* 1362 (2011) mrs11-1362-qq09-24.
- [16] Q. Lu, R. Huang, Nonlinear mechanics of single-atomic-layer graphene sheets, *International Journal of Applied Mechanics* 01(03) (2009) 443-467.
- [17] P. Nayebi, E. Zaminpayma, A molecular dynamic simulation study of mechanical properties of graphene–polythiophene composite with Reax force field, *Physics Letters A* 380(4) (2016) 628-633.
- [18] B.D. Jensen, K.E. Wise, G.M. Odegard, Simulation of the Elastic and Ultimate Tensile Properties of Diamond, Graphene, Carbon Nanotubes, and Amorphous Carbon Using a Revised ReaxFF Parametrization, *The Journal of Physical Chemistry A* 119(37) (2015) 9710-9721.
- [19] R. Ansari, S. Ajori, B. Motevalli, Mechanical properties of defective single-layered graphene sheets via molecular dynamics simulation, *Superlattices and Microstructures* 51(2) (2012) 274-289.

- [20] C.D. Reddy, S. Rajendran, K.M. Liew, Equilibrium configuration and continuum elastic properties of finite sized graphene, *Nanotechnology* 17(3) (2006) 864-870.
- [21] J.-W. Jiang, T. Chang, X. Guo, H.S. Park, Intrinsic Negative Poisson's Ratio for Single-Layer Graphene, *Nano Letters* 16(8) (2016) 5286-5290.
- [22] J.-L. Tsai, J.-F. Tu, Characterizing mechanical properties of graphite using molecular dynamics simulation, *Materials & Design* 31(1) (2010) 194-199.
- [23] Z.W. Ulissi, A. Govind Rajan, M.S. Strano, Persistently Auxetic Materials: Engineering the Poisson Ratio of 2D Self-Avoiding Membranes under Conditions of Non-Zero Anisotropic Strain, *ACS Nano* 10(8) (2016) 7542-7549.
- [24] M. Meo, M. Rossi, Prediction of Young's modulus of single wall carbon nanotubes by molecular-mechanics based finite element modelling, *Composites Science and Technology* 66(11) (2006) 1597-1605.
- [25] F. Liu, P. Ming, J. Li, Ab initio calculation of ideal strength and phonon instability of graphene under tension, *Physical Review B* 76(6) (2007) 064120.
- [26] R.C. Andrew, R.E. Mapasha, A.M. Ukpong, N. Chetty, Mechanical properties of graphene and boronitrene, *Physical Review B* 85(12) (2012) 125428.
- [27] X. Wei, B. Fragneaud, C.A. Marianetti, J.W. Kysar, Nonlinear elastic behavior of graphene: Ab initio calculations to continuum description, *Physical Review B* 80(20) (2009) 205407.
- [28] D. Sánchez-Portal, E. Artacho, J.M. Soler, A. Rubio, P. Ordejón, Ab initio structural, elastic, and vibrational properties of carbon nanotubes, *Physical Review B* 59(19) (1999) 12678-12688.
- [29] Y. Gao, P. Hao, Mechanical properties of monolayer graphene under tensile and compressive loading, *Physica E: Low-dimensional Systems and Nanostructures* 41(8) (2009) 1561-1566.
- [30] A. Sakhaee-Pour, Elastic properties of single-layered graphene sheet, *Solid State Communications* 149(1) (2009) 91-95.
- [31] K.N. Kudin, G.E. Scuseria, B.I. Yakobson, C₂F, BN and C nanoshell elasticity from ab initio computations, *Physical Review B* 64(23) (2001) 235406.
- [32] P.H. Shah, R.C. Batra, Elastic moduli of covalently functionalized single layer graphene sheets, *Computational Materials Science* 95 (2014) 637-650.
- [33] Q. Zheng, Y. Geng, S. Wang, Z. Li, J.-K. Kim, Effects of functional groups on the mechanical and wrinkling properties of graphene sheets, *Carbon* 48(15) (2010) 4315-4322.
- [34] Y.-Y. Zhang, Q.-X. Pei, C.-M. Wang, Y. Cheng, Y.-W. Zhang, A molecular dynamics investigation on mechanical properties of hydrogenated graphynes, *Journal of Applied Physics* 114(7) (2013) 073504.
- [35] Q.X. Pei, Y.W. Zhang, V.B. Shenoy, A molecular dynamics study of the mechanical properties of hydrogen functionalized graphene, *Carbon* 48(3) (2010) 898-904.
- [36] C. Lee, X. Wei, J.W. Kysar, J. Hone, Measurement of the Elastic Properties and Intrinsic Strength of Monolayer Graphene, *Science* 321(5887) (2008) 385.
- [37] J.-U. Lee, D. Yoon, H. Cheong, Estimation of Young's Modulus of Graphene by Raman Spectroscopy, *Nano Letters* 12(9) (2012) 4444-4448.
- [38] X. Liu, T.H. Metcalf, J.T. Robinson, B.H. Houston, F. Scarpa, Shear Modulus of Monolayer Graphene Prepared by Chemical Vapor Deposition, *Nano Letters* 12(2) (2012) 1013-1017.
- [39] J.W. Suk, R.D. Piner, J. An, R.S. Ruoff, Mechanical Properties of Monolayer Graphene Oxide, *ACS Nano* 4(11) (2010) 6557-6564.

[40] B.G. Demczyk, Y.M. Wang, J. Cumings, M. Hetman, W. Han, A. Zettl, R.O. Ritchie, Direct mechanical measurement of the tensile strength and elastic modulus of multiwalled carbon nanotubes, *Materials Science and Engineering: A* 334(1) (2002) 173-178.

APPENDIX B Supplementary materials for Chapter 4

This appendix includes the supplementary material for the paper published from the results of Chapter 4: B. Al-Muhit, F. Sanchez, Nano-engineering of the mechanical properties of tobermorite 14 Å with graphene via molecular dynamics simulations, *Construction and Building Materials*, Volume 233, 2020, 117237, doi.org/10.1016/j.conbuildmat.2019.117237

B1.0 Force field

The consistent valence force field (CVFF) includes both bonded and non-bonded (pair) energy terms, including the bond-stretching energy ($\Psi^{\text{bond-stretching}}$), the angle-bending energy ($\Psi^{\text{angle-bending}}$), the torsion-angle (dihedral) energy (Ψ^{torsion}), the out-of-plane energy (improper torsion) (Ψ^{improper}), the electrostatic energy ($\Psi^{\text{electrostatic}}$), and the van der Waals energy (Ψ^{vdW}). The Clay force-field (ClayFF) includes the bond-stretching energy ($\Psi^{\text{bond-stretching}}$) and the angle-bending energy ($\Psi^{\text{angle-bending}}$) for the bonded energy term, and the electrostatic energy ($\Psi^{\text{electrostatic}}$) and the van der Waals energy (Ψ^{vdW}) for the non-bonded (pair) energy term.

The total potential energy (Ψ^{total}) in the CVFF and ClayFF was calculated as the sum of the bonded energy (Ψ^{bonded}) and non-bonded energy ($\Psi^{\text{non-bonded}}$) using the following expression:

$$\Psi^{\text{total}} = \Psi^{\text{bonded}} + \Psi^{\text{non-bonded}} \quad (32)$$

The bonded energy (Ψ^{bonded}) for the CVFF was defined as follows:

$$\Psi^{\text{bonded}} = \Psi^{\text{bond-stretching}} + \Psi^{\text{angle-bending}} + \Psi^{\text{torsion}} + \Psi^{\text{improper}} \quad (33)$$

The bonded energy (Ψ^{bonded}) for the ClayFF was defined as follows:

$$\Psi^{\text{bonded}} = \Psi^{\text{bond-stretching}} + \Psi^{\text{angle-bending}} \quad (34)$$

The non-bonded energy ($\Psi^{\text{non-bonded}}$) for both CVFF and ClayFF was written as:

$$\Psi^{\text{non-bonded}} = \Psi^{\text{electrostatic}} + \Psi^{\text{vdW}} \quad (35)$$

B1.1 Bonded energy

B1.1.1 Bond-stretching energy

The bond-stretching energy was defined as the energy required to stretch a bond between two atoms from their equilibrium positions. The total bond-stretching energy (Ψ^b) was the sum of the energy from two bond-stretching potentials, i.e., the Morse ($\Psi^{b(\text{Morse})}$) and harmonic ($\Psi^{b(\text{harmonic})}$) potentials, written as follows:

$$\Psi^b = \Psi^{b(\text{Morse})} + \Psi^{b(\text{harmonic})} \quad (36)$$

Morse potential. The Morse bond potential [1] was used to simulate the bond-stretching and bond-breaking of the carbon atoms associated with the graphene sheet (GS) and was defined as:

$$\Psi^{b(\text{Morse})} = \sum_{N_b^{\text{Morse}}} D_b \left[1 - e^{-\alpha(\mathbf{r}-\mathbf{r}_0)} \right]^2 \quad (37)$$

$$\text{with } \alpha = \sqrt{\frac{K_b}{2D_b}} \quad (38)$$

where $\Psi^{b(\text{Morse})}$ is the bond-stretching energy ($\text{kcal mol}^{-1} \text{ \AA}^{-2}$) described by the Morse potential; D_b is the bond dissociation energy; \mathbf{r} and \mathbf{r}_0 are the current and equilibrium bond lengths in angstrom ($1 \text{ \AA} = 10^{-10} \text{ m}$); α is the Morse anharmonicity parameter; N_b^{Morse} is the number of Morse bonds; and K_b is the force constant at the minimum of the potential well.

Harmonic potential. The harmonic potential was used to simulate the bond-stretching between the O–H bonds of water ($\text{O}_w\text{--H}_w$) and hydroxyl ($\text{O}_h\text{--H}_h$) groups in the tobermorite 14\AA (T_{14}) systems as follows:

$$\Psi^{b(\text{harmonic})} = \sum_{N_b^{\text{harmonic}}} \frac{K_0}{2} (\mathbf{r}-\mathbf{r}_0)^2 \quad (39)$$

where $\Psi^{b(\text{harmonic})}$ is the harmonic bond-stretching energy ($\text{kcal mol}^{-1} \text{ \AA}^{-2}$); K_0 is the force constant at the minimum of the potential well; \mathbf{r} and \mathbf{r}_0 are the current and equilibrium bond lengths in angstrom ($1 \text{ \AA} = 10^{-10} \text{ m}$), respectively; and N_b^{harmonic} is the number of Morse bonds.

B1.1.2 Angle-bending potential

The angle-bending energy ($\Psi^{\text{angle-bending}}$) was defined as the energy required for the GS and water molecules in the T₁₄ systems to resist against angular deformation from their equilibrium position. The angle-bending potential expresses the bending energy change of angles as:

$$\Psi^{\text{angle-bending}} = \sum_{N_a} \frac{K_0}{2} (\theta - \theta_0)^2 \quad (40)$$

where K_0 is the angle-bending energy (kcal mol⁻¹ rad⁻²); θ and θ_0 are current and equilibrium bond-angles in degrees, respectively; and N_a is the number of angles. The angle-bending energies for the GS and T₁₄ systems were calculated for the angle types $\angle \text{C-C-C}$ and $\angle \text{H}_w\text{-O}_w\text{-H}_w$ (C: carbon, H_w: water hydrogen, and O_w: water oxygen).

B1.1.3 Torsion potential

The torsional (dihedral) energy (Ψ^{torsion}) was expressed as the angle twisting energy between a quadruple of atoms of the GS, which was defined by the following expression:

$$\Psi^{\text{torsion}} = \sum_{N_t} V [1 + \cos(n\varphi - \varphi_0)] \quad (41)$$

where V is the half-height of the energy barrier (kcal mol⁻¹); n is the periodicity (multiplicity) of torsion (n always equal to 2); φ and φ_0 are the current and equilibrium torsion angles with φ_0 equal to either 0° or 180°; and N_t is the number of torsion angles. The torsion angles were calculated between the quadruples of atoms. The torsional twisting energies were calculated for the C-C-C-C types of torsional angles.

B1.1.4 Out-of-plane bending potential

The improper (out-of-plane) deformation energy (Ψ^{improper}) of the GS was evaluated between a quadruple of atoms using the following expression:

$$\Psi^{\text{improper}} = \sum_{\text{improper}} V [1 + \cos(n\chi - \chi_0)]^2 \quad (42)$$

where V is half of the energy barrier height of the improper angle (kcal mol^{-1}); n is the periodicity (multiplicity) of the improper torsion (n always equal to 2); χ and χ_0 are the current and equilibrium improper torsion angles, respectively, with χ_0 always equal to 180° ; and N_i is the number of improper torsion angles. The CVFF converted the degrees ($^\circ$) into radians automatically. The improper (out-of-plane) bending energies for the GS systems were computed for the quadruple improper bending types C–C–C–C.

B1.2 Non-bonded energy (pair energy)

B1.2.1 Electrostatic energy

The electrostatic (Coulombic) energy ($\Psi^{\text{electrostatic}}$) between any pair of atoms in the GS and T₁₄ systems were calculated and summed over all of the atoms of the GS and T₁₄ using the following expression:

$$\Psi^{\text{electrostatic}} = \sum_i \sum_{j>i} \frac{1}{4\pi \epsilon_0} \cdot \frac{q_i q_j}{r_{ij}^2} \quad (43)$$

$$\text{with } r_{ij} = |\mathbf{r}_i - \mathbf{r}_j| \quad (44)$$

where q_i and q_j are the partial charges on the atoms i and j ; ϵ_0 is the permittivity in the vacuum (8.85419×10^{-12} F/m); and r_{ij} is the interatomic distance (\AA) between the atoms i and j . The short-range electrostatic attraction energy was calculated in the real space, whereas the long-range portion of the electrostatic energy was calculated in the reciprocal space with a cut-off distance of 10 \AA using the Ewald summation approach [2] to increase computational efficiency.

B1.2.2 van der Waals (vdW) energy

The vdW energy observed between atoms was calculated using the 12-6 Lennard-Jones (LJ) potential [3]:

$$\Psi^{\text{vdW}} = \sum_i \sum_{j>i} 4\epsilon \left[\left(\frac{\sigma}{r_{ij}} \right)^{12} - \left(\frac{\sigma}{r_{ij}} \right)^6 \right] \quad (45)$$

where ϵ is the depth of the potential well (kcal mol⁻¹); σ is the distance in angstrom (Å) at which the potential is zero; and \mathbf{r}_{ij} is the interatomic distance (Å) between the atoms i and j .

Although the 12-6 LJ potential was sufficient to calculate the short-range repulsion and long-range attraction energies, the latter part was calculated in the reciprocal space with a vdW cut-off distance of 10 Å using the Ewald summation approach [2] to increase computational efficiency.

B1.3 Interaction between unlike atoms

The Lorentz-Berthelot mixing rules [4, 5] were applied for the calculation of the energy and interatomic distances between unlike atoms. In the CVFF and ClayFF, this rule is known as the arithmetic rule:

$$\sigma_{ij} = \left(\frac{\sigma_{ii} + \sigma_{jj}}{2} \right) \quad (46)$$

$$\epsilon_{ij} = \sqrt{\epsilon_{ii}\epsilon_{jj}} \quad (47)$$

where σ_{ij} is the distance between unlike atoms i and j , which is calculated from the mean distance of the like-atoms i, i and j, j . Similarly, ϵ_{ij} is the energy between unlike atoms i and j , which is termed as the square root of the multiplication of the energy of the like-atoms i, i and j, j .

B1.4 Forcefield parameters for energy calculation

The CVFF parameters necessary to calculate the bonded and non-bonded (pair) interactions of the GS are tabulated in Tables S1 and S2, respectively. The ClayFF parameters for the T₁₄ systems are tabulated in the Tables S3 and S4, respectively.

Table B1.1 CVFF parameters for the bonded energies of the graphene sheet (GS) in the GS reinforced tobermorite 14 Å nanocomposites.

Parameters	Interactions	D_b	α	r_{ij}	K	θ_0	V	n	φ_0	χ_0
Bond-stretching	C–C	120.00	2.0	1.34	---	---	---	---	---	---
Angle-bending	C–C–C	---	---	---	90	120	---	---	---	---
Dihedral/torsional	C–C–C–C	---	---	---	---	---	120	2	-1	---
Improper	C–C–C–C	---	---	---	---	---	0.37	2	---	-1

Notation: D_b = dissociation energy; α = Morse anharmonicity parameter; r_{ij} = distance between interacting atoms; K_0 = angle-bending energy; θ_0 = equilibrium angle; V = half of the energy barrier height; n = periodicity; φ_0 = equilibrium torsion angle; χ_0 = equilibrium improper (out-of-plane bending) angle.

Table B1.2 CVFF parameters of the Lennard-Jones (LJ) potential for the calculation of the vdW non-bonded energies of the graphene sheet (GS) in the GS reinforced tobermorite 14 Å nanocomposites.

Parameters	Interacting types of atoms	Energy, ϵ (kcal mol ⁻¹)	Distance, σ (Å)
Lennard-Jones (LJ)	C–C	0.14799	3.617

Table B1.3 ClayFF partial charges on atoms and parameters for the non-bonded energies (both coulomb and LJ potential) of the tobermorite 14 Å (T₁₄) structure in the pristine T₁₄ systems and graphene reinforced T₁₄ nanocomposites.

Atoms	Charge, q (e ⁻)	Distance, σ (Å)	Energy, ϵ (Kcal mol ⁻¹)
Ca _o	1.36	6.2484	5.0298×10 ⁻⁶
Si _t	2.1	3.302	1.84×10 ⁻⁶
O _b	-1.05	3.1655	0.1554
O _{bts}	-1.1688	3.1655	0.1554
O _h	-0.95	3.1655	0.1554
O _w	-0.82	3.1655	0.1554
H _w	0.41	0.0	0.0
H _h	0.425	0.0	0.0
Ca _w	2.0	3.2237	0.1

Notation: Ca_o: octahedral calcium; Si_t: tetrahedral silicon; O_b: bridging oxygen; O_{bts}: bridging oxygen in tetrahedral; O_h: hydroxyl oxygen; O_w: water oxygen; H_w: water hydrogen; H_h: hydroxyl hydrogen; Ca_w: interlayer calcium; C: carbon in graphene.

Table B1.4 ClayFF parameters for the bonded energies of the tobermorite 14 Å (T₁₄) structure in the pristine T₁₄ systems and graphene reinforced T₁₄ nanocomposites.

Parameters	Interactions	D_b	r_{ij}	K	θ_0
Bond-stretching	O _h -H _h	554.134	1.00	---	---
	O _w -H _w	554.134	1.00	---	---
Angle-bending	H _w -O _w -H _w	---	---	45.769	109.47

Notation: D_b = dissociation energy; r_{ij} = distance between interacting atoms; K_0 = angle-bending energy; θ_0 = equilibrium angle.

Appendix B References

- [1] Morse PM. Diatomic molecules according to the wave mechanics. II. Vibrational levels. *Physical Review* 1929;34(1):57-64. DOI: 10.1103/PhysRev.34.57
- [2] Darden T, York D, Pedersen L. Particle mesh Ewald: An N·log(N) method for Ewald sums in large systems. *The Journal of Chemical Physics* 1993;98(12):10089-10092. DOI: 10.1063/1.464397
- [3] Jones JE, Chapman S. On the determination of molecular fields. —II. From the equation of state of a gas. *Proceedings of the Royal Society of London. Series A, Containing Papers of a Mathematical and Physical Character* 1924;106(738):463-477. DOI: 10.1098/rspa.1924.0082
- [4] Lorentz HA. Ueber die Anwendung des Satzes vom Virial in der kinetischen Theorie der Gase. *Annalen der Physik* 1881;248(1):127-136. DOI: doi:10.1002/andp.18812480110
- [5] Berthelot D. Sur le melange des gaz. *Comptes Rendus Hebdomadaires des Seances de l'Academie des Sciences* 1898;126:1703-1855.

APPENDIX C Molecular dynamics scripts for Chapter 3

This appendix includes the representative LAMMPS scripts for equilibration, tensile simulation, and potential energy derived in Chapter 3.

C1.0 Representative LAMMPS script for X-direction for FGS with 25% -OH in ZZ clustered line pattern

```
## graphene 1 layer
# X- orientation 25 % -OH functionalization
# strain in x-direction (zigzag)

# Variable Initialization
variable          t equal "300"
echo              screen
log               debug_grap1oh25xX.log

units             real
boundary          p p p
newton            on
processors        * * *

# Bonded Interaction
atom_style        full
bond_style        hybrid morse harmonic
angle_style       harmonic
dihedral_style    harmonic
improper_style    cvff

# Non-Bonded Interaction
pair_style         lj/cut/coul/long 10.0 10.0 # cutoff1 = 2.5*sigma
read_data          data.grap1oh25x
neighbor           3.0 bin
neigh_modify       delay 0 every 1 one 10000 check yes
pair_modify        mix arithmetic tail no
kspace_style       ewald 1e-6
#kspace_modify     pressure/scalar no
special_bonds      lj/coul 1e-50 1e-50 1e-50
group              carbon type 1
group              ox type 2
group              hyd type 3
group              graphene type 1
group              hydroxyl type 2 3

bond_coeff 1 morse    120.0    2.0    1.3400 # cp-cp
bond_coeff 2 harmonic 384      1.37      # cp-oh
bond_coeff 3 harmonic 540.6336 0.96      # oh-ho

# Charge Equilibration

compute           mobile_temp all temp
compute           COM all com
```

```

variable      dx equal c_COM[1]
variable      dy equal c_COM[2]
variable      dz equal c_COM[3]
compute       qC carbon property/atom q
compute       qO ox property/atom q
compute       qH hyd property/atom q
compute       q_NC carbon reduce sum c_qC
compute       q_NO ox reduce sum c_qO
compute       q_NH hyd reduce sum c_qH
variable      Ng equal count(graphene)
variable      NO equal count(ox)
variable      NH equal count(hyd)
variable      qC equal c_q_NC/${Ng}
variable      qO equal c_q_NO/${NO}
variable      qH equal c_q_NH/${NH}
compute       MSD all msd com yes
variable      MSD equal c_1[1]
compute       RDF all rdf 500 1 1 1 2 2 3

fix           fix_charge all qeq/point 1 10 1e-6 400 param.qeq2
thermo        100
thermo_style  custom step v_qC v_qO v_qH
run           0
unfix        fix_charge

# Minimization
minimize      1.0e-20 1.0e-20 100 1000
min_style     cg
min_modify    dmax 0.1

# Equilibration Process NVE + NPT

velocity      all create ${t} 12345 temp mobile_temp dist gaussian mom yes rot no
fix           fix_mom all momentum 1 linear 1 1 1
fix           fix_NVT all nvt temp ${t} ${t} 100
fix           fix_BEREND all temp/berendsen ${t} ${t} 100
dump          dump_XYZ all xyz 100 grap1oh25x.xyz

thermo        1000
thermo_style  custom step temp pe etotal press vol density
thermo_modify lost error flush yes
run           200000
unfix        fix_NVT

#-----NPT-----xxx
reset_timestep 0
fix           fix_NPT all npt temp ${t} ${t} 100.0 x 0 0 1000 y 0 0 1000
fix           fix_RDF all ave/time 100 10000 1000000 c_RDF[1] c_RDF[2] c_RDF[3] c_RDF[4] c_RDF[5]
c_RDF[6] c_RDF[7] file grap1oh25x.rdf mode vector
thermo_modify lost error flush yes
run           1000000
unfix        fix_NPT
unfix        fix_RDF
write_restart restart.grap1oh25X.equil

```

```

reset_timestep 0
region leftbdy block INF 0 INF INF INF INF units box
group leftbdy region leftbdy
region rightbdy block 17 INF INF INF INF INF units box
group rightbdy region rightbdy
group mobile subtract all leftbdy rightbdy

variable strainx equal "(lx-v_10x)/v_10x"
variable e1 equal "v_strainx"
variable strainy equal "(ly-v_10y)/v_10y"
variable e2 equal "v_strainy"
variable strainz equal "(lz-v_10z)/v_10z"
variable e3 equal "v_strainz"
variable lxy equal xy
variable lxy0 equal ${lxy}
variable e12 equal (v_lxy-v_lxy0)/v_10y
variable lxz equal xz
variable lxz0 equal ${lxz}
variable e13 equal (v_lxz-v_lxz0)/v_10z
variable lyz equal yz
variable lyz0 equal ${lyz}
variable e23 equal (v_lyz-v_lyz0)/v_10z

# Determination of Strain rates
variable erate equal "1e9"
variable erate1 equal "v_erate/1e15"

compute peratom mobile stress/atom mobile_temp
compute stp mobile reduce sum c_peratom[1] c_peratom[2] c_peratom[3] c_peratom[4] c_peratom[5]
c_peratom[6]

variable tmpx equal "lx"
variable l0x equal ${tmpx}
print "initial length, l0-x: ${l0x}"
variable tmpy equal "ly"
variable l0y equal ${tmpy}
print "initial length in y, l0-y: ${l0y}"
variable tmpz equal "lz"
variable l0z equal ${tmpz}
print "initial length in z, l0-z: ${l0z}"
variable factor equal 1.01325e-4

variable r equal ${l0z}/6.4
variable volinit equal ${l0x}*${l0y}*${l0z}
variable peratom atom c_peratom[1]
variable s11 equal c_stp[1]
variable s22 equal c_stp[2]
variable s33 equal c_stp[3]
variable s12 equal c_stp[4]
variable s13 equal c_stp[5]
variable s23 equal c_stp[6]
variable factor equal 1.01325e-4

variable p11 equal v_s11*v_r*6.4*0.1*${factor}/v_volinit
variable p22 equal v_s22*v_r*6.4*0.1*${factor}/v_volinit

```



```

variable      p33 equal v_s33*v_r*6.4*0.1*${factor}/v_volinit
variable      p12 equal v_s12*v_r*6.4*0.1*${factor}/v_volinit
variable      p13 equal v_s13*v_r*6.4*0.1*${factor}/v_volinit
variable      p23 equal v_s23*v_r*6.4*0.1*${factor}/v_volinit
variable      speratom1 atom c_peratom[1]*v_factor
variable      speratom2 atom c_peratom[2]*v_factor

compute      force all property/atom fx fy fz
variable      fx atom c_force[1]
variable      fy atom c_force[2]
variable      fz atom c_force[3]

compute      pe mobile pe/atom
compute      poteng mobile reduce ave c_pe
compute      ebond mobile pe/atom bond
compute      tbond mobile reduce ave c_ebond
compute      eangle mobile pe/atom angle
compute      tangle mobile reduce ave c_eangle
compute      edihed mobile pe/atom dihedral
compute      tdihed mobile reduce ave c_edihed
compute      epair mobile pe/atom pair
compute      tpair mobile reduce ave c_epair

variable      num_all equal count(mobile)
variable      Epot equal c_poteng
variable      Ebond equal c_tbond
variable      Eangle equal c_tangle
variable      Edihed equal c_tdihed
variable      Epair equal c_tpair

fix          f_DEFORM all deform 1 x erate ${erate1} units box remap x
fix          8 mobile npt temp ${t} ${t} 100 y 0 0 1000 z 0 0 1000
dump         d_movie all movie 4500 grap1oh25xX.movie.mpeg type type axes yes 0.2 0.05 view 0 90
dump         d_vel all custom 9000 grap1oh25xX.lammpstrj id type x y z v_speratom1
dump         d_XYZ all xyz 1000 grap1oh25xX.xyz
fix          9 mobile ave/time 45 100 4500 v_e1 v_p11 mode scalar file grap1oh25xX.profile

fix          f_ENERGY mobile print 450 "${e1} ${Epot} ${Ebond} ${Eangle} ${Edihed} ${Epair}" file
grap1oh25xX.energy screen no
thermo_style custom step temp v_e1 v_p11
run          450000

unfix       f_ENERGY

```

C2.0 Representative LAMMPS scripts for Y-direction of FGS with 25% -OH in ZZ clustered line pattern

```

## graphene 1 layer
# X- orientation 25 % -OH functionalization
# strain in Y-direction (zigzag)

# Variable Initialization
variable      t equal "300"
echo          screen
log           debug_grap1oh25xY.log

```

```

units          real
boundary       p p p
newton         on
processors     * * *

# Bonded Interaction
atom_style     full
bond_style     hybrid morse harmonic
angle_style    harmonic
dihedral_style harmonic
improper_style cvff

# Non-Bonded Interaction
pair_style     lj/cut/coul/long 10.0 10.0 # cutoff1 = 2.5*sigma
read_data      data.grap1oh25x
neighbor       3.0 bin
neigh_modify   delay 0 every 1 one 10000 check yes
pair_modify    mix arithmetic tail no
kspace_style   ewald 1e-6
#kspace_modify pressure/scalar no
special_bonds  lj/coul 1e-50 1e-50 1e-50
group          carbon type 1
group          ox type 2
group          hyd type 3
group          graphene type 1
group          hydroxyl type 2 3

bond_coeff     1 morse          120.0  2.0  1.3400 # cp-cp
bond_coeff     2 harmonic       384    1.37          # cp-oh
bond_coeff     3 harmonic       540.6336 0.96          # oh-ho

# Charge Equilibration

compute        mobile_temp all temp
compute        COM all com
variable       dx equal c_COM[1]
variable       dy equal c_COM[2]
variable       dz equal c_COM[3]
compute        qC carbon property/atom q
compute        qO ox property/atom q
compute        qH hyd property/atom q
compute        q_NC carbon reduce sum c_qC
compute        q_NO ox reduce sum c_qO
compute        q_NH hyd reduce sum c_qH
variable       Ng equal count(graphene)
variable       NO equal count(ox)
variable       NH equal count(hyd)
variable       qC equal c_q_NC/{Ng}
variable       qO equal c_q_NO/{NO}
variable       qH equal c_q_NH/{NH}
compute        MSD all msd com yes
variable       MSD equal c_1[1]
compute        RDF all rdf 500 1 1 1 2 2 3

fix            fix_charge all qeq/point 1 10 1e-6 400 param.qeq2

```

```

thermo          100
thermo_style    custom step v_qC v_qO v_qH
run             0
unfix          fix_charge

# Minimization
minimize        1.0e-20 1.0e-20 100 1000
min_style       cg
min_modify      dmax 0.1

# Equilibration Process NVE + NPT

velocity        all create ${t} 12345 temp mobile_temp dist gaussian mom yes rot no
fix             fix_mom all momentum 1 linear 1 1 1
fix            fix_NVT all nvt temp ${t} ${t} 100
fix            fix_BEREND all temp/berendsen ${t} ${t} 100
dump           dump_XYZ all xyz 100 grap1oh25x.xyz

thermo          1000
thermo_style    custom step temp pe etotal press vol density
thermo_modify   lost error flush yes
run            200000
unfix          fix_NVT

#-----NPT-----xxx
reset_timestep  0
fix            fix_NPT all npt temp ${t} ${t} 100.0 x 0 0 1000 y 0 0 1000
fix            fix_RDF all ave/time 100 10000 1000000 c_RDF[1] c_RDF[2] c_RDF[3] c_RDF[4] c_RDF[5]
c_RDF[6] c_RDF[7] file grap1oh25x.rdf mode vector
thermo_modify   lost error flush yes
run            1000000
unfix          fix_NPT
unfix          fix_RDF
#write_restart restart.grap1oh12x.equil

reset_timestep  0
region         leftbdy block INF INF INF -10 INF INF units box
group          leftbdy region leftbdy
region         rightbdy block INF INF 15 INF INF INF units box
group          rightbdy region rightbdy
group          mobile subtract all leftbdy rightbdy

variable       strainx equal "(lx-v_10x)/v_10x"
variable       e1 equal "v_strainx"
variable       strainy equal "(ly-v_10y)/v_10y"
variable       e2 equal "v_strainy"
variable       strainz equal "(lz-v_10z)/v_10z"
variable       e3 equal "v_strainz"
variable       lxy equal xy
variable       lxy0 equal ${lxy}
variable       e12 equal (v_lxy-v_lxy0)/v_10y
variable       lxz equal xz
variable       lxz0 equal ${lxz}
variable       e13 equal (v_lxz-v_lxz0)/v_10z
variable       lyz equal yz

```

```

variable      lyz0 equal ${lyz}
variable      e23 equal (v_lyz-v_lyz0)/v_l0z

# Determination of Strain rates
variable      erate equal "1e9"
variable      erate1 equal "v_erate/1e15"

compute      peratom mobile stress/atom mobile_temp
compute      stp mobile reduce sum c_peratom[1] c_peratom[2] c_peratom[3] c_peratom[4] c_peratom[5]
c_peratom[6]

variable      tmpx equal "lx"
variable      l0x equal ${tmpx}
print        "initial length, l0-x: ${l0x}"
variable      tmpy equal "ly"
variable      l0y equal ${tmpy}
print        "initial length in y, l0-y: ${l0y}"
variable      tmpz equal "lz"
variable      l0z equal ${tmpz}
print        "initial length in z, l0-z: ${l0z}"
variable      factor equal 1.01325e-4

variable      r equal ${l0z}/6.4
variable      volinit equal ${l0x}*${l0y}*${l0z}
variable      peratom atom c_peratom[1]
variable      s11 equal c_stp[1]
variable      s22 equal c_stp[2]
variable      s33 equal c_stp[3]
variable      s12 equal c_stp[4]
variable      s13 equal c_stp[5]
variable      s23 equal c_stp[6]
variable      factor equal 1.01325e-4

variable      p11 equal v_s11*v_r*6.4*0.1*${factor}/v_volinit
variable      p22 equal v_s22*v_r*6.4*0.1*${factor}/v_volinit
variable      p33 equal v_s33*v_r*6.4*0.1*${factor}/v_volinit
variable      p12 equal v_s12*v_r*6.4*0.1*${factor}/v_volinit
variable      p13 equal v_s13*v_r*6.4*0.1*${factor}/v_volinit
variable      p23 equal v_s23*v_r*6.4*0.1*${factor}/v_volinit
variable      speratom1 atom c_peratom[1]*v_factor
variable      speratom2 atom c_peratom[2]*v_factor

compute      force all property/atom fx fy fz
variable      fx atom c_force[1]
variable      fy atom c_force[2]
variable      fz atom c_force[3]

compute      pe mobile pe/atom
compute      poteng mobile reduce ave c_pe
compute      ebond mobile pe/atom bond
compute      tbond mobile reduce ave c_ebond
compute      eangle mobile pe/atom angle
compute      tangle mobile reduce ave c_eangle
compute      edihed mobile pe/atom dihedral
compute      tdihed mobile reduce ave c_edihed
compute      epair mobile pe/atom pair

```

```

compute          tpair mobile reduce ave c_epair

variable         num_all equal count(mobile)
variable         Epot equal c_poteng
variable         Ebond equal c_tbond
variable         Eangle equal c_tangle
variable         Edihed equal c_tdihed
variable         Epair equal c_tpair

fix              f_DEFORM all deform 1 y erate ${erate1} units box remap x
fix              8 mobile npt temp ${t} ${t} 100 x 0 0 1000 z 0 0 1000
dump             d_movie all movie 4500 grap1oh25xY.movie.mpeg type type axes yes 0.2 0.05 view 0 90
dump             d_vel all custom 9000 grap1oh25xY.lammpstrj id type x y z v_speratom2
dump             d_XYZ all xyz 1000 grap1oh25xY.xyz
fix              9 mobile ave/time 45 100 4500 v_e2 v_p22 mode scalar file grap1oh25xY.profile

fix              f_ENERGY mobile print 450 "${e2} ${Epot} ${Ebond} ${Eangle} ${Edihed} ${Epair}" file
grap1oh25xY.energy screen no
thermo_style     custom step temp v_e2 v_p22
run              450000
unfix            f_ENERGY

```

APPENDIX D Molecular dynamics scripts for Chapter 4

This appendix includes representative LAMMPS scripts for Chapter 4, Section 4.1 and 4.3.

D1.0 Representative LAMMPS scripts for equilibration for the T₁₄/FGS with 25% -OH in ZZ clustered line pattern

```
## LAMMPS input file
```

```
# Tobermorite-14 Ang with Ca/Si = 0.833 and water/Si = 0.857
```

```
# 25% -OH group on Graphene (Full functionalization)
```

```
# ZZ-orientation of Graphene along X-direction
```

```
# (0 0 -1) interface
```

```

# Equilibration
# Declare variable

variable      t equal 300
echo          screen
log           t14grap25X.log

units        real
newton       on
processors    * * *
boundary     p p p

atom_style   full
bond_style   hybrid harmonic morse
angle_style  harmonic
dihedral_style harmonic
improper_style cvff

pair_style   lj/cut/coul/long 12.0 10.0
read_data    t14grap25X.data extra/atom/types 1

bond_coeff   1      harmonic 554.1349 1.0
bond_coeff   2      harmonic 554.1349 1.0
bond_coeff   3      harmonic 554.1349 1.0
bond_coeff   4      morse 120.0    2.0 1.3400
bond_coeff   5      harmonic      384    1.37      # cp-oh
bond_coeff   6      harmonic      540.6336 0.96      # oh-ho

angle_coeff  1      45.7696 109.47
angle_coeff  2      45.7696 109.47
angle_coeff  3      90      120
angle_coeff  4      60.0000 120.0000 # cp-cp-oh*
angle_coeff  5      50.0000 109.0000 # cp-oh*-ho*

dihedral_coeff 1      12.0000 -1 2
dihedral_coeff 2      1.8000 -1 2 # cp-cp-cp-oh*
dihedral_coeff 3      3.0000 -1 2 # oh*-cp-cp-oh*
dihedral_coeff 4      1.5000 1 2 # cp-cp-oh*-ho*

improper_coeff 1 0.3700 -1 2 # cp-cp-cp-cp

pair_coeff    1      1      5.03e-6 6.2484
pair_coeff    2      2      1.8405e-6 3.302
pair_coeff    3      3      0.1554 3.1655
pair_coeff    4      4      0.1554 3.1655
pair_coeff    5      5      0.1554 3.1655
pair_coeff    6      6      0.1554 3.1655
pair_coeff    7      7      0.0      0.0
pair_coeff    8      8      0.1554 3.1655
pair_coeff    9      9      0.0      0.0
pair_coeff   10     10     0.0      0.0
pair_coeff   11     11     0.1      3.2237

```

pair_coeff	12	12	0.148	3.617
pair_coeff	13	13	0.2279965679	3.2100039927 # oh*
pair_coeff	14	14	0.0000000000	0.0000000000 # ho*
pair_coeff	15	15	0.1	3.2237

kspace_style	pppm	1e-6
special_bonds	lj/coul	1e-50 1e-50 1e-50
pair_modify	mix arithmetic	tail no
run_style	verlet	

neighbor	5.0	bin
neigh_modify	delay 0	every 1 one 10000 check yes
comm_style	brick	
comm_modify	mode single	group all cutoff 10

group	cao	type 1
group	st	type 2
group	ob	type 3
group	obts	type 4
group	oh	type 5
group	ow	type 6
group	hw	type 7
group	owd	type 8
group	hwd	type 9
group	ho	type 10
group	Ca	type 11
group	cp	type 12
group	og	type 13
group	hg	type 14

group	wat	type 6 7
group	watd	type 8 9
group	t14	type <= 11
group	solid	subtract t14 wat watd

set	type 1	charge 1.36
set	type 2	charge 2.1
set	type 3	charge -1.311873047
set	type 4	charge -1.311873047
set	type 5	charge -0.95
set	type 6	charge -0.82
set	type 7	charge 0.41
set	type 8	charge -0.82
set	type 9	charge 0.41
set	type 10	charge 0.425
set	type 11	charge 2
set	type 15	charge 2
mass	15	40.007980

group	carbon	type 12
group	grapoh	type 12 13 14


```

compute      qC carbon property/atom q
compute      qO og property/atom q
compute      qH hg property/atom q
compute      q_NC carbon reduce ave c_qC
compute      q_NO og reduce ave c_qO
compute      q_NH hg reduce ave c_qH
variable     qC equal c_q_NC
variable     qO equal c_q_NO
variable     qH equal c_q_NH

fix          fix_charge grapoh qeq/point 1 10 1e-6 1000 param.test
thermo_style custom step v_qC v_qO v_qH
run          1
unfix       fix_charge

# Delete 50% of 2nd type of water (watd) from t14
region      t14box block -0.5 27 -0.75 27 -6 28.75 units box
compute     newtemp all temp
velocity    all create ${t} 71993 temp newtemp dist gaussian mom yes rot no

variable    num_watd equal 0.5*count(watd)
fix         1 watd evaporate 1 ${num_watd} t14box 71993 molecule yes
run         1
unfix      1

# Delete 50% of interlayer Ca atoms from t14
set         type 11 type/fraction 15 0.5 71993
group      delcal type 15
delete_atoms group delcal compress yes bond yes
group      Ca type 11

variable    v equal count(all)

compute     EPOT all pe
compute     EPAIR grapoh group/group t14 pair yes kspace yes
variable    EINTERAC equal c_EPAIR

compute     COM all com
compute     COMG carbon com
compute     COMt14 t14 com
variable    COMG equal c_COMG[3]
variable    COMt14 equal c_COMt14[3]
variable    dCOM equal v_COMt14-v_COMG

compute     MSD_Ca Ca msd com yes
compute     MSD_st st msd com yes
compute     MSD_cao cao msd com yes
compute     MSD_obts obts msd com yes
compute     MSD_ow ow msd com yes
compute     MSD_hw hw msd com yes
compute     MSD_owd owd msd com yes
compute     MSD_hwd hwd msd com yes

```

compute	MSD_oh oh msd com yes
compute	MSD_ho ho msd com yes
compute	MSD_g cp msd com yes
compute	MSD_og og msd com yes
compute	MSD_hg hg msd com yes
compute	RDF_g all rdf 500 12 12 12 13 13 14 13 11
compute	RDF_wat all rdf 500 6 6 6 7 6 11
compute	RDF_watd all rdf 500 8 8 8 9 8 11
compute	RDF_Ca all rdf 500 11 11 11 3 11 2 11 1
compute	RDF_cao all rdf 500 1 1 1 3 1 4
compute	RDF_Si all rdf 500 2 2 2 3 2 4 2 5
compute	dencao1d_Z cao chunk/atom bin/1d z lower 0.01 nchunk once units reduced
compute	denCa1d_Z Ca chunk/atom bin/1d z lower 0.01 nchunk once units reduced
compute	denst1d_Z st chunk/atom bin/1d z lower 0.01 nchunk once units reduced
compute	densOBTS1d_Z obts chunk/atom bin/1d z lower 0.01 nchunk once units reduced
compute	denO1d_Z ow chunk/atom bin/1d z lower 0.01 nchunk once units reduced
compute	denH1d_Z hw chunk/atom bin/1d z lower 0.01 nchunk once units reduced
compute	denOd1d_Z owd chunk/atom bin/1d z lower 0.01 nchunk once units reduced
compute	denHd1d_Z hwd chunk/atom bin/1d z lower 0.01 nchunk once units reduced
compute	denC1d_Z carbon chunk/atom bin/1d z lower 0.01 nchunk once units reduced
compute	denog1d_Z og chunk/atom bin/1d z lower 0.01 nchunk once units reduced
compute	dencao1d_X cao chunk/atom bin/1d x lower 0.01 nchunk once units reduced
compute	denCa1d_X Ca chunk/atom bin/1d x lower 0.01 nchunk once units reduced
compute	denst1d_X st chunk/atom bin/1d x lower 0.01 nchunk once units reduced
compute	densOBTS1d_X obts chunk/atom bin/1d x lower 0.01 nchunk once units reduced
compute	denO1d_X ow chunk/atom bin/1d x lower 0.01 nchunk once units reduced
compute	denH1d_X hw chunk/atom bin/1d x lower 0.01 nchunk once units reduced
compute	denOd1d_X owd chunk/atom bin/1d x lower 0.01 nchunk once units reduced
compute	denHd1d_X hwd chunk/atom bin/1d x lower 0.01 nchunk once units reduced
compute	denC1d_X carbon chunk/atom bin/1d x lower 0.01 nchunk once units reduced
compute	denog1d_X og chunk/atom bin/1d x lower 0.01 nchunk once units reduced
compute	dencao2d cao chunk/atom bin/2d x lower 0.01 y lower 0.01 nchunk once units reduced
compute	denst2d st chunk/atom bin/2d x lower 0.01 y lower 0.01 nchunk once units reduced
compute	denOBTS2d obts chunk/atom bin/2d x lower 0.01 y lower 0.01 nchunk once units reduced
compute	denCa2d Ca chunk/atom bin/2d x lower 0.01 y lower 0.01 nchunk once units reduced
compute	denow2d ow chunk/atom bin/2d x lower 0.01 y lower 0.01 nchunk once units reduced
compute	denhw2d ow chunk/atom bin/2d x lower 0.01 y lower 0.01 nchunk once units reduced
compute	denowd2d owd chunk/atom bin/2d x lower 0.01 y lower 0.01 nchunk once units reduced
compute	denhwd2d ow chunk/atom bin/2d x lower 0.01 y lower 0.01 nchunk once units reduced
compute	denC2d carbon chunk/atom bin/2d x lower 0.01 y lower 0.01 nchunk once units reduced
compute	denog2d og chunk/atom bin/2d x lower 0.01 y lower 0.01 nchunk once units reduced
minimize	1.0e-20 1.0e-20 100 1000
min_style	cg
min_modify	dmax 0.1
reset_timestep	0
fix	f_NVE all nve

```

dump          d_xyz all xyz 5000 t14grap25X.xyz
fix           f_LANG all langevin ${t} ${t} 5 71993

thermo        1000
thermo_style  custom step temp etotal press density v_EINTERAC v_dCOM
run           100000

unfix         f_NVE

reset_timestep 0
fix           f_SHAKE all shake 1e-4 20 0 b 1 a 1
fix           f_NPT all npt temp ${t} ${t} 100 aniso 0 0 1000 pchain 1
dump          d_movie all movie 5000 t14grap25X.mpeg type type axes yes 0.2 0.05 view 0 90
dump          d_vel all custom 5000 t14grap25X.lammpstrj id type x y z vx vy vz
dump          d_hbond all dcd 3000 hbond.dcd

fix           f_RDF_g all ave/time 1000 3000 3000000 c_RDF_g[1] c_RDF_g[2] c_RDF_g[3] c_RDF_g[4]
c_RDF_g[5] c_RDF_g[6] c_RDF_g[7] c_RDF_g[8] c_RDF_g[9] file t14grap25X.rdf.g mode vector

fix           f_RDF_Ca all ave/time 1000 3000 3000000 c_RDF_Ca[1] c_RDF_Ca[2] c_RDF_Ca[3]
c_RDF_Ca[4] c_RDF_Ca[5] c_RDF_Ca[6] c_RDF_Ca[7] c_RDF_Ca[8] c_RDF_Ca[9] file t14grap25X.rdf.Ca
mode vector

fix           f_RDF_wat all ave/time 1000 3000 3000000 c_RDF_wat[1] c_RDF_wat[2] c_RDF_wat[3]
c_RDF_wat[4] c_RDF_wat[5] c_RDF_wat[6] c_RDF_wat[7] file t14grap25X.rdf.wat mode vector

fix           f_RDF_watd all ave/time 1000 3000 3000000 c_RDF_watd[1] c_RDF_watd[2] c_RDF_watd[3]
c_RDF_watd[4] c_RDF_watd[5] c_RDF_watd[6] c_RDF_watd[7] file t14grap25X.rdf.watd mode vector

fix           f_RDF_Si all ave/time 1000 3000 3000000 c_RDF_Si[1] c_RDF_Si[2] c_RDF_Si[3]
c_RDF_Si[4] c_RDF_Si[5] c_RDF_Si[6] c_RDF_Si[7] c_RDF_Si[8] c_RDF_Si[9] file t14grap25X.rdf.Si mode
vector

fix           f_RDF_cao all ave/time 1000 3000 3000000 c_RDF_cao[1] c_RDF_cao[2] c_RDF_cao[3]
c_RDF_cao[4] c_RDF_cao[5] c_RDF_cao[6] c_RDF_cao[7] file t14grap25X.rdf.cao mode vector

fix           f_MSD_Ca all ave/time 10 300 3000 c_MSD_Ca[1] c_MSD_Ca[2] c_MSD_Ca[3] c_MSD_Ca[4]
file t14grap25X.msdc.Ca mode scalar
fix           f_MSD_st all ave/time 10 300 3000 c_MSD_st[1] c_MSD_st[2] c_MSD_st[3] c_MSD_st[4] file
t14grap25X.msdc.st mode scalar
fix           f_MSD_cao all ave/time 10 300 3000 c_MSD_cao[1] c_MSD_cao[2] c_MSD_cao[3]
c_MSD_cao[4] file t14grap25X.msdc.cao mode scalar

fix           f_MSD_obts all ave/time 10 300 3000 c_MSD_obts[1] c_MSD_obts[2] c_MSD_obts[3]
c_MSD_obts[4] file t14grap25X.msdc.obts mode scalar
fix           f_MSD_oh all ave/time 10 300 3000 c_MSD_oh[1] c_MSD_oh[2] c_MSD_oh[3] c_MSD_oh[4]
file t14grap25X.msdc.oh mode scalar

fix           f_MSD_ho all ave/time 10 300 3000 c_MSD_ho[1] c_MSD_ho[2] c_MSD_ho[3] c_MSD_ho[4]
file t14grap25X.msdc.ho mode scalar
fix           f_MSD_ow all ave/time 10 300 3000 c_MSD_ow[1] c_MSD_ow[2] c_MSD_ow[3]
c_MSD_ow[4] file t14grap25X.msdc.ow mode scalar

```

```

fix          f_MSD_hw all ave/time 10 300 3000 c_MSD_hw[1] c_MSD_hw[2] c_MSD_hw[3]
c_MSD_hw[4] file t14grap25X.msd.hw mode scalar
fix          f_MSD_owd all ave/time 10 300 3000 c_MSD_owd[1] c_MSD_owd[2] c_MSD_owd[3]
c_MSD_owd[4] file t14grap25X.msd.owd mode scalar
fix          f_MSD_hwd all ave/time 10 300 3000 c_MSD_hwd[1] c_MSD_hwd[2] c_MSD_hwd[3]
c_MSD_hwd[4] file t14grap25X.msd.hwd mode scalar

fix          f_MSD_g all ave/time 10 300 3000 c_MSD_g[1] c_MSD_g[2] c_MSD_g[3] c_MSD_g[4] file
t14grap25X.msd.g mode scalar
fix          f_MSD_og all ave/time 10 300 3000 c_MSD_og[1] c_MSD_og[2] c_MSD_og[3] c_MSD_og[4]
file t14grap25X.msd.og mode scalar
fix          f_MSD_hg all ave/time 10 300 3000 c_MSD_hg[1] c_MSD_hg[2] c_MSD_hg[3] c_MSD_hg[4]
file t14grap25X.msd.hg mode scalar

fix          f_denscao1d_Z cao ave/chunk 1000 3000 3000000 denscao1d_Z density/number file
den1dcao_Z.txt
fix          f_densCa1d_Z Ca ave/chunk 1000 3000 3000000 denCa1d_Z density/number file den1dCa_Z.txt
fix          f_densst1d_Z st ave/chunk 1000 3000 3000000 densst1d_Z density/number file den1dst_Z.txt
fix          f_densOBTS1d_Z obts ave/chunk 1000 3000 3000000 densOBTS1d_Z density/number file
den1dOBTS_Z.txt

fix          f_densO1d_Z ow ave/chunk 1000 3000 3000000 denO1d_Z density/number file den1dO_Z.txt
fix          f_densH1d_Z hw ave/chunk 1000 3000 3000000 denH1d_Z density/number file den1dH_Z.txt
fix          f_densOd1d_Z owd ave/chunk 1000 3000 3000000 denOd1d_Z density/number file
den1dOd_Z.txt
fix          f_densHd1d_Z hwd ave/chunk 1000 3000 3000000 denHd1d_Z density/number file
den1dHd_Z.txt

fix          f_denscao1d_X cao ave/chunk 1000 3000 3000000 denscao1d_X density/number file
den1dcao_X.txt
fix          f_densCa1d_X Ca ave/chunk 1000 3000 3000000 denCa1d_X density/number file den1dCa_X.txt
fix          f_densst1d_X st ave/chunk 1000 3000 3000000 densst1d_X density/number file den1dst_X.txt
fix          f_densOBTS1d_X obts ave/chunk 1000 3000 3000000 densOBTS1d_X density/number file
den1dOBTS_X.txt

fix          f_densO1d_X ow ave/chunk 1000 3000 3000000 denO1d_X density/number file den1dO_X.txt
fix          f_densH1d_X hw ave/chunk 1000 3000 3000000 denH1d_X density/number file den1dH_X.txt
fix          f_densOd1d_X owd ave/chunk 1000 3000 3000000 denOd1d_X density/number file
den1dOd_X.txt
fix          f_densHd1d_X hwd ave/chunk 1000 3000 3000000 denHd1d_X density/number file
den1dHd_X.txt

fix          f_denscao2d cao ave/chunk 1000 3000 3000000 denscao2d density/number file den2dcao.txt
fix          f_densst2d st ave/chunk 1000 3000 3000000 densst2d density/number file den2dst.txt
fix          f_densCa2d Ca ave/chunk 1000 3000 3000000 denCa2d density/number file den2dCa.txt
fix          f_densOBTS2d obts ave/chunk 1000 3000 3000000 densOBTS2d density/number file
den2dOBTS.txt

fix          f_densow2d ow ave/chunk 1000 3000 3000000 densow2d density/number file den2dow.txt
fix          f_denshw2d hw ave/chunk 1000 3000 3000000 denhw2d density/number file den2dhw.txt
fix          f_densowd2d owd ave/chunk 1000 3000 3000000 densowd2d density/number file den2dowd.txt
fix          f_denshwd2d hwd ave/chunk 1000 3000 3000000 denhwd2d density/number file den2dhwd.txt

```

```

fix          f_densC1d_Z carbon ave/chunk 1000 3000 3000000 denC1d_Z density/mass file den1dC_Z.txt
fix          f_densog1d_Z og ave/chunk 1000 3000 3000000 denog1d_Z density/mass file den1dog_Z.txt
fix          f_densC1d_X carbon ave/chunk 1000 3000 3000000 denC1d_X density/mass file den1dC_X.txt
fix          f_densog1d_X og ave/chunk 1000 3000 3000000 denog1d_X density/mass file den1dog_X.txt
fix          f_densC2d carbon ave/chunk 1000 3000 3000000 denC2d density/number file den2dC.txt
fix          f_densog2d og ave/chunk 1000 3000 3000000 denog2d density/number file den2dog.txt

run          3000000

unfix       f_RDF_Ca
unfix       f_RDF_Si
unfix       f_RDF_cao
unfix       f_RDF_wat
unfix       f_RDF_watd
unfix       f_NPT
unfix       f_SHAKE
unfix       f_LANG
undump      d_movie
undump      d_vel
undump      d_xyz
undump      d_hbond
unfix       f_MSD_Ca
unfix       f_MSD_st
unfix       f_MSD_cao
unfix       f_MSD_obts
unfix       f_MSD_oh
unfix       f_MSD_ho
unfix       f_MSD_ow
unfix       f_MSD_hw
unfix       f_MSD_owd
unfix       f_MSD_hwd
unfix       f_denscao1d_Z
unfix       f_densCa1d_Z
unfix       f_densst1d_Z
unfix       f_densO1d_Z
unfix       f_densH1d_Z
unfix       f_densOd1d_Z
unfix       f_densHd1d_Z
unfix       f_densOBTS1d_Z
unfix       f_denscao1d_X
unfix       f_densCa1d_X
unfix       f_densst1d_X
unfix       f_densO1d_X
unfix       f_densH1d_X
unfix       f_densOd1d_X
unfix       f_densHd1d_X
unfix       f_densOBTS1d_X
unfix       f_denscao2d
unfix       f_densst2d
unfix       f_densCa2d
unfix       f_densOBTS2d

```

```

unfix          f_densow2d
unfix          f_denshw2d
unfix          f_densowd2d
unfix          f_denshwd2d
unfix          f_densC1d_Z
unfix          f_densog1d_Z
unfix          f_densC1d_X
unfix          f_densog1d_X
unfix          f_densC2d
unfix          f_densog2d

write_restart  restart.t14grap25X.equil

```

D2.0 Representative LAMMPS script for tensile deformation simulation along the X-direction for T14/FGS with 25% -OH in ZZ clustered line pattern

```

## Tensile stress-strain simulation (X-direction)

read_restart   restart.t14grap25X.equil
echo           screen
kpace_style    ppm 1e-6
variable       t equal 300

run_style      verlet
bond_coeff     1      harmonic 554.1349 1.0
bond_coeff     2      harmonic 554.1349 1.0
bond_coeff     3      harmonic 554.1349 1.0
bond_coeff     4      morse   120.0   2.0 1.3400
bond_coeff     5      harmonic      384   1.37      # cp-oh
bond_coeff     6      harmonic 540.6336 0.96      # oh-ho

region         leftbdy block INF 3 INF INF INF INF units box
group          leftbdy region leftbdy
region         rightbdy block 20 INF INF INF INF INF units box
group          rightbdy region rightbdy
group          mobile subtract all leftbdy rightbdy
compute        newtemp all temp

#-----Storing Initial lengths-----xxx
variable       tmpx equal "lx"
variable       l0x equal ${tmpx}
print          "initial length, l0-x: ${l0x}"
variable       tmpy equal "ly"
variable       l0y equal ${tmpy}
print          "initial length in y, l0-y: ${l0y}"
variable       tmpz equal "lz"
variable       l0z equal ${tmpz}
print          "initial length in z, l0-z: ${l0z}"

# Calculation of applied strain
variable       strainx equal "(lx-v_10x)/v_10x"
variable       e1 equal "v_strainx"

```

```

variable      strainy equal "(ly-v_10y)/v_10y"
variable      e2 equal "v_strainy"
variable      strainz equal "(lz-v_10z)/v_10z"
variable      e3 equal "v_strainz"
variable      lxy equal xy
variable      lxy0 equal ${lxy}
variable      e12 equal (v_lxy-v_lxy0)/v_10y
variable      lxz equal xz
variable      lxz0 equal ${lxz}
variable      e13 equal (v_lxz-v_lxz0)/v_10z
variable      lyz equal yz
variable      lyz0 equal ${lyz}
variable      e23 equal (v_lyz-v_lyz0)/v_10z

# Determination of Strain rates
variable      erate equal "1e9"
variable      erate1 equal "v_erate/1e15"      # engineering strain rate in fs

compute      peratom mobile stress/atom newtemp
compute      stp mobile reduce sum c_peratom[1] c_peratom[2] c_peratom[3] c_peratom[4] c_peratom[5]
c_peratom[6]

variable      s11 equal c_stp[1]
variable      s22 equal c_stp[2]
variable      s33 equal c_stp[3]
variable      s12 equal c_stp[4]
variable      s13 equal c_stp[5]
variable      s23 equal c_stp[6]
variable      factor equal 1.01325e-4
variable      volinit equal ${10x}*${10y}*${10z}

variable      p11 equal v_s11*${factor}/v_volinit
variable      p22 equal v_s22*${factor}/v_volinit
variable      p33 equal v_s33*${factor}/v_volinit
variable      p12 equal v_s12*${factor}/v_volinit
variable      p13 equal v_s13*${factor}/v_volinit
variable      p23 equal v_s23*${factor}/v_volinit

reset_timestep 0

fix          1 all deform 1 x erate ${erate1} units box remap x
#fix        2 water shake 1e-4 20 0 b 1 a 1
fix          8 mobile npt temp ${t} ${t} 100 y 0 0 1000 z 0 0 1000
dump        d_movie all movie 1000 t14grap25XX.stressx.movie.mpeg type type axes yes 0.2 0.05 view 60 30
fix          9 mobile ave/time 10 100 1000 v_e1 v_p11 mode scalar file t14grap25XX.profile
dump        d_xyz all xyz 1000 t14grap25XX.xyz

thermo      1000
thermo_style custom step temp press vol v_e1 v_p11

run         500000

```

D3.0 Representative LAMMPS script for tensile deformation simulation along the Z-direction for T₁₄/FGS with 25% –OH in ZZ clustered line pattern

Stress-strain simulation

```

read_restart restart.t14grap25X.equil
echo screen
kspace_style pppm 1e-6
variable t equal 300

run_style verlet
bond_coeff 1 harmonic 554.1349 1.0
bond_coeff 2 harmonic 554.1349 1.0
bond_coeff 3 harmonic 554.1349 1.0
bond_coeff 4 morse 120.0 2.0 1.3400
bond_coeff 5 harmonic 384 1.37 # cp-oh
bond_coeff 6 harmonic 540.6336 0.96 # oh-ho

region leftbdy block INF INF INF INF INF -1 units box
group leftbdy region leftbdy
region rightbdy block INF INF INF INF 24.5 INF units box
group rightbdy region rightbdy
group mobile subtract all leftbdy rightbdy
group water union wat watd

compute newtemp all temp

#-----Storing Initial lengths-----xxx
variable tmpx equal "lx"
variable l0x equal ${tmpx}
print "initial length, l0-x: ${l0x}"
variable tmpy equal "ly"
variable l0y equal ${tmpy}
print "initial length in y, l0-y: ${l0y}"
variable tmpz equal "lz"
variable l0z equal ${tmpz}
print "initial length in z, l0-z: ${l0z}"

# Calculation of applied strain
variable strainx equal "(lx-v_l0x)/v_l0x"
variable e1 equal "v_strainx"
variable strainy equal "(ly-v_l0y)/v_l0y"
variable e2 equal "v_strainy"
variable strainz equal "(lz-v_l0z)/v_l0z"
variable e3 equal "v_strainz"
variable lxy equal xy
variable lxy0 equal ${lxy}
variable e12 equal (v_lxy-v_lxy0)/v_l0y
variable lxz equal xz
variable lxz0 equal ${lxz}
variable e13 equal (v_lxz-v_lxz0)/v_l0z
variable lyz equal yz

```



```

variable      lyz0 equal ${lyz}
variable      e23 equal (v_lyz-v_lyz0)/v_l0z

# Determination of Strain rates
variable      erate equal "1e9"
variable      erate1 equal "v_erate/1e15"      # engineering strain rate in fs

compute      peratom mobile stress/atom newtemp
compute      stp mobile reduce sum c_peratom[1] c_peratom[2] c_peratom[3] c_peratom[4] c_peratom[5]
c_peratom[6]

compute      epair1 grapoh group/group water pair yes kspace yes
compute      epair2 grapoh group/group Ca pair yes kspace yes

variable      s11 equal c_stp[1]
variable      s22 equal c_stp[2]
variable      s33 equal c_stp[3]
variable      s12 equal c_stp[4]
variable      s13 equal c_stp[5]
variable      s23 equal c_stp[6]
variable      factor equal 1.01325e-4
variable      volinit equal ${10x}*${10y}*${10z}

variable      p11 equal v_s11*${factor}/v_volinit
variable      p22 equal v_s22*${factor}/v_volinit
variable      p33 equal v_s33*${factor}/v_volinit
variable      p12 equal v_s12*${factor}/v_volinit
variable      p13 equal v_s13*${factor}/v_volinit
variable      p23 equal v_s23*${factor}/v_volinit

reset_timestep 0
fix           1 all deform 1 z erate ${erate1} units box remap x
#fix         2 water shake 1e-4 20 0 b 1 a 1
fix           8 mobile npt temp ${t} ${t} 100 x 0 0 1000 y 0 0 1000
dump         d_movie all movie 1000 t14grap25X-Z.stressx.movie.mpeg type type axes yes 0.2 0.05 view 60
30
dump         5 all xyz 500 t14grap25X-Z.xyz
dump         d_vel all custom 500 t14grap25X-Z.lammpstrj id type x y z

fix           9 mobile ave/time 50 100 5000 v_e3 v_p33 mode scalar file t14grap25X-Z.profile
fix           10 mobile ave/time 50 100 5000 v_e3 c_epair1 c_epair2 mode scalar file t14grap25X-Z.energy
dump         d_xyz all xyz 1000 t14grap25X-Z.xyz

thermo       1000
thermo_style custom step temp press vol v_e3 v_p33 c_epair1 c_epair2

run          500000

```

D4.0 Representative LAMMPS script for stiffness tensor for T₁₄/FGS with 25% –OH in ZZ clustered line pattern

```
## Stress-strain simulation
```

```

read_restart restart.t14grap25X.equil
echo screen
kpace_style pppm 1e-6
variable t equal 300

log log.t14grap25X.elastic
run_style verlet

bond_coeff 1 harmonic 554.1349 1.0
bond_coeff 2 harmonic 554.1349 1.0
bond_coeff 3 harmonic 554.1349 1.0
bond_coeff 4 morse 120.0 2.0 1.3400
bond_coeff 5 harmonic 384 1.37 # cp-oh
bond_coeff 6 harmonic 540.6336 0.96 # oh-ho

region leftbdy block INF INF INF 0 INF INF units box
group leftbdy region leftbdy
region rightbdy block INF INF 25 INF INF INF units box
group rightbdy region rightbdy
group mobile subtract all leftbdy rightbdy
compute newtemp all temp
#velocity all create ${t} 12345 temp newtemp dist gaussian mom yes rot no

```

```
#-----Storing Initial lengths-----xxx
```

```

Variable tmpx equal "lx"
variable l0x equal ${tmpx}
print "initial length, l0-x: ${l0x}"
variable tmpy equal "ly"
variable l0y equal ${tmpy}
print "initial length in y, l0-y: ${l0y}"
variable tmpz equal "lz"
variable l0z equal ${tmpz}
print "initial length in z, l0-z: ${l0z}"

```

```
# Calculation of applied strain
```

```

variable strainx equal "(lx-v_l0x)/v_l0x"
variable e1 equal "v_strainx"
variable strainy equal "(ly-v_l0y)/v_l0y"
variable e2 equal "v_strainy"
variable strainz equal "(lz-v_l0z)/v_l0z"
variable e3 equal "v_strainz"
variable lxy equal xy
variable lxy0 equal ${lxy}
variable e12 equal (v_lxy-v_lxy0)/v_l0y
variable lxz equal xz
variable lxz0 equal ${lxz}
variable e13 equal (v_lxz-v_lxz0)/v_l0z
variable lyz equal yz
variable lyz0 equal ${lyz}
variable e23 equal (v_lyz-v_lyz0)/v_l0z

```

```

# Determination of Strain rates
variable      erate equal "0.5e13"
variable      erate1 equal "v_erate/1e15"      # engineering strain rate in fs

compute      peratom mobile stress/atom newtemp
compute      stp mobile reduce sum c_peratom[1] c_peratom[2] c_peratom[3] c_peratom[4] c_peratom[5]
c_peratom[6]

variable      s11 equal c_stp[1]
variable      s22 equal c_stp[2]
variable      s33 equal c_stp[3]
variable      s12 equal c_stp[4]
variable      s13 equal c_stp[5]
variable      s23 equal c_stp[6]
variable      factor equal 1.01325e-4
variable      volinit equal ${10x}*${10y}*${10z}

variable      p11 equal v_s11*${factor}/v_volinit
variable      p22 equal v_s22*${factor}/v_volinit
variable      p33 equal v_s33*${factor}/v_volinit
variable      p12 equal v_s12*${factor}/v_volinit
variable      p13 equal v_s13*${factor}/v_volinit
variable      p23 equal v_s23*${factor}/v_volinit

reset_timestep 0

fix          1 all deform 1 y erate ${erate1} units box remap x
#fix        2 water shake 1e-4 20 0 b 1 a 1
#fix        3 all temp/berendsen ${t} ${t} 100
fix          4 mobile npt temp ${t} ${t} 100 x 0 0 1000 z 0 0 1000
#dump       d_xyz all xyz 50 t14grap25Xelas.xyz
#fix        5 mobile nvt temp ${t} ${t} 100

thermo      100
thermo_style custom step temp press vol v_e2 v_p33

run         1
unfix      1
unfix      4

fix        6 mobile nvt temp ${t} ${t} 100
thermo_style custom step temp etotal press vol v_e2 v_p33
fix        12 all print 100 "${e2} ${p33}" file C32_3.txt
run        100000

```

APPENDIX E Molecular dynamics scripts for Chapter 5

This appendix includes representative LAMMPS scripts for Chapter 5.

E1.0 Representative LAMMPS script for equilibration of FGS/FGS bilayer with 6% –OH on both sheets and nanoconfined monolayer water

```
## graphene 2-layer (pristine)
# Cohesive Zone Modeling
# Initialization

variable          t equal 300
echo              screen
log               grapoh6oh6RwatVX.log

units             real
boundary         p p p

atom_style        full
bond_style        hybrid morse harmonic
angle_style       harmonic
dihedral_style    harmonic
improper_style    cvff

pair_style         lj/cut/coul/long 10.0 10.0
read_data         grapoh6oh6watRVX.data

bond_coeff        1      morse  120.0   2.0  1.3400
bond_coeff        2      harmonic 384    1.37      # cp-oh
bond_coeff        3      harmonic 540.6336 0.96      # oh-ho
bond_coeff        4      harmonic 540.634  1
bond_coeff        5      morse  120.0   2.0  1.3400
bond_coeff        6      harmonic 384    1.37      # cp-oh
bond_coeff        7      harmonic 540.6336 0.96      # oh-ho

kspace_style      ppm 1e-6
special_bonds     lj/coul 1e-50 1e-50 1e-50
pair_modify       mix arithmetic tail no
run_style         verlet

neighbor          5.0 bin
neigh_modify      delay 0 every 1 one 10000 check yes

group             cp1 type 6
group             og1 type 7
group             hg1 type 8
group             cp2 type 1
group             og2 type 2
group             hg2 type 3
group             ow type 4
```

```

group          hw type 5

group          grapoh1 type 6 7 8
group          grapoh2 type 1 2 3
group          water type 4 5
group          grapoh type 1 2 3 6 7 8

compute        qC1 cp1 property/atom q
compute        qO1 og1 property/atom q
compute        qH1 hg1 property/atom q
compute        q_NC1 cp1 reduce ave c_qC1
compute        q_NO1 og1 reduce ave c_qO1
compute        q_NH1 hg1 reduce ave c_qH1
variable       qC1 equal c_q_NC1
variable       qO1 equal c_q_NO1
variable       qH1 equal c_q_NH1

compute        qC2 cp2 property/atom q
compute        qO2 og2 property/atom q
compute        qH2 hg2 property/atom q
compute        q_NC2 cp2 reduce ave c_qC2
compute        q_NO2 og2 reduce ave c_qO2
compute        q_NH2 hg2 reduce ave c_qH2
variable       qC2 equal c_q_NC2
variable       qO2 equal c_q_NO2
variable       qH2 equal c_q_NH2

fix            fix_charge grapoh qeq/point 1 10 1e-6 1000 param.test
thermo_style   custom step v_qC1 v_qO1 v_qH1 v_qC2 v_qO2 v_qH2
run            0
unfix         fix_charge

variable q equal charge(all)

compute        newtemp all temp
velocity       all create ${t} 71993 temp newtemp dist gaussian mom yes rot no

minimize       1.0e-20 1.0e-20 100 1000
min_style      cg
min_modify     dmax 0.1

fix            f_SHAKE all shake 1e-4 20 0 b 4 a 4
fix            f_NPT all npt temp ${t} ${t} 100 y 0 0 1000 z 0 0 1000
dump           d_xyz all xyz 500 grapoh6oh6RwatVX.xyz
fix            f_LANG all langevin ${t} ${t} 5 71993
dump           coord1 cp1 custom 1500000 dump.cp1X id type x y z
dump           coord2 cp2 custom 1500000 dump.cp2X id type x y z

thermo         1000
thermo_style   custom step temp etotal press density v_q

run            1500000

```

```

undump      coord1
undump      coord2
unfix       f_NPT
unfix       f_LANG
unfix       f_SHAKE
undump      d_xyz

write_restart restart.grapoh6Roh6watVX.equil

```

E2.0 Representative LAMMPS script for normal traction-separation simulation of FGS/FGS bilayer with 6% -OH on both sheets

```
## Stress-strain simulation
```

```

read_restart restart.grapoh6oh6RN.equil
echo screen
kspace_style ewald 1e-6
variable t equal 300
run_style verlet

bond_coeff 1 morse 120.0 2.0 1.3400
bond_coeff 2 harmonic 384 1.37 # cp-oh
bond_coeff 3 harmonic 540.6336 0.96 # oh-ho
bond_coeff 4 morse 120.0 2.0 1.3400
bond_coeff 5 harmonic 384 1.37 # cp-oh
bond_coeff 6 harmonic 540.6336 0.96 # oh-ho

region rightbdy block 18.05 INF INF INF INF -4.4 units box
group rightbdy region rightbdy
region leftbdy block INF 2.23 INF INF INF -4.4 units box
group leftbdy region leftbdy

group bdy union rightbdy leftbdy
group mobile subtract grapoh1 bdy

compute newtemp all temp
compute dispT cp2 com
compute dispB bdy com
variable dT equal c_dispT[3]
variable dB equal c_dispB[3]
variable disp equal (v_dT-v_dB)

fix f_freezeT cp2 setforce 0 0 0
fix f_freezeB bdy setforce 0 0 0
fix f_move bdy move linear 0 0 -1e-5 units box
velocity cp2 set 0 0 0 units box

compute epair grapoh1 group/group grapoh2 pair yes kspace yes
variable ftot equal c_epair[3]*69.4703/1000 # nN unit

variable s equal v_ftot*100/(19.74*28.806) # GPa unit

```

```

compute      fn grapoh1 property/atom fz
compute      fnn grapoh1 reduce sum c_fn
variable     fp atom c_fn

thermo       1000
thermo_style custom step temp etotal press vol v_disp c_epair v_ftot v_s

fix          f_mobile mobile nvt temp ${t} ${t} 100
fix          f_avg all ave/time 100 100 10000 v_disp v_ftot v_s c_epair mode scalar file
            grapoh6oh6RN.profile

dump         d_vel cp2 custom 1000 grapoh6oh6RN.lammpstrj id type x y z v_fp
dump         d_xyz all xyz 1000 grapoh6oh6RN.sim.xyz
dump         d_dump all custom 10000 dump.grapoh6oh6RN.rerun id type x y z vx vy vz

run          1200000

undump       d_vel
undump       d_xyz
undump       d_dump
unfix        f_mobile
unfix        f_avg

write_restart restart.grapoh2oh2RN.rerun

```

E3.0 Representative LAMMPS script for shear traction-separation of FGS/FGS bilayer with 6% –OH on both sheets and nanoconfined monolayer water

Shear traction-separation simulation

```

read_restart restart.grapoh6Roh6watVX.equil
echo         screen
kspace_style ewald 1e-6
variable     t equal 300
run_style    verlet

bond_coeff   1      morse  120.0   2.0  1.3400
bond_coeff   2      harmonic      384   1.37      # cp-oh
bond_coeff   3      harmonic  540.6336 0.96      # oh-ho
bond_coeff   4      harmonic  540.634  1
bond_coeff   5      morse  120.0   2.0  1.3400
bond_coeff   6      harmonic      384   1.37      # cp-oh
bond_coeff   7      harmonic  540.6336 0.96      # oh-ho

region       rightbdy block 16.8 INF INF INF INF -8.1 units box
group        rightbdy region rightbdy
group        mobile subtract all grapoh2 rightbdy

compute      newtemp all temp
compute      dispT cp2 com
compute      dispB rightbdy com

```

```

variable      dT equal c_dispT[1]
variable      dB equal c_dispB[1]
variable      disp equal (v_dB-v_dT)

fix           f_freezeT cp2 setforce 0 0 0
fix           f_freezeB rightbdy setforce 0 0 0
fix           f_move rightbdy move linear 1e-5 0 0 units box
velocity      cp2 set 0 0 0 units box

compute      epair grapoh2 group/group grapoh1 pair yes kspace yes
variable      ftot equal c_epair[1]*69.4703/1000          # nN unit

variable      s equal v_ftot*100/(19.41*27.7)           # GPa unit

compute      fn grapoh2 property/atom fx
compute      fnn grapoh2 reduce sum c_fn
variable      fp atom c_fn

compute      MSD_ow ow msd com yes
compute      MSD_hw hw msd com yes

thermo        1000
thermo_style  custom step temp etotal press vol v_disp c_epair v_ftot v_s

fix           f_mobile mobile nvt temp ${t} ${t} 100
fix           f_avg all ave/time 100 100 10000 v_disp v_ftot v_s c_epair mode scalar file
grapoh6oh6watRVX.profile

dump          d_vel cp1 custom 1000 grapoh6oh6watRVX.lammpstrj id type x y z v_fp
dump          d_angle water custom 10000 grapoh6oh6watRVX.wat.lammpstrj id type x y z
dump          d_xyz all xyz 1000 grapoh6oh6watRVX.sim.xyz
dump          d_dump all custom 10000 dump.grapoh6oh6watRVX.rerun id type x y z vx vy vz

fix           f_MSD_ow all ave/time 10 100 1000 c_MSD_ow[1] c_MSD_ow[2] c_MSD_ow[3]
c_MSD_ow[4] file grapoh6oh6watRVX.msds.ow mode scalar
fix           f_MSD_hw all ave/time 10 100 1000 c_MSD_hw[1] c_MSD_hw[2] c_MSD_hw[3]
c_MSD_hw[4] file grapoh6oh6watRVX.msds.hw mode scalar

run           4000000

undump        d_vel
undump        d_xyz
undump        d_dump
undump        d_angle
unfix         f_mobile
unfix         f_avg
unfix         f_MSD_ow
unfix         f_MSD_hw

write_restart restart.grapoh6oh6watRVX.rerun

```


E4.0 Representative LAMMPS script for interaction energy calculation during shear traction-separation of FGS/FGS bilayer with 6% –OH on both sheets and nanoconfined monolayer water

```

## Energy calculation with rerun
# graphene 2-layer (pristine)
# Cohesive Zone Modeling

read_restart      restart.grapoh6oh6watRVX.rerun
log               grapoh6oh6watRVX.rerun.log

bond_style        hybrid harmonic morse
angle_style        harmonic
dihedral_style     harmonic
improper_style     cvff
kspace_style       ewald 1e-6

pair_style         lj/cut/coul/long 10 10

bond_coeff         1      morse  120.0   2.0  1.3400
bond_coeff         2      harmonic      384   1.37      # cp-oh
bond_coeff         3      harmonic     540.6336 0.96      # oh-ho
bond_coeff         4      harmonic 540.634 1
bond_coeff         5      morse  120.0   2.0  1.3400
bond_coeff         6      harmonic      384   1.37      # cp-oh
bond_coeff         7      harmonic     540.6336 0.96      # oh-ho

pair_coeff          1 1 0.1479999981 3.6170487995 # cp
pair_coeff          2 2 0.2279965679 3.2100039927 # oh*
pair_coeff          3 3 0.0000000000 0.0000000000 # ho*
pair_coeff          4 4 0.1479999981 3.6170487995 # cp
pair_coeff          5 5 0.2279965679 3.2100039927 # oh*
pair_coeff          6 6 0.0000000000 0.0000000000 # ho*

angle_coeff         1      90.0000 120.0000 # cp-cp-cp
angle_coeff         2      60.0000 120.0000 # cp-cp-oh*
angle_coeff         3      50.0000 109.0000 # cp-oh*-ho*
angle_coeff         4      50 109.47
angle_coeff         5      90.0000 120.0000 # cp-cp-cp
angle_coeff         6      60.0000 120.0000 # cp-cp-oh*
angle_coeff         7      50.0000 109.0000 # cp-oh*-ho*

dihedral_coeff      1 12.0000 -1 2 # cp-cp-cp-cp
dihedral_coeff      2 1.8000 -1 2 # cp-cp-cp-oh*
dihedral_coeff      3 1.5000 1 2 # cp-cp-oh*-ho*
dihedral_coeff      4 12.0000 -1 2 # cp-cp-cp-cp
dihedral_coeff      5 1.8000 -1 2 # cp-cp-cp-oh*
dihedral_coeff      6 1.5000 1 2 # cp-cp-oh*-ho*

improper_coeff      1 0.3700 -1 2 # cp-cp-cp-cp
improper_coeff      2 0.3700 -1 2 # cp-cp-cp-cp

special_bonds        lj/coul 1e-50 1e-50 1e-50
pair_modify          mix arithmetic tail no
run_style            verlet

```

```

neighbor      5.0 bin
neigh_modify  delay 0 every 1 one 10000 check yes

compute      1 all pe pair
compute      2 all pe kspace
compute      3 all pe bond
compute      4 all pe angle
compute      5 all pe dihedral
compute      6 all pe improper

variable     num equal count(all)/3
compute      7 grapoh1 pe/atom pair
compute      8 grapoh1 reduce sum c_7
compute      9 grapoh2 pe/atom pair
compute      10 grapoh2 reduce sum c_9
compute      11 water pe/atom pair
compute      12 water reduce sum c_11

reset_timestep 0

fix          f_energy all ave/time 100 1 100 c_12 c_8 c_10 mode scalar file grapoh6oh6watRVX.energy

thermo       100
thermo_style custom step temp etotal press pe c_8 c_10 c_12
rerun       dump.grapoh6oh6watRVX.rerun every 100 dump x y z vx vy vz

```

APPENDIX F Molecular dynamics scripts for Chapter 6

This appendix includes representative LAMMPS scripts for Chapter 6.

F1.0 Representative LAMMPS script for equilibration of T₁₄/FGS nanocomposites with 6% -OH on FGS

```

## LAMMPS input file
# Tobermorite-14 Ang with Ca/Si = 0.833 and water/Si = 0.857
# 6% -OH group on Graphene functionalization
# (0 0 -1) interface
# Equilibration

# Declare variable
variable          t equal 300
echo              screen
log               t14grap6RN.log

units             real
newton            on
processors        * * *
boundary          p p p

atom_style        full
bond_style        hybrid harmonic morse
angle_style       harmonic
dihedral_style    harmonic
improper_style    cvff

pair_style         lj/cut/coul/long 12.0 10.0
read_data          t14grap6RN.data extra/atom/types 1

bond_coeff         1      harmonic 554.1349 1.0
bond_coeff         2      harmonic 554.1349 1.0
bond_coeff         3      harmonic 554.1349 1.0
bond_coeff         4      morse 120.0 2.0 1.3400
bond_coeff         5      harmonic 384 1.37 # cp-oh
bond_coeff         6      harmonic 540.6336 0.96 # oh-ho

angle_coeff        1      45.7696 109.47
angle_coeff        2      45.7696 109.47
angle_coeff        3      90 120
angle_coeff        4      60.0000 120.0000 # cp-cp-oh*
angle_coeff        5      50.0000 109.0000 # cp-oh*-ho*

dihedral_coeff     1      12.0000 -1 2
dihedral_coeff     2      1.8000 -1 2 # cp-cp-cp-oh*
#dihedral_coeff    3      3.0000 -1 2 # oh*-cp-cp-oh*
dihedral_coeff     3      1.5000 1 2 # cp-cp-oh*-ho*

improper_coeff     1      0.3700 -1 2 # cp-cp-cp-cp

pair_coeff          1      1 5.03e-6 6.2484
pair_coeff          2      2 1.8405e-6 3.302

```

pair_coeff	3	3	0.1554	3.1655
pair_coeff	4	4	0.1554	3.1655
pair_coeff	5	5	0.1554	3.1655
pair_coeff	6	6	0.1554	3.1655
pair_coeff	7	7	0.0	0.0
pair_coeff	8	8	0.1554	3.1655
pair_coeff	9	9	0.0	0.0
pair_coeff	10	10	0.0	0.0
pair_coeff	11	11	0.1	3.2237
pair_coeff	12	12	0.148	3.617
pair_coeff	13	13	0.2279965679	3.2100039927 # oh*
pair_coeff	14	14	0.0000000000	0.0000000000 # ho*
pair_coeff	15	15	0.1	3.2237

kpspace_style pppm 1e-6
special_bonds lj/coul 1e-50 1e-50 1e-50
pair_modify mix arithmetic tail no
run_style verlet

neighbor 5.0 bin
neigh_modify delay 0 every 1 one 10000 check yes
comm_style brick
comm_modify mode single group all cutoff 10

group cao type 1
group st type 2
group ob type 3
group obts type 4
group oh type 5
group ow type 6
group hw type 7
group owd type 8
group hwd type 9
group ho type 10
group Ca type 11
group cp type 12
group og type 13
group hg type 14

group wat type 6 7
group watd type 8 9
group t14 type <= 11
group solid subtract t14 wat watd

set type 1 charge 1.36
set type 2 charge 2.1
set type 3 charge -1.1790625
set type 4 charge -1.1790625
set type 5 charge -0.95
set type 6 charge -0.82
set type 7 charge 0.41
set type 8 charge -0.82
set type 9 charge 0.41
set type 10 charge 0.425
set type 11 charge 2
set type 15 charge 2

```

mass          15      40.007980

group        carbon type 12
group        graphene type 12
group        grapoh type 12 13 14

compute      qC carbon property/atom q
compute      qO og property/atom q
compute      qH hg property/atom q
compute      q_NC carbon reduce ave c_qC
compute      q_NO og reduce ave c_qO
compute      q_NH hg reduce ave c_qH
variable     qC equal c_q_NC
variable     qO equal c_q_NO
variable     qH equal c_q_NH

fix          fix_charge grapoh qeq/point 1 10 1e-6 1000 param.test
thermo_style custom step v_qC v_qO v_qH
run          0
unfix       fix_charge

# Delete 50% of 2nd type of water (watd) from t14
region       t14box block 0 27 0 25 0 28 units box
compute      newtemp all temp
velocity     all create ${t} 71993 temp newtemp dist gaussian mom yes rot no

variable     num_watd equal 0.5*count(watd)
fix          1 watd evaporate 1 ${num_watd} t14box 71993 molecule yes
run          1
unfix       1

# Delete 50% of interlayer Ca atoms from t14
set          type 11 type/fraction 15 0.5 71993
group        delcal type 15
delete_atoms group delcal compress yes bond yes
group        Ca type 11

variable     q equal charge(all)

minimize     1.0e-20 1.0e-20 100 1000
min_style    cg
min_modify   dmax 0.1

reset_timestep 0

fix          f_SHAKE all shake 1e-4 20 0 b 1 a 1 2
fix          f_NPT all npt temp ${t} ${t} 100 x 0 0 1000 y 0 0 1000 drag 0.2
dump         d_xyz all xyz 500 t14grap6RN.xyz
dump         coord1 t14 custom 500000 dump.t14 id type x y z
dump         coord2 graphene custom 500000 dump.graphene id type x y z
fix          f_LANG all langevin ${t} ${t} 5 71993

thermo       1000
thermo_style custom step temp etotal press density v_q

run          500000

```

```

undump      coord1
undump      coord2
unfix       f_NPT
unfix       f_LANG
unfix       f_SHAKE
undump      d_xyz

write_restart restart.t14grap6RN.equil

```

F2.0 Representative LAMMPS script for normal traction-separation of T₁₄/FGS nanocomposites with 6% –OH on FGS

```
## Stress-strain simulation
```

```

read_restart restart.t14grap6RN.equil
echo screen
kspace_style pppm 1e-6
variable t equal 300
run_style verlet

bond_coeff 1 harmonic 554.1349 1.0
bond_coeff 2 harmonic 554.1349 1.0
bond_coeff 3 harmonic 554.1349 1.0
bond_coeff 4 morse 120.0 2.0 1.3400
bond_coeff 5 harmonic 384 1.37 # cp-oh
bond_coeff 6 harmonic 540.6336 0.96 # oh-ho

region topbdy block INF INF INF INF 25.6 29.6 units box
group topbdy region topbdy
region rightbdy block 21.18 23.18 INF INF INF -3.3 units box
group rightbdy region rightbdy
region leftbdy block 1.48 3.48 INF INF INF -3.3 units box
group leftbdy region leftbdy

group body subtract t14 topbdy
group bdy union rightbdy leftbdy
group grapmob subtract grapoh bdy
group mobile subtract all topbdy bdy

compute newtemp all temp
compute dispT topbdy com
compute dispG bdy com
variable dT equal c_dispT[3]
variable dG equal c_dispG[3]
variable disp equal (v_dT-v_dG)

fix f_freeze1 topbdy setforce 0 0 0
fix f_freeze2 bdy setforce 0 0 0
fix f_move bdy move linear 0 0 -1e-5 units box
velocity topbdy set 0 0 0 units box

compute epair grapoh group/group body pair yes kspace yes
variable ftot equal c_epair[3]*69.4703/1000 # nN unit

```

```

variable          s equal v_ftot*100/(19.73*26.57)          # GPa unit

compute          peratom mobile stress/atom newtemp
compute          stp mobile reduce sum c_peratom[1] c_peratom[2] c_peratom[3] c_peratom[4] c_peratom[5]
c_peratom[6]

variable         tmpx equal "lx"
variable         l0x equal ${tmpx}
print           "initial length, l0-x: ${l0x}"
variable         tmpy equal "ly"
variable         l0y equal ${tmpy}
print           "initial length in y, l0-y: ${l0y}"
variable         tmpz equal "lz"
variable         l0z equal ${tmpz}
print           "initial length in z, l0-z: ${l0z}"

variable         s11 equal c_stp[1]
variable         s22 equal c_stp[2]
variable         s33 equal c_stp[3]
variable         s12 equal c_stp[4]
variable         s13 equal c_stp[5]
variable         s23 equal c_stp[6]
variable         factor equal 1.01325e-4
variable         volinit equal ${l0x}*${l0y}*30.92

variable         p11 equal v_s11*${factor}/v_volinit
variable         p22 equal v_s22*${factor}/v_volinit
variable         p33 equal v_s33*${factor}/v_volinit
variable         p12 equal v_s12*${factor}/v_volinit
variable         p13 equal v_s13*${factor}/v_volinit
variable         p23 equal v_s23*${factor}/v_volinit

thermo           1000
thermo_style     custom step temp etotal press vol v_disp c_epair v_ftot

fix             f_mobile mobile nvt temp ${t} ${t} 100
fix             f_avg1 all ave/time 100 100 10000 v_disp v_ftot c_epair mode scalar file t14grap6RN.profile
fix             f_avg2 all ave/time 100 100 10000 v_disp v_p11 v_p22 v_p33 v_p23 v_p13 v_p12 mode scalar
file t14grap6RN.stress.profile

dump            d_vel graphene custom 10000 t14grap6RN.lammpstrj id type x y z
dump            d_xyz all xyz 1000 t14grap6RN.sim.xyz
dump            d_dump all custom 10000 dump.t14grap6RN.rerun id type x y z vx vy vz

run            1200000

undump          d_vel
undump          d_xyz
undump          d_dump
unfix          f_mobile
unfix          f_avg1
unfix          f_avg2

write_restart   restart.t14grap6RN.rerun

```

F3.0 Representative LAMMPS script for shear traction-separation of T₁₄/FGS nanocomposites with 6% –OH on FGS

Shear traction-separation

```

read_restart restart.t14grap6RVX.equil
echo screen
kspace_style pppm 1e-6
variable t equal 300
run_style verlet

bond_coeff 1 harmonic 554.1349 1.0
bond_coeff 2 harmonic 554.1349 1.0
bond_coeff 3 harmonic 554.1349 1.0
bond_coeff 4 morse 120.0 2.0 1.3400
bond_coeff 5 harmonic 384 1.37 # cp-oh
bond_coeff 6 harmonic 540.6336 0.96 # oh-ho

region topbdy block INF INF INF INF 24 28 units box
group topbdy region topbdy
region rightbdy block 20.9 23.93 INF INF -4.6 -1.7 units box
group rightbdy region rightbdy

group body subtract t14 topbdy
group grapmob subtract grapoh rightbdy
group mobile subtract all topbdy rightbdy
group graphene type 12

compute newtemp mobile temp
compute dispT topbdy com
compute dispG rightbdy com
variable dT equal c_dispT[1]
variable dG equal c_dispG[1]
variable disp equal (v_dG-v_dT)

fix f_freeze1 rightbdy setforce 0 0 0
fix f_freeze2 topbdy setforce 0 0 0
#fix f_freeze1 grapoh setforce 0 0 0
velocity topbdy set 0 0 0 units box

fix f_move rightbdy move linear 1e-5 0 0 units box

compute epair body group/group grapoh pair yes kspace yes
variable ftot equal c_epair[1]*69.4703/1000 # nN unit

variable s equal v_ftot*100/(20.44*28.22) # GPa unit

compute peratom mobile stress/atom newtemp
compute stp mobile reduce sum c_peratom[1] c_peratom[2] c_peratom[3] c_peratom[4] c_peratom[5]
c_peratom[6]

variable tmpx equal "lx"
variable l0x equal ${tmpx}
print "initial length, l0-x: ${l0x}"

```



```

variable      tmpy equal "ly"
variable      l0y equal ${tmpy}
print        "initial length in y, l0-y: ${l0y}"
variable      tmpz equal "lz"
variable      l0z equal ${tmpz}
print        "initial length in z, l0-z: ${l0z}"

variable      s11 equal c_stp[1]
variable      s22 equal c_stp[2]
variable      s33 equal c_stp[3]
variable      s12 equal c_stp[4]
variable      s13 equal c_stp[5]
variable      s23 equal c_stp[6]
variable      factor equal 1.01325e-4
variable      volinit equal 23.93*${l0y}*${l0z}

variable      p11 equal v_s11*${factor}/v_volinit
variable      p22 equal v_s22*${factor}/v_volinit
variable      p33 equal v_s33*${factor}/v_volinit
variable      p12 equal v_s12*${factor}/v_volinit
variable      p13 equal v_s13*${factor}/v_volinit
variable      p23 equal v_s23*${factor}/v_volinit

#reset_timestep 0

thermo        1000
thermo_style  custom step temp etotal press vol v_disp c_epair v_ftot

fix           f_mobile mobile nvt temp ${t} ${t} 100
fix           f_avg1 all ave/time 100 100 10000 v_disp v_ftot c_epair mode scalar file t14grap6RVX.profile
fix           f_avg2 all ave/time 100 100 10000 v_disp v_p11 v_p22 v_p33 v_p23 v_p13 v_p12 mode scalar
file t14grap6RVX.stress.profile

dump          d_vel graphene custom 10000 t14grap6RVX.lammpstrj id type x y z
dump          d_xyz all xyz 1000 t14grap6RVX.sim.xyz
dump          d_dump all custom 10000 dump.t14grap6RVX.rerun id type x y z vx vy vz

run           4000000

undump        d_vel
undump        d_xyz
undump        d_dump
unfix         f_mobile
unfix         f_avg1
unfix         f_avg2

write_restart restart.t14grap6RVX.rerun

```

F4.0 Representative LAMMPS script for mean squared displacement (MSD) of water molecules in the T₁₄/FGS nanocomposites with 6% –OH on FGS

```

## MSD simulation

read_restart  restart.t14grap6RVX.equil
echo         screen

```

```

kspace_style      pppm 1e-6
variable          t equal 300
run_style         verlet

bond_coeff        1      harmonic 554.1349 1.0
bond_coeff        2      harmonic 554.1349 1.0
bond_coeff        3      harmonic 554.1349 1.0
bond_coeff        4      morse   120.0    2.0  1.3400
bond_coeff        5      harmonic      384    1.37      # cp-oh
bond_coeff        6      harmonic    540.6336 0.96      # oh-ho

kspace_style      pppm 1e-6
special_bonds     lj/coul 1e-50 1e-50 1e-50
pair_modify       mix arithmetic tail no
run_style         verlet

neighbor          5.0 bin
neigh_modify      delay 0 every 1 one 10000 check yes

#compute          newtemp all temp
#velocity         all create ${t} 31562 temp newtemp dist gaussian mom yes rot no

compute          MSD_ow ow msd com yes
compute          MSD_owd owd msd com yes
compute          MSD_hw hw msd com yes
compute          MSD_hwd hwd msd com yes

compute          RDF_g all rdf 500 14 6 14 8 13 7 13 9
compute          RDF_wat all rdf 500 6 6 6 7 6 11
compute          RDF_watd all rdf 500 8 8 8 9 8 11
compute          RDF_Si all rdf 500 5 10 10 6 10 8
compute          RDF_caw all rdf 500 11 3 11 4 11 13

#reset_timestep  0
fix              f_SHAKE all shake 1e-4 20 0 b 2 a 2
dump             d_xyz all xyz 500 t14grap6RVX.msd.xyz

thermo           10000
thermo_style     custom step temp etotal press density c_MSD_ow[4] c_MSD_owd[4]

fix              f_NVE all nve

fix              f_MSD_ow all ave/time 1000 1 1000 c_MSD_ow[1] c_MSD_ow[2] c_MSD_ow[3]
c_MSD_ow[4] file t14grap6RVX.msd.ow mode scalar
fix              f_MSD_owd all ave/time 1000 1 1000 c_MSD_owd[1] c_MSD_owd[2] c_MSD_owd[3]
c_MSD_owd[4] file t14grap6RVX.msd.owd mode scalar
fix              f_MSD_hw all ave/time 1000 1 1000 c_MSD_hw[1] c_MSD_hw[2] c_MSD_hw[3]
c_MSD_hw[4] file t14grap6RVX.msd.hw mode scalar
fix              f_MSD_hwd all ave/time 1000 1 1000 c_MSD_hwd[1] c_MSD_hwd[2] c_MSD_hwd[3]
c_MSD_hwd[4] file t14grap6RVX.msd.hwd mode scalar

fix              f_RDF_g all ave/time 1500000 1 1500000 c_RDF_g[1] c_RDF_g[2] c_RDF_g[3] c_RDF_g[4]
c_RDF_g[5] c_RDF_g[6] c_RDF_g[7] c_RDF_g[8] c_RDF_g[9] file t14grap6RVX.rdf.g mode vector
fix              f_RDF_wat all ave/time 1500000 1 1500000 c_RDF_wat[1] c_RDF_wat[2] c_RDF_wat[3]
c_RDF_wat[4] c_RDF_wat[5] c_RDF_wat[6] c_RDF_wat[7] file 14grap6RVX.rdf.wat mode vector

```

```
fix          f_RDF_watd all ave/time 1500000 1 1500000 c_RDF_watd[1] c_RDF_watd[2] c_RDF_watd[3]
c_RDF_watd[4] c_RDF_watd[5] c_RDF_watd[6] c_RDF_watd[7] file 14grap6RVX.rdf.watd mode vector
fix          f_RDF_Si all ave/time 1500000 1 1500000 c_RDF_Si[1] c_RDF_Si[2] c_RDF_Si[3]
c_RDF_Si[4] c_RDF_Si[5] c_RDF_Si[6] c_RDF_Si[7] file 14grap6RVX.rdf.Si mode vector
fix          f_RDF_caw all ave/time 1500000 1 1500000 c_RDF_caw[1] c_RDF_caw[2] c_RDF_caw[3]
c_RDF_caw[4] c_RDF_caw[5] c_RDF_caw[6] c_RDF_caw[7] file 14grap6RVX.rdf.caw mode vector

run          1500000
```